Petroleum Production Systems

Michael J. Economides
Professor of Petroleum Engineering,
Mining University Leoben

A. Daniel Hill
Professor of Petroleum Engineering,
The University of Texas at Austin

Christine Ehlig-Economides
Technical Advisor,
Schlumberger Oilfield Services Coordination

Prentice Hall PTR
Upper Saddle River, New Jersey 07458

Library of Congress Cataloging-in- Publication Data
Economides, Michael J.
Petroleum production systems / Michael J. Economides, A. Daniel Hill, Christine Ehlig-Economides
p. cm.
ISBN 0-13-658683-X
1. Oil fields—Production methods.. I.Hill, A. D. (A. Daniel)
II. Ehlig–Economides, Christine. III. Title.
TN870.E29 1993
622'.338—dc20–dc20 93-36626
CIP

Buyer: *Alexis Heydt*
Acquisition Editor: *Betty Sun*
Production Editor: *Camille Trentacoste*
Editorial Assistant: *Kim Intindola*
Cover Design: *Wanda Lubelska*

Printed in the United States of America
10 9

ISBN 0-13-658683-X

Prentice-Hall International (UK) Limited, *London*
Prentice-Hall of Australia Pty. Limited, *Sydney*
Prentice-Hall of Canada, Inc., *Toronto*
Prentice-Hall Hispanoamericana, S. A., *Mexico*
Prentice-Hall of India Private Limited, *New Delhi*
Prentice-Hall of Japan, Inc., *Tokyo*
Prentice-Hall Asia Pte. Ltd., *Singapore*
Editora Prentice-Hall do Brasil, Ltda., *Rio de Janeiro*

Contents

Preface

For several years while teaching in academia or in the industry we have recognized a need for a comprehensive and relatively advanced textbook in petroleum production engineering. Currently available texts and monographs failed to provide sufficient scope and depth to be suitable for engineering education. We wanted to develop a petroleum engineering textbook at the level of analogous publications in other engineering disciplines, intended to offer terminal exposure to senior undergraduates or an introduction to graduate students.

All of us have had extensive experience in both university and industrial settings. We feel that our areas of interest are complementary and ideally suited for this textbook, spanning classical production engineering, well testing, production logging, artificial lift, and matrix and hydraulic fracture stimulation. We have been contributors in these areas for several years.

Putting such a textbook together has required long, arduous, and concerted effort. It has also involved a number of our graduate assistants and support staff. Special thanks go to Professor Robert S. Schechter, Dr. Peter Valko, and Dipl.-ing. Michael Prohaska for reviewing some of the text.

The typing of Ms. Marion Flux and Ms. Ellen Hill is gratefully acknowledged for successfully having reproduced a huge number of complicated equations. The drafting of the figures by Ms. Joanna Castillo and special artistic graphics by Michael Prohaska are noted with appreciation. We also thank Ms. Joye Johnson for her assistance in the production of this book.

We would be certainly remiss if we did not acknowledge the hundreds of colleagues, students, and our own professors who, over the years, contributed to the evolution of our thinking in this vital area of engineering. In particular, we thank those students in our recent production engineering courses who have suggested numerous improvements and corrections while using a draft of this text.

We would like to gratefully acknowledge the following organizations and persons for permitting us to reprint some of the figures and tables in this text: for Figs. 2-3, 4-1, 4-2, 4-4, 4-5, 5-4, 5-7, 5-12, 5-14, 5-15, 5-16, 5-17, 6-8, 7-12, 7-13, 7-14, 10-4, 10-6, 10-7, 11-18, 12-10, 13-3, 14-1, 14-2, 14-4, 14-6, 14-9, 14-10, 15-7, 15-11, 16-5, 16-6, 17-7, 18-4, 18-5, and 18-6 and Tables 1-1, 5-1, 5-2, 15-1, and 15-2, the Society of Petroleum Engineers; for Figs. 5-13, 14-3, 14-5, 15-9, 15-10, 15-12, 15-13, 15-14, 15-15, 15-16, 20-1, 20-2, 20-4, 20-6, and 20-7, Prentice Hall; for Figs. 5-5, 5-6, 15-2, 16-10, 17-1, 17-2, 17-3, 17-4, and 17-5 and Table 17-2, Schlumberger; Fig. 7-11, ©1980 AICHE, Fig. 10-5, ©1976 AICHE, and Figs. 15-1 and 15-3, ©1988 AICHE, American Institute of Chemical Engineers, all rights reserved; Figs. 12-2, 12-3, 12-5, 12-6, 12-8, and 12-9, from Petroleum Engineer International, September, 1956, all rights reserved; Figs. 10-2, 20-3, 20-8, 20-12, and 20-13, PennWell Books; Figs. 7-6 and 7-7, American Society of Mechanical Engineers; Fig. 10-11 and Table 10-1, Crane Valves; Figs. 3-2 and 3-3 reprinted with permission of Chevron Research and Technology Company, ©California Research and Technology Corporation, 1947 (now Chevron Research and Technology Company, a division of Chevron U.S.A. Inc.); Figs. 15-4 and 15-5, Dr. Yimei Wang; Fig. 10-8, American Gas Association; Fig. 20-9, Centrilift, a division of Baker Hughes Inteq, Inc.; Fig. 14-7, Dr. E. P. da Motta; Fig. 10-14, Elsevier Science Publishers; Fig. 7-10, World Petroleum Congress; Fig. 10-1, Professor James P. Brill and the University of Tulsa; Fig. 17-8, Stimlab; Fig. 7-9 from Govier, G. W. and Aziz, K., *The Flow of Complex Mixtures in Pipes*, Reprint 1977, Krieger Publishing Co., Malabar, FL; Fig. 10-3, reprinted from International Journal of Multiphase Flow, **1**, Mandhane, J. M., Gregory, G. A., and Aziz, K., "A Flow Pattern Map for Gas-Liquid Flow in Horizontal Pipes", p. 537–553, ©1974, with permission from Pergamon Press Ltd., Headington Hill Hall, Oxford OX3 0BW, UK; Fig. 4-3, reprinted by permission from Hydrocarbon Processing, May, 1972, p. 121, ©1972, Gulf Publishing Co., Houston, Texas, all rights reserved; and Figs. 6-2, 6-3, and 6-5 from *Sand Control Handbook* 2nd Edition by George O. Suman, Jr., Richard C. Ellis, and Robert E. Snyder, Copyright ©1983, by Gulf Publishing Co., Houston, Texas. Used with permission, all rights reserved.

The Authors

CHAPTER 1

The Role of Petroleum Production Engineering

1-1 INTRODUCTION

Petroleum production involves two distinct but intimately connected general systems: the reservoir, which is a porous medium with unique storage and flow characteristics; and the artificial structures, which include the well, bottomhole, and wellhead assemblies, and the surface gathering, separation, and storage facilities.

Production engineering is that part of petroleum engineering which attempts to maximize production (or injection) in a cost-effective manner. One or more wells may be involved. Appropriate production engineering technologies and methods of application are related directly and interdependently with other major areas of petroleum engineering, such as formation evaluation, drilling, and reservoir engineering. Some of the most important connections are summarized below.

Modern formation evaluation provides a composite reservoir description through three-dimensional (3-D) seismic, interwell log correlation, and well testing. This description leads to the identification of geological flow units, each with specific characteristics. Connected flow units form a reservoir.

Drilling creates the all-important well, and with the advent of directional drilling technology it is possible to envision many controllable well configurations, including very long horizontal sections or multiple horizontal completions, targeting individual flow units. Control of drilling-induced, near-wellbore damage is critical, especially in long horizontal wells.

Reservoir engineering in its widest sense overlaps production engineering to a great degree. The distinction is frequently blurred both in the context of study (single versus multiple well) and in the time duration of interest (long versus short term). Single well performance, undeniably the object of production engineering, may serve as a boundary condition

in a field-wide, long-term, reservoir engineering study. Conversely, findings from material balance calculations or reservoir simulation further define and refine the forecasts of well performance and allow for more appropriate production engineering decisions.

In developing a petroleum production engineering thinking process, it is first necessary to understand important parameters that control the performance and the character of the system. Below, several definitions, in certain cases somewhat different from traditional nomenclature, are presented.

1-2 COMPONENTS OF THE PETROLEUM PRODUCTION SYSTEM

1-2.1 Volume and Phase of Reservoir Hydrocarbons

Reservoir. The reservoir consists of one or several interconnected geological flow units. While the shape of the well and converging flow have created in the past the notion of radial flow configuration, modern techniques such as 3-D seismic and new logging and well testing measurements allow for a more precise description of the shape and the ensuing production character of the well and reservoir. This is particularly true in identifying lateral and vertical boundaries and the inherent heterogeneities.

Appropriate reservoir description, including the extent of heterogeneities, discontinuities, and anisotropies, while always important, has become compelling after the emergence of horizontal wells with lengths of several thousand feet.

Figure 1-1 is a schematic showing two wells, one vertical and the other horizontal, contained within a reservoir with potential lateral heterogeneities or discontinuities (sealing faults), vertical boundaries (shale lenses), and anisotropies (stress or permeability).

While appropriate reservoir description and identification of boundaries, heterogeneities, and anisotropies is important, it is somewhat forgiving in the presence of only vertical wells. These issues become critical when long horizontal wells are drilled.

The encountering of lateral discontinuities (including heterogeneous pressure depletion caused by existing vertical wells) has a major impact on the expected horizontal well production. The well trajectory *vis à vis* the azimuth of directional properties also has a great effect on well production. Ordinarily, there would be only one optimum direction.

Understanding the geological history that preceeded the present hydrocarbon accumulation is essential. There is little doubt that the best petroleum engineers are those who understand the geological processes of deposition, fluid migration, and accumulation. Whether a reservoir is an anticline, a fault block, or a channel sand not only dictates the amount of hydrocarbon present but also greatly controls the future well performance.

Porosity. All of petroleum engineering deals with the exploitation of fluids residing within porous media. Porosity, simply defined as the ratio of the pore volume, V_p, to the bulk volume, V_b

$$\phi = \frac{V_p}{V_b} \tag{1-1}$$

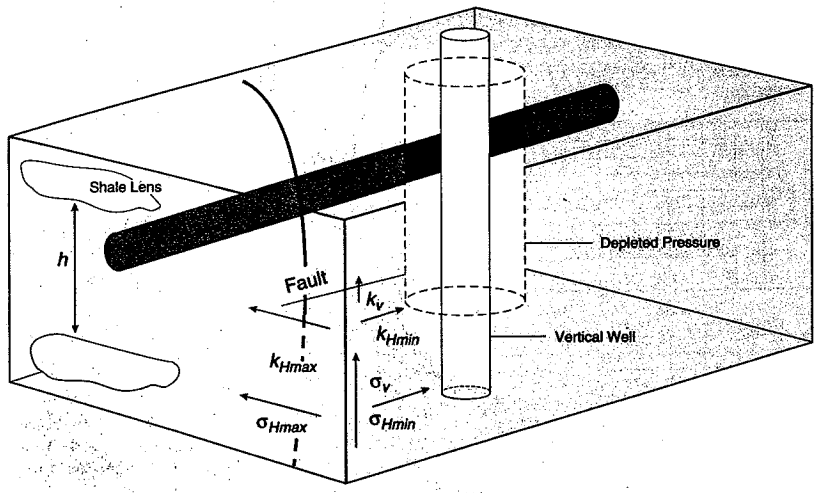

Figure 1-1
Common reservoir heterogeneities, anisotropies, discontinuities, and boundaries affecting the performance of vertical and horizontal wells. (*Courtesy Western Petroleum Services.*)

is a direct indicator of the amount of fluid in place. Porosity values have varied from over 0.3 to less than 0.1. The porosity of the reservoir can be measured with a variety of laboratory techniques using reservoir cores or with field measurements including logs and well tests. Porosity is one of the very first measurements obtained in any exploration scheme, and a desirable value is essential for the continuation of any further activities toward the potential exploitation of a reservoir. In the absence of substantial porosity there is no need to proceed with an attempt to exploit a reservoir.

Reservoir height. Often known as "reservoir thickness" or "pay thickness," or in vernacular as "pay dirt," the reservoir height describes the thickness of a porous medium contained between two layers. These layers are usually considered impermeable. At times the thickness of the hydrocarbon-bearing formation is distinguished from an underlaying water-bearing formation, or aquifer. Well logging techniques have been developed to identify likely reservoirs and quantify their vertical extent. For example, measuring the spontaneous potential (SP) and knowing that sandstones have distinctly different response than shales (a likely lithology to contain a layer), one can estimate the thickness of a formation. In laminated or multilayered formations the terms "gross" and "net" height are used to distinguish between the thickness of an entire sequence and that portion which bears hydrocarbons.

Figure 1-2 is a well log showing clearly the deflection of the spontaneous potential of a sandstone reservoir and the clearly different response of the adjoining shale layers. This deflection corresponds to the thickness of a *potentially* hydrocarbon-bearing, porous medium.

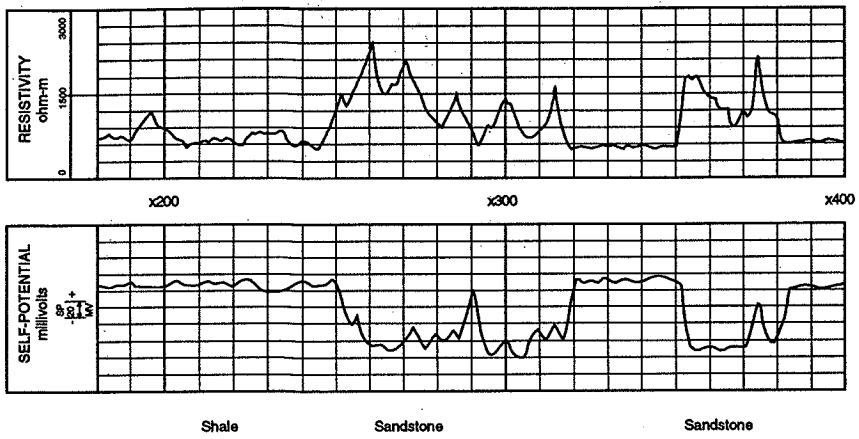

Figure 1-2
Spontaneous potential and electrical resistivity logs identifying sandstones versus shales, and water-bearing versus hydrocarbon-bearing formations.

The presence of satisfactory net reservoir height is an additional imperative in any exploration activity.

Fluid saturations. Oil and/or gas are never alone in "saturating" the available pore space. Water is always present. Certain rocks are "oil-wet," implying that oil molecules cling to the rock surface. More frequently, rocks are "water-wet." Electrostatic forces and surface tension act to create these wettabilities which may change, usually with detrimental consequences, as a result of injection of fluids, drilling, stimulation, or other activity, and in the presence of surface-acting chemicals. If the water is present but does not flow, the corresponding water saturation is known as "connate" or "interstitial." Saturations larger than this value would result in free flow of water along with hydrocarbons.

Petroleum hydrocarbons, which are mixtures of many compounds, are divided into oil and gas. Any mixture depending on its composition and the conditions of pressure and temperature may appear as liquid (oil) or gas or a mixture of the two.

Frequently the use of the terms oil and gas is blurred. Produced oil and gas refer to those parts of the total mixture that would be in liquid and gaseous states, respectively, after surface separation. Usually the corresponding pressure and temperature are "standard conditions," that is, usually (but not always) 14.7 psi and 60°F.

Flowing oil and gas in the reservoir imply, of course, that either the initial reservoir pressure or the induced flowing bottomhole pressure are such as to allow the concurrent presence of two phases. Temperature, except in the case of high-rate gas wells, is for all practical purposes constant.

An attractive hydrocarbon saturation is the third critical variable (along with porosity and reservoir height) to be determined before a well is tested or completed. A classic method, currently performed in a variety of ways, is the measurement of the formation electrical resistivity. Knowing that formation brines are good conductors of electricity (i.e., they have poor resistivity) and hydrocarbons are the opposite, a measurement of this electrical property in a porous formation of sufficient height can detect the presence of hydrocarbons. With proper calibration, not just the presence but also the hydrocarbon saturation (i.e., fraction of the pore space occupied by hydrocarbons) can be estimated.

Figure 1-2 also contains a resistivity log. The previously described SP log along with the resistivity log, showing a high resistivity within the same zone, are good indicators that the identified porous medium is likely saturated with hydrocarbons.

The combination of porosity, reservoir net thickness, and saturations is essential in deciding whether a prospect is attractive or not. These variables can allow the estimation of hydrocarbons near the well.

Classification of reservoirs. All hydrocarbon mixtures can be described by a phase diagram such as the one shown in Fig. 1-3. Plotted are temperature (x axis) and pressure (y axis). A specific point is the *critical point*, where the properties of liquid and gas converge. For each temperature less than the critical-point temperature (to the left of T_c in Fig. 1-3) there exists a pressure called the "bubble-point" pressure, above which only liquid (oil) is present and below which gas and liquid coexist. For lower pressures (at constant temperature), more gas is liberated. Reservoirs above the bubble-point pressure are called "undersaturated."

If the initial reservoir pressure is less than the bubble-point pressure or if the flowing bottomhole pressure is allowed to be at such a value (even if the initial reservoir pressure is above the bubble point), then free gas will at least form and will likely flow in the reservoir. This type of a reservoir is known as "two-phase" or "saturated."

For temperatures larger than the critical point (to the right of T_c in Fig. 1-3), the curve enclosing the two-phase envelop is known as the "dew-point" curve. Outside, the fluid is gas, and reservoirs with these conditions are "lean" gas reservoirs.

The maximum temperature of a two-phase envelop is known as the "cricondentherm." Between these two points there exists a region where, because of the shape of the gas saturation curves, as the pressure decreases, liquid or "condensate" is formed. This happens until a limiting value of the pressure, after which further pressure reduction results in revaporization. The region in which this phenomenon takes place is known as the "retrograde condensation" region, and reservoirs with this type of behavior are known as "retrograde condensate reservoirs."

Each hydrocarbon reservoir has a characteristic phase diagram and resulting physical and thermodynamic properties. These are usually measured in the laboratory with tests per-

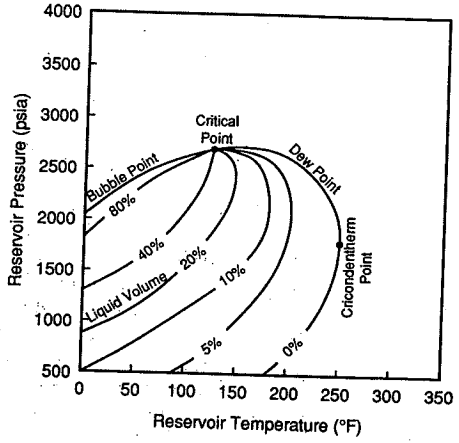

Figure 1-3
Oilfield hydrocarbon phase diagram showing bubble-point and dew-point curves, lines of constant phase distribution, region of retrograde condensation, and the critical and cricondentherm points.

formed on fluid samples obtained from the well in a highly specialized manner. Petroleum thermodynamic properties are known collectively as *PVT* (pressure-volume-temperature) properties.

Areal extent. Favorable conclusions on the porosity, reservoir height, fluid saturations, and pressure (and implied phase distribution) of a petroleum reservoir, based on single well measurements, are insufficient for both the decision to develop the reservoir and for the establishment of an appropriate exploitation scheme.

Recent advances in 3-D and wellbore seismic techniques, in combination with well testing, can increase greatly the region where knowledge of the reservoir extent (with height, porosity, and saturations) is possible. Discontinuities and their locations can be detected. As more wells are drilled, additional information can enhance further the knowledge of the reservoir's peculiarities and limits.

The areal extent is essential in the estimation of the "original-oil-(or gas)-in-place." The hydrocarbon volume, V_{HC}, measured under reservoir conditions, is

$$V_{HC} = Ah\phi(1 - S_w) \tag{1-2}$$

where A is the areal extent, h is the reservoir thickness, ϕ is the porosity, and S_w is the water saturation. (Thus, $1 - S_w$ is the hydrocarbon saturation.) The porosity, height, and saturation can of course vary within the areal extent of the reservoir.

Equation (1-2) can lead to the estimation of the oil or gas volume under standard conditions after dividing by the formation volume factor. This factor is simply a ratio of the volume of a given mass of hydrocarbons under reservoir and under standard conditions. Thus, for oil,

$$N = \frac{Ah\phi(1 - S_w)}{B_o} \tag{1-3}$$

where N is the standard volume of oil. For gas,

$$G = \frac{Ah\phi(1 - S_w)}{B_g} \tag{1-4}$$

where G is the standard volume of gas.

The gas formation volume factor (traditionally, res ft^3/SCF), B_g, simply implies a volumetric relationship and can be calculated readily with an application of the real gas law. The gas formation volume factor is much smaller than 1.

The oil formation volume factor (res bbl/STB), B_o, is not a simple physical property. Instead, it is a thermodynamic relationship allowing for the reintroduction into the liquid (at the elevated reservoir pressure) of all of the gas that would be liberated at standard conditions. Thus the oil formation volume factor is invariably larger than 1, reflecting the swelling of the oil volume because of the gas dissolution.

The reader is referred to the classic textbooks by Muskat (1949), Craft and Hawkins (revised by Terry, 1991), and Amyx, Bass, and Whiting (1960), and the newer book by Dake (1978) for further information. The present textbook assumes basic reservoir engineering knowledge as a prerequisite; for basic production engineering coverage the textbook by Allen and Roberts (1982) is recommended.

1-2.2 Permeability

The presence of a substantial porosity usually (but not always) implies that pores will be interconnected. Therefore the porous medium is also "permeable." The property that describes the ability of fluids to flow in the porous medium is permeability. In certain lithologies (e.g., sandstones), a larger porosity is associated with a larger permeability. In other lithologies (e.g., chalks), very large porosities, at times over 0.4, are not associated with proportionately large permeabilities.

Correlations of porosity versus permeability should be used with a considerable degree of caution. For production engineering calculations these correlations are rarely useful, except when considering matrix stimulation. In this instance, correlations of the *altered* permeability with the *altered* porosity after stimulation are useful.

The concept of permeability was introduced by Darcy (1856) in a classic experimental work from which both petroleum engineering and groundwater hydrology have benefited greatly.

Figure 1-4 is a schematic of Darcy's experiment. The flow rate (or fluid velocity) can be measured against pressure (head) for different porous media.

Darcy observed that the flow rate (or velocity) of a fluid through a specific porous medium is linearly proportional to the head or pressure difference between the inlet and the outlet and a characteristic property of the medium. Thus,

$$u \propto k \Delta p \tag{1-5}$$

where k is the permeability and is a characteristic property of the porous medium. Darcy's experiments were done with water. If fluids of other viscosities flow, then the permeability must be divided by the viscosity.

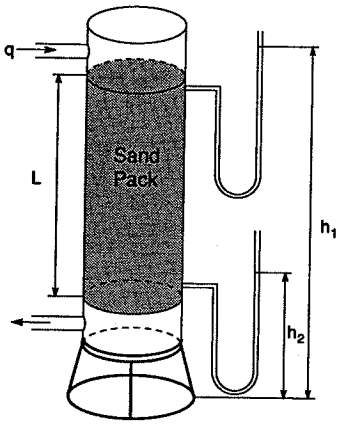

Figure 1-4
Darcy's experiment. Water flows through a sand pack and the pressure difference (head) is recorded.

1-2.3 The Zone near the Well, the Sandface, and the Well Completion

The zone surrounding a well is important. First, all intrusive activities such as drilling, cementing, and well completion are certain to alter the condition of the reservoir near the well. This is invariably detrimental.

Matrix stimulation is intended to recover or even improve the near-wellbore permeability. (There is damage associated even with stimulation. It is the net effect that is expected to be beneficial.)

Many wells are cemented and cased. One of the purposes of cementing is to support the casing, but at formation depths the most important reason is to provide zonal isolation. Contamination of the produced fluid from other formations or the loss of fluid *into* other formations can be envisioned readily in an open hole completion. If no zonal isolation or wellbore stability problems are present, the well can be open-hole. A cemented and cased well must be perforated in order to reestablish communication with the reservoir.

Slotted liners can be used if a cemented and cased well is not deemed necessary and if no wellbore stability problems are likely to be encountered.

Finally, to combat the problems of sand or other fines production, screens can be placed between the well and the formation. Gravel packing can be used as an additional safeguard and as a means to keep permeability-reducing fines away from the well.

The various well completions and the resulting near-wellbore zones are shown in Fig. 1-5.

Ability to direct the drilling of a well allows the creation of highly deviated and horizontal wells. In both cases a longer exposure of the well with the reservoir is accomplished than would be the case for vertical wells.

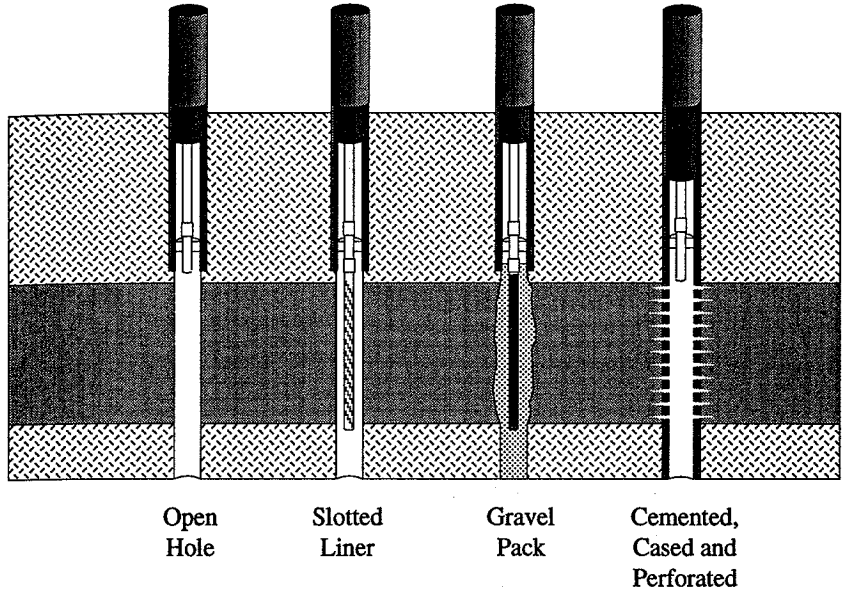

Figure 1-5
Options for well completions.

1-2.4 The Well

Entrance of fluids into the well, following their flow through the porous medium, the near-well zone, and the completion assembly, requires that they are lifted through the well up to the surface.

There is a required flowing pressure gradient between the bottomhole and the wellhead. The pressure gradient consists of the potential energy difference (hydrostatic pressure) and the friction pressure drop. The former depends on the reservoir depth and the latter depends on the well length.

If the bottomhole pressure is sufficient to lift the fluids to the top, then the well is under "natural lift." Otherwise, artificial lift is indicated. Mechanical lift can be supplied by a pump. Another technique is to reduce the density of the fluid in the well and thus to reduce the hydrostatic pressure. This is accomplished by the injection of lean gas in a designated spot along the well. This is known as "gas lift."

1-2.5 The Surface Equipment

After the fluid reaches the top, it is likely to be directed toward a manifold connecting a number of wells. The reservoir fluid consists of oil, gas (even if the flowing bottomhole pressure is larger than the bubble-point pressure, gas is likely to come out of solution along the well), and water.

Traditionally, the oil, gas, and water are not transported long distances as a mixed stream, but instead are separated at a surface processing facility located in close proximity to the wells. An exception that is becoming more common is in some offshore fields, where production from subsea wells, or sometimes the commingled production from several wells, may be transported long distances before any phase separation takes place.

Finally, the separated fluids are transported or stored. In the case of formation water it is usually disposed in the ground through a reinjection well.

The reservoir, well, and surface facilities are sketched in Fig. 1-6. The flow systems from the reservoir to the entrance to the separation facility are the production engineering systems that are the subjects of study in this book.

1-3 Well Productivity and Production Engineering

1-3.1 The Objectives of Production Engineering

All of the components of the petroleum production systems can be condensed into the productivity index. The role of a petroleum production engineer is to maximize the well productivity in a cost-effective manner. Understanding and measuring the variables that control the productivity index (well diagnosis) become imperative.

While these concepts will be dealt with extensively in subsequent chapters, it is useful here to present the productivity index, J, of an oil well (analogous expressions can be written for gas and two-phase wells):

$$J = \frac{q}{p - p_{wf}} = \frac{kh}{\alpha_r B\mu(p_D + s)} \tag{1-6}$$

Equation (1-6) succinctly describes what is possible for a petroleum production engineer. First, the dimensionless pressure p_D depends on the physical model that controls the well flow behavior. These include transient or infinite-acting behavior, steady state (where $p_D = \ln r_e/r_w$) or others.

For a specific reservoir with permeability k, thickness h, and with a fluid with formation volume factor B and viscosity μ, the only variable on the right-hand side of Eq. (1-6) that can be adjusted is the skin effect, s. It can be reduced or eliminated through matrix stimulation if it is caused by damage or can be otherwise remedied if it is caused by mechanical means. A negative skin effect can be imposed if a successful hydraulic fracture is created. Thus stimulation can improve the productivity index. This would ordinarily result in a higher production rate. In reservoirs with pressure drawdown-related problems (fines production, water or gas coning), increasing the productivity can allow lower drawdown with economically attractive production rates.

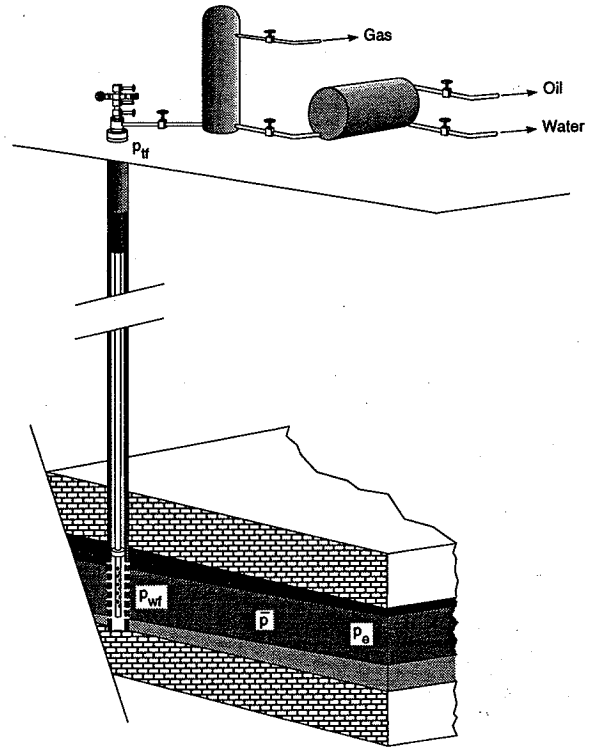

Figure 1-6
The petroleum production system, including the reservoir, underground well completion, the well, wellhead assembly, and surface facilities.

Increasing the drawdown $(p - p_{wf})$ by lowering p_{wf} is the other option available to the production engineer to increase well productivity. While the productivity index remains constant, reduction of the flowing bottomhole pressure would increase the pressure gradient $(p - p_{wf})$ and the flow rate, q, must increase accordingly. The flowing bottomhole pressure may be lowered by minimizing the pressure losses between the bottomhole and the separation facility (by, for example, removing unnecessary restrictions, optimizing tubing size, etc.), or by implementing or improving artificial lift procedures. Improving well productivity by optimizing the flow system from the bottomhole location to the surface production facility is a major role of the production engineer.

In summary, well performance *evaluation* and *enhancement* are the primary charges of the production engineer. The production engineer has three major tools for well performance evaluation: (1) the measurement of (or sometimes, simply the understanding of) the rate-versus-pressure drop relationships for the flow paths from the reservoir to the separator; (2) well testing, which evaluates the reservoir potential for flow and, through measurement of the skin effect, provides information about flow restrictions in the near-wellbore environment; and (3) production logging, which can describe the distribution of flow into the wellbore, as well as diagnose other completion-related problems.

With diagnostic information in hand, the production engineer can then focus on the part or parts of the production engineering flow system that may be optimized to enhance productivity. Remedial steps can range from well stimulation procedures such as hydraulic fracturing that enhance flow in the reservoir to the resizing of surface flow lines to increase productivity. This textbook is aimed at providing the information a production engineer needs to perform these tasks of well performance evaluation and enhancement.

1-3.2 Organization of the Book

This textbook offers a structured approach toward the goal defined above. Chapters 2 to 4 present the inflow performance for oil, two-phase, and gas reservoirs. Chapters 5 and 6 deal with the condition of the near-wellbore zone, such as damage, perforations, and gravel packing. Chapter 7 brings the fluids to the surface. Combination of inflow performance and well performance versus time, taking into account single-well transient flow and material balance, is shown in Chapters 8 and 9. Finally, Chapter 10 describes the surface flow system. Therefore, Chapters 1 to 10 describe the workings of the reservoir and well systems.

For an appropriate production engineering remedy it is essential that well and reservoir diagnosis be done.

Chapters 11 and 12 present the state-of-the-art in modern diagnosis that includes well testing and production logging.

From the well diagnosis it can be concluded whether the well is in need of matrix stimulation, hydraulic fracturing, artificial lift, combinations of the above, or none.

Matrix stimulation for all major types of reservoirs is presented in Chapters 13, 14, and 15, while hydraulic fracturing is treated in Chapters 16, 17, and 18.

Gas lift is outlined in Chapter 19, and mechanical lift in Chapter 20.

To detect the influence of each component of the reservoir and well system, it is necessary to isolate it. This is the purpose of systems analysis, which is presented in Chapter 21.

Finally, environmental issues confronting the petroleum production engineer are described in Chapter 22.

This textbook is designed for a two-semester, 3-contact-hour-per-week sequence of petroleum engineering courses, or a similar training exposure.

Taught as a single course with the presumption that Chapters 2 to 4 have been covered in other courses, it is recommended that the following chapters be emphasized: Chapters 1, 5, 6, 7, 8, 9, 10, 11, 12, 13, 14, 16, 17, 19, and 20.

To simplify the presentation of realistic examples, data for three characteristic reservoir types—an undersaturated oil reservoir, a saturated oil reservoir, and a gas reservoir—are presented in Appendixes. These data sets are used throughout the book.

1-4 Units and Conversions

We have used "oilfield" units throughout the text, even though this system of units is inherently inconsistent. We chose this system because more petroleum engineers "think" in bbl/day and psi than in terms of m^3/s and Pa. All equations presented include the constant or constants needed with oilfield units. To employ these equations with SI units, it will be easiest first to convert the SI units to oilfield units, calculate the desired result in oilfield units, then convert the result to SI units. However, if an equation is to be used repeatedly with the input known in SI units, it will be more convenient to convert the constant or constants in the equation of interest. Conversion factors between oilfield and SI units are given in Table 1-1.

Table 1-1

Typical Units for Reservoir and Production Engineering Calculations[a]

Variable	Oilfield Units	SI	Conversion (Multiply Oilfield Unit)
Area	acre	m^2	4.04×10^3
Compressibility	psi^{-1}	Pa^{-1}	1.45×10^{-4}
Length	ft	m	3.05×10^{-1}
Permeability	md	m^2	9.9×10^{-16}
Pressure	psi	Pa	6.9×10^3
Rate (oil)	STB/d	m^3/s	1.84×10^{-6}
Rate (gas)	MSCF/d	m^3/s	3.28×10^{-4}
Viscosity	cp	Pa-s	1×10^{-3}

[a]From Earlougher (1977).

EXAMPLE 1-1
Conversion from oilfield to SI units

The steady-state, radial-flow form of Darcy's law in oilfield units is given in Chapter 2 as

$$p_e - p_{wf} = \frac{141.2 q B \mu}{kh}\left(\ln \frac{r_e}{r_w} + s\right) \tag{1-7}$$

for p in psi, q in STB/d, B in res bbl/STB, μ in cp, k in md, h in ft, and r_e and r_w in ft (s is dimensionless). Calculate the pressure drawdown ($p_e - p_{wf}$) in Pa for the following SI data,

first by converting units to oilfield units and converting the result to SI units, then by deriving the constant in this equation for SI units.

Data q=0.001 m^3/s, B=1.1 res m^3/ST m^3, $\mu = 2 \times 10^{-3}$ Pa-s, k=10^{-14} m^2, h=10 m, r_e=575 m, r_w=0.1 m, and s=0.

Solution Using the first approach, we first convert all data to oilfield units. Using the conversion factors in Table 1-1,

$$q = (0.001 \text{ m}^3/\text{s})(5.434 \times 10^5) = 543.4 \text{ STB/d} \tag{1-8}$$

$$B = 1.1 \text{ res bbl/STB} \tag{1-9}$$

$$\mu = (2 \times 10^{-3} \text{ Pa-s})(10^3) = 2 \text{ cp} \tag{1-10}$$

$$k = (10^{-14} \text{ m}^2)(1.01 \times 10^{15}) = 10.1 \text{ md} \tag{1-11}$$

$$h = (10 \text{ m})(3.28) = 32.8 \text{ ft} \tag{1-12}$$

Since r_e is divided by r_w, the units for these radii do not have to be converted. Now, from Eq. (1-7),

$$p_e - p_{wf} = \frac{(141.2)(543.4)(1.1)(2)}{(10.1)(32.8)}\left[\ln\left(\frac{575}{0.1}\right) + 0\right] = 4411 \text{ psi} \tag{1-13}$$

and converting this result to Pascals,

$$p_e - p_{wf} = (4411 \text{ psi})(6.9 \times 10^3) = 3.043 \times 10^7 \text{ Pa} \tag{1-14}$$

Alternatively, we can convert the constant 141.2 to the appropriate constant for SI units, as follows (including only-to-be-converted variables):

$$p_e - p_{wf}(\text{Pa}) = \frac{(141.2)\left[q\left(\text{m}^3/s\right)(5.434 \times 10^5)\right]\left[\mu(\text{Pa-s})(10^3)\right]}{\left[k(\text{m}^2)(1.01 \times 10^{15})\right]\left[h(\text{m})(3.28)\right]} \times (6.9 \times 10^3) \tag{1-15}$$

or

$$p_e - p_{wf} = \frac{0.159 q B \mu}{kh}\left(\ln\frac{r_e}{r_w} + s\right) = \frac{qB\mu}{2\pi kh}\left(\ln\frac{r_e}{r_w} + s\right) \tag{1-16}$$

The constant derived, 0.159, is $1/2\pi$, as it should be for this consistent set of units. Substituting the parameters in SI units directly into Eq. (1-15), we again calculate that $p_e - p_{wf} = 3.043 \times 10^7$ Pa.

Often, in regions where metric units are customary, a mix of SI and non-SI units is sometimes employed. For example, in using Darcy's law, the units for flow rate may be m^3/d; for viscosity, cp; for permeability, md; etc. In this instance, units can be converted to oilfield units in the same manner demonstrated here for consistent SI units. ◇

REFERENCES

1. Allen, T. O., and Roberts, A. P., *Production Operations*, Vols. 1 and 2, 2nd ed., Oil & Gas Consultants International, Tulsa, OK, 1982.
2. Amyx, J. W., Bass, D. M., Jr., and Whiting, R. L., *Petroleum Reservoir Engineering*, McGraw-Hill, New York, 1960.

3. Craft, B. C., and Hawkins, M. (Revised by Terry, R. E.), *Applied Petroleum Reservoir Engineering*, 2nd ed., Prentice Hall, Englewood Cliffs, NJ, 1991.
4. Dake, L. P., *Fundamentals of Reservoir Engineering*, Elsevier, Amsterdam, 1978.
5. Darcy, H., *Les Fontaines Publiques de la Ville de Dijon*, Victor Dalmont, Paris, 1856.
6. Earlougher, R. C., Jr., *Advances in Well Test Analysis*, SPE monograph, Vol. 5, SPE, Richardson, TX, 1977.
7. Muskat, M., *Physical Principles of Oil Production*, McGraw-Hill, New York, 1949.

CHAPTER 2

Production from Undersaturated Oil Reservoirs

2-1 INTRODUCTION

This and the following two chapters deal with the well inflow performance and describe the reservoir variables that control the production rate under different conditions. Wells drilled in oil reservoirs drain a porous medium of porosity ϕ, net thickness h, and permeability k. To understand the process of flow from the reservoir and into the well sandface, a simple expression of Darcy's law (1856) in radial coordinates can be used first:

$$q = \frac{kA}{\mu}\frac{dp}{dr} \tag{2-1}$$

where A is a radial area at a distance r and is given by $A = 2\pi rh$.

Equation (2-1) is general and suggests a number of interesting conclusions. The flow rate is large if the pressure gradient dp/dr, the permeability k, and the reservoir height h are large or if the viscosity of the flowing fluid, μ, is small. Also, this expression assumes a single-phase fluid flowing and saturating the reservoir.

2-2 TRANSIENT FLOW OF UNDERSATURATED OIL

The diffusivity equation describes the pressure profile in an infinite-acting, radial reservoir, with a slightly compressible and constant viscosity fluid (undersaturated oil or water). This equation, with similar expressions in wide use in a number of engineering fields such as heat transfer (Carslaw and Jaeger, 1959), has the classic form

$$\frac{\partial^2 p}{\partial r^2} + \frac{1}{r}\frac{\partial p}{\partial r} = \frac{\phi\mu c_t}{k}\frac{\partial p}{\partial t} \tag{2-2}$$

Its generalized solution is

$$p_{r,t} = p_i - \frac{q\mu}{4\pi kh} E_i(x) \tag{2-3}$$

where $E_i(x)$ is the exponential integral and x is given by

$$x = \frac{\phi\mu c_t r^2}{4kt} \tag{2-4}$$

For $x < 0.01$ (i.e., for large values of time or for small distances, such as at the wellbore), the exponential integral $E_i(x)$ can be approximated by $-\ln(\gamma x)$, where γ is Euler's constant and is equal to 1.78.

Therefore, Eq. (2-3), at the wellbore and shortly after production, can be approximated by ($p_{r_w,t} \equiv p_{wf}$)

$$p_{wf} = p_i - \frac{q\mu}{4\pi kh} \ln \frac{4kt}{\gamma\phi\mu c_t r_w^2} \tag{2-5}$$

Finally, introducing variables in oilfield units as listed in Table 1-1 and converting the natural log to log base 10, Eq. (2-5) results in

$$p_{wf} = p_i - \frac{162.6qB\mu}{kh}\left(\log t + \log \frac{k}{\phi\mu c_t r_w^2} - 3.23\right) \tag{2-6}$$

This expression is often known as the pressure drawdown equation describing the declining flowing bottomhole pressure, p_{wf}, while the well is flowing at a constant rate q.

Because a producing well is usually flowing for long times with the same wellhead pressure (which is imposed by the well hardware such as chokes, etc.), the resulting bottomhole pressure is also largely constant. Therefore Eq. (2-6), which is for constant rate, must be adjusted. The more common constant-bottomhole-pressure situation results in a similar expression, which although it appears as a mere algebraic rearrangement, is an approximation of the analytical solution to Eq. (2-2) with the appropriate inner boundary condition (Earlougher, 1977):

$$q = \frac{kh(p_i - p_{wf})}{162.6B\mu}\left(\log t + \log \frac{k}{\phi\mu c_t r_w^2} - 3.23\right)^{-1} \tag{2-7}$$

where the time, t, must be in hours.

EXAMPLE 2-1
Prediction of production rate in an infinite-acting oil well

Using the well and reservoir variables in Appendix A, develop a production rate profile for 1 year assuming that no boundary effects emerge. Do this in increments of 2 months and use a flowing bottomhole pressure equal to 3500 psi.

Solution From Eq. (2-7) and substitution of the appropriate variables in Appendix A, the well production rate is given by

$$q = \frac{(8.2)(53)(5651-3500)}{(162.6)(1.1)(1.7)}\left[\log t + \log \frac{8.2}{(0.19)(1.7)(1.29\times10^{-5})(0.328)^2} - 3.23\right]^{-1}$$

$$= \frac{3074}{\log t + 4.03} \tag{2-8}$$

For $t = 2$ months, from Eq. (2-8) the production rate $q = 428$ STB/d.

Figure 2-1 is a rate-decline curve for this oil well for the first year assuming infinite-acting behavior. The rate decline is from 428 STB/d (after 2 months) to 386 STB/d (after 1 year). ◇

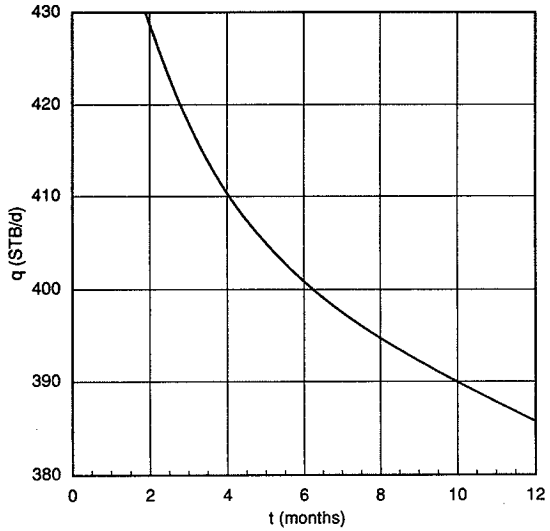

Figure 2-1
Rate decline for an infinite-acting oil reservoir (Example 2-1).

2-3 STEADY-STATE WELL PERFORMANCE

In a well, within a reservoir, as shown in Fig. 2-2, the area of flow at any distance, r, is given by $2\pi rh$, and Eq. (2-1) becomes

$$q = \frac{2\pi krh}{\mu}\frac{dp}{dr} \tag{2-9}$$

Assuming that q is constant, separation of variables and integration leads to

$$\int_{p_{wf}}^{p} dp = \frac{q\mu}{2\pi kh}\int_{r_w}^{r}\frac{dr}{r} \tag{2-10}$$

and finally,

$$p - p_{wf} = \frac{q\mu}{2\pi kh}\ln\frac{r}{r_w} \tag{2-11}$$

Equation (2-11) is logarithmic in nature, meaning that the pressure drop doubles or triples as the radial distance increases by one or two orders of magnitude. Thus, the near-wellbore region is extremely important in well production, because that is where much of the pressure drop occurs.

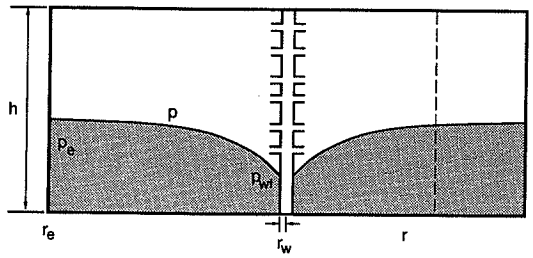

Figure 2-2
Reservoir schematic for steady-state flow into a well.

Van Everdingen and Hurst (1949) quantified the condition of the near-wellbore region with the introduction of the concept of the skin effect. This is analogous to the film coefficent in heat transfer. This skin effect results in an additional steady-state pressure drop, given by

$$\Delta p_s = \frac{q\mu}{2\pi kh}s \tag{2-12}$$

which can be added to the pressure drop in the reservoir. Thus Eq. (2-11) becomes

$$p - p_{wf} = \frac{q\mu}{2\pi kh}\left(\ln\frac{r}{r_w} + s\right) \tag{2-13}$$

If the reservoir exhibits a constant-pressure outer boundary (at r_e), that is, the well operates under steady-state conditions, then if that pressure is p_e, the radial flow equation becomes

$$p_e - p_{wf} = \frac{q\mu}{2\pi kh}\left(\ln\frac{r_e}{r_w} + s\right) \tag{2-14}$$

In oilfield units, where p_e and p_{wf} are in psi, q is in STB/d, μ is in cp, k is in md, h is in ft, and B is the formation volume factor to convert STB into res bbl, Eq. (2-14) becomes

$$p_e - p_{wf} = \frac{141.2\,qB\mu}{kh}\left(\ln\frac{r_e}{r_w} + s\right) \tag{2-15}$$

Two other important concepts are outlined below. They apply to all types of flow.

- The *effective* wellbore radius r'_w can be derived from a simple rearrangement of Eq. (2-15),

$$p_e - p_{wf} = \frac{141.2qB\mu}{kh}\left(\ln\frac{r_e}{r_w} + \ln e^s\right) \tag{2-16}$$

and thus

$$p_e - p_{wf} = \frac{141.2qB\mu}{kh}\left(\ln\frac{r_e}{r_w e^{-s}}\right) \tag{2-17}$$

The effective wellbore radius, r'_w, is defined by

$$r'_w = r_w e^{-s} \tag{2-18}$$

This is an interesting finding. In a damaged well, with, for example, $s = 10$, the reservoir drains into a well with an effective radius equal to $4.5 \times 10^{-5} r_w$. Conversely, in a stimulated well with, for example, $s = -2$ or even $s = -6$ (for a fractured well), then the effective wellbore radii are $7.4r_w$ and $403r_w$, respectively.

- The *productivity index*, J, of a well is simply the production rate divided by the pressure difference. Thus,

$$J = \frac{q}{p_e - p_{wf}} = \frac{kh}{141.2B\mu\,[\ln(r_e/r_w) + s]} \tag{2-19}$$

One of the main purposes of production engineering is to maximize the productivity index in a cost-effective manner, that is, to increase the flow rate for a given driving force (drawdown) or to minimize the drawdown for a given rate. Usually, this can be accomplished with a decrease of the skin effect (through matrix stimulation and removal of near-wellbore damage) or through the superposition of a negative skin effect from an induced hydraulic fracture.

In reservoirs where the viscosity is very large ($\mu > 100$ cp), thermal recovery may be indicated to reduce the viscosity.

EXAMPLE 2-2

Steady-state production rate calculation and rate improvement (stimulation)

Assume that a well in the reservoir described in Appendix A has a drainage area equal to 640 acres ($r_e = 2980$ ft) and is producing at steady state with an outer boundary (constant) pressure equal to 5651 psi. Calculate the steady-state production rate if the flowing bottomhole pressure is equal to 4500 psi. Use a skin effect equal to +10.

Describe two mechanisms to increase the flow rate by 50%. Show calculations.

Solution From Eq. (2-15) and rearrangement,

$$q = \frac{(8.2)(53)(5651 - 4500)}{(141.2)(1.1)(1.7)\,[\ln(2980/0.328) + 10]} = 100 \text{ STB/d} \tag{2-20}$$

To increase the production rate by 50%, one possibility is to increase the drawdown, $p_e - p_{wf}$, by 50%. Therefore

$$(5651 - p_{wf})_2 = 1.5(5651 - 4500) \tag{2-21}$$

leading to $p_{wf} = 3925$ psi.

A second possibility is to reduce the skin effect. In this case

$$\left(\ln\frac{2980}{0.328} + s_2\right) = \left(\ln\frac{2980}{0.328} + 10\right)/1.5 \tag{2-22}$$

leading to $s = 3.6$. ◇

EXAMPLE 2-3

Effect of drainage area on well performance

Demonstrate the effect of drainage area on oilwell production rate by calculating the ratios of production rates from 80-, 160-, and 640-acre drainage areas to that obtained from a 40-acre drainage area. The well radius is 0.328 ft.

Solution Assuming that the skin effect is zero (this would result in the most pronounced difference in the production rate), the ratios of the production rates (or productivity index) can be given by an expression of the form

$$\frac{q}{q_{40}} = \frac{(\ln r_e/r_w)_{40}}{(\ln r_e/r_w)} \tag{2-23}$$

The drainage radius for a given drainage area is calculated by assuming that the well is in the center of a circular drainage area. Thus,

$$r_e = \sqrt{\frac{(A)(43,560)}{\pi}}$$

The results are shown in Table 2-1. These ratios indicate that the drainage area assigned to a well has a small impact on the production rate. For tight reservoirs, cumulative production differences are particularly immune to the drainage area, because transient behavior is evident for much of the time. ◇

Table 2-1

Production Rate Increases (over a 40-acre spacing)

A (acres)	r_e (ft)	$\ln(r_e/r_w)$	q/q_{40}
40	745	7.73	1
80	1053	8.07	0.96
160	1489	8.42	0.92
640	2980	9.11	0.85

2-4 PSEUDO-STEADY-STATE FLOW

Almost all wells eventually "feel" their assigned boundaries. In the previous section the steady-state condition implied a constant-pressure outer boundary. Naturally, this

boundary can approximate the impact of a large aquifer. Induced constant pressure may be the result of injector-producer configurations.)

For no-flow boundaries, drainage areas can either be described by natural limits such as faults, pinchouts, etc., or can be artificially induced by the production of adjoining wells.

This condition is often referred to as "pseudo-steady state." The pressure at the outer boundary is no longer constant but instead declines at a constant rate with time, that is, $\partial p_e/\partial t = \text{const}$.

From the radial diffusivity equation, the pressure p at any point r in a reservoir of radius r_e is given by (Dake, 1978)

$$p = p_{wf} + \frac{141.2qB\mu}{kh}\left(\ln\frac{r}{r_w} - \frac{r^2}{2r_e^2}\right) \tag{2-24}$$

At $r = r_e$, Eq. (2-24) can be converted to

$$p_e = p_{wf} + \frac{141.2qB\mu}{kh}\left(\ln\frac{r_e}{r_w} - \frac{1}{2}\right) \tag{2-25}$$

This equation is not particularly useful under pseudo-steady state, since p_e is not known at any given time. However, as shown in Chapter 11, the average reservoir pressure, $\bar{p}$, can be obtained from periodic pressure buildup tests. Therefore a more useful expression for the pseudo-steady-state equation would be one using the average reservoir pressure. This is defined as a volumetrically weighted pressure,

$$\bar{p} = \frac{\int_{r_w}^{r_e} p\,dV}{\pi(r_e^2 - r_w^2)h\phi} \approx \frac{\int_{r_w}^{r_e} p\,dV}{\pi r_e^2 h\phi} \tag{2-26}$$

and since $dV = 2\pi rh\phi\,dr$, Eq. (2-26) becomes

$$\bar{p} = \frac{2}{r_e^2}\int_{r_w}^{r_e} pr\,dr \tag{2-27}$$

The expression for the pressure at any point r can be substituted from Eq. (2-24), and therefore

$$\bar{p} - p_{wf} = \frac{2}{r_e^2}\frac{141.2qB\mu}{kh}\int_{r_w}^{r_e}\left(\ln\frac{r}{r_w} - \frac{r^2}{2r_e^2}\right)dr \tag{2-28}$$

Performing the integration results in

$$\bar{p} - p_{wf} = \frac{141.2qB\mu}{kh}\left(\ln\frac{r_e}{r_w} - \frac{3}{4}\right) \tag{2-29}$$

Introducing the skin effect and incorporating the term 3/4 into the logarithmic expression leads to the inflow relationship for a no-flow boundary oil reservoir:

$$\bar{p} - p_{wf} = \frac{141.2qB\mu}{kh}\left(\ln\frac{0.472r_e}{r_w} + s\right) \tag{2-30}$$

Equation (2-30) is particularly useful because it provides the relationship between the average reservoir pressure, $\bar{p}$, and the rate q. The average pressure, $\bar{p}$, is a variable that *can* be determined. It depends on the drainage area and the properties of the fluid and rock. Material balance calculations, presented in Chapter 9, permit combination of depletion mechanisms and inflow relationships and lead toward forecasts of well performance and cumulative production.

Finally, while Eq. (2-30) appears similar to Eq. (2-15) (for steady-state flow), they should never be confused. They represent distinctly different reservoir production mechanisms.

EXAMPLE 2-4

Production from a no-flow boundary reservoir

What would be the average reservoir pressure if the outer boundary pressure is 6000 psi, the flowing bottomhole pressure is 3000 psi, the drainage area is 640 acres, and the well radius is 0.328 ft? What would be the ratio of the flow rates before (q_1) and after (q_2) the average reservoir pressure drops by 1000 psi? Assume that $s = 0$.

Solution A ratio of Eqs. (2-25) and (2-30) results in

$$\frac{p_e - p_{wf}}{\bar{p} - p_{wf}} = \frac{\ln(r_e/r_w) - 1/2}{\ln(r_e/r_w) - 3/4} \tag{2-31}$$

The drainage area $A = 640$ and therefore $r_e = 2980$ ft. Substituting the given variables in Eq. (2-31) results in

$$\bar{p} = \frac{(6000 - 3000)(8.36)}{8.61} + 3000 = 5913 \text{ psi} \tag{2-32}$$

The flow-rate ratio would be

$$\frac{q_2}{q_1} = \frac{4913 - 3000}{5913 - 3000} = 0.66 \tag{2-33}$$

◇

2-4.1 Transition to Pseudo-steady State from Infinite Acting Behavior

Earlougher (1977) has shown that the time, t_{pss}, at which pseudo-steady state begins is given by

$$t_{pss} = \frac{\phi\mu c_t A}{0.000264k} t_{DA} \tag{2-34}$$

where A is the drainage area and t_{DA} has a characteristic value that depends on the drainage shape. For a regular shape such as a circle or a square, it is equal to 0.1. For a well in a 1×2 rectangle, t_{DA} is equal to 0.3; and for a 1×4 rectangle it is equal to 0.8. Off-centered wells in irregular patterns have even larger values of t_{DA}, implying that the well will "feel" the farther-off boundaries after a significantly longer time. The reader is referred to Earlougher's monograph for a complete list of t_{DA} values.

If the drainage area can be approximated by a circle with an equivalent drainage radius r_e, then Eq. (2-34) (with t_{DA}=0.1) yields

$$t_{pss} \approx 1200 \frac{\phi\mu c_t r_e^2}{k} \tag{2-35}$$

for the onset of pseudo-steady state. The time t_{pss} is in hours, and all other variables are in the customary oilfield units.

2-5 Wells Draining Irregular Patterns

Rarely do wells drain regular-shaped drainage areas. Even if they are assigned regular *geographic* drainage areas, these are distorted after production commences, either because of the presence of natural boundaries or because of lopsided production rates in adjoining wells. The drainage area is then *shaped* by the assigned production duty of a particular well.

To account for irregular drainage shapes or asymmetrical positioning of a well within its drainage area, a series of "shape" factors was developed by Dietz (1965).

Equation (2-29) is for a well at the center of a circle. The logarithmic expression can be modified (by multiplying and dividing the expressions within the logarithm by 4π and performing a simple property of logarithms) into

$$\ln\frac{r_e}{r_w} - \frac{3}{4} = \frac{1}{2}\ln\frac{4\pi r_e^2}{4\pi e^{3/2} r_w^2} \tag{2-36}$$

The argument πr_e^2 is, of course, the drainage area of a circle of radius r_e. The product $4\pi e^{3/2}$ in the denominator is equal to 56.32 or (1.78)(31.6), where 1.78 is Euler's constant, denoted by γ, and 31.6 is a shape factor for a circle with a well at the center, denoted by C_A. Dietz (1965) has shown that all well/reservoir configurations that depend on drainage shape and well position have a characteristic shape factor. Therefore, Eq. (2-29) can be generalized for any shape into

$$\bar{p} - p_{wf} = \frac{141.2qB\mu}{kh}\left(\frac{1}{2}\ln\frac{4A}{\gamma C_A r_w^2} + s\right) \tag{2-37}$$

Figure 2-3 (Earlougher, 1977) contains some commonly encountered (approximate) drainage shapes and well positions.

EXAMPLE 2-5

Impact of irregular well positioning on production rate

Assume that two wells in the reservoir described in Appendix A each drain 640 acres. Furthermore, assume that $\bar{p} = 5651$ psi (same as p_i) and that $s = 0$. The flowing bottomhole pressure in both is 3500 psi. However, well A is placed at the center of a square, whereas well B is at the

1.		31.6	12.		10.8
2.		31.6	13.		4.5
3.		27.6	14.		2.08
4.		27.1	15.		3.16
5.	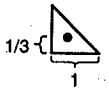	21.9	16.		0.58
6.		0.098	17.	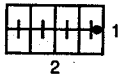	0.11
7.		30.9	18.	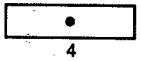	5.38
8.		13	19.		2.69
9.		4.5	20.	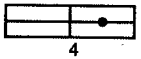	0.23
10.		3.3	21.		0.12
11.		21.8	22.	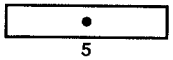	2.36

Figure 2-3
Shape factors for various closed, single-well drainage areas. (*From Earlougher, 1977.*)

center of the upper right quadrant of a square drainage shape. Calculate the production rates from the two wells at the onset of pseudo-steady state. (This calculation is valid only at very early time. At late time, either drainage shapes will change, if they are artificially induced, or the average reservoir pressure will not decline uniformly within the drainage areas because of different production rates and resulting different rates of depletion.)

Solution Well A The shape factor, C_A, from Fig. 2-3 is equal to 30.9. Therefore from Eq. (2-37),

$$q = \frac{(8.2)(53)(2151)}{(141.2)(1.1)(1.7)(0.5)\ln\left[(4)(640)(43560)/(1.78)(30.9)(0.328)^2\right]} \qquad (2\text{-}38)$$

$$= 423 \text{ STB/d}$$

Well B Since it is located at the center of the upper right quadrant, its shape factor (from Fig. 2-3) is equal to 4.5. All other variables in Eq. (2-37) remain the same. The flow rate calculated is then equal to 379 STB/d, representing a 10% reduction. ◇

EXAMPLE 2-6
Determining average reservoir pressure within adjoining drainage areas

The following data were obtained on a three-well fault block. A map with well locations is shown in Fig. 2-4. (Use properties as for the reservoir described in Appendix A.)

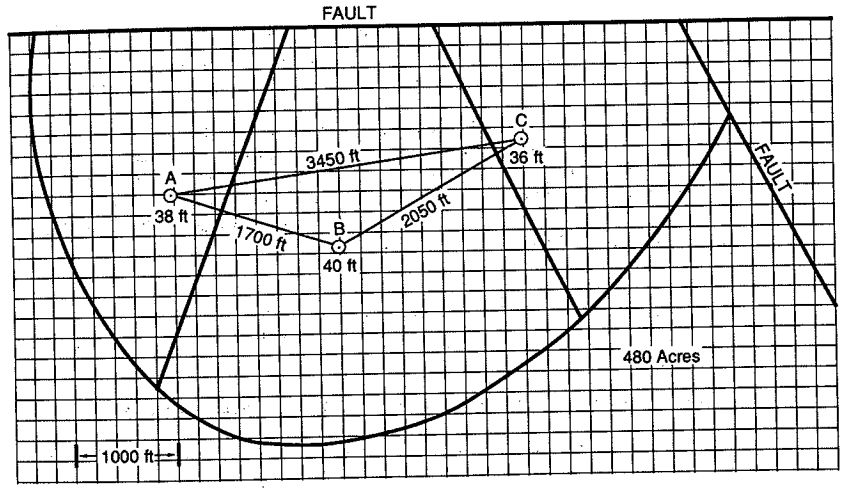

Figure 2-4
Three-well fault block for Example 2-6. (*From a problem by H. Dykstra, class notes, 1976.*)

Each well produced for 200 days since the previous shut-in. At the end of the 200 days, the following rates and skin effects were obtained from each well:

	A	B	C
q_o (STB/d at time of shut-in)	100	200	80
h (ft)	38	40	36
s (skin effect)	2	0	5

If the bottomhole pressure is 2000 psi for each well, calculate the average reservoir pressure within each drainage area.

Solution The drainage volumes *formed* by the production rate of each well are related by

$$\frac{V_A}{V_B} = \frac{q_A}{q_B} \tag{2-39}$$

and

$$\frac{V_A}{V_C} = \frac{q_A}{q_C} \tag{2-40}$$

If the reservoir thickness were the same throughout, then the ratios of the areas would have sufficed. However, since h varies, the volumes can be replaced by the product $h_i A_i$, where i refers to each well. Finally, a third equation is needed:

$$A_A + A_B + A_C = A_{\text{total}} = 480 \text{ acres} \tag{2-41}$$

Equations (2-39), (2-40), and (2-41) result in $A_A = 129$ acres (5.6×10^6 ft^2), $A_B = 243$ acres (1.06×10^7 ft^2), and $A_C = 108$ acres (4.7×10^6 ft^2). The next step is to sketch these areas on the fault block map.

Each map square represents 40,000 ft^2 (200 × 200 ft), and therefore the three areas are to be allocated 140, 265, and 118 squares, respectively. The drainage divide must be normal to the tieline between adjoining wells. Thus, counting squares, the approximate drainage areas, shown in Fig. 2-4, can be drawn. These describe shapes and therefore approximate shape factors. From Fig. 2-3, well A is shape no. 12 ($C_A = 10.8$), well B is shape no. 7 ($C_A = 30.9$), and well C is shape no. 10 ($C_A = 3.3$).

From Eq. (2-37) and for well A,

$$\bar{p} = 2000 + \frac{(141.2)(100)(1.1)(1.7)}{(8.2)(38)}\left[(0.5)\ln\frac{(4)(5.6\times10^6)}{(1.78)(10.8)(0.328)^2} + 2\right] \tag{2-42}$$

$$= 2856 \text{ psi}$$

The average pressures in the drainage areas for wells B and C are calculated to be 3271 and 2974 psi, respectively.

Such uneven depletion is common and is an important variable to know in any reservoir exploitation strategy. ◇

2-6 INFLOW PERFORMANCE RELATIONSHIP

All well deliverability equations relate the well production rate and the driving force in the reservoir, that is, the pressure difference between the initial, outer boundary or average reservoir pressure and the flowing bottomhole pressure.

If the bottomhole pressure is given, the production rate can be obtained readily. However, the bottomhole pressure *is* a function of the wellhead pressure, which, in turn, depends on production engineering decisions, separator or pipeline pressures, etc. Therefore, what a well will actually produce must be the combination of what the reservoir can deliver and what the imposed wellbore hydraulics would allow.

It is then useful to present the well production rate as a function of the bottomhole pressure. This type of presentation is known as an "inflow performance relationship" (IPR) curve. Usually, the bottomhole pressure, p_{wf}, is graphed on the ordinate and the production rate, q, is graphed on the abscissa.

Equations (2-7), (2-15), and (2-37) can be used for transient, steady-state, and pseudo-steady-state IPR curves. The following examples will illustrate these concepts.

EXAMPLE 2-7
Transient IPR

Using the well and reservoir data in Appendix A, construct transient IPR curves for 1, 6, and 24 months. Assume zero skin.

Solution Equation (2-7) with substituted variables takes the form

$$q = \frac{1.43(5651 - p_{wf})}{\log t + 4.03} \tag{2-43}$$

The relationship between q and p_{wf} of course will depend on time, t [which in Eq. (2-43) must be entered in hours]. Figure 2-5 is a graph of the *transient* IPR curves for the three different times. ◇

EXAMPLE 2-8
Steady-state IPR: Influence of the skin effect

Assume that the initial reservoir pressure of the well described in Appendix A is also the constant pressure of the outer boundary, p_e (steady state). Draw IPR curves for skin effects equal to 0, 5, 10, and 50, respectively. Use a drainage radius of 2980 ft ($A = 640$ acres).

Solution Equation (2-15) describes a straight-line relationship between q and p_{wf} for any skin effect. For example, after substitution of variables for a skin equal to 5, Eq. (2-15) becomes

$$p_{wf} = 5651 - 8.58q \tag{2-44}$$

Similarly, the multipliers of the rate for the 0, 10, and 50 skin effects are 5.54, 11.6, and 35.9, respectively.

Figure 2-6 gives the steady-state IPR curves for the four skin effects. ◇

EXAMPLE 2-9
Pseudo-steady-state IPR: Influence of average reservoir pressure

This calculation is the most useful and the one most commonly done for the forecast of well performance. Each IPR curve reflects a "snapshot" of well performance at a given reservoir

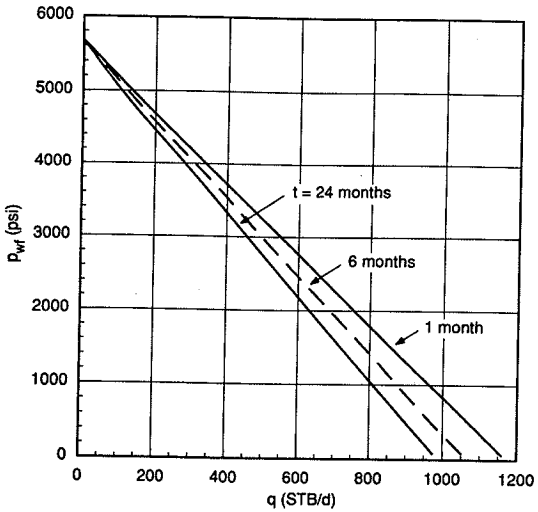

Figure 2-5
Transient IPR curves for Example 2-7.

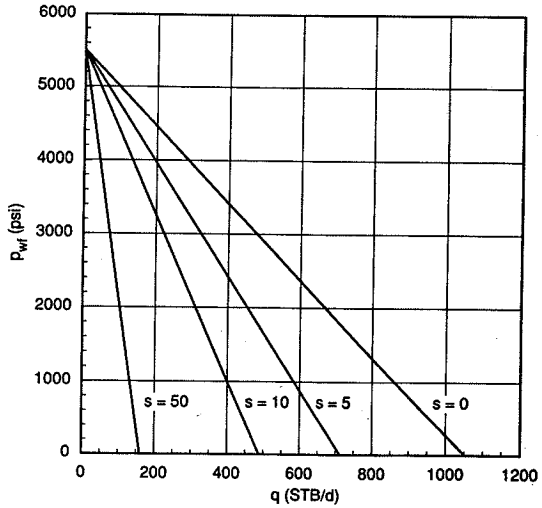

Figure 2-6
Steady-state IPR curves and impact of skin effect for Example 2-8.

pressure. This is a time-dependent calculation, done in discrete intervals. Combination with volumetric material balances (treated in Chapter 9) will allow the forecast of rate and cumulative production versus time.

For this exercise, calculate the IPR curves for zero skin effect but for average reservoir pressures in increments of 500 psi from the "initial" 5651 to 3500 psi. Use all other variables from Appendix A. Drainage radius is 2980 ft.

Solution Equation (2-37) is the generalized pseudo-steady-state equation for any drainage shape and well position. For a circular drainage shape, Eq. (2-30) is sufficient.

Substituting the variables from Appendix A into Eq. (2-30) results (for $\bar{p} = 5651$) in

$$p_{wf} = 5651 - 5q \tag{2-45}$$

For all average reservoir pressures, the slope in Eq. (2-45) will remain the same. The intercept will simply be the average pressure. Therefore, as shown in Fig. 2-7, the pseudo-steady-state IPR curves are depicted as parallel straight lines, each reflecting an average reservoir pressure. ◇

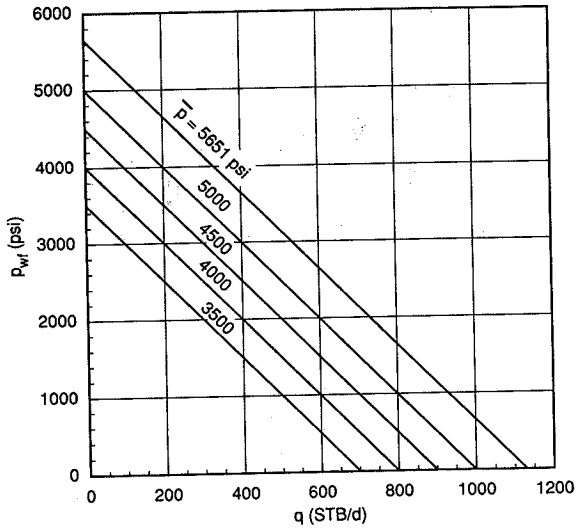

Figure 2-7
Pseudo-steady-state IPR curves for a range of average reservoir pressures (Example 2-9).

2-7 Horizontal Well Production

Starting in the 1980s, horizontal wells began capturing an ever-increasing share of hydrocarbon production. They proved to be excellent producers for thin ($h < 50$ ft) reservoirs or for thicker reservoirs with good vertical permeability, k_v.

A horizontal well of length L penetrating a reservoir with horizontal permeability k_H and vertical permeability k_V creates a drainage pattern that is different from that for a vertical well. Figure 2-8 presents this drainage pattern, together with important variables affecting well performance. The drainage shape formed is ellipsoidal, with the large half-axis of the drainage ellipsoid, a, related to the length of the horizontal well.

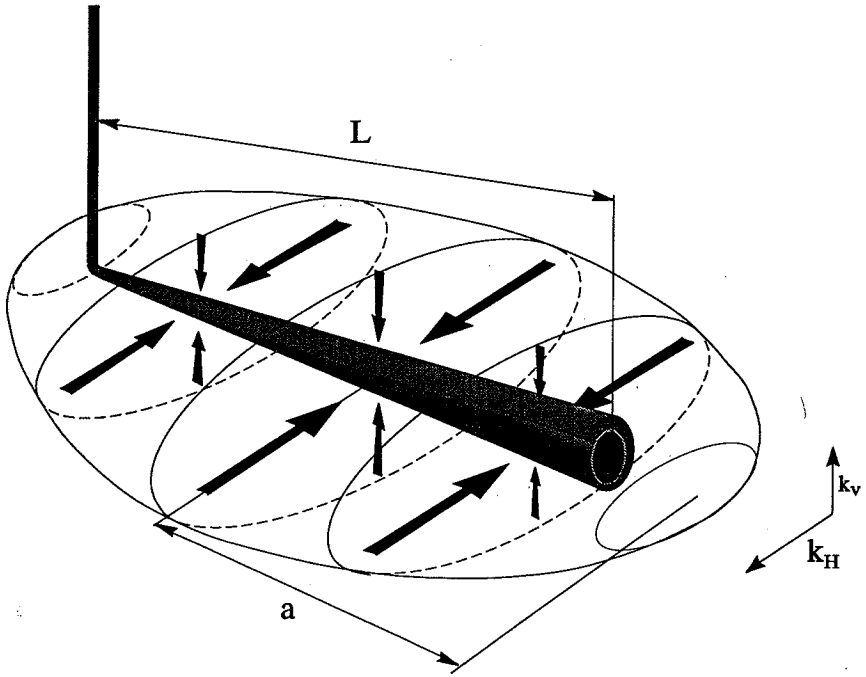

Figure 2-8
Drainage pattern formed around a horizontal well.

Of particular importance in the production of the horizontal well is the horizontal-to-vertical permeability anisotropy. The larger the vertical permeability, the higher the productivity index from the horizontal well will be. Low vertical permeability may render horizontal wells unattractive.

An often-ignored, but important, issue is the permeability anisotropy in the *horizontal* plane. A well drilled normal to the larger horizontal permeability would be a much better producer than one drilled in any arbitrary direction or normal to the smaller horizontal permeability.

Measurements are always indicated before a horizontal well is drilled. These measurements should be done in a vertical pilot hole. Testing techniques to estimate the vertical and horizontal permeabilities are described in Chapter 11. For the horizontal permeability anisotropy, stress measurements in the pilot hole can identify the maximum and minimum horizontal stress directions. Usually, they coincide with the maximum and minimum horizontal permeability directions. Therefore, a horizontal well that is not intended to be hydraulically fractured should be drilled along the direction of minimum horizontal stress.

Joshi (1988) presented a horizontal well deliverability relationship that was augmented by Economides et al. (1990). The relationship (mixed steady state in the horizontal plane and pseudo-steady state in the vertical plane) is

$$q = \frac{k_H h\,\Delta p}{141.2B\mu\left(\ln\left\{\frac{\left[a+\sqrt{a^2-(L/2)^2}\right]}{L/2}\right\}+\left(\frac{I_{ani}h}{L}\right)\ln\frac{I_{ani}h}{[r_w(I_{ani}+1)]}\right)} \tag{2-46}$$

where I_{ani} is a measurement of vertical-to-horizontal permeability anisotropy and is given by

$$I_{ani} = \sqrt{\frac{k_H}{k_V}} \tag{2-47}$$

In Eq. (2-46), a is the large half-axis of the drainage ellipsoid formed by a horizontal well of length L. The expression for this ellipsoid is

$$a = \frac{L}{2}\left\{0.5+\left[0.25+\left(\frac{r_{eH}}{L/2}\right)^4\right]^{0.5}\right\}^{0.5} \quad \text{for } \frac{L}{2} < 0.9r_{eH} \tag{2-48}$$

The productivity index ratio between a horizontal and a vertical well in a specific reservoir may be large, (assuming that an appropriate candidate is selected, the well is drilled in the optimum direction, and it is stimulated effectively). This productivity index ratio can be manifested by an increase in the production rate, a decrease in the pressure drawdown, or both. Therefore, horizontal wells can be excellent means of reservoir management where problems of water or gas coning or sand production are present.

EXAMPLE 2-10

Production rate from a horizontal well: Effects of reservoir thickness and vertical permeability

Using the variables for the well in Appendix A, calculate the expected production rate from a horizontal well of several lengths up to a maximum length of 2000 ft. Graph length versus production rate. Use $r_{eH} = 2980$ ft and $p_{wf} = 3500$ psi.

Repeat the calculation for reservoir heights equal to 25 and 250 ft and for k_V equal to 8.2 md ($I_{ani} = 1$) and 131 md ($I_{ani} = 0.25$).

Also graph the productivity index ratios between these horizontal wells and vertical wells in the same reservoirs.

Solution The calculations below are done for a horizontal well of length L, equal to 2000 ft. From Eq. (2-48),

$$a = \frac{2000}{2}\left\{0.5 + \left[0.25 + \left(\frac{2980}{1000}\right)^4\right]^{0.5}\right\}^{0.5} = 3065 \text{ ft} \tag{2-49}$$

From Eq. (2-46), and remembering that for the base case,

$$I_{ani} = \sqrt{\frac{8.2}{0.9}} = 3 \tag{2-50}$$

then

$$q = \frac{(8.2)(53)(5651 - 3500)}{(141.2)(1.1)(1.7)\left\{\ln\left[\frac{3065+\sqrt{3065^2-1000^2}}{1000}\right] + \left[\frac{(3)(53)}{2000}\right]\ln\left[\frac{(3)(53)}{(0.328)(3+1)}\right]\right\}} \tag{2-51}$$
$$= 1634 \text{ STB/d}$$

If $I_{ani} = 1$ then $q = 1862$ STB/d; and if $I_{ani} = 0.25$, then $q = 1958$ STB/d.

These results suggest the moderate significance of the vertical-to-horizontal permeability anisotropy for a moderate-thickness formation. However, if $h = 250$ ft, then for I_{ani} equal to 3, 1, and 0.25, the flow rates q are 4009, 6607, and 8600 STB/d, respectively, denoting the great significance of permeability anisotropy for thicker reservoirs.

Figure 2-9 shows the flow rates for all three thicknesses and three permeability anisotropies for a range of horizontal well lengths. Figure 2-10 is a graph of the productivity index ratios between these horizontal wells and vertical wells in the same reservoirs. In both graphs the great impact of good vertical permeability in thick formations is evident. In thinner formations this requirement is relaxed. ◇

EXAMPLE 2-11

Equivalent skin effect and effective wellbore radius from a horizontal well

For a vertical well, the effective wellbore radius, r'_w, is given by Eq. (2-18). The horizontal well production rate is given by Eq. (2-46). Develop an expression for a vertical well effective wellbore radius that would result in equivalent production from a horizontal well. Using the data in Example 2-10, estimate the equivalent vertical well skin effect.

Solution The logarithmic expression inside the large parentheses in Eq. (2-46) can be gathered:

$$\ln\left[\frac{a+\sqrt{a^2-(L/2)^2}}{L/2}\right] + \frac{I_{ani}h}{L}\ln\frac{I_{ani}h}{r_w(I_{ani}+1)}$$
$$= \ln\left[\frac{a+\sqrt{a^2-(L/2)^2}}{L/2}\right]\left[\frac{I_{ani}h}{r_w(I_{ani}+1)}\right]^{I_{ani}h/L} \tag{2-52}$$

Comparison between Eq. (2-17) [and the definition of the effective wellbore in Eq. (2-18)] and Eq. (2-46) [and the expression in Eq. (2-52)] results in

$$r'_w = \frac{r_e}{\left\{[a+\sqrt{a^2-(L/2)^2}]/(L/2)\right\}[I_{ani}h/r_w(I_{ani}+1)]^{I_{ani}h/L}} \tag{2-53}$$

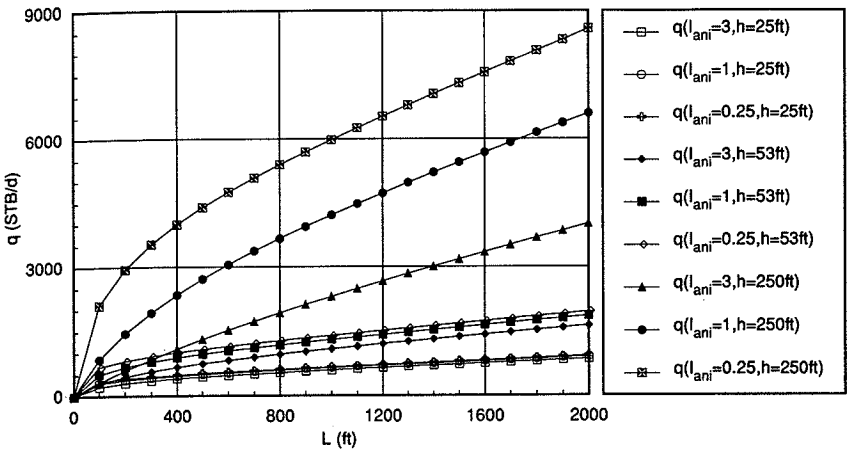

Figure 2-9
Horizontal well production rates and impact of formation thickness and permeability anisotropy for Example 2-10.

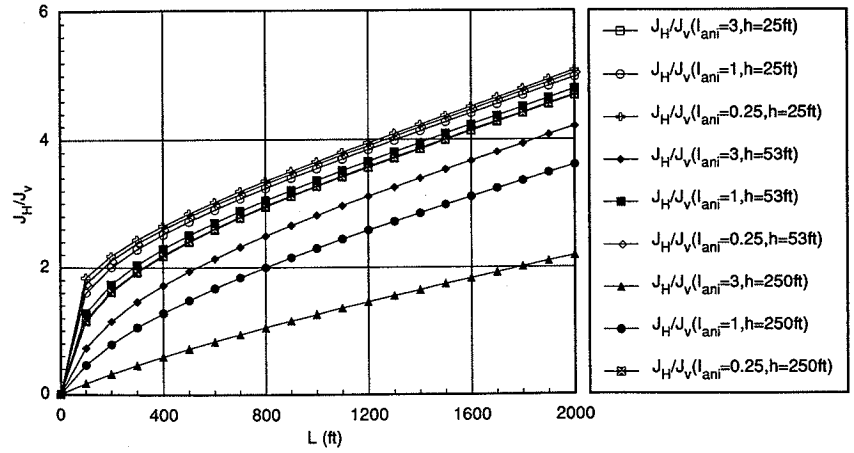

Figure 2-10
Productivity index ratios between horizontal and vertical wells (Example 2-10).

For a given r_w, the resulting skin effect can be calculated.

In Example 2-10, $L = 2000$ ft, $h = 53$ ft, $a = 3065$ ft, $I_{ani} = 3$ and $r_{eH} = 2980$ ft. Therefore, from Eq. (2-53), $r'_w = 341$ ft, and from Eq. (2-18), $s = -6.9$. ◇

2-8 Impact of Skin Effect on Horizontal Well Performance

The horizontal well skin effect is added to the denominator of Eq. (2-46) in the following manner:

$$q = \frac{k_H h\,\Delta p}{141.2B\mu\left(\ln\left\{\frac{[a+\sqrt{a^2-(L/2)^2}]}{L/2}\right\}+\left(\frac{I_{ani}h}{L}\right)\left\{\ln\left[\frac{I_{ani}h}{r_w(I_{ani}+1)}\right]+s'_{eq}\right\}\right)} \tag{2-54}$$

This skin effect, denoted as s'_{eq}, is characteristic of the shape of damage in horizontal wells, taking into account the permeability anisotropy and the likelihood of larger damage penetration nearest to the vertical section. This point is expounded upon in Chapter 5. Expressions for s'_{eq} are also presented in the same chapter.

The impact of this skin effect on the production rate reduction can be very large.

The first logarithmic expression in the denominator of Eq. (2-54) ranges between 1.5 and 3 for most applications. The second logarithmic expression ranges between 2.5 and 4.5, whereas s'_{eq} can be as high as 50 with common values about 20. Even if it is multiplied by $I_{ani}h/L$, which ranges between 10^{-2} and 0.3, its effect on the production rate can be substantial. For example, if $I_{ani} = 3$, $h = 100$ ft, $L = 2000$ ft, $a = 2500$ ft, and $s'_{eq} = 20$, then the three terms in the denominator of Eq. (2-54) would be 1.6, 0.65, and 3, respectively. This results in a 58% reduction of the production rate compared to the case of an undamaged well.

This issue, the magnitude of damage, its relative impact, and stimulation considerations will be addressed in Chapter 5.

2-9 Effects of Water Production; Relative Permeability

All previous sections in this chapter provided volumetric flow rates of undersaturated oil reservoirs as functions of the permeability, k. This permeability was used as a reservoir property. In reality this is only an approximation, since such a use of permeability is correct only if the flowing fluid is *also* the only saturating fluid. In such case the "absolute" and "effective" permeabilities are the same.

In petroleum reservoirs, however, water is always present at least as connate water, denoted as S_{wc}. Thus, in all previous equations in this chapter the permeability should be considered as effective, and it would be invariably less (in certain cases significantly less) than the one obtained from core flooding or other laboratory techniques using a single fluid.

If both oil *and* free water are flowing, then effective permeabilities must be used. The sum of these permeabilities is invariably less than the absolute permeability of the formation (to either fluid).

These effective permeabilities are related to the "relative" permeabilities (also rock properties) by

$$k_o = kk_{ro} \tag{2-55}$$

and

$$k_w = kk_{rw} \tag{2-56}$$

Relative permeabilities are determined in the laboratory and are characteristic of a given reservoir rock and its saturating fluids. It is not a good practice to use relative permeabilities obtained for one reservoir to predict the performance of another.

Usually, relative permeability curves are presented as functions of the water saturation, S_w, as shown in Fig. 2-11. When the water saturation, S_w, is the connate water saturation, S_{wc}, no free water would flow and therefore its effective permeability, k_w, would be equal to zero. Similarly, when the oil saturation becomes the residual oil saturation, S_{or}, then no oil would flow and its effective permeability would be equal to zero.

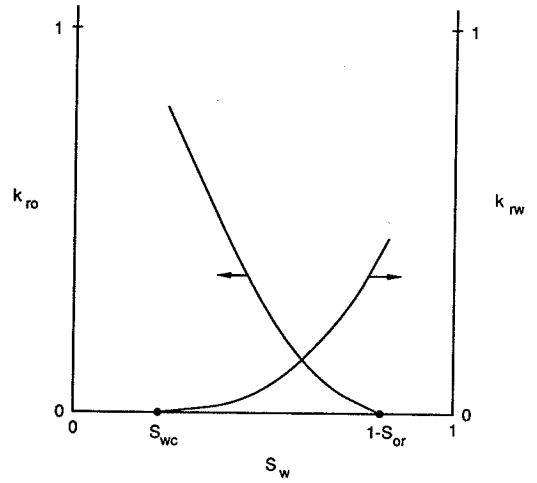

Figure 2-11
Water production; relative permeability effects.

Thus, in an undersaturated oil reservoir, inflow equations must be written for both oil and water. For example, for steady-state production,

$$q_o = \frac{kk_{ro}h(p_e - p_{wf})_o}{141.2B_o\mu_o\,[\ln(r_e/r_w)+s]} \tag{2-57}$$

and

$$q_w = \frac{kk_{rw}h(p_e - p_{wf})_w}{141.2B_w\mu_w\,[\ln(r_e/r_w)+s]} \tag{2-58}$$

with the relative permeabilities, k_{ro} and k_{rw}, being functions of S_w, as shown in Fig. 2-11.

Note that the pressure gradients have been labeled with subscripts for oil and water to allow for different pressures within the oil and water phases.

The ratio q_w/q_o is referred to as the water–oil ratio. In an almost depleted reservoir it would not be unusual to obtain water–oil ratios of 10 or larger. Such a well is often referred to as a "stripper" with production rates of less than 10 STB/d of oil.

In mature petroleum areas, stripper wells may constitute the overwhelming majority of producers. Their economic viability is frequently one of the most important questions confronting production engineers.

REFERENCES

1. Carslaw, H. S., and Jaeger, J. C., *Conduction of Heat in Solids*, 2nd ed., Clarendon Press, Oxford, 1959.
2. Dake, L. P., *Fundamentals of Reservoir Engineering*, Elsevier, Amsterdam, 1978.
3. Darcy, H., *Les Fontaines Publiques de la Ville de Dijon*, Victor Dalmont, Paris, 1856.
4. Dietz, D. N., "Determination of Average Reservoir Pressure from Build-up Surveys," *JPT*, 955–959, August 1965.
5. Earlougher, R. C., *Advances in Well Test Analysis*, Society of Petroleum Engineers, Dallas, 1977.
6. Economides, M. J., Deimbacher, F. X., Brand, C. W., and Heinemann, Z. E., "Comprehensive Simulation of Horizontal Well Performance," SPE 20717, 1990, and *SPEFE*, 418–426, December 1991.
7. Joshi, S. D., "Augmentation of Well Productivity with Slant and Horizontal Wells," *JPT*, 729–739, June 1988.
8. Van Everdingen, A. F., and Hurst, W., "The Application of the Laplace Transformation to Flow Problems in Resevoirs," *Trans. AIME*, **186:** 305–324, 1949.

PROBLEMS

2-1. Using the variables for the well in Appendix A, develop a cumulative production curve for 1 year. At what time will the well produce 50% of the total? The flowing bottomhole pressure is 3500 psi.

2-2. In Eq. (2-7), the skin effect must be added inside the large parentheses as $0.87s$. Assuming that the skin effect is equal to 10, calculate the performance for 1 year and compare it with the performance of a well with zero skin. What will the ratio of the flow rates be after 6 months?

2-3. Continue Problem 2-2. Assume that the price of oil is $25. The discount rate (time value of money) is 0.15. Calculate the net present value (NPV) for the expected cumulative production of the first 3 years. [NPV $= (\Delta N_p)_n/(1+i)^n$, where $(\Delta N_p)_n$ is the cumulative production in year n and i is the discount rate.] What are the fractional contributions from each year on the 3-year NPV?

2-4. Wells produce under steady-state conditions in four reservoirs of permeabilities, 0.01, 0.1, 1, and 10 md, respectively. The skin effect is equal to 10 in all four cases. Calculate the production rate before and after skin removal. The drainage area is 640 acres, the outer boundary pressure is 5500, and the flowing bottomhole pressure is 3500 psi. Obtain all other variables from Appendix A. (Note: The improvements in the production rate that are calculated in this problem would provide an insight as to the decision for an appropriate stimulation treatment: fracturing versus matrix.)

2-5. Assume a production rate of 80 STB/d and a drainage area of 640 acres. Use the well and reservoir properties in Appendix A. Calculate the total pressure gradient required for values of skin of 0, 5, 10, and 20. In each case, what fraction of this pressure gradient is across the damage zone?

2-6. The average pressure in a reservoir is 6000 psi. If the well drainage area in another reservoir is half that of the first reservoir (e.g., 640 versus 320 acres), what should be its average reservoir pressure to produce the same well flow rate? Use zero skin and 3000-psi bottomhole flowing pressure for both wells. All other variables are also the same.

2-7. What would be the impact on the well production rate if the well were placed within the drainage area as depicted in configurations no. 7, no. 8, and no. 9 in Fig. 2-3? Assume a drainage area of 640 acres and $r_w = 0.328$. How would the presence of a skin effect distort this comparison? Use skins equal to 0, 10, and 30 and p_{wf} equal to 3000 psi.

2-8. Equation (2-35) provided the time for the beginning of pseudo-steady state. Calculate this time for the well described in Appendix A if the drainage area is 640 acres. What would be the average reservoir pressure at that time? The flowing bottomhole pressure is 3500 psi. (Note: Calculate flow rate from transient relationship. Use this flow rate to solve for $\bar{p}$ from the pseudo-steady state relationship).

2-9. Construct a transient IPR for the well in Problem 2-8 at the time of the beginning of pseudo-steady state. Repeat for half the time.

2-10. A horizontal well, 1000 ft long, is drilled in a reservoir with $I_{ani} = 1$. What should be the horizontal well length to produce the same flow rate if $I_{ani} = 3$? The drainage radius, r_{eH}, is 2980 ft, and the flowing bottomhole pressure, p_{wf}, is 3500 psi. All other necessary variables are in Appendix A.

2-11. A horizontal well, 2000 ft long, is drilled in a reservoir as described in Appendix A. Additionally, $r_{eH} = 2980$ ft and $p_{wf} = 3500$ psi. What would be the skin effect, s'_{eq} that would halve the well production rate?

CHAPTER 3

Production from Two-Phase Reservoirs

3-1 INTRODUCTION

The performance relationships presented in Chapter 2 were for single-phase oil wells and, while gas may come out of solution after oil enters the well, the use of those relationships does not consider free gas to be present in the reservoir. Expansion of oil itself as a means of recovery is a highly inefficient mechanism because of the oil's small compressibility. It is likely that even in the best of cases (the issue will be addressed in Chapter 9), keeping the bottomhole pressure above the *bubble*-point pressure would result in a very small fractional recovery of the original-oil-in-place. Therefore, frequently, oil will be produced along with free gas in the reservoir, either because the reservoir pressure is naturally below the bubble-point pressure (saturated reservoirs) or because the flowing bottomhole pressure is set below that point to provide adequate driving force. In terms of ultimate recovery, expansion of free or solution gas is a much more efficient mechanism than the expansion of oil.

Figure 3-1 is a schematic of a classic phase diagram, plotting pressure versus temperature and identifying the important variables. Depending on the initial and flowing pressures and the reservoir temperature, a diagram such as Fig. 3-1 can indicate whether single-phase deliverability relationships as presented in Chapter 2 apply, or if the two-phase equations presented in this chapter are needed.

In Fig. 3-1, the initial reservoir conditions for an undersaturated oil reservoir are marked as p_i, T. In this depiction, the reservoir is above the bubble-point pressure. The flowing bottomhole pressure, p_{wf}, is marked within the two-phase region. The flowing bottomhole temperature is taken as equal to the reservoir temperature, reflecting the typically isothermal flow in the reservoir. The wellhead flowing conditions, with pressure p_{tf} and temperature T_{tf} are also marked. Thus the reservoir fluid would follow a path from the reservoir to the surface, joining these three points. In an initially saturated reservoir, all three points would be within the two-phase envelope. For comparison, the paths for the

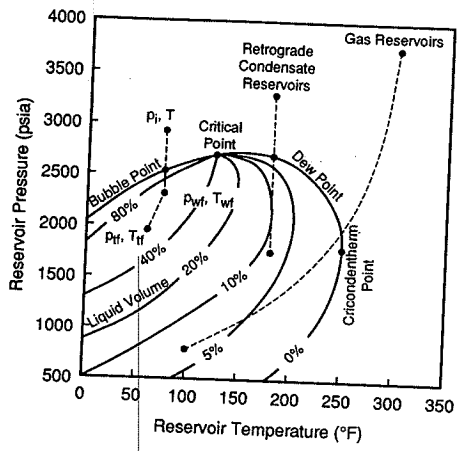

Figure 3-1
Schematic phase diagram of a hydrocarbon mixture. Marked are reservoir, bottomhole, and wellhead flowing conditions for an oil reservoir.

fluids in a retrograde gas condensate reservoir and in a single-phase gas reservoir are shown. In the latter case there is a much more pronounced reduction in the temperature along the path, reflecting Joule-Thomson expansion effects associated with gas flow.

3-2 Properties of Saturated Oil

3-2.1 General Properties of Saturated Oil

The bubble-point pressure is the important variable in characterizing a saturated oil. At pressures above the bubble point, oil behaves like a liquid; below the bubble point, gas comes out of solution, becoming free gas.

The formation volume factor, B_o, for oil above the bubble-point pressure includes all of the solution gas. At a pressure below the bubble point, the B_o refers to the liquid phase and the remaining dissolved gas at that pressure.

Figure B-1a in Appendix B shows a plot of B_o versus pressure for an example, two-phase well. Above p_b, the B_o declines with increasing pressure, reflecting the compression of the undersaturated oil. This decline is, as should be expected, slight. Below p_b, B_o increases with pressure, reflecting the dissolution of gas in the oil.

In Fig. B-1b the formation volume factor of the gas, B_g, shows the predictable decline at increasing pressure. Finally, Fig. B-1c shows the solution gas–oil ratio, R_s, increasing to the value at the bubble point and remaining constant above the p_b. This gas–oil ratio is the amount of gas that would be liberated from a unit volume of oil at standard conditions.

The variables B_o, B_g, and R_s are related through the total formation volume factor, B_t, which accounts for both oil and free gas:

$$B_t = B_o + (R_{sb} - R_s)B_g \tag{3-1}$$

where R_{sb} is the solution gas–oil ratio at the bubble-point pressure. If B_g is given in res ft^3/SCF, then B_g must be divided by 5.615 to convert to res bbl/SCF. These *PVT* properties are usually obtained in the laboratory and are unique to a given reservoir fluid.

Figures 3-2 and 3-3, from Standing's (1977) significant work in oilfield hydrocarbon correlations, relate important variables such as R_s, γ_g, γ_o, T, p_b, and B_o for a large number of hydrocarbons. These correlations should be used only in the absence of *PVT* properties obtained for the specific reservoir.

EXAMPLE 3-1
PVT properties below the bubble-point pressure: Impact on oil reserves

Calculate the total formation volume factor at 3000 psi for the reservoir fluid described in Appendix B. What would be the reduction in volume of oil (STB) in 4000 acres of the reservoir described in the same Appendix when the average pressure is reduced from the initial pressure to 3000 psi? Assume that the initial pressure is the bubble-point pressure and is equal to 4350 psi.

Solution From Fig. B-1, B_o= 1.31 res bbl/STB, $B_g = 5 \times 10^{-3}$ res ft^3/SCF, R_{sb}= 850 SCF/STB, and R_s= 550 SCF/STB. Then from Eq. (3-1),

$$B_t = 1.31 + \frac{5 \times 10^{-3}}{5.615}(850 - 550) = 1.58 \text{ res bbl/STB} \tag{3-2}$$

The original-oil-in-place at p_i=p_b is (B_{ob}=1.43 res bbl/STB from Fig. B-1a)

$$N = \frac{Ah\phi(1 - S_w)}{B_{oi}} = \frac{(7758)(4000)(115)(0.21)(0.7)}{(1.43)} = 3.7 \times 10^8 \text{ STB} \tag{3-3}$$

For B_t=1.58 res bbl/STB, $N(-N_p) = 3.3 \times 10^8$ STB, a reduction of 4×10^7 STB. ◇

EXAMPLE 3-2
Use of correlations to obtain PVT properties of saturated oil reservoirs

Supposing that R_s=500 SCF/STB, γ_g=0.7, γ_o=28°API, and T=160°F, calculate the bubble-point pressure. What would be the impact if R_s=1000 SCF/STB but all other variables remain the same?

If R_s=500 SCF/STB, B_{ob}=1.2 res bbl/STB, T=180°F, and γ_o=32°API, what should be the gas gravity, γ_g?

Solution Reading from Fig. 3-2 in a stairstep manner with the first set of variables, p_b=2750 psi. If R_s=1000 SCF/STB, then p_b=5200 psi.

Figure 3-3 can be used for the last question. Starting from the right at B_{ob}=1.2 res bbl/STB, T=180°F, and γ_o=32°API and then from the left at R_s=500 SCF/STB, the intersection of the two lines results in γ_g=0.7. ◇

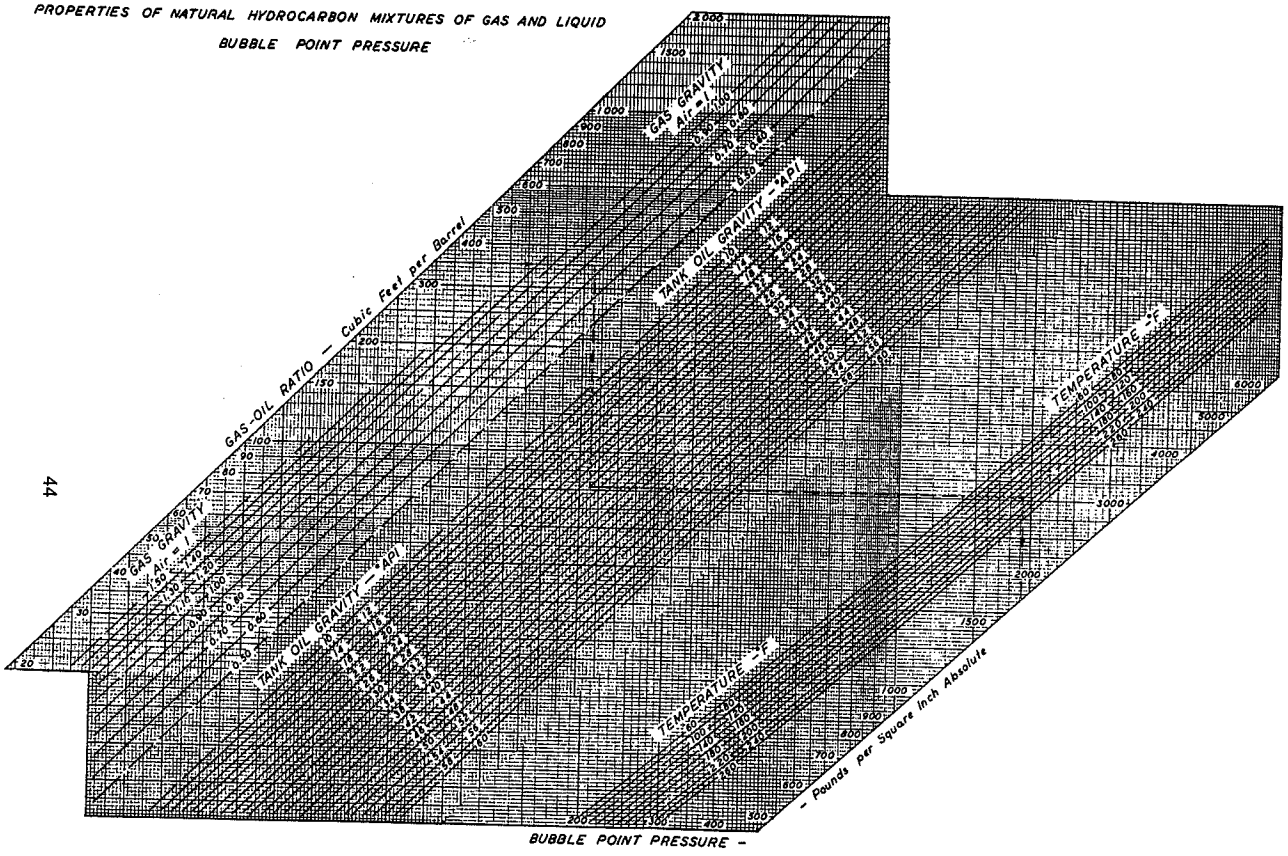

Figure 3-2

Properties of natural mixtures of hydrocarbon gas and liquids, bubble-point pressure. (*After Standing, 1977.*)

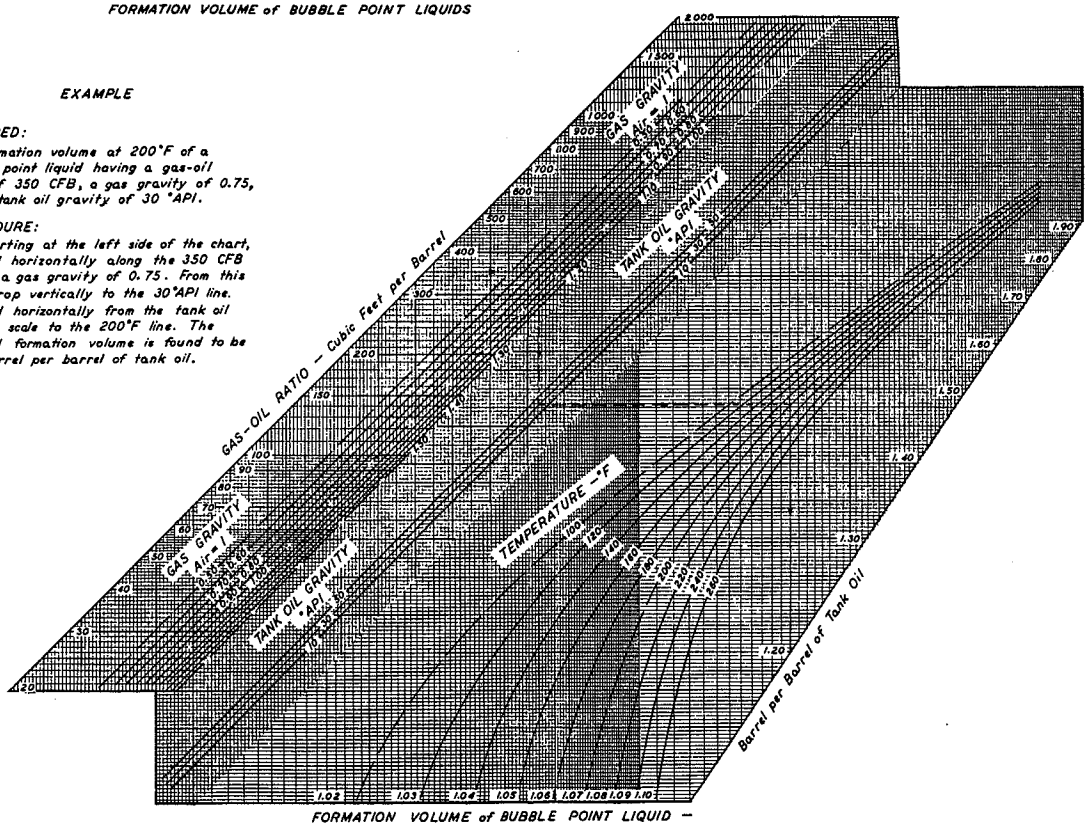

Figure 3-3

Properties of natural mixtures of hydrocarbon gas and liquids, formation volume of bubble-point liquids. (*After Standing, 1977.*)

3-2.2 Property Correlations for Two-Phase Systems

This Subsection presents the most widely used property correlations for two-phase oilfield hydrocarbon systems.

The downhole volumetric flow rate of oil is related to the surface rate through the formation volume factor, B_o:

$$q_l = B_o q_o \tag{3-4}$$

Here q_l is the actual liquid flow rate at some location in the well or reservoir. The downhole gas rate depends on the solution gas–oil ratio, R_s, according to

$$q_g = B_g(\text{GOR} - R_s)q_o \tag{3-5}$$

where B_g is the gas formation volume factor and will be addressed further in Chapter 4, and GOR is the gas–oil ratio in SCF/STB.

The oil-formation volume factor and the solution gas–oil ratio, R_s, will vary with temperature and pressure. They can be obtained from laboratory PVT data, such as those in Appendix B, or from correlations. One common correlation is that of Standing, given in Figs. 3-2 and 3-3. Another correlation that is accurate for a wider range of crude oils is that of Vasquez and Beggs (1980), given here.

First, the gas gravity is corrected to the reference separator pressure of 100 psig (114.7 psia):

$$\gamma_{gs} = \gamma_{gsep}\left[1 + 5.912 \times 10^{-5}\gamma_l T_{sep} \log\left(\frac{p_{sep}}{114.7}\right)\right] \tag{3-6}$$

where T_{sep} is in °F, p_{sep} is in psia, and γ_l is in °API. The solution gas–oil ratio is then, for $\gamma_l \leq 30$°API,

$$R_s = \frac{\gamma_{gs} p^{1.0937}}{27.64} \times 10^{11.172A} \tag{3-7}$$

and for $\gamma_l > 30$°API,

$$R_s = \left(\frac{\gamma_{gs} p^{1.187}}{56.06}\right) \times 10^{10.393A} \tag{3-8}$$

where

$$A = \frac{\gamma_l}{T + 460} \tag{3-9}$$

For pressures below the bubble-point pressure, the oil-formation volume factor for $\gamma_l \leq 30$°API is

$$B_o = 1.0 + 4.677 \times 10^{-4} R_s + 0.1751 \times 10^{-4} F - 1.8106 \times 10^{-8} R_s F \tag{3-10}$$

and for $\gamma_l > 30$°API is

$$B_o = 1.0 + 4.67 \times 10^{-4} R_s + 0.11 \times 10^{-4} F + 0.1337 \times 10^{-8} R_s F \tag{3-11}$$

where

$$F = (T - 60)\left(\frac{\gamma_l}{\gamma_{gs}}\right) \tag{3-12}$$

and for pressures above the bubble point is

$$B_o = B_{ob} e^{c_o(p_b - p)} \tag{3-13}$$

where

$$c_o = \frac{-1.433 + 5R_s + 17.2T - 1.180\gamma_{gs} + 12.61\gamma_l}{p \times 10^5} \tag{3-14}$$

and B_{ob} is the formation volume factor at the bubble point. At the bubble point, the solution gas–oil ratio is equal to the produced gas–oil ratio (GOR), so the bubble-point pressure can be estimated from Eqs. (3-7) or (3-8) setting R_s=GOR and solving for p. Then Eq. (3-10) or (3-11) may be used to calculate B_{ob}.

Fluid Density. The oil density at pressures below the bubble point is

$$\rho_o = \frac{[8,830/(131.5 + \gamma_l)] + 0.01361\gamma_{gd} R_s}{B_o} \tag{3-15}$$

where ρ_o is in lb_m/ft^3 and γ_{gd} is the dissolved gas gravity because of the changing gas composition with temperature. It can be estimated from Fig. 3-4 (Katz et al., 1959). Above the bubble point, the oil density is

$$\rho_o = \rho_{ob}\left(\frac{B_o}{B_{ob}}\right) \tag{3-16}$$

where B_o is calculated from Eq. (3-13) and B_{ob} from Eq. (3-10) or (3-11), with R_s=GOR.

Fluid Viscosity. Oil viscosity can be estimated with the correlations of Beggs and Robinson (1975) and Vasquez and Beggs (1980). The "dead" oil viscosity is

$$\mu_{od} = 10^A - 1 \tag{3-17}$$

where

$$A = BT^{-1.163} \tag{3-18}$$

$$B = 10^C \tag{3-19}$$

$$C = 3.0324 - 0.02023\gamma_l \tag{3-20}$$

The oil viscosity at any other pressure below the bubble point is

$$\mu_o = a\mu_{od}^b \tag{3-21}$$

where

$$a = 10.715(R_s + 100)^{-0.515} \tag{3-22}$$

$$b = 5.44(R_s + 150)^{-0.338} \tag{3-23}$$

If the stock tank oil viscosity is known, this value can be used for μ_{od} with Eqs. (3-21) through (3-23).

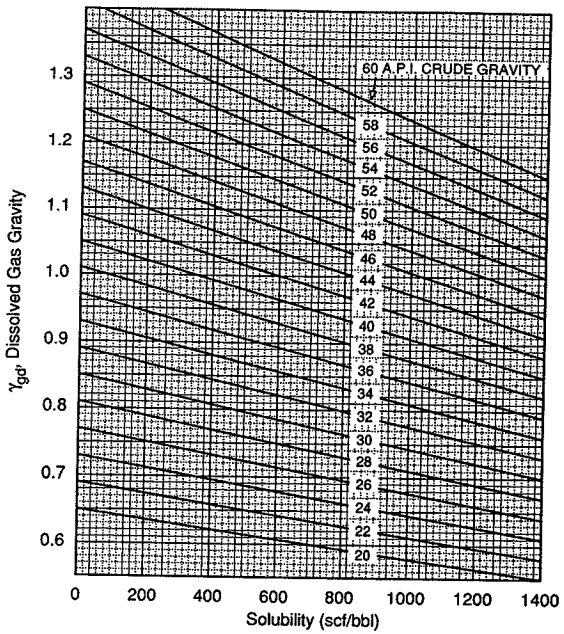

Figure 3-4
Prediction of gas gravity from solubility and crude-oil gravity. *(After Katz et al., Handbook of Natural Gas Engineering, copyright 1959, McGraw-Hill, reproduced with permission of McGraw-Hill.)*

For pressures above the bubble point, the viscosity at the bubble point is first computed with Eqs. (3-17) through (3-23). Then

$$\mu_o = \mu_{ob}\left(\frac{p}{p_b}\right)^m \tag{3-24}$$

where

$$m = 2.6p^{1.187}\exp(-11.513 - 8.98 \times 10^{-5}p) \tag{3-25}$$

Gas viscosity can be estimated with the correlation that will be given in Chapter 4.

Accounting for the presence of water. When water is produced, the liquid flow properties are generally taken to be averages of the oil and water properties. If there is no slip between the oil and water phases, the liquid density is the volume fraction-weighted average of the oil and water densities. The volume fraction-weighted averages will be used

to estimate liquid viscosity and surface tension, though there is no theoretical justification for this approach. The reader should note that in the petroleum literature it has been common practice to use volume fraction-weighted average liquid properties in oil-water-gas flow calculations. Also, the formation volume factor for water is normally assumed to be 1.0 because of low compressibility and gas solubility. Thus, when water and oil are flowing,

$$q_l = q_o(\text{WOR} + B_o) \tag{3-26}$$

$$\rho_l = \frac{\text{WOR}\rho_w + B_o\rho_o}{\text{WOR} + B_o} \tag{3-27}$$

$$\mu_l = \left(\frac{\text{WOR}\rho_w}{\text{WOR}\rho_w + B_o\rho_o}\right)\mu_w + \left(\frac{B_o\rho_o}{\text{WOR}\rho_w + B_o\rho_o}\right)\mu_o \tag{3-28}$$

$$\sigma_l = \left(\frac{\text{WOR}\rho_w}{\text{WOR}\rho_w + B_o\rho_o}\right)\sigma_w + \left(\frac{B_o\rho_o}{\text{WOR}\rho_w + B_o\rho_o}\right)\sigma_o \tag{3-29}$$

where WOR is the water–oil ratio, and σ is the surface tension.

EXAMPLE 3-3
Estimating downhole properties

Suppose that 500 bbl/d of the oil described in Appendix B is being produced at a WOR of 1.5 and a GOR of 500. The separator conditions for properties given in Appendix B are 100 psig and 100°F. Using the correlations presented in Section 3-2.2, estimate the volumetric flow rates of the gas and liquid and the density and viscosity of the liquid at a point in the tubing where the pressure is 2000 psia and the temperature is 150°F.

Solution The first step is to calculate R_s and B_o. Since the separator is at the reference condition of 100 psig, $\gamma_{gs} = \gamma_g$. From Eqs. (3-8) and (3-9),

$$A = \frac{32}{150 + 460} = 0.0525 \tag{3-30}$$

$$R_s = \left[\frac{(0.71)(2000)^{1.187}}{56.06}\right]10^{10.393(0.0525)} = 369 \text{ ft}^3/\text{bbl} \tag{3-31}$$

$$F = (150 - 60)\left(\frac{32}{0.71}\right) = 4.056 \times 10^3 \tag{3-32}$$

$$B_o = 1 + (4.67 \times 10^{-4})(369) + 0.11 \times 10^{-4}(4.056 \times 10^3) + 0.1337 \times 10^{-8}(369)(4.056 \times 10^3) = 1.22 \text{ res bbl/STB} \tag{3-33}$$

The gas-formation volume factor, B_g, can be calculated from the real gas law. For T=150°F and p=2000 psi, it is 6.97×10^{-3} res ft^3/SCF. (This type of calculation will be shown explicitly in Chapter 4.)

The volumetric flow rates are [Eqs. (3-26) and (3-27)]

$$q_l = (500)(1.5 + 1.22) = 1360 \text{ bbl/day} = 7640 \text{ ft}^3/\text{d} \tag{3-34}$$

$$q_g = (6.97 \times 10^{-3})(500 - 369)(500) = 457 \text{ ft}^3/\text{d} \quad (3\text{-}35)$$

To calculate the oil density, the dissolved gas gravity, γ_{gd}, must be estimated. From Fig. 3-4 it is found to be equal to 0.85. Then, from Eq. (3-15),

$$\rho_o = \frac{[8,830/(131.5 + 32)] + (0.01361)(0.85)(369)}{1.22} = 47.8 \text{ lb}_m/\text{ft}^3 \quad (3\text{-}36)$$

and, from Eq. (3-27),

$$\rho_l = \frac{1.5(62.4) + 1.22(47.8)}{1.5 + 1.22} = 55.9 \text{ lb}_m/\text{ft}^3 \quad (3\text{-}37)$$

The oil viscosity can be estimated with Eqs. (3-17) through (3-23):

$$C = 3.0324 - (0.02023)(32) = 2.385 \quad (3\text{-}38)$$

$$B = 10^{2.385} = 242.7 \quad (3\text{-}39)$$

$$A = (242.7)(150)^{-1.163} = 0.715 \quad (3\text{-}40)$$

$$\mu_{od} = 10^{0.715} - 1 = 4.19 \text{ cp} \quad (3\text{-}41)$$

$$a = 10.715(369 + 100)^{-0.515} = 0.451 \quad (3\text{-}42)$$

$$b = 5.44(369 + 150)^{-0.338} = 0.657 \quad (3\text{-}43)$$

$$\mu_o = 0.451(4.19)^{0.657} = 1.16 \text{ cp} \quad (3\text{-}44)$$

The liquid viscosity is then found from Eq. (3-28), using the given value of 1 cp for μ_w:

$$\mu_l = \frac{(1.5)(62.4)}{(1.5)(62.4) + (1.22)(47.8)}(1) + \frac{(1.22)(47.8)}{(1.5)(62.4) + (1.22)(47.8)}(1.16) = 1.06 \text{ cp} \quad (3\text{-}45)$$

◇

3-3 Two-Phase Flow in a Reservoir

Although a rigorous treatment of two-phase flow in a reservoir is outside the scope of this textbook, it is necessary to understand the impact of competing phases on the flow of a fluid through the porous medium.

If there are two or three fluids flowing at the same time in a porous medium, the absolute reservoir permeability, k, is necessarily divided into "effective" permeabilities, one for each fluid. Therefore, in multiphase flow, oil flows with an effective permeability, k_o, water with k_w, and gas with k_g.

Even the presence of a nonflowing phase, such as connate water, whose saturation is denoted by S_{wc}, would cause some reduction in the effective permeability to oil, when compared to a core fully saturated with oil. Thus laboratory-derived core permeabilities

with air or water should not be used automatically for reservoir calculations. Pressure transient test-derived permeabilities are far more reliable (not only because of the reason outlined above but also because they account for reservoir heterogeneities; cores reflect only local permeabilities). The effective permeabilities are related to the relative permeabilities by simple expressions:

$$k_{ro} = \frac{k_o}{k}, \qquad k_{rw} = \frac{k_w}{k}, \qquad k_{rg} = \frac{k_g}{k} \quad (3\text{-}46)$$

Relative permeabilities are laboratory-derived relationships, are functions of fluid saturations, and, although frequently misapplied, are functions of the specific reservoir rock. Thus, relative permeability data developed for a reservoir cannot be readily transferred to another, even seemingly similar, formation.

Figure 3-5 is a schematic diagram of laboratory-derived oil and gas relative permeability data. The effective permeabilities are analogous, being simply the relative permeabilities multiplied by the absolute permeability, k.

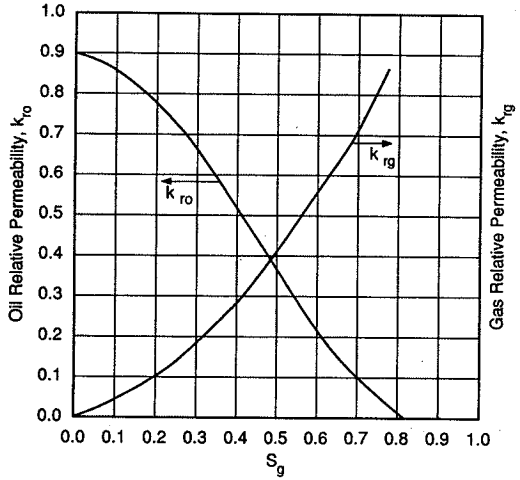

Figure 3-5
Oil and gas relative permeability.

The rate equations developed in Chapter 2 for single-phase flow of oil must then be adjusted to reflect effective permeabilities in the presence of gas. Therefore, Eq. (2-15) for steady state, rearranged for the flow of oil, becomes

$$q_o = \frac{k_o h(p_e - p_{wf})_o}{141.2 B_o \mu_o [\ln (r_e/r_w) + s]} \quad (3\text{-}47)$$

where $k_o = k_{ro}\,k$. Also note that the pressure gradient is denoted with a subscript o, indicating that it must be within the oil phase, which may be different from that in the gas phase.

The generalized expression for the flow of oil, taking into account property variation and relative permeability effects, can be written for steady state as

$$q_o = \frac{kh}{141.2[\ln(r_e/r_w) + s]} \int_{p_{wf}}^{p_e} \frac{k_{ro}}{\mu_o B_o}\, dp \tag{3-48}$$

For pseudo-steady state, $\ln(r_e/r_w)$ and p_e can be changed to $\ln(0.472r_e/r_w)$ and $\bar{p}$, respectively. Finally, in the brackets in the denominator of Eq. (3-48), the term Dq can be added to account for turbulence effects in high-rate wells, where D is the turbulence coefficient.

EXAMPLE 3-4

The effect of relative permeability on the flow of oil in a two-phase reservoir

Using the experimentally determined relative permeability data in Appendix B, calculate the well flow rate if the flowing bottomhole pressure is 3000 psi. Compare the ideal flow rate (assuming no oil relative permeability reduction) and the true flow rate reflecting the relative permeability at a free gas saturation S_g=0.08. The drainage radius is 1490 ft and the skin effect is zero.

Solution From Eq. (2-15),

$$q_o = \frac{(13)(115)(4350 - 3000)}{(141.2)(1.37)(1.7)[\ln(1490/0.406)]} = 748 \text{ STB/d} \tag{3-49}$$

(Note: The value of B_o is the average value between 4350 and 3000 psi in Fig. B-1a).

The permeability used in Eq. (3-49) is the test-derived effective permeability without free gas. From Fig. B-2 in Appendix B at S_g=0.08, the relative permeability to oil k_{ro}=0.21 and, from Eq. (3-47),

$$q_o = q_{o,\text{ideal}} k_{ro} \tag{3-50}$$

resulting in q_o=157 STB/d, a significant reduction from the ideal value. ◇

3-4 Oil Inflow Performance for a Two-Phase Reservoir

Vogel (1968) introduced an empirical relationship for q_o based on a number of history-matching simulations. The relationship, normalized for the absolute open flow potential, $q_{o,\max}$ is

$$\frac{q_o}{q_{o,\max}} = 1 - 0.2\frac{p_{wf}}{\bar{p}} - 0.8\left(\frac{p_{wf}}{\bar{p}}\right)^2 \tag{3-51}$$

where, for pseudo-steady state,

$$q_{o,\max} = \left(\frac{1}{1.8}\right) \frac{k_o h \bar{p}}{141.2 B_o \mu_o [\ln(0.472 r_e/r_w) + s]} \tag{3-52}$$

and therefore

$$q_o = \frac{k_o h \bar{p}[1 - 0.2(p_{wf}/\bar{p}) - 0.8(p_{wf}/\bar{p})^2]}{254.2 B_o \mu_o [\ln(0.472 r_e/r_w) + s]} \tag{3-53}$$

The convenience of the Vogel correlation is that it allows the use of the properties of only oil in a two-phase system. The viscosity and the formation volume factor must be taken at $\bar{p}$.

EXAMPLE 3-5

Calculation of inflow performance using Vogel's correlation

Develop an IPR curve for the well described in Appendix B. The drainage radius is 1490 ft and the skin effect is zero.

Solution Equation (3-53) for $\bar{p}$=4350 psi becomes

$$q_o = 1411\left[1 - 0.2\frac{p_{wf}}{\bar{p}} - 0.8\left(\frac{p_{wf}}{\bar{p}}\right)^2\right] \tag{3-54}$$

The flow-rate prediction with Eq. (3–54) is simple. For example, if p_{wf} = 3000 psi, from Eq. (3–54), q_o = 680 STB/d.

Figure 3-6 is a plot of the IPR curve for this well. Note the shape of the curve which is no longer a straight line as for the single-phase oil in Chapter 2. ◇

3-5 Generalized Vogel Inflow Performance

If the reservoir pressure is above the bubble point and yet the flowing bottomhole pressure is below, a generalized inflow performance can be written. This can be done for transient, steady state, and pseudo-steady state.

At first, q_b, the flow rate, where p_{wf}=p_b, can be written as

$$q_b = \frac{kh(p_i - p_b)}{141.2 B\mu(p_D + s)} \tag{3-55}$$

where p_D is the transient dimensionless pressure drop or is equal to $\ln(r_e/r_w)$ for steady state or $\ln(0.472\,r_e/r_w)$ for pseudo-steady state.

The productivity index above the bubble point is simply

$$J = \frac{q_b}{p_i - p_b} \tag{3-56}$$

and is related to q_V (denoted here as "Vogel" flow) by

$$q_V = \frac{p_b J}{1.8} \tag{3-57}$$

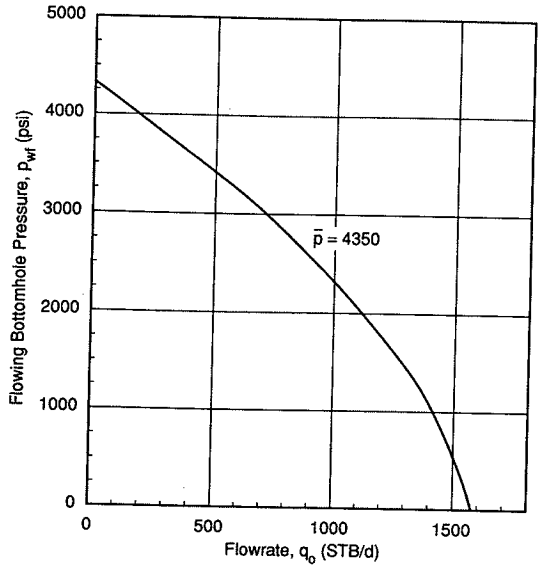

Figure 3-6
Inflow performance curve for a two-phase well.

Finally,

$$q_o = q_b + q_V \left[1 - 0.2\frac{p_{wf}}{p_b} - 0.8\left(\frac{p_{wf}}{p_b}\right)^2\right] \tag{3-58}$$

3-6 FETKOVICH'S APPROXIMATION

Vogel's correlation, normalizing q_o by $q_{o,\max}$, is frequently not in accordance with field data. Fetkovich (1973) suggested a normalization with $q_{o,\max} = C\bar{p}^{2n}$, and in a flow equation of the form

$$q_o = C(\bar{p}^2 - p_{wf}^2)^n \tag{3-59}$$

the relationship becomes

$$\frac{q_o}{q_{o,\max}} = \left[1 - \left(\frac{p_{wf}}{\bar{p}}\right)^2\right]^n \tag{3-60}$$

Equation (3-60) requires the determination of two unknowns, the absolute open flow potential, $q_{o,\max}$, and the exponent n. Both of them are characteristic of a specific well and therefore a test at two stabilized flow rates can allow the calculation of the corresponding p_{wf} and therefore can lead to the determination of $q_{o,\max}$ and n.

Equations (3-53) and (3-60) are both empirical fits and thus should be used accordingly.

REFERENCES

1. Beggs, H. D., and Robinson, J. R., "Estimating the Viscosity of Crude Oil Systems," *JPT*, 1140–1141, September 1975.
2. Fetkovich, M. J., "The Isochronal Testing of Oil Wells," SPE Paper 4529, 1973.
3. Katz, D. L., Cornell, D., Kobayashi, R. L., Poettmann, F. H., Vary, J. A., Elenbaas, J. R., and Weinang, C. F., *Handbook of Natural Gas Engineering*, McGraw-Hill, New York, 1959.
4. Standing, M. B., *Volumetric and Phase Behavior of Oil Field Hydrocarbon Systems*, Society of Petroleum Engineers, Dallas, 1977.
5. Vasquez, M., and Beggs, H. D., "Correlations for Fluid Physical Property Predictions," *JPT*, 968–970, June 1990.
6. Vogel, J. V., "Inflow Performance Relationships for Solution-Gas Drive Wells," *JPT*, 83–92, January 1968.

PROBLEMS

3-1. Plot B_t versus pressure for the data in Appendix B.

3-2. Suppose that R_S=1000 SCF/STB, γ_g=0.7, and γ_o=30° API. What would be the maximum B_o, regardless of the temperature?

3-3. Plot the bubble-point pressure versus γ_o for R_S=500 SCF/STB and γ_g=0.7. The temperature is 180°F.

3-4. Assume that each 0.02 in the gas saturation in Fig. B-2 represents a reduction in the bottomhole pressure of 200 psi. With these relative permeability data, the *PVT* properties in Fig. B-1, and the data in Appendix B, use Eq. (3-48) to forecast the well oil flow rate. Skin effect is equal to zero, r_e=1490 ft, and the p_{wf} is 3000 psi.

3-5. Plot IPR curves as in Example 3-5 but for a range of average reservoir pressures in increments of 500 psi. Do these curves follow a similar pattern, as would be the case for a single-phase oil well? Do they approach each other more or less? Why?

3-6. Assume that the initial pressure of the well described in Appendix B is 1000 psi above the given initial (which also is the bubble-point) pressure. Calculate the flow rate if p_{wf}=3350 psi (1000 psi below p_b), r_e=1490, and s=0. What are the relative contributions to the flow rate from the pressure difference above and the one below the bubble point?

3-7. For the problem in Example 3-5, calculate the $q_{o,\max}$ and n in Fetkovich's approximation given by Eq. (3-60). Hint: You must plot the data on log-log paper.

CHAPTER 4

Production from Natural Gas Reservoirs

4-1 INTRODUCTION

Natural gas reservoirs produce hydrocarbons that exist primarily in the gas phase at reservoir conditions. In order to predict the production rate from these reservoirs, there is a need to review some of the fundamental properties of hydrocarbon gases. This is particularly important (more so than in the case of oil reservoirs) because certain physical properties of gases and gas mixtures vary significantly with pressure, temperature, and gas composition. Following is a brief outline of gas gravity, the real gas law, gas compressibility factor (and the impact of nonhydrocarbon gases), gas viscosity, and gas isothermal compressibility.

4-1.1 Gas Gravity

The gas gravity, as used in natural gas production and reservoir engineering, is the ratio of the molecular weight of a natural gas to that of air, itself a mixture of gases. The molecular weight of air is usually taken as equal to 28.97 (approximately 79% nitrogen and 21% oxygen). Therefore the gas gravity, symbolized by γ_g, is

$$\gamma_g = \frac{\text{MW}}{28.97} = \frac{\sum y_i \text{MW}_i}{28.97} \tag{4-1}$$

where y_i and MW_i are the mole fraction and molecular weight, respectively, of an individual component.

Table 4-1 gives the molecular weights and critical properties for most hydrocarbon and nonhydrocarbon gases likely to be found in a natural gas reservoir. A *light* gas reservoir is one that contains primarily methane with some ethane. Pure methane would have a gravity equal to $(16.04/28.97) = 0.55$. A *rich* or *heavy* gas reservoir may have a gravity equal to 0.75 or, in some rare cases, higher than 0.9.

Table 4-1

Molecular Weights and Critical Properties of Pure Components of Natural Gases

Compound	Chemical Composition	Symbol (for calculations)	Molecular Weight	Critical Pressure (psi)	Critical Temperature (°)R
Methane	CH_4	C_1	16.04	673	344
Ethane	C_2H_6	C_2	30.07	709	550
Propane	C_3H_8	C_3	44.09	618	666
iso-Butane	C_4H_{10}	i-C_4	58.12	530	733
n-Butane	C_4H_{10}	n-C_4	58.12	551	766
iso-Pentane	C_5H_{12}	i-C_5	72.15	482	830
n-Pentane	C_5H_{12}	n-C_5	72.15	485	847
n-Hexane	C_6H_{14}	n-C_6	86.17	434	915
n-Heptane	C_7H_{16}	n-C_7	100.2	397	973
n-Octane	C_8H_{18}	n-C_8	114.2	361	1024
Nitrogen	N_2	N_2	28.02	492	227
Carbon dioxide	CO_2	CO_2	44.01	1072	548
Hydrogen Sulfide	H_2S	H_2S	34.08	1306	673

EXAMPLE 4-1

Calculation of the gravity of a natural gas

A natural gas consists of the following (molar) composition: $C_1 = 0.880$, $C_2 = 0.082$, $C_3 = 0.021$, and $CO_2 = 0.017$. Calculate the gas gravity to air.

Solution With the data in Table 4-1 and the given composition, the contributions to the natural gas molecular weight are

Compound	Composition	y_i MW$_i$
C_1	0.880	14.115
C_2	0.082	2.466
C_3	0.021	0.926
CO_2	0.017	0.748
		18.255

Therefore, the gas gravity is 18.225/28.97 = 0.63. ◇

4-1.2 Real Gas Law

The behavior of natural gas mixtures can be approximated by the real gas law

$$pV = ZnRT \tag{4-2}$$

where Z is the compressibility factor, also called the gas deviation factor in the petroleum literature. The universal gas constant, R, is equal to 10.73 psi ft^3/lb-mol-°R. Equation (4-2) is a general equation of state for gases. The gas deviation factor for mixtures of hydrocarbon gases can be obtained from Fig. 4-1 (Standing and Katz, 1942). This well-known graph was constructed for hydrocarbon gas mixtures. In the presence of large amounts of nonhydrocarbon gases, the gas deviation factor must be adjusted, as will be demonstrated in a later section.

To use Fig. 4-1 it is necessary to calculate the pseudo-reduced properties (pressure and temperature) of the mixture. These properties are simply

$$p_{pr} = \frac{p}{p_{pc}} \tag{4-3}$$

and

$$T_{pr} = \frac{T}{T_{pc}} \tag{4-4}$$

where p_{pc} and T_{pc} are the pseudo-critical pressure and temperature of the mixture, respectively. The temperature must be absolute (R or K), which is simply °F+ 460°F or °C + 273.

Finally, as can be seen from Fig. 4-1, at the standard conditions of $p_{sc} = 14.7$ psi and $T_{sc} = 60°F = 520°R$, the gas deviation factor, Z_{sc}, can be taken as equal to 1.

EXAMPLE 4-2

Use of the real gas law to calculate the volume of a gas mixture at reservoir conditions

Assume that a natural gas has the following molar composition (this is the fluid in the reservoir described in Appendix C): C_1=0.875, C_2=0.083, C_3=0.021, i-C_4=0.006, n-C_4=0.002, i-C_5=0.003, n-C_5=0.008, n-C_6=0.001, and C_7+=0.001.

Calculate the volume of 1 lb-mol of this mixture at reservoir conditions of $T = 180°F$ and $p = 4000$ psi.

Solution The first step is to calculate the pseudo-critical properties of the mixture. These properties are simply the summation of the individual contributions of the component gases, weighted by their molar fractions. This is based on the classical thermodynamics law for ideal mixtures and Dalton's law of partial pressures. Table 4-2 gives the results of this calculation.

The pseudo-reduced properties are then p_{pr} = 4000/671 = 5.96 and T_{pr} = (180 + 460)/378 = 1.69. From Fig. 4-1, $Z = 0.855$. Then, from Eq. (4-2) and rearrangement,

$$V = \frac{(0.855)(1)(10.73)(640)}{4000} = 1.47 \text{ ft}^3 \tag{4-5}$$

◇

4-2 Correlations and Useful Calculations for Natural Gases

Several important works have presented correlations for natural gas properties. Following is a summary of these, with brief descriptions of the use of these correlations.

4-2.1 Pseudo-critical Properties from Gas Gravity

Figure 4-2 relates the gas gravity (to air) with the pseudo-critical properties of gas mixtures. Using the results of Example 4-2, the calculated molecular weight is 18.92,

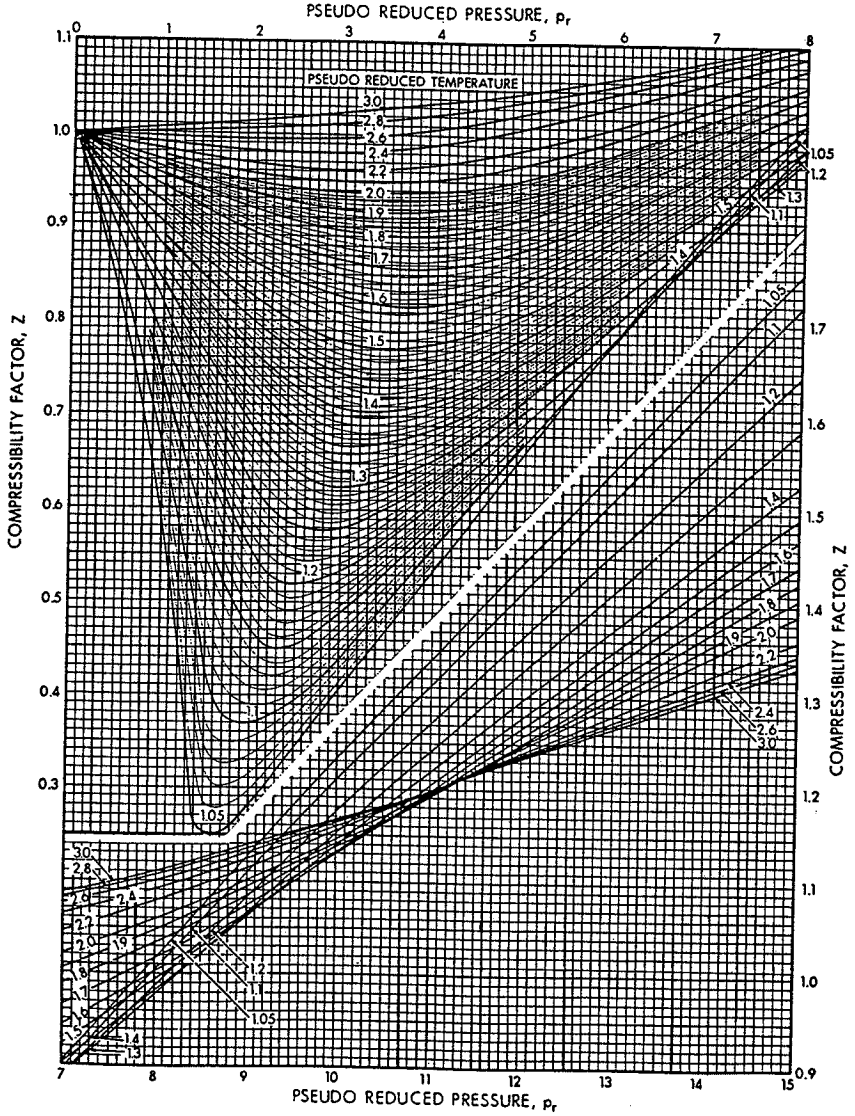

Figure 4-1

The gas deviation factor for natural gases. (*From Standing and Katz, 1942.*)

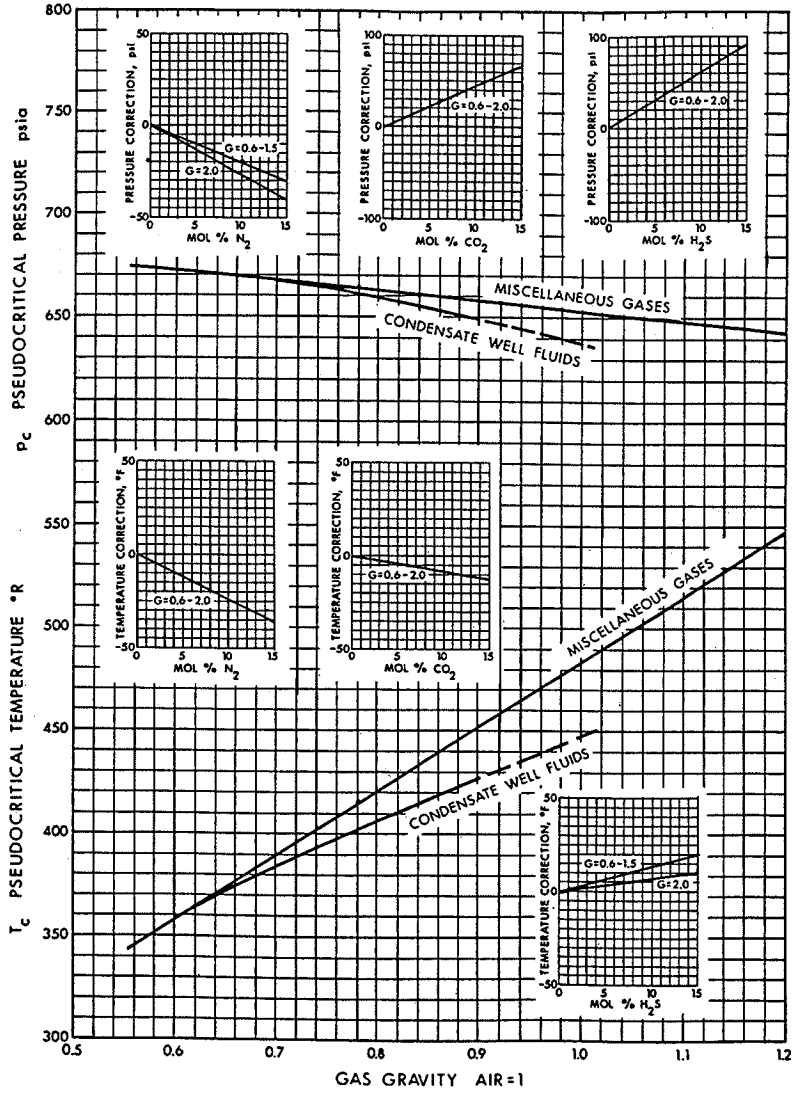

Figure 4-2

Pseudo-critical properties of natural gases. (*From Brown et al., 1948; inserts from Carr et al., 1954.*)

Table 4-2

Calculation of Pseudo-critical Properties for Example 4-2

Compound	y_i	MW_i	$y_i MW_i$	p_{ci}	$y_i p_{ci}$	T_{ci}	$y_i T_{ci}$
C_1	0.875	16.04	14.035	673	588.87	344	301
C_2	0.083	30.07	2.496	709	58.85	550	45.65
C_3	0.021	44.1	0.926	618	12.98	666	13.99
i-C_4	0.006	58.12	0.349	530	3.18	733	4.4
n-C_4	0.002	58.12	0.116	551	1.1	766	1.53
i-C_5	0.003	72.15	0.216	482	1.45	830	2.49
n-C_5	0.008	72.15	0.577	485	3.88	847	6.78
n-C_6	0.001	86.18	0.086	434	0.43	915	0.92
C_7+	0.001	114.23[a]	0.114	361[a]	0.36	1024[a]	1.02
	1.000		18.92		671=p_{pc}		378=T_{pc}

[a]Use the properties of n-octane.

leading to $\gamma_g = 18.92/28.97 = 0.65$. From Fig. 4-2, $p_{pc} = 670$ psi and $T_{pc} = 375°R$, which compare with 671 psi and 378°R calculated explicitly in Example 4-2.

Figure 4-2 can be used as an approximation when only the gas gravity is known or when a quick calculation is indicated.

4-2.2 Presence of Nonhydrocarbon Gases

The inserts in Fig. 4-2 can be used to adjust the pseudo-critical properties of a gas mixture to account for the presence of nonhydrocarbon gases. A gas with a high content of H_2S is often referred to as a "sour" gas. The gas gravity used is for the whole mixture. Of course, a more proper calculation is to calculate the pseudo-critical properties, taking into account the nonhydrocarbon gases, in the same manner as for Example 4-2.

4-2.3 Gas Deviation Factor Correction for Nonhydrocarbon Gases

Wichert and Aziz (1972) have presented a correlation that allows the use of the Standing-Katz graph (Fig. 4-1) in the presence of nonhydrocarbon gases. The pseudo-critical properties, T_{pc} and p_{pc}, can be corrected by

$$T'_{pc} = T_{pc} - \varepsilon_3 \tag{4-6}$$

and

$$p'_{pc} = \frac{p_{pc}\, T'_{pc}}{T_{pc} + y_{H_2S}(1 - y_{H_2S})\varepsilon_3} \tag{4-7}$$

where y_{H_2S} is the mole fraction of hydrogen sulfide and the term ε_3 is a function of the H_2S and CO_2 concentrations and can be obtained from Fig. 4-3.

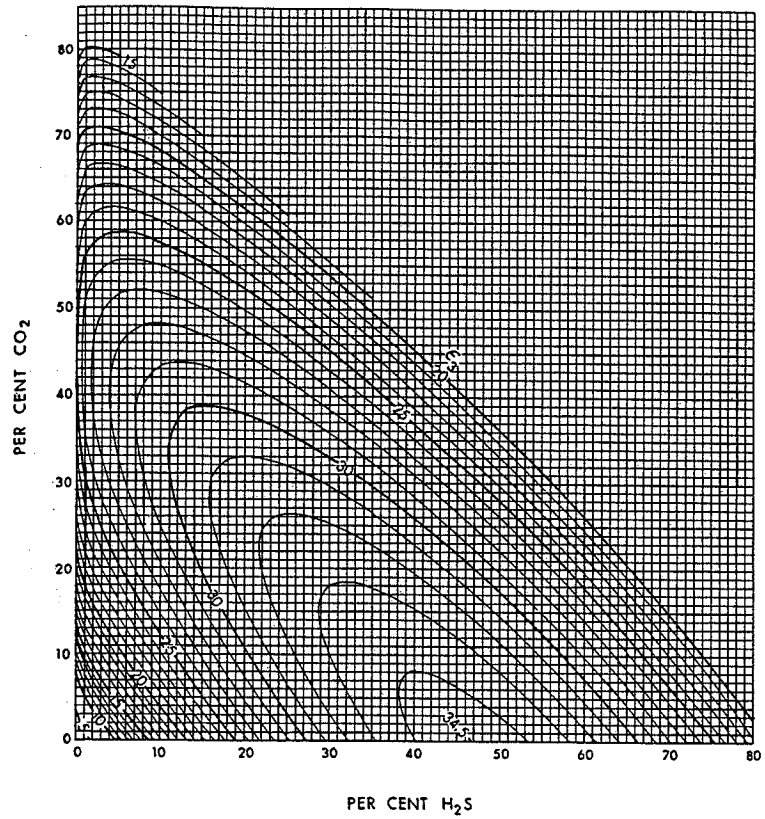

Figure 4-3
Pseudo-critical temperature adjustment factor, ε_3. (*From Wichert and Aziz, 1972.*)

EXAMPLE 4-3
Calculation of the gas deviation factor of a sour gas

A natural gas has the following composition: C_1=0.7410, C_2=0.0245, C_3=0.0007, i-C_4=0.0005, n-C_4=0.0003, i-C_5=0.0001 n-C_5=0.0001, C_6+=0.0005, N_2=0.0592, CO_2=0.021, and H_2S=0.152. Calculate the gas deviation factor, Z, at 180°F and 4000 psi.

Solution The pseudo-reduced properties are calculated as shown in Table 4-3. From Fig. 4-3 and using the compositions of CO_2 and H_2S, the adjustment factor ε_3 = 23.5°R. Therefore, from Eq. (4-6)

$$T'_{pc} = 397.4 - 23.5 = 373.9°\text{R} \tag{4-8}$$

and from Eq. (4-7),

$$p'_{pc} = \frac{(767.44)(373.9)}{397.4 + (0.152)(1 - 0.152)(23.5)} = 716.6 \text{ psi} \tag{4-9}$$

The pseudo-reduced properties are then $T_{pr} = (180 + 460)/373.9 = 1.71$ and $p_{pr} = 4000/716.6 = 5.58$, respectively. From Fig. 4-1, $Z = 0.908$.

Table 4-3

Pseudo-reduced Properties for Example 4-3

Compound	y_i	MW_i	$y_i\ MW_i$	p_{ci}	$y_i\ p_{ci}$	T_{ci}	$y_i\ T_{ci}$
C_1	0.7410	16.04	11.886	673	498.69	344	254.90
C_2	0.0246	30.07	0.740	709	17.44	550	13.53
C_3	0.0007	44.01	0.031	618	0.43	666	0.47
i-C_4	0.0005	58.12	0.029	530	0.26	733	0.37
n-C_4	0.0003	58.12	0.017	551	0.17	766	0.23
i-C_5	0.0001	72.15	0.007	482	0.05	830	0.08
n-C_5	0.0001	72.15	0.007	485	0.05	847	0.08
C_6+	0.0005	100.2	0.050	397	0.20	973	0.49
N_2	0.0592	28.02	1.659	492	29.13	227	13.44
CO_2	0.021	44.01	0.924	1072	22.51	548	11.51
H_2S	0.152	34.08	5.180	1306	198.51	673	102.30
	1.0000		20.53		767.44		397.4

In addition to the calculation shown in this example, it is possible to calculate the pseudo-critical properties from Fig. 4-2. The molecular weight is 20.53, so $\gamma_g = 20.53/28.97 = 0.709$. Therefore, from Fig. 4-2, $T_{pc} = 394°\text{R}$ and $p_{pc} = 667$ psi. These must be corrected by the inserts in Fig. 4-2. Thus,

$$T_{pc} = 394 - 15 - 2 + 20 = 397°\text{R} \tag{4-10}$$

and

$$p_{pc} = 667 - 10 + 5 + 92 = 754 \text{ psi} \tag{4-11}$$

The adjustments are for N_2, CO_2, and H_2S, respectively. The values from Eqs. (4-10) and (4-11) compare with 397.4 and 767, as calculated explicitly. To use the Z graph, these values must be adjusted again using Eqs. (4-6) and (4-7). ◇

4-2.4 Gas Viscosity

Gas viscosity correlations have been presented by a number of authors. The Carr, Kobayashi, and Burrows (1954) correlation has been the most popular. It is presented in Figs. 4-4 and 4-5. Figure 4-4 allows the calculation of the viscosity at any temperature and at a pressure of 1 atm. Figure 4-5 provides the estimation of μ/μ_{1atm}, which is the ratio of the viscosity at an elevated pressure to the viscosity at 1 atm.

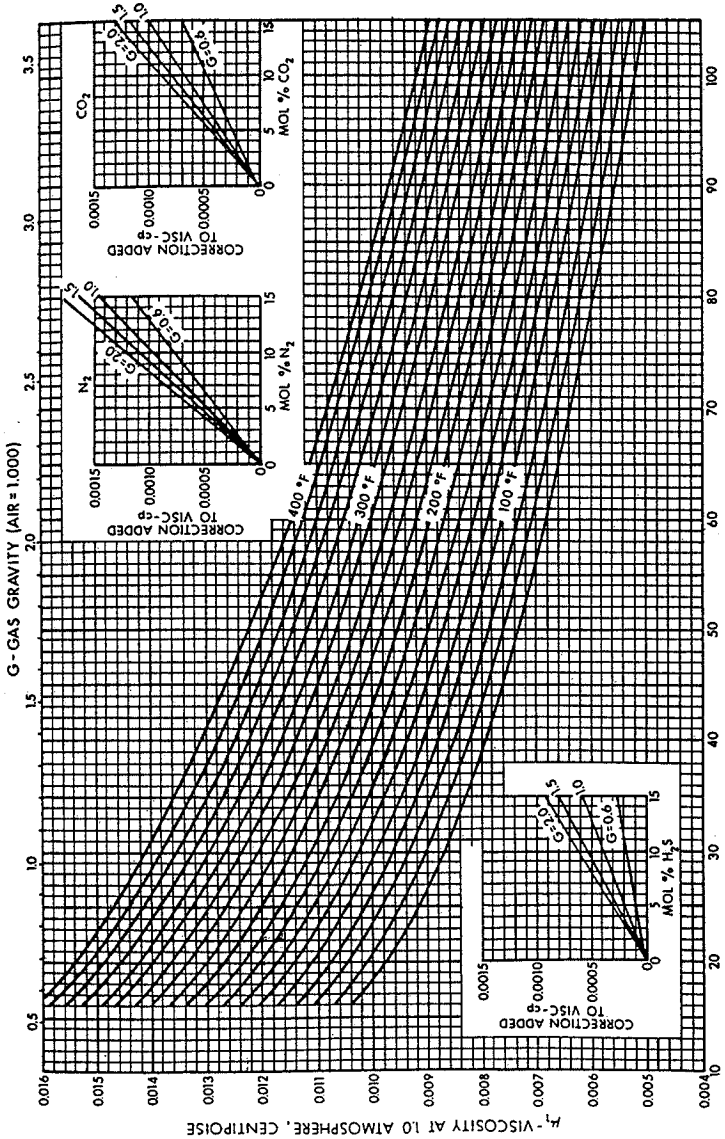

Figure 4-4
Viscosity of natural gases at 1 atm. (*From Carr et al., 1954.*)

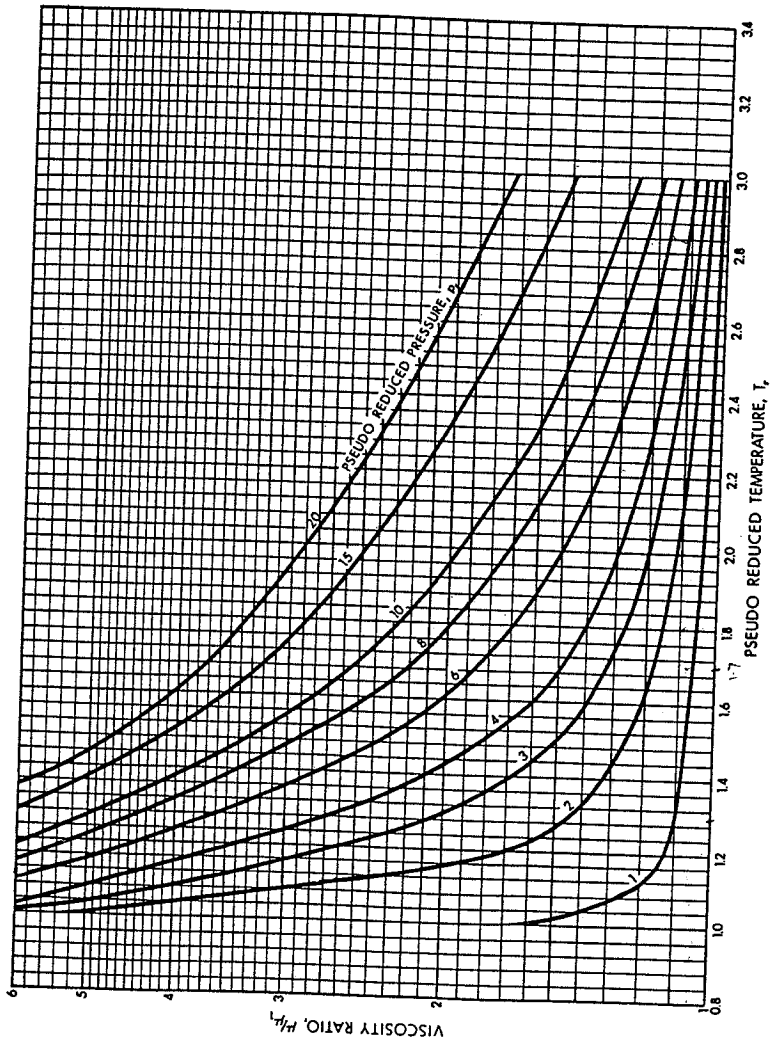

Figure 4-5
Viscosity ratio at elevated pressures and temperatures. (*From Carr et al., 1954.*)

EXAMPLE 4-4
Calculation of the viscosity of a natural gas and a sour gas

Calculate the viscosity at 180°F and 4000 psi of the natural gas described in Examples 4-2 and 4-3.

Solution For the natural gas in Example 4-2, the gas gravity is 0.65 and therefore from Fig. 4-4 and at $T = 180°F$, $\mu_{1atm} = 0.0122$ cp. Since the pseudo-reduced properties are $p_{pr} = 5.96$ and $T_{pr} = 1.69$, then from Fig. 4-5, $\mu/\mu_{1\ atm} = 1.85$ and therefore $\mu = (1.85)(0.0122) = 0.0226$ cp.

For the sour gas in Example 4-3, the gas gravity is 0.709, which results (from Fig. 4-4) in $\mu_{1\ atm} = 0.0119$ cp. However, the presence of nonhydrocarbon gases require the adjustments given in the inserts in Fig. 4-4. These adjustments are to be added to the viscosity value and are 0.0005, 0.0001, and 0.0004 cp for the compositions of N_2, CO_2, and H_2S (in Example 4-3), respectively. Therefore, $\mu_{1\ atm} = 0.0129$ cp. Since p_{pc} and T_{pc} are 767.44 psi and 397.4°R, respectively, then $p_{pr} = 4000/767.44 = 5.2$ and $T_{pr} = 640/397.4 = 1.61$. From Fig. 4-5, $\mu/\mu_{1\ atm} = 1.8$, resulting in $\mu = (0.0129)(1.8) = 0.0232$ cp. ◇

4-2.5 Gas Formation Volume Factor

The formation volume factor relates the reservoir volume to the volume at standard conditions of any hydrocarbon mixture. In the case of a natural gas, the formation volume factor, B_g, can be related with the application of the real gas law for reservoir conditions and for standard conditions. Thus,

$$B_g = \frac{V}{V_{sc}} = \frac{ZnRT/p}{Z_{sc}nRT_{sc}/p_{sc}} \tag{4-12}$$

For the same mass, nR can be cancelled out and, after substitution of $Z_{sc} \approx 1$, $T_{sc} = 60 + 460 = 520°R$, and $p_{sc} = 14.7$ psi, Eq. (4-12) becomes

$$B_g = 0.0283 \frac{ZT}{p} \text{ (res ft}^3\text{/SCF)} \tag{4-13}$$

EXAMPLE 4-5
Initial gas-in-place

Calculate the initial gas-in-place, G_i, in 1900 acres of the reservoir described in Appendix C. Properties are also listed in Appendix C.

Solution The initial formation volume factor, B_{gi}, is given by Eq. (4-13) and therefore

$$B_{gi} = \frac{(0.0283)(0.945)(640)}{4613} = 3.71 \times 10^{-3} \text{ res ft}^3\text{/SCF} \tag{4-14}$$

Then

$$G_i = \frac{Ah\phi S_g}{B_{gi}} \tag{4-15}$$

and

$$G_i = \frac{(43{,}560)(1{,}900)(78)(0.14)(0.73)}{3.71 \times 10^{-3}} = 1.78 \times 10^{11} \text{ SCF} \tag{4-16}$$

◇

4-2.6 Gas Compressibility

The gas compressibility, c_g, often referred to as isothermal compressibility, has an exact thermodynamic expression:

$$c_g = -\frac{1}{V}\left(\frac{\partial V}{\partial p}\right)_T \tag{4-17}$$

For an ideal gas, it can be shown readily that c_g is exactly equal to $1/p$. For a real gas, using Eq. (4-2), the derivative $\partial V/\partial p$ can be evaluated:

$$\frac{\partial V}{\partial p} = -\frac{ZnRT}{p^2} + \frac{nRT}{p}\left(\frac{\partial Z}{\partial p}\right)_T \tag{4-18}$$

Substitution of the volume, V, by its equivalent from Eq. (4-2) and the derivative $\partial V/\partial p$ from Eq. (4-18) into Eq. (4-17) results in

$$c_g = \frac{1}{p} - \frac{1}{Z}\left(\frac{\partial Z}{\partial p}\right)_T \tag{4-19}$$

or, more conveniently,

$$c_g = \frac{1}{p} - \frac{1}{Z\,p_{pc}}\left(\frac{\partial Z}{\partial p_{pr}}\right)_T \tag{4-20}$$

Equation (4-20) is useful because it allows the calculation of the compressibility of a real gas at any temperature and pressure. Needed are the gas deviation factor Z and the *slope* of the Standing-Katz correlation, $\partial Z/\partial p_{pr}$, at the corresponding temperature (i.e., the associated pseudo-reduced temperature curve).

4-3 Approximations of Gas Well Deliverability

The steady-state relationship developed from Darcy's law for an incompressible fluid (oil) was presented as Eq. (2-15) in Chapter 2. That relationship can be adjusted for a natural gas well by converting the flow rate from STB/d to MSCF/d and using an *average* value of the gas formation volume between p_e and p_{wf}. Therefore,

$$\bar{B}_g = \frac{0.0283\bar{Z}\,T}{(p_e + p_{wf})/2} \tag{4-21}$$

and from Eq. (2-15),

$$p_e - p_{wf} = \frac{141.2(1000/5.615)q(\text{MSCF/d})(0.0283)\bar{Z}T\bar{\mu}}{[(p_e + p_{wf})/2]kh}\left(\ln\frac{r_e}{r_w} + s\right) \tag{4-22}$$

which results, after rearrangement and gathering of terms, in

$$p_e^2 - p_{wf}^2 = \frac{1424q\bar{\mu}\bar{Z}T}{kh}\left(\ln\frac{r_e}{r_w} + s\right) \tag{4-23}$$

Equation (4-23) suggests that a gas well production rate is approximately proportional to the pressure squared difference. The properties $\bar{\mu}$ and $\bar{Z}$ are average properties between p_e and p_{wf}. (Henceforth the bars will be dropped for simplicity).

A similar approximation can be developed for pseudo-steady state. It has the form

$$\bar{p}^2 - p_{wf}^2 = \frac{1424q\mu ZT}{kh}\left(\ln 0.472\,\frac{r_e}{r_w} + s\right) \tag{4-24}$$

Equations (4-23) and (4-24) are not only approximations in terms of properties but also because they assume Darcy flow in the reservoir. For reasonably small gas flow rates this approximation is acceptable. A common presentation of Eq. (4-24) [or Eq. (4-23)] is

$$q = C(\bar{p}^2 - p_{wf}^2) \tag{4-25}$$

For larger flow rates, where non-Darcy flow is evident in the reservoir,

$$q = C(\bar{p}^2 - p_{wf}^2)^n \tag{4-26}$$

where $0.5 < n < 1$.

A log-log plot of q versus $\bar{p}^2 - p_{wf}^2$ would yield a straight line with slope equal to n and intercept C.

EXAMPLE 4-6

Flow rate versus bottomhole pressure for a gas well

Graph the gas flow rate versus flowing bottomhole pressure for the well described in Appendix C. Use the steady-state relationship given by Eq. (4-23). Assume that $s = 0$ and $r_e = 1490$ ft ($A = 160$ acres).

Solution Equation (4-23) after substitution of variables becomes

$$2.128 \times 10^7 - p_{wf}^2 = (5.79 \times 10^5)q\bar{\mu}\bar{Z} \tag{4-27}$$

For p_{wf} increments of 500 psi from 1000 psi to 4000 psi, calculations are shown in Table 4-4. (Note that $\mu_{1\text{ atm}} = 0.0122$ cp and $T_{pr} = 1.69$ throughout, since the reservoir is considered isothermal.)

As an example calculation, for $p_{wf} = 3000$, Eq. (4-27) yields

$$q = \frac{2.128 \times 10^7 - 3000^2}{(5.79 \times 10^5)(0.022)(0.903)} = 1.07 \times 10^3 \text{ MSCF/d} \tag{4-28}$$

If the initial μ_i and Z_i were used (i.e., not averages) the flow rate q would be 9.22×10^2 MSCF/d, a deviation of 14%. Figure 4-6 is a graph of p_{wf} versus q for this example. Although this is done in the style of IPR curves as shown in the previous two chapters, this is not a common construction for gas reservoirs, as will be shown in a later section of this chapter.

The "irregular" shape of the curve in Fig. 4-6 reflects the changes in the Z factor, which for this example reaches a minimum between 2500 and 3000 psi. ◇

Table 4-4

Viscosity and Gas Deviation Factor for Example 4-6

p_{wf} (psi)	$p_{pr,w}$	$\mu/\mu_{1\ atm}$[a]	μ (cp)	$\bar{\mu}$ (cp)[b]	Z[c]	$\bar{Z}$[d]
1000	1.49	1.10	0.0134	0.0189	0.920	0.933
1500	2.24	1.20	0.0146	0.0195	0.878	0.912
2000	2.98	1.35	0.0165	0.0205	0.860	0.903
2500	3.73	1.45	0.0177	0.0211	0.850	0.898
3000	4.47	1.60	0.0195	0.022	0.860	0.903
3500	5.22	1.70	0.0207	0.0226	0.882	0.914
4000	5.96	1.85	0.0226	0.0235	0.915	0.930

[a] From Fig. 4-5, following $T_{pr} = 1.69$.

[b] Arithmetic average with $\mu_i = 0.0244$ cp (at $p_e = 4613$ psi).

[c] From Fig. 4-1, following $T_{pr} = 1.69$.

[d] Arithmetic average with $Z_i = 0.945$ (at $p_e = 4613$ psi).

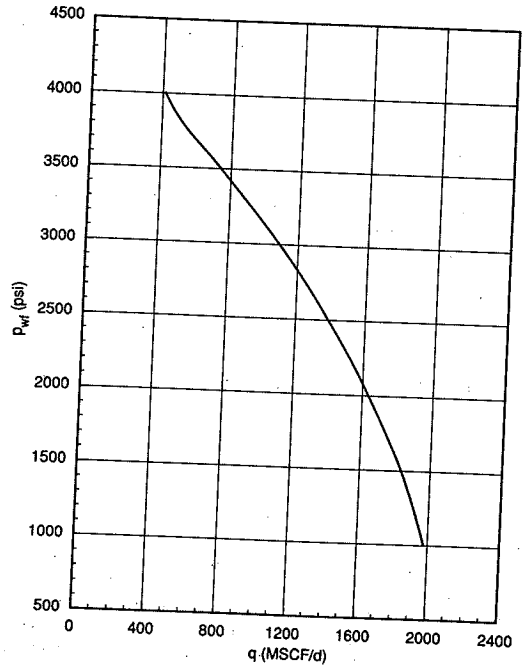

Figure 4-6
Production rate versus flowing bottomhole pressure for the gas well in Example 4-6.

4-4 Gas Well Deliverability for Non-Darcy Flow

A more "exact" deliverability relationship for stabilized gas flow was developed by Aronofsky and Jenkins (1954) from the solution of the differential equation for gas flow through porous media using the Forchheimer (rather than the Darcy) equation for flow. This solution is

$$q(\text{MSCF/d}) = \frac{kh(\bar{p}^2 - p_{wf}^2)}{1424\bar{\mu}\bar{Z}T[\ln(r_d/r_w) + s + Dq]} \tag{4-29}$$

where D is the non-Darcy coefficient and r_d is the Aronofsky and Jenkins "effective" drainage radius, and is time dependent until $r_d = 0.472r_e$. Otherwise

$$\frac{r_d}{r_w} = 1.5\sqrt{t_D} \tag{4-30}$$

where

$$t_D = \frac{0.000264kt}{\phi\mu c_t r_w^2} \tag{4-31}$$

The term Dq is often referred to as the turbulence skin effect, and for certain high rate wells it can be substantial. The non-Darcy coefficient, D, is frequently of the order of 10^{-3} and therefore a rate of 10 MMSCF/d would make the term Dq near the value of $\ln r_d/r_w$ (usually between 7 and 9). Smaller values of q would result in proportionately smaller values of Dq.

Frequently, Eq. (4-29) is rearranged as

$$\bar{p}^2 - p_{wf}^2 = \frac{1424\bar{\mu}\bar{Z}T}{kh}\left(\ln\frac{0.472\,r_e}{r_w} + s\right)q + \frac{1424\bar{\mu}\bar{Z}T\,D}{kh}q^2 \tag{4-32}$$

The first term on the right-hand side of Eq. (4-32) is identical to the one developed earlier [Eq. (4-24)] for Darcy flow. The second term accounts for non-Darcy effects. All multipliers of q and q^2 can be considered as constant, and therefore Eq. (4-32) may take the form

$$\bar{p}^2 - p_{wf}^2 = aq + bq^2 \tag{4-33}$$

In field applications the constants a and b in Eq. (4-33) can be calculated from a "four-point test" where $(\bar{p}^2 - p_{wf}^2)/q$ is graphed on Cartesian coordinates against q. The flowing bottomhole pressure, p_{wf}, is calculated for four different stabilized flow rates. The intercept of the straight line is a, and the slope is b. From b and its definition [see Eq. (4-32)], the non-Darcy coefficient, D can be obtained.

Approximations for the non-Darcy coefficient have been given by a number of authors. In the absence of field measurements, an empirical relationship is proposed:

$$D = \frac{6 \times 10^{-5}\,\gamma k_s^{-0.1}\,h}{\mu r_w h_{\text{perf}}^2} \tag{4-34}$$

where γ is the gas gravity, k_s is the near-wellbore permeability in md, h and h_{perf} the net and perforated thicknesses, both in ft, and μ is the gas viscosity in cp, evaluated at the flowing bottomhole pressure.

EXAMPLE 4-7

Development of a gas well deliverability curve

Use the data in Appendix C and r_e=1490 ft (A = 160 acres), $\bar{\mu}$=0.022 cp, $\bar{Z}$=0.93, and $c_t = 1.5 \times 10^{-4}$ psi^{-1}. Develop a deliverability relationship, and graph the Darcy and non-Darcy components and the correct deliverability curve. Show the absolute open flow potential (AOF), that is, what the flow rate would be if p_{wf}=0. The skin effect is equal to 3, and the non-Darcy coefficient, D, is equal to 4.9×10^{-2} (this is a very large coefficient).

Solution The first step is to calculate the time required for stabilized flow. From Eqs. (4-30) and (4-31),

$$\left(\frac{0.472 r_e}{1.5 r_w}\right)^2 = \frac{0.000264kt}{\phi \mu c_t r_w^2} \tag{4-35}$$

which leads to

$$t = \left[\frac{(0.472)(1490)}{(1.5)(0.328)}\right]^2 \frac{(0.14)(0.022)(1.5 \times 10^{-4})(0.328)^2}{(0.000264)(0.17)}$$
$$= 2260 \text{ hr} = 94 \text{ d} \tag{4-36}$$

Therefore, the stabilized relationship implied by Eq. (4-32) will be in effect after this time.

The coefficients a and b in Eq. (4-33) can be calculated next:

$$a = \frac{(1424)(0.022)(0.93)(640)}{(0.17)(78)}\left[\ln \frac{(0.472)(1490)}{0.328} + 3\right] = 1.5 \times 10^4 \tag{4-37}$$

and

$$b = \frac{(1424)(0.022)(0.93)(640)(4.9 \times 10^{-2})}{(0.17)(78)} = 68.5 \tag{4-38}$$

The deliverability relationship for this well is then

$$\bar{p}^2 - p_{wf}^2 = 1.5 \times 10^4 q + 68.5 q^2 \tag{4-39}$$

Figure 4-7 is a log-log graph of the Darcy and the correct curve incorporating non-Darcy effects.

The absolute open flow potential (AOF) for the correct curve (at p_{wf}=0 and therefore $\bar{p}^2 = 2.13 \times 10^7$ psi^2) is 460 MSCF/d, whereas this AOF, when taking into account only the Darcy flow contribution, would be 1420 MSCF/d. ◇

EXAMPLE 4-8

Estimation of the non-Darcy coefficient

Calculate the non-Darcy coefficient for the well in Appendix C. Assume that k_s is the same as the reservoir permeability, but that h_{perf}=39 ft (half the net thickness). Use a viscosity μ=0.02 cp. What would happen if the near-wellbore permeability is reduced by damage to one-tenth?

Solution From Eq. (4-34) and substitution of the variables in Appendix C,

$$D = \frac{(6 \times 10^{-5})(0.65)(0.17^{-0.1})(78)}{(0.02)(0.328)(39)^2} = 3.6 \times 10^{-4} \text{ (MSCF/d)}^{-1} \tag{4-40}$$

If k_s=0.017 md, then $D = 4.5 \times 10^{-4}$ (MSCF/d)$^{-1}$. ◇

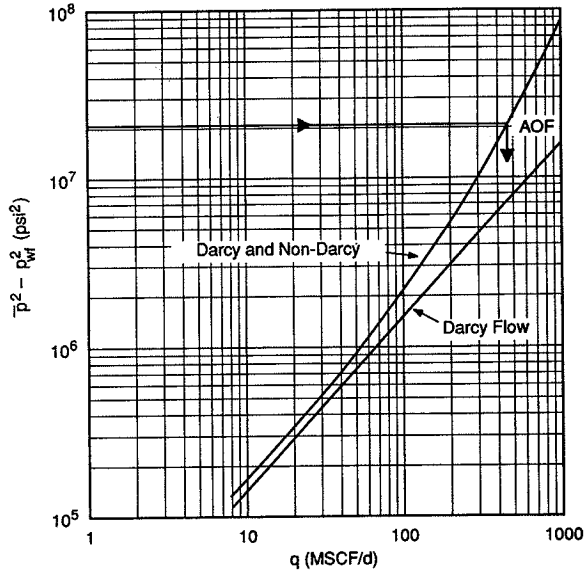

Figure 4-7

Deliverability relationship for the gas well in Example 4-7. Non-Darcy and Darcy effects.

4-5 TRANSIENT FLOW OF A GAS WELL

Gas flow in a reservoir under transient conditions can be approximated by the combination of Darcy's law (rate equation) and the continuity equation. In general,

$$\phi \frac{\partial \rho}{\partial t} = \nabla\left(\rho \frac{k}{\mu} \nabla p\right) \tag{4-41}$$

which in radial coordinates reduces to

$$\phi \frac{\partial \rho}{\partial t} = \frac{1}{r}\frac{\partial}{\partial r}\left(\rho \frac{k}{\mu} r \frac{\partial p}{\partial r}\right) \tag{4-42}$$

From the real gas law,

$$\rho = \frac{m}{V} = \frac{pMW}{ZRT} \tag{4-43}$$

and therefore

$$\phi \frac{\partial}{\partial t}\left(\frac{p}{Z}\right) = \frac{1}{r}\frac{\partial}{\partial r}\left(\frac{k}{\mu Z} r p \frac{\partial p}{\partial r}\right) \tag{4-44}$$

If the permeability k is considered constant, then Eq. (4-44) can be approximated further:

$$\frac{\phi}{k}\frac{\partial}{\partial t}\left(\frac{p}{Z}\right) = \frac{1}{r}\frac{\partial}{\partial r}\left(\frac{p}{\mu Z} r \frac{\partial p}{\partial r}\right) \tag{4-45}$$

Performing the differentiation on the right-hand side of Eq. (4-45) and assuming that Z and μ are either constant or they change uniformly and slowly with pressure, then

$$\frac{1}{\mu Z}\left[\frac{p}{r}\frac{\partial p}{\partial r} + p\frac{\partial^2 p}{\partial r^2} + \left(\frac{\partial p}{\partial r}\right)^2\right] = \text{RHS} \tag{4-46}$$

Via rearrangement and remembering that

$$\frac{1}{2}\frac{\partial^2 p^2}{\partial r^2} = p\frac{\partial^2 p}{\partial r^2} + \left(\frac{\partial p}{\partial r}\right)^2 \tag{4-47}$$

it becomes

$$\frac{1}{2\mu Z}\left(\frac{1}{r}\frac{\partial p^2}{\partial r} + \frac{\partial^2 p^2}{\partial r^2}\right) = \text{RHS} \tag{4-48}$$

Therefore, Eq. (4-45) can be written as

$$\frac{\phi\mu}{kp}\frac{\partial p^2}{\partial t} = \frac{\partial^2 p^2}{\partial r^2} + \frac{1}{r}\frac{\partial p^2}{\partial r} \tag{4-49}$$

For an ideal gas, $c_g = 1/p$ and, as a result, Eq. (4-49) leads to

$$\frac{\partial^2 p^2}{\partial r^2} + \frac{1}{r}\frac{\partial p^2}{\partial r} = \frac{\phi\mu c}{k}\frac{\partial p^2}{\partial t} \tag{4-50}$$

This approximation is in the form of the diffusivity equation [see Eq. (2-2) in Chapter 2] and its solution, under the assumptions listed in this section, could have the shape of the solutions of the equation for oil, presuming that p^2 instead of p is used. This approximation was used in earlier sections of this chapter and was developed independently. Pressure squared differences can be used as a reasonable approximation. However, the assumptions used to derive Eq. (4-50) are limiting and, in fact, they can lead to large errors in high-rate wells with large variations in the flowing pressure. Therefore a better solution can be developed, using the Al-Hussainy and Ramey (1966) real gas pseudo-pressure function.

The real gas pseudo-pressure function, $m(p)$, is defined as

$$m(p) = 2\int_{p_o}^{p} \frac{p}{\mu Z}\, dp \tag{4-51}$$

where p_o is some arbitrary reference pressure (could be zero). The differential pseudo-pressure $\Delta m(p)$, defined as $m(p) - m(p_{wf})$, is then the driving force in the reservoir.

For low pressure it can be shown that

$$2\int_{p_{wf}}^{p_i} \frac{p}{\mu Z}\, dp \approx \frac{p_i^2 - p_{wf}^2}{\mu Z} \tag{4-52}$$

whereas for high pressure (both p_i and p_{wf} higher than 3000 psi),

$$2\int_{p_{wf}}^{p_i} \frac{p}{\mu Z}\, dp \approx 2\frac{\bar{p}}{\bar{\mu}\bar{Z}}(p_i - p_{wf}) \tag{4-53}$$

The real gas pseudo-pressure can be used instead of pressure squared difference in any gas well deliverability relationship (properly adjusted for the viscosity and the gas deviation factor). For example, Eq. (4-29) would be of the form

$$q\ (\text{MSCF/d}) = \frac{kh\left[m(\bar{p}) - m(p_{wf})\right]}{1424T[\ln(0.472r_e/r_w) + s + Dq]} \tag{4-54}$$

Of course, more appropriately, the real gas pseudo-pressure can be used as an integrating factor for an exact solution of the diffusivity equation for a gas. Equation (4-45) can be the basis for this analysis.

From the definition of the real gas pseudo-pressure [Eq. (4-51)] and the chain rule, it can be written readily that

$$\frac{\partial m(p)}{\partial t} = \frac{\partial m(p)}{\partial p}\frac{\partial p}{\partial t} = \frac{2p}{\mu Z}\frac{\partial p}{\partial t} \tag{4-55}$$

Similarly,

$$\frac{\partial m(p)}{\partial r} = \frac{2p}{\mu Z}\frac{\partial p}{\partial r} \tag{4-56}$$

Therefore, Eq. (4-45) becomes

$$\frac{\partial^2 m(p)}{\partial r^2} + \frac{1}{r}\frac{\partial m(p)}{\partial r} = \frac{\phi\,\mu\,c_t}{k}\frac{\partial m(p)}{\partial t} \tag{4-57}$$

The solution of Eq. (4-57) is exactly similar to the solution for the diffusivity equation in terms of pressure. Dimensionless time has (by convention) been defined as

$$t_D = \frac{0.000264kt}{\phi(\mu\, c_t)_i\, r_w^2} \tag{4-58}$$

and dimensionless pressure as

$$p_D = \frac{kh\left[m(p_i) - m(p_{wf})\right]}{1424qT} \tag{4-59}$$

All solutions (such as the line source solution and the wellbore storage and skin effect solution) that have been developed for oil wells using the diffusivity equation in terms of pressure are applicable for a gas well using the real gas pseudo-pressure. For example, the logarithmic approximation to the exponential integral [compare Eqs. (2-3) and (2-5)] would lead to an analogous expression for a natural gas. Thus,

$$q\ (\text{MSCF/d}) = \frac{kh\left[m(p_i) - m(p_{wf})\right]}{1638\,T}\left[\log t + \log\frac{k}{\phi(\mu\, c_t)_i\, r_w^2} - 3.23\right]^{-1} \tag{4-60}$$

This expression can be used for transient IPR curves for a gas well.

EXAMPLE 4-9

Transient IPR for a gas well

With the data for the well in Appendix C, calculate transient IPR curves for 10 days, 3 months, and 1 year.

Solution Table 4-5 gives the viscosity, gas deviation factor, and real gas pseudo-pressure for the reservoir fluid described in Appendix C. For the initial condition of $p_i = 4613$ psi, the real gas pseudo-pressure, viscosity, and gas deviation factor are 1.265×10^9 psi^2/cp, 0.0235 cp, and 0.968, respectively. (These values, derived from numerical fits, are slightly different from the ones in Appendix C.) Figure 4-8 is a graph of pressure versus the real gas pseudo-pressure. This graph will be used for the remainder of the solution to this problem.

Equation (4-60) can be used for the transient IPR calculations if real gas pseudo-pressures are to be used. If pressure squared differences are to be used, then the denominator $1638T$ must be replaced by $1638\mu ZT$.

The gas compressibility can be calculated from Eq. (4-20). At initial conditions,

$$c_g = \frac{1}{4613} - \frac{0.045}{(0.968)(671)} = 1.475 \times 10^{-4} \text{ psi}^{-1} \tag{4-61}$$

The slope 0.045 was obtained from Fig. 4-1 at $T_{pr} = 1.69$ and $p_{pr} = 6.87$. Thus the total system compressibility is

$$c_t \approx S_g c_g \approx 0.73 \times 1.475 \times 10^{-4} = 1.08 \times 10^{-4} \text{ psi}^{-1} \tag{4-62}$$

Hence for time equal to 10 days (240 hr), Eq. (4-60) becomes

$$q = \frac{(0.17)(78)[1.265 \times 10^9 - m(p_{wf})]}{(1638)(640)} \left[\log 240 + \log \frac{(0.17)}{(0.14)(0.0235)(1.08 \times 10^{-4})(0.328)^2} - 3.23\right]^{-1} \tag{4-63}$$

and finally,

$$q = 2.18 \times 10^{-6}[1.265 \times 10^9 - m(p_{wf})] \tag{4-64}$$

Similar expressions can be developed readily for the other times.

Figure 4-9 is a graph of the transient IPR curves for 10 days, 3 months, and 1 year. ◇

Table 4-5

Calculated Viscosity, Gas Deviation Factor, and Real Gas Pseudo-pressure for Example 4-9

p (psi)	μ (cp)	Z	$m(p)$ (psi^2/cp)
100	0.0113	0.991	8.917×10^5
200	0.0116	0.981	3.548×10^6
300	0.0118	0.972	7.931×10^6
400	0.0120	0.964	1.401×10^7
500	0.0123	0.955	2.174×10^7
600	0.0125	0.947	3.108×10^7
700	0.0127	0.939	4.202×10^7
800	0.0130	0.931	5.450×10^7
900	0.0132	0.924	6.849×10^7
1000	0.0135	0.917	8.396×10^7
1100	0.0137	0.910	1.009×10^8
1200	0.0140	0.904	1.192×10^8
1300	0.0142	0.899	1.389×10^8
1400	0.0145	0.894	1.598×10^8
1500	0.0147	0.889	1.821×10^8
1600	0.0150	0.885	2.056×10^8
1700	0.0153	0.881	2.303×10^8
1800	0.0155	0.878	2.562×10^8
1900	0.0158	0.876	2.831×10^8
2000	0.0161	0.874	3.111×10^8
2100	0.0163	0.872	3.401×10^8
2200	0.0166	0.872	3.700×10^8
2300	0.0169	0.871	4.009×10^8
2400	0.0171	0.871	4.326×10^8
2500	0.0174	0.872	4.651×10^8
2600	0.0177	0.873	4.984×10^8
2700	0.0180	0.875	5.324×10^8
2800	0.0183	0.877	5.670×10^8
2900	0.0185	0.879	6.023×10^8
3000	0.0188	0.882	6.381×10^8
3100	0.0191	0.885	6.745×10^8
3200	0.0194	0.889	7.114×10^8
3300	0.0197	0.893	7.487×10^8
3400	0.0200	0.897	7.864×10^8
3500	0.0203	0.902	8.245×10^8
3600	0.0206	0.907	8.630×10^8
3700	0.0208	0.912	9.018×10^8

Table 4-5 (Continued)

Calculated Viscosity, Gas Deviation Factor, and Real Gas Pseudo-pressure for Example 4-9

p (psi)	μ (cp)	Z	$m(p)$ (psi^2/cp)
3800	0.0211	0.917	9.408×10^8
3900	0.0214	0.923	9.802×10^8
4000	0.0217	0.929	1.020×10^9
4100	0.0220	0.935	1.059×10^9
4200	0.0223	0.941	1.099×10^9
4300	0.0226	0.947	1.139×10^9
4400	0.0229	0.954	1.180×10^9
4500	0.0232	0.961	1.220×10^9
4600	0.0235	0.967	1.260×10^9
4700	0.0238	0.974	1.301×10^9
4800	0.0241	0.982	1.342×10^9
4900	0.0244	0.989	1.382×10^9
5000	0.0247	0.996	1.423×10^9

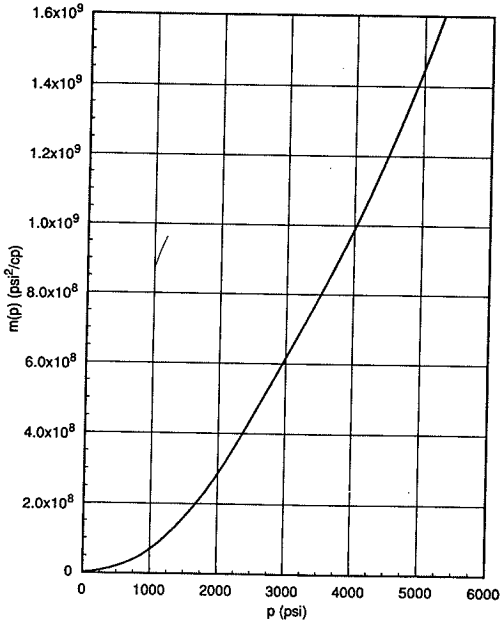

Figure 4-8
Real-gas pseudo-pressure versus pressure for Example 4-8.

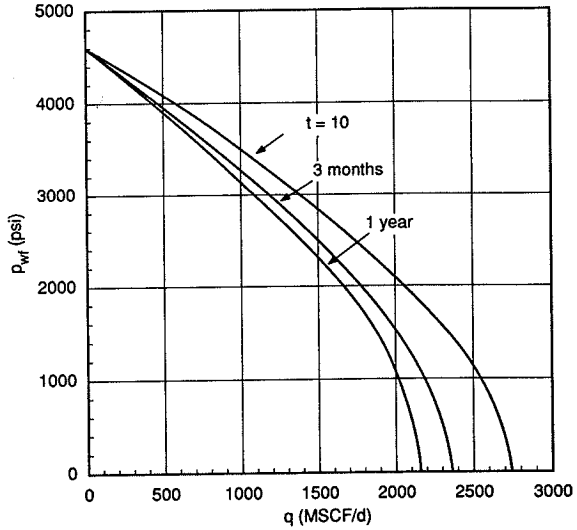

Figure 4-9
Transient IPR curves for Example 4-9.

4-6 Horizontal Well IPR in a Gas Reservoir

Analogs to Eqs. (4-23) (for steady state) and (4-24) (for pseudo-steady state) can be written for a horizontal well. Allowing for turbulence effects, the inflow performance relationships for a horizontal well in a gas reservoir are as follows

For steady state:

$$q = \frac{k_H h(p_e^2 - p_{wf}^2)}{1424\mu ZT\left(\ln\left\{\frac{a+\sqrt{a^2-(L/2)^2}}{L/2}\right\} + \frac{I_{ani}h}{L}\left\{\ln\frac{I_{ani}h}{r_w(I_{ani}+1)} + Dq\right\}\right)} \tag{4-65}$$

For pseudo-steady state:

$$q = \frac{k_H h(\bar{p}^2 - p_{wf}^2)}{1424\,\mu ZT\left(\ln\left\{\frac{a+\sqrt{a^2-(L/2)^2}}{L/2}\right\} + \frac{I_{ani}h}{L}\left\{\ln\frac{I_{ani}h}{r_w(I_{ani}+1)} - \frac{3}{4} + Dq\right\}\right)} \tag{4-66}$$

In both cases, the damage skin effect can be added within the second set of braces in the denominators of Eqs. (4-65) and (4-66). Also, instead of the approximation $(\bar{p}^2 - p_{wf}^2)/\mu Z$,

the real-gas pseudo-pressure difference can be used. As for the horizontal oil well cases, a is the large axis of the drainage ellipsoid and is given by Eq. (2-48) in Chapter 2.

Turbulence effects in horizontal wells usually can be neglected, since they are multiplied by the scaled aspect ratio $I_{ani}h/L$. Thus, the turbulence coefficient calculated in Example 4-8 would be reduced (if L=2000 ft and I_{ani}=1) to 1.3×10^{-7}. This would reduce the associated pressure drop from the near-wellbore turbulence. Equations (4-65) and (4-66) can be used without the terms Dq. An exception would be a horizontal well that is only partially open to flow.

EXAMPLE 4-10
Horizontal gas well deliverability

Calculate the gas well flow rate for a 1000-ft and a 2000-ft horizontal well and compare results with the vertical well in Example 4-6 for p_{wf}=3000 psi. Use the data in Appendix C and Example 4-6. Use $I_{ani} = 3$. In the case of the 2000-ft well, calculate the bottomhole pressure that *could* deliver the same flow rate in the horizontal well as with the 3000 psi bottomhole pressure in the vertical well.

Solution From Eq. (2-48) and r_{eH}=1490 ft, a=1533 ft for L=1000 ft and a=1667 ft for L=2000 ft.

For p_{wf}=3000 psi and p_e=4613 psi, the flow rate for the vertical well is 1.07×10^3 MSCF/d.

From Eq. (4-65), and μ=0.022 cp and Z=0.903 (see Example 4-6), T=640°R, p_e=4613 psi, and p_{wf}=3000 psi,

$$q = \frac{8994}{\ln\left\{\frac{\left[a+\sqrt{a^2-(L/2)^2}\right]}{L/2}\right\} + \left(\frac{I_{ani}h}{L}\right)\ln\left[\frac{I_{ani}h}{r_w(I_{ani}+1)}\right]} \qquad (4\text{-}67)$$

Equation (4-67) results in q=2995 MSCF/d for L=1000 ft and q=5270 MSCF/d for L=2000 ft. These rates compare with q=1070 MSCF/d calculated in Example 4-6 for the vertical well.

To calculate the required drawdowns to deliver 1070 MSCF/d in a 2000-ft well,

$$\frac{4613^2 - p_{wf}^2}{4613^2 - 3000^2} \simeq \frac{1070}{5270} \qquad (4\text{-}68)$$

[Equation (4-68) is not exactly true, since it assumes that $\mu Z \approx$ const. This is not a major issue and would be eliminated if real-gas pseudo-pressures are used.]

From Eq. (4-68), p_{wf}=4334 psi, which implies a much smaller pressure drawdown to deliver the same flow rate. Thus, horizontal wells eliminate both the pressure drop due to turbulence *and* allow considerable decrease in the drawdown, which can have major effects in reducing water coning and sand production. ◇

REFERENCES

1. Al-Hussainy, R., and Ramey, H. J., Jr., "Application of Real Gas Theory to Well Testing and Deliverability Forecasting," *JPT*, 637–642, May 1966.
2. Aronofsky, J. S., and Jenkins, R., "A Simplified Analysis of Unsteady Radial Gas Flow," *Trans. AIME*, **201**, 149–154, 1954.

3. Brown, G. G., Katz, D. L., Oberfell, C. G., and Alden, R. C., "Natural Gasoline and the Volatile Hydrocarbons," NGAA, Tulsa, OK, 1948.
4. Carr, N. L., Kobayashi, R., and Burrows, D. B., "Viscosity of Hydrocarbon Gases Under Pressure," *Trans. AIME*, **201**, 264–272, 1954.
5. Standing, M. B., and Katz, D. L., "Density of Natural Gases," *Trans. AIME*, **146**, 140–149, 1942.
6. Wichert, E., and Aziz, K., "Calculation of Z's for Sour Gases," *Hydrocarbon Processing*, **51** (5), 1972.

PROBLEMS

4-1. It is commonly assumed that Z at standard conditions (p_{sc} = 14.7 psi and T_{sc}=60°F) is equal to 1. Show whether this is a good assumption using the fluid data in Appendix C. Plot the volume versus pressure of 1 lb-mol of this gas from atmospheric pressure to the reservoir pressure, which is equal to 4613 psi. (Use a temperature of 180°F.) Comment on the shape of this curve.

4-2. In Eq. (4-23) and other deliverability expressions, the product $\bar{\mu}\bar{Z}$ is at the average pressure between p_e and p_{wf}. Temperature is constant. With the data in Appendix C, show the difference in the production rate if the $\bar{\mu}\bar{Z}$ is calculated at the initial pressure rather than the average. Flowing bottomhole pressures are 1000 and 3000 psi.

4-3. Suppose that the composition of the gas in Appendix C was altered. While all gases other than methane remain the same and with the same composition, assume that 20% of the methane is replaced by CO_2 or H_2S. Calculate the change in the gas deviation factor and viscosity at reservoir conditions. Compare with the exclusively hydrocarbon mixture. What comments can you make on the results?

4-4. In Appendix C the initial reservoir pressure is 4613 psi. Suppose that the drainage area is 4000 acres. What would be the initial gas-in-place at the given pressure, and what would be the residual gas if the pressure dropped to 3000 psi?

4-5. What would be the difference in the production rate at the two instances described in Problem 4-4? Assume that p_{wf}=1000 psi.

4-6. Assume that a gas well reached stabilized flow as described by Eq. (4-32). With the data in Appendix C and r_e = 1490 ft, $\bar{\mu}$=0.022 cp, Z=0.93, $c_t = 1.5 \times 10^{-4}$psi^{-1}, D=10^{-3}, and p_{wf}=1000 psi, compute the expected flow rate for the given permeability of 0.17 md and for permeabilities 10 and 100 times larger.

4-7. The real-gas pseudo-pressure data in Table 4-5 can be used for a number of calculations along with Eq. (4-60). With the data in Appendix C, calculate the required flowing bottomhole pressure after 6 months if the flow rate is 1000 MSCF/d.

4-8. What would the flow rate be for the bottomhole pressure calculated in Problem 4-7 if the permeability is 17 md (instead of 0.17 md)?

4-9. Calculate a cumulative production curve for the gas well in Appendix C, assuming infinite-acting behavior [Eq. (4-60)] for 1 year. Bottomhole pressure is 2000 psi. What fraction of the original gas-in-place will be produced if A=4000 acres?

4-10. How would the cumulative production obtained in Problem 4-9 compare with a calculated value using the pseudo-steady-state relationship? (That is, assume that the well reached pseudo-steady state and that for the duration of the year the "average" pressure was equal to the initial reservoir pressure, p_i=4613 psi). Comment on the results.

CHAPTER 5

The Near-Wellbore Condition and Damage Characterization; Skin Effects

5-1 INTRODUCTION

The semilogarithmic nature of the pressure-versus-distance relationship presented in Chapter 2 [Eq. (2-11)] suggests that the condition of the near-wellbore region is critical. Van Everdingen and Hurst (1949) introduced the skin effect as a means to characterize this region with a steady-state pressure difference Δp_s, which is proportional to the skin effect [Eq. (2-12)].

Mathematically, the skin effect has no physical dimension and is analogous to the film coefficient in heat transfer. Conveniently, though, the additional pressure drop associated with the skin effect is defined in terms of the same group of constants as the dimensionless solutions to the pressure drop in the porous medium. The skin effect can then be added to $\ln(r_e/r_w)$ for steady state, $\ln(0.472r_e/r_w)$ for pseudo-steady state, or p_D for the transient solutions. Therefore, the sum becomes proportional to the total (reservoir plus near-wellbore) pressure drop.

The well skin effect is a composite variable. In general, any phenomenon that causes a distortion of the flow lines from the perfectly normal to the well direction or a restriction to flow (which could be viewed as a distortion at the pore-throat scale) would result in a positive value of the skin effect.

Positive skin effects can be created by "mechanical" causes such as partial completion (i.e., a perforated height that is less than the reservoir height) and inadequate number of perforations (again, causing a distortion of flow lines), by phase changes (relative permeability reduction to the main fluid), turbulence, and, of course, by damage to the natural reservoir permeability.

A negative skin effect denotes that the pressure drop in the near-wellbore zone is less than would have been from the normal, undisturbed, reservoir flow mechanisms. Such a negative skin effect, or a negative contribution to the total skin effect, may be the result

of matrix stimulation (the near-wellbore permeability exceeds the natural value), hydraulic fracturing, or a highly inclined wellbore.

In Chapter 2, the impact of the skin effect was quantified through the concept of the effective wellbore radius, r'_w [Eq. (2-18)]. A positive skin value has the effect of reducing the wellbore radius, whereas a negative skin has the opposite effect. An interesting, extreme case is when a large conductivity fracture penetrates the well. As is shown in Chapter 16, this situation leads to an effective wellbore radius equal to half the fracture half-length.

It is important to realize that there may be high contrasts in skin along the length of the productive interval. This is particularly likely in wells in which production from two or more dissimilar and vertically separated intervals is commingled. Different formation properties (permeability, stress, mechanical stability, fluids) and differential pressure create an environment for uneven damage due to drilling fluid invasion, poor perforation cleanup, and other causes. Similar reasoning also implies the likelihood of uneven damage along a horizontal borehole. Chapter 15 describes stimulation techniques for commingled wells.

In this chapter, the skin effect, its components, and the estimation of the mechanical contributions are presented in detail. Skin effects characterizing the damage and the (potentially) partial stimulation around a horizontal well are also introduced. Finally, the nature of formation damage and the types of formation damage are outlined as a precursor to the appropriate choice of matrix stimulation treatments.

5-2 HAWKINS' FORMULA

While the skin effect is dimensionless, the associated damage zone is not. Figure 5-1 is a typical depiction of the near-wellbore condition, with r_s and k_s being the penetration of damage and permeability, respectively. Outside this zone the reservoir remains undisturbed, with permeability k.

A well-known equation relating the skin effect and the above variables has been presented by Hawkins (1956) and is frequently referred to as Hawkins' formula. Figure 5-2 provides an easy means for the development of this relationship.

If the near-wellbore permeability is the reservoir permeability (i.e., no damage), then a steady-state pressure drop between the outer boundary pressure (p_s) and the well would result in a $p_{wf,\text{ideal}}$ given by

$$p_s - p_{wf,\text{ideal}} = \frac{q\mu}{2\pi kh} \ln \frac{r_s}{r_w} \tag{5-1}$$

If, though, the near-wellbore permeability is altered to k_s, then the real bottomhole pressure is related by

$$p_s - p_{wf,\text{real}} = \frac{q\mu}{2\pi k_s h} \ln \frac{r_s}{r_w} \tag{5-2}$$

The difference between $p_{wf,\text{ideal}}$ and $p_{wf,\text{real}}$ is exactly the pressure drop due to the skin effect, Δp_s, which was given in Chapter 2 by Eq. (2-12). Therefore, from Eqs. (5-1), (5-2), and (2-12),

$$\frac{q\mu}{2\pi kh} s = \frac{q\mu}{2\pi k_s h} \ln \frac{r_s}{r_w} - \frac{q\mu}{2\pi kh} \ln \frac{r_s}{r_w} \tag{5-3}$$

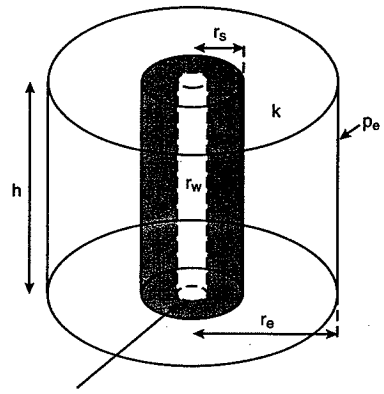

Figure 5-1
Near-wellbore zone with altered permeability.

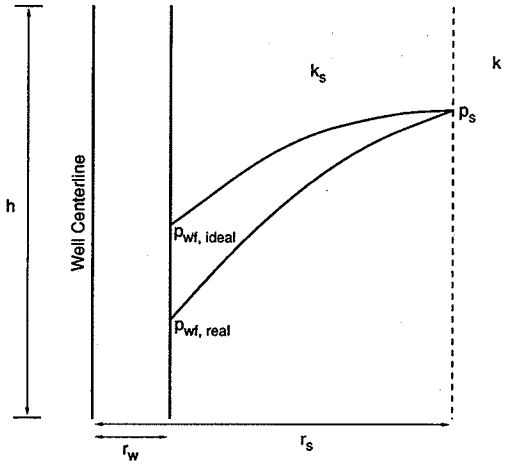

Figure 5-2
Near-wellbore zone. Ideal and real flowing bottomhole pressures.

and simply

$$s = \left(\frac{k}{k_s} - 1\right) \ln \frac{r_s}{r_w} \tag{5-4}$$

Equation (5-4) is Hawkins' formula and is useful in assessing the relative effects of permeability impairment and the penetration of damage.

EXAMPLE 5-1

Permeability impairment versus damage penetration

Assume that a well has a radius r_w equal to 0.328 ft and a penetration of damage 3 ft beyond the well (i.e., r_s=3.328 ft). What would be the skin effect if the permeability impairment results in k/k_s equal to 5 and 10, respectively. What would be the required penetration of damage to provide the same skin effect as the latter case but with k/k_s=5?

Solution From Eq. (5-4), k/k_s=5, and the given r_s and r_w,

$$s = (5-1)\ln\frac{3.328}{0.328} = 9.3 \tag{5-5}$$

For k/k_s=10 and r_s=3.328 then, similarly, s=20.9.

However, if s=20.9 and k/k_s=5, then

$$r_s = r_w e^{20.9/4} = 61 \text{ ft} \tag{5-6}$$

This exercise suggests that permeability impairment has a much larger effect on the value of the skin effect than the penetration of damage. Except for a phase change-dependent skin effect, a penetration of damage such as the one calculated in Eq. (5-6) is impossible. Thus, skin effects derived from well tests (frequently ranging between 5 and 20) are likely to be caused by substantial permeability impairment very near the well. This is a particularly important point in the design of matrix stimulation treatments. ◇

EXAMPLE 5-2

Pressure drop in the near-wellbore zone versus in the reservoir

With the skin effects calculated in Example 5-1, compare the portions of the pressure drop due to damage within the near-wellbore zone versus the total pressure drop. (The difference will be in the reservoir). Assume that A=640 acres (r_e=2980 ft).

Solution The ratio of the pressure drop due to damage within the near-wellbore zone to the total pressure drop is proportional to $s/[\ln(r_e/r_w) + s]$ (for steady-state flow), as can be seen readily from Eq. (2-13). For r_e=2980 ft and r_w=0.328 ft, $\ln r_e/r_w$=9.1. This quantity will be largely constant for almost all drainage/wellbore radius combinations. The skin effects calculated in Example 5-1 for the 3-ft damage zone are 9.3 and 20.9, suggesting that the portions of the total pressure drop due to damage would be 0.51 and 0.70, respectively. Possible elimination of these skin effects, at a constant $p_e - p_{wf}$, would result in production rate increases of 104% and 233%, respectively. ◇

5-3 THE SKIN COMPONENTS

The total skin effect for a well, s, consists of a number of components. Generally these can be added together, and therefore

$$s = s_d + s_{c+\theta} + s_p + \sum s_{\text{pseudo}} \tag{5-7}$$

where s_d is the damage skin, $s_{c+\theta}$ is the skin due to partial completion and slant, and s_p is the perforation skin effect. All "pseudo-skins" are grouped together within the summation sign.

These pseudo-skins include all phase- and rate-dependent effects. Following is a discussion of these skin effects. Subsequent sections will discuss the mechanical skin components.

The rate-dependent effect has been discussed in Chapter 4 in conjunction with the turbulence in high-rate gas producers. (It can also affect very high-rate oil wells.) This skin effect is equal to Dq, where D is the non-Darcy coefficient (see Section 4-4). The skin effect extracted from a well test in a high-rate gas well is likely to be larger and, in certain instances, much larger than the non-rate-dependent skin effect. Thus, from a well test, an apparent skin, s' can be obtained that is equal to

$$s' = s + Dq \tag{5-8}$$

Tests performed at several different rates can be used to isolate the skin effect, s. A plot such as the one shown in Fig. 5-3 of s' versus q suggests that s is the intercept and D is the slope. This is the proper manner for the field determination of D and the forecast of the impact of the rate-dependent skin on future well production.

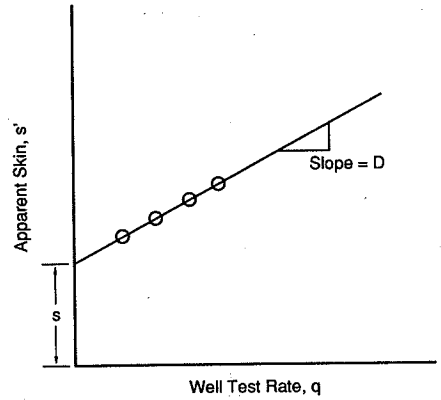

Figure 5-3
Field determination of skin effect and non-Darcy coefficient from multiple-rate well tests.

Phase-dependent skin effects are associated with phase changes because of the near-wellbore pressure gradient.

In the case of oil wells, if the flowing bottomhole pressure is below the bubble-point pressure, then a gas saturation will form, causing a reduction in the effective permeability to oil even if the gas phase is not mobile. A version of Hawkins' formula with k/k_s substituted by the ratio of the effective (or relative) permeabilities can be used.

A similar phenomenon can be observed in the case of gas retrograde condensate reservoirs, where liquid is formed around the well, causing a reduction in the gas permeability.

This is a particularly adverse occurrence. While in the case of gas that is formed in an oil reservoir the gas will reenter solution at an elevated pressure (e.g., as the pressure builds up when the well is shut in), in the case of a gas condensate reservoir much of the formed condensate will not reenter the gas. Several authors (Fussell, 1973; Cvetkovic et al., 1990) have studied the process of liquid condensate deposition with time and have shown that permeability impairment to gas in gas condensate reservoirs is not eliminated following a shut-in. Thus, after reopening the well, the gas flow rate is still affected by the near-wellbore permeability reduction. A method to combat this skin effect is by the injection of neat natural gas, which may redissolve the condensate and displace it into the reservoir. This "huff and puff" operation can be repeated periodically.

The skin effects in Eq. (5-7) are those that cause an alteration of the flow near a vertical or inclined well in a radial reservoir. Other skin effects have been introduced for other flow configurations, especially associated with fractures (choke, fracture face) or fracture-to-well contact as in the case of a largely vertical fracture intersecting a horizontal well transversely. These skins are addressed in Chapter 18. However, the reader must be alerted here that once a hydraulic fracture is generated, most pretreatment skin effects (s_d, $s_{c+\theta}$, s_p) are bypassed and have no impact on the posttreatment well performance.

Similar phenomena may be in effect in the case of a deeply penetrating perforation that may bypass the near-wellbore damage. Phase- and rate-dependent skin effects are either eliminated or contribute in the calculation of the fracture skin effects. In general, it is not correct to add pretreatment skin effects to any postfracture skin effects.

5-4 Skin from Partial Completion and Slant

Frequently, wells are partially completed; that is, the height that is open to the formation is smaller than the reservoir height. Sometimes this is known as partial penetration. This situation can occur as a result of a bad perforation job or by deliberate undercompletion to retard or avoid coning effects. In certain modern reservoir testing practices, partial penetration may be created to form early-time spherical flow to allow the calculation of the vertical permeability. Late-time radial flow would have the distinguishing characteristics of partial completion. If the well is not completed at the middle of the reservoir height, the problem will be aggravated further.

In all of these cases the ensuing bending of the flow lines would result in a skin effect denoted by s_c. The smaller the perforated interval compared to the reservoir height and the more skewed the completion, the larger the skin effect would be. If the completed interval is 75% of the reservoir height or more, this skin effect becomes negligible.

While partial completion generates a positive skin effect by reducing the well exposure to the reservoir, a deviated well results in the opposite. The larger the angle of slant, the larger the negative contribution to the total skin effect will be. The skin effect due to slant is denoted by s_θ, and the composite skin from partial completion and slant is denoted by $s_{c+\theta}$.

Cinco-Ley et al. (1975) solved the problem semianalytically and presented tables of these skin effects for various combinations of partial completion, completion elevation, and well deviation. Figure 5-4 shows the relevant variables. Here h_w is the perforated height, z_w is the elevation of the perforation midpoint from the base of the reservoir, h is the reservoir height, θ is the angle of well deviation, and r_w is the well radius.

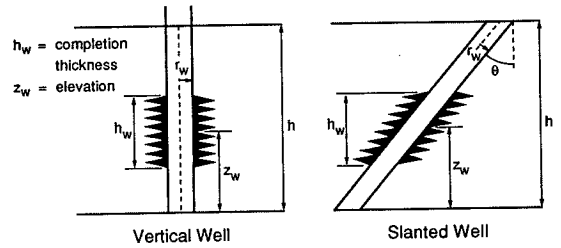

Figure 5-4
Inclined, partially completed, and skewed well configuration. (*After Cinco-Ley et al., 1975.*)

Tables 5-1 and 5-2 give the results for reservoir dimensionless thicknesses, h_D (=h/r_w) equal to 100 and 1000, respectively. Relevant ratios are z_w/h (elevation ratio) and h_w/h (completion ratio). The composite skin effect, $s_{c+\theta}$, and the individual parts, s_c and s_θ, are listed. As can be seen, the absolute value of s_θ increases with the angle of slant and in certain cases may render $s_{c+\theta}$ negative in spite of the positive s_c associated with a partial completion. Finally, the corresponding skins for the same completion and elevation ratios are larger when h_D=1000 rather than 100, reflecting the longer penetration of flowline distortion.

EXAMPLE 5-3
Partial penetration and slant skin effect

A well with a radius r_w=0.328 ft is completed in a 33-ft reservoir. In order to avoid severe water coning problems, only 8 ft are completed and the midpoint of the perforations is 29 ft above the base of the reservoir. Calculate the skin effect due to partial completion for a vertical well. What would be the composite skin effect if θ=45°?

Repeat this problem for h=330 ft, h_w=80 ft, and z_w=290 ft.

Solution The dimensionless reservoir thickness h_D is h/r_w=33/0.328 ≈ 100, the elevation ratio is z_w/h=29/33 = 0.875, and the completion ratio is h_w/h=8/33 = 0.25. From Table 5-1 for a vertical well (θ=0°), $s_{c+\theta}$=8.6, of which s_c=8.6 and s_θ=0. If θ=45°, then s_c=8.6 but s_θ=-2.7, resulting in $s_{c+\theta} \approx 6$.

If h_D=330/0.328 ≈ 1000 although all other ratios are the same, from Table 5-2, $s_{c+\theta}$=15.7 for the vertical well and $s_{c+\theta}$=10.4 for the 45° slant. ◇

Table 5-1

Skins from Partially Penetrating Slanted Wells (h_D = 100)[a]

$\theta°$	h_D	z_W/h	h_w/h	$s_{\theta+c}$	s_c	s_θ
0	100	0.95	0.1	20.810	20.810	0
15				20.385	20.810	-0.425
30				18.948	20.810	-1.861
45				16.510	20.810	-4.299
60				12.662	20.810	-8.147
75				6.735	20.810	-14.074
0	100	0.8	0.1	15.809	15.809	0
15				15.449	15.809	-0.36
30				14.185	15.809	-1.623
45				12.127	15.809	-3.682
60				8.944	15.809	-6.864
75				4.214	15.809	-11.594
0	100	0.6	0.1	15.257	15.257	0
15				14.898	15.257	-0.359
30				13.636	15.257	-1.621
45				11.583	15.257	-3.674
60				8.415	15.257	-6.842
75				3.739	15.257	-11.517
0	100	0.5	0.1	15.213	15.213	0
15				14.854	15.213	-0.359
30				13.592	15.213	-1.620
45				11.540	15.213	-3.673
60				8.372	15.213	-6.841
75				3.699	15.213	-11.514
0	100	0.875	0.25	8.641	8.641	0
15				8.359	8.641	-0.282
30				7.487	8.641	-1.154
45				5.968	8.641	-2.673
60				3.717	8.641	-4.924
75				0.464	8.641	-8.177
0	100	0.75	0.25	7.002	7.002	0
15				6.750	7.002	-0.251
30				5.969	7.002	-1.032
45				4.613	7.002	-2.388
60				2.629	7.002	-4.372
75				-0.203	7.002	-7.206
0	100	0.6	0.25	6.658	6.658	0
15				6.403	6.658	-0.249
30				5.633	6.658	-1.024
45				4.290	6.658	-2.447
60				2.337	6.658	-4.32
75				0.418	6.658	-7.076
0	100	0.5	0.25	6.611	6.611	0
15				6.361	6.611	-0.249
30				5.587	6.611	-1.023

Table 5-1 (Continued)

Skins from Partially Penetrating Slanted Wells (h_D = 100)[a]

$\theta°$	h_D	z_W/h	h_w/h	$s_{\theta+c}$	s_c	s_θ
45				4.245	6.611	-2.365
60				2.295	6.611	-4.315
75				-0.451	6.611	-7.062
0	100	0.75	0.5	3.067	3.067	0
15				2.878	3.067	-0.189
30				2.308	3.067	-0.759
45				1.338	3.067	-1.729
60				-0.082	3.067	-3.150
75				-2.119	3.067	-5.187
0	100	0.6	0.5	2.430	2.430	0
15				2.254	2.430	-0.176
30				1.730	2.430	-0.700
45				0.838	2.430	-1.592
60				-0.466	2.430	-2.897
75				-2.341	2.430	-4.772
0	100	0.5	0.5	2.369	2.369	0
15				2.149	2.369	-0.175
30				1.672	2.369	-0.697
45				0.785	2.369	-1.584
60				-0.509	2.369	-2.879
75				-2.368	2.369	-4.738
0	100	0.625	0.75	0.924	0.924	0
15				0.778	0.924	-0.145
30				0.337	0.924	-0.587
45				-0.411	0.924	-1.336
60				-1.507	0.924	-2.432
75				-3.099	0.924	-4.024
0	100	0.5	0.75	0.694	0.694	0
15				0.554	0.694	-0.139
30				0.134	0.694	-0.560
45				-0.581	0.694	-1.275
60				-1.632	0.694	-2.326
75				-3.170	0.694	-3.864
0	100	0.5	1	0	0	0
15				-0.128	0	-0.128
30				-0.517	0	-0.517
45				-1.178	0	-1.178
60				-2.149	0	-2.149
75				-3.577	0	-3.577

[a]From Cinco-Ley et al., 1975.

Table 5-2

Skins from Partially Penetrating Slanted Wells (h_D = 1000)[a]

$\theta°$	h_D	z_W/h	h_w/h	$s_{\theta+c}$	s_c	s_θ
0	1000	0.95	0.1	41.521	41.521	0
15				40.343	41.521	-1.178
30				36.798	41.521	-4.722
45				30.844	41.521	-10.677
60				22.334	41.521	-19.187
75				10.755	41.521	-30.766
0	1000	0.8	0.1	35.840	35.840	0
15				34.744	35.840	-1.095
30				31.457	35.840	-4.382
45				25.973	35.840	-9.867
60				18.261	35.840	-17.599
75				8.003	35.840	-27.837
0	1000	0.6	0.1	35.290	35.290	0
15				34.195	35.290	-1.095
30				30.910	35.290	-4.380
45				25.430	35.290	-9.860
60				17.710	35.290	-17.580
75				7.522	35.290	-27.768
0	1000	0.5	0.1	35.246	35.246	0
15				34.151	35.246	-1.095
30				30.866	35.246	-4.380
45				25.386	35.246	-9.860
60				17.667	35.246	-17.579
75				7.481	35.246	-27.765
0	1000	0.875	0.25	15.733	15.733	0
15				15.136	15.733	-0.597
30				13.344	15.733	-2.389
45				10.366	15.733	-5.367
60				6.183	15.733	-9.550
75				0.632	15.733	-15.101
0	1000	0.75	0.25	14.040	14.040	0
15				13.471	14.040	-0.569
30				11.770	14.040	-2.270
45				8.959	14.040	-5.081
60				5.047	14.040	-8.993
75				-0.069	14.040	-14.109
0	1000	0.6	0.25	13.701	13.701	0
15				13.133	13.701	-0.568
30				11.437	13.701	-2.264
45				8.638	13.701	-5.063

Table 5-2 (Continued)

Skins from Partially Penetrating Slanted Wells (h_D = 1000)[a]

$\theta°$	h_D	z_W/h	h_w/h	$s_{\theta+c}$	s_c	s_θ
60				4.753	13.701	-8.948
75				-0.288	13.701	-13.989
0	1000	0.5	0.25	13.655	13.655	0
15				13.087	13.655	-0.568
30				11.391	13.655	-2.264
45				8.593	13.655	-5.062
60				4.711	13.655	-8.944
75				-0.321	13.655	-13.976
0	1000	0.75	0.5	5.467	5.467	0
15				5.119	5.467	-0.348
30				4.080	5.467	-1.387
45				2.363	5.467	-3.104
60				-0.031	5.467	-5.498
75				-3.203	5.467	-8.670
0	1000	0.6	0.5	4.837	4.837	0
15				4.502	4.837	-0.335
30				3.503	4.837	-1.334
45				1.858	4.837	-2.979
60				-0.424	4.837	-5.261
75				-0.431	4.837	-8.268
0	1000	0.5	0.5	4.777	4.777	0
15				4.443	4.777	-0.334
30				3.446	4.777	-1.331
45				1.806	4.777	-2.971
60				-0.467	4.777	-5.244
75				-3.458	4.777	-8.235
0	1000	0.625	0.75	1.735	1.735	0
15				1.483	1.735	-0.252
30				0.731	1.735	-1.004
45				-0.512	1.735	-2.247
60				-2.253	1.735	-3.988
75				-4.595	1.735	-6.330
0	1000	0.5	0.75	1.508	1.508	0
15				1.262	1.508	-0.246
30				0.528	1.508	-0.980
45				-0.683	1.508	-2.191
60				-2.380	1.508	-3.888
75				-4.665	1.508	-6.173
0	1000	0.5	1	0	0	0
15				-0.206	0	-0.206
30				-0.824	0	-0.824
45				-1.850	0	-1.850
60				-3.298	0	-3.298
75				-5.282	0	-5.282

[a]From Cinco-Ley et al., 1975.

5-5 Well Perforation and Skin Effect

Modern well perforation is done with perforating guns that are attached either to a wireline or to coiled tubing. Figure 5-5 shows a schematic of a gun system with the shape charges arranged in a helical pattern. This pattern allows good perforation density with small phasing (i.e., the angle between adjoing perforations.)

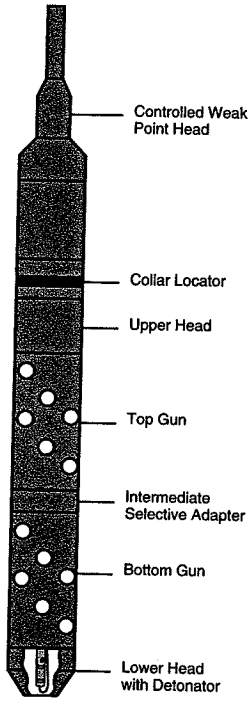

Figure 5-5
Drawing of a perforating gun string. (*Courtesy of Schlumberger.*)

The perforating string contains a cable head, a correlation device, a positioning device, and the perforation guns. The cable head connects the string to the wireline and at the same time provides a weak point at which to disconnect the cable if problems arise. The correlation device is used to identify the exact position with a previously run correlation log, and frequently it locates casing collars.

The positioning device orients the shots toward the casing for more optimum perforation geometry.

The perforating guns are loaded with shape charges, which consist of the case, the explosive, and the liner, as shown in Fig. 5-6. Electric current initiates an explosive wave; the phases of the detonation are shown in Fig. 5-6. Perforations with a diameter between 0.25 and 0.4 in. and a tunnel between 6 and 12 in. are typically created.

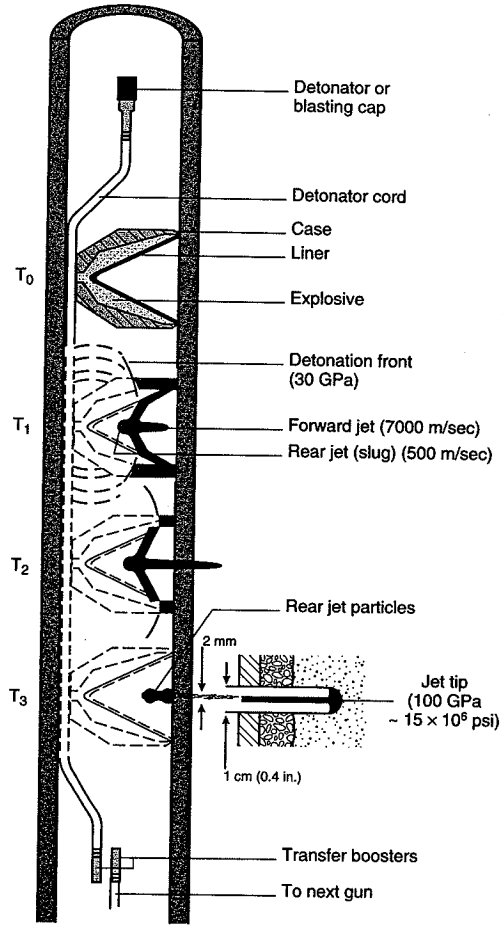

Figure 5-6
Detonation process of a shaped charge. (*Courtesy of Schlumberger.*)

Perforating is usually done at underbalance; that is, the pressure in the well is less than the reservoir pressure. This facilitates immediate flowback following the detonation, carrying the debris and resulting in a cleaner perforation tunnel. The dimensions, number, and phasing of perforations have a controlling role in well performance.

5-5.1 Calculation of the Perforation Skin Effect

Karakas and Tariq (1988) have presented a semianalytical solution for the calculation of the perforation skin effect, which they divide into components: the plane flow effect, s_H; the vertical converging effect, s_V; and the wellbore effect, s_{wb}. The total perforation skin effect is then

$$s_p = s_H + s_V + s_{wb} \tag{5-9}$$

Figure 5-7 gives all relevant variables for the calculation of the perforation skin. These include the well radius, r_w, the perforation radius, r_{perf}, the perforation length, l_{perf}, the angle of perforation phasing, θ, and, very important, the distance between the perforations, h_{perf}, which is exactly inversely proportional to the perforation density (e.g., 2 shots per foot, SPF, result in h_{perf}=0.5 ft). Below, the method of estimating the individual components of the perforation skin is outlined.

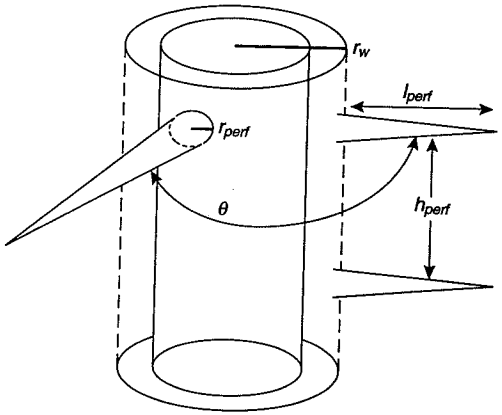

Figure 5-7
Well variables for perforation skin calculation. (*From Karakas and Tariq, 1988.*)

Calculation of s_H.

$$s_H = \ln \frac{r_w}{r'_w(\theta)} \tag{5-10}$$

where $r'_w(\theta)$ is the effective wellbore radius and is a function of the phasing angle θ:

$$r'_w(\theta) = \begin{cases} \dfrac{l_{\text{perf}}}{4} & \text{for } \theta = 0 \\ a_\theta \left(r_w + l_{\text{perf}}\right) & \text{for } \theta \neq 0 \end{cases} \tag{5-11}$$

The constant a_θ depends on the perforation phasing and can be obtained from Table 5-3. This skin effect is negative (except for θ=0), but its total contribution is usually small.

Table 5-3

Constants for Perforation Skin Effect Calculation[a]

Perforation Phasing	a_θ	a_1	a_2	b_1	b_2	c_1	c_2
0° (360°)	0.250	-2.091	0.0453	5.1313	1.8672	1.6E−1	2.675
180°	0.500	-2.025	0.0943	3.0373	1.8115	2.6E−2	4.532
120°	0.648	-2.018	0.0634	1.6136	1.7770	6.6E−3	5.320
90°	0.726	-1.905	0.1038	1.5674	1.6935	1.9E−3	6.155
60°	0.813	-1.898	0.1023	1.3654	1.6490	3.0E−4	7.509
45°	0.860	-1.788	0.2398	1.1915	1.6392	4.6E−5	8.791

[a]From Karakas and Tariq, 1988.

Calculation of s_V. To obtain s_V, two dimensionless variables must be calculated:

$$h_D = \frac{h_{\text{perf}}}{l_{\text{perf}}} \sqrt{\frac{k_H}{k_V}} \tag{5-12}$$

where k_H and k_V are the horizontal and vertical permeabilities, respectively, and

$$r_D = \frac{r_{\text{perf}}}{2h_{\text{perf}}} \left(1 + \sqrt{\frac{k_V}{k_H}}\right) \tag{5-13}$$

The vertical pseudo-skin is then

$$s_V = 10^a h_D^{b-1} r_D^b \tag{5-14}$$

with

$$a = a_1 \log r_D + a_2 \tag{5-15}$$

and

$$b = b_1 r_D + b_2 \tag{5-16}$$

The constants a_1, a_2, b_1, and b_2 are also functions of the perforation phasing and can be obtained from Table 5-3. The vertical skin effect, s_V, is potentially the largest contributor to s_p; for small perforation densities, that is, large h_{perf}, s_V can be very large.

Calculation of s_{wb}. For the calculation of s_{wb}, a dimensionless quantity is calculated first:

$$r_{wD} = \frac{r_w}{l_{perf} + r_w} \tag{5-17}$$

Then

$$s_{wb} = c_1 e^{c_2 r_{wD}} \tag{5-18}$$

The constants c_1 and c_2 also can be obtained from Table 5-3.

EXAMPLE 5-4
Perforation skin effect

Assume that a well with r_w=0.328 ft is perforated with 2 SPF, r_{perf}=0.25 in., (0.0208 ft), l_{perf}=8 in. (0.667 ft), and θ=180°. Calculate the perforation skin effect if k_H/k_V=10.

Repeat the calculation for θ=0° and θ=60°.

If θ=180°, show the effect of the horizontal-to-vertical permeability anisotropy with k_H/k_V=1.

Solution From Eq. (5-11) and Table 5-3 (θ=180°),

$$r'_w(\theta) = (0.5)(0.328 + 0.667) = 0.5 \tag{5-19}$$

Then, from Eq. (5-10),

$$s_H = \ln \frac{0.328}{0.5} = -0.4 \tag{5-20}$$

From Eq. (5-12) and remembering that h_{perf}=1/SPF,

$$h_D = \frac{0.5}{0.667}\sqrt{10} = 2.37 \tag{5-21}$$

and

$$r_D = \frac{0.0208}{(2)(0.5)}\left(1 + \sqrt{0.1}\right) = 0.027 \tag{5-22}$$

From Eqs. (5-15) and (5-16) and the constants in Table 5-3,

$$a = -2.025 \log(0.027) + 0.0943 = 3.271 \tag{5-23}$$

and

$$b = (3.0373)(0.027) + 1.8115 = 1.894 \tag{5-24}$$

From Eq. (5-14),

$$s_V = 10^{3.271} 2.37^{0.894} 0.027^{1.894} = 4.3 \tag{5-25}$$

Finally, from Eq. (5-17),

$$r_{wD} = \frac{0.328}{0.667 + 0.328} = 0.33 \tag{5-26}$$

and with the constants in Table 5-3 and Eq. (5-18),

$$s_{wb} = \left(2.6 \times 10^{-2}\right) e^{(4.532)(0.33)} = 0.1 \tag{5-27}$$

The total perforation skin effect is then

$$s_p = -0.4 + 4.3 + 0.1 = 4 \tag{5-28}$$

If θ=0°, then s_H=0.3, s_V=3.6, s_{wb}=0.4, and therefore s_p=4.3.

If θ=60°, then s_H=-0.9, s_V=4.9, s_{wb}=0.004, and s_p=4.

For θ=180° and k_H/k_V=1, s_H and s_{wb} do not change; s_V, though, is only 1.2, leading to s_p=0.9, reflecting the beneficial effects of good vertical permeability even with relatively unfavorable perforation density (2 SPF). ◇

EXAMPLE 5-5
Perforation density

Using typical perforation characteristics such as r_{perf}=0.25 in. (0.0208 ft), l_{perf}=8 in. (0.667 ft), θ=120°, in a well with r_w=0.328 ft, develop a table of s_V versus perforation density for permeability anisotropies k_H/k_V=10, 5, and 1.

Solution Table 5-4 presents the skin effect s_V for perforation densities from 0.5 SPF to 4 SPF using Eqs. (5-12) to (5-16). For high perforation densities (3 to 4 SPF), this skin contribution becomes small. For low shot densities, this skin effect in normally anisotropic formations can be substantial. For the well in this problem, s_H=-0.7 and s_{wb}=0.04. ◇

Table 5-4

Vertical Contribution to Perforation Skin Effect

	s_V		
SPF	$k_H/k_V = 10$	$k_H/k_V = 5$	$k_H/k_V = 1$
0.5	21.3	15.9	7.7
1	10.3	7.6	3.6
2	4.8	3.5	1.3
3	3.0	2.1	0.9
4	2.1	1.5	0.6

5-5.2 Near-Well Damage and Perforations

Karakas and Tariq (1988) have also shown that damage and perforations can be characterized by a composite skin effect,

$$(s_d)_p = \left(\frac{k}{k_s} - 1\right)\left(\ln\frac{r_s}{r_w} + s_p\right) + s_p = (s_d)_o + \frac{k}{k_s}\, s_p \tag{5-29}$$

if the perforations terminate within the damage zone ($l_{\text{perf}} < r_s$). In Eq. (5-29), $(s_d)_o$ is the open-hole equivalent skin effect given by Hawkins' formula [Eq. (5-4)]. If the perforations terminate outside the damage zone, then

$$(s_d)_p = s'_p \tag{5-30}$$

where s'_p is evaluated at a modified perforation length l'_{perf} and a modified radius, r'_w. These are

$$l'_{\text{perf}} = l_{\text{perf}} - \left(1 - \frac{k_s}{k}\right) r_s \tag{5-31}$$

and

$$r'_w = r_w + \left(1 - \frac{k_s}{k}\right) r_s \tag{5-32}$$

These variables are used in Eqs. (5-10) to (5-18) for the calculation of the skin effects contributing to the composite skin effect in Eq. (5-30).

5-6 Horizontal Well Damage Skin Effect

In Eq. (2-54), the damage skin effect, s'_{eq}, was added to the horizontal well production rate equation. Frick and Economides (1991) developed equations for the skin effect that reflect the damage around a horizontal well. Figure 5–8 describes the shape of damage along and normal to a horizontal well.

Permeability anisotropy would generate an elliptical shape normal to the well. The shape of damage depends on the permeability anisotropy index I_{ani} given by Eq. (2-47). Simulated responses are shown in Fig. 5-8 for three different values of I_{ani}.

The time of exposure during drilling and completion would result in a truncated elliptical cone with the larger base near the vertical section of the well. Also, during production, the pressure profile in the well would imply the largest pressure gradient normal to the well trajectory nearer to the vertical section. Therefore, production-induced damage would also be elliptical.

The geometry of the shape of damage resulted in a skin effect analogous to Hawkins' formula for a vertical well:

$$s'_{\text{eq}} = \left(\frac{k}{k_s} - 1\right) \ln\left[\frac{1}{(I_{\text{ani}} + 1)}\sqrt{\frac{4}{3}\left(\frac{a^2_{H,\max}}{r_w^2} + \frac{a_{H,\max}}{r_w} + 1\right)}\right] \tag{5-33}$$

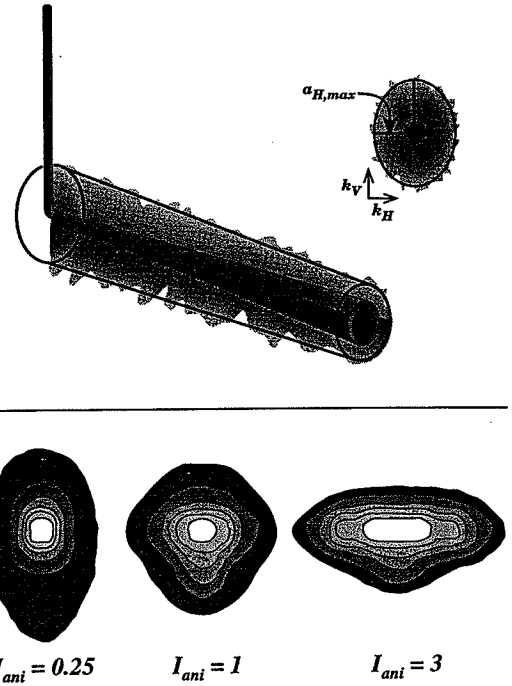

Figure 5-8
Distribution of damage along and normal to a horizontal well. Effect of vertical-to-horizontal permeability anisotropy.

where $a_{H,\max}$ is the largest horizontal axis (near the vertical section) of the cone of damage (Fig. 5-8).

Equation (5-33) assumes no damage at the end of the well.

The skin effect can be added to the denominator of the horizontal well production rate equation, but it must be multiplied by hI_{ani}/L, called the anisotropic scaled aspect ratio, as shown in Eq. (2-54).

The matrix stimulation of a horizontal well is a far more involved process than the stimulation of a vertical well. First, the required volumes are much larger, as would be expected. Second, the placement of the stimulation fluids along the well is much more difficult. Therefore, techniques have been developed to handle both difficulties. These include mechanical methods of stimulation fluid distribution (coiled tubing, zonal isolation devices) and deliberate understimulation (leaving a collar of damage around a stimulated zone) or

deliberate undercompletion of the well (i.e., leaving sections that are not perforated vis à vis other sections that are fully stimulated). These issues will be addressed in Chapters 14 and 15.

If a collar of damage with a large axis of the damage ellipse, $a_{sH,\max}$ is left surrounding a zone of stimulation with a maximum axis of the stimulation ellipse, $a_{iH,\max}$, then the resulting skin effect is

$$s'_{eq} = \frac{1}{2}\left(\frac{k}{k_s} - 1\right) \ln\left(\frac{a^2_{sH,\max}}{r_w^2} + \frac{a_{sH,\max}}{r_w} + 1\right) + \frac{1}{2}\left(\frac{k}{k_i} - \frac{k}{k_s}\right) \ln\left(\frac{a^2_{iH,\max}}{r_w^2} + \frac{a_{iH,\max}}{r_w} + 1\right) - \left(\frac{k}{k_i} - 1\right) \ln\left[(I_{\text{ani}} + 1)\sqrt{\frac{3}{4}}\right] \tag{5-34}$$

In Eq. (5-34), k, k_s, and k_i are the virgin, damaged, and stimulated permeabilities, respectively. This expression is for the situation where the shape of stimulation mimics the shape of damage. This is likely the case for a sandstone reservoir, where the stimulation fluids will penetrate the pore space, eliminating foreign damage.

If the reservoir is a carbonate, then it is possible that the shape of the stimulated zone, affected by reaction kinetics and not by flow in the porous medium, is cylindrical (a subject of current research), and the partial stimulation skin effect with elliptical damage but cylindrical stimulated zone (with $r_{i,\max}$, the largest radius) is

$$s'_{eq} = \frac{1}{2}\left(\frac{k}{k_s} - 1\right) \ln\left(\frac{a^2_{sH,\max}}{r_w^2} + \frac{a_{sH,\max}}{r_w} + 1\right) + \frac{1}{2}\left(\frac{k}{k_i} - \frac{k}{k_s}\right) \ln\left[I_{\text{ani}}\left(\frac{r^2_{i,\max}}{r_w^2} + \frac{r_{i,\max}}{r_w} + 1\right)\right] - \left(\frac{k}{k_i} - 1\right) \ln\left[(I_{\text{ani}} + 1)\sqrt{\frac{3}{4}}\right] \tag{5-35}$$

EXAMPLE 5-6

Calculation of a horizontal well skin effect and impact on well performance

Use the data for the well in Appendix A, L=2000 ft, p_{wf}=3500 psi, r_w=0.328 ft, and A=640 acres. Show the productivity index ratio between a vertical and a horizontal well versus skin effect. (Note that I_{ani}=3.)

Also plot the skin effect versus penetration of damage ($a_{H,\max}$) for different permeability impairment ratios (k/k_s=20, 10, and 5).

Solution Application of the given variables to Eq. (2-54) for the productivity index (J) of a horizontal well and division by the productivity index for a vertical well [Eq. (2-19) with $s = 0$] results in the productivity index ratio between a damaged horizontal and an undamaged vertical well. This is plotted in Fig. 5-9. These results are significant because they denote that the productivity index benefits (either increased production rate or decreased drawdown) may be affected greatly by damage in the horizontal well that is not removed.

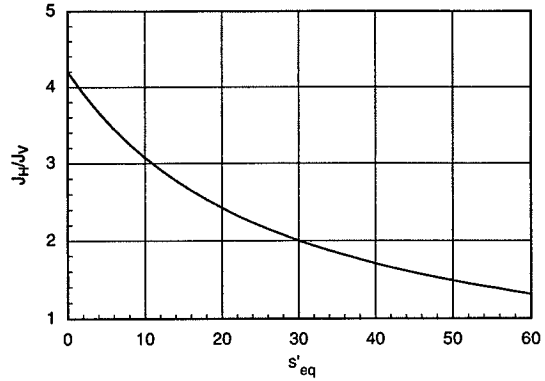

Figure 5-9

Productivity index ratios between a damaged horizontal and an undamaged vertical well (Example 5-6).

The range of skin effects, s'_{eq}, plotted on the abscissa of Fig. 5-9 are reasonable, as can be seen in Fig. 5-10. Here penetrations of damage (maximum axis of the ellipse near the vertical section of the well) up to 5 ft and plausible permeability impairment ratios are plotted. Equivalent skin effects up to 30 can be calculated. ◇

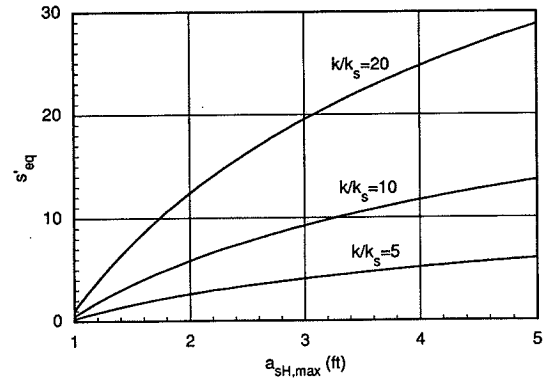

Figure 5-10

Horizontal well equivalent skin effect for range of penetrations of damage and permeability impairments (Example 5-6).

EXAMPLE 5-7

Partial stimulation in a horizontal well

Calculate the partial stimulation effects (i.e., the reduction in the skin effect) if k/k_s=20, $a_{sH,\max}$=5 ft, and k/k_i=1 for a sandstone reservoir. Show on the same graph the productivity index ratio (between a horizontal and a vertical well) improvement if L=2000 ft and all other variables are as for Example 5-6.

Solution Figure 5-11 is a summary of the results of this example. The maximum penetration of stimulation, $a_{iH,\max}$, is on the abscissa. The posttreatment skin effect is obtained with Eq. (5-34), assuming that the shape of stimulation imitates the shape of damage. This shape would require the appropriate distribution of the stimulation fluids. When $a_{iH,\max}=a_{sH,\max}$, then $s'_{eq}=0$. The corresponding J_H/J_V can be used in an economic evaluation of the benefits versus costs of the treatment. ◇

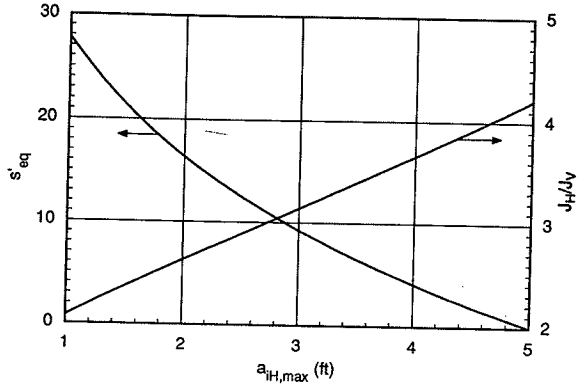

Figure 5-11

Partial stimulation of a horizontal well and associated productivity index ratio increase (over that of a vertical well). The original maximum penetration of damage $a_{sH,\max}$ is 5 ft. The maximum penetration of stimulation is $a_{iH,\max}$ (Example 5–7).

5-7 Formation Damage Mechanisms

In the next two sections, the underlying causes of formation damage and the source of damage during well operations are described. Formation damage can be caused by plugging of the pore spaces by solid particles, by mechanical crushing or disaggregation of the porous media, or by fluid effects such as the creation of emulsions or changes in relative permeability. Plugging of pores by solid particles is the most pervasive of these mechanisms and can result from many sources, including the injection of solids into the formation, dispersion of clays present in the rock, precipitation, and the growth of bacteria.

5-7.1 Particle Plugging of Pore Spaces

A porous medium is a complex assembly of irregularly shaped mineral grains with void spaces (pores), which are likewise irregularly shaped and distributed, providing the pathway for fluid transport. Scanning electron microscope (SEM) photographs, such as that shown in Fig. 5-12 (Krueger, 1986), have illustrated the tortuous nature of the pore spaces and the common presence of small particles, called fines, in naturally occurring porous media. This complicated structure can be idealized as a collection of relatively large chambers, the pore bodies, connected by narrower openings, the pore throats. The permeability of the medium is controlled largely by the number and conductivity of the pore throats.

Figure 5-12

Scanning electron micrograph of pore space in a sandstone. (*From Krueger, 1986.*)

When fines are moving through a porous medium, they will often be deposited, and if this deposition occurs in the pore throats, a severe reduction in the permeability may result. Figure 5-13 (Schechter, 1992) illustrates possible modes of particle entrapment. Large particles transported to the surface of the porous medium will bridge over the surface pores and form a filter cake external to the porous medium. An example of surface bridging and

filter cake formation is the mud cake formed on the wellbore wall during drilling operations. Such a filter cake greatly reduces the ability to transport fluids to or from the porous medium, but is also relatively easily removed or bypassed.

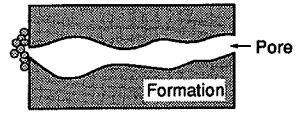

Cake Formation by Large Particles

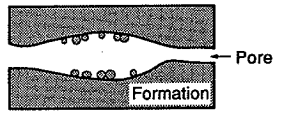

Surface Deposits of Adhering Particles

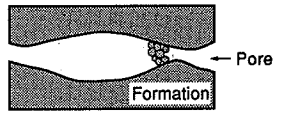

Plugging Type Deposits

Figure 5-13
Modes of particle entrapment. (*From Schechter, 1992.*)

Small fines passing through the porous medium may adhere to the surfaces of the pore bodies, resulting in little permeability impairment, or may bridge in the pore throats, effectively plugging the pore. Bridging can occur when the particles are on the order of one-third to one-seventh the size of the pore throat, or larger; thus, the relative sizes of the fines and the pore throats is a primary factor in determining whether formation damage due to fines movement will occur.

EXAMPLE 5-8
Change in permeability due to pore throat plugging

A capillary model of pore structure (Schechter and Gidley, 1969) describes the porous medium as a collection of capillary tubes, with their sizes given by a pore size density function, $\eta(A)$, defined as the number of pores per unit volume with a cross-sectional area between A and $A + dA$. With this model, the permeability is

$$k = F \int_0^\infty A^2 \eta(A)\, dA \tag{5-36}$$

where F is the average pore length multiplied by a tortuosity factor. For Berea sandstone, the pore size density function is approximately

$$\eta = 0 \qquad \text{for } A < 10^{-10} \text{ cm}^2 \tag{5-37}$$

$$\eta = A^{-2} \qquad \text{for } 10^{-10} \text{ cm}^2 < A < 10^{-4} \text{ cm}^2 \tag{5-38}$$

$$\eta = 0 \qquad \text{for } A > 10^{-4} \text{ cm}^2 \tag{5-39}$$

where η is the number of pores per cubic centimeter. It can be assumed that this describes the distribution of pore throats.

Particles with a radius of 5μm (5×10^{-4} cm) are injected into the porous medium described above until the permeability no longer changes. If particles bridge over and completely plug all pore throats that are less than seven times larger than the particles, what would be the ratio of the permeability after injection of the particles to that before?

Solution All pores small enough to be plugged will be eliminated from the pore size distribution contributing to permeability. The smallest pore that would be plugged is seven times the size of the particles or has a radius of (7) (5×10^{-4} cm) or 3.5×10^{-3} cm. Thus, the area of the smallest effective pore in the damaged porous medium is

$$A_d = \pi(r_d)^2 = \pi(3.5 \times 10^{-3} \text{ cm})^2 = 3.85 \times 10^{-5} \text{ cm}^2 \tag{5-40}$$

The ratio of the damaged to the original permeability is then

$$\frac{k_d}{k} = \frac{F \int_{A_d}^{A_{\max}} A^2 \eta\, dA}{F \int_{A_{\min}}^{A_{\max}} A^2 \eta\, dA} = \frac{\int_{A_d}^{A_{\max}} A^2 (A^{-2}) dA}{\int_{A_{\min}}^{A_{\max}} A^2 (A^{-2}) dA} = \frac{A_{\max} - A_d}{A_{\max} - A_{\min}} \tag{5-41}$$

so

$$\frac{k_d}{k} = \frac{10^{-4} - (3.85 \times 10^{-5})}{10^{-4} - 10^{-10}} = 0.61 \tag{5-42}$$

Most of the pores would be plugged by the particles; however, since the largest pores are not affected, the permeability impairment is not severe. Using Hawkins' formula and assuming that r_s=3 ft and r_w=0.5 ft, this permeability impairment would result in a skin effect approximately equal to 1. ◇

5-7.2 Mechanisms for Fines Migration

The fines responsible for particle plugging may come from external sources or may originate in the porous medium itself. Fines in the porous medium may be mobilized by a change in the chemical composition of the water or simply mechanically entrained due to the shear forces applied by the moving fluid. Formation damage is often caused by the dispersion of fine clay particles when the salinity of the interstitial water is reduced or the ionic composition is changed. Thus, any fluids that may come in contact with the producing formation (drilling fluid filtrate, completion fluids, stimulation fluids, etc.) should have an ionic composition that will be nondamaging.

Numerous studies have shown that a sudden decrease in salinity of the brine flowing through a sandstone will cause formation damage by dispersing clay particles. This phenomenon, called water sensitivity, depends on the cations present in the brine, the pH, and the rate of salinity change. In general, monovalent cations are much more damaging than

divalent or trivalent cations; the water sensitivity is greatest for NaCl brines and decreases in the order Na > K > NH_4. The higher the pH, the more sensitive the porous medium will be to salinity changes. To prevent clay dispersion because of a salinity change, any aqueous fluid that may come in contact with the formation should have a minimum concentration of a monovalent ion or a sufficient fraction of divalent ions. Commonly used criteria to prevent damage are for brines to contain at least 2 wt% of KCl or that at least one-tenth of the cations are divalent cations. The reader is referred to Schechter (1992) for a complete discussion of clay particle dispersion.

5-7.3 Chemical Precipitation

Precipitation of solids from the brine or the crude oil in the formation can cause severe formation damage when these solids plug the pore spaces. The formed precipitates can be either inorganic compounds precipitating from brine or organic species precipitating from the oil; in either case, the precipitation can be due to changes in temperature or pressure near the wellbore or from alterations in the composition of the phase by injected fluids.

Inorganic precipitates causing formation damage are usually divalent cations, such as calcium or barium, combined with carbonate or sulfate ions. The ionic species in solution in the connate water in a reservoir are initially in chemical equilibrium with the formation minerals. A change in the composition of the brine may lead to precipitation.

For example, the equilibrium reaction between calcium and bicarbonate ions can be expressed as

$$Ca^{2+} + 2HCO_3^- \longleftrightarrow CaCO_3(s) + H_2O + CO_2(g) \tag{5-43}$$

If the brine is initially saturated with respect to calcium bicarbonate, an increase in the concentration of species on the left side of the equation or a decrease in the concentration of any species on the right side of the equation will drive the reaction to the right and calcium carbonate will precipitate. Addition of calcium ions will cause calcium carbonate to precipitate; likewise, removal of CO_2 will lead to precipitation. Thus, in a reservoir with high bicarbonate concentrations, injection of fluids high in calcium, such as $CaCl_2$ completion fluids, may cause severe formation damage. Likewise, as the pressure decreases near a production well, CO_2 will be liberated from the brine, and again precipitation may occur. Precipitation of $CaCO_3$ from the bicarbonate-rich connate water is a common source of formation damage at the Prudhoe Bay field (Tyler et al., 1984).

The most common organic species that cause formation damage are waxes (paraffins) and asphaltenes. Waxes are long-chain hydrocarbons that precipitate from certain crude oils when the temperature is reduced, or the oil composition changes because of the liberation of gas as the pressure is reduced. Asphaltenes are high-molecular-weight aromatic and napthenic compounds that are thought to be colloidally dispersed in crude oils (Schechter, 1992). This colloidal state is stabilized by the presence of resins in the crude oil; when these resins are removed, the asphaltenes can flocculate, creating particles large enough to cause

formation damage. Chemical changes to the crude oil that reduce the resin concentration can thus lead to asphaltene deposition in the formation.

5-7.4 Fluid Damage: Emulsions, Relative Permeability, and Wettability Changes

Formation damage can be caused by changes in the fluids themselves rather than a change in the permeability of the rock. The damage caused by fluids is due either to a change in the apparent viscosity of the oil phase or to a change in relative permeability. These types of damage can be thought of as temporary, because the fluids are mobile and theoretically can all be removed from the near-well vicinity. However, such removal is sometimes difficult.

The formation of water-in-oil emulsions in the reservoir rock around the wellbore can cause damage because the apparent viscosity of the emulsion may be more than an order or magnitude higher than that of the oil. In addition, emulsions are often non-Newtonian and may require sufficient force to overcome a yield stress to be mobilized. Emulsions are most commonly caused by mechanical mixing of oil and water, which breaks one of the phases into small droplets dispersed in the other phase. In the formation, it is more likely that emulsions are formed chemically, through the introduction of surfactants or fines that tend to stabilize small droplets.

Apparent formation damage can also be due simply to an increase in the water saturation around the wellbore, resulting in a reduction of the permeability to oil. This effect, called a water block, can occur any time aqueous fluids are introduced into the formation.

Finally, certain chemicals can alter the wettability of the formation, changing the relative permeability characteristics of the formation entirely. If a water-wet formation is changed to oil-wet around the wellbore, the oil relative permeability may be greatly reduced in the near-wellbore region. This was addressed also in Section 5-3.

5-7.5 Mechanical Damage

The formation near the wellbore can also be damaged by physical crushing or compaction of the rock. Pulverization and compaction of the rock in the vicinity of a perforation is an unavoidable consequence of perforating, leading to a damaged region around a perforation like that shown schematically in Fig. 5-14 (Krueger, 1986). Based on laboratory testing of perforating into sandstone cores, Krueger (1986) reported the damaged zone around a perforation to be 1/4 to 1/2 in. thick with a permeability of 7% to 20% of the undamaged permeability. Because of the convergent flow to a perforation, this small layer of damage around a perforation can significantly impair the productivity of the perforation. For example, Lea et al. (1991) showed that a crushed zone with a permeability of 10% of the original permeability results in a perforation skin factor of about 15.

Mechanical damage around the wellbore can also result from the collapse of weak formation material around the wellbore. This type of damage is possible in friable formations or those weakened by acidizing in the near-wellbore region.

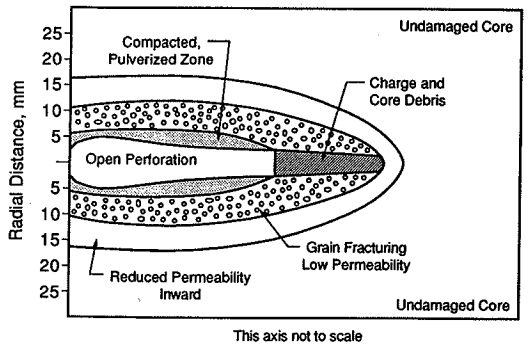

Figure 5-14
Damaged regions around a perforation. (*From Krueger, 1986.*)

5-7.6 Biological Damage

Some wells, particularly water injection wells, are susceptible to damage caused by bacteria in the near-wellbore environment. Bacteria injected into the formation, particularly anaerobic bacteria, may grow rapidly in the formation, plugging the pore spaces with the bacteria themselves or with precipitates that result from the biological activity of the organisms. The permeability reduction caused by bacteria can be so significant that the injection of bacteria to intentionally reduce the permeability of thief zones is under active study as an enhanced oil recovery method (Zajic et al., 1983). Biological damage is best prevented by treating injection waters with bactericides.

5-8 Sources of Formation Damage During Well Operations

5-8.1 Drilling Damage

The most common source of formation damage in wells is the drilling process itself. Drilling damage results from the invasion of the formation by drilling fluid particles and drilling fluid filtrate. The damage caused by the drilling fluid particles is likely to be the more severe.

The deposition of drilling mud particles in the formation around the wellbore can severely reduce the permeability in this critical region; fortunately, however, the depth of particle invasion is usually small, ranging from less than an inch to a maximum of about 1 ft. To minimize this damage, the mud particles should be larger than the pores; Abrams (1977) suggests that having 5 vol% of the mud particles with a diameter greater than one-third of the mean pore size will prevent significant particle invasion. Since the invasion depth is

small, it is often possible to overcome drilling mud particle damage by perforating through the damaged region or by acidizing.

Drilling mud filtrate will invade the formation to a greater depth than drilling mud particles, with depths of invasion of 1 to 6 ft being common (Hassen, 1980). As filtrate enters the formation, a filter cake of drilling mud solids is built up on the formation face, decreasing the rate of filtrate invasion. However, the filter cake will also be eroded by the shear force of the drilling fluid. The dynamic filtration rate accounts for this balance between filter cake formation and erosion and is given by

$$u_f = \frac{C}{\sqrt{t}} + 3600b\dot{\gamma} \tag{5-44}$$

where u_f is the filtrate flux, C is the dynamic fluid loss coefficient for the filter cake, t is the exposure time (hr), b is a constant accounting for the mechanical stability of the filter cake, and $\dot{\gamma}$ is the shear rate at the wall (sec^{-1}). Hassen (1980) reports values of b of 2×10^{-8} to 5×10^{-7} cm^3/cm^2. The fluid loss coefficient can be obtained from a laboratory dynamic fluid loss test.

The drilling of horizontal wells with reported horizontal lengths up to 8000 ft poses new problems of significant penetrations of damage because of the long exposures to drilling fluids while the horizontal well is drilled. The shape of damage along a horizontal well is likely to reflect the longer exposure near the vertical section. This issue was addressed in a previous section of this chapter.

EXAMPLE 5-9
The depth of filtrate invasion

Calculate the depth of drilling mud filtrate invasion after 10 hr and after 100 hr of drilling mud exposure to the formation for a mud with a dynamic fluid loss coefficient of 5 $\text{in.}^3/\text{in.}^2\text{-hr}^{1/2}$. The wellbore radius is 6 in., and the formation porosity is 0.2. Assume that b is 5×10^{-7} cm^3/cm^2 and that the shear rate at the wall is 20 sec^{-1}.

Solution Equation (5-44) gives the filtrate flux at the wellbore; the volumetric flow rate per unit thickness of formation is just the flux multiplied by the borehole circumference. The volume of filtrate is then the integral of the volumetric flow rate with time:

$$q_f = 2\pi r_w u_f = 2\pi r_w \left(\frac{C}{\sqrt{t}} + 3600b\dot{\gamma}\right) \tag{5-45}$$

$$V = \int_0^t q_f \, dt \tag{5-46}$$

$$V = \int_0^t 2\pi r_w \left(\frac{C}{\sqrt{t}} + 3600b\dot{\gamma}\right) dt = 2\pi r_w \left(2C\sqrt{t} + 3600b\dot{\gamma}t\right) \tag{5-47}$$

The volume of filtrate injected per unit thickness is related to the depth of penetration of the filtrate by

$$V = \pi\phi(r_p^2 - r_w^2) \tag{5-48}$$

Equating V from (5-47) and (5-48), we obtain

$$r_p = \sqrt{r_w^2 + \frac{2r_w}{\phi}\left(2Ct^{1/2} + 3600b\dot{\gamma}t\right)} \tag{5-49}$$

and for the data given with appropriate unit conversions,

$$r_p = \sqrt{6^2 + \frac{(2)(6)}{0.2}\left[(2)(5)t^{1/2} + (3600)\left(\frac{5\times10^{-7}}{2.54}\right)(20)t\right]} \tag{5-50}$$

From Eq. (5-50), we find that for t=10 hr, r_p=44 in.; and for t=100 hr, r_p=78 in. Thus, the filtrate has invaded 38 in. into the formation after 10 hr and 72 in. into the formation after 100 hr. The actual filtrate invasion is likely to be somewhat higher than that calculated here because of higher fluid loss rates that occur before a stable filter cake is formed. ◇

Drilling fluid filtrate can damage the formation by fines movement, by precipitation, or by water blocking, as discussed in Section 5-7. Fines migration and precipitation damage can be minimized by tailoring the ionic composition of the drilling fluid to be compatible with that of the formation. If water blocking is a serious problem, water-based muds may have to be avoided.

5-8.2 Completion Damage

Damage to the formation during well completion operations can be caused by invasion of completion fluids into the formation, by cementing, by perforating, or by well stimulation techniques. Since a primary purpose of the completion fluid is to maintain a higher pressure in the wellbore than in the formation (overbalance), completion fluids will be forced into the formation. Thus, if the completion fluids contain solids or are chemically incompatible with the formation, damage can result similar to the damage caused by drilling mud. It is particularly important that completion fluids be filtered well to prevent injection of solids into the formation. It is recommended that completion fluids contain no more than 2 ppm of solids of a size less than 2 μm (Millhone, 1982).

Cement filtrate is another potentially damaging fluid when it enters the formation. Since cement filtrate will usually contain a high concentration of calcium ions, precipitation damage may occur.

Perforating will inevitably result in some crushing of the formation in the immediate vicinity of the perforation. This damage is minimized by perforating underbalanced, that is, with the wellbore pressure lower than the formation pressure. Guidelines for the amount of underbalance needed in gas and oil zones are given in Figs. 5-15 and 5-16 (King et al., 1985). The minimum overbalance needed for a given formation permeability can be read from the correlation lines drawn on these figures.

Well stimulation fluids, though intended to increase the productivity of a well, can cause formation damage themselves by solids invasion of the formation or precipitation. The potential for damage from stimulation fluids is discussed in the chapters on well stimulation.

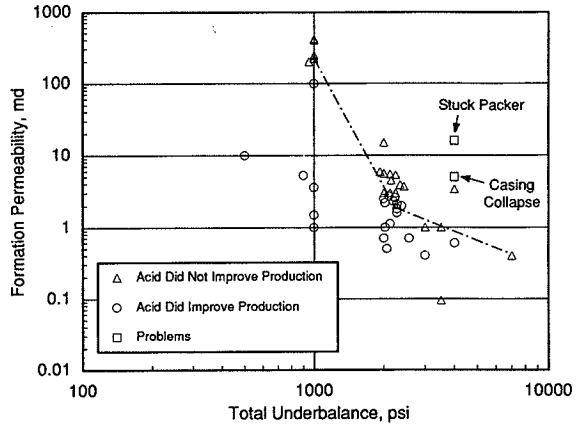

Figure 5-15
Underbalance needed to minimize perforation damage in gas zones. (*From King et al., 1985.*)

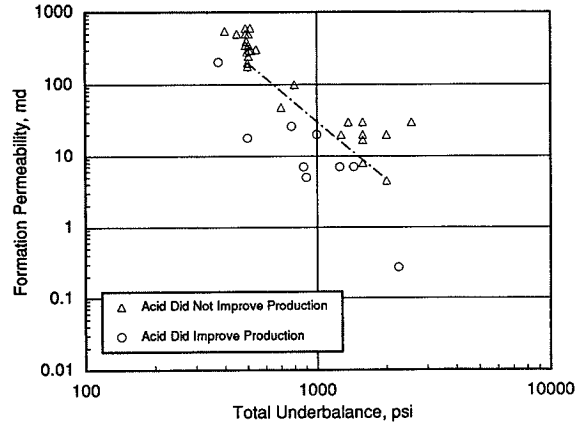

Figure 5-16
Underbalance needed to minimize perforation damage in oil zones. (*From King et al., 1985.*)

5-8.3 Production Damage

Formation damage during production can be caused by fines migration in the formation or by precipitation. The high velocity in the porous medium near the well is sometimes sufficient to mobilize fines that can then plug pore throats. Numerous studies have shown that a critical velocity exists, above which formation damage by particle migration occurs (Schechter, 1992). Unfortunately, this critical velocity depends on the particular rock and fluids in a complex manner; the only means of determining the critical velocity is through laboratory coreflood tests.

Fines may be mobilized in the vicinity of a production well when water production begins. Figure 5-17 (Muecke, 1979) illustrates this mechanism. Fines are most likely to move when the phase they wet is mobile, and since most formation fines are water-wet, the presence of a mobile water phase can cause fines migration and subsequent formation damage.

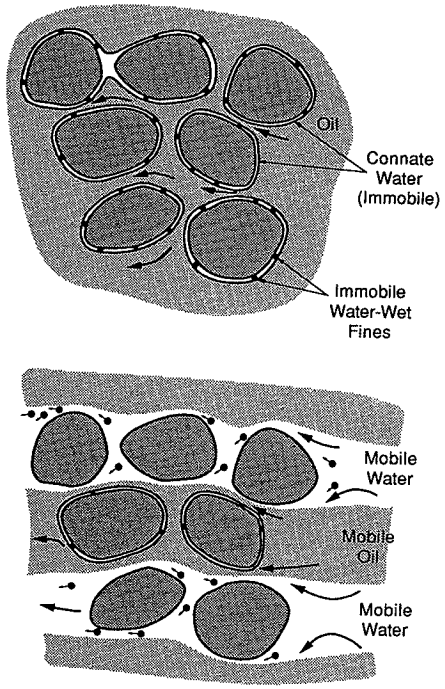

Figure 5-17
Fines mobilization caused by water movement. (*From Muecke, 1979.*)

Precipitation of solids, either inorganic material from the brine or organic solids from the crude oil, may occur near a production well because of the reduced pressure in the

near-wellbore region. These sources of formation damage can often be overcome with occasional stimulation treatments (e.g., acids to remove carbonate precipitates or solvents to remove waxes) or can be prevented with chemical squeeze treatments using sequestering agents.

5-8.4 Injection Damage

Injection wells are susceptible to formation damage caused by the injection of solid particles, by precipitation due to incompatibility of injected and formation water, or by the growth of bacteria. Solids injection is always a danger if the injected water is not well filtered; filtration to remove all particles larger than 2 μm is recommended.

Damage by precipitated solids can occur whenever mixing of the injected water with the formation water leads to supersaturation of one or more chemical species. The most common problem of this type is the injection of water with relatively high concentrations of sulfate or carbonate ions into formations with divalent cations, such as calcium, magnesium, or barium present. Because cation exchange with clays in the formation can release divalent cations into solution when a water with a different ionic composition is injected, precipitation may occur in the formation even when the injected water is apparently compatible with the formation water. In other words, the fact that no precipitation occurs when a sample of formation water is mixed with a sample of injection water is not sufficient to guarantee that no precipitation will occur in the formation. Dynamic processes such as cation exchange must be considered. Modeling of these processes is beyond the scope of this book.

Injection water may contain bacteria, which can plug the formation just like any other solid particles. Injected bacteria may also grow in the near-wellbore vicinity, causing severe formation damage. Injection water should be tested for the presence of bacteria, and bactericides should be added to the water if the potential for formation damage is indicated.

REFERENCES

1. Abrams, A., "Mud Design to Minimize Rock Impairment Due to Particle Invasion," *JPT*, 586–592, May 1977.
2. Cinco-Ley, H., Ramey, H. J., Jr., and Miller, F. G., "Pseudoskin Factors for Partially Penetrating Directionally Drilled Wells," SPE Paper 5589, 1975.
3. Cvetkovic, B., Economides, M. J., Omrcen, B., and Longaric, B., "Production from Heavy Gas Condensate Reservoirs," SPE Paper 20968, 1990.
4. Frick, T. P., and Economides, M. J., "Horizontal Well Damage Characterization and Removal," SPE Paper 21795, 1991.
5. Fussell, D. D., "Single-Well Performance Predictions for Gas Condensate Reservoirs," *JPT*, 860–870, July 1973.
6. Hassen, B. R., "New Technique Estimates Drilling Fluid Filtrate Invasion," SPE Paper 8791, 1980.
7. Hawkins, M. F., Jr., "A Note on the Skin Effect," *Trans. AIME*, **207**: 356–357, 1956.
8. Karakas, M., and Tariq, S., "Semi-Analytical Production Models for Perforated Completions," SPE Paper 18247, 1988.
9. King, G. E., Anderson, A., and Bingham, M., "A Field Study of Underbalance Pressures Necessary to Obtain Clean Perforations Using Tubing-Conveyed Perforating," SPE Paper 14321, 1985.
10. Krueger, R. F., "An Overview of Formation Damage and Well Productivity in Oilfield Operations," *JPT*, 131–152, February 1986.

11. Lea, C. M., Hill, A. D., and Sepehrnoori, K., "The Effect of Fluid Diversion on the Acid Stimulation of a Perforation," SPE Paper 22853, 1991.
12. Millhone, R. S., "Completion Fluids—Maximizing Productivity," SPE Paper 10030, 1982.
13. Muecke, T. W., "Formation Fines and Factors Controlling Their Movement in Porous Media," *JPT*, 144–150, February 1979.
14. Schechter, R. S., *Oil Well Stimulation*, Prentice Hall, Englewood Cliffs, NJ, 1992.
15. Schechter, R. S., and Gidley, J. L., "The Change in Pore Size Distributions from Surface Reactions in Porous Media," *AICHE J.*, 339–350, May 1969.
16. Tyler, T. N., Metzger, R. R., and Twyford, L. R., "Analysis and Treatment of Formation Damage at Prudhoe Bay, AK," SPE Paper 12471, 1984.
17. Van Everdingen, A. F., and Hurst, N., "The Application of the Laplace Transformation to Flow Problems in Reservoirs," *Trans. AIME*, **186**: 305–324, 1949.
18. Zajic, J. E., Cooper, D. G., Jack, T. R., and Kosaric, N., *Microbial Enhanced Oil Recovery*, PennWell Publishing Co., Tulsa, OK, 1983.

PROBLEMS

5-1. If the permeability impairment k/k_s is 8, the damage penetration is 3 ft, and r_w=0.328 ft, calculate the well skin effect. What should the k/k_s be for the same skin effect if the penetrations of damage are 1, 2, and 4 ft, respectively?

5-2. Suppose that the pressure value 10 ft away from the well in Appendix B is the bubble-point pressure. (S_g=0). If the bottomhole pressure would result in a gas saturation at the sandface equal to 0.04, estimate the phase-dependent skin effect. (Hint: Use Fig. B-2 to obtain the relative permeability-to-oil reduction in the near-wellbore zone).

5-3. If r_w=0.328 ft, h=165 ft, h_w=75 ft, and z_w=82.5 ft (midpoint of the reservoir), calculate the partial completion skin effect for a vertical well.

5-4. At which angle of well deviation would the contribution from s_θ nullify the effects of s_c (i.e., $s_{c+\theta} \approx 0$)?

5-5. For θ=120°, r_{perf}=0.25 in., r_w=0.328 ft, k_H/k_V=10, and 2 SPF, show the impact of the perforation length on the perforation skin effect. Try l_{perf} equal to 6, 9, 12, and 15 in.

5-6. For θ=120°, l_{perf}=8 in., r_w=0.328 ft, k_H/k_V=10, and 2 SPF, calculate the perforation skin for r_{perf}=0.33 and 0.5 in.

5-7. If the penetration of damage, r_s=2 ft, l_{perf}=8 in., k/k_s=10, r_{perf}=0.25 in., k_H/k_V=10, θ=120°, r_w=0.328 ft, and 4 SPF, calculate the combined skin effect from damage and perforations.

5-8. Repeat Problem 5-7 but with r_s=6 in.

5-9. If a horizontal well is drilled in the reservoir of Appendix A and p_{wf}=3500 psi, r_w=0.328 ft, and A=640 acres, what length L is required to provide a 2:1 productivity ratio over a vertical well with no skin if the damage skin effect in the horizontal well is 15?

5-10. A drilling mud has a dynamic fluid loss coefficient of 10 in.^{3}/in.^{2}-hr$^{1/2}$. During the 20 hr that the formation is exposed to this mud during drilling, the shear rate at the wall is 50 sec^{-1} and b is 5×10^{-7} cm^3/cm^2. What is the depth of drilling filtrate invasion assuming that ϕ = 0.19? What is the skin factor if the filtrate reduces the permeability to 50% of the original value? The drainage radius is 660 ft, and r_w=0.328 ft.

5-11. In addition to the filtrate loss and resulting damage, assume that, in the well of Problem 5-10, drilling mud particles penetrate 5 in. into the formation, reducing the permeability to 10% of the original reservoir permeability. What is the skin factor resulting from the combined particle and filtrate damage?

CHAPTER 6

Gravel Pack Completions

6-1 INTRODUCTION

Many reservoirs comprised of relatively young sediments are so poorly consolidated that sand will be produced along with the reservoir fluids unless the rate is restricted significantly. Sand production leads to numerous production problems, including erosion of downhole tubulars; erosion of valves, fittings, and surface flow lines; the wellbore filling up with sand; collapsed casing because of the lack of formation support; and clogging of surface processing equipment. Even if sand production can be tolerated, disposal of the produced sand is a problem, particularly at offshore fields. Thus, a means to eliminate sand production without greatly limiting production rates is desirable. Sand production is controlled by using gravel pack completions, slotted liner completions, or sand consolidation treatments, with gravel pack completions being by far the most common approach. A review of sand-control completion practices is given by Suman et al. (1983).

In a gravel pack completion, sand that is larger than the average formation sand grain size is placed between the formation and a screen or slotted liner. The gravel pack sand (referred to as gravel, though it is actually sand in grain size), should retain most of the formation sand, but let very fine particles pass through it and be produced. The two most common types of gravel pack completions are an inside-casing gravel pack and an open-hole or underreamed-casing gravel pack (Fig. 6-1). The underreamed-casing gravel pack provides better conductivity through the gravel, but is limited to single-zone completions. A successful gravel pack completion must retain the formation sand and offer the least possible resistance to flow through the gravel itself.

6-2 GRAVEL PACK PLACEMENT

For a successful gravel pack completion, gravel must be adjacent to the formation without having mixed with formation sand, and the annular space between the screen and

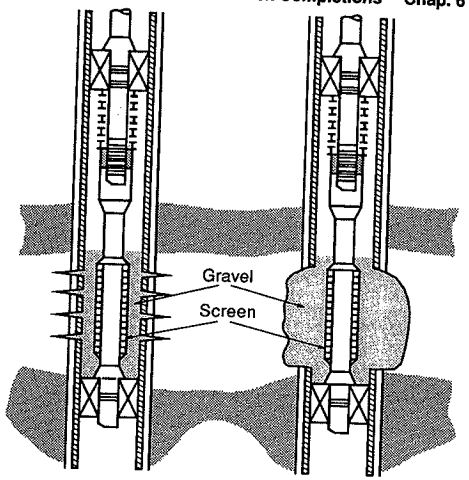

Figure 6-1
Common types of gravel pack completions.

the casing or formation must be completely filled with gravel. Special equipment and procedures have been developed over the years to accomplish good gravel placement.

Water or other low-viscosity fluids were first used as transporting fluids in gravel pack operations. Because these fluids could not suspend the sand, low sand concentrations and high velocities were needed. Now, viscosified fluids, most commonly, solutions of hydroxyethylcellulose (HEC), are used so that high concentrations of sand can be transported without settling (Scheuerman, 1984). Just as with the fluids used in hydraulic fracturing, it is desirable that these solutions degrade to low viscosity with little residue, requiring the addition of breakers to the polymer solution.

In open-hole completions, the gravel-laden fluid can be pumped down the tubing casing annulus, after which the carrier fluid passes through the screen and flows back up the tubing. This is the reverse-circulation method depicted in Fig. 6-2a (Suman et al., 1983). A primary disadvantage of this method is the possibility of rust, pipe dope, or other debris being swept out of the annulus and mixed with the gravel, damaging the pack permeability. More commonly, a crossover method is used, in which the gravel-laden fluid is pumped down the tubing, crosses over to the screen-open hole annulus, flows into a wash pipe inside the screen, leaving the gravel in the annulus, and then flows up the casing-tubing annulus to the surface (Fig. 6-2b). Notice that the open-hole section is usually underreamed through the productive interval to increase well productivity.

For inside-casing gravel packing, washdown, reverse-circulation, and crossover methods are used (Fig. 6-3) (Suman et al., 1983). In the washdown method, the gravel is placed opposite the productive interval before the screen is placed, and then the screen is washed down to its final position. The reverse-circulation and crossover methods are analogous to

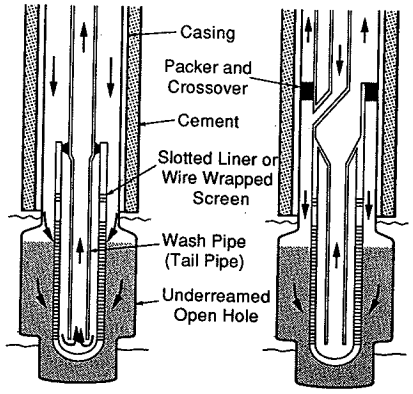

Figure 6-2
Gravel placement methods in open-hole or underreamed casing completions. (*From Suman et al., 1983.*)

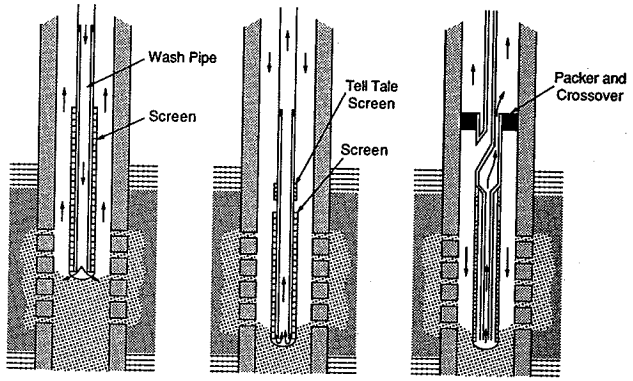

Figure 6-3
Gravel placement methods for inside-casing gravel packs. (*After Suman et al., 1983.*)

those used in open holes. A modern crossover method, described in detail by Schechter (1992), is shown in Fig. 6-4. Gravel is first placed below the perforated interval by circulation through a section of screen called the telltale screen. When this has been covered, the pressure increases, signaling the beginning of the squeeze stage. During squeezing, the carrier fluid leaks off to the formation, placing gravel in the perforation tunnels. After

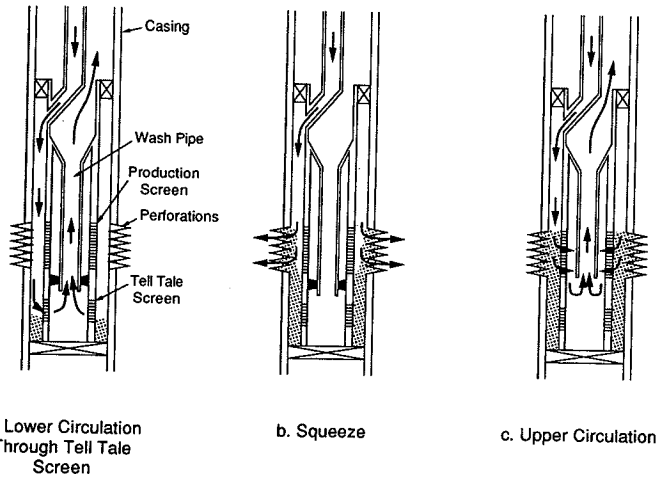

Figure 6-4
Steps in a crossover method of gravel pack placement. (*From Schechter, 1992.*)

squeezing, the washpipe is raised, and the carrier fluid circulates through the production screen, filling the casing-production screen annulus with gravel. Gravel is also placed in a section of blank pipe above the screen to provide a supply of gravel as the gravel settles.

In deviated wells, gravel packing is greatly complicated by the fact that the gravel tends to settle to the low side of the hole, forming a dune in the casing-screen annulus. This problem is significant at deviations greater than 45° from vertical (Shryock, 1983). Gravel placement is improved in deviated wells by using a washpipe that is large relative to the screen (Gruesbeck et al., 1979); this causes a higher velocity over the dune in the annulus between the screen and the casing by increasing the resistance to flow in the screen-washpipe annulus. Shryock's results also suggest that an intermediate-viscosity carrier fluid may be preferable to high-viscosity fluids in deviated wellbores.

6-3 Gravel and Screen Design

A critical element in designing a gravel pack completion is the proper sizing of the gravel and the screen or slotted liner. To perform its sand control function and maximize the permeability of the gravel pack, the gravel must be small enough to retain the formation sand, yet large enough that clay particles and other formation fines flow through the pack. Thus, the optimal gravel size is related to the formation particle size distribution. The screen must be sized to retain all of the gravel.

The first step in determining the gravel size is to measure accurately the formation particle size distribution. A representative sample of formation material can be obtained, in order of preference, from rubber-sleeve cores, conventional cores, or sidewall cores. Produced sand samples or bailed samples should not be used to size gravel. Produced sand will tend to have a larger proportion of smaller grain sizes, while bailed sand will have a larger proportion of larger grain sizes.

The formation grain size is obtained with a sieve analysis, using a series of standard sieve trays; the sieve opening sizes for U.S. standard mesh sizes are given in Table 6-1 (Perry, 1963). The results of the sieve analysis are usually reported as a semilog plot of cumulative weight of formation material retained versus grain size. Typical grain size distributions from California and U.S. Gulf Coast unconsolidated sands are shown in Fig. 6-5 (Suman et al, 1983).

Schwartz (1969) and Saucier (1974) presented similar (but slightly different) correlations for optimal gravel size based on the formation grain size distribution. Schwartz's

Table 6-1

Standard Sieve Sizes[a]

U.S. Standard Mesh Size	Sieve Opening (in.)	(mm)
2 1/2	0.315	8.00
3	0.265	6.73
3 1/2	0.223	6.68
4	0.187	4.76
5	0.157	4.00
6	0.132	3.36
7	0.111	2.83
8	0.0937	2.38
10	0.0787	2.00
12	0.0661	1.68
14	0.0555	1.41
16	0.0469	1.19
18	0.0394	1.00
20	0.0331	0.840
25	0.0280	0.710
30	0.0232	0.589
35	0.0197	0.500
40	0.0165	0.420
45	0.0138	0.351
50	0.0117	0.297
60	0.0098	0.250
70	0.0083	0.210
80	0.0070	0.177

Table 6-1 (Cont.)

Standard Sieve Sizes[a]

U.S. Standard Mesh Size	Sieve Opening (in.)	Sieve Opening (mm)
100	0.0059	0.149
120	0.0049	0.124
140	0.0041	0.104
170	0.0035	0.088
200	0.0029	0.074
230	0.0024	0.062
270	0.0021	0.053
325	0.0017	0.044
400	0.0015	0.037

[a]From Perry, (1963).

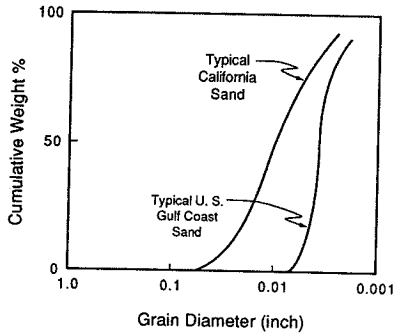

Figure 6-5
Grain size distributions for California and U.S. Gulf Coast sands. (*From Suman et al., 1983.*)

correlation depends on the uniformity of the formation and the velocity through the screen, but for most conditions (nonuniform sands) is

$$D_{g40} = 6D_{f40} \tag{6-1}$$

where D_{g40} is the recommended gravel size and D_{f40} is the diameter of formation sand for which 40 wt% of the grains are of a larger diameter. To fix the gravel size distribution, Schwartz recommends that the gravel size distribution should plot as a straight line on the standard semilog plot, and a uniformity coefficient, U_c, defined as

$$U_c = \frac{D_{g40}}{D_{g90}} \tag{6-2}$$

should be 1.5 or less. From these requirements, we find

$$D_{g,\,\text{min}} = 0.615D_{g40} \tag{6-3}$$

and

$$D_{g,\,\text{max}} = 1.383D_{g40} \tag{6-4}$$

where $D_{g,\,\text{min}}$ and $D_{g,\,\text{max}}$ are the minimum and maximum sizes of gravel to be used, respectively. Equations (6-3) and (6-4) define the range of recommended gravel size.

Saucier recommends that the geometric mean gravel size be five or six times the mean formation grain size, or

$$D_{g50} = (5 \text{ or } 6)\, D_{f50} \tag{6-5}$$

Saucier gave no recommendation about gravel size distribution. If we apply Schwartz's criteria, then

$$D_{g,\,\text{min}} = 0.667D_{g50} \tag{6-6}$$

$$D_{g,\,\text{max}} = 1.5D_{g50} \tag{6-7}$$

The screen openings should be small enough to retain all of the gravel, requiring that the screen openings be slightly less than the smallest gravel size.

EXAMPLE 6-1
Selecting the optimum gravel and screen sizes

Using both the Schwartz and Saucier correlations, determine the optimal gravel and screen size for the California unconsolidated sand for which the grain size distribution was given in Fig. 6-5.

Solution

Schwartz correlation The grain size distribution for the California unconsolidated sand is replotted in Fig. 6-6. Reading from the plot for a cumulative weight fraction of 40%, we find that $D_{f40} = 0.0135$ in. The 40% grain size for the gravel is then (6)(0.0135 in.) = 0.081 in. The 90% grain size is $D_{g40}/1.5 = 0.054$ in. The recommended grain size distribution is shown graphically as the dashed line on Fig. 6-6; the intersections with the cumulative weight % = 100 and = 0 lines define the minimum and maximum gravel sizes, respectively, calculated with Eqs. (6-3) and (6-4) to be 0.05 and 0.11 in.

From Table 6-1, the sieve sizes most closely corresponding to the maximum and minimum gravel sizes are 7 mesh and 16 mesh; an 8/16 mesh sand would probably be chosen, since 7 mesh is rarely used. The screen size should be less than 0.0469 in., so that all of the 16 mesh gravel is retained by the screen.

Saucier correlation From the formation grain size distribution, the mean grain size (D_{f50}) is found to be 0.0117 in. The recommended mean gravel size is (5 or 6)(0.0117 in.) = 0.059 or 0.070 in., and from Eqs. (6-6) and (6-7), the minimum gravel size is 0.039 to 0.047 in., while the maximum gravel size is 0.088 to 0.105 in. This range is shown as the shaded region in Fig. 6-6. From Table 6-1, these grain sizes correspond to sieve sizes of 8 mesh and 16 or 18 mesh. An 8/16 mesh sand would again be chosen, with a screen size of less than 0.0469 in. ◇

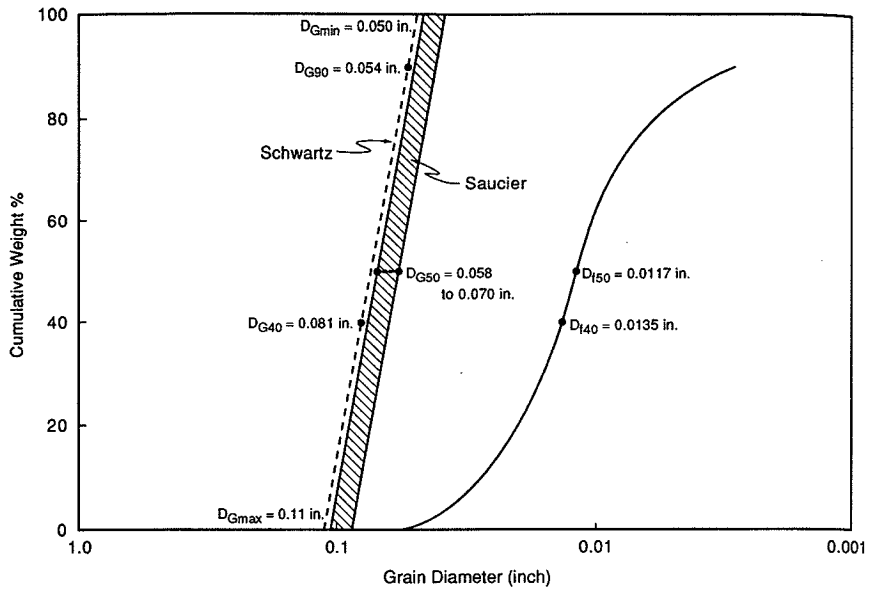

Figure 6-6
Gravel size distributions predicted by Saucier and Schwartz correlations.

Once the gravel size has been chosen, it is important to check that the gravel used conforms closely to this size. The API (1986) recommends that a minimum of 96% of the gravel pack sand should pass the course designated sieve and be retained on the fine designated sieve. More detail about gravel pack sand quality control is given in API RP 58.

6-4 Productivity of Gravel-Packed Wells

The productivity of a gravel-packed well is affected by the pressure drop through the gravel pack, if this pressure drop is significant compared with the pressure drop in the formation. In an open-hole gravel pack, the pressure drop through the gravel should be very small compared with the formation, unless the gravel permeability has been severely reduced by formation particles. If the productivity is expressed based on the radius of the liner, the gravel pack should contribute a small negative skin effect, since it will behave like a larger-diameter wellbore.

For inside-casing gravel pack completions, the pressure drop through the gravel-packed perforations can contribute significantly to the overall pressure drop. Also, since the

productivity of an unconsolidated sand requiring gravel packing is often high, turbulence in the perforations may add to the laminar (Darcy flow) pressure drop through the perforations. The Darcy and non-Darcy contributions to the pressure drop through the perforations can be represented by a gravel-pack skin factor, s_g, and the non-Darcy flow coefficient for the gravel-filled perforation, D_g.

Golan and Whitson (1991) presented the following equations for inside-casing gravel packs:

$$s_g = \frac{96khl_{perf}}{k_g D_{perf}^2 n} \tag{6-8}$$

and for gas wells,

$$D_{gg} = \frac{2.45 \times 10^{-10} \gamma_g khl_{perf}\beta_g}{\mu D_{perf}^4 n^2} \tag{6-9}$$

while for oil wells,

$$D_{go} = \frac{1.80 \times 10^{-11} B_o \rho khl_{perf}\beta_g}{\mu D_{perf}^4 n^2} \tag{6-10}$$

In these equations, kh is the formation permeability-thickness product (md-ft), l_{perf} is the gravel-packed perforation length (in.), k_g is the permeability of the gravel (md), D_{perf} is the perforation diameter (in.), γ_g is the gas gravity, μ is viscosity (cp), ρ is fluid density (lb_m/ft^3), n is the number of perforations, and β_g is the gravel turbulence factor. The turbulence factor is correlated with the gravel permeability (Cooke, 1973), as

$$\beta_g = bk_g^{-a} \tag{6-11}$$

Values of the constants a and b for common gravel sizes are given in Table 6-2 (Golan and Whitson, 1991).

Table 6-2

Gravel Properties

U.S. Mesh Size	Approx. Mean Diam. (in.)	Permeability (md)	$\beta_g = bk_g^{-a}$ a	b
40/60	0.014	$1.2 \times 10^5 - 1.7 \times 10^5$	1.6	2.12×10^{12}
20/40	0.025	1.2×10^5	1.54	3.37×10^{12}
10/20	0.056	$5 \times 10^5 - 6.5 \times 10^5$	1.34	8.4×10^{11}
8/12	0.080	1.7×10^6	1.24	5.31×10^{11}

[a] After Golan and Whitson (1991).

Equations (6-8) through (6-11) are based on the the use of the casing radius, not the screen radius, as r_w in deliverability calculations. The term, $s_g + D_g q$, when added to the [ln $(r_e/r_w) + s$] term, in for example Eq. (2-15) or Eq. (4-23), accounts for the apparent skin effect of the gravel pack. Other skin effects will still be present; in particular, the perforation skin effects discussed in Chapter 5 will also occur in inside-casing gravel packs and will be in addition to the gravel-pack skin effect discussed here.

Finally, in using Eqs. (6-8) though (6-11), the perforation length should be the length through the casing and cement only, that is, the difference between the drilled hole radius and the casing inside radius. This is because it is unlikely that a perforation tunnel can be maintained in an unconsolidated medium.

EXAMPLE 6-2

IPR for a high-rate, gravel-packed gas well

Develop a plot of p_{wf} versus q for the gas well described in Appendix C (as in Example 4-6), with the following change: $k = 100$ md, instead of 0.17 md. The well is gravel-packed inside the 7 7/8-in. casing with 10/20 mesh sand, the drilled hole diameter is 11 in., $r_e = 1490$ ft, and the well is perforated 4 shots/ft with 1/2-in.-diameter perforations.

Solution Since the skin effect, other than due to the gravel pack, is zero, Eq. (4-29) can be written for this case as

$$p_e^2 - p_{wf}^2 = \frac{1424 q \mu \bar{Z} T}{kh}\left(\ln \frac{r_e}{r_w} + s_g + D_g q\right) \tag{6-12}$$

We must evaluate s_g and D_g; then, the problem is analogous to Example 4-6. From Table 6-2, for 10/20 mesh sand, $k = 5 \times 10^5$ md, $a = 1.34$, and $b = 8.4 \times 10^{11}$. The I.D. of the casing is about 7 in., so the perforation length through the casing and cement is (11 in. $-$ 7 in.)/2 = 2 in. From Eq. (6-8),

$$s_g = \frac{(96)(100)(78)(2)}{(5 \times 10^5)(0.5)^2[(4)(78)]} = 0.04 \tag{6-13}$$

so the Darcy flow skin effect through the gravel-packed perforation is insignificant. Now, from Eq. (6-11),

$$\beta_g = (8.4 \times 10^{11})(5 \times 10^5)^{-1.34} = 1.94 \times 10^4 \tag{6-14}$$

so, D_g from Eq. (6-9), is

$$D_g = \frac{(2.45 \times 10^{-10})(0.65)(100)(78)(2)(1.94 \times 10^4)}{(0.5)^4[(4)(78)]^2 \mu} = \frac{7.92 \times 10^{-6}}{\mu} \tag{6-15}$$

Notice that D_g is a function of μ, which will vary depending on the pressure. We will use the viscosity evaluated at p_{wf} for the viscosity of the fluid in the perforation—these have been calculated in Example 4-6.

Equation (6-12) is quadratic in q, and rearranging, we have

$$D_g q^2 + \left(\ln \frac{r_e}{r_w} + s_g\right) q - \frac{kh(p_e^2 - p_{wf}^2)}{1424 \mu \bar{Z} T} = 0 \tag{6-16}$$

which, after substituting for all known quantities, is

$$\left(\frac{7.92 \times 10^{-6}}{\mu}\right) q^2 + 8.64q - \frac{8.56 \times 10^{-3}(2.128 \times 10^7 - p_{wf}^2)}{\mu \bar{Z}} = 0 \tag{6-17}$$

As in Example 4-6, for increments of 500 psi in p_{wf}, we use the values of μ, $\bar{\mu}$, and $\bar{Z}$, and solve the quadratic equation for q. The results are given in Table 6-3 and plotted in Fig. 6-7. Notice how large the non-Darcy flow term, $D_g q$, is for this high-rate well. At low values of p_{wf}, the flow rate actually decreases with a decrease in p_{wf} because of this term. In actual practice, this would probably not occur, because of other restrictions on the flow rate. ◇

Table 6-3

Example 6-2 Results

p_{wf} (psi)	$\mu@p_{wf}$ (cp)	$\bar{\mu}$(cp)	$\bar{Z}$	q (MMSCF/d)	$D_g q$
1000	0.0134	0.0189	0.933	124.8	73.7
1500	0.0146	0.0195	0.912	125.2	67.9
2000	0.0165	0.0205	0.903	123.6	59.3
2500	0.0177	0.0211	0.898	117.5	52.6
3000	0.0195	0.0220	0.903	108.1	43.9
3500	0.0207	0.0226	0.914	93.0	35.6
4000	0.0226	0.0235	0.93	71.6	25.1

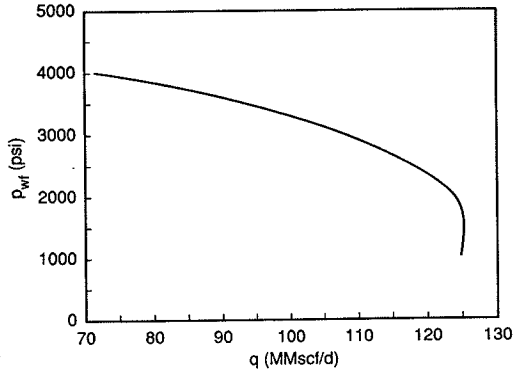

Figure 6-7
IPR curve for a high-rate, gravel-packed gas well.

6-5 GRAVEL PACK EVALUATION

Unfocused γ-ray density logs can be used to locate the top of the gravel-packed section and to detect voids in gravel packs by measuring the density of the materials in the region of the well completion. The tools used are gamma-gamma density devices having a gamma-ray source, typically cesium-137, and a single γ-ray detector. In a gravel-packed well, the material through which the γ-rays travel should be constant except for the amount of gravel present in the annular space between the liner and the casing or formation. Thus the γ-ray intensity measured at the detector should provide at least a qualitative measure of the amount of gravel present—where the annulus is completely filled, the detector response is a minimum while void spaces yield higher count rates.

An unfocused γ-ray density log displays regions of high γ-ray intensity in the packed zone when the gravel pack contains voids, as illustrated in Fig. 6-8 (Neal and Carroll, 1985). Though a portion of the gravel-packed region produces a low count level, through a large region of the completion the γ-ray intensity is high, indicating an incomplete pack of gravel.

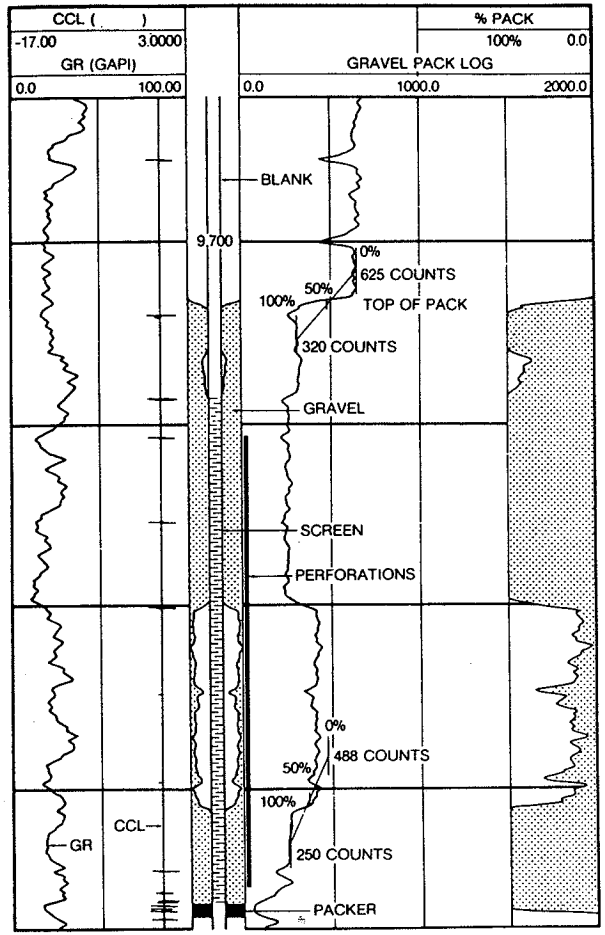

CCL = casing collar log
GR = gamma ray log

Figure 6-8

Gravel pack evaluation response to voids in gravel pack. (*From Neal and Carroll, 1985.*)

REFERENCES

1. American Petroleum Institute, "Recommended Practices for Testing Sand Used in Gravel Packing Operations," API Recommended Practice 58 (RP 58), 1st ed., March 1986.
2. Cooke, C. E., Jr., "Conductivity of Fracture Proppants in Multiple Layers," *JPT*, 1101–1107, September 1973.
3. Golan, M., and Whitson, C. H., *Well Performance*, 2nd ed., Prentice Hall, Englewood Cliffs, NJ, 1991.
4. Gruesbeck, C., Salathiel, W. M., and Echols, E. E., "Design of Gravel Packs in Deviated Wellbores," *JPT*, **31**: 109–115, January 1979.
5. Neal, M. R., and Carroll, J. F., "A Quantitative Approach to Gravel Pack Evaluation," *JPT*, 1035–1040, June 1985.
6. Perry, J. H., *Chemical Engineer's Handbook*, 4th ed., McGraw-Hill, New York, 1963.
7. Saucier, R. J., "Considerations in Gravel Pack Design," *JPT*, 205–212, February 1974.
8. Schechter, R. S., *Oil Well Stimulation*, Prentice Hall, Englewood Cliffs, NJ, 1992.
9. Scheuerman, R. F., "New Look at Gravel Pack Carrier Fluid," SPE 12476, presented at the Seventh Formation Damage Control Symposium, Bakersfield, CA, 1984.
10. Schwartz, D. H., " Successful Sand Control Design for High-Rate Oil and Water Wells," *JPT*, 1193–1198, September 1969.
11. Shryock, S. G., "Gravel-Packing Studies in Full-Scale Deviated Model Wellbore," *JPT*, 603–609, March 1983.
12. Suman, G. O., Jr., Ellis, R. C., and Snyder, R. E., *Sand Control Handbook*, 2nd ed., Gulf Pub. Co., Houston, 1983.

PROBLEMS

6-1. Determine the optimal gravel size for the Gulf Coast formation sand grain size distribution given in Fig. 6-5, using both the Schwartz and Saucier correlations.

6-2. The undersaturated oil described in Appendix A is being produced from a 50-ft.-thick, 800-md unconsolidated sand reservoir with a drainage radius of 1490 ft. The well is completed with an inside-casing gravel pack with 20/40 mesh gravel. The casing is 7 in. (6 in. I.D.), and the drilled hole is 10 in. in diameter. Plot p_{wf} versus q for a range of p_{wf} from 2000 to 5000 psi, assuming 0.5-in.-diameter perforations and a shot density of (a) 1 shot/ft; (b) 2 shot/ft; (c) 4 shot/ft.

6-3. For the well described in Example 6-2, calculate the total apparent skin effect (skin + non-Darcy flow term) if the damage skin effect is 20 and the flow rate is 20 MMSCF/d.

6-4. Assume that the grain size distribution for a sand plots as a straight line on the usual semi-log plot of percent sand retained versus grain size. Show the relationship between the predicted mean particle sizes of the gravel from the Schwartz and Saucier correlations (i. e., compare D_{g50} from the two correlations).

CHAPTER 7

Wellbore Flow Performance

7-1 INTRODUCTION

Wellbore flow can be divided into several broad categories, depending on the flow geometry, the fluid properties, and the flow rate. First, the flow in a wellbore will be either single-phase or multiphase; in most production wells, the flow is multiphase, with at least two phases (e.g., gas and liquid) present. Some production wells and most injection wells experience single-phase flow. The flow geometry of interest in wellbores is usually flow through a circular pipe, though flow in an annular space, such as between tubing and casing, sometimes occurs. Furthermore, the flow of interest may be in any direction relative to the gravitational field. The properties of the fluids, both their PVT behavior and their rheological characteristics, must be considered in describing wellbore flow performance. Finally, depending on the flow rate and the fluid properties, flow in a wellbore may be either laminar or turbulent, and this will strongly influence the flow behavior.

In considering wellbore flow performance, the objective is usually to predict the pressure as a function of position between the bottomhole location and the surface. In addition, the velocity profile and the distribution of the phases in multiphase flow are sometimes of interest, particularly when interpreting production logs.

In this chapter the fluid flow relationships assume Newtonian behavior, which is appropriate for most hydrocarbon fluids. However, when injecting gelled fracturing fluids, the flow behavior is non-Newtonian, and this will be covered in Chapter 17.

7-2 SINGLE-PHASE FLOW OF AN INCOMPRESSIBLE, NEWTONIAN FLUID

7-2.1 Laminar or Turbulent Flow

Single-phase flow can be characterized as being either laminar or turbulent, depending on the value of a dimensionless group, the Reynolds number, N_{Re}. The Reynolds number

is the ratio of the inertial forces to the viscous forces in a flowing fluid, and for flow in a circular pipe is given by

$$N_{Re} = \frac{Du\rho}{\mu} \tag{7-1}$$

When the flow is laminar, the fluid moves in distinct laminae, with no fluid motion transverse to the bulk flow direction. Turbulent flow, on the other hand, is characterized by eddy currents that cause fluctuating velocity components in all directions. Whether the flow is laminar or turbulent will strongly influence the velocity profile in the pipe, the frictional pressure drop behavior, and the dispersion of solutes contained in the fluid, among other factors; all of these attributes are considerations at times in production operations.

The transition from laminar to turbulent flow in circular pipes generally occurs at a Reynolds number of 2100, though this value can vary somewhat depending on the pipe roughness, entrance conditions, and other factors (Govier and Aziz, 1977). To calculate the Reynolds number, all variables must be expressed in consistent units so that the result is dimensionless.

EXAMPLE 7-1

Determining the Reynolds number for flow in an injection well

For the injection of 1.03-specific gravity water ($\rho = 64.3$ lb$_m$/ft^3) in an injection well with 7-in., 32-lb/ft casing, construct a graph of Reynolds number versus volumetric flow rate (in bbl/d). The viscosity of the water at bottomhole conditions is 0.6 cp. At what volumetric flow rate will the transition from laminar to turbulent flow occur?

Solution Equation (7-1) relates the Reynolds number to the average velocity, pipe size, and fluid properties. The average velocity is simply the volumetric flow rate divided by the cross-sectional area of flow,

$$u = \frac{q}{A} \tag{7-2}$$

and for flow in a circular pipe, the cross-sectional area is

$$A = \frac{\pi}{4}D^2 \tag{7-3}$$

so

$$u = \frac{4q}{\pi D^2} \tag{7-4}$$

Substituting for u in Eq. (7-1),

$$N_{Re} = \frac{4q\rho}{\pi D\mu} \tag{7-5}$$

The units must now be converted to a consistent set. For this problem, English engineering units will be most convenient. The appropriate conversion factors are given in Table 1-1.

$$N_{Re} = \frac{4(q \text{ bbl/d})(5.615 \text{ ft}^3\text{/bbl})(\text{day}/86,400 \text{ s})(64.3 \text{ lb}_m/\text{ft}^3)}{\pi(6.094 \text{ in.})(\text{ft}/12 \text{ in.})(0.6 \text{ cp})(6.72 \times 10^{-4} \text{ lb}_m/\text{ft-s-cp})} = 26.0q \tag{7-6}$$

where q is in bbl/d, ρ is in lb$_m$/ft^3, D is in in., and μ is in cp. Of course, the constant 26.0 is specific to the pipe size and fluid properties of this example. For these oilfield units, the Reynolds number can be expressed in general as

$$N_{Re} = \frac{1.48q\rho}{D\mu} \tag{7-7}$$

We see that the Reynolds number varies linearly with the volumetric flow rate for a given pipe size and fluid (Fig. 7-1). The transition from laminar to turbulent flow occurs at $N_{Re} = 2100$, so for this example $2100 = 26.0q$ and therefore $q = 81$ bbl/d. Below about 81 bbl/d, the flow will be laminar; at rates higher than 81 bbl/d, flow is turbulent. ◇

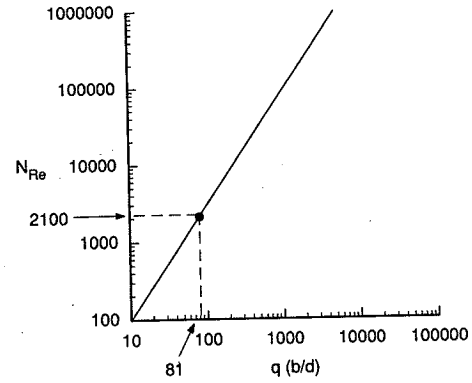

Figure 7-1
Variation of Reynolds number with volumetric flow rate.

Example 7-1 illustrates that laminar flow occurs at low flow rates, generally less than about 100 bbl/d, when the fluid is a low-viscosity liquid. As the viscosity increases, the likelihood of laminar flow will also increase. Figure 7-2 shows the variation of Reynolds number with flow rate, with pipe size and viscosity as parameters. Laminar flow will occur at relatively high flow rates in wells in which a viscous fluid is being produced or injected.

7-2.2 Velocity Profiles

The velocity profile, or variation of velocity with radial position, is sometimes an important consideration when analyzing flow in wellbores, particularly with regard to certain production logging measurements. In laminar flow, the velocity profile in a circular pipe can be derived analytically and is given by

$$u(r) = \frac{(\Phi_0 - \Phi_L)r^2}{4\mu L}\left[1 - \left(\frac{r}{R}\right)^2\right] \tag{7-8}$$

where $\Phi_0 = p_0 + \rho g z_0$; $\Phi_L = p_L + \rho g z_L$; p_0 and p_L are the pressures at longitudinal positions a distance L apart; z_0 and z_L are the heights above some datum at these axial positions; R is the inside pipe radius; r is the radial distance from the center of the pipe;

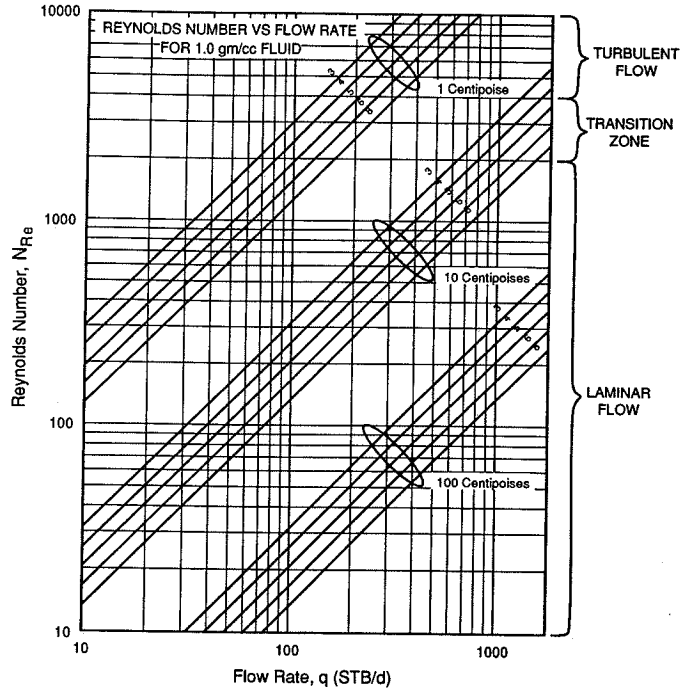

Figure 7-2
Variation of Reynolds number with volumetric flow rate, viscosity, and pipe size.

and $u(r)$ is velocity as a function of radial position. This equation shows that the velocity profile is parabolic in laminar flow with the maximum velocity occurring at the center of the pipe as shown in Fig. 7-3. It can be readily shown from Eq. (7-8) that the average velocity, u, and maximum or centerline velocity, u_{max}, are

$$u = \frac{(\Phi_0 - \Phi_L)R^2}{8\mu L} \tag{7-9}$$

$$u_{max} = \frac{(\Phi_0 - \Phi_L)R^2}{4\mu L} \tag{7-10}$$

so that the ratio of mean velocity to maximum velocity in laminar flow in a circular pipe is

$$\frac{u}{u_{max}} = 0.5 \tag{7-11}$$

Equation (7-9) is a form of the Hagen-Poiseuille equation for laminar flow in a pipe.

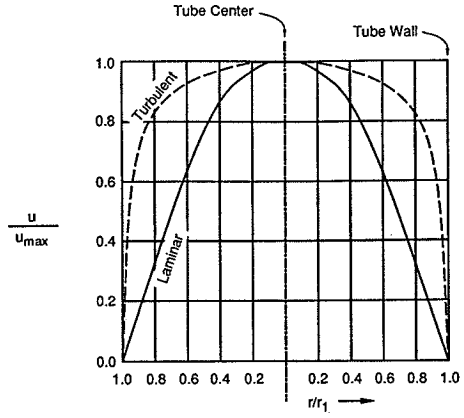

Figure 7-3
Velocity profiles in laminar and turbulent flow.

Turbulent flow does not lend itself to a simple analytical treatment as applied to laminar flow because of the fluctuating nature of turbulent flow. From experiments, empirical expressions have been developed to describe the velocity profile in turbulent flow. One such expression that is fairly accurate for $10^5 > N_{Re} > 3000$ is the power law model

$$\frac{u(r)}{u_{max}} = \left[1 - \left(\frac{r}{R}\right)\right]^{1/7} \tag{7-12}$$

From this expression, it can be shown that

$$\frac{u}{u_{max}} \approx 0.8 \tag{7-13}$$

Thus, in turbulent flow, the velocity profile is much flatter than that found in laminar flow and the average velocity is closer to the maximum velocity (Fig. 7-3). The ratio u/u_{max} in turbulent flow varies with Reynolds number and the roughness of the pipe, but is generally in the range 0.75–0.86.

7-2.3 Pressure Drop Calculations

The pressure drop over a distance, L, of single-phase flow in a pipe can be obtained by solving the mechanical energy balance equation, which in differential form is

$$\frac{dp}{\rho} + \frac{u\,du}{g_c} + \frac{g}{g_c}dz + \frac{2f_f u^2\,dL}{g_c D} + dW_s = 0 \tag{7-14}$$

If the fluid is incompressible (ρ = constant), and there is no shaft work device in the pipeline

(a pump, compressor, turbine, etc.), this equation is readily integrated to yield

$$\Delta p = p_1 - p_2 = \frac{g}{g_c}\rho\,\Delta z + \frac{\rho}{2g_c}\Delta u^2 + \frac{2f_f\rho u^2 L}{g_c D} \tag{7-15}$$

for fluid moving from position 1 to position 2. The three terms on the right-hand side are the potential energy, kinetic energy, and frictional contributions to the overall pressure drop, or

$$\Delta p = \Delta p_{PE} + \Delta p_{KE} + \Delta p_F \tag{7-16}$$

Δp_{PE}, the pressure drop due to potential energy change. Δp_{PE} accounts for the pressure change due to the weight of the column of fluid (the hydrostatic head); it will be zero for flow in a horizontal pipe. From Eq. (7-15), the potential energy pressure drop is given by

$$\Delta p = \frac{g}{g_c}\rho\Delta z \tag{7-17}$$

In this equation, Δz is the difference in elevation between positions 1 and 2, with z increasing upward. θ is defined as the angle between horizontal and the direction of flow. Thus, θ is $+90°$ for upward, vertical flow, $0°$ for horizontal flow, and $-90°$ for downward flow in a vertical well (Fig. 7-4). For flow in a straight pipe of length L with flow direction θ,

$$\Delta z = z_2 - z_1 = L\sin\theta \tag{7-18}$$

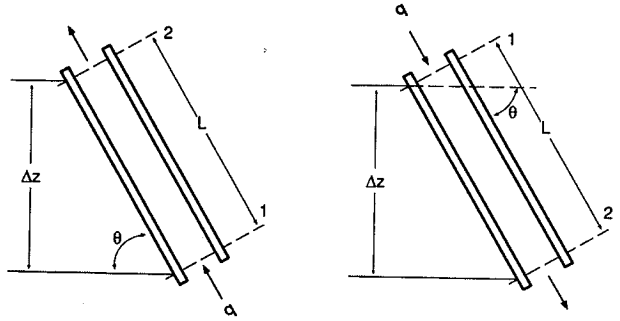

Figure 7-4
Flow geometry for pipe flow.

EXAMPLE 7-2
Calculation of the potential energy pressure drop

Suppose that 1000 bbl/d of brine ($\gamma_w = 1.05$) is being injected through 2 7/8-in., 8.6-lb_m/ft tubing in a well that is deviated 50° from vertical. Calculate the pressure drop over 1000 ft of tubing due to the potential energy change.

Solution Combining Eqs. (7-17) and (7-18),

$$\Delta p_{PE} = \frac{g}{g_c}\rho L\sin\theta \tag{7-19}$$

For downward flow in a well deviated 50° from vertical, the flow direction is $-40°$ from horizontal, so θ is $-40°$. Converting to oilfield units, $\rho = (1.05)(62.4)lb_m/ft^3 = 65.5\ lb_m/ft^3$ and $\Delta p_{PE} = -292$ psi from Eq. (7-19).

Shortcut solution For fresh water with $\gamma_w = 1(\rho = 62.4\ lb_m/ft^3)$, the potential energy pressure drop per foot of vertical distance is

$$\frac{dp}{dz} = \frac{g}{g_c}\rho = \left(1\frac{lb_f}{lb_m}\right)\left(62.4\frac{lb_m}{ft^3}\right)\left(\frac{1\ ft^2}{144\ in.^2}\right) = 0.433 psi/ft \tag{7-20}$$

For a fluid of any other specific gravity, γ_w,

$$\frac{dp}{dz} = 0.433\gamma_w \tag{7-21}$$

where γ_w is the specific gravity. Thus,

$$\Delta p_{PE} = 0.433\gamma_w\,\Delta z \tag{7-22}$$

For the example given, $\gamma_w = 1.05$, and $\Delta z = L\sin\theta$, so $\Delta p_{PE} = 0.433\gamma_w L\sin\theta = -292$ psi. ◇

Δp_{KE}, the pressure drop due to kinetic energy change. Δp_{KE} is the pressure drop resulting from a change in the velocity of the fluid between positions 1 and 2. It will be zero for an incompressible fluid unless the cross-sectional area of the pipe is different at the two positions of interest. From Eq. (7-15),

$$\Delta p_{KE} = \frac{\rho}{2g_c}(\Delta u^2) \tag{7-23}$$

or

$$\Delta p_{KE} = \frac{\rho}{2g_c}\left(u_2^2 - u_1^2\right) \tag{7-24}$$

If the fluid is incompressible, the volumetric flow rate is constant. The velocity then varies only with the cross-sectional area of the pipe. Thus,

$$u = \frac{q}{A} \tag{7-25}$$

and since $A = \pi D^2/4$, then

$$u = \frac{4q}{\pi D^2} \tag{7-26}$$

Combining Eqs. (7-24) and (7-26), the kinetic energy pressure drop due to a pipe diameter change for an incompressible fluid is

$$\Delta p_{KE} = \frac{8\rho q^2}{\pi^2 g_c}\left(\frac{1}{D_2^4} - \frac{1}{D_1^4}\right) \tag{7-27}$$

EXAMPLE 7-3

Calculation of the kinetic energy pressure drop

Suppose that 2000 bbl/d of oil with a density of 58 lb_m/ft^3 is flowing through a horizontal pipeline having a diameter reduction from 4 in. to 2 in., as illustrated in Fig. 7-5. Calculate the kinetic energy pressure drop caused by the diameter change.

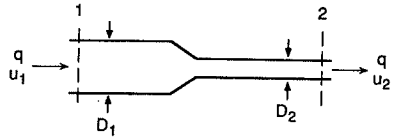

Figure 7-5
Flow with a reduction in pipe size (Example 7-3).

Solution Equation (7-27) can be used if the fluid is incompressible. First, the volumetric flow rate must be converted to ft^3/sec:

$$q = (2000 \text{ bbl/d})(5.615 \text{ ft}^3/\text{bbl})\left(\frac{\text{day}}{86400 \text{ sec}}\right) = 0.130 \text{ ft}^3/\text{sec} \tag{7-28}$$

and from Eq. (7-27),

$$\Delta p_{KE} = \frac{8\left(58 \text{ lb}_m/\text{ft}^3\right)\left(0.130 \text{ ft}^3/\text{sec}\right)^2}{\pi^2\left(32.17 \text{ ft-lb}_m/\text{lb}_f\text{-sec}^2\right)}\left[\frac{1}{\left(\frac{2}{12} \text{ ft}\right)^4} - \frac{1}{\left(\frac{4}{12} \text{ ft}\right)^4}\right]\left(\frac{1 \text{ ft}^2}{144 \text{ in.}^2}\right) \tag{7-29}$$
$$= 0.28 \text{ psi}$$

For oilfield units of bbl/d for flow rate, lb_m/ft^3 for density, and in. for diameter, the constants in Eq. (7-27) and unit conversions can be combined to yield

$$\Delta p_{KE} = 1.3 \times 10^{-8} q^2 \rho \left(\frac{1}{D_2^4} - \frac{1}{D_1^4}\right) \tag{7-30}$$

where q is in bbl/d, ρ is in lb_m/ft^3, and D is in in. ◇

Δp_F, the frictional pressure drop. The frictional pressure drop is obtained from the Fanning equation,

$$\Delta p_F = \frac{2 f_f \rho u^2 L}{g_c D} \tag{7-31}$$

where f_f is the Fanning friction factor. In laminar flow, the friction factor is a simple function of the Reynolds number,

$$f_f = \frac{16}{N_{Re}} \tag{7-32}$$

whereas in turbulent flow, the friction factor may depend on both the Reynolds number and the relative pipe roughness, ϵ. The relative roughness is a measure of the size of surface features on the pipe wall protruding into the flow stream compared with the pipe diameter, or

$$\epsilon = \frac{k}{D} \tag{7-33}$$

where k is the length of the protrusions on the pipe wall. The relative roughnesses of some common types of pipes are given in Fig. 7-6 (Moody, 1944). However, it should be remembered that the pipe roughness may change with service, so that the relative roughness is essentially an empirical parameter that can be obtained through pressure drop measurements.

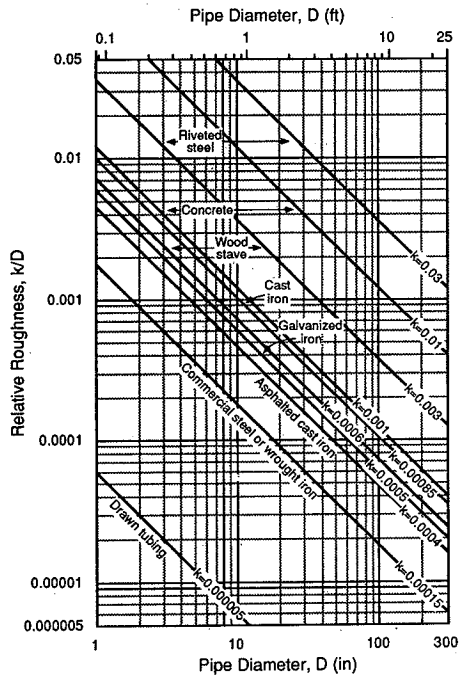

Figure 7-6
Relative roughness of common piping material. (*From Moody, 1944.*)

The Fanning friction factor is most commonly obtained from the Moody friction factor chart (Fig. 7-7; Moody, 1944). This chart was generated from the Colebrook-White equation,

$$\frac{1}{\sqrt{f_f}} = -4\log\left(\frac{\epsilon}{3.7065} + \frac{1.2613}{N_{\text{Re}}\sqrt{f_f}}\right) \tag{7-34}$$

The Colebrook-White equation is implicit in f_f, requiring an iterative procedure, such as the Newton-Raphson method, for solution. An explicit equation for the friction factor with similar accuracy to the Colebrook-White equation (Gregory and Fogarasi, 1985) is the Chen equation (Chen, 1979):

$$\frac{1}{\sqrt{f_f}} = -4\log\left\{\frac{\epsilon}{3.7065} - \frac{5.0452}{N_{\text{Re}}}\log\left[\frac{\epsilon^{1.1098}}{2.8257} + \left(\frac{7.149}{N_{\text{Re}}}\right)^{0.8981}\right]\right\} \tag{7-35}$$

EXAMPLE 7-4
Calculating the frictional pressure drop

Calculate the frictional pressure drop for the 1000 bbl/d of brine injection described in Example 7-2. The brine has a viscosity of 1.2 cp, and the pipe relative roughness is 0.001.

Solution First, the Reynolds number must be calculated to determine if the flow is laminar or turbulent. Using Eq. (7-7),

$$N_{\text{Re}} = \frac{(1.48)(1000\text{ bbl/d})(65.5\text{ lb}_m/\text{ft}^3)}{(2.259\text{ in.})(1.2\text{ cp})} = 35,700 \tag{7-36}$$

Note that the oilfield units used here are obviously not consistent; however, the constant 1.48 converts the units to a consistent set. The Reynolds number is well above 2100, so the flow is turbulent. Either the Moody diagram (Fig. 7-7) or the Chen equation [Eq. (7-35)] can be used to determine the friction factor. Using the Chen equation,

$$\frac{1}{\sqrt{f_f}} = -4\log\left\{\frac{0.001}{3.7065} - \frac{5.0452}{3.57\times10^4}\log\left[\frac{(0.001)^{1.1098}}{2.8257} + \left(\frac{7.149}{3.57\times10^4}\right)^{0.8981}\right]\right\} \tag{7-37}$$

and

$$f_f = \left(\frac{1}{12.57}\right)^2 = 0.0063 \tag{7-38}$$

Now using Eq. (7-31), and noting that 2 7/8-in., 8.6-lb_m/ft tubing has an I.D. of 2.259 in.,

$$u = \frac{q}{A} = \frac{4q}{\pi D^2} = \frac{4(1000\text{ bbl/day})(5.615\text{ ft}^3/\text{bbl})(1\text{ d}/86,400\text{ s})}{\pi[(2.259/12)\text{ ft}]^2} = 2.33\text{ ft/s} \tag{7-39}$$

then,

$$\Delta p_F = \frac{2(0.0063)(65.5\text{ lb}_m/\text{ft}^3)(2.33\text{ ft/s})^2(1000\text{ ft})}{(32.17\text{ ft-lb}_m/\text{lb}_f\text{-s}^2)[(2.259/12)\text{ ft}]} = (740\text{ lb}_f/\text{ft}^2)(\text{ft}^2/144\text{ in.}^2) = 5.14\text{ psi} \tag{7-40}$$

Notice that the frictional pressure drop is considerably less than the potential energy or hydrostatic pressure drop, which we calculated to be −292 psi in Example 7-2. ◇

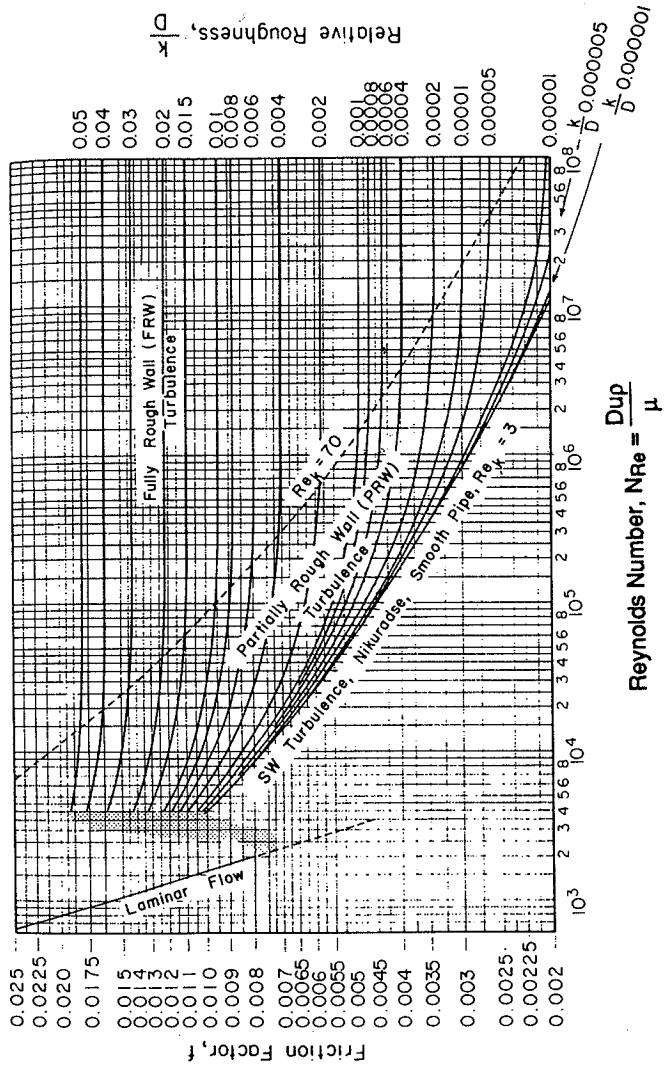

Figure 7-7
Moody friction factor diagram. (*From Moody, 1944.*)

7-3 SINGLE-PHASE FLOW OF A COMPRESSIBLE, NEWTONIAN FLUID

To calculate the pressure drop in a gas well, the compressibility of the fluid must be considered. When the fluid is compressible, the fluid density and fluid velocity vary along the pipe, and these variations must be included when integrating the mechanical energy balance equation.

To derive an equation for the pressure drop in a gas well, we begin with the mechanical energy balance, Eq. (7-14). With no shaft work device and neglecting for the time being any kinetic energy changes, the equation simplifies to

$$\frac{dp}{\rho} + \frac{g}{g_c}dz + \frac{2f_f u^2\, dL}{g_c D} = 0 \tag{7-41}$$

Since dz is $\sin\theta\, dL$, the last two terms can be combined as

$$\frac{dp}{\rho} + \left(\frac{g}{g_c}\sin\theta + \frac{2f_f u^2}{g_c D}\right) dL = 0 \tag{7-42}$$

From the real gas law (Chapter 4), the density is expressed as

$$\rho = \frac{MWp}{ZRT} \tag{7-43}$$

or, in terms of gas gravity,

$$\rho = \frac{28.97\gamma_g p}{ZRT} \tag{7-44}$$

The velocity can be written in terms of the volumetric flow rate at standard conditions, q,

$$u = \frac{4}{\pi D^2} qZ\left(\frac{T}{T_{sc}}\right)\left(\frac{p_{sc}}{p}\right) \tag{7-45}$$

Then, substituting for ρ and u from Eqs. (7-44) and (7-45), Eq. (7-42) becomes

$$\frac{ZRT}{28.97\gamma_g p}dp + \left\{\frac{g}{g_c}\sin\theta + \frac{32f_f}{\pi^2 g_c D^5}\left[\left(\frac{T}{T_{sc}}\right)\left(\frac{p_{sc}}{p}\right)qZ\right]^2\right\} dL = 0 \tag{7-46}$$

This equation still contains three variables that are functions of position: Z, the compressibility factor, temperature, and pressure. To solve Eq. (7-46) rigorously, the temperature profile can be provided and the compressibility factor replaced by a function of temperature and pressure using an equation of state. This approach will likely require numerical integration.

Alternatively, single, average values of temperature and compressibility factor over the segment of pipe of interest can be assumed. If the temperature varies linearly between upstream position 1 and downstream position 2, the average temperature can be estimated as the mean temperature $(T_1 + T_2)/2$ or the log-mean temperature (Bradley, 1987), given by

$$T_{lm} = \frac{T_2 - T_1}{\ln(T_2/T_1)} \tag{7-47}$$

An estimate of the average compressibility factor, $\bar{Z}$, can be obtained as a function of average temperature, $\bar{T}$, and the known pressure, p_1, as described in Chapter 4. Once the pressure, p_2, has been calculated, $\bar{Z}$ can be checked using $\bar{T}$ and the mean pressure, $(p_1 + p_2)/2$. If the new estimate differs significantly, the pressure calculation can be repeated using a new estimate of $\bar{Z}$.

Using average values of Z and T, Eq. (7-46) can be integrated for nonhorizontal flow to yield

$$p_2^2 = e^s p_1^2 + \frac{32f_f}{\pi^2 D^5 g_c \sin\theta}\left(\frac{\overline{ZT}qp_{sc}}{T_{sc}}\right)^2 (e^s - 1) \tag{7-48}$$

where s is defined as

$$s = \frac{-(2)(28.97)\gamma_g(g/g_c)\sin\theta L}{\bar{Z}R\bar{T}} \tag{7-49}$$

For the special case of horizontal flow, $\sin\theta$ and s are zero; integration of Eq. (7-46) gives

$$p_1^2 - p_2^2 = \frac{(64)(28.97)\gamma_g f_f \overline{ZT}}{\pi^2 g_c D^5 R}\left(\frac{p_{sc}q}{T_{sc}}\right)^2 L \tag{7-50}$$

To complete the calculation, the friction factor must be obtained from the Reynolds number and the pipe roughness. Since the product, ρu, is a constant for flow of a compressible fluid, N_{Re} can be calculated based on standard conditions as

$$N_{Re} = \frac{4(28.97)\gamma_g q p_{sc}}{\pi D\bar{\mu}R\bar{T}_{sc}} \tag{7-51}$$

The viscosity should be evaluated at the average temperature and pressure as was the compressibility factor, $\bar{Z}$.

The constants and conversion factors for oilfield units for Eqs. (7-48)–(7-51) can be combined to give

For vertical or inclined flow:

$$p_2^2 = e^s p_1^2 + 2.685\times 10^{-3}\frac{f_f(\overline{ZT}q)^2}{\sin\theta\, D^5}(e^s - 1) \tag{7-52}$$

where

$$s = \frac{-0.0375\gamma_g \sin\theta L}{\overline{ZT}} \tag{7-53}$$

For horizontal flow:

$$p_1^2 - p_2^2 = 1.007\times 10^{-4}\frac{\gamma_g f_f \overline{ZT}q^2 L}{D^5} \tag{7-54}$$

$$N_{Re} = 20.09\frac{\gamma_g q}{D\mu} \tag{7-55}$$

In Eqs. (7-51) through (7-55), p is in psia, q is in MSCF/d, D is in in., L is in ft, μ is in cp, T is in °R, and all other variables are dimensionless.

Frequently, in production operations, the unknown pressure may be the upstream pressure, p_1. For example, in a gas production well, in calculating the bottomhole pressure from the surface pressure, the upstream pressure is the unknown. Rearranging Eq. (7-52) to solve for p_1, we have

$$p_1^2 = e^{-s} p_2^2 - 2.685 \times 10^{-3} \frac{f_f (\overline{ZT} q)^2}{\sin\theta \, D^5} (1 - e^{-s}) \tag{7-56}$$

Equations (7-51) through (7-56) are the working equations for computing the pressure drop in gas wells. Remember that these equations are based on the use of an average temperature, compressibility factor, and viscosity over the pipe segment of interest. The longer the flow distance, the larger will be the error due to this approximation. It is advantageous to divide the well into multiple segments and calculate the pressure drop for each segment if the length (well measured depth) is large. We have also neglected changes in kinetic energy to develop these equations, even though we know that velocity will be changing throughout the pipe. The kinetic energy pressure drop can be checked after using these equations to estimate the pressure drop and corrections made, if necessary.

EXAMPLE 7-5

Calculation of the bottomhole flowing pressure in a gas well

Suppose that 2 MMSCF/d of natural gas is being produced through 10,000 ft of 2 7/8-in. tubing in a vertical well. At the surface, the temperature is 150°F and the pressure is 800 psia; the bottomhole temperature is 200°F. The gas has the composition given in Example 4-3, and the relative roughness of the tubing is 0.0006 (this is a common value used for new tubing.)

Calculate the bottomhole flowing pressure directly from the surface pressure. Repeat the calculation, but this time dividing the well into two equal segments. Show that the kinetic energy pressure drop is negligible.

Solution Equations (7-53), (7-55), and (7-56) are needed to solve this problem. From Example 4-3, T_{pc} is 374°R, p_{pc} is 717 psia, and γ_g is 0.709. Using the mean temperature, 175°F, the pseudo-reduced temperature is $T_{pr} = (175 + 460)/374 = 1.70$; and using the known pressure at the surface to approximate the average pressure, $p_{pr} = 800/717 = 1.12$. From Fig. 4-1, $\bar{Z} = 0.935$. Following Example 4-4, the gas viscosity is estimated: from Fig. 4-4, $\mu_{1\text{ atm}} = 0.012$ cp; from Fig. 4-5, $\mu/\mu_{1\text{ atm}} = 1.07$, and therefore $\mu = (0.012\text{ cp})(1.07) = 0.013$ cp.

The Reynolds number is, from Eq. (7-55),

$$N_{\text{Re}} = \frac{(20.09)(0.709)(2000\text{ MSCF/d})}{(2.259\text{ in.})(0.013\text{ cp})} = 9.70 \times 10^5 \tag{7-57}$$

and $\epsilon = 0.0006$, so, from the Moody diagram (Fig. 7-7), $f_f = 0.0044$. Since the flow direction is vertical upward, $\theta = +90°$.

Now, using Eq. (7-53),

$$s = \frac{-(0.0375)(0.709)[\sin(90)](10,000)}{(0.935)(635)} = -0.448 \tag{7-58}$$

The bottomhole pressure is calculated from Eq. (7-56):

$$p_1^2 = e^{0.448}(800)^2 - 2.685 \times 10^{-3} \left\{ \frac{0.0044[(0.935)(635)(2000)]^2}{\sin(90)(2.259)^5} \right\} (1 - e^{0.448}) \tag{7-59}$$

and $p_1 = p_{wf} = 1078$ psia.

The well is next divided into two equal segments and the calculation of bottomhole pressure repeated. The first segment is from the surface to a depth of 5000 ft. For this segment, $\bar{T}$ is 162.5°F, T_{pr} is 1.66, and p_{pr} is 1.12 as before. From Fig. 4-1, $\bar{Z} = 0.93$. The viscosity is essentially the same as before, 0.0131 cp. Thus, the Reynolds number and friction factor will be the same as in the previous calculation. From Eqs. (7-53) and (7-56),

$$s = -\frac{(0.0375)(0.709)[\sin(90)](5000)}{(0.93)(622.5)} = -0.2296 \tag{7-60}$$

$$p_1^2 = e^{0.2296}(800)^2 - 2.685 \times 10^{-3} \left\{ \frac{(0.0044)[(0.93)(622.5)(2000)]^2}{2.259^5} \right\} (1 - e^{0.2296}) \tag{7-61}$$

and $p_{5000} = 935$ psia.

For the second segment, from a depth of 5000 ft to the bottomhole depth of 10,000 ft, we use $\bar{T} = 187.5$°F and $p = 935$ psia. Thus, $T_{pr} = 1.73$, $p_{pr} = 1.30$, and from Fig. 4-1, $\bar{Z} = 0.935$. Viscosity is again 0.0131 cp. So, for this segment,

$$s = -\frac{(0.0375)(0.709)[\sin(90)](5000)}{(0.935)(647.5)} = -0.2196 \tag{7-62}$$

$$p_1^2 = e^{0.2196}(935)^2 - 2.685 \times 10^{-3} \left\{ \frac{(0.0044)[(0.935)(647.5)(2000)]^2}{2.259^5} \right\} (1 - e^{0.2196}) \tag{7-63}$$

and $p_1 = p_{wf} = 1078$ psia.

Since neither temperature nor pressure varied greatly throughout the well, little error resulted from using average T and Z for the entire well. It is not likely that kinetic energy changes are significant, also because of the small changes in temperature and pressure, but this can be checked.

The kinetic energy pressure drop in this well can be estimated by

$$\Delta p_{\text{KE}} \approx \frac{\bar{\rho}}{2g_c} \Delta u^2 \approx \frac{\bar{\rho}}{2g_c} \left(u_2^2 - u_1^2 \right) \tag{7-64}$$

This calculation is approximate, since an average density is being used. The velocities at points 1 and 2 are

$$u_1 = \frac{Z_1 (p_{sc}/p_1)(T_1/T_{sc}) q}{A} \tag{7-65}$$

and

$$u_2 = \frac{Z_2 (p_{sc}/p_2)(T_2/T_{sc}) q}{A} \tag{7-66}$$

and the average density is

$$\bar{\rho} = \frac{28.97 \gamma_g \bar{p}}{\bar{Z} R \bar{T}} \tag{7-67}$$

At position 2 (surface), T is 150°F, $T_{pr} = 1.63$, $p = 800$ psia, $p_{pr} = 1.12$, and $Z = 0.925$; while at 1 (bottomhole), $T = 200$°F, $T_{pr} = 1.76$, $p = 1078$ psia, $p_{pr} = 1.50$, and $Z = 0.93$. For 2 7/8-in., 8.6-lb$_m$/ft tubing, the I.D. is 2.259 in., so the cross-sectional area is 0.0278 ft^2. To calculate average densities, the average pressure, 939 psia, average temperature, 175°F, and average compressibility factor, 0.93, are used. We then calculate $\Delta p_{KE} = 0.06$ psia. The kinetic energy pressure drop is negligible compared with the potential energy and frictional contributions to the overall pressure drop. ◇

7-4 Multiphase Flow in Wells

Multiphase flow—the simultaneous flow of two or more phases of fluid—will occur in almost all oil production wells, in many gas production wells, and in some types of injection wells. In an oil well, whenever the pressure drops below the bubble point, gas will evolve, and from that point to the surface, gas-liquid flow will occur. Thus, even in a well producing from an undersaturated reservoir, unless the surface pressure is above the bubble point, two-phase flow will occur in the wellbore and/or tubing. Many oil wells also produce significant amounts of water, resulting in oil-water flow or oil-water-gas three-phase flow.

Two-phase flow behavior depends strongly on the distribution of the phases in the pipe, which in turn depends on the direction of flow relative to the gravitational field. In this chapter, upward vertical and inclined flow are described; horizontal and near-horizontal flow are treated in Chapter 10.

7-4.1 Holdup Behavior

In two-phase flow, the amount of the pipe occupied by a phase is often different from its proportion of the total volumetric flow rate. As an example of a typical two-phase flow situation, consider the upward flow of two phases, α and β, where α is less dense than β, as shown in Fig. 7-8. Typically, in upward two-phase flow, the lighter phase (α) will be moving faster than the denser phase (β). Because of this fact, called the *holdup phenomenon*, the in-situ volume fraction of the denser phase will be greater than the input volume fraction of the denser phase—that is, the denser phase is "held up" in the pipe relative to the lighter phase.

This relationship is quantified by defining a parameter called *holdup*, y , as

$$y_\beta = \frac{V_\beta}{V} \tag{7-68}$$

where V_β = volume of denser phase in pipe segment and V = volume of pipe segment. The holdup, y_β, can also be defined in terms of a local holdup, $y_{\beta l}$, as

$$y_\beta = \frac{1}{A}\int_0^A y_{\beta l}\, dA \tag{7-69}$$

The local holdup, $y_{\beta l}$, is a time-averaged quantity—that is, $y_{\beta l}$ is the fraction of the time a given location in the pipe is occupied by phase β.

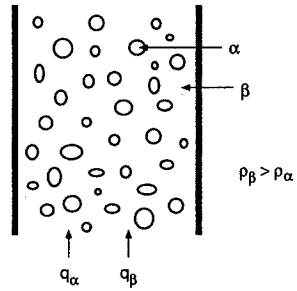

Figure 7-8
Schematic of two-phase flow.

The holdup of the lighter phase, y_α, is defined identically to y_β as

$$y_\alpha = \frac{V_\alpha}{V} \tag{7-70}$$

or, because the pipe is completely occupied by the two phases,

$$y_\alpha = 1 - y_\beta \tag{7-71}$$

In gas-liquid flow, the holdup of the gas phase, y_α, is sometimes called the *void fraction.*

Another type of parameter used in describing two-phase flow is the input fraction of each phase, λ, defined as

$$\lambda_\beta = \frac{q_\beta}{q_\alpha + q_\beta} \tag{7-72}$$

and

$$\lambda_\alpha = 1 - \lambda_\beta \tag{7-73}$$

where q_α and q_β are the volumetric flow rates of the two phases. The input volume fractions, λ_α and λ_β, are also referred to as the "no-slip holdups."

Another measure of the holdup phenomenon that is commonly used in production log interpretation is the "slip velocity," u_s. Slip velocity is defined as the difference between the average velocities of the two phases. Thus,

$$u_s = \bar{u}_\alpha - \bar{u}_\beta \tag{7-74}$$

where $\bar{u}_\alpha$ and $\bar{u}_\beta$ are the average in-situ velocities of the two phases. Slip velocity is not an independent property from holdup, but is simply another way to represent the holdup

phenomenon. In order to show the relationship between holdup and slip velocity, we introduce the definition of superficial velocity, $u_{s\alpha}$ or $u_{s\beta}$, defined as

$$u_{s\alpha} = \frac{q_\alpha}{A} \tag{7-75}$$

and

$$u_{s\beta} = \frac{q_\beta}{A} \tag{7-76}$$

The superficial velocity of a phase would be the average velocity of the phase if that phase filled the entire pipe; that is, if it were single-phase flow. In two-phase flow, the superficial velocity is not a real velocity that physically occurs, but simply a convenient parameter.

The average in-situ velocities, $\bar{u}_\alpha$ and $\bar{u}_\beta$ are related to the superficial velocities and the holdup by

$$\bar{u}_\alpha = \frac{u_{s\alpha}}{y_\alpha} \tag{7-77}$$

and

$$\bar{u}_\beta = \frac{u_{s\beta}}{y_\beta} \tag{7-78}$$

Substituting these expressions into the equation defining slip velocity (7-74) yields

$$u_s = \frac{1}{A}\left(\frac{q_\alpha}{1-y_\beta} - \frac{q_\beta}{y_\beta}\right) \tag{7-79}$$

Correlations for holdup are generally used in two-phase pressure gradient calculations; the slip velocity is usually used to represent holdup behavior in production log interpretation.

EXAMPLE 7-6

Relationship between holdup and slip velocity

If the slip velocity for a gas-liquid flow is 60 ft/min and the superficial velocity of each phase is also 60 ft/min, what is the holdup of each phase?

Solution From Eq. (7-79), since superficial velocity of a phase is q/A,

$$u_s = \frac{u_{sg}}{1-y_l} - \frac{u_{sl}}{y_l} \tag{7-80}$$

Solving for y_l, a quadratic equation is obtained:

$$u_s y_l^2 - (u_s - u_{sg} - u_{sl})y_l - u_{sl} = 0 \tag{7-81}$$

For $u_s = u_{sg} = u_{sl} = 60$ ft/min, the solution is $y_l = 0.62$. The holdup of the gas phase is then $y_g = 1 - y_l = 0.38$. The holdup of the liquid is greater than the input fraction (0.5), as is typical in upward gas-liquid flow. ◇

7-4.2 Two-Phase Flow Regimes

The manner in which the two phases are distributed in the pipe significantly affects other aspects of two-phase flow, such as slippage between phases and the pressure gradient. The "flow regime" or flow pattern is a qualitative description of the phase distribution. In gas-liquid, vertical, upward flow, four flow regimes are now generally agreed upon in the two-phase flow literature: bubble, slug, churn, and annular flow. These occur as a progression with increasing gas rate for a given liquid rate. Figure 7-9 (Govier and Aziz, 1977) shows these flow patterns and the approximate regions in which they occur as functions of superficial velocities for air-water flow. A brief description of these flow regimes is as follows.

1. Bubble flow: Dispersed bubbles of gas in a continuous liquid phase.
2. Slug flow: At higher gas rates, the bubbles coalesce into larger bubbles, called Taylor bubbles, that eventually fill the entire pipe cross section. Between the large gas bubbles are slugs of liquid that contain smaller bubbles of gas entrained in the liquid.
3. Churn flow: With a further increase in gas rate, the larger gas bubbles become unstable and collapse, resulting in churn flow, a highly turbulent flow pattern with both phases dispersed. Churn flow is characterized by oscillatory, up-and-down motions of the liquid.
4. Annular flow: At higher gas rates, gas becomes the continuous phase, with liquid flowing in an annulus coating the surface of the pipe and with liquid droplets entrained in the gas phase.

The flow regime in gas-liquid vertical flow can be predicted with a flow regime map, a plot relating flow regime to flow rates of each phase, fluid properties, and pipe size. One such map that is used for flow regime discrimination in some pressure drop correlations is that of Duns and Ros (1963), shown in Fig. 7-10. The Duns and Ros map correlates flow regime with two dimensionless numbers, the liquid and gas velocity numbers, N_{vl} and N_{vg}, defined as

$$N_{vl} = u_{sl}\sqrt[4]{\frac{\rho_l}{g\sigma}} \tag{7-82}$$

and

$$N_{vg} = u_{sg}\sqrt[4]{\frac{\rho_l}{g\sigma}} \tag{7-83}$$

where ρ_l is liquid density, g is the acceleration of gravity, and σ is the interfacial tension of the liquid-gas system. This flow pattern map does account for some fluid properties; note, however, that for a given gas-liquid system, the only variables in the dimensionless groups are the superficial velocities of the phases.

Duns and Ros defined three distinct regions on their map, but also included a transition region where the flow changes from a liquid continuous to a gas continuous system. Region I contains bubble and low-velocity slug flow, Region II is high-velocity slug and churn flow, and Region III contains the annular flow pattern.

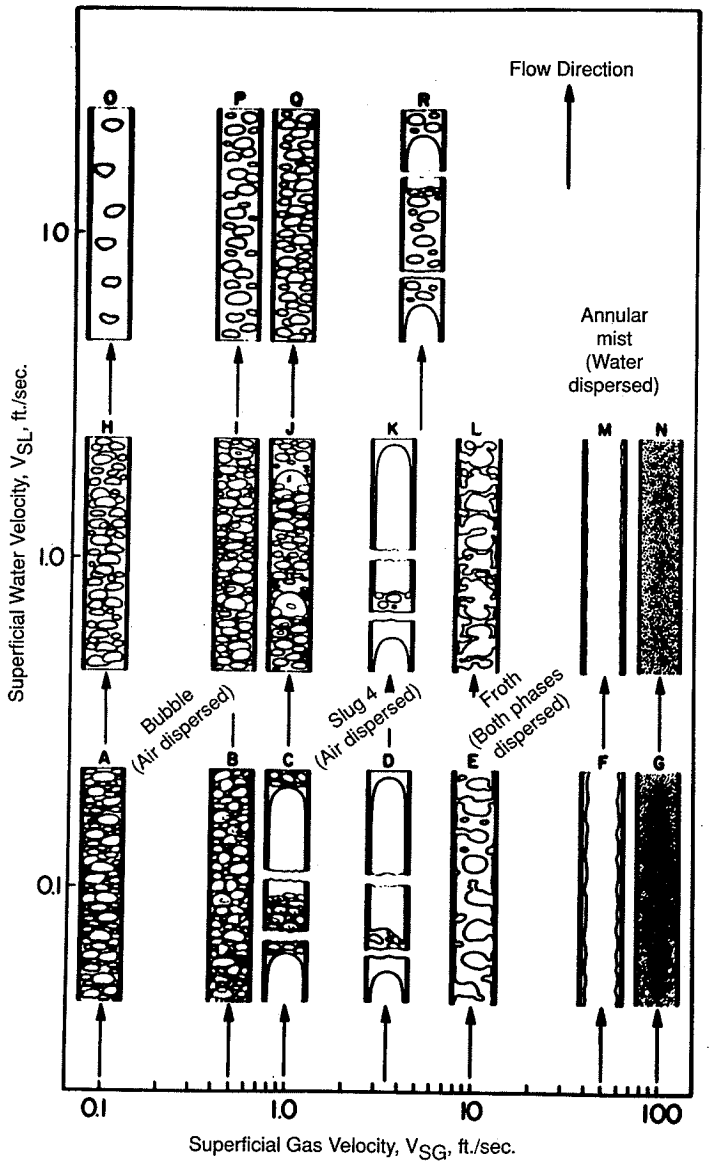

Figure 7-9
Flow regimes in gas-liquid flow. (*From Govier and Aziz, 1977.*)

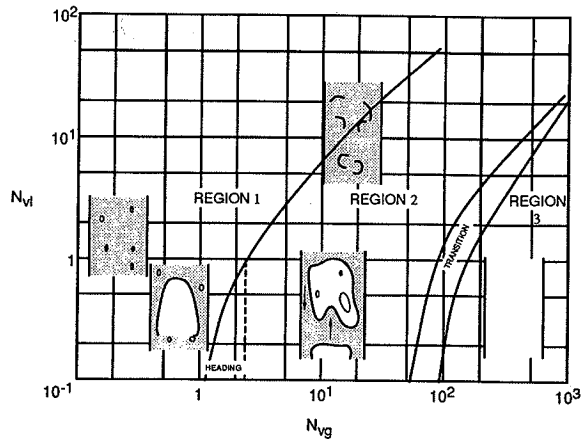

Figure 7-10
Duns and Ros flow regime map. (*From Duns and Ros, 1963.*)

A flow regime map that is based on a theoretical analysis of the flow regime transitions is that of Taitel and Dukler (Taitel et al., 1976). This map must be generated for particular gas and liquid properties and for a particular pipe size; a Taitel-Dukler map for air-water flow in a 2-in.-I.D. pipe is shown in Fig. 7-11. This map identifies five possible flow regimes: bubble, dispersed bubble (a bubble regime in which the bubbles are small enough that no slippage occurs), slug, churn, and annular. The slug/churn transition is significantly different than that of other flow regime maps in that churn flow is thought to be an entry phenomenon leading to slug flow in the Taitel-Dukler theory. The D lines show how many pipe diameters from the pipe entrance churn flow is expected to occur before slug flow develops. For example, if the flow conditions fell on the D line labeled $L_E/D = 100$, for a distance of 100 pipe diameters from the pipe entrance, churn flow is predicted to occur; beyond this distance slug flow is the predicted flow regime.

EXAMPLE 7-7
Predicting two-phase flow regime

200 bbl/d of water and 10,000 ft^3/day of air are flowing in a 2-in. vertical pipe. The water density is 62.4 lb_m/ft^3 and the surface tension is 74 dynes/cm. Predict the flow regime that will occur using the Duns-Ros and the Taitel-Dukler flow regime maps.

Solution First, the superficial velocities are calculated as

$$u_{sl} = \frac{q_l}{A} = \left[\frac{(200 \text{ bbl/d})(5.615 \text{ ft}^3/\text{bbl})(1 \text{ d}/86,400 \text{ s})}{0.02182 \text{ ft}^2}\right] = 0.6 \text{ ft/s} = 0.18 \text{ m/s} \qquad (7\text{-}84)$$

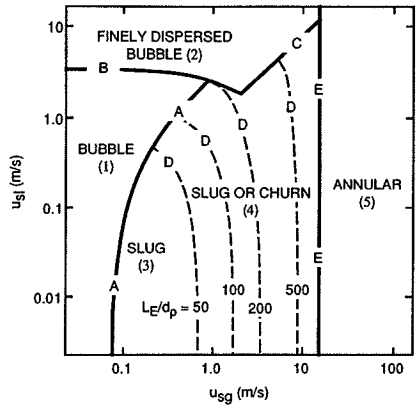

Figure 7-11
Taitel-Dukler flow regime map.
(From Taitel et al., 1976.)

$$u_{sg} = \frac{q_g}{A} = \left[\frac{(10,000 \text{ ft}^3/\text{d})(1 \text{ d}/86,400 \text{ s})}{0.02182 \text{ ft}^2}\right] = 5.3 \text{ ft/s} = 1.62 \text{ m/s} \tag{7-85}$$

For the Duns and Ros map, the liquid and gas velocity numbers must be calculated. For units of ft/s for superficial velocity, lb_m/ft^3 for density, and dynes/cm for surface tension, these are

$$N_{vl} = 1.938 u_{sl} \sqrt[4]{\frac{\rho_l}{\sigma}} \tag{7-86}$$

$$N_{vg} = 1.938 u_{sg} \sqrt[4]{\frac{\rho_l}{\sigma}} \tag{7-87}$$

Using the physical properties and flow rates given, we find $N_{vl} = 1.11$ and $N_{vg} = 9.8$. Referring to Fig. 7-10, the flow conditions fall in region 2; the predicted flow regime is high-velocity slug or churn flow. Using the Taitel-Dukler map (Fig. 7-11), the flow regime is also predicted to be slug or churn, with L_E/D of about 150. Thus, the Taitel-Dukler map predicts that churn flow will occur for the first 150 pipe diameters from the entrance; beyond this position, slug flow is predicted. ◇

7-4.3 Two-Phase Pressure Gradient Models

In this section we will consider correlations used to calculate the pressure drop in gas-liquid two-phase flow in wells. As in single-phase flow, the starting point is the mechanical energy balance given by Eq. (7-16). Since the flow properties may change significantly along the pipe (mainly the gas density and velocity) in gas-liquid flow, we must calculate

the pressure gradient for a particular location in the pipe; the overall pressure drop is then obtained with a pressure traverse calculation procedure (Section 7-4.4). A differential form of the mechanical energy balance equation is

$$\frac{dp}{dz} = \left(\frac{dp}{dz}\right)_{\text{PE}} + \left(\frac{dp}{dz}\right)_{\text{KE}} + \left(\frac{dp}{dz}\right)_{\text{F}} \tag{7-88}$$

In most two-phase flow correlations, the potential energy pressure gradient is based on the in-situ average density, $\bar{\rho}$,

$$\left(\frac{dp}{dz}\right)_{\text{PE}} = \frac{g}{g_c}\bar{\rho}\sin\theta \tag{7-89}$$

where

$$\bar{\rho} = (1 - y_1)\rho_g + y_1\rho_l \tag{7-90}$$

Various definitions of the two-phase average velocity, viscosity, and friction factor are used in the different correlations to calculate the kinetic energy and frictional pressure gradients.

We will consider two of the most commonly used two-phase flow correlations: the modified Hagedorn and Brown method (Brown, 1977), and the Beggs and Brill method (Beggs and Brill, 1973). The first of these was developed for vertical, upward flow and is recommended only for near-vertical wellbores; the Beggs and Brill correlation can be applied for any wellbore inclination and flow direction.

The modified Hagedorn and Brown method. The modified Hagedorn and Brown method (mH-B) is an empirical two-phase flow correlation based on the original work of Hagedorn and Brown (1965). The heart of the Hagedorn-Brown method is a correlation for liquid holdup; the modifications of the original method include using the no-slip holdup when the original empirical correlation predicts a liquid holdup value less than the no-slip holdup and the use of the Griffith correlation (Griffith and Wallis, 1961) for the bubble flow regime.

These correlations are selected based on the flow regime as follows. Bubble flow exists if $\lambda_g < L_B$, where

$$L_B = 1.071 - 0.2218\left(\frac{u_m^2}{D}\right) \tag{7-91}$$

and $L_B \geq 0.13$. Thus, if the calculated value of L_B is less than 0.13, L_B is set to 0.13. If the flow regime is found to be bubble flow, the Griffith correlation is used; otherwise, the original Hagedorn-Brown correlation is used.

Flow regimes other than bubble flow: The original Hagedorn-Brown correlation. The form of the mechanical energy balance equation used in the Hagedorn-Brown correlation is

$$\frac{dp}{dz} = \frac{g}{g_c}\bar{\rho} + \frac{2f\bar{\rho}u_m^2}{g_c D} + \bar{\rho}\frac{\Delta(u_m^2/2g_c)}{\Delta z} \tag{7-92}$$

which can be expressed in oilfield units as

$$144\frac{dp}{dz} = \bar{\rho} + \frac{f\dot{m}^2}{(7.413 \times 10^{10} D^5)\bar{\rho}} + \bar{\rho}\frac{\Delta(u_m^2/2g_c)}{\Delta z} \tag{7-93}$$

where f is the friction factor, $\dot{m}$ is the total mass flow rate (lb_m/d), $\bar{\rho}$ is the in-situ average density [Eq. (7-90)] (lb_m/ft^3), D is the diameter (ft), u_m is the mixture velocity (ft/sec), and the pressure gradient is in psi/ft. The mixture velocity used in H-B is the sum of the superficial velocities,

$$u_m = u_{sl} + u_{sg} \tag{7-94}$$

To calculate the pressure gradient with Eq. (7-93), the liquid holdup is obtained from a correlation and the friction factor is based on a mixture Reynolds number. The liquid holdup, and hence, the average density, is obtained from a series of charts using the following dimensionless numbers.

Liquid velocity number, N_{vl}:

$$N_{vl} = u_{sl}\sqrt[4]{\frac{\rho_l}{g\sigma}} \tag{7-95}$$

Gas velocity number, N_{vg}:

$$N_{vg} = u_{sg}\sqrt[4]{\frac{\rho_l}{g\sigma}} \tag{7-96}$$

Pipe diameter number, N_D:

$$N_D = D\sqrt{\frac{\rho_l g}{\sigma}} \tag{7-97}$$

Liquid viscosity number, N_L:

$$N_L = \mu_l\sqrt[4]{\frac{g}{\rho_l\sigma^3}} \tag{7-98}$$

In field units, these are

$$N_{vl} = 1.938u_{sl}\sqrt[4]{\frac{\rho_l}{\sigma}} \tag{7-99}$$

$$N_{vg} = 1.938u_{sg}\sqrt[4]{\frac{\rho_l}{\sigma}} \tag{7-100}$$

$$N_D = 120.872D\sqrt{\frac{\rho_l}{\sigma}} \tag{7-101}$$

$$N_L = 0.15726\mu_l\sqrt[4]{\frac{1}{\rho_l\sigma^3}} \tag{7-102}$$

where superficial velocities are in ft/sec, density is in lb_m/ft^3, surface tension is in dynes/cm, viscosity is in cp, and diameter is in ft. The holdup is obtained from Figs. 7-12 through

7-14. First, CN_L is read from Fig. 7-12. Then the group

$$\frac{N_{vl}p^{0.1}(CN_L)}{N_{vg}^{0.575}p_a^{0.1}N_D}$$

is calculated; from Fig. 7-13, we get y_l/ψ. Here p is the absolute pressure at the location where pressure gradient is wanted, and p_a is atmospheric pressure. Finally, compute

$$\frac{N_{vg}N_L^{0.380}}{N_D^{2.14}}$$

and read ψ from Fig. 7-14. The liquid holdup is then

$$y_l = \left(\frac{y_l}{\psi}\right)\psi \tag{7-103}$$

The mixture density is then calculated from Eq. (7-90).

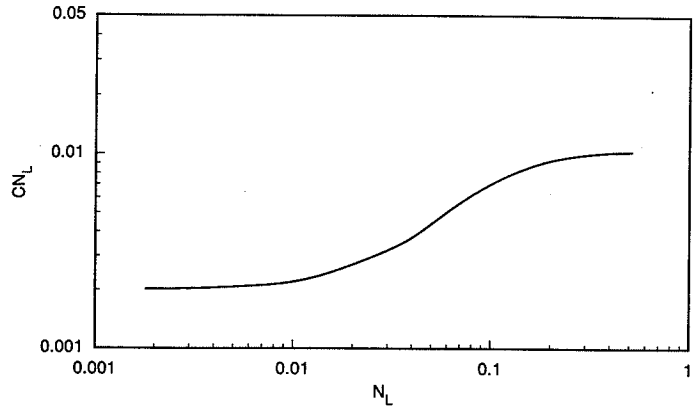

Figure 7-12
Hagedorn and Brown correlation for CNL. (*From Hagedorn and Brown, 1965.*)

The frictional pressure gradient is based on a Fanning friction factor using a mixture Reynolds number, defined as

$$N_{\text{Re}} = \frac{Du_m\bar{\rho}}{\mu_l^{y_l}\mu_g^{(1-y_l)}} \tag{7-104}$$

or, in terms of mass flow rate and using field units,

$$N_{\text{Re}} = \frac{2.2 \times 10^{-2}\dot{m}}{D\mu_l^{y_l}\mu_g^{(1-y_l)}} \tag{7-105}$$

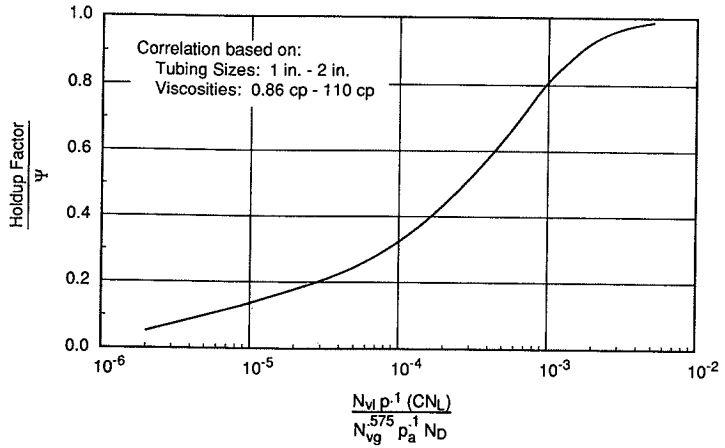

Figure 7-13
Hagedorn and Brown correlation for holdup/ψ. (*From Hagedorn and Brown, 1965.*)

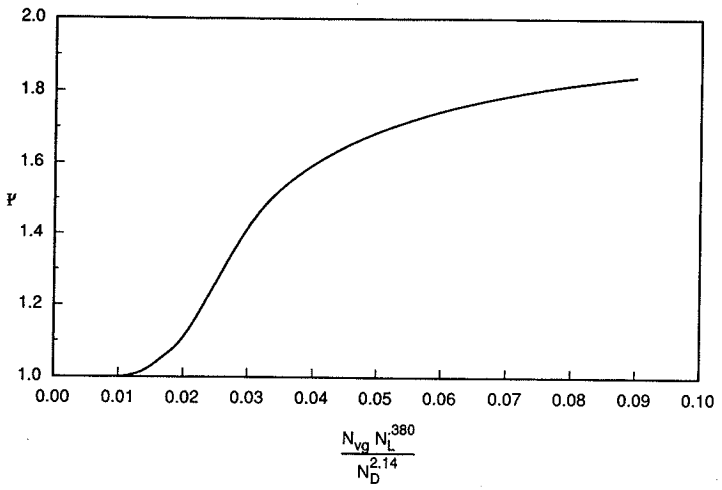

Figure 7-14
Hagedorn and Brown correlation for ψ. (*From Hagedorn and Brown, 1965.*)

where mass flow rate, $\dot{m}$, is in lb_m/day, D is in ft, and viscosities are in cp. The friction factor is then obtained from the Moody diagram (Fig. 7-7) or calculated with the Chen equation [Eq. (7-35)] for the calculated Reynolds number and the pipe relative roughness.

The kinetic energy pressure drop will in most instances be negligible; it is calculated from the difference in velocity over a finite distance of pipe, Δz.

Bubble flow: The Griffith correlation. The Griffith correlation uses a different holdup correlation, bases the frictional pressure gradient on the in-situ average liquid velocity, and neglects the kinetic energy pressure gradient. For this correlation,

$$\frac{dp}{dz} = \frac{g}{g_c}\bar{\rho} + \frac{2f\rho_l \bar{u}_l^2}{g_c D} \tag{7-106}$$

where u_l is the in-situ average liquid velocity, defined as

$$\bar{u}_l = \frac{u_{sl}}{y_l} = \frac{q_l}{A y_l} \tag{7-107}$$

For field units, Eq. (7-106) is

$$144\frac{dp}{dz} = \bar{\rho} + \frac{f\dot{m}_l^2}{(7.413 \times 10^{10}) D^5 \rho_l y_l^2} \tag{7-108}$$

where m_l is the mass flow rate of the liquid only. The liquid holdup is

$$y_l = 1 - \frac{1}{2}\left[1 + \frac{u_m}{u_s} - \sqrt{\left(1 + \frac{u_m}{u_s}\right)^2 - 4\frac{u_{sg}}{u_s}}\right] \tag{7-109}$$

where $u_s = 0.8$ ft/sec. The Reynolds number used to obtain the friction factor is based on the in-situ average liquid velocity,

$$N_{\text{Re}} = \frac{D\bar{u}_l \rho_l}{\mu_l} \tag{7-110}$$

or

$$N_{\text{Re}} = \frac{2.2 \times 10^{-2}\dot{m}_l}{D\mu_l} \tag{7-111}$$

EXAMPLE 7-8

Pressure gradient calculation using the modified Hagedorn and Brown method

Suppose that 2000 bbl/d of oil ($\rho = 0.8$ g/cm^3, $\mu = 2$ cp) and 1 MM SCF/d of gas of the same composition as in Example 7-5 are flowing in 2 7/8-in. tubing. The surface tubing pressure is 800 psia and the temperature is 175°F. The oil-gas surface tension is 30 dynes/cm, and the pipe relative roughness is 0.0006. Calculate the pressure gradient at the top of the tubing, neglecting any kinetic energy contribution to the pressure gradient.

Solution From Example 7-5, we have $\mu_g = 0.0131$ cp and $Z = 0.935$. Converting volumetric flow rates to superficial velocities with $A = (\pi/4)(2.259/12)^2 = 0.0278$ ft^2,

$$u_{sl} = \frac{(2000 \text{ bbl/d})(5.615 \text{ ft}^3/\text{bbl})(\text{d}/86,400 \text{ s})}{0.0278 \text{ ft}^2} = 4.67 \text{ ft/s} \tag{7-112}$$

The gas superficial velocity can be calculated from the volumetric flow rate at standard conditions with Eq. (7-45),

$$u_{sg} = \frac{4}{\pi(2.259/12)^2}(10^6 \text{ ft}^3/\text{d})(0.935)\left(\frac{460+175}{460+60}\right)\left(\frac{14.7}{800}\right)\frac{\text{d}}{86,400 \text{ s}} \tag{7-113}$$
$$= 8.72 \text{ ft/s}$$

The mixture velocity is

$$u_m = u_{sl} + u_{sg} = (4.67 + 8.72) = 13.39 \text{ ft/s} \tag{7-114}$$

and the input fraction of gas is

$$\lambda_g = \frac{u_{sg}}{u_m} = \frac{8.72}{13.39} = 0.65 \tag{7-115}$$

First, we check whether the flow regime is bubble flow. Using Eq. (7-91),

$$L_B = 1.071 - 0.2218\left[\frac{(13.39)^2}{2.259/12}\right] = -210 \tag{7-116}$$

but L_B must be ≥ 0.13, so $L_B = 0.13$. Since $\lambda_g(0.65)$ is greater than L_B, the flow regime is not bubble flow and we proceed with the Hagedorn-Brown correlation.

We next compute the dimensionless numbers, N_{vl}, N_{vg}, N_D, and N_L. Using Eqs. (7-99) through (7-102), we find $N_{vl} = 10.28$, $N_{vg} = 19.20$, $N_D = 29.35$, and $N_L = 9.26\times10^{-3}$. Now, we determine liquid holdup, y_l, from Figs. 7-12 through 7-14. From Fig. 7-12, $CN_L = 0.0022$. Then

$$\frac{N_{vl}}{N_{vg}^{0.575}}\left(\frac{p}{p_a}\right)^{0.1}\frac{CN_L}{N_D} = \frac{10.28}{(19.2)^{0.575}}\left(\frac{800}{14.7}\right)^{0.1}\frac{(0.0022)}{29.35} = 2.1\times10^{-4} \tag{7-117}$$

and, from Fig. 7-13, $y_l/\psi = 0.46$. Finally, we calculate

$$\frac{N_{vg}N_L^{0.38}}{N_D^{2.14}} = \frac{(19.2)(9.26\times10^{-3})^{0.38}}{(29.35)^{2.14}} = 2.34\times10^{-3} \tag{7-118}$$

and from Fig. 7-14, $\psi = 1.0$. Note that ψ will generally be 1.0 for low-viscosity liquids. The liquid holdup is thus 0.46. This is compared with the input liquid fraction, λ_l, which in this case is 0.35. If y_l is less than λ_l, y_l is set to λ_l.

Next, we calculate the two-phase Reynolds number using Eq. (7-105). The mass flow rate is

$$\dot{m} = \dot{m}_l + \dot{m}_g = A\left(u_{sl}\rho_l + u_{sg}\rho_g\right) \tag{7-119}$$

The gas density is calculated from Eq. (7-44),

$$\rho_g = \frac{(28.97)(0.709)(800 \text{ psi})}{(0.935)(10.73 \text{ psi-ft}^3/\text{lb-mol-°R})(635°\text{R})} = 2.6 \text{ lb}_m/\text{ft}^3 \tag{7-120}$$

so

$$\dot{m} = (0.0278 \text{ ft}^2)[(4.67 \text{ ft/s})(49.9 \text{ lb}_m/\text{ft}^3) + (8.72 \text{ ft/s})(2.6 \text{ lb}_m/\text{ft}^3)](86,400 \text{ s/d})$$
$$= 614,000 \text{ lb}_m/\text{d} \tag{7-121}$$

and

$$N_{\text{Re}} = \frac{(2.2\times10^{-2})(6.14\times10^5)}{(2.259/12)(2)^{0.46}(0.0131)^{0.54}} = 5.42\times10^5 \tag{7-122}$$

From Fig. 7-7 or Eq. (7-35), $f = 0.0046$. The in-situ average density is

$$\bar{\rho} = y_l\rho_l + (1-y_l)\rho_g = (0.46)(49.9) + (0.54)(2.6) = 24.4 \text{ lb}_m/\text{ft}^3 \tag{7-123}$$

Finally, from Eq. (7-93),

$$\frac{dp}{dz} = \frac{1}{144}\left[\bar{\rho} + \frac{f\dot{m}^2}{(7.413\times10^{10})D^5\bar{\rho}}\right]$$
$$= \frac{1}{144}\left[24.4 + \frac{(0.0046)(614,000)^2}{(7.413\times10^{10})(2.259/12)^5(24.4)}\right] \tag{7-124}$$
$$= \frac{1}{144}(24.4 + 4.1) = 0.198 \text{ psi/ft} \quad \diamond$$

The Beggs and Brill method. The Beggs and Brill correlation differs significantly from that of Hagedorn and Brown in that the Beggs and Brill correlation is applicable to any pipe inclination and flow direction. This method is based on the flow regime that would occur if the pipe were horizontal; corrections are then made to account for the change in holdup behavior with inclination. It should be kept in mind that the flow regime determined as part of this correlation is the flow regime that would occur if the pipe were perfectly horizontal and is probably not the actual flow regime that occurs at any other angle. The Beggs and Brill method is the recommended technique for any wellbore that is not near vertical.

The Beggs and Brill method uses the general mechanical energy balance [Eq. (7-88)] and the in-situ average density [Eq. (7-90)] to calculate the pressure gradient and is based on the following parameters:

$$N_{\text{FR}} = \frac{u_m^2}{gD} \tag{7-125}$$

$$\lambda_l = \frac{u_{sl}}{u_m} \tag{7-126}$$

$$L_1 = 316\lambda_l^{0.302} \tag{7-127}$$

$$L_2 = 0.0009252\lambda_l^{-2.4684} \tag{7-128}$$

$$L_3 = 0.10\lambda_l^{-1.4516} \tag{7-129}$$

$$L_4 = 0.5\lambda_l^{-6.738} \tag{7-130}$$

The horizontal flow regimes used as correlating parameters in the Beggs-Brill method are segregated, transition, intermittent, and distributed (see Chapter 10 for a discussion of horizontal flow regimes). The flow regime transitions are given by the following.

Segregated flow exists if

$$\lambda_l < 0.01 \text{ and } N_{\text{FR}} < L_1 \quad \text{or} \quad \lambda_l \geq 0.01 \text{ and } N_{\text{FR}} < L_2 \tag{7-131}$$

Transition flow occurs when

$$\lambda_l \geq 0.01 \text{ and } L_2 < N_{\text{FR}} \leq L_3 \tag{7-132}$$

Intermittent flow exists when

$$0.01 \leq \lambda_l < 0.4 \text{ and } L_3 < N_{\text{FR}} \leq L_1 \quad \text{or} \quad \lambda_l \geq 0.4 \text{ and } L_3 < N_{\text{FR}} \leq L_4 \tag{7-133}$$

Distributed flow occurs if

$$\lambda_l < 0.4 \text{ and } N_{\text{FR}} \geq L_1 \quad \text{or} \quad \lambda_l \geq 0.4 \text{ and } N_{\text{FR}} > L_4 \tag{7-134}$$

The same equations are used to calculate the liquid holdup, and hence, the average density, for the segregated, intermittent, and distributed flow regimes. These are

$$y_l = y_{lo}\psi \tag{7-135}$$

$$y_{lo} = \frac{a\lambda_l^b}{N_{\text{FR}}^c} \tag{7-136}$$

with the constraint that $y_{lo} \geq \lambda_l$ and

$$\psi = 1 + C[\sin(1.8\,\theta) - 0.333\sin^3(1.8\,\theta)] \tag{7-137}$$

where

$$C = (1 - \lambda_l)\ln(d\lambda_l^e N_{vl}^f N_{FR}^g) \tag{7-138}$$

where a, b, c, d, e, f, and g depend on the flow regime and are given in Table 7-1. C must be ≥ 0.

If the flow regime is transition flow, the liquid holdup is calculated using both the segregated and intermittent equations and interpolated using the following:

$$y_l = Ay_l(\text{segregated}) + By_l(\text{intermittent}) \tag{7-139}$$

where

$$A = \frac{L_3 - N_{\text{FR}}}{L_3 - L_2} \tag{7-140}$$

Table 7-1

Beggs and Brill holdup constants

Flow regime	a	b	c	
Segregated	0.98	0.4846	0.0868	
Intermittent	0.845	0.5351	0.0173	
Distributed	1.065	0.5824	0.0609	
	d	e	f	g
Segregated uphill	0.011	−3.768	3.539	−1.614
Intermittent uphill	2.96	0.305	−0.4473	0.0978
Distributed uphill	No correction, $C = 0$, $\psi = 1$			
All regimes downhill	4.70	−0.3692	0.1244	−0.5056

and

$$B = 1 - A \tag{7-141}$$

The frictional pressure gradient is calculated from

$$\left(\frac{dp}{dz}\right)_F = \frac{2f_{tp}\rho_m u_m^2}{g_c D} \tag{7-142}$$

where

$$\rho_m = \rho_l\lambda_l + \rho_g\lambda_g \tag{7-143}$$

and

$$f_{\text{tp}} = f_n\frac{f_{\text{tp}}}{f_n} \tag{7-144}$$

The no-slip friction factor, f_n, is based on smooth pipe $(\epsilon/D) = 0$) and the Reynolds number,

$$N_{\text{Re}_m} = \frac{\rho_m u_m D}{\mu_m} \tag{7-145}$$

where

$$\mu_m = \mu_l\lambda_l + \mu_g\lambda_g \tag{7-146}$$

The two-phase friction factor, f_{tp} is then

$$f_{\text{tp}} = f_n e^S \tag{7-147}$$

where

$$S = \frac{[\ln(x)]}{\{-0.0523 + 3.182\ln(x) - 0.8725[\ln(x)]^2 + 0.01853[\ln(x)]^4\}} \tag{7-148}$$

and

$$x = \frac{\lambda_l}{y_l^2} \tag{7-149}$$

Since S is unbounded in the interval $1 < x < 1.2$, for this interval,

$$S = \ln(2.2x - 1.2) \tag{7-150}$$

The kinetic energy contribution to the pressure gradient is accounted for with a parameter E_k as follows:

$$\frac{dp}{dz} = \frac{(dp/dz)_{PE} + (dp/dz)_F}{1 - E_k} \tag{7-151}$$

where

$$E_k = \frac{u_m u_{sg} \rho_m}{g_c p} \tag{7-152}$$

EXAMPLE 7-9

Pressure gradient calculation using the Beggs and Brill method

Repeat Example 7-8, using the Beggs and Brill method.

Solution First, we determine the flow regime that would exist if the flow were horizontal. Using Eqs. (7-125) through (7-130) and the values of u_m (13.39 ft/sec) and λ_l (0.35) calculated in Example 7-8, we find $N_{FR} = 29.6$, $L_1 = 230$, $L_2 = 0.0124$, $L_3 = 0.459$, and $L_4 = 590$. Checking the flow regime limits [Eqs. (7-131) through (7-134)], we see that

$$0.01 \le \lambda_l < 0.4 \quad \text{and} \quad L_3 < N_{FR} \le L_1$$

and therefore, the horizontal flow regime is intermittent. From Eq. (7-136) and Table 7-1,

$$y_{lo} = \frac{0.845(0.35)^{0.5351}}{(29.6)^{0.0173}} = 0.454 \tag{7-153}$$

Then, using Eqs. (7-137) and (7-138),

$$C = (1 - 0.35)\ln[2.96(0.35)^{0.305}(10.28)^{-0.4473}(29.6)^{0.0978}] = 0.0351 \tag{7-154}$$

$$\psi = 1 + 0.0351\{\sin[1.8(90)] - 0.333\sin^3[1.8(90)]\} = 1.01 \tag{7-155}$$

so that, from Eq. (7-135),

$$y_l = (0.454)(1.01) = 0.459 \tag{7-156}$$

The in-situ average density is

$$\bar{\rho} = y_l \rho_l + y_g \rho_g = (0.459)(49.9) + (1 - 0.459)(2.6) = 24.29 \text{ lb}_m/\text{ft}^3 \tag{7-157}$$

and the potential energy pressure gradient is

$$\left(\frac{dp}{dz}\right)_{PE} = \frac{g}{g_c}\bar{\rho}\sin\theta = \frac{(24.29)\sin(90)}{144} = 0.169 \text{ psi/ft} \tag{7-158}$$

To calculate the frictional pressure gradient, we first compute the input fraction weighted density and viscosity from Eqs. (7-143) and (7-146):

$$\rho_m = (0.35)(49.9) + (0.65)(2.6) = 19.1 \text{ lb}_m/\text{ft}^3 \tag{7-159}$$

$$\mu_m = (0.35)(2) + (0.65)(0.0131) = 0.709 \text{ cp} \tag{7-160}$$

The Reynolds number from Eq. (7-145) is

$$N_{Re_m} = \frac{(19.1)(13.39)(2.259/12)(1488)}{0.709} = 101{,}000 \tag{7-161}$$

From the smooth pipe curve on the Moody diagram, the no-slip friction factor, f_n, is 0.0045. Then, using Eqs. (7-147) through (7-149),

$$x = \frac{0.35}{(0.459)^2} = 1.66 \tag{7-162}$$

$$S = \frac{\ln(1.66)}{\{-0.0523 + 3.182\ln(1.66) - 0.8725[\ln(1.66)]^2 + 0.01853[\ln(1.66)]^4\}} \tag{7-163}$$

$$= 0.379$$

$$f_{tp} = 0.0045e^{0.379} = 0.0066 \tag{7-164}$$

From Eq. (7-142), the frictional pressure gradient is

$$\left(\frac{dp}{dz}\right)_F = \frac{(2)(0.0066)(19.1)(13.39)^2}{(32.17)(2.259/12)} = 7.5 \text{ lb}_f/\text{ft}^3 = 0.05 \text{ psi/ft} \tag{7-165}$$

and the overall pressure gradient is

$$\left(\frac{dp}{dz}\right) = \left(\frac{dp}{dz}\right)_{PE} + \left(\frac{dp}{dz}\right)_F = 0.169 + 0.05 = 0.219 \text{ psi/ft} \tag{7-166}$$

◇

7-4.4 Pressure Traverse Calculations

We have examined several methods for calculating the pressure gradient, dp/dz, which can be applied at any location in a well. However, our objective is often to calculate the overall pressure drop, Δp, over a considerable distance, and over this distance the pressure gradient in gas-liquid flow may vary significantly as the downhole flow properties change with temperature and pressure. For example, in a well such as that pictured in Figure 7-15, in the lower part of the tubing the pressure is above the bubble point and the flow is single-phase oil. At some point, the pressure drops below the bubble point and gas comes out of solution, causing gas-liquid bubble flow; and as the pressure continues to drop, other flow regimes may occur farther up the tubing.

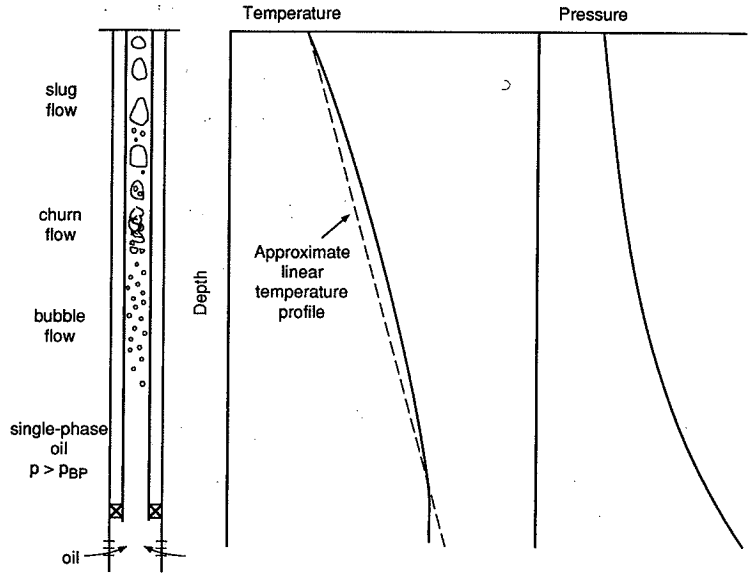

Figure 7-15
Pressure, temperature, and flow regime distribution in a well.

Thus, we must divide the total distance into increments small enough that the flow properties, and hence, the pressure gradient, are almost constant in each increment. Summing the pressure drop in each increment, we obtain the overall pressure drop. This stepwise calculation procedure is generally referred to as a pressure traverse calculation.

Since both the temperature and pressure will be varying, a pressure traverse calculation is usually iterative. The temperature profile is usually approximated as being linear between the surface temperature and the bottomhole temperature, as shown in Fig. 7-15. Pressure traverse calculations can be performed either by fixing the length increment and finding the pressure drop over this increment or by fixing the pressure drop and finding the depth interval over which this pressure drop would occur (Brill and Beggs, 1978). Fixing the length interval is often more convenient when programming a pressure traverse calculation for computer solution; fixing the pressure drop increment is more convenient for hand calculations.

Pressure traverse with fixed length interval. Starting with a known pressure p_1 at position L_1 (normally the surface or bottomhole conditions), the following procedure is followed:

1. Select a length increment, ΔL. A typical value for flow in tubing is 200 ft.
2. Estimate the pressure drop, Δp. A starting point is to calculate the no-slip average density and from this, the potential energy pressure gradient. The estimated Δp is then the potential energy pressure gradient times the depth increment. This will generally underestimate the pressure drop.
3. Calculate all fluid properties at the average pressure $(p_1 + \Delta p/2)$ and average temperature $(T_1 + \Delta T/2)$.
4. Calculate the pressure gradient, dp/dz, with a two-phase flow correlation.
5. Obtain a new estimate of Δp from

$$\Delta p_{\text{new}} = \left(\frac{dp}{dz}\right)\Delta L \tag{7-167}$$

6. If $\Delta p_{\text{new}} \neq \Delta p_{\text{old}}$ within a prescribed tolerance, go back to step 3 and repeat the procedure with the new estimate of Δp.

Pressure traverse with fixed pressure increment. Starting with a known pressure p_1 at position L_1 (normally the surface or bottomhole conditions), the following procedure is followed:

1. Select a pressure drop increment, Δp. The pressure drop in the increment should be less than 10% of the pressure p_1 and can be varied from one step to the next.
2. Estimate the length increment. This can be done using the no-slip density to estimate the pressure gradient, as was suggested for the fixed-length-traverse procedure.
3. Calculate all necessary fluid properties at the average pressure, $p_1 + \Delta p/2$ and the estimated average temperature, $T_1 + \Delta T/2$.
4. Calculate the estimated pressure gradient, dp/dz, using a two-phase flow correlation.
5. Estimate the length increment by

$$\Delta L_{\text{new}} = \frac{\Delta p}{(dp/dz)} \tag{7-168}$$

6. If $\Delta L_{\text{new}} \neq \Delta L_{\text{old}}$ within a prescribed tolerance, go back to step 3 and repeat the procedure. In this procedure, since temperature is changing more slowly in a well and the average pressure of the increment is fixed, convergence should be rapid. If the well can be assumed to be isothermal, no iteration is required.

Since the pressure traverse calculations are iterative, and the fluid properties and pressure gradient calculations are tedious, it is most convenient to write computer programs for pressure traverse calculations.

EXAMPLE 7-10

Pressure traverse calculation for a vertical well

Using the modified Hagedorn and Brown method, generate plots of pressure versus depth, from the surface to 10,000 ft, for gas–oil ratios ranging from 0 to 4000 for the following flow conditions in a vertical well: $q_o = 400$ bbl/d, WOR = 1, $p_{sep} = 100$ psig, average $T = 140°$F, $\gamma_g = 0.65$, $\gamma_o = 35°$API, $\gamma_w = 1.074$, tubing size = 2.5 in. I.D.

Solution A series of pressure traverse calculations must be performed, one for each GOR. This is best done with a simple computer program. Using the modified Hagedorn and Brown method and calculating fluid properties with the correlations presented in Section 3-2, the results shown in Fig. 7-16 were obtained. Plots such as this one are often called gradient curves; those presented by Brown (1977) were generated with the modified Hagedorn and Brown method, as illustrated here. ◇

EXAMPLE 7-11

Pressure drop in a high-rate horizontal well

A horizontal well with a 5-in. I.D. is producing 15,000 bbl/d at a GOR of 1000 along a 3000-ft interval from the saturated reservoir described in Appendix B. From a production log, the fluid entries were found to be distributed approximately as shown in Fig. 7-17. The pressure at the beginning of the horizontal section is 3000 psia. Estimate the pressure profile along the horizontal production interval.

Solution We can use the Beggs and Brill method to calculate the pressure drops between each fluid entry location, since this method is applicable to horizontal flow. This may underestimate the overall pressure drop because there will be additional turbulence at the fluid entry locations that is not considered in our calculations.

Beginning with the known pressure at location 1, the total liquid rate at this point is 15,000 STK bbl/d and the temperature is 180°F (the temperature is assumed constant throughout the well and equal to the reservoir temperature.) First, we calculate the downhole flow conditions. Following the correlations in Sections 3-2 and 4-2, and Examples 3-3, 4-2, and 4-4, we find:

$R_s = 562$ ft^3/bbl $\quad B_o = 1.29 \quad B_g = 5.071 \times 10^{-3}$

$\rho_o = 46.8$ lb$_m$/ft^3 $\quad \rho_g = 10.7$ lb$_m$/ft^3

$\mu_o = 0.69$ cp $\quad \mu_g = 0.02$ cp

$q_l = 19,350$ bbl/d $= 1.26$ ft^3/sec $\quad q_g = 3.33 \times 10^4$ ft^3/d $= 0.39$ ft^3/sec

From the downhole volumetric flow rates and the well cross-sectional area, we calculate

$$\lambda_l = 0.766 \qquad \lambda_g = 0.234$$
$$u_m = 12.05 \text{ ft/sec}$$

From Eqs. (7-125) through (7-130), we find $N_{FR} = 10.8$, $L_1 = 292$, $L_2 = 1.79 \times 10^{-3}$, $L_3 = 0.147$, and $L_4 = 3.01$. Since $\lambda_l \geq 0.4$ and $N_{FR} > L_4$, the flow regime is distributed.

Since the well is horizontal, the potential energy pressure drop is zero. However, we still must calculate the holdup, y_l, for the frictional pressure gradient. Using the constants for

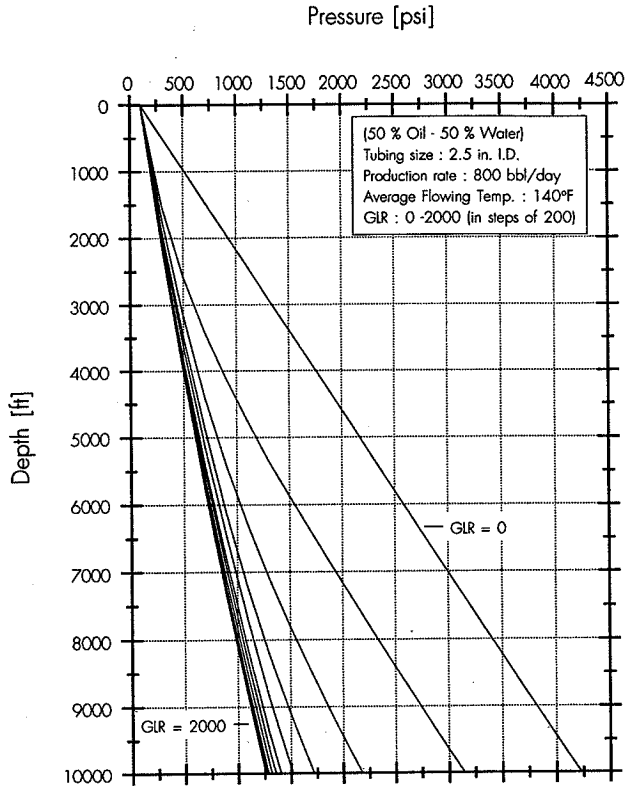

Figure 7-16
Pressure gradient curves generated with the modified Hagedorn and Brown correlation.

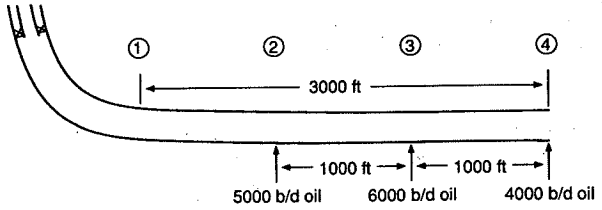

Figure 7-17
Horizontal well of Example 7-11.

distributed flow, from Eq. (7-136),

$$y_{lo} = \frac{1.065(0.766)^{0.5824}}{(10.8)^{0.0609}} = 0.788 \tag{7-169}$$

Since the well is horizontal, $\psi = 1$ and $y_l = y_{lo}$. Next, we calculate the mixture density and viscosity from Eqs. (7-143) and (7-146):

$$\rho_m = (0.766)(46.8) + (0.234)(10.7) = 38.4 \text{ lb}_m/\text{ft}^3 \tag{7-170}$$

$$\mu_m = (0.766)(0.69) + (0.234)(0.02) = 0.533 \text{ cp} \tag{7-171}$$

The mixture Reynolds number is [from Eq. (7-145)]

$$N_{\text{Re}_m} = \frac{(38.4)(12.05)(5/12)(1488)}{0.533} = 538{,}000 \tag{7-172}$$

and from the Moody diagram, the no-slip friction factor, f_n, = 0.0032. Using Eqs. (7-147) through (7-149), the two-phase friction factor, f_{tp}, is computed to be 0.0046. Finally,

$$\frac{dp}{dz} = \left(\frac{dp}{dz}\right)_F = \frac{2f\rho_m u_m^2}{g_c D} = \frac{(2)(0.0046)(38.4)(12.05)^2}{(32.17)(5/12)} \tag{7-173}$$
$$= 3.82 \text{ lb}_f/\text{ft}^3 = 0.0265 \text{ psi/ft}$$

and the pressure drop over the first 1000 ft of wellbore is

$$\Delta p = \left(\frac{dp}{dz}\right)(L) = (0.0265)(1000) = 26.5 \text{ psi} \tag{7-174}$$

For the next 1000 ft of wellbore, the oil flow rate at surface conditions is 10,000 bbl/d. Since the pressure has changed so little, we can use the same downhole fluid properties as before. Thus the gas and liquid flow rates will be in the same proportion, and the only significant difference is that u_m is now 8.03 ft/sec. Repeating the calculation procedure, the flow regime is also distributed flow between points 2 and 3 and the pressure drop is 11 psi.

In the last 1000 ft of wellbore, the oil flow rate at surface conditions is 4000 bbl/d, so $u_m = 3.21$ ft/sec. The flow regime in this section is predicted to be intermittent and the overall pressure drop is 1.7 psi. The total pressure drop over the entire horizontal section is predicted to be only 39 psi. For these calculations to be valid, the well must be perfectly horizontal; slight changes in inclination would lead to some potential energy contributions to the pressure drop and may significantly change the pressure profile in a "horizontal" well. ◇

REFERENCES

1. Beggs, H. D., and Brill, J. P., "A Study of Two-Phase Flow in Inclined Pipes," *JPT*, 607–617, May 1973.
2. Bradley, H. B., ed., *Petroleum Engineering Handbook*, Society of Petroleum Engineers, Richardson, TX, chap. 34, 1987.
3. Brill, J. P., and Beggs, H. D., *Two-Phase Flow in Pipes*, University of Tulsa, Tulsa, OK, 1978.
4. Brown, K. E., *The Technology of Artificial Lift Methods*, Vol. 1, Pennwell Books, Tulsa, OK, 1977.
5. Chen, N. H., "An Explicit Equation for Friction Factor in Pipe," *Ind. Eng. Chem. Fund.*, **18**: 296, 1979.

6. Duns, H., Jr., and Ros, N. C. J., "Vertical Flow of Gas and Liquid Mixtures in Wells," Proc., Sixth World Petroleum Congress, Frankfurt, Vol. 2, Paper 22, 1963.
7. Govier, G. W., and Aziz, K., *The Flow of Complex Mixtures in Pipes*, Robert E. Drieger Publishing Co., Huntington, NY, 1977.
8. Gregory, G. A., and Fogarasi, M., "Alternate to Standard Friction Factor Equation," *Oil and Gas J.*, 120–127, April 1, 1985.
9. Griffith, P., and Wallis, G. B., "Two-Phase Slug Flow," *J. Heat Transfer, Trans. ASME*, Ser. C, **83**, 307–320, August 1961.
10. Hagedorn, A. R., and Brown, K. E., "Experimental Study of Pressure Gradients Occurring During Continuous Two-Phase Flow in Small-Diameter Vertical Conduits," *JPT*, 475–484, April, 1965.
11. Moody, L. F., "Friction Factors for Pipe Flow," *Trans. ASME*, **66**, 671, 1944.
12. Taitel, Y., Barnea, D., and Dukler, A. E., "Modelling Flow Pattern Transitions for Steady Upward Gas-Liquid Flow in Vertical Tubes," *AIChE J.*, **26** (6): 345–354, May 1980.

PROBLEMS

7-1. Calculate the bottomhole pressure for the injection of 1500 bbl/d of brine with a density of 1.08 g/cm^3 and a viscosity of 1.3 cp in an 8000-ft vertical well having a surface pressure of 200 psi and (a) 2-in., 3.4-lb$_m$/ft tubing; (b) 2 7/8-in., 8.6-lb$_m$/ft tubing; (c) 3 1/2-inch, 12.70-lb$_m$/ft tubing.

7-2. In order to supply a pipeline, a particular gas well must maintain a wellhead pressure of 600 psia. The vertical well is 15,000 ft deep, and the production is through new, 2 7/8-in., 8.6-lb$_m$/ft tubing. What gas flow rate can be obtained with (a) $p_{wf} = 1000$ psia; (b) $p_{wf} = 1500$ psia; (c) $p_{wf} = 2000$ psia?

The gas gravity is 0.65. Assume that an average temperature of 200°F can be used in all calculations.

7-3. Calculate the slip velocity for the flow of 5-ft^3/sec of oil and 10-ft^3/sec of gas in a 6-in.-I.D. pipe when the liquid holdup is 0.8.

7-4. Calculate the bottomhole flowing pressure for a gas well producing 10 MM SCF/d through 2 7/8-in. tubing in a well deviated 50° from vertical and having a measured depth of 15,000 ft. The surface tubing pressure is 1000 psia, the surface temperature is 150°F, and the bottomhole temperature is 250°F. The gas is the same composition as that in Example 7-5 ($\gamma_g = 0.70$, $T_{\text{pc}} = 374$°R, $p_{pc} = 717$ psia).

7-5. For a flow of 1000 bbl/d of oil with a density of 0.8 g/cm^3 and a surface tension of 30 dynes/cm in a 3-in.-I.D. vertical pipe, at what gas rate will the transition from region I to region II (Duns and Ros flow regime map) occur?

7-6. Using the modified Hagedorn and Brown method, calculate the pressure gradient for the flow of 1200 STB/d of the oil in Appendix B with a GOR of 1000 and a WOR of 1.0 in 2 7/8-in. vertical tubing at (a) the surface, where $T = 100$°F and $p = 100$ psig; (b) the bottomhole, where $T = 180$°F and $p = 3000$ psia.

7-7. Repeat problem 7-6, using the Beggs and Brill correlation.

7-8. Write a computer program to implement a two-phase pressure traverse calculation with fixed length increment incorporating both correlations presented in this chapter as user options. Assume that the surface pressure is known and the bottomhole pressure is the desired result.

CHAPTER 8

Well Deliverability

8-1 INTRODUCTION

Chapters 2, 3, and 4 described well inflow performance of oil, two-phase, and gas reservoirs, respectively. Inflow performance relationships (IPR) were presented in a standardized manner, with the flowing bottomhole pressure on the ordinate of a graph and the corresponding production rate on the abscissa. This type of depiction gives a comprehensive picture of what the reservoir can deliver into the well at a specific time. Except for the case of steady-state flow, the well IPR would change with time. This would be both under infinite-acting conditions and under pseudo-steady-state conditions where the *reservoir* pressure declines with time.

The reservoir's ability to deliver into the bottom of a well must be combined with the well's vertical lift performance (VLP). Wellbore flow was outlined in Chapter 7. For a required wellhead flowing pressure, p_{tf}, there exists a corresponding bottom hole flowing pressure, p_{wf}, which is a function of the hydrostatic pressure difference and the friction pressure losses. Both of these variables are related implicitly to the pressure values themselves. Density differences and phase changes affect both the hydrostatic pressure and the friction pressure drop. For two-phase flow an increase in the imposed wellhead pressure would result in a proportionately larger increase in the corresponding bottomhole pressure, because gas will be redissolved, increasing the density of the fluid in the wellbore. Two-phase flow in the well is common for almost all oil reservoirs, even if the flowing bottomhole pressure is above the bubble point. The wellhead pressure is likely to be significantly below. Thus, it is common to combine single-phase oil IPR with two-phase VLP.

Increasing the flowing gas–liquid ratio (GLR) would result in a reduction in the bottomhole pressure. This is the purpose of gas lift. However, there exists a limiting GLR where the decrease in the hydrostatic pressure will be offset by the increase in the frictional pressure drop. Gas lift performance will be outlined in Chapter 19, while pump-assisted lift will be treated in Chapter 20.

In this chapter natural vertical lift performance is combined with the IPR to estimate the well deliverability. The material consists largely of examples, each intended to demonstrate an important issue.

8-2 Combination of Inflow Performance Relationship (IPR) and Vertical Lift Performance (VLP)

The traditional manner of solving the problem is depicted graphically in Fig. 8-1. The IPR curve is shown in the p_{wf}-versus-q plot. Then, for a given wellhead pressure, p_{tf}, the flowing bottomhole pressure, p_{wf}, is calculated for each flow rate through an application of the mechanical energy balance. (See Chapter 7 and, especially, Section 7-2.3.) This is plotted as shown in Fig. 8-1. The intersection of the two curves provides the expected production rate and the flowing bottomhole pressure. Usually, the VLP curve is largely linear, with a relatively small slope. For low GLR fluids the hydrostatic pressure would comprise the overwhelming portion of the pressure gradient in the well. Therefore, the frictional pressure drop would be relatively small and, since it is the only pressure component affected by the flow rate, the associated VLP curve is likely to be flat. For higher GLR values or for a gas well, the VLP curve is not expected to be linear. At low flow rates and where laminar flow may be in effect, while the friction pressure drop is proportional to the velocity squared [i.e., flow rate squared—see Eq. (7-31)], the friction factor declines rapidly as shown in the Moody diagram of Fig. 7-7. Therefore, there may be a flow rate where the resulting flowing bottomhole pressure may be minimum. Also, the shape of the VLP curve at lower rates may be affected by liquid accumulation, since there may not be sufficient momentum to carry the fluid. Thus the overall composition in the wellbore may be more liquidlike. At increasing flow rates, or in turbulent flow, the friction factor-versus-Reynolds number (i.e., rate) relationship is much flatter, resulting in an increase in the frictional pressure drop and an associated increase in the flowing bottomhole pressure.

EXAMPLE 8-1

Calculation of VLP for single-phase fluid and combination with single-phase IPR

Use the well in Appendix A. Assume that the depth is 8000 ft, the oil gravity, γ_o, is equal to 0.88 (API°=28, ρ_o=55 lb/ft^3), the tubing size is 2 3/8 in. (I.D.≈2 in.) with a roughness ε=0.0006. What would be the expected production rate and the corresponding bottomhole pressure if the wellhead pressure is 0 psi? (Assume for this problem that p_b=0 psi.) The reservoir operates under steady-state conditions (use the IPR curve developed in Example 2-8 for s=0).

Solution The IPR curve for this problem is [from Eq. (2-15)]

$$p_{wf} = 5651 - 5.54\,q \tag{8-1}$$

Ignoring the kinetic energy pressure drop, as indicated by Example 7-3, the potential and frictional pressure drops must be calculated for each flow rate.

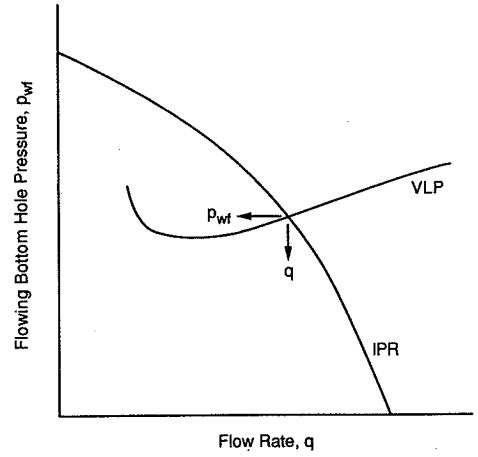

Figure 8-1
Combination of inflow performance relationship (IPR) and vertical lift performance (VLP).

Since the fluid in this example is considered as single phase, and largely incompressible, the potential energy pressure drop (hydrostatic pressure) would be the same, regardless of the wellhead pressure and rate. Therefore, from Eq. (7-22),

$$\Delta p_{PE} = (0.433)(0.88)(8000) = 3048 \text{ psi} \tag{8-2}$$

The frictional pressure drop must then be calculated for each flow rate. For example, if q_o=100 STB/d, the Reynolds number is [from Eq. (7-7) and using the properties in Appendix A]

$$N_{Re} = \frac{(1.48)(100)(55)}{(2)(1.7)} = 2400 \tag{8-3}$$

which implies turbulent flow.

From Eq. (7-35) and ε=0.0006, the Fanning friction factor, f_f, is 0.0117. The velocity, u, is

$$u = \frac{(4)(100)(5.615)(1/86,400)}{\pi(2/12)^2} = 0.3 \text{ ft/sec} \tag{8-4}$$

and therefore, from Eq. (7-31),

$$\Delta p_F = \frac{(2)(0.0117)(55)(0.3)^2(8000)}{(32.17)(2/12)} = 173 \text{ lb}_f/\text{ft}^2 = 1.2 \text{ psi} \tag{8-5}$$

which is insignificant when compared to the hydrostatic pressure drop.

The total pressure drop is the sum of the results of Eqs. (8-2) and (8-5), that is, 3049 psi. This is equal to p_{wf}, since p_{tf}=0. Similar calculations for flow rates of 300, 500, and 700 STB/d result in Δp_F equal to 8, 20, and 35 psi, respectively.

Figure 8-2 shows the combination of the IPR and VLP (largely a flat, straight line) for this problem. The intersection is at p_{wf}=3060 psi with q=468 STB/d. ◇

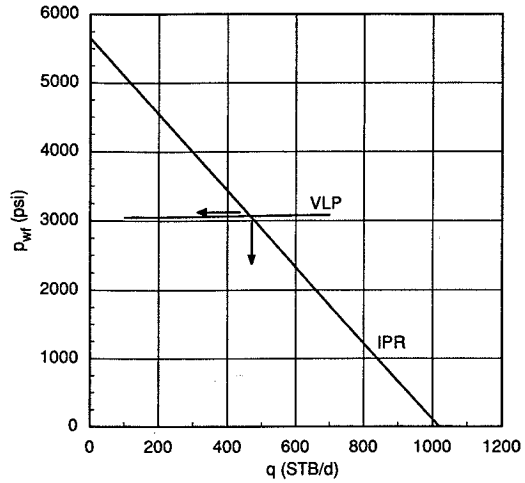

Figure 8-2
Well deliverability from a single-phase fluid (Example 8-1).

EXAMPLE 8-2

Impact of the gas–liquid ratio (GLR) on vertical lift performance (VLP)

Assume that the reservoir in Appendix A (R_S=150 SCF/STB) is completed with a well with 2 3/8-in. (I.D.≈2 in.) tubing. If the wellhead flowing pressure, p_{tf}, is 100 psi, develop gradient curves for q=500 STB/d and GLR values from 100 to 800 SCF/STB. All GLRs larger than 150 must be supplied artificially. What would be the bottomhole flowing pressures and the flowing pressure gradients (between 5000 and 8000 ft) for GLRs equal to 300 and 800 SCF/STB, respectively? The average flowing temperature is 130°F.

Solution Using the modified Hagedorn and Brown method (see Section 7-4.3 and Example 7-11), Fig. 8-3 can be constructed readily. The flowing bottomhole pressures with GLR values of 300 and 800 SCF/STB are 1900 and 1200 psi, respectively. The corresponding flowing gradients (between 5000 and 8000 ft) are 0.32 and 0.17 psi/ft. ◇

EXAMPLE 8-3

Increasing the flowing wellhead pressure

For the well in Appendix A (GLR=150 SCF/STB and tubing-size I.D.≈2 in.) develop VLP curves for p_{tf}=0, 100, and 500 psi, respectively. What would be the production rates with the steady-state IPR (used in Example 8-1)?

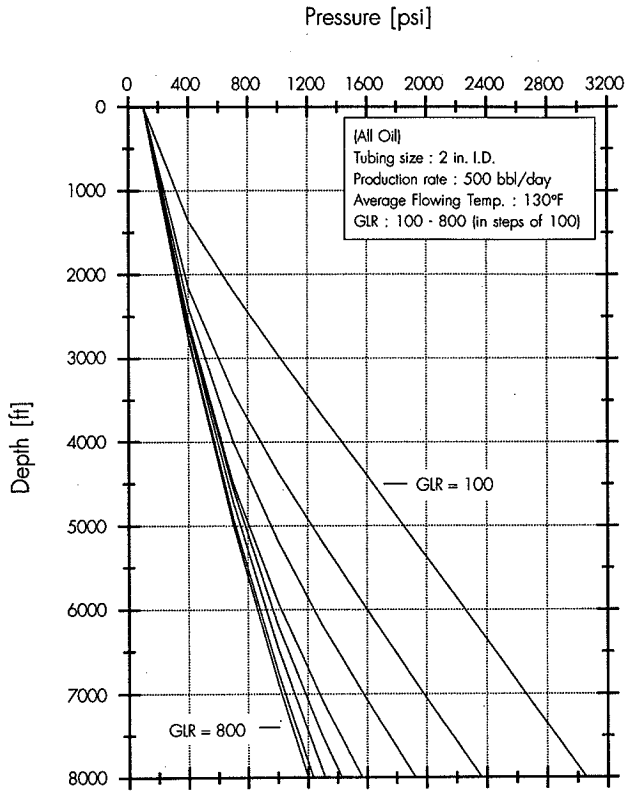

Figure 8-3
Gradient curves for a range of GLR values (Example 8-2).

Solution Table 8-1 contains the calculated flowing bottomhole pressures for a range of flow rates using the modified Hagedorn and Brown correlation. These results demonstrate the effect of phase change as the fluids in the well are pressurized. An increase in the wellhead flowing pressure by 100 psi (from 0 to 100) results in an increase in the flowing bottomhole pressure by almost 500 psi when the flow rate is 100 STB/d, reflecting the impact of the hydrostatic pressure component on the total pressure drop.

The combination of the IPR with the three VLP curves shown in Fig. 8-4 results in flow rates of 600, 530, and 390 STB/d for the 0-, 100-, and 500-psi wellhead pressures, respectively.

This problem demonstrates the necessity for the appropriate design of wellhead and surface equipment that are inherently related to the wellhead pressure. ◇

Table 8-1

Flowing Bottomhole Pressures for Various Production Rates for Example 8-3

	p_{wf} (psi)		
q_o (STB/d)	p_{tf}=0 psi	p_{tf}=100 psi	p_{tf}=500 psi
100	2150	2618	3383
300	2156	2639	3473
500	2305	2697	3547
700	2426	2750	3603

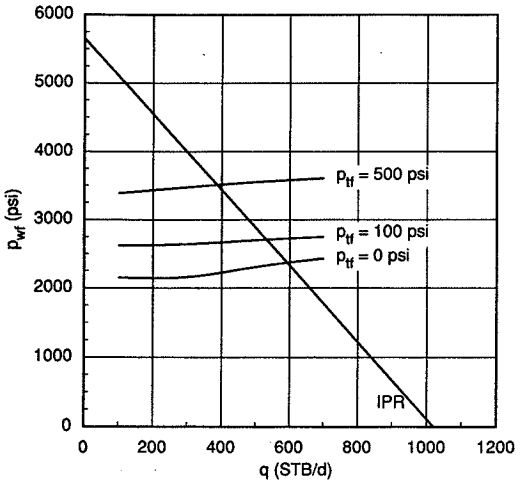

Figure 8-4
Effect of flowing wellhead pressure on well deliverability (Example 8-3).

EXAMPLE 8-4
Changes in the IPR

Well deliverability is affected both by the well lift performance and the reservoir inflow. The previous two examples examined the influence of GLR and the wellhead pressure on well performance and, hence, well deliverability. The reservoir inflow is affected by the near-well situation (damage or stimulation) and the evolution of the average reservoir pressure.

In this example, use the IPR curves of Example 2-8 (different skin effects) and Example 2-9 (declining reservoir pressure) with the VLP curve for p_{tf}=100 psi, developed in Example 8-3, to show the effects of skin and declining reservoir pressure on well deliverability.

Solution Figure 8-5 is the graphical solution of the skin effect impact on the IPR and the resulting changes in well deliverability. While the production rate would be 530 STB/d with zero skin, it would be reduced to 270 and less than 90 STB/d with skins equal to 10 and 50, respectively.

The declining reservoir pressure and its impact on well deliverability is shown on Fig. 8-6. [The IPR curve using the pseudo-steady-state relationship is given by Eq. (2-45).] The flow rates for $\bar{p}$=5651, 5000, and 4000 psi are 580, 470, and 270 STB/d, respectively.

Reduction in the bottomhole pressure, either by lowering the wellhead pressure (usually not feasible) or, especially, through artificial lift, would shift the VLP curve downward, resulting in the maintenance of the original production rate or retardation of its decline. ◇

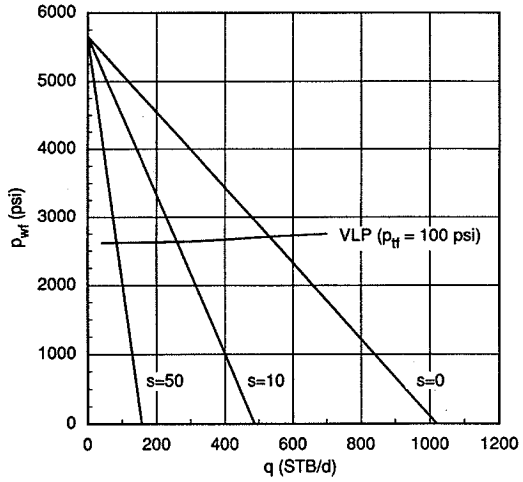

Figure 8-5
Skin effect and well deliverability (Example 8-4).

8-3 IPR AND VLP OF TWO-PHASE RESERVOIRS

The main difference between single-phase and two-phase reservoirs is that the producing GLR in the latter will vary with time as the reservoir pressure declines. Gas coming out of solution in the reservoir will enter a growing gas cap, causing a free-flowing gas. This will be mixed in the well with the oil flow, which will also contain an amount of solution gas. As a result, the VLP curve will change with time and will shift downward. However, a new IPR at the lower reservoir pressure will be in effect. The composite effect is that while the well producing rate will decline, it will do so at a lower pace than the producing rate of single-phase reservoirs. Graphically, this process is shown in Fig. 8-7. The flowing wellhead pressure is constant. A comprehensive example of a forecast of well performance, taking into account the reservoir decline behavior, will be presented in Chapter 9.

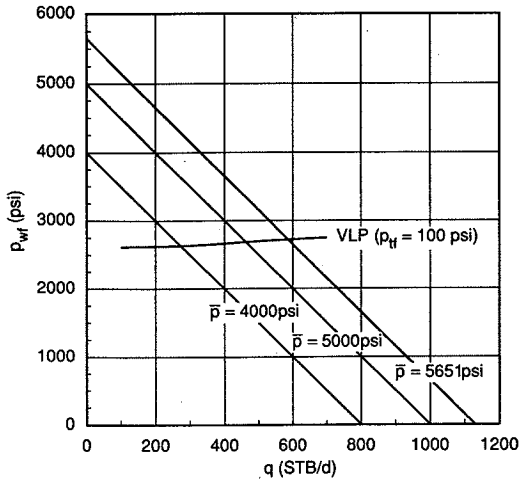

Figure 8-6
Declining reservoir pressure and VLP (Example 8-4).

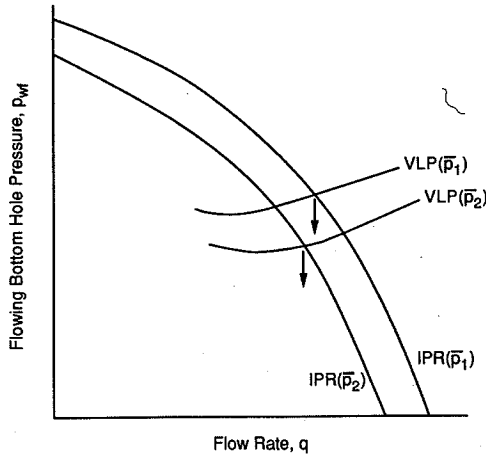

Figure 8-7
IPR and VLP curves at two average reservoir pressures ($\bar{p}_2 < \bar{p}_1$). The flowing wellhead pressure is constant.

The behavior depicted in Fig. 8-7 will be observed under natural lift conditions. This process will be more pronounced at early time in reservoirs with high initial pressure and which contain fluids with high solution gas–oil ratios. At a later time, as the producing GLR increases with time, the gap between the corresponding VLP curves is reduced. Ultimately, they are likely to overlap.

EXAMPLE 8-5
Well deliverability from a two-phase reservoir

Using the well in Appendix B, a drainage radius equal to 1490 ft, and a skin effect equal to 2, develop an IPR curve for the (initial) average reservoir pressure of 4350 psi. Show the influence of the wellhead flowing pressure by using p_{tf}=100 and 300 psi, respectively.

Solution The IPR expression for a two-phase reservoir was given in Section 3-4 [Eq. (3-51)]. With the variables in Appendix B and the ones given in this example, it becomes

$$q_o = \frac{1591}{\bar{B}_o}\left[1 - 0.2\frac{p_{wf}}{\bar{p}} - 0.8\left(\frac{p_{wf}}{\bar{p}}\right)^2\right] \tag{8-6}$$

The IPR curve with average values of the formation volume factor, B_o, is plotted in Fig. 8-8. Also on Fig. 8-8 are the two VLP curves for the two wellhead pressures (100 and 300 psi). The corresponding production rates are 995 and 925 STB/d, respectively. The flowing bottomhole pressures are approximately 1535 and 1835 psi, a difference of 300 psi, instead of 200, reflecting the more liquidlike phase distribution at the higher wellhead pressure. ◇

8-4 IPR AND VLP IN GAS RESERVOIRS

Equations (4-54) and (4-60) in Chapter 4 describe the inflow performance of a gas well under pseudo-steady-state and transient conditions, respectively. Both of these expressions use the real-gas pseudo-pressure function $m(p)$, and they are the most appropriate forms of the gas IPR.

Approximate expressions can be obtained by substituting for the real-gas pseudo-pressures with the pressure-squared difference divided by the product of the average values of the viscosity and the gas deviation factor. For example, the pseudo-steady-state IPR is given by Eq. (4-32). The same expression contains the non-Darcy coefficient, D, which accounts for turbulence effects evident in high-rate gas wells.

The vertical lift performance of a gas well would consist of the hydrostatic and friction pressure drop components, just as for any other well. However, the friction pressure contribution is likely to be large, in contrast to largely liquid reservoirs. Hence, the tubing diameter and its selection become critical for gas wells. (This, of course, is true for all high-rate reservoirs.)

Section 7-3 and Example 7-5 presented the methodology for the calculation of the flowing bottomhole pressure for a gas well. A graph of flowing bottomhole pressure versus the gas rate is the VLP curve for the well.

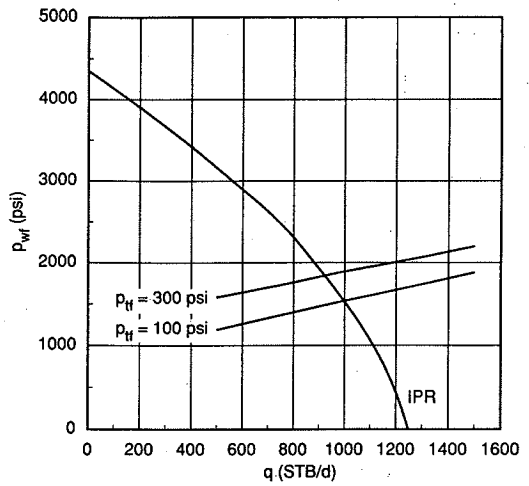

Figure 8-8
IPR and VLP for two flowing wellhead pressures in a two-phase reservoir (Example 8-5).

EXAMPLE 8-6
Well deliverability for a gas reservoir

With the data for the gas well in Appendix C, r_e=1490 ft, $\bar{\mu}$=0.022 cp, $\bar{Z}$=0.93, $c_t = 1.5\times10^{-4}$ psi^{-1}, s=0, and $D = 1.5\times10^{-4}$ (MSCF/d)$^{-1}$, construct an IPR curve using Eqs. (4-32) and (4-33) (i.e., assume that the well is stabilized).

What would be the well deliverability if the flowing wellhead pressure is 500 psi? The depth of the well is 10,000 ft, the inside tubing diameter is 2 7/8 in., and the relative roughness is 0.0006. Assume that the wellhead temperature is 140°F.

Solution The coefficients a and b in Eq. (4-33) are

$$a = \frac{(1424)(0.022)(0.93)(640)}{(0.17)(78)}\left[\ln\frac{(0.472)(1490)}{0.328}\right] = 1.08\times10^4 \qquad (8\text{-}7)$$

$$b = \frac{(1424)(0.022)(0.93)(640)(1.5\times10^{-4})}{(0.17)(78)} = 0.21 \qquad (8\text{-}8)$$

leading to an IPR given by

$$\bar{p}^2 - p_{wf}^2 = (1.08\times10^4)\,q + 0.21q^2 \qquad (8\text{-}9)$$

The IPR curve is plotted in Fig. 8-9 ($\bar{p}$=4613 psi). The absolute open-flow potential (at p_{wf}=0) is 1900 MSCF/d. For such a small D the non-Darcy effects are minimal. Ignoring the second term in Eq. (8-9) would result in an absolute open-flow potential equal to 1970 MSCF/d.

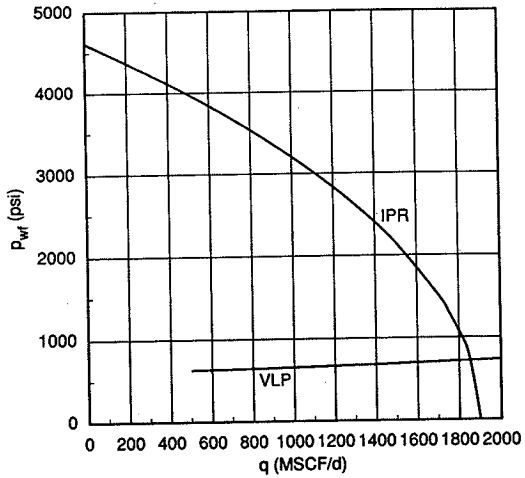

Figure 8-9
Gas well deliverability for Example 8-6.

From the intersection of the VLP curve, developed as shown in Example 7-5, the expected gas production rate would be 1860 MSCF/d. ◇

EXAMPLE 8-7
High-rate gas well: Effect of tubing size

A gas well in a reservoir with $\bar{p}$=4613 psi has an IPR given by

$$\bar{p}^2 - p_{wf}^2 = 25.8q + 0.115q^2 \qquad (8\text{-}10)$$

Assuming that all physical properties are as for the gas well in Appendix C, show with combinations of IPR and VLP the impact of the tubing size.

Solution The absolute open-flow potential for this well is 13.6×10^3 MSCF/d. The IPR curve for this problem is Fig. 8-10, along with the VLP curves for four common tubing sizes (2 3/8, 2 7/8, 3 1/2, and 4 in. with corresponding I.D.s of 2, 2.44, 3, and 3.48 in.) As can be extracted readily from Fig. 8-10, production rates from the well would be 10.7, 12.3, 13, and 13.2 MMSCF/d for the four tubing sizes, respectively. This exercise shows the relative benefits from the appropriate tubing size selection in a gas well. This is particularly important for gas wells that are likely candidates for hydraulic fracturing (such as the well in Appendix C with permeability k=0.17 md). The anticipated benefits from the improved IPR, following a

successful fracturing treatment, may be reduced if the tubing size is not selected on the basis of the expected posttreatment rather than the pretreatment inflow. ◇

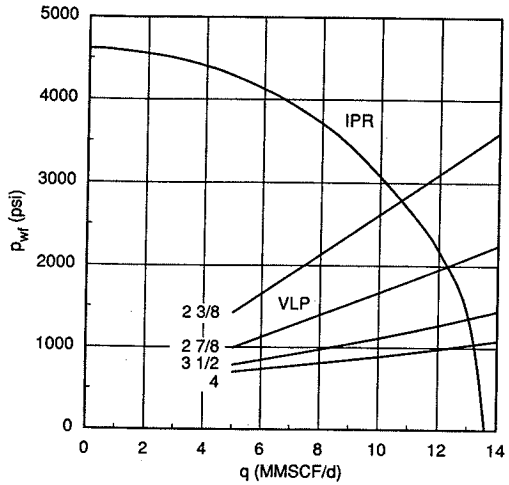

Figure 8-10
Deliverability from a high-rate gas well with a range of tubing diameters.

PROBLEMS

8-1. With the well in Appendix A, a depth of 8000 ft, and a flowing wellhead pressure of 100 psi, estimate the tubing diameter at which the friction pressure drop is 20% of the total. Assume single phase throughout the tubing flow.

8-2. Suppose that the IPR curve for a well is

$$q_o = 10,000\left[1 - 0.2\frac{p_{wf}}{\bar{p}} - 0.8\left(\frac{p_{wf}}{\bar{p}}\right)^2\right] \tag{8-11}$$

with $\bar{p}$=5000 psi (and using an average B_o). If GOR=300 SCF/STB, $\bar{T}$ = 150°F, p_{tf}=100 psi and tubing I.D.=3 in., calculate the well deliverability for depths of 4000, 6000, and 8000 ft. For all other properties use the well in Appendix B.

8-3. Is it possible for the tubing diameter in Problem 8-2 to be 2 in.? If so, what would be the well deliverability if the depth is 6000 ft?

8-4. Suppose that a horizontal well with L=2000 ft and I_{ani}=3 were to be drilled in the reservoir described in Problem 8-2. What would be the well deliverability? (Assume that the well has an average trajectory of 45° and that there is negligible pressure drop in the horizontal portion of the well.)

8-5. The gas well in Appendix C is hydraulically fractured, and the treatment results in an equivalent skin effect equal to −6. Develop a gas well IPR with the data in Appendix C and Example 8-6. The flowing wellhead pressure is 500 psi. How does the performance compare with the results of Example 8-6 for the well in the pretreatment state and with a tubing I.D. equal to 1 in.? What would be the performance with a tubing with 2-in. I.D.?

8-6. Assume that a horizontal well with L=2500 ft is drilled in the reservoir described in Appendix C and Example 8-6. If the horizontal well r_w=0.328 ft, what is the well deliverability? The vertical well has a 3-in. tubing I.D. Calculate the pressure drop in the horizontal section.

CHAPTER 9

Forecast of Well Production

9-1 INTRODUCTION

In the previous chapter the well inflow and vertical lift performances (IPR and VLP) were combined to provide the well deliverability. The intersection of the plots of flow rate versus flowing bottomhole pressure of those two components of the reservoir and well system is the expected well deliverability. This intersection point describes a specific instant in the life of the well. It depends greatly on the type of flow regime controlling the well performance.

For infinite-acting behavior, transient IPR curves can be drawn from a single pressure value on the p_{wf} axis. This is the initial reservoir pressure. The intersections with the VLP curve at different times are the expected flow rates (and corresponding p_{wf} values).

By definition, for steady-state flow, a single IPR curve would intersect the VLP curve. For pseudo-steady-state flow the situation is more complicated, because the average reservoir pressure will change with time. Given the values of the average reservoir pressure, $\bar{p}$, a family of IPR curves can be drawn, each intersecting the p_{wf} axis at the individual reservoir pressures. What is needed is the element of time. Material balance calculations, relating underground withdrawal and reservoir pressure depletion, can provide the crucial pressure-versus-time relationship. Therefore, the associated well deliverability would be the forecast of well production.

In all cases, integration of the flow rate versus time would lead to the cumulative production, which is an essential element in any economic decision making about the viability of any petroleum production engineering project.

9-2 TRANSIENT PRODUCTION RATE FORECAST

In an infinite-acting reservoir, the well IPR can be calculated from the solution to the diffusivity equation. The classic approximations for the well flow rate were given in

Chapter 2 for an oil well [Eq. (2-7)] and in Chapter 4 for a gas reservoir [Eq. (4-60)]. For a two-phase reservoir, Eq. (2-7) can be adjusted further, as shown in Section 3-5. These expressions would lead to transient IPR curves, one for each production time. Example 2-7 and associated Fig. 2-5 demonstrate the method of calculation and presentation for the transient IPR curves.

Unless the wellhead pressure changes, there will be only one VLP curve for the well, and its intersections with the IPR curves will be the well production rate. The cumulative production under any flow regime is simply

$$N_p = \int_0^t q(t)\,dt \tag{9-1}$$

EXAMPLE 9-1

Forecast of well production with transient IPR

Use the transient IPR curves for the well in Appendix A as developed in Example 2-7. Then, with the VLP curve of Example 8-1, calculate and plot the expected well flow rate and cumulative production versus time.

Solution Equation (2-43) is the transient IPR curve relationship for this well. If t=1 month (t must be converted into hours), Eq. (2-43) becomes

$$q = 0.208(5651 - p_{wf}) \tag{9-2}$$

Figure 9-1 shows on an expanded scale (all IPR curves would merge at $p_{wf}=p_i$=5651 psi) the intersections between the IPR curves at 1, 6, and 12 months and the VLP curve. The corresponding production rates would be 537, 484, and 465 STB/d, respectively.

Figure 9-2 is a graph of the well production rate versus time. The associated cumulative production is also shown on the same figure. ◇

9-3 Material Balance for an Undersaturated Reservoir and Production Forecast under Pseudo-Steady-State Conditions

The fluid recovery from an undersaturated oil reservoir depends entirely on the fluid expansion as a result of underground withdrawal and associated pressure reduction. This can be evaluated by starting with the expression for isothermal compressibility.

The isothermal compressibility is defined as

$$c = -\frac{1}{V}\frac{\partial V}{\partial p} \tag{9-3}$$

where V is the volume of the fluid. By separation of variables, assuming that c is small and largely constant for an oil reservoir,

$$\int_{p_i}^{\bar{p}} c\,dp = \int_{V_i}^{V} \left(-\frac{dV}{V}\right) \tag{9-4}$$

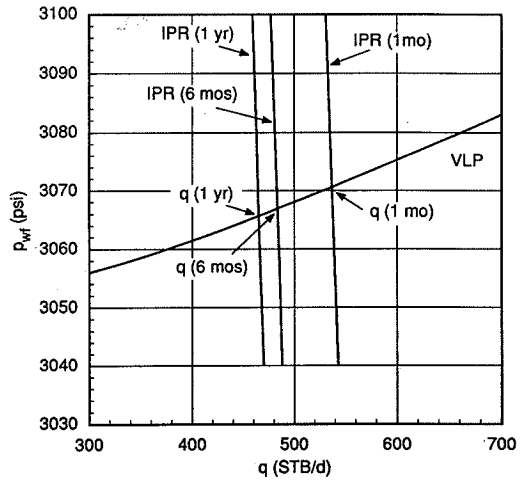

Figure 9-1
Transient IPR and VLP curves for Example 9-1.

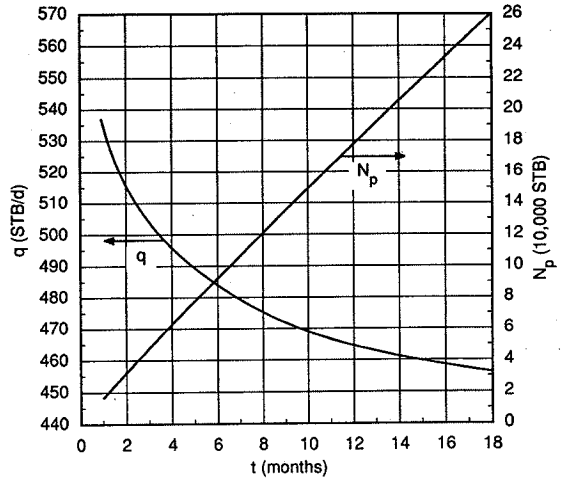

Figure 9-2
Flow rate and cumulative production forecast for Example 9-1.

and therefore

$$c(\bar{p} - p_i) = \ln \frac{V_i}{V} \tag{9-5}$$

Rearrangement of Eq. (9-5) results in

$$\frac{V}{V_i} = e^{c(p_i - \bar{p})} \tag{9-6}$$

The volume V is equal to $V_i + V_p$, that is, the original plus that produced at the lower pressure. For the case of an undersaturated oil reservoir, the total compressibility is equal to $c_t = c_o S_o + c_w S_w + c_f$, where c_o, c_w, and c_f are the compressibilities of oil, water, and rock, respectively and S_o and S_w are the oil and water saturations. Finally, the recovery ratio, r, is

$$r = \frac{V_p}{V_i} = e^{c_t(p_i - \bar{p})} - 1 \tag{9-7}$$

If the original oil-in-place, N, is known, the cumulative recovery, N_p, is simply rN.

The general approach to the problem of forecasting the well performance under pseudo-steady-state conditions is as follows.

- Assume an average reservoir pressure, $\bar{p}$. From Eq. (9-7), the recovery ratio (and the corresponding cumulative recovery) can be calculated. Within each average reservoir pressure interval, an incremental cumulative production ΔN_p can be calculated.
- With the average reservoir pressure (a mean value within the pressure interval can be considered), the pseudo-steady state IPR relationship can be used. Equation (2-30) is for an undersaturated oil reservoir.
- The time is simply $t = \Delta N_p / q$, where q is the calculated average flow rate within the interval.

Thus the well flow rate and the cumulative recovery are related to time.

EXAMPLE 9-2

Well production from an oil reservoir under pseudo-steady-state conditions

Assume that the well in Appendix A operates under pseudo-steady-state conditions draining a 40-acre spacing. Calculate the well production rate and cumulative production versus time. If artificial lift is required when $\bar{p}$=4000, calculate the time of its onset.

What is the maximum possible cumulative production from this drainage area at $\bar{p}=p_b$ =1323 psi? Use the VLP curve of Example 8-1.

Solution The pseudo-steady-state IPR for an undersaturated oil reservoir is given by Eq. (2-30). With the variables in Appendix A, the 40-acre drainage area (r_e=745 ft), s=0, and allowing for the average reservoir pressure to vary, Eq. (2-30) becomes

$$q = 0.236(\bar{p} - p_{wf}) \tag{9-8}$$

Figure 9-3 is the combination of IPR curves at different reservoir pressures $\bar{p}$ and the single VLP for the well. At $\bar{p}$=5651, 5000, 4500, and 4000 psi, the corresponding well production rates would be approximately 610, 455, 340, and 225 STB/d, respectively.

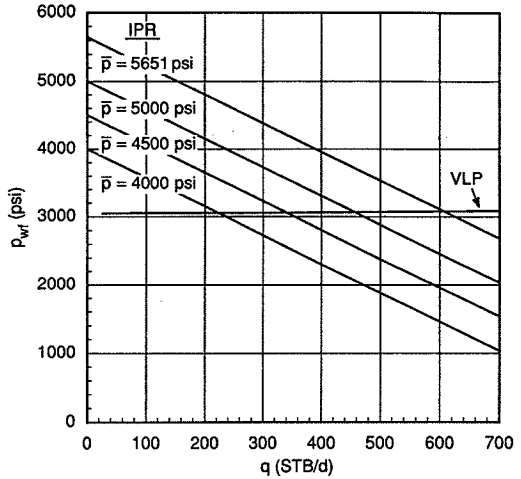

Figure 9-3

IPR and VLP curves for an oil well under pseudo-steady-state conditions (Example 9-2).

The next step is to calculate the cumulative production after each pressure interval. At first, the initial oil in place must be estimated. Using the variables in Appendix A, the initial oil in place within 40 acres is

$$N = \frac{(7758)(40)(53)(0.19)(1 - 0.34)}{1.1} = 1.87 \times 10^6 \text{ STB} \tag{9-9}$$

Then, following the approach described in Section 9-3, a sample calculation is presented below. If $\bar{p}$=5000 psi, from Eq. (9-7) the recovery ratio can be obtained,

$$r = e^{1.29 \times 10^{-5}\,(5651 - 5000)} - 1 = 8.43 \times 10^{-3} \tag{9-10}$$

and therefore

$$N_p = (1.87 \times 10^6)(8.43 \times 10^{-3}) = 15,770 \text{ STB} \tag{9-11}$$

If the average production rate in this interval (from Fig. 9-3) is 533 STB/d, the time required to produce the cumulative production of Eq. (9-11) would be (15770/533) $\approx$ 30 days.

Table 9-1 gives the production rate, incremental, and total cumulative recovery for the well in this example.

After 105 days the reservoir pressure would decline by 1650 psi, the rate would decline from 610 to 225 STB/d, while the total recovery would be only 2% of the original oil-in-place.

This calculation shows the inefficient recovery from highly undersaturated oil reservoirs. Also, after 105 days is when artificial lift must start, since this time coincides with $\bar{p}$=4000 psi.

Finally, if $\bar{p}=p_b$, the maximum recovery ratio [Eq. (9-7)] would be

$$r = e^{1.29\times10^{-5}(5651-1323)} - 1 = 0.057 \tag{9-12}$$

◇

Table 9-1

Production Rate and Cumulative Recovery Forecast for a Well in Example 9-2

$\bar{p}$ (psi)	q (STB/d)	N_p (STB)	ΔN_p (STB)	Δt (days)	t (days)
5651	610				
			1.58×10^4	30	
5000	455	1.58×10^4			30
			1.22×10^4	31	
4500	340	2.80×10^4			61
			1.23×10^4	44	
4000	225	4.03×10^4			105

9-4 The General Material Balance for Oil Reservoirs

Havlena and Odeh (1963, 1964) introduced the application of material balance to oil reservoirs that have initial oil-in-place N and a ratio m relating the initial hydrocarbon volume in the gascap to the initial hydrocarbon volume in the oil zone.

9-4.1 The Generalized Expression

The generalized expression as presented by Dake (1978) (and ignoring water influx and production) is

$$N_p[B_o + (R_p - R_s)B_g] = NB_{oi}\left[\frac{(B_o - B_{oi}) + (R_{si} - R_s)B_g}{B_{oi}} + m\left(\frac{B_g}{B_{gi}} - 1\right) + (1+m)\left(\frac{c_w S_{wc} + c_f}{1 - S_{wc}}\right)\Delta p\right] \tag{9-13}$$

In Eq. (9-13), N_p is the cumulative oil production, R_p is the producing gas–oil ratio, and S_{wc} is the interstitial water saturation. All other variables are the usual thermodynamic and physical properties of a two-phase system. Groups of variables, as defined below, correspond to important components of production.

- Underground withdrawal:

$$F = N_p[B_o + (R_p - R_s)B_g] \tag{9-14}$$

- Expansion of oil and originally dissolved gas:

$$E_o = (B_o - B_{oi}) + (R_{si} - R_s)B_g \tag{9-15}$$

- Expansion of gas cap:

$$E_g = B_{oi}\left(\frac{B_g}{B_{gi}} - 1\right) \tag{9-16}$$

- Expansion of connate water and reduction of pore volume:

$$E_{f,w} = (1+m)B_{oi}\left(\frac{c_w S_{wc} + c_f}{1 - S_{wc}}\right)\Delta p \tag{9-17}$$

Finally, from Eqs. (9-13) through (9-17),

$$F = N(E_o + mE_g + E_{f,w}) \tag{9-18}$$

9-4.2 Calculation of Important Reservoir Variables

As shown by Havlena and Odeh (1963), Eq. (9-18) can be used in the form of straight lines for the calculation of important reservoir variables, by observing the well performance and using the properties of the fluids produced.

Saturated reservoirs. For saturated reservoirs,

$$E_{f,w} \simeq 0 \tag{9-19}$$

since the compressibility terms can be ignored, and hence

$$F = NE_o + NmE_g \tag{9-20}$$

With no original gas cap (m= 0),

$$F = NE_o \tag{9-21}$$

a plot of F versus E_o would result in a straight line with slope N, the original oil-in-place.

With an original gas cap (N and m are unknown),

$$F = NE_o + NmE_g \tag{9-22}$$

or

$$\frac{F}{E_o} = N + Nm\left(\frac{E_g}{E_o}\right) \tag{9-23}$$

A graph of F/E_o versus E_g/E_o would result in a straight line with N the intercept and Nm the slope.

Undersaturated reservoirs. In undersaturated reservoirs, since m=0 and R_p=R_s, Eq. (9-13) becomes

$$N_p B_o = N B_{oi}\left[\frac{B_o - B_{oi}}{B_{oi}} + \left(\frac{c_w S_{wc} + c_f}{1 - S_{wc}}\right)\Delta p\right] \tag{9-24}$$

Equation (9-6) can be written in terms of the formation volume factors and simplified as a Taylor series dropping all terms with powers of 2 and larger:

$$B_o = B_{oi} e^{c_o \Delta p} \simeq B_{oi}(1 + c_o \Delta p) \tag{9-25}$$

Therefore

$$\frac{B_o - B_{oi}}{B_{oi}} = c_o \Delta p \tag{9-26}$$

Multiplying and dividing by S_o results in

$$\frac{B_o - B_{oi}}{B_{oi}} = \frac{c_o S_o \Delta p}{S_o} \tag{9-27}$$

Since S_o=1 − S_{wc}, then also

$$\frac{B_o - B_{oi}}{B_{oi}} = \frac{c_o S_o \Delta p}{1 - S_{wc}} \tag{9-28}$$

and therefore Eq. (9-24) becomes

$$N_p B_o = N B_{oi}\left[\frac{c_o S_o \Delta p}{1 - S_{wc}} + \frac{c_w S_{wc} + c_f}{1 - S_{wc}}\Delta p\right] \tag{9-29}$$

From the definition of the total compressibility, c_t=$c_o S_o$+$c_w S_{wc}$+c_f, this is

$$N_p B_o = \frac{N B_{oi} c_t \Delta p}{1 - S_{wc}} \tag{9-30}$$

A graph of $N_p B_o$ versus $B_{oi} c_t \Delta p/(1 - S_{wc})$ would result in a straight line with a slope equal to N.

Equations (9-21), (9-23), and (9-30) describe straight lines, the slope and/or intercepts of which provide the original oil-in-place and, if present, the size of the gascap. The groups of variables to be plotted include production history, reservoir pressure, and associated fluid properties. Hence, well performance history can be used for the calculation of these important reservoir variables.

EXAMPLE 9-3

Material balance for saturated reservoirs[1]

An oil field produced as in the schedule in Table 9-2. Fluid properties are also given. The reservoir pressure in the oil and gas zones varied somewhat, therefore, fluid properties are given

[1] After an example from Class Notes by M. B. Standing, 1978.

Table 9-2

Production and Fluid Data for Example 9-3

Date	N_p (STB)	G_p (MSCF)
5/1/89	—	—
1/1/91	492,500	751,300
1/1/92	1.015,700	2,409,600
1/1/93	1.322,500	3,901,600

Date	$\bar{p}_o$ (psia)	$\bar{p}_g$ (psia)	B_t at $\bar{p}_o$ (res bbl/STB)	B_g at $\bar{p}_g$ (res ft³/SCF)
5/1/89	4415	4245	1.6291	0.00431
1/1/91	3875	4025	1.6839	0.00445
1/1/92	3315	3505	1.7835	0.00490
1/1/93	2845	2985	1.9110	0.00556

p_b = 4290 psia

R_{si} = 975 SCF/STB

B_{ob} = 1.6330 res bbl/STB

B_{oi} = 1.6291 res bbl/STB

for the simultaneous pressures in the two zones. Calculate the best value of the initial oil in place (STB) and the initial *total* gas in place (MM SCF).

The oil zone thickness is 21 ft, the porosity is 0.17, and the water saturation is 0.31. Calculate the areal extent of the initial gas cap and the reservoir pore volume.

Reservoir simulation has shown that a good time for a waterflood start is when 16% of the original oil-in-place is produced. When will this happen if a constant flow rate is maintained?

Since B_t data are given in this example, the already-developed equations for F, E_o and E_g are developed below in terms of B_t. Because

$$B_t = B_o + (R_{si} - R_s)B_g \tag{9-31}$$

then

$$B_o = B_t - (R_{si} - R_s)B_g \tag{9-32}$$

and therefore

$$F = N_p[B_t + (R_p - R_{si})B_g] \tag{9-33}$$

$$E_o = B_t - B_{oi} \tag{9-34}$$

$$E_g = B_{oi}\left(\frac{B_g}{B_{gi}} - 1\right) \tag{9-35}$$

Solution Table 9-3 contains the calculated R_p (= G_p/N_p) and the variables F, E_o, and E_g as given by Eqs. (9-33) through (9-35). Also, in the manner suggested by Eq. (9-23), the variables F/E_o and E_g/E_o are listed.

Table 9-3

Calculated Variables for the Material Balance Straight Line of Example 9-3

Date	R_p (SCF/STB)	F	E_o	E_g	F/E_o	E_g/E_o
1/1/91	1525	2.04×10^6	5.48×10^{-2}	5.29×10^{-2}	3.72×10^7	0.96
1/1/92	2372	8.77×10^6	1.54×10^{-1}	2.22×10^{-1}	5.69×10^7	1.44
1/1/93	2950	17.05×10^6	2.82×10^{-1}	4.72×10^{-1}	6.0×10^7	1.67

Figure 9-4 is a plot of the results, providing an intercept of 9×10^6 STB (= N, the initial oil-in-place) and a slope equal to 3.1×10^7 (= Nm). This leads to $m = 3.44$. [If there were no initial gas cap, the slope would be equal to zero. In general, the use of Eq. (9-23) instead of Eq. (9-21) is recommended, since the latter is included in the former.]

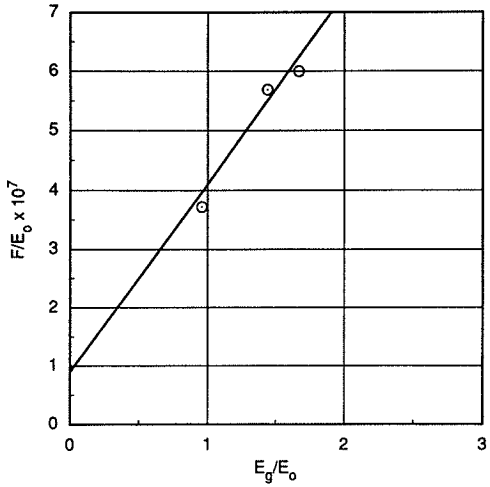

Figure 9-4
Material balance calculation for a two-phase reservoir (Example 9-3).

The pore volume of oil is then

$$V_{po} = NB_{oi} = (9 \times 10^6)(1.6291) = 1.47 \times 10^7 \text{ res bbl} \tag{9-36}$$

and the pore volume of the gas cap is

$$V_{pg} = mV_{po} = (3.44)(1.47 \times 10^7) = 5.04 \times 10^7 \text{ res bbl} \tag{9-37}$$

The drainage area of the oil zone in acres is

$$A = \frac{V_{po}}{7758\,\phi\,h\,(1 - S_w)} \tag{9-38}$$

and therefore

$$A = \frac{(1.47 \times 10^7)}{(7758)\,(0.17)(21)(1 - 0.31)} = 770 \text{ acres} \tag{9-39}$$

If 16% of initial oil-in-place is to be produced, then

$$N_p = (0.16)(9 \times 10^6) = 1.44 \times 10^6 \text{ STB} \tag{9-40}$$

From Table 9-2 the flow rate between 1/1/92 and 1/1/93 is approximately 840 STB/d. From 1/1/93 until the required date for water flooding, there will be a need for an additional 1.12×10^5 STB of production. With the same production rate it would require 140 days of additional production. Thus water flooding should begin at about May 1993. ◇

9-5 PRODUCTION FORECAST FROM A TWO-PHASE RESERVOIR: SOLUTION GAS DRIVE

The general material balance of Eq. (9-13) can be simplified further if the reservoir is assumed to have no initial gascap but rapidly passes below the bubble-point pressure after production commences. These assumptions encompass a large number of reservoirs. This mode of recovery is known as solution gas drive, and the calculation method outlined below is referred to as Tarner's (1944) method. It was described further by Craft and Hawkins (1991).

With the assumption that m=0 and with gas evolving out of solution immediately (i.e., the water and rock compressibility terms can be neglected), Eq. (9-13) becomes

$$N_p[B_o + (R_p - R_s)B_g] = N[(B_o - B_{oi}) + (R_{si} - R_s)B_g] \tag{9-41}$$

Since G_p (gas produced) = N_pR_p, then

$$N_p(B_o - R_sB_g) + G_pB_g = N[(B_o - B_{oi}) + (R_{si} - R_s)B_g] \tag{9-42}$$

and therefore

$$N = \frac{N_p(B_o - R_sB_g) + G_pB_g}{(B_o - B_{oi}) + (R_{si} - R_s)B_g} \tag{9-43}$$

Equation (9-43) has two distinct components, the oil cumulative production, N_p, and the gas cumulative production, G_p. Multiplying these components are groups of thermodynamic variables. With the following definitions,

$$\Phi_n = \frac{B_o - R_sB_g}{(B_o - B_{oi}) + (R_{si} - R_s)B_g} \tag{9-44}$$

and

$$\Phi_g = \frac{B_g}{(B_o - B_{oi}) + (R_{si} - R_s)B_g} \tag{9-45}$$

Eq. (9-43) becomes

$$N = N_p\Phi_n + G_p\Phi_g \tag{9-46}$$

Let R = GOR, the instantaneous, producing gas–oil ratio. Then

$$R = \frac{\Delta G_p}{\Delta N_p} \tag{9-47}$$

If N=1 STB, Eq. (9-46) in terms of increments of production becomes

$$\begin{aligned} 1 &= (N_p + \Delta N_p)\Phi_n + (G_p + \Delta G_p)\Phi_g \\ &= (N_p + \Delta N_p)\Phi_n + (G_p + R\ \Delta N_p)\Phi_g \end{aligned} \tag{9-48}$$

The instantaneous value of R is the GOR within a production interval with incremental cumulative production ΔN_p. Therefore, in a stepwise fashion between intervals i and $i+1$,

$$1 = (N_{pi} + \Delta N_{pi\to i+1})\Phi_{n,\text{av}} + (G_{pi} + R_{\text{av}}\ \Delta N_{pi\to i+1})\Phi_{g,\text{av}} \tag{9-49}$$

and solving for $\Delta N_{pi\to i+1}$,

$$\Delta N_{pi\to i+1} = \frac{1 - N_{pi}(\Phi_n)_{\text{av}} - G_{pi}(\Phi_g)_{\text{av}}}{(\Phi_n)_{\text{av}} + R_{\text{av}}(\Phi_g)_{\text{av}}} \tag{9-50}$$

This is an important finding. It can predict incremental production for a decline in the reservoir pressure in the same manner as shown in Section 9–3 for an undersaturated reservoir. The following steps are needed:

- Define Δp for calculation.
- Calculate Φ_n and Φ_g for the two different pressure values. Obtain averages for the interval.
- Assume a value of R_{av} in the interval.
- Calculate $\Delta N_{pi\to i+1}$ from Eq. (9-50).
- Calculate $N_{pi\to i+1}$.
- Calculate G_{pi+1} ($\Delta G_{pi\to i+1} = \Delta N_{pi\to i+1}R_{\text{av}}$).
- Calculate the oil saturation from

$$S_o = \left(1 - \frac{N_p}{N}\right)\frac{B_o}{B_{oi}}(1 - S_w) \tag{9-51}$$

- Obtain the relative permeability ratio k_g/k_o from a plot versus S_o. Relative permeability curves are usually available.

- Calculate R_{av} from

$$R_{\text{av}} = R_s + \frac{k_g\mu_o B_o}{k_o\mu_g B_g} \tag{9-52}$$

- Compare calculated R_{av} in the interval with the assumed.

With the average pressure within the interval, the Vogel correlation [Eq. (3-11)] can be used for the calculation of the well IPR. Combination with VLP will lead to the well production rate. Finally, with the material balance outlined above, rate and cumulative production versus time can be established.

EXAMPLE 9-4

Forecast of well performance in a two-phase reservoir

The well described in Appendix B is 8000 ft deep, completed with a 3-in.-I.D. tubing and with 100 psi flowing wellhead pressure. If the drainage area is 40 acres, develop a forecast of oil rate and oil and gas cumulative productions versus time until the average reservoir pressure declines to 3350 psi (i.e., $\Delta\bar{p}$=1000 psi).

Solution Since p_i=p_b=4350, the solution gas drive material balance and Tarner's method outlined in Section 9-5 are appropriate. With the properties in Fig. B-1 in Appendix B, the variables Φ_n and Φ_g can be calculated for a range of reservoir pressures.

The following is a sample calculation. Suppose a pressure interval between 4350 and 4150. The average B_o, B_g, and R_s are 1.42 res bbl/STB, 7.1×10^{-4} res bbl/SCF, and 820 SCF/STB, respectively. Noting that B_{oi} and R_{si} (at p_i) are 1.43 res bbl/STB and 840 SCF/STB, Eq. (9-44) yields

$$\Phi_n = \frac{1.42 - (820)(7.1 \times 10^{-4})}{(1.42 - 1.43) + (840 - 820)(7.1 \times 10^{-4})} = 199 \tag{9-53}$$

From Eq. (9-45),

$$\Phi_g = \frac{7.1 \times 10^{-4}}{(1.42 - 1.43) + (840 - 820)(7.1 \times 10^{-4})} = 0.17 \tag{9-54}$$

Similarly, these variables are calculated for four additional 200-psi intervals and are shown in Table 9-4.

For the first interval, assume that the producing R_{av}=845 SCF/STB. Then, from Eq. (9-50).

$$\Delta N_{pi\to i+1} = \frac{1}{199 + (845)(0.17)} = 2.92 \times 10^{-3}\ \text{STB} \tag{9-55}$$

which, for the first interval, is the same as $N_{pi\to i+1}$. The incremental gas cumulative production is (845)(2.92×10^{-3})=2.48 SCF, which, for the first interval, also coincides with G_p.

From Eq. (9-51),

$$S_o = (1 - 2.92 \times 10^{-3})\left(\frac{1.42}{1.43}\right)(1 - 0.3) = 0.693 \tag{9-56}$$

Table 9-4

Physical Properties for Tarner's Calculations (Example 9-4) for Well in Appendix B

$\bar{p}$ (psi)	B_o (res bbl/STB)	B_g (res bbl/SCF)	R_s (SCF/STB)	Φ_n	Φ_g
4350	1.43	6.9×10^{-4}	840		
	1.42	7.1×10^{-4}	820	199	0.17
4150					
	1.395	7.4×10^{-4}	770	49	0.044
3950					
	1.38	7.8×10^{-4}	730	22.6	0.022
3750					
	1.36	8.1×10^{-4}	680	13.6	0.014
3550					
	1.345	8.5×10^{-4}	640	9.42	0.010
3350					

and from the relative permeability curves in Fig. B-2 (noting that $S_g = 0.007$), $k_g/k_o = 8 \times 10^{-5}$ (extrapolated)/0.48 = 1.7×10^{-4}. From Eq. (9-52), using μ_o=1.7 cp and μ_g=0.023 cp,

$$R_{av} = 820 + 1.7 \times 10^{-4} \frac{(1.7)}{(0.023)} \frac{(1.42)}{(7.1 \times 10^{-4})} = 845 \text{ SCF/STB} \qquad (9\text{-}57)$$

which agrees with the assumed value.

The calculation is repeated for all intervals and appears in summary form in Table 9-5. There is an interesting comparison between the results in Table 9-5 and those in Table 9-1 for the undersaturated case. In the latter, after about 1000 psi reservoir pressure drop (from 5651 to 4500 psi), the recovery ratio would be less than 1.5% (i.e., $2.8 \times 10^4/1.87 \times 10^6$). For a similar pressure drop, the recovery ratio for the two-phase well in this example is more than three times higher, demonstrating the far more efficient recovery in a solution-gas drive reservoir.

For A=40 acres, the initial oil-in-place (using the variables in Appendix B) is

$$N = \frac{(7758)(40)(115)(0.21)(1 - 0.3)}{1.43} = 3.7 \times 10^6 \text{ STB} \qquad (9\text{-}58)$$

The IPR expression for this two-phase reservoir can be obtained from the Vogel correlation [Eq. (3-53)]. With k_o=13 md, h=115 ft, r_e=1490 ft, r_w=0.328 ft, μ_o=1.7 cp, s=0, and allowing B_o to vary with the pressure, Eq. (3-53) becomes

$$q_o = 0.45 \frac{\bar{p}}{B_o} \left[1 - 0.2 \frac{p_{wf}}{\bar{p}} - 0.8 \left(\frac{p_{wf}}{\bar{p}} \right)^2 \right] \qquad (9\text{-}59)$$

The IPR curves for six average reservoir pressures (from 4350 to 3350 in increments of 200 psi) are shown in expanded form in Fig. 9-5. At q_o=0, each curve would intersect the p_{wf} axis at the corresponding $\bar{p}$.

Table 9-5

Cumulative Production with Depleting Pressure for Well in Example 9-4 (N=1 STB)

$\bar{p}$ (psi)	ΔN_p (STB)	N_p (STB)	R_{av} (SCF/STB)	ΔG_p (SCF)	G_p (SCF)
4350					
	2.92×10^{-3}		845	2.48	
4150		2.92×10^{-3}			2.48
	8.41×10^{-3}		880	7.23	
3950		1.1×10^{-2}			9.71
	1.2×10^{-2}		1000	12	
3750		2.3×10^{-2}			21.71
	1.26×10^{-2}		1280	16.1	
3550		3.56×10^{-2}			37.81
	1.1×10^{-2}		1650	18.2	
3350		4.66×10^{-2}			56.01

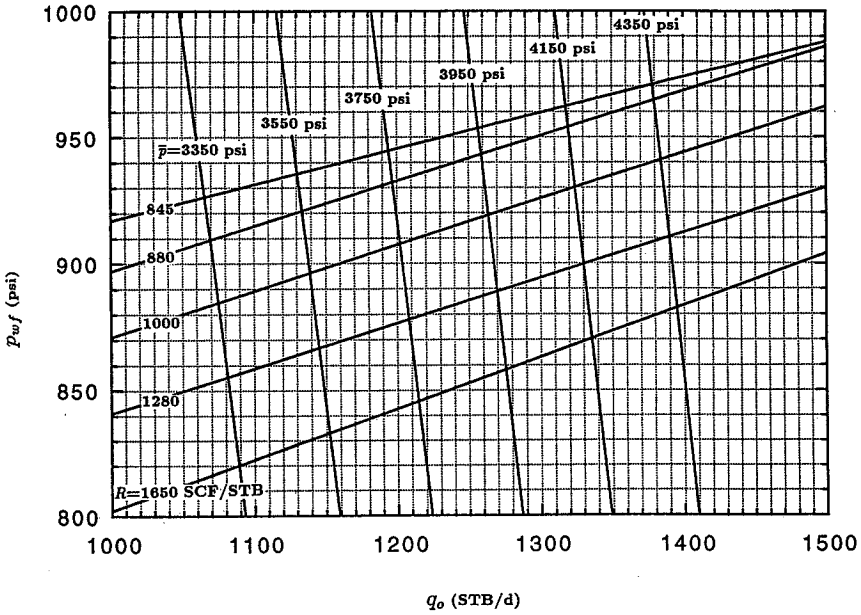

Figure 9-5
IPR and VLP curves for a solution-gas-drive reservoir (Example 9-4).

Also plotted are five VLP curves for this well, each for the average producing gas–liquid ratio within the pressure interval. These values are listed in Table 9-5. The expected oil flow rates within each interval can be obtained from Fig. 9-5.

All necessary variables are now available for the calculation of the time duration of each interval. For example, the recovery ratio ($=\Delta N_p$ with N=1 STB) in the interval between 4350 and 4150 psi is 2.92×10^{-3}, and since $N = 3.7 \times 10^6$ STB,

$$\Delta N_p = (2.92 \times 10^{-3}) \times (3.7 \times 10^6) = 1.08 \times 10^4 \text{ STB} \tag{9-60}$$

Also,

$$\Delta G_p = (1.08 \times 10^4)(845) = 9.1 \times 10^6 \text{ SCF} \tag{9-61}$$

The average production rate within the interval is 1346 STB/d (from Fig. 9-5), and therefore

$$t = \frac{1.08 \times 10^4}{1346} = 8 \text{ d} \tag{9-62}$$

The results for all intervals are shown in Table 9-6.

Table 9-6

Production Rate and Oil and Gas Cumulative Recovery Forecast for Well in Example 9-4

$\bar{p}$ (psi)	q_o (STB/d)	ΔN_p (10^4 STB)	N_p (10^4 STB)	ΔG_p (10^6 SCF)	G_p (10^6 SCF)	Δt (d)	t (d)
4350							
	1346	1.08		9.1		8	
4150			1.08		9.1		8
	1288	3.11		27.4		24	
3950			4.19		36.5		32
	1234	4.44		44.4		36	
3750			8.63		80.9		68
	1176	4.66		59.6		40	
3550			13.29		140.5		108
	1120	4.07		67.2		36	
3350			17.36		207.7		144

(Note: This example was set up to illustrate both the recovery and time contrasts with the undersaturated reservoir of Example 9-2. Thus a drainage area of 40 acres was used for both cases. Ordinarily, a well such as the one in Example 9-5 would be assigned a much larger drainage area, e.g., 640 acres. In such a case, while the production rate would not be affected markedly—being inversely proportional to the respective ln r_e—the time values in Table 9-6 would be more than 16 times larger.) ◇

9-6 GAS MATERIAL BALANCE AND FORECAST OF GAS WELL PERFORMANCE

If G_i and G are the initial and current gas-in-place within a drainage area, the cumulative production from a gas reservoir, considering the expansion of the fluid, is

$$G_p = G_i - G = G_i - G_i \frac{B_{gi}}{B_g} \tag{9-63}$$

when B_{gi} and B_g are the corresponding formation volume factors.

Equation (4-13) in Chapter 4 provides B_g in terms of pressure, temperature, and the gas deviation factor. Substitution in Eq. (9-63), assuming isothermal operation throughout, and rearrangement results in

$$G_p = G_i \left(1 - \frac{\bar{p}/Z}{p_i/Z_i}\right) \tag{9-64}$$

This expression suggests that if G_p, the cumulative production, is plotted against $\bar{p}/Z$, it should form a straight line. Usually, the variable $\bar{p}/Z$ is plotted on the ordinate and the cumulative production on the abscissa. At $G_p = 0$, then, $\bar{p}/Z$=p_i/Z_i, and at $\bar{p}/Z$=0, $G_p = G_i$. For any value of the reservoir pressure (and associated Z), there exists a corresponding G_p. Coupled with the gas well IPR expressions for pseudo-steady-state flow [Eq. (4-24)] or accounting for non-Darcy flow [Eq. (4-32)], or using the more exact form [Eq. (4-54)], a forecast of well performance versus time can be developed readily.

EXAMPLE 9-5

Forecast of gas well performance

Assume that a well in the gas reservoir in Appendix C drains 40 acres. The calculation of the initial gas-in-place with p_i=4613 psi was presented in Example 4-5 (for 1900 acres). Develop a forecast of this well's performance versus time until the average reservoir pressure declines to 3600 psi. Use five pressure intervals of 200 psi each. The flowing bottomhole pressure is 1500 psi. Estimate the time to pseudo-steady state using the approximation of Eq. (2-35). The total compressibility, c_t, is 1.5×10^{-4} psi^{-1}. For the solution to this problem, assume pseudo-steady-state conditions throughout and ignore the non-Darcy effects on the flow rate.

Solution From Eq. (2-35) and r_e=745 ft (for A=40 acres),

$$t_{pss} = 1200 \frac{(0.14)(0.0244)(1.5 \times 10^{-4})(745^2)}{0.17} = 2007 \text{ hr} \tag{9-65}$$

After about 84 days the well will "feel" the no-flow boundaries.

Similar to Example 4-5, the initial gas-in-place within 40 acres (and using the calculated B_{gi}) is

$$G_i = \frac{(43,560)(40)(78)(0.14)(0.73)}{3.71 \times 10^{-3}} = 3.7 \times 10^9 \text{ SCF} \tag{9-66}$$

With Z_i=0.969 (from Table 4-5—This value is used for consistency; it was obtained from correlations and is slightly different from the Z_i listed in Appendix C),

$$\frac{p_i}{Z_i} = \frac{4613}{0.969} = 4761 \text{ psi} \tag{9-67}$$

From Eq. (9-64), the gas cumulative production is

$$G_p = 3.7 \times 10^9 \left(1 - \frac{\bar{p}/Z}{4761}\right) \tag{9-68}$$

at any reservoir pressure $\bar{p}$.

Table 9-7 lists the average reservoir pressures, the calculated gas deviation factors (see Table 4-5), and the corresponding cumulative production.

Table 9-7

Production Rate and Cumulative Production Forecast for Gas Well in Example 9-5

$\bar{p}$ (psi)	Z (10^8 SCF)	G_p (10^8 SCF)	ΔG_p (10^8 SCF)	q (10^3 MSCF/d)	Δt (d)	t (d)
4613	0.969	0				
			1.16	2.16	54	
4400	0.954	1.16				54
			1.15	2.0	58	
4200	0.941	2.31				112
			1.23	1.83	67	
4000	0.929	3.54				179
			1.26	1.66	76	
3800	0.917	4.80				255
			1.35	1.5	90	
3600	0.907	6.15				345

The production rate is obtained from Eq. (4-24), cast in real-gas pseudo-pressures, and calculated with the average $\bar{p}$ within each pressure interval. Assuming that s=0, Eq. (4-24), rearranged, becomes

$$q = \frac{m(\bar{p}) - 1.821 \times 10^8}{4.8 \times 10^5} \tag{9-69}$$

where $m(p_{wf}) = 1.821 \times 10^8$ psi^2/cp.

The values for $m(\bar{p})$ are obtained from Table 4-5 at the average value within a pressure interval. ◇

REFERENCES

1. Craft, B. C., and Hawkins, M. (Revised by Terry, R. E.), *Applied Petroleum Reservoir Engineering*, 2nd ed., Prentice Hall, Englewood Cliffs, NJ, 1991.
2. Dake, L. P., *Fundamentals of Reservoir Engineering*, Elsevier, Amsterdam, 1978.

3. Havlena, D., and Odeh, A. S., "The Material Balance as an Equation of a Straight Line," *JPT*, 896–900, August 1963.
4. Havlena, D., and Odeh, A. S., "The Material Balance as an Equation of a Straight Line. Part II—Field Cases," *JPT*, 815–822, July 1964.
5. Tarner, J., "How Different Size Gas Caps and Pressure Maintenance Programs Affect Amount of Recoverable Oil," *Oil Weekly*, **144**: 32–34, June 12, 1944.

PROBLEMS

9-1. Estimate the time during which the oil well in Appendix A would be infinite acting. Perform the calculations for drainage areas of 40, 80, 160, and 640 acres.

9-2. Develop a forecast of well performance using the VLP curve of Example 8-1 and a transient IPR for the 640-acre drainage area (i.e., until boundaries are felt). Use the data in Appendix A.

9-3. Calculate the average reservoir pressure of the well in Appendix A after 2 years. Use the VLP curve of Example 8-1. Plot production rate and cumulative production versus time.

9-4. Suppose that the drainage area of the well in Appendix B is 640 acres. Assuming that the flowing bottomhole pressure is held constant at 1500 psi, calculate the average reservoir pressure after 3 years. Graph the oil production rate and the oil and gas cumulative productions versus time.

9-5. A well in a gas reservoir has been producing 3.1×10^3 MSCF/d for the last 470 days. The rate was held constant. The reservoir temperature is 624°R, and the gas gravity is 0.7. Assuming that h=31 ft, S_g=0.75, and ϕ=0.21, calculate the areal extent of the reservoir.

The initial reservoir pressure, p_i, is 3650 psi. Successive pressure buildup analysis reveals the following average reservoir pressures at the corresponding times from the start of production: 3424 psi (209 days), 3310 psi (336 days), and 3185 psi (470 days).

9-6. Assume that the production rate of the well in Problem 9-5 is reduced after 470 days from 3.1×10^3 MSCF/d to 2.1×10^3 MSCF/d. What would be the average reservoir pressure after 600 days from the start of production?

9-7. Repeat the calculation of Example 9-5 but use the non-Darcy coefficient calculated in Example 4-8 [$D = 3.6 \times 10^{-4}$ (MSCF/d)$^{-1}$]. After how many days would the well cumulative production compare with the cumulative production after 345 days obtained in Example 9-5 and listed in Table 9-7?

CHAPTER 10

Wellhead and Surface Gathering Systems

10-1 INTRODUCTION

This chapter is concerned with the transport of fluids from the wellhead to the facility where processing of the fluids begins. For oil production, this facility is typically a two- or three-phase separator; for gas production, the facility may be a gas plant, a compressor station, or simply a transport pipeline; and, for injection wells, the surface transport of interest is from a water treating/pumping facility to the wells. We are not concerned here with pipeline transport over large distances; thus we will not consider the effect of hilly terrain or changes in fluid temperature in our calculations.

As in wellbore flow, we are interested primarily in the pressure as a function of position as fluids move through the wellhead and surface flow lines. In addition to flow through pipes, flows through fittings and chokes are important considerations for surface transport.

10-2 FLOW IN HORIZONTAL PIPES

10-2.1 Single-Phase Flow: Liquid

Single-phase flow in horizontal pipes is described by the same equations as those for single-phase flow in wellbores presented in Chapter 7, but with the simplification that the potential energy pressure drop is zero. If the fluid is incompressible and the pipe diameter is constant, the kinetic energy pressure drop is also zero, and the mechanical energy balance [Eq. (7-15)] simplifies to

$$\Delta p = p_1 - p_2 = \frac{2 f_f \rho u^2 L}{g_c D} \tag{10-1}$$

CHAPTER 10

Wellhead and Surface Gathering Systems

10-1 INTRODUCTION

This chapter is concerned with the transport of fluids from the wellhead to the facility where processing of the fluids begins. For oil production, this facility is typically a two- or three-phase separator; for gas production, the facility may be a gas plant, a compressor station, or simply a transport pipeline; and, for injection wells, the surface transport of interest is from a water treating/pumping facility to the wells. We are not concerned here with pipeline transport over large distances; thus we will not consider the effect of hilly terrain or changes in fluid temperature in our calculations.

As in wellbore flow, we are interested primarily in the pressure as a function of position as fluids move through the wellhead and surface flow lines. In addition to flow through pipes, flows through fittings and chokes are important considerations for surface transport.

10-2 FLOW IN HORIZONTAL PIPES

10-2.1 Single-Phase Flow: Liquid

Single-phase flow in horizontal pipes is described by the same equations as those for single-phase flow in wellbores presented in Chapter 7, but with the simplification that the potential energy pressure drop is zero. If the fluid is incompressible and the pipe diameter is constant, the kinetic energy pressure drop is also zero, and the mechanical energy balance [Eq. (7-15)] simplifies to

$$\Delta p = p_1 - p_2 = \frac{2 f_f \rho u^2 L}{g_c D} \tag{10-1}$$

The friction factor is obtained as in Chapter 7 by the Chen equation [Eq. (7-35)] or the Moody diagram (Fig. 7-7).

EXAMPLE 10-1

Pressure drop in a water injection supply line

The 1000 bbl/d of injection water described in Examples 7-2 and 7-4 is supplied to the wellhead through a 3000-ft-long, 1 1/2-in.-I.D. flow line from a central pumping station. The relative roughness of the galvanized iron pipe is 0.004. If the pressure at the wellhead is 100 psia, what is the pressure at the pumping station, neglecting any pressure drops through valves or other fittings? The water has a specific gravity of 1.05 and a viscosity of 1.2 cp.

Solution Equation (10-1) applies, with the Reynolds number and the friction factor calculated as in Chapter 7. Using Eq. (7-7), the Reynolds number is calculated to be 53,900; from the Chen equation [Eq. (7-35)], the friction factor is 0.0076. Dividing the volumetric flow rate by the pipe cross-sectional area, we find the mean velocity to be 5.3 ft/sec. Then, from Eq. (10-1),

$$\Delta p = p_1 - p_2 = \frac{(2)(0.0076)(65.5\ \text{lb}_m/\text{ft}^3)(5.3\ \text{ft/sec})^2(3000\ \text{ft})}{(32.17\ \text{ft-lb}_m/\text{lb}_{f\text{-sec}^2})[(1.5/12)\ \text{ft}]} = 20{,}800\ \text{lb}_f/\text{ft}^2 = 145\ \text{psi} \tag{10-2}$$

so

$$p_1 = p_2 + 145\ \text{psi} = 100\ \text{psi} + 145\ \text{psi} = 245\ \text{psi} \tag{10-3}$$

This is a significant pressure loss over 3000 ft. It can be reduced substantially by using a larger pipe for this water supply, since the frictional pressure drop depends approximately on the pipe diameter to the fifth power. ◇

10-2.2 Single-Phase Flow: Gas

The pressure drop for the horizontal flow of a compressible fluid (gas), neglecting the kinetic energy pressure drop, was given by Eqs. (7-50) and (7-54). This equation was based on using average values of Z, T, and μ for the entire length of pipe being considered. In a high-rate, low-pressure line, the change in kinetic energy may be significant. In this case, for a horizontal line, the mechanical energy balance is

$$\frac{dp}{\rho} + \frac{u\,du}{g_c} + \frac{2f_f u^2\,dL}{g_c D} = 0 \tag{10-4}$$

For a real gas, ρ and u are given by Eqs. (7-44) and (7-45), respectively. The differential form of the kinetic energy term is

$$u\,du = -\left(\frac{4qZT}{\pi D^2}\frac{p_{sc}}{T_{sc}}\right)^2 \frac{dp}{p^3} \tag{10-5}$$

Substituting for ρ and $u\,du$ in Eq. (10-4), assuming average values of Z and T over the length of the pipeline, and integrating, we obtain

$$p_1^2 - p_2^2 = \frac{32}{\pi^2}\frac{28.97\gamma_g \overline{ZT}}{Rg_c D^4}\left(\frac{p_{sc}q}{T_{sc}}\right)^2\left(\frac{2f_f L}{D} + \ln\frac{p_1}{p_2}\right) \tag{10-6}$$

which for field units is

$$p_1^2 - p_2^2 = (4.195 \times 10^{-6})\frac{\gamma_g \overline{ZT} q^2}{D^4}\left(\frac{24 f_f L}{D} + \ln\frac{p_1}{p_2}\right) \tag{10-7}$$

where p_1 and p_2 are in psi, T is in °R, q is in MSCF/d, D is in in., and L is in ft. The friction factor is obtained from the Reynolds number and pipe roughness, with the Reynolds number for field units given by Eq. (7-55).

Equation (10-7) is identical to Eq. (7-50) except for the additional $\ln(p_1/p_2)$ term, which accounts for the kinetic energy pressure drop. Equation (10-7) is an implicit equation in p and must be solved iteratively. The equation can be solved first by neglecting the kinetic energy term; then, if $\ln(p_1/p_2)$ is small compared with $24 f_f L/D$, the kinetic energy pressure drop is negligible.

EXAMPLE 10-2

Flow capacity of a low-pressure gas line

Gas production from a low-pressure gas well (wellhead pressure = 100 psia) is to be transported through 1000 ft of a 3-in.-I.D. line ($\epsilon = 0.001$) to a compressor station, where the inlet pressure must be at least 20 psia. The gas has a specific gravity of 0.7, a temperature of 100°F and an average viscosity of 0.012 cp. What is the maximum flow rate possible through this gas line?

Solution We can apply Eq. (10-7), solving for q. We need the Reynolds number to find the friction factor. However, we can begin by assuming that the flow rate, and hence the Reynolds number, is high enough that the flow is fully rough wall turbulent so that the friction factor depends only on the pipe roughness. From the Moody diagram (Fig. 7-7), we find that $f_f = 0.0049$ for high Reynolds number and a relative roughness of 0.001. Then

$$q = \sqrt{\frac{(p_1^2 - p_2^2)D^4}{(4.195 \times 10^{-7})\gamma_g \overline{ZT}\left[\left(24 f_f L/D\right) + \ln(p_1/p_2)\right]}} \tag{10-8}$$

Assuming $Z = 1$ at these low pressures,

$$q = \sqrt{\frac{(100^2 - 20^2)(3)^4}{(4.195 \times 10^{-7})(0.7)(1)(560)\{[(24)(0.0049)(1000)/3] + \ln(100/20)\}}} \tag{10-9}$$

$$= \sqrt{\frac{4.73 \times 10^9}{39.2 + 1.61}} = 10{,}800\ \text{MSCF/d} \tag{10-10}$$

Checking the Reynolds number using Eq. (7-55),

$$N_{Re} = \frac{(20.09)(0.7)(10{,}800)}{(3)(0.012)} = 4.2 \times 10^6 \tag{10-11}$$

so the friction factor based on fully rough wall turbulence is correct.

We find that we can transport over 10 MMSCF/d through this line. Notice that even at this high flow rate and with a velocity five times higher at the pipe outlet than at the entrance, the kinetic energy contribution to the overall pressure drop is still small relative to the frictional pressure drop. ◇

10-2.3 Two-Phase Flow

Two-phase flow in horizontal pipes differs markedly from that in vertical pipes; except for the Beggs and Brill correlation (Beggs and Brill, 1973), which can be applied for any flow direction, completely different correlations are used for horizontal flow than for vertical flow. In this section, we first consider flow regimes in horizontal gas-liquid flow, then a few commonly used pressure drop correlations.

Flow regimes. The flow regime does not affect the pressure drop as significantly in horizontal flow as it does in vertical flow, because there is no potential energy contribution to the pressure drop in horizontal flow. However, the flow regime is considered in some pressure drop correlations and can affect production operations in other ways. Most important, the occurrence of slug flow necessitates designing separators or sometimes special pieces of equipment (slug catchers) to handle the large volume of liquid contained in a slug. Particularly in offshore operations, where gas and liquid from subsea completions are transported significant distances to a platform, the possibility of slug flow, and its consequences, must be considered.

Figure 10-1 (Brill and Beggs, 1978) depicts the commonly described flow regimes in horizontal gas-liquid flow. These can be classified as three types of regimes: *segregated* flows, in which the two phases are for the most part separate; *intermittent* flows, in which gas and liquid are alternating; and *distributive* flows, in which one phase is dispersed in the other phase.

Segregated flow is further classified as being stratified smooth, stratified wavy (ripple flow), or annular. Stratified smooth flow consists of liquid flowing along the bottom of the pipe and gas flowing along the top of the pipe, with a smooth interface between the phases. This flow regime occurs at relatively low rates of both phases. At higher gas rates, the interface becomes wavy, and stratified wavy flow results. Annular flow occurs at high gas rates and relatively high liquid rates and consists of an annulus of liquid coating the wall of the pipe and a central core of gas flow, with liquid droplets entrained in the gas.

The intermittent flow regimes are slug flow and plug (also called elongated bubble) flow. Slug flow consists of large liquid slugs alternating with high-velocity bubbles of gas that fill almost the entire pipe. In plug flow, large gas bubbles flow along the top of the pipe, which is otherwise filled with liquid.

Distributive flow regimes described in the literature include bubble, dispersed bubble, mist, and froth flow. The bubble flow regimes differ from those described for vertical flow in that the gas bubbles in a horizontal flow will be concentrated on the upper side of the pipe. Mist flow occurs at high gas rates and low liquid rates and consists of gas with liquid droplets entrained. Mist flow will often be indistinguishable from annular flow, and many flow regime maps use "annular mist" to denote both of these regimes. "Froth flow" is used by some authors to describe the mist or annular mist flow regime.

Flow regimes in horizontal flow are predicted with flow regime maps. One of the first of these, and still one of the most popular, is that of Baker (1953), later modified by Scott (1963), shown in Fig. 10-2. The axes for this plot are G_l/λ and $G_l\lambda\phi/G_g$, where G_l and G_g are the mass fluxes of liquid and gas, respectively ($lb_m/hr\text{-}ft^2$) and the parameters λ

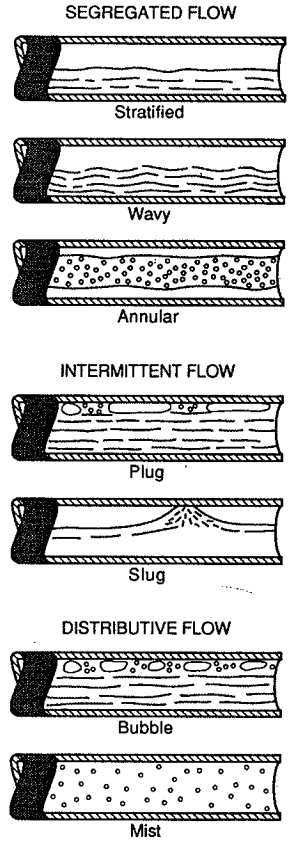

Figure 10-1
Flow regimes in two-phase horizontal flow. (*From Brill and Beggs, 1978.*)

and ϕ are

$$\lambda = \left[\left(\frac{\rho_g}{0.075}\right)\left(\frac{\rho_l}{62.4}\right)\right]^{1/2} \tag{10-12}$$

$$\phi = \frac{73}{\sigma_l}\left[\mu_l\left(\frac{62.4}{\rho_l}\right)^2\right]^{1/3} \tag{10-13}$$

where densities are in lb_m/ft^3, μ is in cp, and σ_l is in dynes/cm. The shaded regions on this

diagram indicate that the transitions from one flow regime to another are not abrupt, but occur over these ranges of flow conditions.

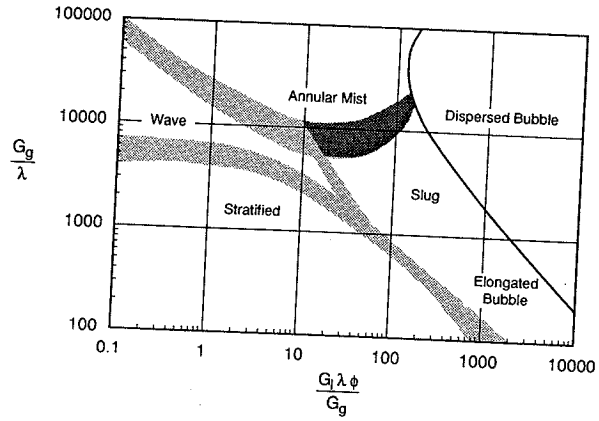

Figure 10-2
Baker flow regime map. (*From Baker, 1953.*)

Another commonly used flow regime is that of Mandhane et al. (1974) (Fig. 10-3). Like many vertical flow regime maps, this map uses the gas and liquid superficial velocities as the coordinates.

The Beggs and Brill correlation is based on a horizontal flow regime map that divides the domain into the three flow regime categories, segregated, intermittent and distributed. This map, shown in Fig. 10-4, plots the mixture Froude number defined as

$$N_{\text{Fr}} = \frac{u_m^2}{gD} \tag{10-14}$$

versus the input liquid fraction, λ_l.

Finally, Taitel and Dukler (1976) developed a theoretical model of the flow regime transitions in horizontal gas-liquid flow; their model can be used to generate flow regime maps for particular fluids and pipe size. Figure 10-5 shows a comparison of their flow regime predictions with those of Mandhane et al. for air-water flow in a 2.5-cm pipe.

EXAMPLE 10-3
Predicting horizontal gas-liquid flow regime

Using the Baker, Mandhane, and Beggs and Brill flow regime maps, determine the flow regime for the flow of 2000 bbl/d of oil and 1 MM SCF/d of gas at 800 psia and 175°F in a 2 1/2-in.-I.D. pipe. The fluids are the same as in Example 7-8.

Solution From Example 7-8, we find the following properties:

Liquid: $\rho = 49.92$ lb$_m$/ft^3; $\mu_l = 2$ cp; $\sigma_l = 30$ dynes/cm; $q_l = 0.130$ ft^3/sec

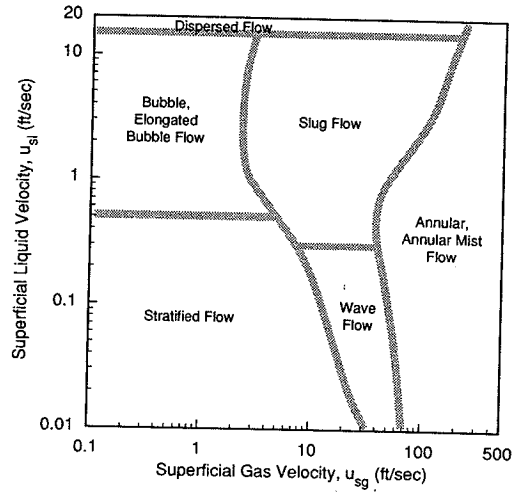

Figure 10-3
Mandhane flow regime map. (*From Mandhane et al., 1974.*)

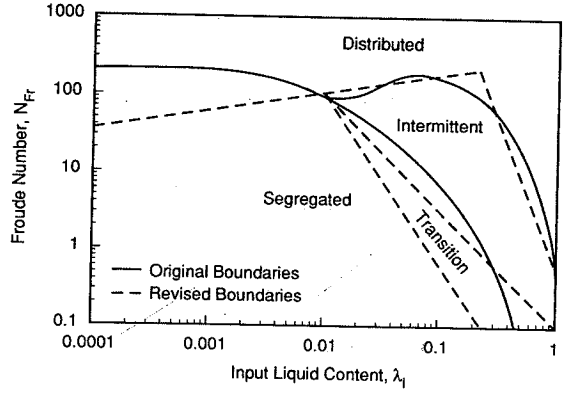

Figure 10-4
Beggs and Brill flow regime map. (*From Beggs and Brill, 1973.*)

Gas: $\rho = 2.6$ lb$_m$/ft^3; $\mu_g = 0.0131$ cp; $Z = 0.935$; $q_g = 0.242$ ft^3/sec

The 2 1/2-in. pipe has a cross-sectional area of 0.0341 ft^2; dividing the volumetric flow rates by the cross-sectional area, we find $u_{sl} = 3.81$ ft/sec, $u_{sg} = 7.11$ ft/sec, and $u_m = 10.9$ ft/sec.

For the Baker map, we compute the mass fluxes, G_l and G_g, and the parameters, λ and

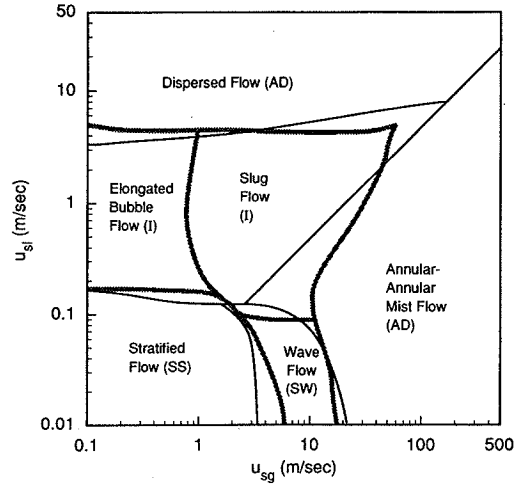

Figure 10-5
Taitel-Dukler flow regime map. (*From Taitel and Dukler, 1976.*)

ϕ. The mass flux is just the superficial velocity times density, so

$$G_l = u_{sl}\rho_l = (3.81 \text{ ft/sec})\left(49.92 \text{ lb}_m/\text{ft}^3\right)(3600 \text{ sec/hr}) = 6.84 \times 10^5 \text{ lb}_m/\text{hr-ft}^2 \quad (10\text{-}15)$$

$$G_g = u_{sg}\rho_g = (7.11 \text{ ft/sec})\left(2.6 \text{ lb}_m/\text{ft}^3\right)(3600 \text{ sec/hr}) = 6.65 \times 10^4 \text{ lb}_m/\text{hr-ft}^2 \quad (10\text{-}16)$$

Then, from Eqs. (10-12) and (10-13),

$$\lambda = \left[\left(\frac{2.6}{0.075}\right)\left(\frac{49.92}{62.4}\right)\right]^{1/2} = 5.27 \quad (10\text{-}17)$$

$$\phi = \frac{73}{30}\left[2\left(\frac{62.4}{49.92}\right)^2\right]^{1/3} = 3.56 \quad (10\text{-}18)$$

The coordinates for the Baker map are

$$\frac{G_g}{\lambda} = \frac{6.65 \times 10^4}{5.27} = 1.26 \times 10^4 \quad (10\text{-}19)$$

$$\frac{G_l\lambda\phi}{G_g} = \frac{(6.84 \times 10^5)(5.27)(3.56)}{6.65 \times 10^4} = 193 \quad (10\text{-}20)$$

Reading from Fig. 10-2, the flow regime is predicted to be dispersed bubble, though the conditions are very near the boundaries with slug flow and annular mist flow.

The Mandhane map (Fig. 10-3) is simply a plot of superficial liquid velocity versus superficial gas velocity. For our values of $u_{sl} = 3.81$ ft/sec and $u_{sg} = 7.11$ ft/sec, the flow regime is predicted to be slug flow.

The Beggs and Brill map plots the mixture Froude number, defined by Eq. (7-125), against the input fraction of liquid. These parameters are

$$N_{Fr} = \frac{(10.9 \text{ ft/sec})^2}{(32.17 \text{ ft/sec}^2)[(2.5/12) \text{ ft}]} = 17.8 \quad (10\text{-}21)$$

$$\lambda_l = \frac{3.81}{10.9} = 0.35 \quad (10\text{-}22)$$

From Fig. 10-4, the flow regime is predicted to be intermittent.

The prediction of dispersed bubble flow with the Baker map disagrees with that of Mandhane and Beggs and Brill, which predict slug flow. However, the conditions were very near the flow regime transition on the Baker map, and slug flow is the likely flow regime. ◇

Pressure gradient correlations. Over the years, numerous correlations have been developed to calculate the pressure gradient in horizontal gas-liquid flow. The most commonly used in the oil and gas industry today are those of Beggs and Brill (1973), Eaton et al. (1967), and Dukler (1969). These correlations all include a kinetic energy contribution to the pressure gradient; however, this can be considered negligible unless the gas rate is high and the pressure is low.

Beggs and Brill correlation. The Beggs and Brill correlation presented in Chapter 7 can be applied to horizontal flow, as well as flow in any other direction. For horizontal flow, the correlation is somewhat simplified, since the angle θ is 0, making the factor ψ equal to 1. This correlation is presented in Section 7-4.3, Eqs. (7-125) through (7-152).

EXAMPLE 10-4
Pressure gradient calculation using the Beggs and Brill correlation

Calculate the pressure gradient for the flow of 2000 bbl/d oil and 1 MMSCF/d of gas described in Example 10-3.

Solution The first step in using this correlation is to determine the flow regime using Eqs. (7-131) through (7-134); however, we have already found the flow regime to be intermittent by using the flow regime map in Example 10-3. Note that the dashed lines in Fig. 10-4 correspond to Eqs. (7-131) through (7-134).

Next, we calculate the holdup for horizontal flow with Eq. (7-136). From Example 10-3, $\lambda_l = 0.35$ and $N_{Fr} = 17.8$, so

$$y_{l0} = \frac{(0.845)(0.35)^{0.5351}}{(17.8)^{0.0173}} = 0.458 \quad (10\text{-}23)$$

Even though there is no potential energy contribution to the pressure gradient in horizontal flow, the holdup is used as a parameter in calculating the frictional pressure gradient.

To calculate the frictional gradient, we first obtain the no-slip friction factor based on the mixture Reynolds number. Using Eqs. (7-143), (7-145), and (7-146),

$$\rho_m = (49.92)(0.35) + (2.6)(0.65) = 19.2 \text{ lb}_m/\text{ft}^3 \quad (10\text{-}24)$$

$$\mu_m = (2)(0.35) + (0.0131)(0.65) = 0.71 \text{ cp} \tag{10-25}$$

$$N_{\text{Re}_m} = \frac{(19.2 \text{ lb}_m/\text{ft}^3)(10.92 \text{ ft/sec})[(2.5/12) \text{ ft}]}{((0.71)(6.72 \times 10^{-4}) \text{ lb}_m/\text{ft-sec})} = 91,600 \tag{10-26}$$

and from the Moody diagram (Fig. 7-7) or the Chen equation [Eq. (7-35)], $f_n = 0.0046$. Now, we calculate the parameters x, S, and f_{tp} using Eqs. (7-149), (7-148), and (7-147), respectively.

$$x = \frac{0.35}{(0.458)^2} = 1.67 \tag{10-27}$$

$$S = \frac{\ln(1.67)}{\{-0.0523 + 3.182\ln(1.67) - 0.8725[\ln(1.67)]^2 + 0.01853[\ln(1.67)]^4\}} \tag{10-28}$$

$$= 0.379$$

$$f_{tp} = (0.0046)e^{0.379} = 0.0067 \tag{10-29}$$

Finally, from Eq. (7-142),

$$\frac{dp}{dx} = \frac{(2)(0.0067)(19.2 \text{ lb}_m/\text{ft}^3)(10.92 \text{ ft/sec})^2}{(32.17 \text{ ft-lb}_m/\text{lb}_f\text{-sec}^2)[(2.5/12) \text{ ft}]} = 4.6 \text{ lb}_f/\text{ft}^3 = 0.03 \text{ psi/ft} \tag{10-30}$$

◇

Eaton correlation. The Eaton correlation (Eaton et al., 1967) was developed empirically from a series of tests in 2-in.- and 4-in.-diameter, 1700-ft-long lines. It consists primarily of correlations for liquid holdup and friction factor. The Eaton correlation is derived by applying mechanical energy balances to both the gas and liquid phases, then adding these together. Integrating this equation over a finite distance of pipe, Δx, yields

$$\frac{\Delta p}{\Delta x} = \frac{f\bar{\rho}_m u_m^2}{2g_c D} + \frac{\lambda_l \bar{\rho}_l \, \Delta(u_l)^2 + \lambda_g \bar{\rho}_g \, \Delta(u_g)^2}{2g_c \, \Delta x} \tag{10-31}$$

In this equation, the overbars indicate properties evaluated at the average pressure over the distance Δx and the velocities, u_l and u_g, are the in-situ average velocities. If the kinetic energy term is neglected, the equation can be applied at a point, or

$$\left(\frac{dp}{dx}\right)_F = \frac{f\rho_m u_m^2}{2g_c D} \tag{10-32}$$

The friction factor, f, is obtained from the correlation shown in Fig. 10-6 as a function of the mass flow rate of the liquid, m_l, and the total mass flow rate, m_m. For the constant given in this figure to compute the abscissa, mass flow rates are in lb_m/sec, diameter is in ft, and viscosity is in lb_m/ft-sec.

To compute the kinetic energy pressure drop, the liquid holdup is needed so that the in-situ average velocities of the phases can be calculated. Liquid holdup is given by the correlation of Fig. 10-7, using the same dimensionless groups as the Hagedorn and Brown correlation (see Section 7-4.3). The base pressure, p_b, is 14.65 psi.

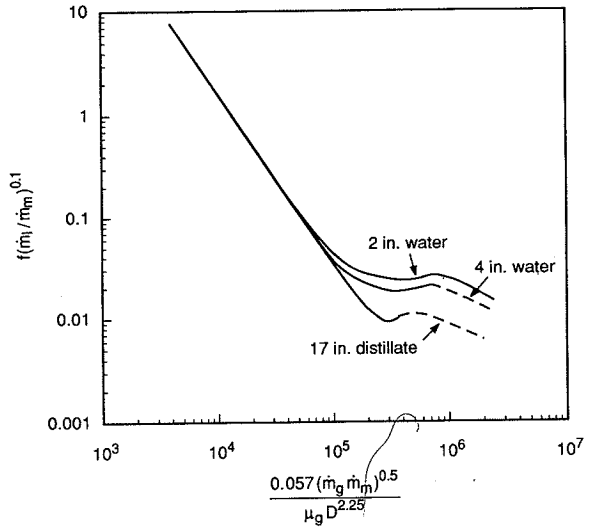

Figure 10-6
Eaton friction factor correlation. (*From Eaton et al., 1966.*)

EXAMPLE 10-5

Pressure gradient calculation using the Eaton correlation

For the same conditions as Examples 10-3 and 10-4, calculate the pressure gradient using the Eaton correlation. Neglect the kinetic energy pressure drop, but determine the liquid holdup.

Solution First, we compute the mass flow rates of gas, liquid, and the combined stream:

$$\dot{m}_l = q_l \rho_l = (0.130 \text{ ft}^3/\text{sec})(49.92 \text{ lb}_m/\text{ft}^3) = 6.5 \text{ lb}_m/\text{sec} \tag{10-33}$$

$$\dot{m}_g = q_g \rho_g = (0.242 \text{ ft}^3/\text{sec})(2.6 \text{ lb}_m/\text{ft}^3) = 0.63 \text{ lb}_m/\text{sec} \tag{10-34}$$

$$\dot{m}_m = \dot{m}_l + \dot{m}_g = 6.5 + 0.63 = 7.13 \text{ lb}_m/\text{sec} \tag{10-35}$$

The gas viscosity is

$$\mu_g = (0.0131 \text{ cp})(6.72 \times 10^{-4} \text{ lb}_m/\text{ft-sec-cp}) = 8.8 \times 10^{-6} \text{ lb}_m/\text{ft-sec} \tag{10-36}$$

To find f with Fig. 10-6, we calculate

$$\frac{(0.057)(\dot{m}_g \dot{m}_m)^{0.5}}{\mu_g D^{2.25}} = \frac{(0.057)[(0.63)(7.13)]^{0.5}}{(8.8 \times 10^{-6})(2.5/12)^{2.25}} = 4.7 \times 10^5 \tag{10-37}$$

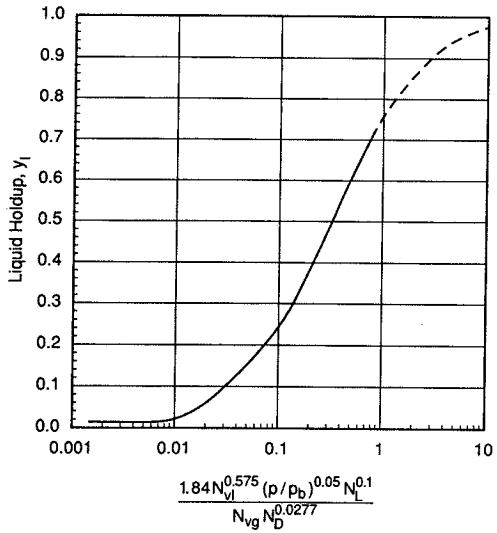

Figure 10-7
Eaton holdup correlation. (*From Eaton et al., 1966.*)

and reading from the correlation line for water in a 2-in. pipe (we choose this line because the pipe is closest to this size),

$$f\left(\frac{\dot{m}_l}{\dot{m}_m}\right)^{0.1} = 0.01 \tag{10-38}$$

so

$$f = \frac{0.01}{(6.5/7.13)^{0.1}} = 0.021 \tag{10-39}$$

Neglecting the kinetic energy term, the pressure gradient is given by Eq. (10-32),

$$\left(\frac{dp}{dx}\right)_F = \frac{(0.021)(19.16)(10.92)^2}{(2)(32.17)(2.5/12)} = 3.57 \text{ lb}_f/\text{ft}^3 = 0.025 \text{ psi/ft} \tag{10-40}$$

The liquid holdup is obtained from the correlation given by Fig. 10-7. The dimensionless numbers needed are given by Eqs. (7-99) through (7-102).

$$N_{vl} = (1.938)(3.81)\sqrt[4]{\frac{49.92}{30}} = 8.39 \tag{10-41}$$

$$N_{vg} = (1.98)(7.11)\sqrt[4]{\frac{49.92}{30}} = 15.65 \tag{10-42}$$

$$N_D = (120.872)\left(\frac{2.5}{12}\right)\sqrt{\frac{49.92}{30}} = 32.48 \tag{10-43}$$

$$N_L = (0.15726)(2)\sqrt[4]{\frac{1}{(49.92)(30)^3}} = 0.00923 \tag{10-44}$$

Calculating the abscissa value, we have

$$\frac{(1.84)N_{vl}^{0.575}(p/p_b)^{0.05}N_L^{0.1}}{N_{vg}N_D^{0.0277}} = \frac{(1.84)(8.39)^{0.575}(800/14.65)^{0.05}(0.00923)^{0.1}}{(15.65)(32.48)^{0.0277}} \tag{10-45}$$

$$= 0.277$$

and from Fig. 10-7, $y_l = 0.45$.

The liquid holdup predictions from the Beggs and Brill and Eaton correlations agree very closely; the Eaton correlation predicts a lower pressure gradient. ◇

Dukler correlation. The Dukler correlation (Dukler, 1969), like that of Eaton, is based on empirical correlations of friction factor and liquid holdup. The pressure gradient again consists of frictional and kinetic energy contributions:

$$\frac{dp}{dx} = \left(\frac{dp}{dx}\right)_F + \left(\frac{dp}{dx}\right)_{KE} \tag{10-46}$$

The frictional pressure drop is

$$\left(\frac{dp}{dx}\right)_F = \frac{f\rho_k u_m^2}{2g_c D} \tag{10-47}$$

where

$$\rho_k = \frac{\rho_l \lambda_l^2}{y_l} + \frac{\rho_g \lambda_g^2}{y_g} \tag{10-48}$$

Notice that the liquid holdup enters the frictional pressure drop through ρ_k. The friction factor is obtained from the no-slip friction factor, f_n, defined as

$$f_n = 0.0056 + 0.5(N_{\text{Re}_k})^{-0.32} \tag{10-49}$$

where the Reynolds number is

$$N_{\text{Re}_k} = \frac{\rho_k u_m D}{\mu_m} \tag{10-50}$$

The two-phase friction factor is given by the correlation

$$\frac{f}{f_n} = 1 - \frac{\ln \lambda_l}{1.281 + 0.478 \ln \lambda_l + 0.444(\ln \lambda_l)^2 + 0.094(\ln \lambda_l)^3 + 0.00843(\ln \lambda_l)^4} \tag{10-51}$$

The liquid holdup is given as a function of the input liquid fraction, λ_l, in Fig. 10-8, with N_{Re_k} as a parameter. Since the holdup is needed to calculate N_{Re_k} (ρ_k depends on y_l), determining the liquid holdup is an iterative procedure. We can begin by assuming that $y_l = \lambda_l$; an estimate of ρ_k and N_{Re_k} is then calculated. With these estimates, y_l is obtained from Fig. 10-8. We then compute new estimates of ρ_k and N_{Re_k}, repeating this procedure until convergence is achieved.

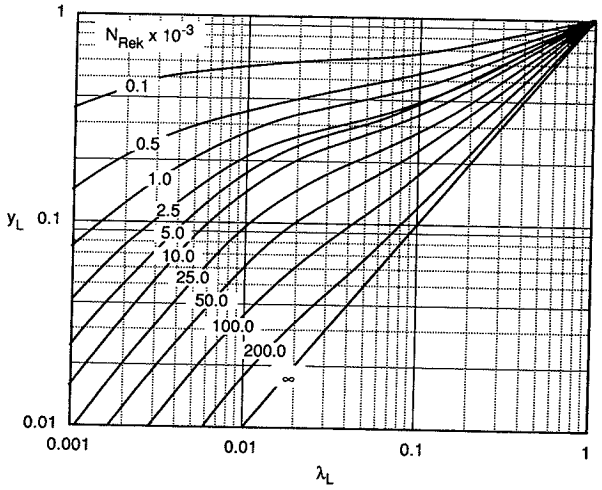

Figure 10-8
Dukler holdup correlation. (*From Dukler, 1969.*)

The pressure gradient due to kinetic energy changes is given by

$$\left(\frac{dp}{dx}\right)_{\mathrm{KE}} = \frac{1}{g_c\,\Delta x}\Delta\left(\frac{\rho_g u_{sg}^2}{y_g} + \frac{\rho_l u_{sl}^2}{y_l}\right) \tag{10-52}$$

EXAMPLE 10-6
Pressure gradient calculation using the Dukler correlation

Repeat Examples 10-4 and 10-5, using the Dukler correlation.

Solution An iterative procedure is required to find the liquid holdup. We begin by assuming that $y_l = \lambda_l$. In this case, $\rho_k = \rho_m$, found previously to be 19.16 $\mathrm{lb}_m/\mathrm{ft}^3$, and $N_{\mathrm{Re}_k} = N_{\mathrm{Re}_m}$, which was 91,600. From Fig. 10-8, we estimate y_l to be 0.44. Using this new value of liquid holdup,

$$\rho_k = \frac{(49.92)(0.35)^2}{0.44} + \frac{(2.6)(0.65)^2}{(1-0.44)} = 15.86\ \mathrm{lb}_m/\mathrm{ft}^3 \tag{10-53}$$

and

$$N_{\mathrm{Re}_k} = (91,600)\left(\frac{15.86}{19.16}\right) = 75,800 \tag{10-54}$$

Again reading y_l from Fig. 10-8, $y_l = 0.46$. This is the converged value.

The no-slip friction factor from Eq. (10-49) is

$$f_n = 0.0056 + (0.5)(75{,}800)^{-0.32} = 0.019 \tag{10-55}$$

From Eq. (10-51), we find

$$\frac{f}{f_n} = 1 - \frac{\ln(0.35)}{1.281 + 0.478[\ln(0.35)] + 0.444[\ln(0.35)]^2 + 0.094[\ln(0.35)]^3 + 0.00843[\ln(0.35)]^4}$$

$$= 1.90 \tag{10-56}$$

so

$$f = (1.90)(0.019) = 0.036 \tag{10-57}$$

Finally, from Eq. (10-47), we find the frictional pressure gradient to be

$$\left(\frac{dp}{dx}\right)_F = \frac{(0.036)(15.86)(10.92)^2}{(2)(32.17)(2.5/12)} = 5.08\ \mathrm{lb}_f/\mathrm{ft}^3 = 0.035\ \mathrm{psi/ft} \tag{10-58}$$

We see that all three correlations predict essentially the same liquid holdup, but the pressure gradient predictions differ. ◇

Pressure traverse calculations. The correlations we have just examined provide a means of calculating the pressure gradient at a point along a pipeline; to determine the overall pressure drop over a finite length of pipe, the variation of the pressure gradient as the fluid properties change in response to the changing pressure must be considered. The simplest procedure is to evaluate fluid properties at the mean pressure over the distance of interest and then calculate a mean pressure gradient. For example, integrating the Dukler correlation over a distance L of pipe, we have

$$\Delta_P = \frac{\overline{f}\rho_k \bar{u}_m^2 L}{2g_c D} + \frac{1}{g_c}\Delta\left(\frac{\rho_g u_{sg}^2}{y_g} + \frac{\rho_l u_{sl}^2}{y_l}\right) \tag{10-59}$$

The overbars indicate that f, ρ_k, and u_m are evaluated at the mean pressure, $(p_1 + p_2)/2$. In the kinetic energy term, the Δ means the difference between conditions at point 1 and point 2. If the overall pressure drop, $p_1 - p_2$, is known, the pipe length, L, can be calculated directly with this equation. When L is fixed, Δp must be estimated to calculate the mean pressure; using this mean pressure, Δp is calculated with Eq. (10-59), and, if necessary, the procedure is repeated until convergence is reached.

Since the overall pressure drop over the distance L is being calculated based on the mean properties over this distance, the pressure should not change too much over this

distance. In general, if the Δp over the distance L is greater than 10% of p_1, the distance L should be divided into smaller increments and the pressure drop over each increment calculated. The pressure drop over the distance L is then the sum of the pressure drops over the smaller increments.

EXAMPLE 10-7
Calculating the overall pressure drop

Just downstream from the wellhead choke, 2000 bbl/d of oil and 1 MM SCF/d of gas enters a 2.5-in. pipeline at 800 psia and 175°F (the same fluids as in the previous four examples). If these fluids are transported 3000 ft through this flow line to a separator, what is the discharge pressure at the separator? Use the Dukler correlation and neglect kinetic energy pressure losses.

Solution We found in Example 10-6 that the pressure gradient at the entrance conditions is 0.035 psi/ft. If this value holds over the entire line, the overall pressure drop would be (0.035)(3000) = 105 psi. Since this pressure drop is slightly greater than 10% of the entrance condition, we will divide the pipe into two length increments and calculate a mean pressure gradient over each increment.

It is most convenient to fix the Δp for the first increment and solve for the length of the increment. The remainder of the pipeline will then comprise the second section. We will choose a Δp of 60 psi for the first increment, L_1. Thus, for this section, $\bar{p} = 800 - 60/2 = 770$ psi. We previously calculated the properties of the fluids at 800 psi; the only property that may differ significantly at 770 psi is the gas density.

Following Example 4-3 for this gas, at 770 psi and 175°F, $p_{pr} = 1.07$ and $T_{pr} = 1.70$. From Fig. 4-1, $Z = 0.935$, and using Eq. (7-67),

$$\bar{\rho}_g = \frac{(28.97)(0.709)(770)}{(0.935)(10.73)(635)} = 2.5 \text{ lb}_m/\text{ft}^3 \tag{10-60}$$

The gas volumetric flow rate is then

$$\bar{q}_g = \frac{\dot{m}_g}{\bar{\rho}_g} = \frac{0.63 \text{ lb}_m/\text{sec}}{2.5 \text{ lb}_m/\text{ft}^3} = 0.252 \text{ ft}^3/\text{sec} \tag{10-61}$$

Since the liquid density is essentially the same at 770 psi as at the entrance condition, q_l is 0.13 ft^3/sec, as before, and the total volumetric flow rate is 0.252 + 0.13 = 0.382 ft^3/sec.

The input liquid fraction is 0.13/0.382 = 0.34, and the mixture velocity ($\bar{u}_m$) is found to be 11.2 ft/sec by dividing the total volumetric flow rate by the pipe cross-sectional area.

We can now use the Dukler correlation to calculate the pressure gradient at the mean pressure. We begin by estimating the liquid holdup at mean conditions to be the same as that found at the entrance, or $y_l = 0.46$. Then

$$\rho_k = \frac{(49.92 \text{ lb}_m/\text{ft}^3)(0.34)^2}{0.46} + \frac{(2.5 \text{ lb}_m/\text{ft}^3)(0.66)^2}{0.56} = 14.56 \text{ lb}_m/\text{ft}^3 \tag{10-62}$$

and

$$\mu_m = (2 \text{ cp})(0.34) + (0.0131 \text{ cp})(0.66) = 0.689 \text{ cp} \tag{10-63}$$

so,

$$N_{\text{Re}_k} = \frac{(14.56)(11.2)(2.5/12)}{(0.689)(6.72 \times 10^{-4})} = 73{,}400 \tag{10-64}$$

Checking Fig. 10-8, we find that $y_l = 0.46$, so no iteration is required. Using Eqs. (10-49) and (10-51), $f_n = 0.019$ and $f/f_n = 1.92$, so $f = 0.036$. From Eq. (10-47), we find that dp/dx is 0.034 psi/ft. The length of the first increment is

$$L_1 = \frac{\Delta p}{dp/dx} = \frac{60 \text{ psi}}{0.034 \text{ psi/ft}} = 1760 \text{ ft} \tag{10-65}$$

The remaining section of the pipeline is 3000 − 1760 = 1240 ft long. If the pressure gradient over this section is also 0.034 psi/ft, the pressure drop will be 42 psi; thus we can estimate the mean pressure over the second increment to be $740 - 42/2 \approx 720$ psi.

With this mean pressure, we repeat the procedure to calculate the mean pressure gradient using the Dukler correlation and find that $dp/dx = 0.036$ psi/ft, giving an overall pressure drop for the second segment of 45 psi. Adding the two pressure drops, the pressure drop over the 3000-ft pipe is 105 psi. This happens to be exactly what we estimated using the pressure gradient at the pipe entrance conditions, illustrating that the pressure gradient is not varying significantly at these relatively high pressures. ◇

10-2.4 Pressure Drop through Pipe Fittings

When fluids pass through pipe fittings (tees, elbows, etc.) or valves, secondary flows and additional turbulence create pressure drops that must be included to determine the overall pressure drop in a piping network. The effects of valves and fittings are included by adding the "equivalent length" of the valves and fittings to the actual length of straight pipe when calculating the pressure drop. The equivalent lengths of many standard valves and fittings have been determined experimentally (Crane, 1957) and are given in Table 10-1. The equivalent lengths are given in pipe diameters; this value is multiplied by the pipe diameter to find the actual length of pipe to be added to account for the pressure drop through the valve or fitting.

10-3 Flow through Chokes

The flow rate from almost all flowing wells is controlled with a wellhead choke, a device that places a restriction in the flow line (Fig. 10-9.) A variety of factors may make it desirable to restrict the production rate from a flowing well, including the prevention of coning or sand production, satisfying production rate limits set by regulatory authorities, and meeting limitations of rate or pressure imposed by surface equipment.

When gas or gas-liquid mixtures flow through a choke, the fluid may be accelerated sufficiently to reach sonic velocity in the throat of the choke. When this condition occurs, the flow is called "critical," and changes in the pressure downstream of the choke do not affect the flow rate, because pressure disturbances cannot travel upstream faster than the sonic velocity. (Note: Critical flow is not related to the critical point of the fluid.) Thus, to predict the flow rate-pressure drop relationship for compressible fluids flowing through a choke, we must determine whether or not the flow is critical. Figure 10-10 shows the dependence of flow rate through a choke on the ratio of the downstream to upstream pressure for a compressible fluid, with the rate being independent of the pressure ratio when the flow is critical.

Table 10-1

Equivalent Lengths of Valves and Fittings[a]

		Description of Fitting		Equivalent Length in Pipe Diameters
Globe valves	Stem perpendicular to run	With no obstruction in flat, bevel, or plug type seat	Fully open	340
		With wing or pin guided disk	Fully open	450
	Y-pattern	(No obstruction in flat, bevel, or plug type seat) —With stem 60° from run of pipe line	Fully open	175
		—With step 45° from run of pipe line	Fully open	145
Angle valves		With no obstruction in flat, bevel, or plug type seat	Fully open	145
		With wing or pin-guided disk	Fully open	200
Gate valves	Wedge, disk		Fully open	13
	Double disk or plug disk		Three-quarters open	35
			One-half open	160
			One-quarter open	900
	Pulp stock		Fully open	17
			Three-quarters open	50
			One-half open	260
			One-quarter open	1200
Conduit pipe line gate, ball, and plug valves			Fully open	3
Check valves	Conventional swing		Fully open	135
	Clearway swing		Fully open	50
	Globe life or stop; stem perpendicular to run or Y-pattern		Fully open	Same as globe
	Angle lift or stop			Fully open
	Same as angle			
	In-line ball		Fully open	150

Table 10-1 (Continued)

Equivalent Lengths of Valves and Fittings[a]

		Description of Fitting		Equivalent Length in Pipe Diameters
Foot valves with strainer		With poppet lift-type disk	Fully open	420
		With leather-hinged disk	Fully open	75
Butterfly valves (8 in. and larger)			Fully open	40
Cocks	Straight-through	Rectangular plug port area equal to 100% of pipe area	Fully open	18
	Three-way	Rectangular plug port area equal to 80% of pipe area (fully open)	Flow straight through	44
			Flow through branch	140
Fittings	90° standard elbow			30
	45° standard elbow			16
	90° long radius elbow			20
	90° street elbow			50
	45° street elbow			26
	Square corner elbow			57
	Standard tee	With flow through run		20
		With flow through branch		60
	Close-pattern return bend			50

[a]From Crane (1957).

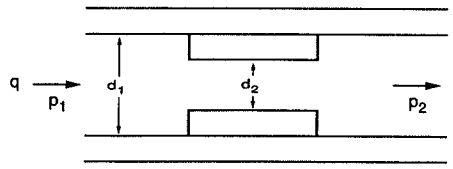

Figure 10-9
Choke schematic.

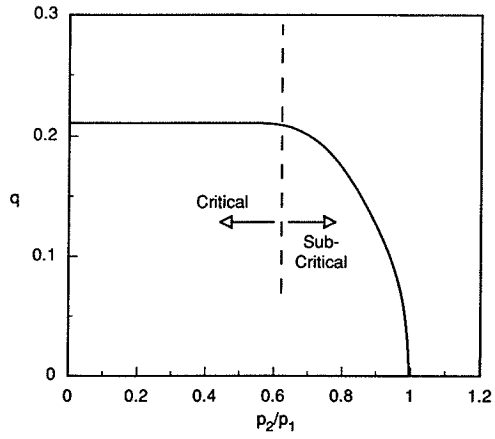

Figure 10-10
Dependence of flow rate through a choke on the ratio of the upstream to the downstream pressure.

In this section, we will examine the flow of liquid, gas, and gas-liquid mixtures through chokes.

10-3.1 Single-Phase Liquid Flow

The flow through a wellhead choke will rarely consist of single-phase liquid, since the flowing tubing pressure is almost always below the bubble point. However, when this does occur, the flow rate is related to the pressure drop across the choke by

$$q = CA\sqrt{\frac{2g_c\,\Delta p}{\rho}} \tag{10-66}$$

where C is the flow coefficient of the choke and A is the cross-sectional area of the choke. The flow coefficient for flow through nozzles is given in Fig. 10-11 (Crane, 1957) as a function of the Reynolds number in the choke and the ratio of the choke diameter to the pipe diameter. Equation (10-66) is derived by assuming that the pressure drop through the

choke is equal to the kinetic energy pressure drop divided by the square of a drag coefficient. This equation applies for subcritical flow, which will usually be the case for single-phase liquid flow.

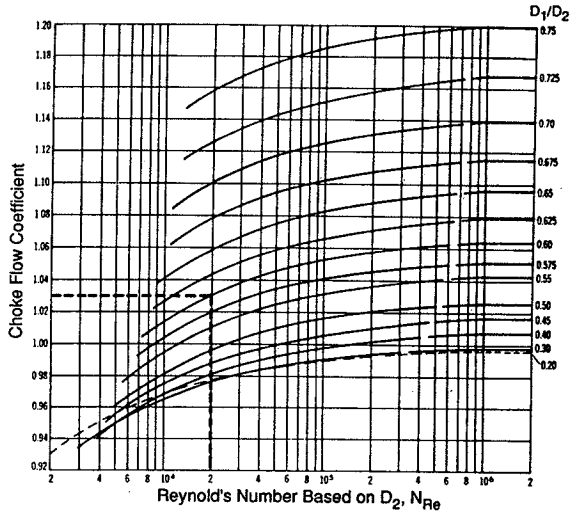

Figure 10-11
Flow coefficient for liquid flow through a choke. (*From Crane, 1957.*)

For oilfield units, Eq. (10-66) becomes

$$q = 22{,}800C(D_2)^2\sqrt{\frac{\Delta p}{\rho}} \tag{10-67}$$

where q is in bbl/d, D_2 is the choke diameter in in., Δp is in psi, and ρ is in lb_m/ft^3. The choke diameter is often referred to as the "bean size," because the device in the choke that restricts the flow is called the bean. Bean sizes are usually given in 64ths of an inch.

EXAMPLE 10-8
Liquid flow through a choke

What will be the flow rate of a 0.8-specific gravity, 2-cp oil through a 20/64-in. choke if the pressure drop across the choke is 20 psi and the line size in 1 in.?

Solution Figure 10-11 gives the flow coefficient as a function of the diameter ratio and the Reynolds number through the choke. Since we do not know the Reynolds number until we know the flow rate, we assume that the Reynolds number is high enough that the flow coefficient is independent of Reynolds number. For $D_2/D_1 = 0.31$, C is approximately 1.00. Then, from

Eq. (10-67),

$$q = (22{,}800)(1.00)\left(\frac{20}{64}\right)^2\sqrt{\frac{20}{49.92}} = 1410 \text{ bbl/d} \tag{10-68}$$

Checking the Reynolds number through the choke [Eq. (7-7)], we find $N_{Re} = 1.67 \times 10^5$. From Fig. 10-11, $C = 0.99$ for this N_{Re}; using this value, the flow rate is 1400 bbl/d. ◇

10-3.2 Single-Phase Gas Flow

When a compressible fluid passes through a restriction, the expansion of the fluid is an important factor. For isentropic flow of an ideal gas through a choke, the rate is related to the pressure ratio, p_2/p_1, by (Szilas, 1975)

$$q_g = \frac{\pi}{4}D_2^2 p_1 \frac{T_{sc}}{p_{sc}}\alpha\sqrt{\left(\frac{2g_c R}{28.97\gamma_g T_1}\right)\left(\frac{\gamma}{\gamma-1}\right)\left[\left(\frac{p_2}{p_1}\right)^{2/\gamma} - \left(\frac{p_2}{p_1}\right)^{(\gamma+1)/\gamma}\right]} \tag{10-69}$$

which can be expressed in oilfield units as

$$q_g = 3.505 D_{64}^2\left(\frac{p_1}{p_{sc}}\right)\alpha\sqrt{\left(\frac{1}{\gamma_g T_1}\right)\left(\frac{\gamma}{\gamma-1}\right)\left[\left(\frac{p_2}{p_1}\right)^{2/\gamma} - \left(\frac{p_2}{p_1}\right)^{(\gamma+1)/\gamma}\right]} \tag{10-70}$$

where q_g is in MSCF/d, D_{64} is the choke diameter (bean size) in 64ths of inches (e.g., for a choke diameter of 1/4 in., $D_2 = 16/64$ in. and $D_{64} = 16$), T_1 is the temperature upstream of the choke in °R, γ is the heat capacity ratio, C_p/C_v, α is the flow coefficient of the choke, γ_g is the gas gravity, p_{sc} is standard pressure, and p_1 and p_2 are the pressures upstream and downstream of the choke, respectively.

Equations (10-69) and (10-70) apply when the pressure ratio is equal to or greater than the critical pressure ratio, given by

$$\left(\frac{p_2}{p_1}\right)_c = \left(\frac{2}{\gamma+1}\right)^{\gamma/(\gamma-1)} \tag{10-71}$$

When the pressure ratio is less than the critical pressure ratio, p_2/p_1 should be set to $(p_2/p_1)c$ and Eq. (10-70) used, since the flow rate is insensitive to the downstream pressure whenever the flow is critical. For air and other diatomic gases, γ is approximately 1.4, and the critical pressure ratio is 0.53; in petroleum engineering operations, it is commonly assumed that flow through a choke is critical whenever the downstream pressure is less than about half of the upstream pressure.

EXAMPLE 10-9

The effect of choke size on gas flow rate

Construct a chart of gas flow rate versus pressure ratio for choke diameters (bean sizes) of 8/64, 12/64, 16/24, 20/64, and 24/64 of an inch. Assume that the choke flow coefficient is 0.85, the gas gravity is 0.7, γ is 1.25, and the wellhead temperature and flowing pressure are 100°F and 600 psia.

Solution From Eq. (10-71), we find that the critical pressure ratio is 0.56 for this gas. Using Eq. (10-70),

$$q_g = 3.505 D_{64}^2\left(\frac{600}{14.7}\right)(0.85)\sqrt{\left(\frac{1}{(0.7)(560)}\right)\left(\frac{1.25}{1.25-1}\right)\left[\left(\frac{p_2}{p_1}\right)^{2/1.25} - \left(\frac{p_2}{p_1}\right)^{(1.25+1)/1.25}\right]} \tag{10-72}$$

or

$$q_g = 13.73 D_{64}^2\sqrt{\left(\frac{p_2}{p_1}\right)^{1.6} - \left(\frac{p_2}{p_1}\right)^{1.8}} \tag{10-73}$$

The maximum gas flow rate will occur when the flow is critical, that is, when $(p_2/p_1) = 0.56$. For any value of the pressure ratio below the critical value, the flow rate will be the critical flow rate. Using values of p_2/p_1 from 0.56 to 1 for each choke size, Fig. 10-12 is constructed. ◇

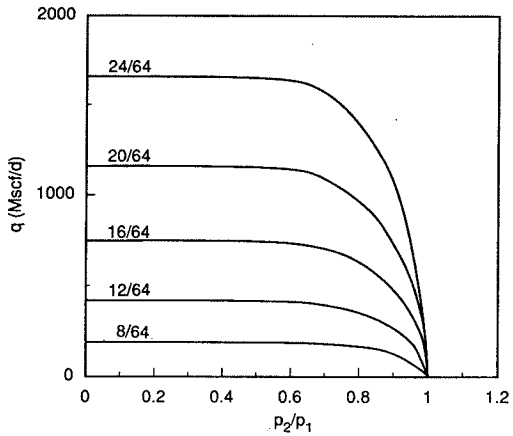

Figure 10-12
Gas flow performance for different choke sizes.

10-3.3 Gas-Liquid Flow

Two-phase flow through a choke has not been described well theoretically. To determine the flow rate of two phases through a choke, empirical correlations for critical flow are generally used. Some of these correlations are claimed to be valid up to pressure ratios of 0.7 (Gilbert, 1954). One means of estimating the conditions for critical two-phase flow through a choke is to compare the velocity in the choke with the two-phase sonic velocity, given by Wallis (1969) for homogeneous mixtures as

$$v_c = \left\{\left[\lambda_g\rho_g + \lambda_l\rho_l\right]\left[\frac{\lambda_g}{\rho_g v_{gc}^2} + \frac{\lambda_l}{\rho_l v_{lc}^2}\right]\right\}^{-1/2} \tag{10-74}$$

where v_c is the sonic velocity of the two-phase mixture and v_{gc} and v_{lc} are the sonic velocities of the gas and liquid, respectively.

The empirical correlations of Gilbert (1954) and Ros (1960) have the same form, namely,

$$p_1 = \frac{Aq_l(\text{GLR})^B}{D_{64}^C} \tag{10-75}$$

differing only in the empirical constants A, B, and C, given in Table 10-2. The upstream pressure, p_1, is in psig in the Gilbert correlation and psia in Ros's correlation. In these correlations, q_l is the liquid rate in bbl/d, GLR is the producing gas–liquid ratio in SCF/bbl, and D_{64} is the choke diameter in 64ths of an inch.

Table 10-2

Empirical Constants in Two-Phase Critical Flow Correlations

Correlation	A	B	C
Gilbert	10.00	0.546	1.89
Ros	17.40	0.500	2.00

Another empirical correlation that may be preferable for certain ranges of conditions is that of Omana et al. (1969). Based on dimensional analysis and a series of tests with natural gas and water, the correlation is

$$N_{ql} = 0.263 N_\rho^{-3.49} N_{pl}^{3.19} \lambda_l^{0.657} N_D^{1.80} \tag{10-76}$$

with dimensionless groups defined as

$$N_\rho = \frac{\rho_g}{\rho_l} \tag{10-77}$$

$$N_{p1} = 1.74 \times 10^{-2} p_1 \left(\frac{1}{\rho_l \sigma_l}\right)^{0.5} \tag{10-78}$$

$$N_D = 0.1574 D_{64} \sqrt{\frac{\rho_l}{\sigma_l}} \tag{10-79}$$

$$N_{ql} = 1.84 q_l \left(\frac{\rho_l}{\sigma_l}\right)^{1.25} \tag{10-80}$$

For the constants given, the oilfield units are q, bbl/d; ρ, lb_m/ft^3; σ_l, dynes/cm; D_{64}, 64ths of an inch; and p_1, psia. The Omana correlation is restricted to critical flow, requiring that $q_g/q_l > 1.0$ and $p_2/p_1 < 0.546$. It is best suited to low-viscosity liquids (near the viscosity of water) and choke diameters (bean sizes) of 14/64 in. or less. The fluid properties are evaluated at the upstream conditions.

EXAMPLE 10-10

Finding the choke size for gas-liquid flow

For the flow of 2000 bbl/d of oil and 1 MMSCF/d of gas at a flowing tubing pressure of 800 psia as described in Example 10-3, find the choke diameter (bean size) using the Gilbert, Ros, and Omana correlations.

Solution For the Gilbert and Ros correlations, solving Eq. (10-75) for the choke diameter, we have

$$D_{64} = \left(\frac{Aq_l(\text{GLR})^B}{p_1}\right)^{1/C} \tag{10-81}$$

For the given flow rate of 2000 bbl/d, a GLR of 500 SCF/bbl, and an absolute pressure of 800 psi upstream of the choke, from the Gilbert correlation,

$$D_{64} = \left(\frac{(10)(2000)(500)^{0.546}}{800 - 14.7}\right)^{1/1.89} = 33 \text{ 64ths of an inch} \tag{10-82}$$

and, from the Ros correlation,

$$D_{64} = \left(\frac{(17.4)(2000)(500)^{0.5}}{800}\right)^{0.5} = 31 \text{ 64ths of an inch} \tag{10-83}$$

With the Omana correlation, we solve Eq. (10-76) for N_D:

$$N_D = \left(\frac{1}{0.263} N_{ql} N_\rho^{3.49} N_{p1}^{-3.19} \lambda_l^{-0.657}\right)^{1/1.8} \tag{10-84}$$

From Example 10-3, $\lambda_l = 0.35$, $\rho_l = 49.92$ lb_m/ft^3, $\rho_g = 2.6$ lb_m/ft^3, and $\sigma_l = 30$ dynes/cm. From Eqs. (10-77), (10-78), and (10-80),

$$N_\rho = \frac{2.6}{49.92} = 0.0521 \tag{10-85}$$

$$N_{p1} = (1.74 \times 10^{-2})(800)\left[\frac{1}{(49.92)(30)}\right]^{0.5} = 0.36 \tag{10-86}$$

$$N_{ql} = (1.84)(2000)\left(\frac{49.92}{30}\right)^{1.25} = 6.95 \times 10^3 \tag{10-87}$$

Then

$$N_D = \left[\left(\frac{1}{0.263}\right)(6.95 \times 10^3)(0.0521)^{3.49}(0.36)^{-3.19}(0.35)^{-0.657}\right]^{1/1.8} = 8.35 \tag{10-88}$$

Solving Eq. (10-79) for the choke diameter, we have

$$D_{64} = \frac{N_D}{(0.1574)\sqrt{\frac{\rho_l}{\sigma_l}}} \tag{10-89}$$

so

$$D_{64} = \frac{8.35}{(0.1574)\sqrt{49.92/30}} = 41 \text{ 64ths of an inch} \qquad (10\text{-}90)$$

The Gilbert and Ros correlations predict a choke size of about 1/2 in. (32/64 in.), while the Omana correlation predicts a larger choke size of 41/64 in. Since the Omana correlation was based on liquid flow rates of 800 bbl/d or less, the Gilbert and Ros correlations are probably the more accurate in this case. ◇

When a well is being produced with critical flow through a choke, the relationship between the wellhead pressure and the flow rate is controlled by the choke, since downstream pressure disturbances (such as a change in separator pressure) do not affect the flow performance through the choke. Thus, the attainable flow rate from a well for a given choke can be determined by matching the choke performance with the well performance, as determined by a combination of the well IPR and the vertical lift performance. The choke performance curve is a plot of the flowing tubing pressure versus the liquid flow rate, and can be obtained from the two-phase choke correlations, assuming that the flow is critical.

EXAMPLE 10-11
Choke performance curves

Construct performance curves for 16/64-, 24/64-, and 32/64-in. chokes for a well with a GLR of 500, using the Gilbert correlation.

Solution The Gilbert correlation predicts that the flowing tubing pressure is a linear function of the liquid flow rate, with an intercept at the origin. Using Eq. (10-75), we find

$$p_{tf} = 1.57 q_l \quad \text{for 16/64-in. choke} \qquad (10\text{-}91)$$

$$p_{tf} = 0.73 q_l \quad \text{for 24/64-in. choke} \qquad (10\text{-}92)$$

$$p_{tf} = 0.43 q_l \quad \text{for 32/64-in. choke} \qquad (10\text{-}93)$$

These relationships are plotted in Fig. 10-13, along with a well performance curve. The intersections of the choke performance curves with the well performance curve are the flow rates that would occur with these choke sizes. Note that the choke correlation is valid only when the flow through the choke is critical; for each choke, there will be a flow rate below which flow through the choke is subcritical. This region is indicated by the dashed portions of the choke performance curves—the predictions are not valid for these conditions. ◇

10-4 SURFACE GATHERING SYSTEMS

In most oil and gas production installations, the flow from several wells will be gathered at a central processing station or combined into a common pipeline. Two common types of gathering systems were illustrated by Szilas (1975) (Fig. 10-14). When the individual well flow rates are controlled by critical flow through a choke, there is little interaction among the wells. However, when flow is subcritical, the downstream pressure can influence the performance of the wells, and the flow through the entire piping network may have to be treated as a system.

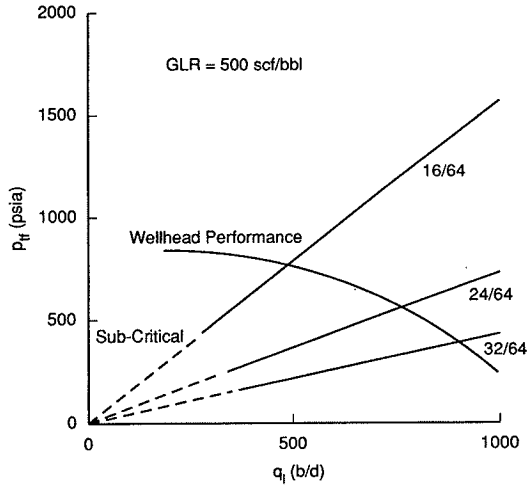

Figure 10-13
Choke performance curves (Example 10-11).

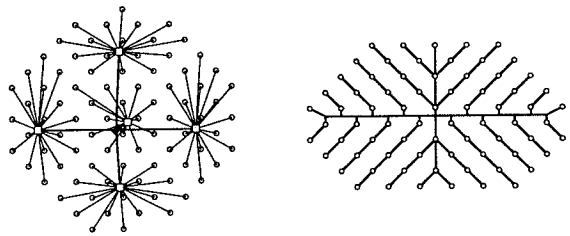

Figure 10-14
Oil and gas production gathering systems. (*From Szilas, 1975.*)

When individual flow lines all join at a common point (Fig. 10-14, left), the pressure at the common point is equal for all flow lines. The common point is typically a separator in an oil production system. The flowing tubing pressure of an individual well i is related to the separator pressure by

$$ptfi = p_{sep} + \Delta p_{Li} + \Delta p_{Ci} + \Delta p_{fi} \qquad (10\text{-}94)$$

where Δp_{Li} is the pressure drop through the flow line, Δp_{Ci} is the pressure drop through the choke (if present), and Δp_{fi} is the pressure drop through fittings.

In a gathering system where individual wells are tied into a common pipeline, so that the pipeline flow rate is the sum of the upstream well flow rates as in Fig. 10-14, right, each

well has a more direct effect on its neighbors. In this type of system, individual wellhead pressures can be calculated by starting at the separator and working upstream.

Depending on the lift mechanism of the wells, the flow rates of the individual wells may depend on the flowing tubing pressures. In this case, the IPRs and vertical lift performance characteristics of the wells and surface gathering system must all be considered together to predict the performance of the well network. This will be treated in Chapter 21.

EXAMPLE 10-12

Analysis of a surface gathering system

The liquid production from three rod-pumped wells is gathered in a common 2-in. line, as shown in Fig. 10-15. One-inch flow lines connect each well to the gathering line, and each well line contains a ball valve and a conventional swing check valve. Well 1 is tied into the gathering line with a standard 90° elbow, while wells 2 and 3 are connected with standard tees. The oil density is 0.85 g/cm^3 (53.04 lb$_m$/ft^3), and its viscosity is 5 cp. The separator pressure is 100 psig. Assuming the relative roughness of all lines to be 0.001, calculate the flowing tubing pressures of the three wells.

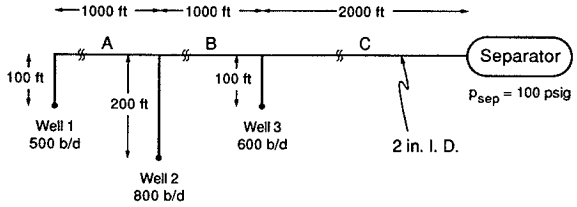

Figure 10-15
Surface gathering system (Example 10-12).

Solution Since the flow rates are all known (and are assumed independent of the wellhead pressures for these rod-pumped wells), the pressure drop for each pipe segment can be calculated independently using Eq. (10-1). The friction factors are obtained from the Chen equation [Eq. (7-35)] or the Moody diagram (Fig. 7-7). The pressure drops through the fittings and valves in the well flow lines are considered by adding their equivalent lengths from Table 10-1 to the well flow line lengths. For example, for well flow line 2, the ball valve adds 3 pipe diameters, the check valve 135 pipe diameters, and the tee (with flow through a branch) 60 pipe diameters. The equivalent length of flow line 2 is then (3 + 135 + 60)(1/12 ft) + 200 ft = 216.5 ft. A summary of the calculated results are given in Table 10-3.

The pressure at each point in the pipe network is obtained by starting with the known separator pressure and adding the appropriate pressure drops. The resulting system pressures are shown in Fig. 10-16. The differences in the flowing tubing pressures in these wells would result in different fluid levels in the annuli, if the IPRs and elevations are the same in all three wells. ◇

Table 10-3

Pressure Drop Calculation Results

Gathering Line

Segment	q (bbl/d)	N_{Re}	f	u (ft/sec)	Δp (psi)
A	500	3,930	0.0103	1.49	3
B	1,300	10,200	0.0081	3.88	17
C	1,900	14,900	0.0077	5.66	68

Well Flow Lines

Well No.	N_{Re}	f	u (ft/sec)	$(L/D)_{fittings}$	L (ft)	Δp (psi)
1	7,850	0.0086	5.96	168	114	10
2	12,600	0.0077	9.54	198	216.5	42
3	9,420	0.0082	7.16	198	116.5	13

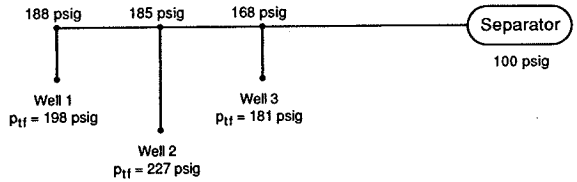

Figure 10-16
Pressure distribution in gathering system (Example 10-12).

REFERENCES

1. Baker, O., "Design of Pipelines for the Simultaneous Flow of Oil and Gas," *Oil and Gas J.*, **53**: 185, 1953.
2. Beggs, H. D., and Brill, J. P., "A Study of Two-Phase Flow in Inclined Pipes," *JPT*, 607–617, May 1973.
3. Brill, J. P., and Beggs, H. D., *Two-Phase Flow in Pipes*, University of Tulsa, Tulsa, OK, 1978.
4. Crane Co., "Flow of Fluids through Valves, Fittings, and Pipe," Technical Paper No. 410, Chicago, 1957.
5. Dukler, A. E., "Gas-Liquid Flow in Pipelines," American Gas Association, American Petroleum Institute, Vol. 1, *Research Results*, May 1969.
6. Eaton, B. A., Andrews, D. E., Knowles, C. E., and Silberberg, I. H., and Brown, K. E., "The Prediction of Flow Patterns, Liquid Holdup, and Pressure Losses Occurring during Continuous Two-Phase Flow in Horizontal Pipelines, *Trans. AIME*, **240**: 815–828, 1967.
7. Gilbert, W. E., "Flowing and Gas-Lift Well Performance," *API Drilling and Production Practice*, p. 143, 1954.
8. Mandhane, J. M., Gregory, G. A., and Aziz, K., "A Flow Pattern Map for Gas-Liquid Flow in Horizontal Pipes," *Int. J. Multiphase Flow*, **1**: 537–553, 1974.

9. Omana, R., Houssiere, C., Jr., Brown, K. E., Brill, J. P., and Thompson, R. E., "Multiphase Flow through Chokes", SPE Paper 2682, 1969.
10. Ros, N. C. J., "An Analysis of Critical Simultaneous Gas/Liquid Flow through a Restriction and Its Application to Flowmetering," *Appl. Sci. Res.*, **9**, Sec. A, p. 374, 1960.
11. Scott, D. S., "Properties of Cocurrent Gas-Liquid Flow," *Advances in Chemical Engineering, Volume 4*, Drew, T. B., Hoopes, J. W., Jr., and Vermeulen, T., eds., Academic Press, New York, pp. 200–278, 1963.
12. Szilas, A. P., *Production and Transport of Oil and Gas*, Elsevier, Amsterdam, 1975.
13. Taitel, Y., and Dukler, A. E., "A Model for Predicting Flow Regime Transitions in Horizontal and Near Horizontal Gas-Liquid Flow," *AICHE J.*, **22** (1): 47–55, January 1976.
14. Wallis, G. B., *One Dimensional Two-Phase Flow*, McGraw-Hill, New York, 1969.

PROBLEMS

10-1. Suppose that 3000 bbl/d of injection water is supplied to a well by a central pumping station located 2000 ft away, where the pressure is 400 psig. The water has a specific gravity of 1.02 and a viscosity of 1 cp. Determine the smallest diameter flow line (within the nearest 1/2 in.) that can be used to maintain a wellhead pressure of at least 300 psig if the pipe relative roughness is 0.001.

10-2. Suppose that 2 MMSCF/d of natural gas with specific gravity of 0.7 is connected to a pipeline with 4000 ft of 2-in. flow line. The pipeline pressure is 200 psig and the gas temperature is 150°F. Calculate the wellhead pressure assuming: (a) smooth pipe; (b) $\epsilon = 0.001$.

10-3. A 20/64-in. choke ($\alpha = 0.9$) is added to the flowline of Problem 10-2. Repeat the calculations of wellhead pressure.

10-4. Using the Baker, Mandhane, and Beggs and Brill flow regime maps, find the flow regime for the flow of 500 bbl/d oil and 1000 SCF/bbl of associated gas in a 2-in. flow line. The oil and gas are those described in Appendix B, $\sigma_l = 20$ dynes/cm, the temperature is 120°F, and the pressure is 1000 psia.

10-5. Repeat Problem 10-4, but for a pressure of 100 psia.

10-6. Using the Beggs and Brill, Eaton, and Dukler correlations, calculate the pressure gradient for the flow of 4000 bbl/d of oil and 500 SCF/bbl of associated gas (Appendix B oil and gas) flowing in a 3-in.-I.D. line with a relative roughness of 0.001. $T = 150$°F, $p = 200$ psia, and $\sigma_l = 20$ dynes/cm. Neglect the kinetic energy pressure gradient.

10-7. Repeat Problem 10-6 for 1000 bbl/d oil, GOR = 1000, $p = 400$ psia, in a 1 1/2-in. flow line.

10-8. Repeat Problem 10-6 for 2000 bbl/d, GOR = 1000, $p = 100$ psia in a 2-in. flow line.

10-9. For the flow described in Problem 10-6, assume that the pressure given is the wellhead pressure. What is the maximum possible length of this flow line?

10-10. Construct choke performance curves for flowing tubing pressures up to 1000 psi for the well of Appendix A for choke sizes of 8/64, 12/64, and 16/64 in.

10-11. Construct choke performance curves for flowing tubing pressures up to 1000 psi for the well of Appendix B for choke sizes of 8/64, 12/64, and 16/64 in.

10-12. Construct choke performance curves for flowing tubing pressures up to 1000 psi for the gas well of Appendix C for choke sizes of 8/64, 12/64, and 16/64 in.

10-13. The liquid production from several rod-pumped wells producing from the reservoir of Appendix A are connected to a separator with the piping network shown in Fig. 10-17. The relative roughness of all pipes is 0.001. For a separator pressure of 150 psig and assuming that the temperature is approximately 100°F throughout the system, find the wellhead pressures of the wells.

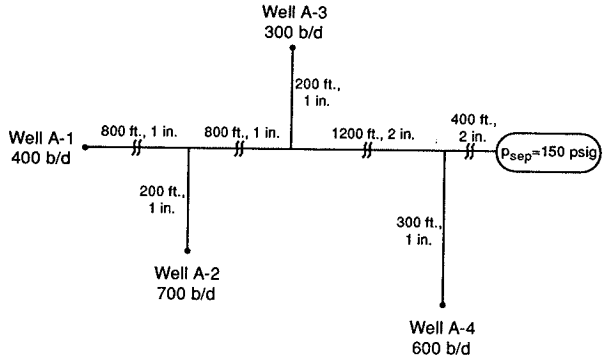

Figure 10-17
Surface gathering system (Problem 10-13).

10-14. Redesign the piping network of Problem 10-13 so that no wellhead pressure is greater than 225 psig by changing the pipe diameters of as few pipe segments as possible.

CHAPTER 11

Well Test Design and Data Acquisition

11-1 INTRODUCTION

Modern testing techniques are based on a methodology for reservoir test interpretation that can be applied to many types of tests in essentially the same way. This chapter will describe how to design a test that can accomplish specific objectives in a cost-effective manner.

In general, tests, like other measurements in a wellbore, should be justified and planned in advance. When the test interpretation can provide quantitative information about a reservoir that cannot be learned otherwise and that is essential to decision making or to forecasting production, the test can be justified provided that its costs are not prohibitive and the chances for success are high. The testing timeline in Fig. 11-1 illustrates the opportunities for various types of tests during the productive life of a vertical or horizontal well.

In wildcat, exploration, and appraisal wells, safety and logistical considerations often severely constrain the choices for test duration and hardware. This can, in turn, limit what can be learned from these tests. However, tests performed before the onset of field production have the distinct advantage that flow in the reservoir may remain single phase throughout the test duration. This is also the optimal time to obtain a reservoir fluid sample for *PVT* (pressure, volume, temperature) analysis.

In the first few wells drilled in a new formation, collecting representative samples of the reservoir fluids is of primary importance. Once the field has been in production and the reservoir pressure drops below the bubble point (below which gas evolves from solution in oil) or the dew point of a gas condensate (below which retrograde liquids evolve), it is no longer possible to acquire a fluid sample from which the hydrocarbon composition can be determined. This is because gas and liquid phases are not produced from the formation in the same proportions as they exist in a single phase above the bubble- or

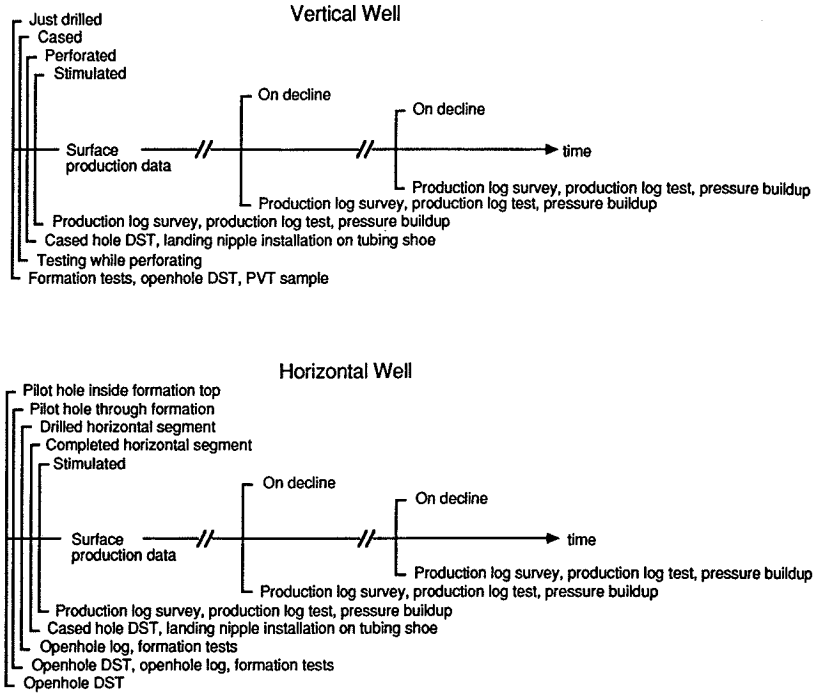

Figure 11-1
Testing timelines.

dew-point pressure. Conversely, when a representative sample of the undersaturated oil or gas is acquired, laboratory *PVT* measurements can determine the hydrocarbon composition and the composition and quantity of each phase at pressures below the original saturation (bubble-point or dew-point) pressure at reservoir temperature and under depletion conditions that resemble those occurring in the formation. The laboratory measurements also provide values for the reservoir fluid formation volume factor, viscosity, and compressibility that are required for transient test interpretation. Reservoir temperature must also be measured.

Once the reservoir is put on production and the pressure drops below the fluid bubble or dew point, the chance to interpret transient data influenced only by well and reservoir features and uncomplicated by multiphase flow is lost. However, when the formation is tested and thoroughly understood in single-phase flow, later tests can be designed to quantify multiphase-flow characteristics such as relative permeability.

In development wells, the first priority should be the inclusion of wireline formation tests as part of the open-hole logging suite. The information derived from formation-test pressure profiles is essential for understanding flow communication from well to well and in the vertical direction. These tests offer more information as successive wells are drilled over time and can be performed in every well except when unusual circumstances cause the results to be unreliable.

Well tests in development wells have the inherent cost of stalling production during the test period. Since these wells are drilled for their economic importance to production, testing strategies focus on minimizing time on the well site. Techniques of testing while perforating offer an attractive means for evaluating the completion and reservoir permeability before a stimulation treatment. The cased-hole drillstem test provides data for completion evaluation and (in long-duration tests) reservoir limits.

In wells with production tubing, installing a landing nipple at the base of the tubing at the time the well is completed can permit testing with downhole shutin thereafter and can make testing in gas-lift wells feasible. Without this provision, subsequent tests may be dominated by wellbore storage effects for prohibitively long time periods, masking near-wellbore transients in early time and prolonging the time required to evaluate reservoir permeability, sometimes so long that nearby wells interfere or outer boundary effects appear before wellbore transients die out. As discussed in Section 11-2, when the radial flow regime is not visible in the transient response, accurate quantification of wellbore damage, formation permeability, and average reservoir pressure may be impossible.

Figure 11-1 shows that after stimulation and in established wells in decline, production log surveys, production log tests, and pressure buildup tests may be conducted periodically.

Production systems with accurate, continuous monitoring of surface pressure and flow rate can provide data that will be useful for completion and reservoir evaluation over long periods of time. Using interpretation techniques analogous to those designed for continuously acquired downhole flow rate and pressure data, production data can yield quantitative information about reservoir permeability and hydraulic fracture or horizontal well characterization.

Horizontal wells are challenging for both testing and interpretation. However, the main problem with horizontal well tests is that much of the information they provide is too late if the well would not have been drilled given this information in advance. To avoid this situation, one or more tests can be conducted in the pilot hole drilled before the horizontal segment. Tests in the pilot hole should determine horizontal and vertical permeability in the formation and should verify vertical communication over the formation thickness. Open-hole log and stress measurements in the pilot hole may show evidence of horizontal permeability and/or stress anisotropy that indicates the direction in which the well should be drilled. After drilling in a developed reservoir, formation tests along the horizontal borehole can provide considerable information about lateral reservoir communication. After completion, production log and transient measurements acquired from a horizontal well can be used to quantify additional reservoir and well parameters.

This brief discussion has shown some key reasons for planning transient tests. In the sections that follow, details are provided to help ensure reliable and useful results from tests.

The main issues in designing a test are test objectives, test duration, sensor characteristics, and hardware requirements. Because all of these items are interrelated, computer programs for test design can provide considerable assistance.

11-2 WELL TEST OBJECTIVES

Two basic categories of well tests are stabilized and transient tests. Interpretation of stabilized test data yields the average reservoir pressure in the well drainage area and the well productivity or injectivity index. Data for stabilized tests are acquired when the well is flowing in a stabilized condition that results when either pressures in the well drainage area are unchanging (steady-state flow) or are changing linearly with respect to time (pseudo-steady-state flow) while the well is being flowed at a constant rate. Once the well is in a stabilized flow condition, single values for the flowing bottomhole pressure and the surface flow rate are recorded. Stabilized flow tests may acquire data for more than one stabilized rate. Data for transient tests are acquired over a range of time, starting with the instant the well flow rate is changed (usually in a stepwise manner at the surface) and continuing for a few minutes to several hours or days. Both stabilized and transient tests can be conducted on either production or injection wells.

Often production engineers are asked to evaluate well productivity, as measured by a stabilized flow test. The productivity index is given by the well flow rate, q, divided by the drop in pressure from the average reservoir pressure, $\bar{p}$, to the flowing wellbore pressure, p_{wf}. In terms of quantities that are either known or can be determined from a well test, the ideal productivity index, J_{ideal}, is defined by the following:

$$J_{\text{ideal}} = \frac{q}{(\bar{p} - p_{wf})} = \frac{kh}{\alpha_p B \mu \ln(0.472 r_e / r_w)} \tag{11-1}$$

where k is permeability, h is the formation thickness, B is the fluid formation volume factor, μ is the fluid viscosity, r_e is the drainage radius, and r_w is the wellbore radius. The units conversion factor, α_p, depends on the system of units used for analysis. Values for common units systems are provided in Table 11-4 later in this chapter.

Equation (11-1) applies in the ideal case when the skin effect for the well is negligible. When the skin effect is nonzero, the actual productivity index, J_{actual}, is

$$J_{\text{actual}} = \frac{q}{(\bar{p} - p_{wf} + \Delta p_{\text{skin}})} = \frac{kh}{\alpha_p B \mu \left[\ln(0.472 r_e / r_w) + s\right]} \tag{11-2}$$

where s is the wellbore skin factor. Although the formation thickness, fluid formation volume factor, viscosity, and the wellbore radius are usually known values, the reservoir permeability, drainage radius, and the skin factor affect the productivity, and their values are typically not known.

No single measurement of stabilized flow rate and pressure can provide values for permeability, skin factor, average pressure, or the effective drainage radius, nor can this predict at what rate the well will flow at other bottomhole flowing pressure values. If a well

is severely damaged, the productivity index is reduced. However, the productivity index is also reduced when the formation permeability is low. Acid stimulation or other workover treatments may improve productivity when there is damage near the wellbore, but if the reason for low productivity is low permeability, the way to improve production may be to fracture the well hydraulically. The ratio of the actual productivity index to the ideal value is defined as the flow efficiency, FE:

$$\text{FE} = \frac{J_{\text{actual}}}{J_{\text{ideal}}} \tag{11-3}$$

The productivity index can be determined from a series of measurements of flowing pressure at different surface flow rates.

EXAMPLE 11-1

Determination of the productivity index and average reservoir pressure from stabilized flow tests

From the stabilized flow test data in Table 11-1, determine the well productivity index and the average reservoir pressure. Determine at what rate the well will flow for a surface pressure of 500 psi.

Table 11-1

Stabilized Flow Test Data

Measured Surface Rate	Computed Downhole Rate[a]	Measured Surface Pressure	Computed Downhole Pressure[b]
1223	1296	1594	4725
1835	1945	1400	4587
2447	2594	1203	4449
3058	3241	1006	4312
3670	3890	806	4174
4282	4539	607	4037
4894	5188	405	3900
6117	6484	0	3624

[a] $B_o = 1.06$ RB/STB.

[b] Beggs and Brill (1973) Method.

Solution In Table 11-1, surface pressure and flow rate measurements are provided along with bottomhole pressure values computed using the techniques indicated in Chapter 7. Figure 11-2 shows a plot of flowing bottomhole pressure versus downhole flow rate. Rearranging Eq. (11-2):

$$p_{wf} = \bar{p} - \frac{q}{J} \tag{11-4}$$

For the data in Table 11-1, this plot makes a line with a slope corresponding to the reciprocal of the productivity index for the well. Extrapolating the line to zero flow rate provides a value

for the average reservoir pressure, provided that the pressure drop due to skin is zero. A least-squares line fit through these data points yields a slope of −0.212 psi/bpd and an intercept of 5000 psi. Thus, the productivity index is

$$J = \frac{-1}{-0.212} = 4.72 \text{ bpd/psi} \tag{11-5}$$

The average pressure is given by the intercept, 5000 psi.

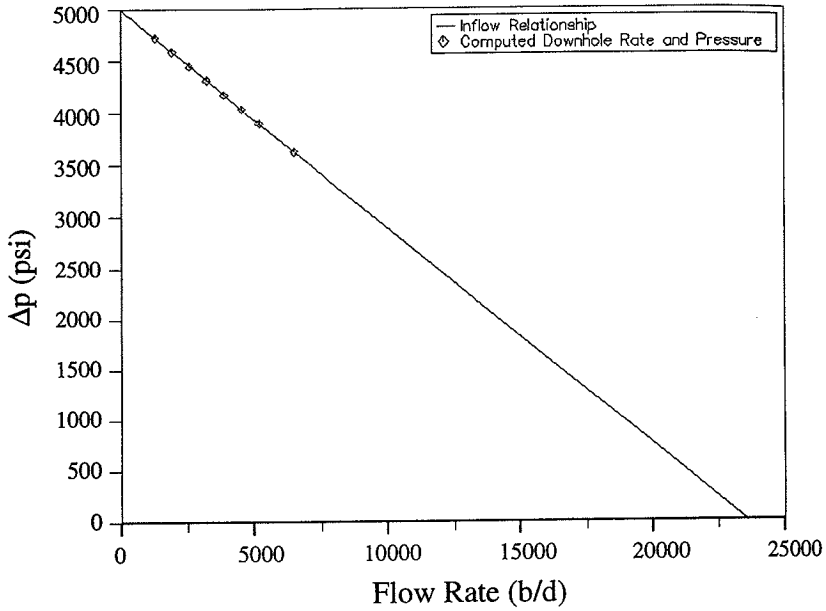

Figure 11-2
Inflow performance plot for Example 11-1.

To determine the well flow rate at 500 psi surface pressure, it is necessary to interpolate the data in the table to compute the bottomhole pressure, 3964 psi, that corresponds to this value of surface pressure. Then the corresponding bottomhole flow rate is determined from the equation of the line through the data to be 4883 bbl/d. The well flow rate for any flowing bottomhole pressure above the bubble-point pressure can be determined from this plot. Finally, using the formation volume factor, the surface flow rate is 4607 bbl/d. ◇

As Eq. (11-2) shows, the actual productivity index is a function of permeability, skin factor, average reservoir pressure, and the effective drainage radius of the well. However, knowing the productivity index does not provide any one of these values unless the others

are known. A pressure transient test can provide values for permeability and the skin factor, thus taking the guesswork out of deciding the best way to improve well productivity. Provided that the shape and extent of the well drainage area are known, the average reservoir pressure and the productivity index can also be determined from the transient test analysis of a pressure buildup or falloff test.

Most wells require from several hours to several days (or even months) to reach the stabilized flow behavior modeled by the productivity index in Eq. (11-1). During that time, a constant surface flow rate should be maintained. If pressure is continuously monitored following a change in the surface rate, the acquired data can be analyzed as a pressure transient test. The fundamental modes for pressure transient testing in a production well are drawdown and buildup tests. In an injection well, the analogs are injection and falloff tests.

Pressure transient data are obtained by measuring bottomhole pressures in the wellbore. Drawdown and injection tests are conducted with the well flowing at a constant rate. Buildup and falloff tests are conducted by measuring the pressure variations that result from shutting the well in after it has flowed at a constant rate. There are several testing configurations that can be used to acquire the pressure transient data. These are addressed in the next section.

The simplest drawdown test is initiated by opening the well to flow from a shutin condition. As the well flows, the pressure measured in the wellbore drops or is drawn down, hence the name drawdown test. The surface flow rate and the resultant bottomhole pressure response for a simulated drawdown test are shown in Fig. 11-3. Pressure buildup data are also shown in the figure. The pressure data can be plotted in other ways to assist in the computation of parameters concerning the well and the formation.

In Fig. 11-3, the drawdown and buildup pressure data do not appear to display the same behavior. In addition to the change in the direction of variation (pressure dropping during the drawdown, rising during the buildup), even the trends in the data appear to be distinct. The pressure drop during the initial part of the drawdown response appears to be more gradual than in the buildup, and the behavior near the end of the responses also appears different. In Fig. 11-4, both the drawdown and buildup data shown in Fig. 11-3 are plotted in a way that shows that, in fact, each represents the same transient trend in late time, although they are distinct in early time. The different early-time behavior is due to wellbore storage. In the simulation, as in most drillstem tests, the well was shut in downhole, thus minimizing wellbore storage during the buildup by reducing the wellbore volume in hydraulic communication with the downhole pressure gauge.

Wellbore storage is caused by movement or expansion/compression of wellbore fluids in response to a change in the wellbore pressure. The duration of the wellbore storage effect is dependent on the depth of the well and the type of completion and is greatly prolonged when fluid phase changes occur. On a log-log diagnostic plot like that shown in Fig. 11-4, constant wellbore storage appears as a "hump" in the pressure derivative. This behavior can mask transient pressure trends due to near-wellbore geometry or reservoir heterogeneity. Wellbore storage is not constant when phase redistribution occurs in the wellbore. Variable wellbore storage can exhibit trends that appear similar to patterns associated with a reservoir response. Distinguishing wellbore and reservoir response patterns can be difficult even for

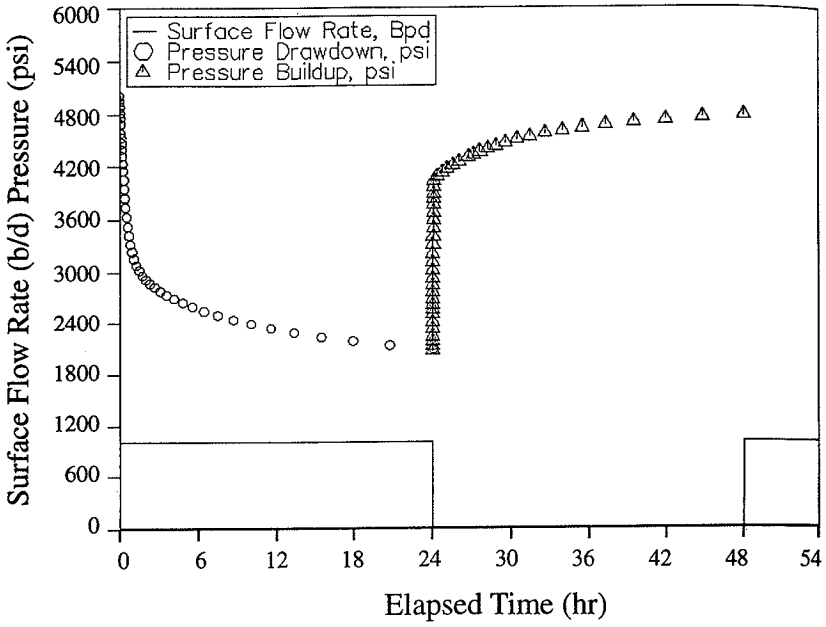

Figure 11-3
Simulated test data.

experts. Thus, the use of downhole shutin is recommended in pressure buildup tests to avoid loss of early-time data that may help to characterize damage and to avoid error in the test interpretation. Minimizing wellbore storage is an important consideration in test design.

Figure 11-4 shows the pressure change for the drawdown (squares) and buildup (circles) data. The pressure change is computed as follows:

$$\Delta p(\Delta t) = p_i - p_{wf}(\Delta t) \qquad \text{for drawdown data} \qquad (11\text{-}6)$$

and

$$\Delta p(\Delta t) = p_{ws}(\Delta t) - p_{wf}(t_p) \qquad \text{for buildup data} \qquad (11\text{-}7)$$

where Δp is the pressure change, Δt is the elapsed time since the instant the surface rate was initiated or stopped, p_i is the initial reservoir pressure at the test datum level, p_{wf} is the flowing bottomhole pressure (FBHP), p_{ws} is the shutin bottomhole pressure (SIBHP), and t_p is the production time, or the length of time the well was flowed before shutin. Also shown in Fig. 11-4 is a plot of the derivative of the pressure change with respect to the superposition time function for the drawdown data (shaded circles) and the buildup data

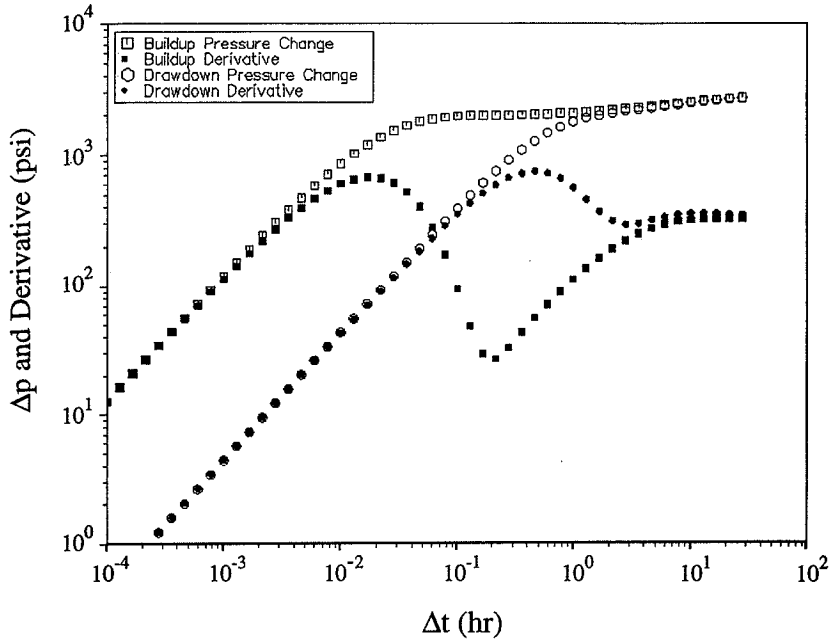

Figure 11-4
Log-log diagnostic plot for data in Fig. 11-3.

(shaded squares). Computation of the superposition time function and the derivative of pressure change with respect to the superposition time function is explained in Bourdet et al. (1983), Horne (1990), and Ehlig-Economides et al. (1990a).

The standard way of plotting pressure buildup data is the Horner plot shown for the simulated data in Fig. 11-5. In this plot, the logarithm of the Horner time function, $(t_p + \Delta t)/\Delta t$, is plotted on the abscissa, and the shutin pressure, $p_{ws}(\Delta t)$, is plotted on the ordinate. When plotted in this way, the data acquired first are plotted on the right, and each successive point is plotted to the left of the previous point. If the analyst is not using a computer for the analysis, the plot is drawn on special graph paper that has a logarithmic scale for the x axis. If this paper is not available, the analyst must first compute the logarithm of each value of the Horner time function. Otherwise, the points can be plotted directly on the semilog graph paper.

The simulated drawdown data are plotted as shown in Fig. 11-6, again on a semilog graph. In this case, the log of elapsed time, Δt, is plotted on the x axis, the flowing pressure $p_{wf}(\Delta t)$ is plotted on the y axis, and successive data points are plotted from left to right.

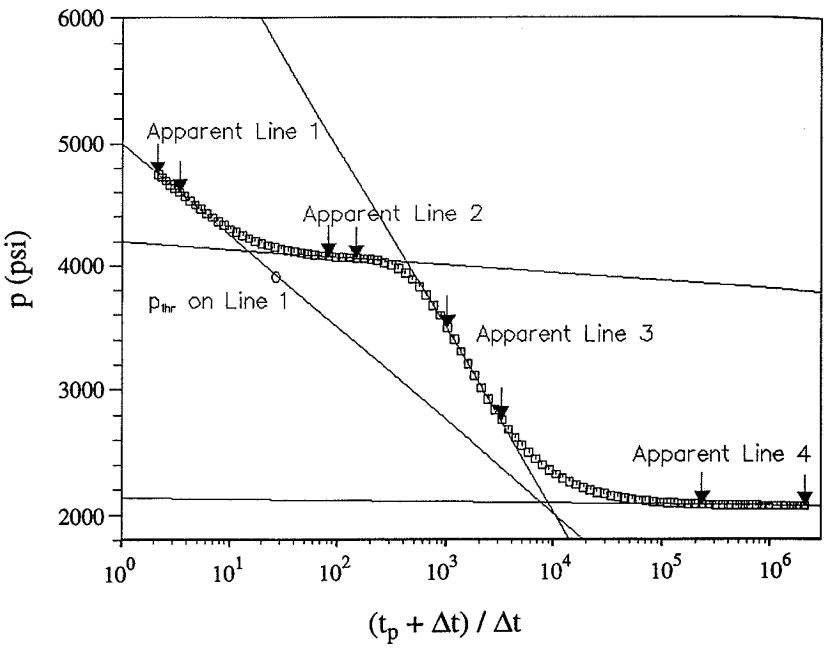

Figure 11-5
Horner plot of the buildup data in Fig. 11-3.

From a semilog line, the slope, m, can be used to compute permeability as follows:

$$k = \frac{1.151 \alpha_p \Delta q B \mu}{mh} \tag{11-8}$$

The computed value of k along with the pressure value on the semilog line at an elapsed time of 1 hr, p_{1hr}, are used to compute the skin:

$$s = 1.151 \left(\frac{\Delta p_{1hr}}{m} - \log \frac{\alpha_t k}{\phi \mu c_t r_w^2} - 0.351 \right) \tag{11-9}$$

where $\Delta p_{1hr} = p_{wf} - p_{1hr}$ for a buildup test, and $\Delta p_{1hr} = p_i - p_{1hr}$ for a drawdown test.

The purpose in plotting the buildup or drawdown data on a semilog plot is the determination of permeability, skin factor, and, for buildup tests, the average reservoir pressure. Other reservoir parameters that can be determined from a semilog plot are the distance to a permeability barrier, such as a fault, and values that are used to quantify the effects of

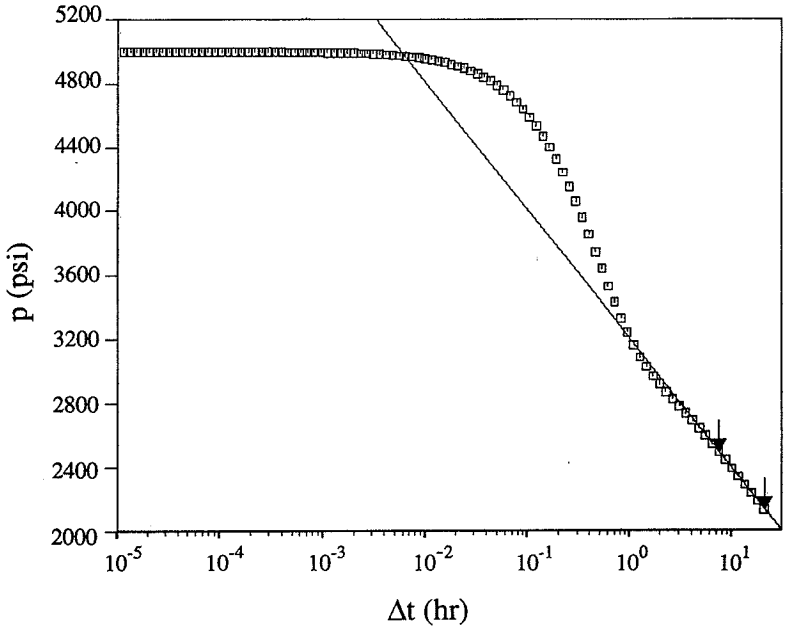

Figure 11-6
Semilog plot of drawdown data in Fig. 11-3.

reservoir heterogeneities, such as natural fractures, layering, or other phenomena classified as dual porosity effects.

Permeability, skin factor, and average reservoir pressure are computed from slope and intercept values for a line that fits some portion of the data. Often, as in Fig. 11-5, the data exhibit more than one apparent straight line on the semilog plot. Sometimes, no apparent line on the plot represents the response from which these values can be determined correctly. If an incorrect line is used for computation of permeability, skin factor, and average reservoir pressure, the values will be wrong. Although the use of computers minimizes computational errors, if the analyst fails to identify the correct straight line, the results will be in error.

Identification of the correct straight line on a semilog plot is aided considerably with the use of the log-log diagnostic plot consisting of the pressure change and its derivative, as in Fig. 11-4. Because the derivative is computed with respect to the superposition time function (logarithm of time for a drawdown, Horner time function for a buildup), on this plot, the data that can be correctly analyzed as a straight line on a Horner or semilog plot follow a constant or flat trend. Apparent lines on a semilog plot that do not correspond to

a flat trend for the same data points on the log-log diagnostic plot cannot provide correct values for permeability, skin, and the average reservoir pressure. The following example illustrates the computation of permeability, skin factor, and extrapolated reservoir pressure.

EXAMPLE 11-2
Horner plot analysis

Reservoir rock and fluid data for the simulated example are the following: $B = 1.06$, $\mu = 4.35$ cp, $\phi = 0.1$, $h = 100$ ft, $c_t = 6 \times 10^{-6}$ psi^{-1}, and $r_w = 0.35$ ft. The drawdown duration was 24 hr, and the flowing pressure at the end of the drawdown was 2087 psi. The well was flowing at a rate of 1000 bbl/d during the drawdown. Determine permeability, skin factor, and the extrapolated pressure from the Horner plot in Fig. 11-5.

Solution Permeability, skin factor, and average reservoir pressure are frequently the parameters sought from a pressure transient test. These parameters are easily computed from the line that appears on a semilog plot of the data. However, as shown in Fig. 11-5, there are several apparent straight-line trends on the semilog plot. Once the correct line has been identified on a Horner plot, three values must be determined from the line, its slope, m, the value on the line corresponding to an elapsed time of 1 hr, $p_{1\text{hr}}$, and the value on the line corresponding to a Horner time ratio of 1, p^*.

The slope determined from the first apparent line (from the left of the plot) in Fig. 11-5 is -748 psi/log cycle, the value for $p_{1\text{hr}}$ is 3954 psi, and the value for p^* is 5000 psi. Using the slope of the line, and values for the flow rate change, Δq, and the formation thickness, h, determined independently, the permeability, k, is computed as follows:

$$k = \frac{(162.6)(-1000)(1.06)(4.35)}{(-748)(100)} = 10 \text{ md} \tag{11-10}$$

The value of α_p depends on the units of the data used for the computation. Since these data are in oilfield units, the value of α_p is 141.2. The factor 1.151 that appears in Eq. (11-8) is used whenever the slope, m, is computed from a plot drawn with base 10 logarithms. If natural logarithms are used, this factor is 0.5.

Using $p_{1\text{hr}}$ determined from the line, the permeability determined from the previous step, and values for porosity, ϕ, fluid viscosity, μ, compressibility, c_t, and the wellbore radius, r_w, the wellbore skin factor, s, is determined as follows:

$$s = 1.151\left[\frac{2087 - 3954}{-748} - \log\frac{(0.000264)(10)}{(0.1)(4.35)(6 \times 10^{-6})(0.35)^2} - 0.351\right]$$
$$= -2 \tag{11-11}$$

As above, the value of α_t depends on the units of the data.

Using the second apparent line, $k = 123$ md, $s = 32$, and $p^* = 4194$ psi. From the third apparent line, $k = 5$ md, $s = -1.6$, and $p^* = 8200$ psi. Clearly, the answers are significantly different depending on which line is used for the analysis. However, by consulting Fig. 11-4, the points that provide a correct analysis must be on the flat portion of the derivative, which appears in the late-time data. The data that lie on the third apparent semilog line appear on the crest of the hump in the derivative data, which does not appear as flat on the log-log diagnostic plot. This hump is an indication of wellbore storage. Frequently, the most prominent line on a semilog buildup plot corresponds to the crest of the wellbore storage response on the log-log plot. Use of the log-log diagnostic plot avoids mistaking this behavior for a reservoir response and provides a means to identify the correct line on the Horner plot.

The second apparent line on the Horner plot in Fig. 11-5 indicates an extrapolated pressure that is succeeded in value by data acquired in late time. When this occurs for a Horner line correctly identified as a flat trend on a log-log diagnostic plot, this is an indication of reservoir limits. In that case, the extrapolated pressure from the Horner line has no meaning. The fourth apparent line on the Horner plot is not a likely choice for analysis because it corresponds to data acquired during the first few minutes of the buildup. Data acquired this early in time would rarely represent a reservoir response. ◇

Data for both drawdown and buildup tests in the same well are rarely collected. Even when such data are acquired, often only the buildup data are analyzed. The reason that buildup data are desirable is illustrated in the data plotted in Fig. 11-7. As shown in the figure, the buildup pressure change and derivative response are smooth, while the drawdown data contain high-frequency noise due primarily to small variations in the surface flow rate. Each change in surface flow rate, however small, results in a detectable jump in the pressure transient data that are particularly visible in the pressure derivative. The difficulty of maintaining a constant flow rate is avoided when the well is shut in. In Fig. 11-7, surface rate variation causes distortion in the drawdown pressure data that masks the meaningful response and renders the data essentially uninterpretable. This difficulty is revisited in Problem 11-9.

In Fig. 11-4, the late-time pressure derivative data for both the drawdown and the buildup data are constant. In Fig. 11-7, none of the buildup pressure derivative data follow a constant trend. Instead, the buildup data on the log-log plot follow a straight line that has a slope of 1/4. Although permeability and skin can be determined only from the portion of the data with a flat derivative, other parameters can be determined from other straight-line trends that appear in the derivative response.

Derivative responses that are commonly found and readily recognized in transient test data are termed "flow regimes." The reason for this term is that the flow regimes are associated with flow geometries like those shown in Fig. 11-8. Derivative response patterns for the flow regimes diagrammed in this figure are shown in Fig. 11-9. For each flow regime there is a specialized plot of the portion of the data exhibiting the characteristic derivative response pattern. On the specialized plot, the data identified with the characteristic derivative response pattern lie on a straight line, and the slope and intercepts of the line are used to compute well and/or reservoir parameters. Figure 11-9 shows the specialized plot associated with respective trends identified on the log-log diagnostic plot of pressure change and its derivative.

Table 11-2 describes the observed derivative response patterns in simple terms. Table 11-3 provides the equations that describe the flow regimes diagrammed in Figs. 11-8 and 11-9, and the units conversion coefficients (α values) are indicated in Table 11-4. Use of Fig. 11-9 and Tables 11-2 through 11-4 is illustrated in the following example.

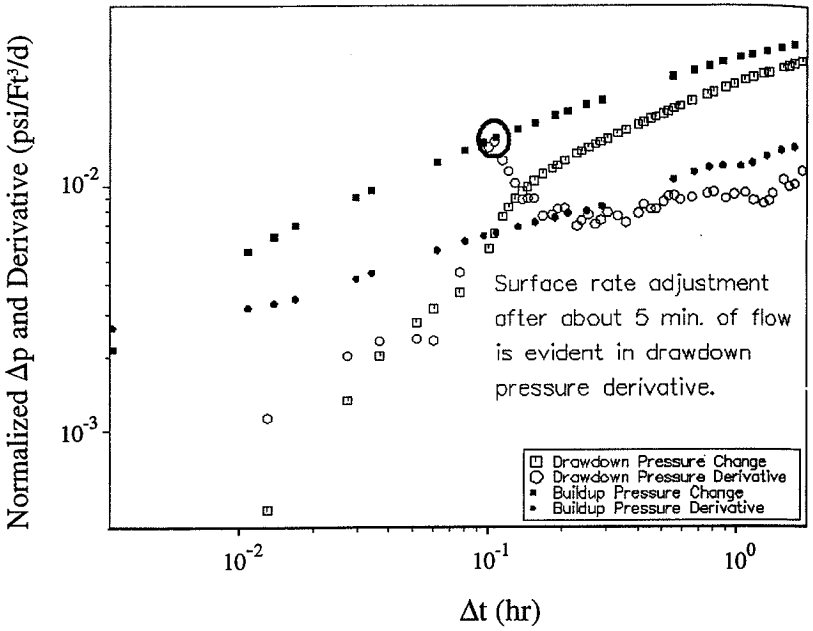

Figure 11-7
Comparative diagnostic plot of drawdown and buildup date. In this plot the pressure change and its derivative for each transient are divided by the flowrate change that induced the transient.

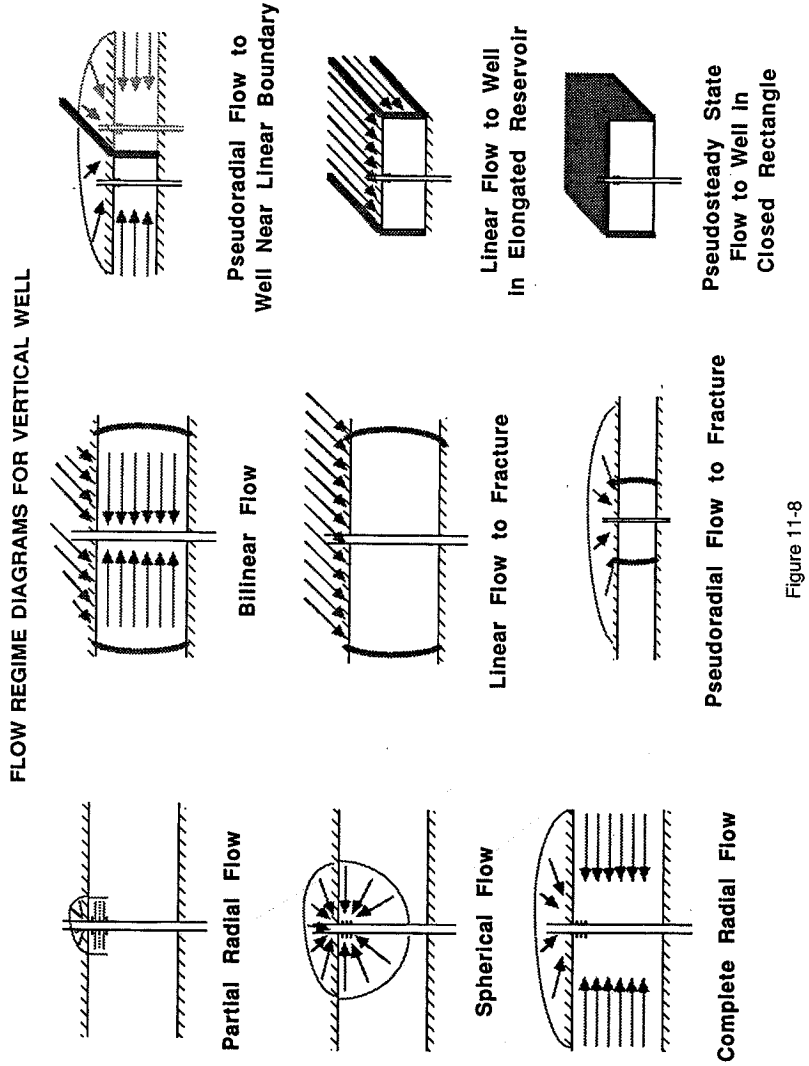

Figure 11-8
Predominant flow streamlines for flow regimes identifiable in pressure transient data. (*From Ehlig-Economides, 1992.*)

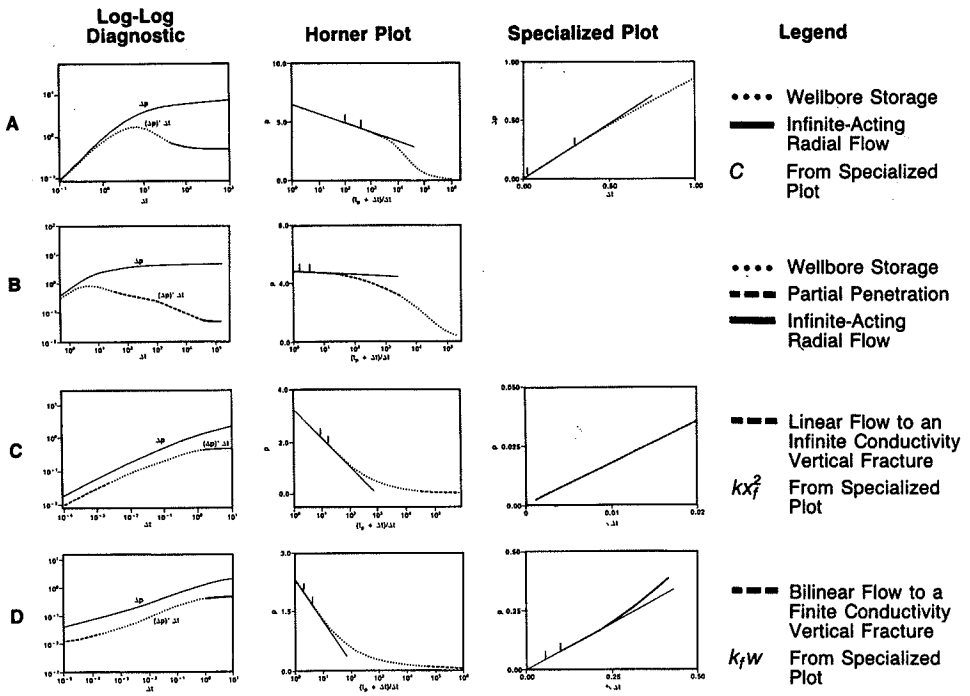

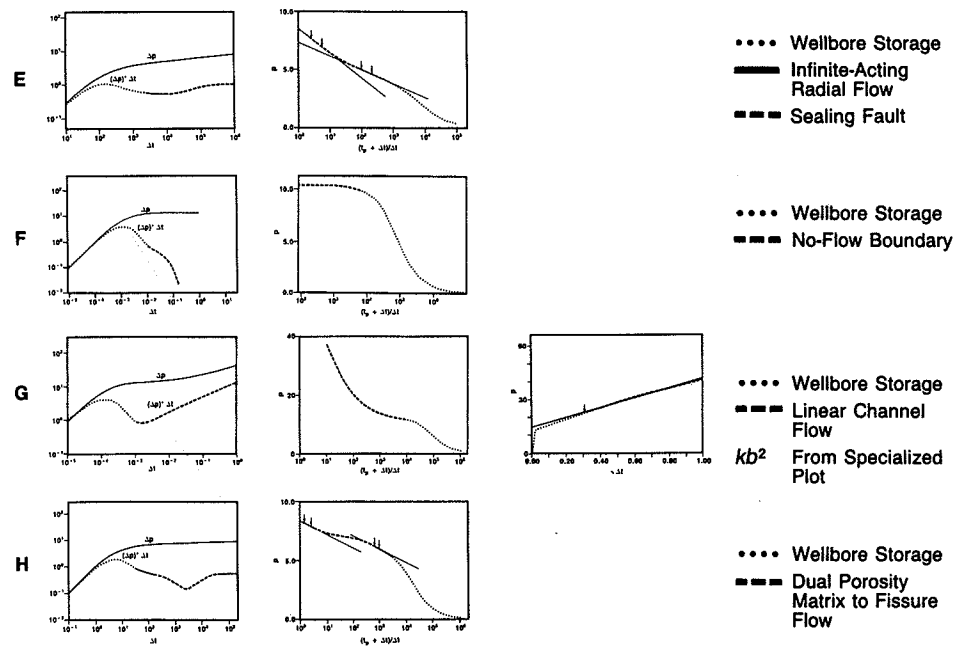

Figure 11-9
Appearance of common flow regimes on log-log diagnostic, Horner, and specialized plots.

Table 11-2

Pressure Derivative Trends for Common Flow Regimes

Flow Regime	Pressure Change Slope	Pressure Derivative Slope	Additional Distinguishing Characteristic
Wellbore storage (WBS) (fluid expansion/ compression)	1	1	Early-time pressure change and derivative are overlain
Finite-conductivity vertical fracture (FCVF) (bilinear flow)	$\frac{1}{4}$	$\frac{1}{4}$	Early-time (after WBS) pressure change and derivative are offset by factor of 4
Infinite-conductivity vertical fracture (ICVF) (linear flow)	$\frac{1}{2}$	$\frac{1}{2}$	Early-time (after WBS and/or FCVF) pressure change and derivative are offset by factor of 2
Partial penetration (PPEN) (spherical flow)	Leveling off	$-\frac{1}{2}$	Middle time (after WBS and before IARF)
Infinite-acting radial flow (IARF)	Increasing	0	Middle-time flat derivative
Dual porosity with pseudo-steady-state interporosity flow	Increasing, leveling off, increasing	0, valley, 0	Middle-time valley trend; duration is more than 1 log cycle
Dual porosity with transient interporosity flow	Steepening	0, upward trend, 0	Middle-time slope doubles
Single sealing fault (pseudo-radial flow)	Steepening	0, upward trend, 0	Late-time slope doubles
Elongated reservoir (linear flow)	$\frac{1}{2}$	$\frac{1}{2}$	Late-time pressure change and derivative are offset by factor of 2; slope of $\frac{1}{2}$ occurs much earlier in the derivative
Pseudo-steady-state (fluid expansion/ compression)	1 for drawdown; 0 for buildup	1 for drawdown; steeply descending for buildup	Late-time drawdown pressure change and derivative are overlain; slope of 1 occurs much earlier in the derivative
Constant-pressure boundary (steady state)	0	steeply descending	Cannot be distinguished from pseudo-steady state in pressure buildup data

Table 11-3a **Pressure Transient Flow Regimes for Early and Middle Time Analysis**

Flow Regime	Plot Axes	Equation[a]	Parameters to Compute
Infinite-acting radial flow (radial flow)[b]	t_{sup}, p_{wf} for flowing well, p_{ws} for shutin well	$\Delta p = mt_{sup} + \Delta p_{1hr}$ $\Delta p = p_i - p_{wf}(\Delta t)$ for flowing well $\Delta p = p_{ws}(\Delta t) - p_{wf}(t_p)$ for shutin well $m = \frac{1.151\alpha_p \Delta q B \mu}{kh}$ $\Delta p_{1hr} = m(\log \frac{\alpha_t k}{\phi \mu c_t r_w^2} + 0.351 + 0.87s)$	$k = \frac{1.151\alpha_p \Delta q B \mu}{mh}$ $s = 1.151(\frac{\Delta p_{1hr}}{m} - \log \frac{\alpha_t k}{\phi \mu c_t r_w^2} - 0.351)$ $\Delta p_{1hr} = p_i - p_{1hr}$ for flowing well $\Delta p_{1hr} = p_{wf} - p_{1hr}$ for shutin well
Wellbore storage (fluid expansion/ compression)[b]	Δt, Δp	$\Delta p = m_c \Delta t$ $m_c = \frac{\Delta q B}{\alpha_c C}$	$C = \frac{\Delta q B}{\alpha_c m_c}$
Finite-conductivity vertical fracture (bilinear flow)[c]	$\sqrt[4]{\Delta t}$, Δp	$\Delta p = m_{bf} \sqrt[4]{\Delta t}$ $m_{bf} = \frac{2.45\alpha_p \Delta q B \mu}{kh\sqrt{k_f w/kx_f}} (\frac{\alpha_t k}{\phi \mu c_t x_f^2})^{0.25}$	$k_f w\sqrt{k} = (\frac{\alpha_{bf} \Delta q B \mu}{m_{bf} h})^2 (\frac{1}{\phi \mu c_t})^{0.5}$
Infinite-conductivity vertical fracture (linear flow)[c]	$\sqrt{\Delta t}$, Δp	$\Delta p = m_{lf}\sqrt{\Delta t} + (\frac{\pi}{3}) \frac{m}{1.151} \frac{kx_f}{k_f w}$ $m_{lf} = \frac{\alpha_p \Delta q B \mu}{kh} (\frac{\pi \alpha_t k}{\phi \mu c_t x_f^2})^{0.5}$	$x_f\sqrt{k} = (\frac{\alpha_{lf} \Delta q B}{m_{lf} h})(\frac{\mu}{\phi c_t})^{0.5}$ $\frac{k_f w}{kx_f} = (\frac{\pi}{3}) \frac{m}{1.151} (\frac{1}{\Delta p_{int}})$
Partial penetration (spherical flow)[d]	$\frac{1}{\sqrt{\Delta t}}$, p_{wf}, p_{ws}	$\Delta p = \frac{\alpha_p \Delta q B \mu}{2k_{sph} r_w} - \frac{m_{pp}}{\sqrt{\Delta t}}$ $m_{pp} = \frac{\alpha_p \Delta q B \mu}{2k_{sph} r_w} (\frac{\phi \mu c_t r_w^2}{\pi \alpha_t k_{sph}})^{0.5}$	$k_{sph} = (\frac{\alpha_{pp} \Delta q B \mu}{m_{pp}} \sqrt{\phi \mu c_t})^{2/3}$

[a] In this table and Table 11-3b, the equations refer to the generalized superposition time function, t_{sup}. For a simple drawdown test, this simplifies to log Δt, and for a buildup after a single drawdown flow period, this simplifies to the Horner time function given by $(t_p + \Delta t)/\Delta t$, where t_p is the flow time before shutting in the well. The expression Δq is the change in surface flow rate that initiated transient. For a drawdown or a buildup following a drawdown flow period at a single constant flow rate, Δq is equivalent to q.

[b] Earlougher (1977).

[c] Economides and Nolte (1989).

[d] Chatas (1966).

TABLE 11-3b

Pressure Transient Flow Regimes for Late-Time Analysis

Flow Regime	Plot Axes	Equation	Parameters to Compute
Single sealing fault (pseudo-radial flow)[a]	t_{sup}, p_{wf} for flowing well, p_{ws} for shutin well	$\Delta p = 2mt_{sup} + p(t_x)$ t_x is the time of intersection for two semilog lines, the first corresponding to radial flow, the second with a slope exactly twice that of the first line. $t_x = (\frac{2.2456\alpha_t k}{4\phi\mu c_t L^2})^{0.5}$	$L = (\frac{\alpha_t k t_x}{\phi\mu c_t})^{0.5}$
Elongated reservoir (linear flow)[b]	Δt, p_{wf}, p_{ws}	$\Delta p = m_{cf}\sqrt{\Delta t}$ $m_{cf} = \frac{\alpha_{cf}\Delta q B\mu}{2\alpha_p \Delta q B\mu}(\frac{\pi\alpha_t k}{\phi\mu c_t b^2})^{0.5}$	$b\sqrt{k} = (\frac{\alpha_{cf}\Delta q B}{m_{cf} h})(\frac{\mu}{\phi c_t})^{0.5}$
Pseudo-steady state (fluid expansion/ compression)[a]	Δt, p_{wf}, p_{ws}	$p_i - p_{wf} = m_{pss}t + p_{int}$ for drawdown $\bar{p} - p^* = \frac{m}{2.302}p_{DMDH}(\frac{\alpha_t k t_p}{\phi\mu c_t A})$ for buildup $m_{pss} = -\frac{2\pi\alpha_p\alpha_t \Delta q B}{\phi c_t hA}$ $p_{int} = p_i - m(\frac{1}{2}\log\frac{A}{C_A r_w^2} + 0.351 + 0.87s)$ m from IARF plot p_{DMDH} from ref. a	$\phi hA = \frac{\alpha_{pss}\Delta q B}{c_t m_{pss}}$ for drawdown $C_A = \frac{\alpha_{cA} kt}{m_{pss}}\exp([2.303\frac{(p_{1hr}-p_{int})}{m}])$ for flowing well (m, p_{1hr} from IARF plot) $\bar{p} = p^* - \frac{m}{2.302}p_{DMDH}(\frac{\alpha_t k t_p}{\phi\mu c_t A})$ for shutin well

[a] Earlougher (1977).

[b] Ehlig-Economides and Economides (1985).

TABLE 11-4

Units Conversion Factors

Quantity	Oilfield Units	SI Units	Preferred API Standard Units	cgs Units
Production rate, q	STB/D	m^3/s	dm^3/s	cm^3/s
Formation thickness, h	ft	m	m	cm
Permeability, k	md	m^2	μm^2	darcy
Viscosity, μ	cp	Pa-s	Pa-s	cp
Mobility, k/μ	md/cp	m^2/Pa-s	μm^2/Pa-s	darcy/cp
Mobility-thickness product, kh/μ	md-ft/cp	m^3/Pa-s	μm^2-m/Pa-s	darcy-cm/cp
Pressure difference, Δp	psi	Pa	kPa	atm
Pressure, p	psi	Pa	kPa	atm
Radius, r	ft	m	m	cm
Fracture half-length, x_f				
Fracture width, w				
Distance to sealing fault, L				
Channel length, b				
Effective horizontal well length, L_p				
Time, t	hr	s	hr	s
Porosity, ϕ, fraction	unitless	unitless	unitless	unitless
Total system compressibility, c_t	psi^{-1}	Pa^{-1}	kPa^{-1}	atm^{-1}
Porosity-compressibility-thickness product, $\phi c_t h$	ft/psi	m/Pa	m/kPa	cm/atm
Wellbore storage, C	bbl/psi	m^3/Pa-s	dm^3/kPa-s	cm^3/atm-s
Skin, s	unitless	unitless	unitless	unitless
Horizontal well early pseudo-radial skin, s_{epr}				
Horizontal well damage skin, s_m				
α_p	141.2	$1/(2\pi) = 0.1592$	$1/(2\pi) = 0.1592$	$1/(2\pi) = 0.1592$
α_t	0.0002637	1	3.6×10^{-6}	1
α_c	24	1	1/3600	1
α_{lf}	4.064	$1/(2\sqrt{\pi}) = 0.2821$	1.016×10^{-6}	$1/(2\sqrt{\pi}) = 0.2821$
α_{bf}	44.1	0.3896	0.01697	0.3896
α_{pp}	2453	0.00449	2.366	0.00449
α_f	0.000148	0.7493	2.698×10^{-6}	0.7493
α_{cf}	8.168	$1/(\sqrt{\pi}) = 0.5642$	0.508×10^{-6}	$1/(\sqrt{\pi}) = 0.5642$
α_{pss}	0.234	1	3.6×10^{-6}	1
α_{CA}	5.456	5.456	5.456	5.456

EXAMPLE 11-3
Hydraulically fractured well

Data from a posttreatment test in a hydraulically fractured well are plotted in Fig. 11-10. Determine the hydraulic fracture half-length and conductivity. Required well and reservoir data are as follows: $r_w = 0.365$ ft, $\phi = 0.135$, $h = 46$ ft, $T_R = 80°F$, $\gamma_g = 0.57$, $\bar{\mu}_g = 0.014$ cp, $\bar{B}_g = 0.0523$, $\bar{c}_t = \bar{c}_g = 0.00304$ psi^{-1}. This buildup follows an extended period of flow at 58.75 MSCF/d.

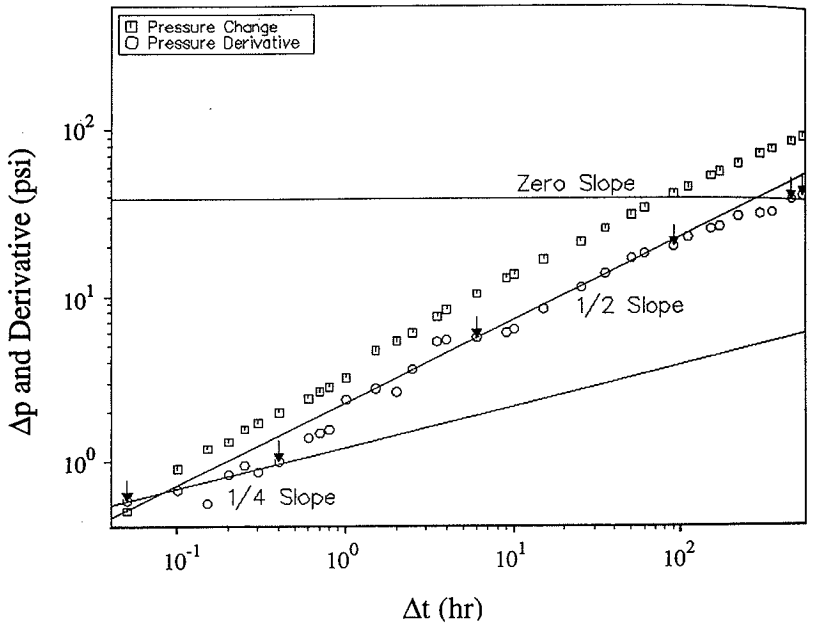

Figure 11-10
Flow regime identification on log-log diagnostic plot of data for Example 11-3.

Solution This example concerns posttreatment evaluation of a hydraulically fractured well. In general, a successful hydraulic fracture treatment cannot be evaluated by a posttreatment pressure buildup test, because the transient response is dominated by linear flow to the fracture. However, if a transient test performed before the treatment provides a value for the formation permeability, then the posttreatment test provides values for the fracture length and/or the fracture conductivity.

Since this is a gas well, the pressure dependence of the gas properties can affect the analysis. For simplicity, average values are used in the analysis for this example. The equivalent

flow rate of 10,460 bbl/d is computed using a conversion factor of 5.615 ft^3/bbl. Use of the real-gas pseudo-pressure described by Govier (1975) is recommended for gas well tests.

The log-log diagnostic plot in Fig. 11-10 shows that nearly all of the data lie on a line of slope 1/2. The pressure derivative in this case is parallel to pressure change and offset by a factor of 2. This corresponds to the response labeled linear flow in Figs. 11-8 and 11-9 and in Tables 11-2 and 11-3.

Since there are no data exhibiting a flat pressure derivative trend, an accurate value for permeability cannot be determined from these data. An estimate determined for the last few data points provides a maximum value for permeability. The actual value may be considerably less. The Horner plot in Fig. 11-11 shows that a value of permeability equal to 0.28 md is determined from the last data points.

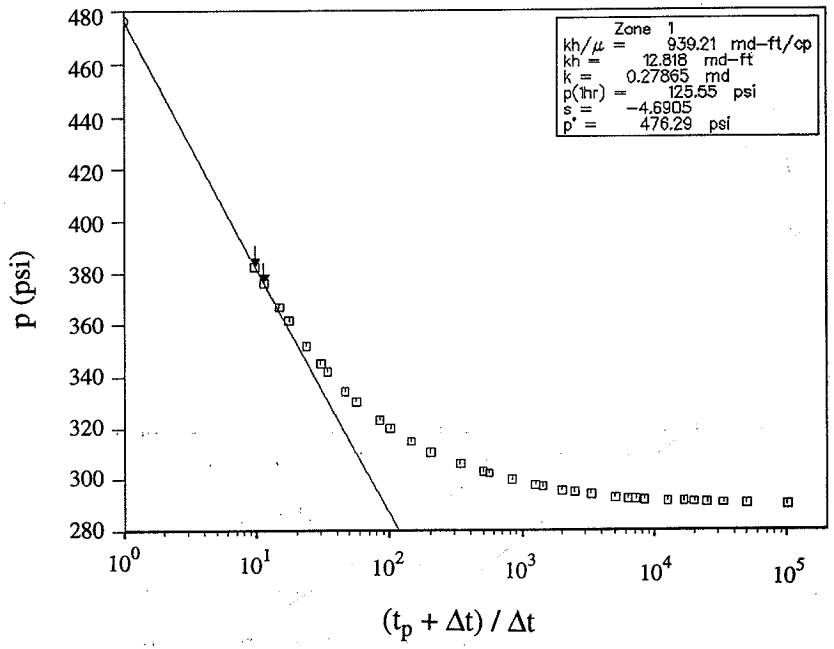

Figure 11-11
Estimation of permeability, skin, and extrapolated pressure on specialized plot of data for Example 11-3.

On the specialized plot in Fig. 11-12, all but a few late-time data points fit on the same line, which has a slope of $m_{1f} = 4.41$. Using the equation in Table 11-3, the fracture half-length is computed as follows:

$$kx_f^2 = \left(\frac{(4.064)(10{,}460)(0.0523)}{(4.41)(46)}\right)^2 \frac{(0.014)}{(0.135)(0.00304)} = 4097 \text{ md-ft}^2 \qquad (11\text{-}12)$$

Using the maximum permeability value estimated from the Horner plot, $x_f = 121$ ft. Since the permeability could be less, this value is a minimum. The value for Δp_{int} determined from Fig. 11-12 is approximately zero. Referring to Table 11-3, this indicates that the fracture conductivity is effectively infinite.

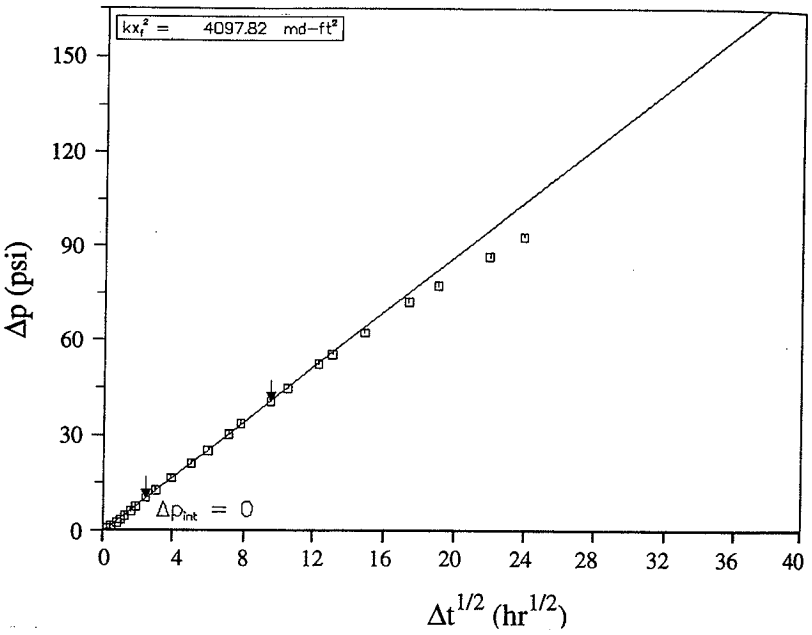

Figure 11-12
Determination of vertical fracture half-length on specialized plot of data for Example 11-3.

Figure 11-13 shows a bilinear flow specialized plot for the first few data points. From Table 11-3:

$$k(k_f w)^2 = \left[\frac{(44.1)(10{,}460)(0.0523)(0.014)}{(4.69)(46)}\right]^4 \left[\frac{1}{(0.135)(0.014)(0.00304)}\right] \qquad (11\text{-}13)$$

$$= 1.05 \times 10^6 \text{ md}^3\text{-ft}^2$$

Using the estimated maximum permeability value, $k_f w = 1930$ md-ft, which serves as a minimum estimate.

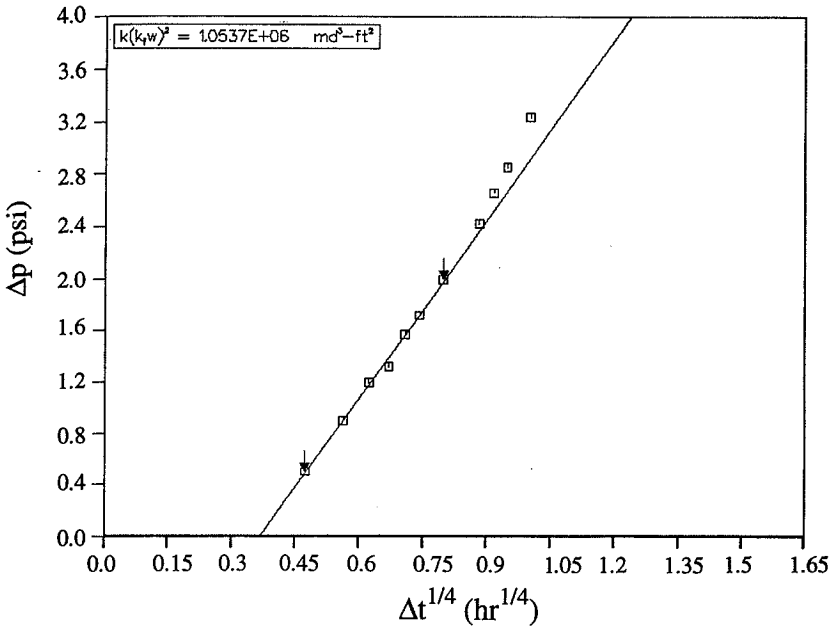

Figure 11-13
Estimation of vertical fracture conductivity on specialized plot of data for Example 11-3.

For fractures that have effectively infinite conductivity, a conventional technique for determining fracture half-length from the skin value determined from Horner analysis is discussed in Economides and Nolte (1989):

$$x_f = 2r_w e^{-s} = (2)(0.365)e^{(4.7)} = 80 \text{ ft} \qquad (11\text{-}14)$$

In this case, although the buildup data were acquired for more than 600 hr, the pseudo-radial flow regime was still not developed in late time. Massive hydraulic fractures are designed to reach up to 2000-ft half-lengths. Such fractures should produce a transient response dominated by bilinear and linear flow for several months. Thus, Eq. (11-14) can rarely be used in practice. Further, this equation applies only for infinite-conductivity fractures, and the fracture half-length can be severely underestimated for finite-conductivity fractures using this approach. This example shows, however, that if the permeability has been determined, perhaps from a pretreatment transient test, then fracture length and/or fracture conductivity can be computed from the bilinear and/or linear flow regimes. ◇

To appreciate the distinction among various testing strategies and what they can deliver, it is important to know what transient test data look like and how well and reservoir parameters are determined from these data. Additional information on test interpretation is found in Earlougher (1977) and Horne (1990). The next section describes techniques for acquiring well test data.

11-3 Test Types

The purpose of this section is to describe briefly the list of test types shown in Table 11-5. This will provide terminology that is useful for specifying test requirements. Each test type listed in Table 11-5 is described, including information on the condition at the time of testing, the type of hardware required, the typical test duration and test radius of investigation, and objectives that may be addressed.

Lee (1982) indicates that the radius of investigation can be computed for any test from the following equation:

$$r_i = \left(\frac{4\alpha_t kt}{\phi\mu c_t}\right)^{0.5} \tag{11-15}$$

For a low-mobility reservoir ($k/\mu < 0.1$) and a 1-hr drawdown, this equation yields a radius of less than 10 ft. For a reservoir with moderate mobility ($k/\mu = 100$ md-ft), a 12-hr drawdown investigates a radius of 3600 ft. For the buildup, the effective radius of investigation may be less if the late-time transient pressure response varies less than the gauge resolution or is distorted by superposition effects. Ehlig-Economides (1992) has provided equations for the area investigated in nonradial geometries.

11-3.1 Closed Chamber Test

The closed chamber test is a specialized form of a drillstem test shown in Fig. 11-14 that can be conducted under open-hole conditions or after casing and perforating. The inclusion of an additional valve in the drillstem some length above the standard downhole shutin valve increases test safety. When pressure is recorded both at the sandface and inside the chamber while formation fluids flow into the closed chamber, it is possible to estimate production versus time during drawdown. Stanislav and Kabir (1990) have shown that more accurate accounting for production during drawdown enhances the buildup interpretation. This configuration can thus be an improvement over the standard drillstem test.

The closed chamber test equipment may be lowered in a cased hole along with perforating guns. The formation interval is perforated under mud hydrostatic pressure. When the test valve is opened, the formation is subjected to the pressure in the drillstem, which can be increased by partially filling the chamber with a water cushion [see Eq. (11-15)]. Because the pressure in the drillstem is much less than in the formation, this results in a flow surge that helps to clean the perforations.

The closed chamber test is programmed as a typical drillstem test sequence lasting 4 to 5 hr. The chamber pressure can be lowered before the second flow by opening the

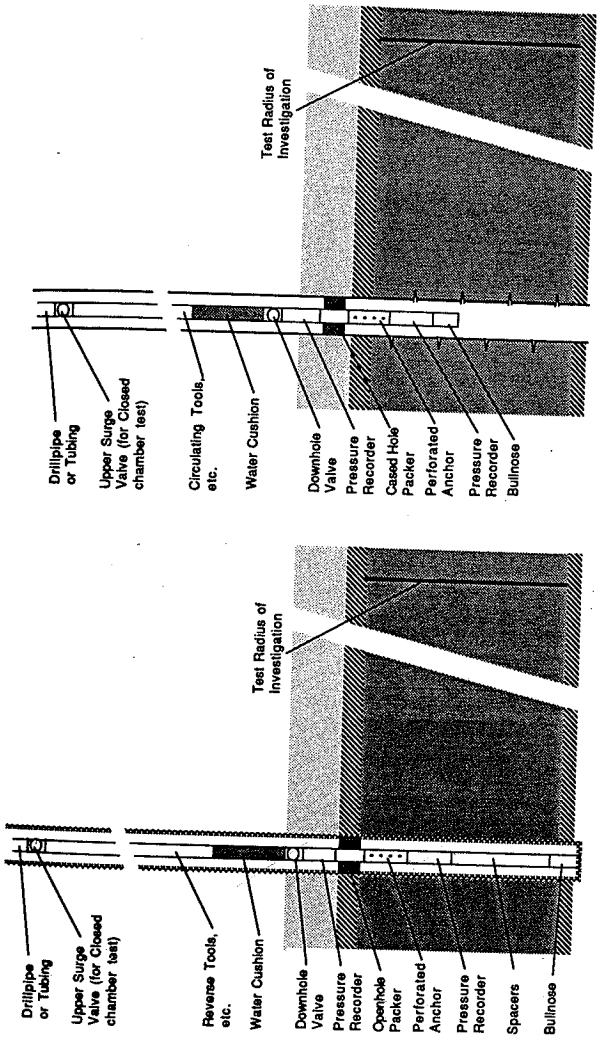

Figure 11-14
Drillstem test in: (a) open hole; (b) cased hole.

TABLE 11-5

Types of Modern Reservoir Tests[a]

Test Type	Measurement Condition[b] F	SI	P	S	Distinguishing Characteristics	Design Considerations
Closed chamber test	C	Y		Y	Downhole shutin; controllable wellbore condition	Chamber and cushion lengths; valve open/shut sequence
Constant-pressure flow test	Y			Y	Requires transient flow rate measurement	Flow rate sensitivity
Drillstem test	C	Y			Downhold shutin; open or cased hole	Flow and shutin sequence/duration
Exploration well test	Y				Special provision for well control and disposal of produced fluids	*PVT* fluid sample collection
Formation test	Y	Y			Test conducted on borehole wall; formation fluid sampling	Tool module sizing/selection; pressure sensitivity
Horizontal well test	Y	Y			Testing hardware usually located in vertical segment	Minimize wellbore storage effects; requires long-duration test
Impulse test	Y	Y			Transients initiated by short-rate impulse	Trade-off between impulse duration and pressure sensitivity
Multilayer transient test	Y	Y			Multirate test; pressure and rate measured at several depths	Flow rate/pressure sensitivity; test sequence; measurenment depths
Multirate test	Y				Transient measurements for a succession of surface flow rates	Magnitude of test flow rates and duration of the flow periods
Multiwell interference test	Y	Y			Transient induced in active well and measured in observation well(s)	Test duration; pressure sensitivity
Production data analysis	Y				Uses surface pressure and rate as transient data for analysis	Computation of downhole rate and pressure from surface measurements
Production/injection well test	Y	Y			Transient test in an established production or injection well	Possibility of testing with downhole shutin to avoid excessive wellbore storage

TABLE 11-5 (Continued)

Types of Modern Reservoir Tests[a]

Test Type	Measurement Condition[b] F	SI	P	S	Distinguishing Characteristics	Design Considerations
Production log test	Y	Y			Downhole measurement of pressure and flow rate, temperature, and (usually) density	Flow rate/pressure sensitivity
Pulse test			Y		Multiwell interference test sequence of flow and shutin pulses	Pulse magnitude and duration
Pumped well test		Y			Downhole pressure measured or computed from liquid-level soundings	Downhole pressure sensor versus surface acoustic device
Stabilized flow test	Y				Includes isochronal, flow-after-flow, inflow performance, production logs, etc.	Time to reach stabilization
Testing while perforating	Y	Y		Y	Testing hardware and perforating guns on the same string	Underbalance determination
Vertical interference test	C	Y	C		Transient induced at one depth and measured at another	Test duration; pressure sensitivity; checking packer seal

[a]Adapted from Ehlig-Economides et al. (1990b).

[b]F = flow, SI = shutin, P = pulse, S = slug; Y = yes, commonly; C = under certain conditions.

upper chamber valve. Test radius of investigation and objectives are the same as for any short-term drillstem test equipped with mechanical gauges.

11-3.2 Constant-Pressure Flow Test

The constant-pressure test (Jacob and Lohman, 1952) is distinguished from standard flow tests because the test is initiated with a step change in pressure from one constant-pressure value to another instead of the conventional step change in flow rate. Although, in theory, continuous measurement of flow rate, ideally at the sandface, can provide the same interpretation results as the conventional continuous bottomhole pressure measurement, the practical concern is whether the flow rate measurements have sufficient resolution for accurate interpretation. The most common downhole flow rate measurement device is the spinner flow meter found on production logging tool strings. The interpretation methods that have been developed for continuous wellbore flow rate measurement may be used for flow rates measured at the surface, provided downhole flow rates can be computed. Downhole flow rates are measured only in cased holes.

11-3.3 Drillstem Test

The drillstem test hardware diagrammed in Fig. 11-14 is lowered with drillpipe or tubing. Required equipment include packers, a downhole shutin valve, reverse-circulation ports that permit the tool to bypass wellbore fluids while being lowered into or pulled out of the wellbore, and a pressure gauge. Frequently, transient pressure data are recorded downhole and retrieved when the tool is pulled out of the hole. Pressure may be recorded mechanically or in battery-powered electronic memory. Mechanical pressure recording has a low maximum sampling rate and limits resolution to about 10 psi. Electronic pressure records can be programmed for variable sampling rates starting at 1- 2-sec sampling at the beginning of each flow period and ending with a few samples per hour or less depending on the transient duration. Electronic pressure gauges and battery-powered memory can achieve much higher resolution than a mechanical gauge, provided that the test is conducted according to the preprogrammed test sequence. If there are delays, the memory may be filled before the actual test is finished.

The flow and shutin sequence is usually controlled mechanically from the surface. Often, for safety reasons there can be no wireline lowered into the hole. When permitted, devices on wirelines may be used to retrieve data from electronic memory during transient acquisition. The introduction of wireless telemetry has enabled surface readout during testing without a wireline. With surface readout, the data can be examined on the log-log diagnostic plot described in Section 11-2 to determine when sufficient data have been acquired to satisfy test objectives.

Full-bore drillstem test equipment packages the test equipment in such a way that there is a clear path with the same radius as the drill pipe through the entire test string, as in Fig. 11-14b. This enables completion operations such as perforation or acid injection to be conducted while the test equipment is in the hole.

When fluids flow to the surface during the drillstem test, the flow rate is accurately determined by surface flow rate measurements. When the reservoir pressure is not high

enough for fluids to flow to the surface, the rate during drawdown is not known accurately. In some cases, the rate is determined by measuring the volume of fluid in the drillstem as it is retrieved to the surface. Produced gas is difficult to measure in tests that do not flow to the surface. With the exception of the closed chamber test, drillstem tests are conducted with atmospheric pressure in the drillstem. Liquid flow open to atmospheric pressure is termed slug flow. (This is not the same as the two-phase slug flow described in Chapter 7.)

A back pressure can be applied to the formation at the start of the test by filling part of the drillstem or the chamber in a closed chamber test with water, which is called a cushion. The magnitude of the applied back pressure is computed from the length of the cushion:

$$p_{\text{cushion}} = \rho_w g h_{\text{cushion}} = 0.433 h_{\text{cushion}} \tag{11-16}$$

for pure water and for cushion pressure in psi and cushion length in ft. The objective of the cushion may be to avoid two-phase flow in the formation (below the bubble- or dew-point pressure of the reservoir fluid), but the back pressure with a cushion is usually designed to be small enough to avoid killing the well during flow.

A typical open-hole drillstem test is programmed with an initial flow for 30 min, an initial shutin for 1 hr, a second drawdown for 1 hr and a final buildup for 2 hr. Downhole shutin minimizes wellbore storage effects, but the low sampling rate provided by mechanical gauges limits what can be interpreted from the early-time data. Higher sampling rates afforded by electronic gauges may permit quantification of the radius and permeability of near-well radial damage or partial penetration effects. If radial flow occurs during the buildup, reservoir pressure, permeability and the total skin factor can be determined.

Drillstem tests in wells that flow to the surface may have several initial short flows to clean up the perforations followed by an extended drawdown of 12 hr or more and a buildup of 24 hr or more. Reservoir limit tests designed to sense reservoir boundaries may be of even longer duration. A good test design may be particularly effective for these tests because they may combine the highest testing technologies: high-resolution gauges, high sampling rate in early time, long duration, and surface readout of transient data during acquisition.

11-3.4 Exploration Well Test

For wildcat and exploration wells drilled to find or delineate newly found reservoirs, the first testing objective is to determine the well flow potential. As shown in Fig. 11-15, a temporary production facility is required for this kind of testing, along with special safety measures and a means for the disposal of fluids produced. The main safety concern is well control, because in exploration the flow behavior and composition of the reservoir fluids is largely unknown. Since wells drilled for field development usually exhibit similar flow behavior as in neighboring wells, well control can focus on known problems. In exploration wells, preventive measures must be prepared for a wide range of potential problems. Special precautions are taken to see that sand production, corrosion-causing compounds in the hydrocarbons, or other unexpected events will not create blowout conditions during the well test.

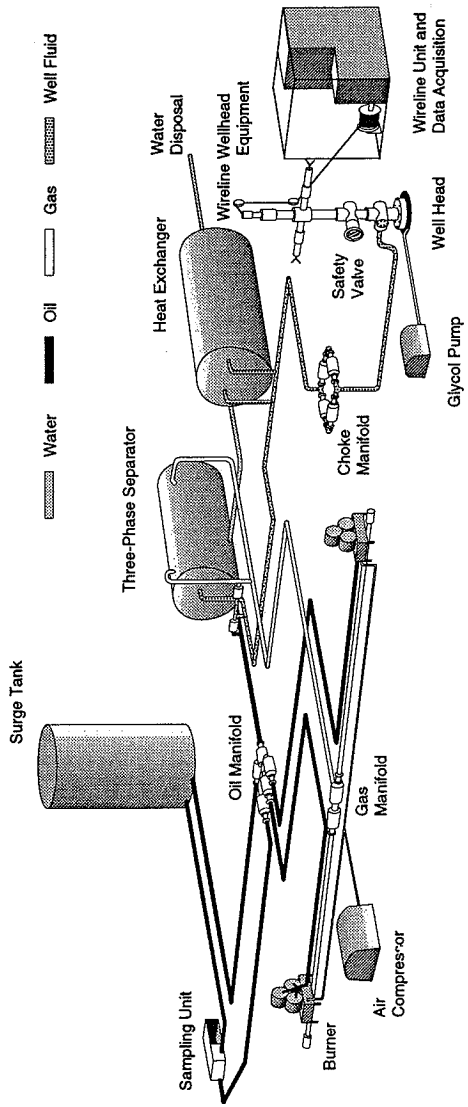

Figure 11-15
Exploration well test.

Once a field has been put into production, gathering systems are in place for collecting, separating, and transporting produced fluids. In exploration wells, produced hydrocarbons are often burned, and produced water must be purified for disposal. The paths of gas, oil, and water can be traced in Fig. 11-15.

Frequently, adverse and unknown conditions discourage transient testing in an exploration well. Instead, a stabilized flow test is performed to determine the well flow rate at a measured wellhead pressure, and often a hydrocarbon fluid sample is acquired for *PVT* analysis. Fluid sampling is done by collecting pressurized hydrocarbon samples from the separator outlets. Oil and gas rates are carefully metered during stabilized flow so that the two phases can be recombined later in the same proportions, thus yielding a representative sample of the reservoir fluid. In some cases, instead of recombining the hydrocarbon samples collected at the surface, a special tool is lowered into the well to collect a bottomhole sample.

If a transient test is performed, the objectives of the test usually focus more on reservoir characterization than on completion evaluation. Hence, reservoir pressure, permeability, heterogeneity, and limits are sought in the transient response. In some cases, real-time surface readout of acquired data is transmitted by satellite from the remote test location to corporate offices for diagnosis and interpretation during acquisition. The test is terminated by the desired test radius of investigation or the detection of reservoir boundaries.

11-3.5 Formation Test

The formation test (Moran and Finklea, 1962) is not a well test. As shown in Fig. 11-16a, the wireline formation test is usually performed only in a mud-filled open hole. Hydraulically operated arms press against one side of the borehole, forcing the testing device against the opposing side. A doughnut-shaped rubber packer provides a seal, inside which a probe is forced into the formation. When exposed to low pressure, reservoir fluids flow into the tool. When a valve is shut, flow stops and a buildup occurs. Because the flow is for only a few seconds or minutes, the pressure builds up to the reservoir pressure in a short period of time. The test radius of investigation is at most only a few feet, but unlike most well tests, the perturbation is spherical, not radial. This test is repeated at successive locations, providing a measure of reservoir pressure versus depth. Because the test is usually conducted on a newly drilled well, the pressure measurements represent the static pressure profile with depth for the area in hydraulic communication with the well horizontally. This area is independent of the test radius of investigation. However, if the transient pressures recorded during the drawdown and buildup are analyzed, they can provide estimates for spherical permeability and sometimes even for horizontal and vertical permeability that are representative only within the test radius of investigation. Such permeability estimates must be used with care, because two-phase flow occurs in the zone of mud filtrate invasion from drilling, which occupies much of the test radius of investigation.

Recent improvements in the wireline formation test tool include the addition of observation probes located opposite the active probe and offset at another depth, as shown in Fig. 11-16b. The observation probes permit reliable determination of vertical and horizontal permeability between the source and sink locations and can also characterize partial

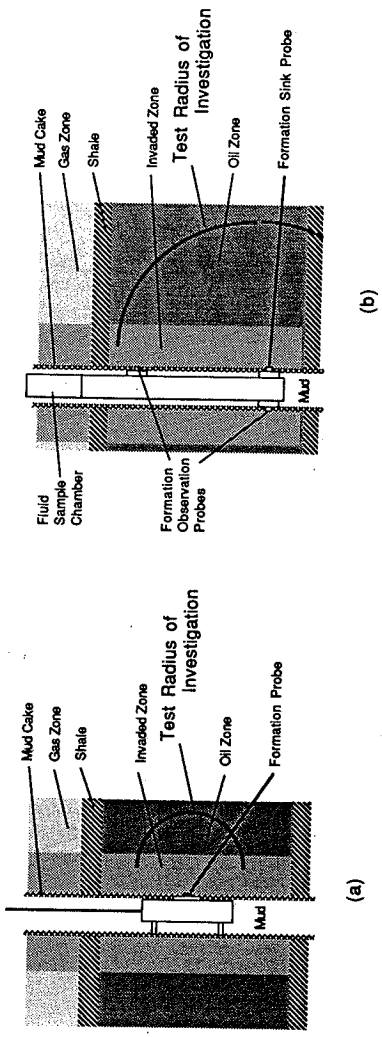

Figure 11-16
(a) Formation test; (b) multiprobe formation test.

barriers to vertical flow. In addition, larger flow chambers permit longer flow periods, thus extending the test radius of investigation and enabling determination of more representative permeability values. A device has been developed that senses the phase of fluids withdrawn from the reservoir so that representative samples of reservoir fluids can be obtained, and multiple chambers are available that permit collection of fluid samples at more than one depth in one logging trip.

Fluid samples and formation pressure measurements also help to locate barriers to flow. Gross changes in fluid composition from one depth to another or from one well to another may suggest that the hydrocarbon samples have different origins, or at least have not been in communication in the recent geologic past. Formation pressure measurements that exhibit an abrupt change with depth, as in Fig. 11-17, indicate the existence of a barrier to vertical flow. When pressures vary abruptly from well to well in zones that are correlated in the geological model of the reservoir, also seen in Fig. 11-17, there is an indication of impaired or obstructed flow between wells. Formation pressure measurements may show clearer indications of vertical and/or areal barriers in wells drilled after the field is put on production and differential depletion effects have become evident in the pressure data.

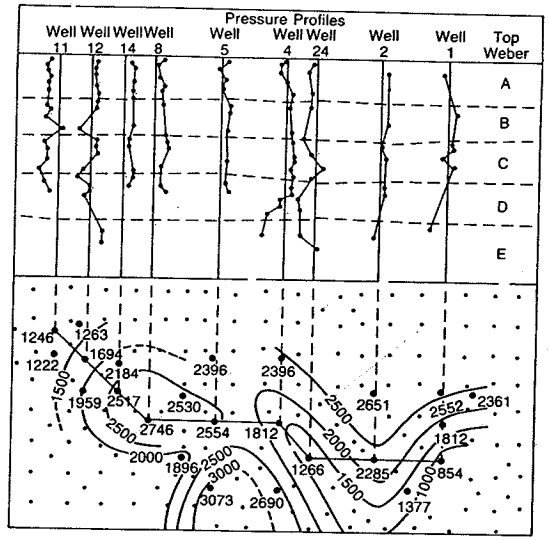

Figure 11-17
Formation test measurements and reservoir description. (*From Schlumberger, 1986b.*)

Differential depletion occurs when two or more intervals of high permeability contrast are commingled in the well. The high conductivity interval is produced with less pressure drop in the wellbore than in the other(s), which remain at a much higher pressure. Whenever a well with differential depletion among commingled units is shut in, fluids flow from the higher-pressure intervals into the more depleted zones, resulting in wellbore crossflow. In such a case, to enable production of the lower permeability reserves it may be necessary eventually to plug off the depleted zone(s).

Formation test pressures measured along a horizontal borehole, as in Fig. 11-18, often show significant pressure variation laterally in the formation. These measurements are often an eye opener, but in addition, they signal cause for caution in planning a pressure buildup test too early in the life of a horizontal well. Since such a test would be dominated by backflow in the horizontal wellbore as reservoir fluids seek pressure equilibrium, a drawdown test would have a better chance for success. Otherwise, an even better plan would be to put the well on production for some time before testing.

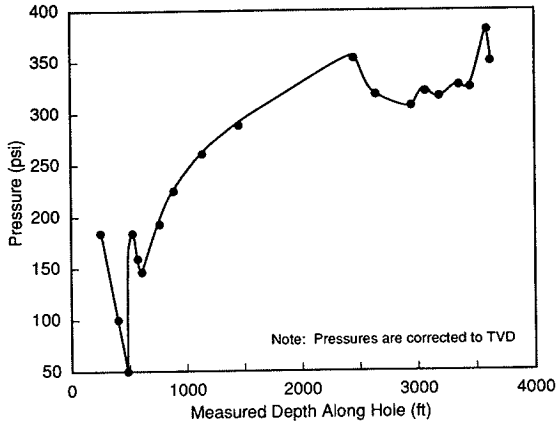

Figure 11-18
Formation test measurements along a horizontal borehole. (*From Chauvel and Oosthoek, 1990.*)

11-3.6 Horizontal Well Test

Usually, any point along the horizontal segment of a wellbore is part of the productive interval. Hence, since transient test measurements are acquired in most wells just above the productive interval, and in addition because the test string is frequently too rigid and too long to pass through a curved wellbore, the measurements are usually conducted above the horizontal wellbore, as in Fig. 11-19. Thus conventional hardware can be used for horizontal well tests.

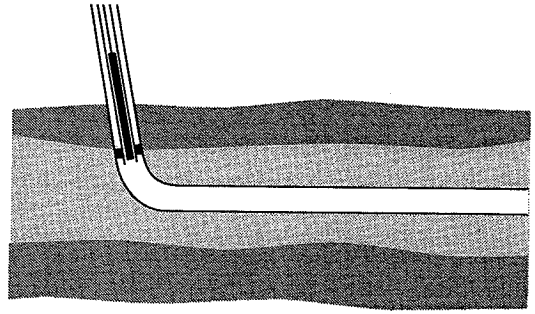

Figure 11-19
Horizontal well test configuration.

Because of the longer borehole, wellbore storage is an inherent problem in testing horizontal wells, even for buildup tests conducted with downhole shutin. For horizontal wells in developed reservoirs as in Fig. 11-19, a buildup test conducted before the well has been on production may be dominated by wellbore crossflow. The list of parameters affecting the transient response includes horizontal permeability (normal and parallel to the well trajectory), vertical permeability, drilling damage, and completion damage. Additionally, the producing interval may be effectively much less than the drilled length, and the standoff (distance of the well from the nearest reservoir bed boundary) may vary along the length of the well. Hence, counting the wellbore storage coefficient, there may be seven or more parameters affecting the interpretation for a horizontal well in a homogeneous reservoir with no evidence of boundaries. For all of these reasons, horizontal well tests frequently provide inconclusive results.

While wellbore storage inhibits determination of parameters associated with the early-time transient behavior (vertical permeability, drilling and completion damage), the middle- and late-time response behaviors (yielding horizontal permeability anisotropy, and values for effective production length and standoff) may require several hours, days, or months to appear in the transient data. Since there are many factors that threaten the success of horizontal well tests, careful test design is a must.

First, tests in the pilot hole drilled before kicking off to drill the horizontal borehole segment can yield horizontal and vertical permeability. Second, a good directional drilling survey can frequently provide an adequate estimate of the standoff. Third, a production log flow survey conducted with coiled tubing can determine what portion of the wellbore length is actually producing, thus indicating the effective production length. Fourth, as mentioned above, wells in developed reservoirs should be flowed for a sufficient length of time to equilibrate pressures along the wellbore. For wells that flow at sufficiently high rates, continuous borehole pressure and flow rate measurements (see the production log test) can be acquired while flowing and used to interpret the drawdown transient response. Finally, if

downhole flow rates are not measured, the buildup test should be conducted with downhole shutin. With all or several of these provisions, the horizontal well test has a reasonable chance of providing values for horizontal permeability anisotropy and the damage skin, which cannot otherwise be quantified.

11-3.7 Impulse Test

In theory, the impulse test introduced by Ayoub et al. (1988) replaces the step rate change used to initiate conventional tests, with its derivative with respect to time, which is a rate impulse of zero duration and unit magnitude, as in Fig. 11-20. The resultant pressure response is the pressure derivative with respect to time, which, when multiplied by elapsed time, becomes the form of the pressure derivative used for test interpretation. Hence there is no need to differentiate the data for diagnosis.

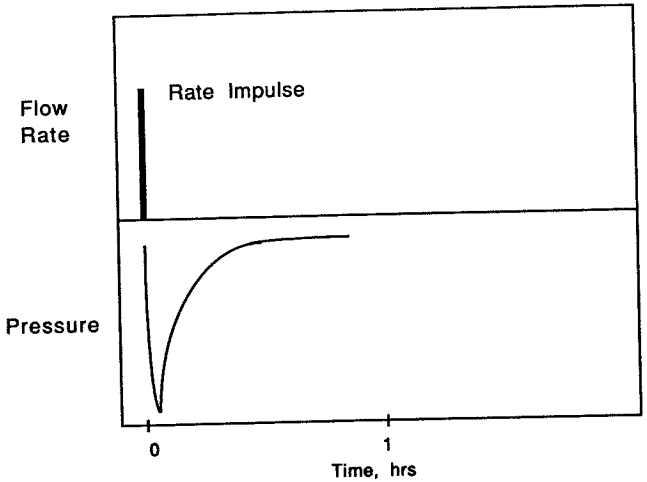

Figure 11-20
Theoretical impulse test sequence.

In practice, the rate impulse that can be achieved in a test is not of zero duration, and its magnitude depends on many factors. As such, early-time information is lost, and the late-time response is valid only while the pressure variations measured by the gauge are larger than the gauge resolution. Usually, this type of test is of very short duration (less than 1 hr), and has a consequently small radius of investigation.

The practical application of this test has proved to be in testing during underbalanced perforation. Two common types of impulse tests are shown in Fig. 11-21. Figure 11-21a shows a way to achieve the "true" impulse test configuration by running testing equipment along with tubing-conveyed perforating guns. With sufficient underbalance, the perforations

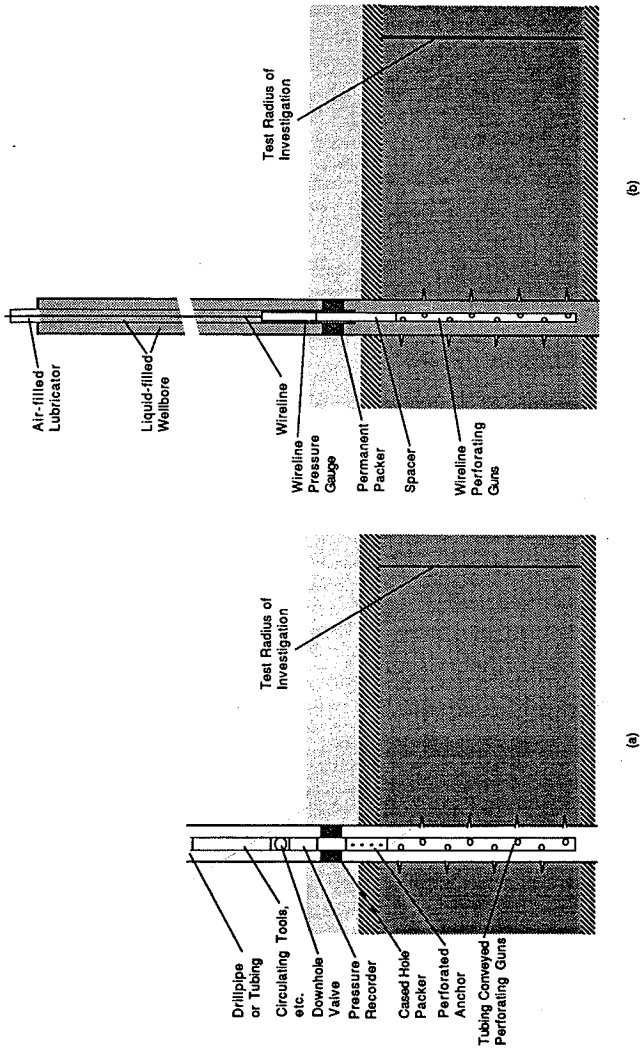

Figure 11-21
Impulse test configurations for (a) tubing-conveyed perforating and (b) wireline perforating in underbalanced conditions.

begin flowing once the interval is shot, which is an effective means of perforation cleanup. After a few seconds or minutes, depending on the test design, the downhole test valve is shut. The subsequent pressure transient lasts up to 1–2 hr, but sometimes radial flow is visible in the impulse diagnostic plot after about 15 min, and often the last part of the pressure variation is less than the gauge resolution, particularly in high-permeability formations. The technique of flowing the well for a very short time has been particularly attractive in wells that are likely to produce sand.

The other test configuration in Fig. 11-21b is not a true impulse test because flow is never actually shut in. As in Fig. 11-21a, the test is conducted while perforating underbalanced. Here, the perforations are conveyed on a wireline perforating device equipped with a pressure gauge. This technique has been particularly effective in overpressured gas wells for which underbalance is achieved by displacing drilling mud with diesel oil. A small pocket of air in the lubricator used for lowering the wireline tool is compressed when fluids flow into the wellbore immediately after perforating. Once the air volume has been compressed to the maximum, the well stops flowing without shutting a downhole valve. For gas wells, the liquid-filled wellbore minimizes wellbore storage effects, so that radial flow that would require 12 hr or more to overcome in a conventional buildup test appears in a few minutes.

11-3.8 Multilayer Transient Test

The multilayer transient test is described in Ehlig-Economides (1987). By combining techniques for multirate, production log, and stabilized testing and analysis, this test offers a means to determine permeability, skin, static pressure, and boundaries on a layer-by-layer basis for layers in a commingled completion.

11-3.9 Multirate Test

In a multirate test, pressure measurements are acquired while flowing at a succession of surface rates. Usually flow and pressure are stabilized at each rate before proceeding to the next rate. If the only data acquired are at stabilized conditions, the multirate test is equivalent to a stabilized flow test.

In general, the reason for acquiring transient data at more than one surface rate involves changing near-wellbore conditions, particularly rate-dependent skin, as described in Chapter 5. By analyzing transient pressure behavior at different production rates, it is possible to resolve the apparent skin into the actual damage skin and the rate-dependent part of the skin due to non-Darcy flow.

Another well condition that results in an apparent rate-dependent skin is in fractured injection wells. In this case, the higher the injection pressure (rate), the longer is the induced hydraulic fracture. When such wells are shut in, the fracture due to injection may close partially or completely. Thus, analysis of the falloff may not suggest that the well is fractured. The two-rate injection test (Singh et al., 1987) is designed to evaluate the pressure at which the fracture opens (parts) by detecting fracture parting in the transient data. Another strategy for determination of fracture parting pressure uses a multirate stabilized flow test.

11-3.10 Multiwell Interference Test

A multiwell interference test requires at least one active well and one or more observation wells. The active well is flowed and then shut in. Gauges in the observation well(s), which is (are) shut in during the test, record transient pressures that result from changes in flow rate in the active well. If no response is observed in an observation well, this is an indication that there is no flow communication between it and the active well.

Depending on the distances between wells, interference tests require sufficient duration for the radius of investigation of the disturbance caused by rate changes in the active well to be sensed by gauges in the observation well(s). In all but very-high-permeability reservoirs, the time required for a measurable pressure interference response is significant. Typically, these tests require at least a week and are conducted only with careful planning and design.

11-3.11† Production Data Analysis

Wellhead pressure and flow rate data can be used in some wells to estimate downhole transients. Using data processing techniques like those applied in production log testing, such data can provide characterization of features that require a transient test duration that exceeds the practical limit. These features include late-time hydraulic fracture and horizontal well flow regimes and evidence of far drainage boundaries. Additionally, such data can be used for permeability and skin determination and evaluation of changing skin over time. This technique works only during periods of uneventful production and when the fluid content of the wellbore during flowing conditions permits straightforward estimation of the downhole pressure from surface pressure data.

These data are also used for numerical simulation of well flow behavior. Because such models may be sensitive to reservoir and well parameters, they help to determine these values. Numerical simulation is the only choice when multiphase flow renders the analytical models used for transient test interpretation invalid.

11-3.12 Production / Injection Well Test

A transient test can be conducted by lowering sensors into the cased well or through production tubing, as in Fig. 11-22. This can be done at any time in many production or injection wells, and for some reservoirs tests are conducted in all or a number of the wells as part of routine well and reservoir production monitoring. The advent of reliable downhole shutin tools that can be lowered on a wireline or slick line has significantly improved the quality of the data that can be acquired in production wells by minimizing wellbore storage. Joseph et al. (1988) illustrates how the wellbore storage-dominated period in a production well test was reduced from more than 100 hr with surface shutin to about 2 hr with downhole shutin. Wellbore damage and the reservoir pressure in the well drainage volume are computed from the radial flow regime in the transient data. Since these are usually the main values sought in routine production tests, the transient data must be acquired for long enough to detect this flow regime.

The duration of wellbore storage in production wells can be significant due to fluid phase redistribution in the wellbore, a likelihood because both gas and oil flow in many

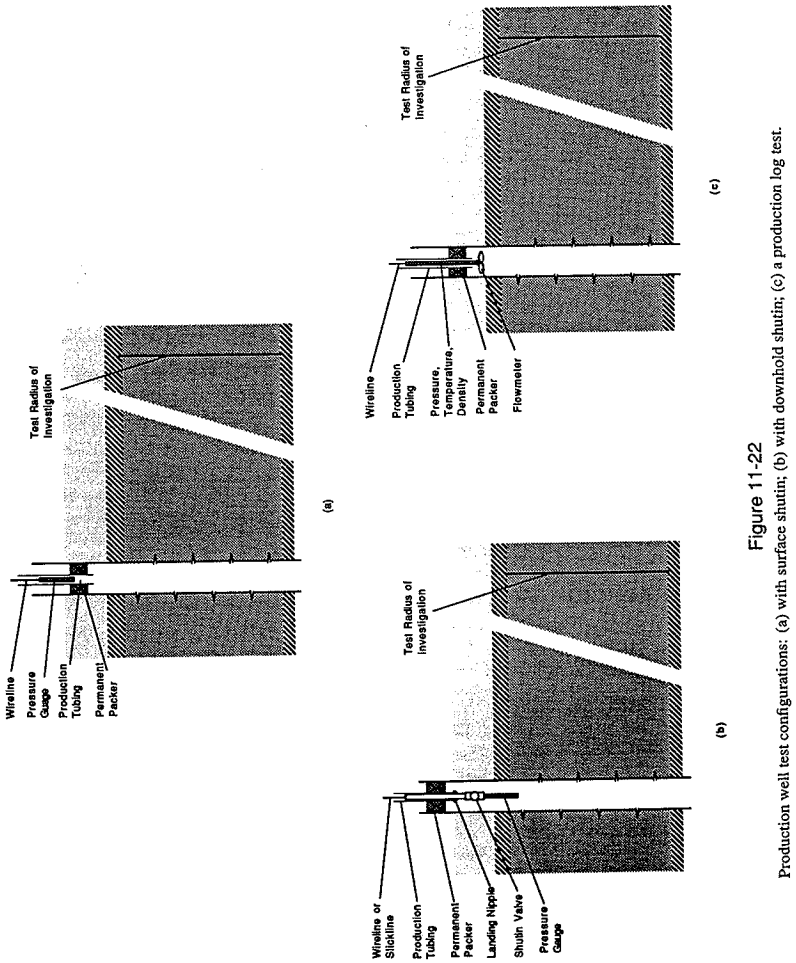

Figure 11-22 Production well test configurations: (a) with surface shutin; (b) with downhold shutin; (c) a production log test.

production wells, even if the production at the sandface is single phase. If wellbore storage effects have not ended before the effects of interfering wells appear in the transient response, determination of skin and reservoir pressure is much more difficult. The installation of a landing nipple in the tubing shoe, as in Fig. 11-22b, at the time the well is completed permits testing with downhole shutin later in the life of the well. Another alternative is to measure continuously both pressure and flow rate at the sandface using a production logging tool, as in Fig. 11-22c. This technique is termed a production log test, and is feasible in wells that flow at sufficiently high rates.

With downhole shutin or continuous pressure and flow rate monitoring, skin, permeability, and reservoir pressure frequently can be determined from a test lasting less than 10 hr. Completion evaluation and characterization of heterogeneity or boundaries inside the test radius of investigation are possible test objectives. However, since wells on production usually have multiphase flow near the wellbore, interpretation of the transient data may require advanced techniques.

11-3.13 Production Log Test

The production log test combines a production log acquired while the well is flowing and/or shut in with a drawdown and/or buildup transient test for which both pressure and flow rate are measured continuously at the sandface. As described in Chapter 12, the production log provides the velocity and phase of fluids entering the wellbore versus depth. Parts of a perforated interval that do not produce may indicate nonproductive sands or plugged perforations. This measurement helps to determine the formation thickness and/or the penetration ratio that should be used in the transient interpretation.

As shown in Fig. 11-22c, the transient data are acquired with a production logging tool that is positioned just above the sandface. Kuchuk (1990) and Ehlig-Economides et al. (1990a) describe how the convolution or deconvolution derivative of the transient pressure and flow rate measurements provides an analog to the pressure derivative that resembles the signal that could be acquired from a buildup test with a downhole shutin valve at the same depth as the flow rate measurement. Access to the early-time transient response enables determination of near-wellbore components of skin such as the radius and permeability of a radial damage zone around the well, or vertical permeability for a partially penetrated formation. When downhole flow rates are acquired continuously during drawdown, boundary effects that appear in the late-time response are less susceptible to superposition effects that can introduce errors in the transient data interpretation.

11-3.14 Pulse Test

The term "pulse test" (Kamal, 1983) refers to a multiwell interference test in which the active well is repeatedly pulsed, with each drawdown/buildup sequence lasting only a few hours. Although the frequency of the pulses makes the response more easily identified in the observation well(s), superposition effects may make the interpretation of the data somewhat more complex. Otherwise, the test configurations, objectives, and sensor requirements are like those of the conventional interference test.

11-3.15 Pumped Well Test

Testing in a sucker-rod pump is inhibited by the pump assembly in the tubing, which prevents downhole shutin or the lowering of a gauge to the formation depth (except a slim gauge or a permanent gauge installed with the completion). As shown in Fig. 11-23, when the well is shut in, formation fluids flow into the annulus. Thus, if pressure is sensed at the sandface, the initial response is a lengthy period of wellbore storage, often lasting for several days. In the absence of a pressure gauge measurement, an acoustic technique can be used. An acoustic pulse is regularly transmitted in the annulus. The pulse reflected off the gas/liquid interface in the annulus returns to the acoustic receiver, and is readily distinguished from reflections due to casing collars. As the liquid level rises in the annulus, its depth versus time is determined by the acoustic reflections. Knowing the annular volume per unit depth, the liquid flow rate into the annulus can be computed. Knowing the density of the liquid produced, the pressure at the sandface can be computed. Stanislav and Kabir (1990) have described how even multiphase flow from the formation can be resolved.

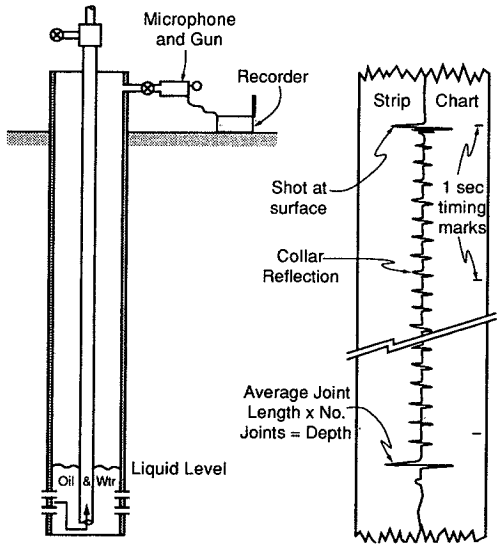

Figure 11-23
Testing in a well equipped with a rod pump.

Interpretation of continuously measured sandface pressure and flow rate is described in Joseph et al. (1988) and Ehlig-Economides et al. (1990b). The acoustic measurements are frequently sufficiently accurate for monitoring reservoir pressure and well productivity and for permeability determination.

Transient pressure data can be acquired with a downhole gauge in wells produced with an electric submersible pump (ESP). Some wells are specially completed with a Y-tool for this purpose.

11-3.16 Stabilized Flow Test

A stabilized flow test measures the bottomhole flowing pressure at one or more surface flow rates. The "flow-after-flow test" consists of a series of flow tests at a succession of surface rates. When stabilized flow conditions are established, the flowing bottomhole pressure is recorded. In gas wells this procedure is called a "back-pressure test." Such tests provide direct measurement of the inflow performance relationship, and the productivity index for single-phase reservoir flow. In addition, these measurements can be used to quantify turbulence or non-Darcy flow coefficients in producing wells, and parting pressures in water injection wells.

Pressures are usually recorded after a few hours in flow-after-flow tests. Theoretically, results of such tests apply in the fixed area inside the well drainage boundary. In practice, these measurements are frequently recorded when the well is in radial flow, which means that the test area of investigation is still expanding at the time of the stabilized flow measurement. This limitation can and should be remedied by taking care to record the pressures after the same length of time following the change of surface rate. In this way, the test area of investigation, although it is changing, will be approximately equal for each stabilized flow measurement. The strategy of making stabilized pressure measurements for flow periods of equal duration defines an "isochronal" deliverability test.

The "selective inflow performance test," published by Stewart et al. (1981), permits direct measurement of inflow performance on a layer-by-layer basis. This technique uses the same test sequence as for flow-after-flow, isochronal, or modified isochronal tests, but measures both stabilized pressure and the stabilized flow profile each time stabilized flow conditions are reached. With this strategy, the same parameters that can be determined for a single layer using conventional stabilized flow analysis can be determined for each layer in a commingled completion.

The "step rate test" is used in water injection wells to determine the parting pressure for an unpropped hydraulic fracture induced during injection.

Stabilized test data acquisition requires considerable time, and the measurements are rarely made in the appropriate stabilized condition for rigorous analysis. Further, as shown in Section 11-2, these tests cannot be used to quantify most of the well and reservoir parameters that can be determined from analysis of a transient test. For wells that flow at sufficiently high rates, the information learned from a stabilized test can be determined more efficiently from a transient test in which both pressure and flow rate are measured continuously in the wellbore.

11-3.17 Testing While Perforating

When perforating guns are run along with drillstem, tubing-conveyed, or wireline testing equipment, the well can be tested just after perforating. The presence of the pressure

gauge can also provide information that can help to monitor completion operations. The pressure gauge must be able to withstand the shock of the perforation shots. Impulse and closed chamber tests can both be conducted during perforating. This type of test is run primarily on development wells, and is usually of short duration to minimize costs. The test provides reservoir pressure, permeability, and completion skin.

11-3.18 Vertical Interference Test

The vertical interference test configuration (Burns, 1969) is designed to permit production at one depth in a well and observation at another depth. This can provide a measure of the vertical permeability in a given layer or the vertical permeability of a low-permeability bed between two higher-permeability beds. Similar measurements are possible with the multiprobe formation test shown in Fig. 11-16b, except that the vertical interference test is conducted after completion, whereas the multiprobe formation test is performed in an open hole. The vertical interference test conducted in the completed well can have an arbitrarily large radius of investigation dependent on the duration of the test. As with multiwell interference testing, some vertical interference tests are conducted using rate pulses instead of a lengthy drawdown/buildup sequence.

One practical drawback with this test type is that the pressure differential between the active and observation depths can cause leaks behind the casing or across the packer used to separate the two points in the wellbore. The test design should include provision to check for packer leaks, but leaks behind the casing are difficult to assess and can cause erroneous interpretation of the transient data.

11-4 Pressure Gauge Characteristics

Wellbore pressure measurements were introduced in the 1920s. At first, only the maximum wellbore pressure was measured using a Bourdon gauge or a device capable of recording the liquid level in the well, such as a float or a sonic echo. A Bourdon gauge consists of a helical tube that uncoils as pressure is increased on the fluid in the tube, thus lengthening the tube. This principle was used in the first continuously recording downhole gauges, introduced by Amerada. The movement of the coil is recorded by a stylus that makes a fine scratch on a metal plate with a black coating. A gauge that senses and records pressure variation without any electrical power source is termed a mechanical gauge.

Modern gauges rely on pressure transducers that convert a mechanical displacement induced by a change in pressure to an electrical signal. The electrical signal can be stored in a downhole memory device or transmitted to acquisition computers at the surface via wireline telemetry. Many types of transducers are used in electronic gauges. The principle behind a strain gauge is an electrical resistor mounted to a force-summing device such as a Bourdon tube, a diaphragm, or bellows, the displacement of which changes the length of the resistor, and thereby changes its resistance. With current flowing through the strain gauge, the resistance is calibrated to dead-weight pressure. The resistors found in strain gauges are composed of wire, foil, thin film, or semiconductor material. The sapphire gauge

was recently introduced to improve on the strain gauge technology by depositing a strain gauge bridge circuit on a box-shaped sapphire crystal. When a change in pressure alters the sapphire crystal, the circuit resistance is altered. The advantage of this technology is that the distortion and relaxation in response to changes in pressure are less complex for the crystal than for metallic substances used in conventional strain gauge transducers. The principle of a capacitance transducer is that the displacement in the force-summing element in the gauge causes a change in capacitance instead of resistance as in the case of the strain gauge.

The Hewlett-Packard gauge, introduced in 1972, offers much greater accuracy than any of the above gauges. This gauge uses a vibrating quartz crystal for the transducer. Just as a timepiece relies on the constant vibrational frequency of a resonating quartz crystal, the quartz transducer resonating frequency shifts in proportion to the stress on a crystal that is linked mechanically to a force-summing element. The disadvantage of the original Hewlett-Packard gauge was its sensitivity to temperature. Temperature-compensated quartz gauges have been recently introduced that provide correction for temperature effects by sensing the temperature with the same crystal as that which senses the pressure.

Pressure gauge characteristics are important to both test design and interpretation. Pressure gauges do not exactly reproduce the wellbore pressure, and additional errors are introduced in recording the data, whether in a downhole memory device or at the surface via wireline telemetry. Following is a list of pressure gauge characteristics and their potential effects on test results. Table 11-6 compares various gauges on the basis of some of these characteristics.

11-4.1 Range

Pressure gauges are designed to perform up to a certain maximum pressure. Outside the specified range, the gauge reading may be in error, or the gauge may be destroyed.

11-4.2 Accuracy

Accuracy refers to how close the gauge reading is to the actual pressure to be sensed. Gauges can be calibrated to provide a correct reading with a dead-weight tester. Most gauges need frequent calibration to maintain accuracy. Gauge accuracy may be specified as a maximum absolute error (e.g., ± 2 psi) or as a relative error such a ratio of the error to the gauge output, expressed as a percent.

Gauge accuracy is apparent whenever more than one gauge is run at the same time. Often, after correcting all pressures to a common datum, although trends measured by the gauges may be similar, absolute values may be different. When the differences in the gauge readings are greater than reported gauge accuracy values, one or more of the gauges may be out of calibration. It is important not to attempt to use absolute pressure measurements for applications that require accuracy beyond what is practically feasible.

Gauges can lose calibration while downhole, particularly when subject to pressure shocks that may be produced by perforating guns, or even from opening and shutting flow in the well. For high accuracy, it may be necessary to check the gauge calibration before and after the measurements.

Table 11-6

Pressure Gauge Comparison Chart, from Villa et al. (1992)

	Mechanical Gauge	Metal Strain Gauge	Capacitance Gauge	Sapphire Gauge	Standard Quartz Gauge	Compensated Quartz Gauge
Advantages	Reliable Simple Rugged	Improved resolution Fast p response Rugged and small	Greater stability Lower power requirement	Improved stability Improved accuracy Fast p, T response Good resolution Very rugged	Best resolution Best stability Best accuracy	Best resolution Best stability Best accuracy Best dynamics Higher pressure range
Disadvantages	Poor resolution Poor stability Poor accuracy Tedious to read	Moderate stability Moderate accuracy Moderate T-response time	Poor dynamic response Slower sampling Temperature and vibration sensitivity Pressure hysteresis	Moderate temperature sensitivity	Poor dynamic response High-temperature sensitivity Limited psi range Cost	More electronics Cost
Maximum range	20,000 psi 200°C	20,000 psi 175°C	20,000 psi 175°C	20,000 psi 175°C	11,000 psi 175°C	15,000 psi 175°C
Resolution (full scale and sampling time):	(analog chart)					
20 kpsi and 1 sec	~ 5 psi	0.50 psi	0.20 psi	0.20 psi	N.A.	N.A.
15 kpsi and 1 sec	~ 2 psi	0.20 psi	0.15 psi	0.10 psi	N.A.	0.003 psi
10 kpsi and 10 sec	~ 2 psi	0.10 psi	0.05 psi	0.05 psi	0.001 psi	0.001 psi
Accuracy						
20 kpsi	~ 20 psi	18 psi	N.A.	6 psi	N.A.	N.A.
15 kpsi	~ 15 psi	12 psi	~ 12 psi	5 psi	N.A.	± (0.01% of reading + 2.0 psi)
10 kpsi	~ 10 psi	10 psi	~ 10 psi	4 psi	± (0.025% of reading + 0.5 psi)	± (0.01% of reading + 2.0 psi)

Table 11-6 (Continued)

Pressure Gauge Comparison Chart, from Villa et al. (1992)

	Mechanical Gauge	Metal Strain Gauge	Capacitance Gauge	Sapphire Gauge	Standard Quartz Gauge	Compensated Quartz Gauge
Drift (10 kpsi and 150°C):						
first day	~ 5 psi	< 2–10 psi	< 3 psi	< 3 psi	< 2 psi	< 0.2 psi
first 4 days	~ 10 psi	< 3–12 psi	< 5 psi	< 5 psi	± 0.2 psi in 18 days	± 0.2 psi in 7 days
Long term	~ 5 psi/week	< 2–4 psi/week	± 1–7 psi/week	< 1 psi/week	< 0.1 psi/week	< 0.1 psi/week
Stabilization time:						
After a 5-kpsi step	10 min est.	30 sec	8 min	20 sec est.	6 min	Always within 1 psi
After a 10°C step	10 min est.	10 min	40 min	10 min	25 min	Stable within 25 sec
Relative cost	Low	Low	Medium-high	Low-medium	High	High
Notes	Note 1	Note 2	Note 1	Note 2	Note 2	Note 2

Note 1: These are estimated figures based on published literature and manufacturers' commercial data.

Note 2: These figures are based on Schlumberger laboratory and field test data.

Another characteristic, the gauge linearity, is a measure of how close the gauge calibration is to a straight line. Highly linear response implies the need for only two calibration points to specify the gauge response completely. When the gauge response is not sufficiently linear, its accuracy will decline for measured pressure values far from the calibration pressures. Also related to accuracy and calibration is the gauge repeatability, or its ability to reproduce the same reading when subjected to the same conditions. This is tested by running two successive calibration cycles. Some gauges exhibit hysteresis; that is, the gauge response is different when calibrated with increasing pressures than with decreasing pressures.

11-4.3 Resolution

Resolution or precision refers to what minimum change in pressure can be sensed by the gauge and ranges from ± 0.01 psi for high-resolution gauges to ± 2 psi for some mechanical gauges. The gauge sensitivity is a ratio of the change in transducer output to a change in pressure.

The variation in the pressure transient response should be large compared to the gauge resolution. The limits of gauge resolution are more evident in data sampled at a high rate, such as that shown in Fig. 11-24. The stair-step appearance results as the gauge reports discrete values approximating the actual signal. The quality of the data can be improved by filtering out the high-frequency variation in the data, as shown by the dotted line. The pressure variation between any two times during the radial flow regime can be predicted for a given test design with the following equation:

$$\Delta p = \pm m \log\left(\frac{t_2}{t_1}\right) \tag{11-17}$$

where m is computed using the equation in Table 11-3a with the design values for Δq, B, μ, and h, and assumed values for k. The test simulation described in Section 11-5.3 predicts the expected pressure variation, so that a gauge with sufficient precision can be selected that will avoid this kind of response. Alternatively, an increase in the flow rate change, Δq, may increase the pressure change, Δp, sufficiently to exceed the gauge resolution.

Sometimes, low precision in pressure data is a result of how the data are acquired, not the resolution of the gauge itself. Since usually the electronic gauge response is digitized, an insufficient number of bits allotted for wireline telemetry or for downhole data storage can reduce the resolution below what the gauge can deliver.

11-4.4 Response Time

Response time refers to the length of time required for the gauge to indicate the pressure following a step change. For a large step, gauges may require from a few seconds to a few minutes. The response time for quartz gauges is lengthened due to temperature sensitivity.

There are two sources of gauge errors associated with temperatures. First, some gauges register a pressure change when, in reality, only temperature has changed while

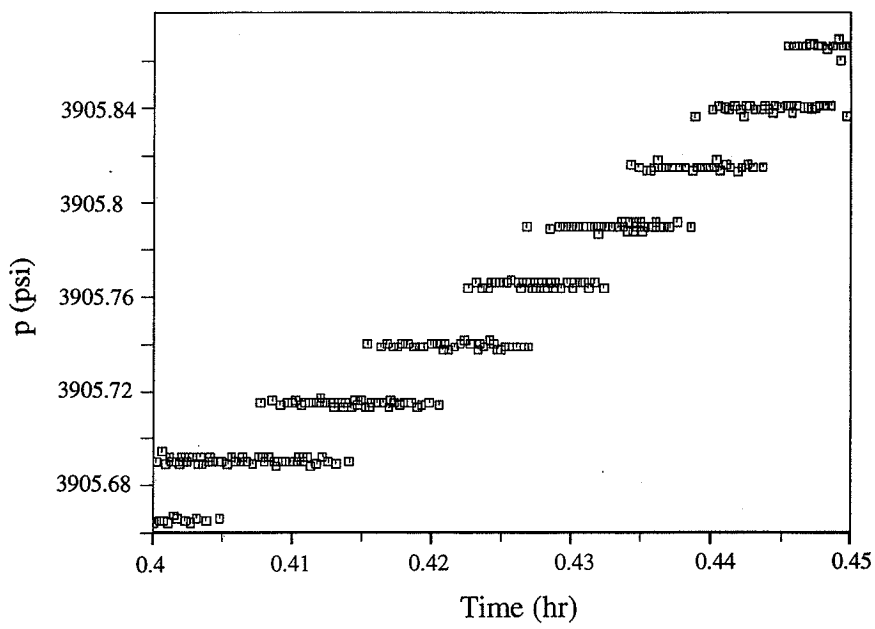

Figure 11-24
Transient data with pressure variation less than the gauge resolution.

pressure remained constant. Second, the thermodynamic properties of the gauge imply a temperature change associated with any pressure change. If the gauge could somehow be isolated from the surrounding temperature, the first source of temperature error could be eliminated. However, the second source of temperature change can never be eliminated completely. Hence, some gauges have built-in temperature sensors, and the pressure response is compensated by correcting for the known behavior of the temperature-related errors. In quartz crystal gauges, the effectiveness of the temperature compensation was constrained by the differences in temperature between the locations of the pressure and temperature sensors. The latest technology has packaged both sensors in the same crystal, eliminating a lag in the temperature compensation that previously degraded considerably the quartz gauge response time in variable temperature conditions.

Errors in pressure measurement associated with temperature variation are most evident in gas well transient tests. Frequently, in such wells, once wellbore storage has diminished, the variation in pressure associated with the reservoir response is small due to the high mobility of gas, even for reservoirs with moderately low permeability. This,

coupled with the increase or decrease in temperature associated with gas compression or expansion, results in temperature-caused errors that can dominate the pressure response.

Temperature errors affect the early-time response most detrimentally. After an hour or so, temperature is normally stable during testing. Thus, quartz gauges favor long-term testing, such as for reservoir limits. The feasibility of near-wellbore characterization based on the early-time response is dependent on appropriate gauge selection.

11-4.5 Stability

The stability of a transducer is its ability to retain its performance characteristics over time. The obvious measure of gauge stability is whether it provides the same calibration from one time to another. Gauge calibration should be updated periodically to maintain high accuracy.

A problem associated with transducer stability is the phenomenon of gauge drift. The calibration for mechanical gauges and strain gauge transducers is known to drift over time. The magnitude of gauge drift ranges from less than 0.1 psi/d for quartz gauges to 1.5 psi/d for strain gauges to 2 psi/d for capacitance gauges. Since the drift represents a continuous change in the gauge response, if its magnitude is comparable to the pressure variation being measured, the interpreted response may be more representative of gauge characteristics than reservoir characteristics. This problem is important for reservoir limit testing in high-mobility reservoirs. Because early-time pressure variations are normally well in excess of gauge drift, near-wellbore characterization is not affected by this potential source of error.

11-4.6 Sampling Rate

The highest data rate seen in most tests is one pressure sample per second, and this is common in data acquired at the surface in real time, e.g., during testing. Data recorded in a downhole memory device may be sampled at a lower rate in order to be able to record data over a long period of time without expending the memory capacity. Since the analog response from a mechanical gauge is digitized manually, it is difficult to read the data at intervals of less than 1 min.

In reality, since the response patterns in pressure transient data are viewed as a function of the logarithm of elapsed time, a logarithmic variation in sampling rate is implied. Completion and near-wellbore characterization require enough data in the first few minutes to define the transient trends, while the data usually associated with radial, linear, bilinear, pseudo-radial, or boundary-limit flow regimes are often sufficiently defined with data sampled once an hour, or even once a day. Formation tests, typically lasting only a few minutes, require a high sampling rate. The net result is that most tests have a surplus of data.

For test design, the main issue is to ensure that the sampling rate is sufficiently high to provide adequate representation of the transient response sought in the test objective. Modern downhole recording equipment can be programmed to achieve a variable sampling rate that enables accurate representation of the early-time response. However, the success of this technique relies on execution of the test according to plan. Some downhole processors

are capable of filtering the recorded response to include only those changes that exceed a certain rate of pressure variation or other related criteria.

11-4.7 Shock Resistance

Testing while perforating or stimulating puts additional demands on a gauge. The pressure shock that may be associated with these operations may render a gauge inoperable or may at least affect its calibration. In general, the more rugged gauges do not employ the most accurate transducer technology.

11-5 Test Design

Having addressed many of the selections available to the test design, this section suggests ways to facilitate the decision-making process. Figure 11-25 suggests how to organize the main considerations in test design.

11-5.1 Defining the Test Interval

The first step in test design is to determine what is being tested. This requires a look at external data about the formation, derived mainly from openhole log data and completion information. Seeking this information before testing helps one to develop realistic test objectives and ensures that it is available when the transient data are interpreted. This, in turn, may enable the interpreter to quantify additional near-well features or to detect more distant heterogeneities, and it will help to avoid interpretation conclusions that are inconsistent with external data.

Using the logs, the hydrocarbon-bearing interval can be organized into flow units based on expected fluid flow behavior. A flow unit is a rock volume with identifiable internal fluid flow characteristics (including heterogeneity or anisotropy) that can be modeled, and with known or hypothesized boundary shape and behavior. Flow unit boundaries can include barriers such as faults, nonconformities, and impermeable beds, communication with another flow unit such as a partially sealing fault or a leaking shale bed, and fluid contacts (gas-oil, water-oil, gas-water). Since different flow units have different permeabilities, mechanical properties, boundaries, and perhaps reservoir drive mechanisms, they should be tested separately to provide the most meaningful results.

A geologist may be able to estimate areal extent and continuity of various flow units based on the understanding of their likely depositional, stratigraphic, or structural interrelationships. Seismic data may suggest the location of the areal flow unit limits and the geometry of the bedding surface. A borehole image derived from televiewer, resistivity, or core photographs can be particularly helpful for defining a vertical flow unit partition and detecting a likelihood of permeability anisotropy due to natural fractures or laminations as in Fig. 11-26.

For well testing, the completion is a major factor in what is observed in the transient data, and it controls which flow units are tested. Accounting for known information about the completion enables more realistic expectations in the test design.

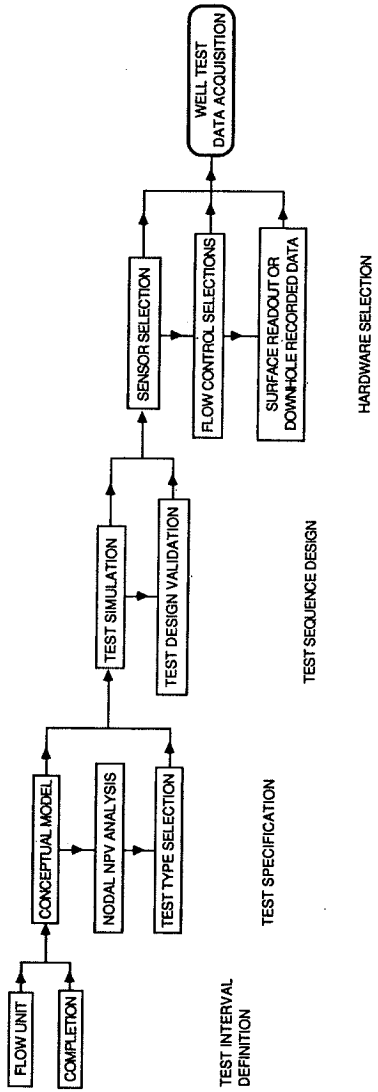

Figure 11-25
Test design strategy.

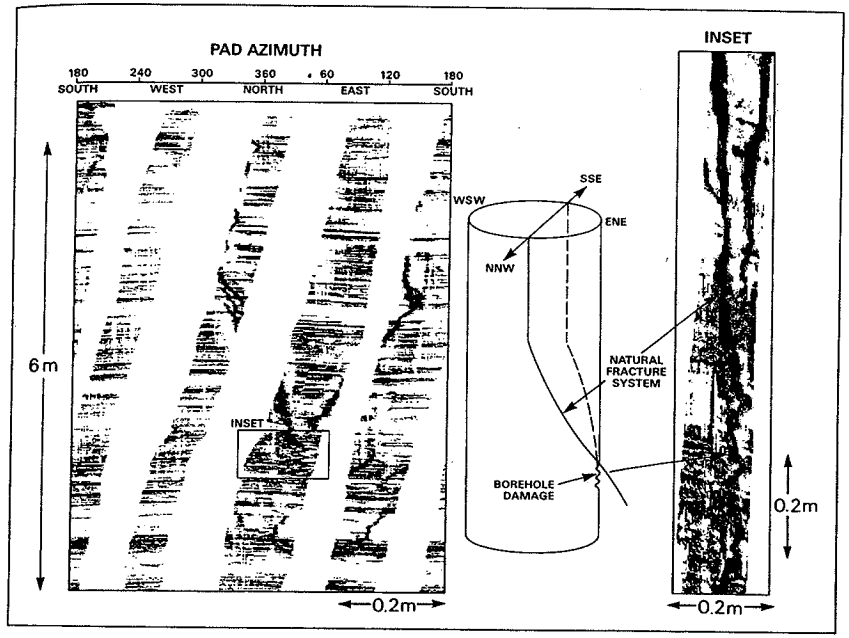

Figure 11-26
Borehole image showing natural and drilling-induced fractures in a laminated carbonate formation. (*From Schlumberger, 1986a.*)

The internal characteristics of the flow unit to be tested, its expected vertical and areal delineations, and reservoir drive mechanisms that may be visible in transient data, coupled with an anticipated or actual completion or stimulation geometry, define a conceptual model for each test interval.

11-5.2 Test Specification

The essential considerations in the test specification step are to define objectives and to select a test type or technique. The conceptual model for the test interval can help indicate what are the unquantified parameters that a transient test or a production log survey might provide. Further, coupled systems and net present value economic analyses may demonstrate the cost effectiveness of testing for parameters required to optimize the completion, or stimulation design can use the same model. If no parameters are identified as economically essential test objectives, the merits of performing measurements during the

completion and/or stimulation procedure should be explored as inexpensive means for acquiring additional data about the formation that may be useful for reservoir characterization or posttreatment productivity evaluation.

11-5.3 Test Sequence

With a conceptual model or models of what the transient test may encounter, clear objectives, and a selected test type, the test can be simulated under various possible test sequences using modern computerized well test analysis tools. When data required for the simulation can be retained in a database for subsequent interpretation of the test, this is a useful exercise that is not time consuming. When presented as a log-log diagnostic plot, the simulated test data reveal whether patterns sensitive to parameters sought in the test objectives are present, masked by wellbore storage or requiring a longer test duration. Sometimes an alternative test design can greatly increase what can be expected from the test.

When a test is conducted without surface readout, many or all of the steps in the test sequence must be planned in advance. Some downhole recorders can be programmed to increase the sampling rate at a predetermined elapsed time after the start of the test sequence, so that data are sampled adequately in early time. To conserve downhole memory, such devices can even be programmed not to acquire any data during certain periods, such as during cleanup of the well, or when running the equipment in and out of the hole. In such cases, the test is often programmed to follow certain standard procedures, but often the program can be altered if necessary.

The three main factors to consider are flow period duration(s), test initiation, and the magnitude and direction of planned surface rate changes.

Flow period duration(s). Even with surface readout, it is recommended that one establish a plan before going to the well site and try to stick to the plan if possible. The test plan can optimized to achieve certain objectives when it has been laid out in advance. One useful step is to simulate the test using whatever parameters are known and estimating the others. By varying unknown values, the sensitivity to these values of the length of various flow regimes of interest can be evaluated. For example, if determination of vertical permeability from a partially penetrated formation is sought from the test, the necessity for downhole shutin or downhole flow rate measurement is readily justified with a test simulation. Further, if determination of horizontal permeability is also desired from the same transient test, a family of simulations can be generated for the known total thickness and the known penetration ratio and for various values of vertical and horizontal permeability values within an expected range. In this way, if determining the horizontal permeability within an acceptable transient duration is judged to be feasible, a sufficient test length can be planned that ensures the establishment of the essential radial flow regime. This discussion applies for any sort of test objective.

Sometimes daylight is a factor in planning a test sequence. On land, changes of rate or the onset of a buildup frequently must be planned during daylight hours. Additionally, it is not an unusual requirement that the entire test sequence must be completed during one day. Such constraints can greatly inhibit the feasibility of certain test objectives.

Tests run with continuous surface readout of acquired transient data permit examination during testing of the transient data, termed real-time test validation. Barring other constraints, the test can be terminated as soon as the required data have been acquired or can be extended if necessary. However, it is important to remember that the flow regimes of interest are established with respect to the logarithm of elapsed time. Hence, if radial flow begins after 4 hr, the test must continue for two to three times this duration (e.g., 10–12 hr) to provide a well-defined radial flow regime. If, because of wellbore storage, radial flow is not visible for more than 10 hr, the test must be continued for 20 to 30 h. In each of these cases, only about one-half a log cycle of radial flow will be developed.

One purpose of test design simulation is to anticipate when a longer test is or may be needed. Table 11-7 provides equations that can be used to estimate the time required

Table 11-7a

Flow Regime Durations for Test Design[a]

Time Mark	Expression
End of wellbore storage for drawdown or injection for well with no vertical fracture and homogeneous reservoir without natural fractures	$\alpha_w(60+3.5s)\frac{\mu C}{kh}$, where $C=\frac{V_u}{(\rho g/\alpha_l g_c)}$ for changing liquid level, and $C=V_w c_w$ for single-phase fluid
End of wellbore storage for buildup or falloff, and same well and reservoir conditions as above	$50\,\alpha_w\frac{\mu C}{kh}e^{0.14s}$
End of linear flow to vertical fracture	$0.016\,\phi\mu c_t x_f^2/\alpha_l k$
Change of slope for sealing boundary	$\phi\mu c_t L^2/\alpha_f k$
Start of pseudo-steady state	$\phi\mu c_t A(t_{DA})_{pss}/\alpha_l k$

[a]From Earlougher (1977).

Table 11-7b

Units Conversion Factors (See Table 11-4)

Quantity	Oilfield Units	SI Units	Preferred API Standard Units	cgs Units
Wellbore volume per unit length, V_u	bbl/ft	m^2	dm^3/m	cm^2
Wellbore volume, V_w	bbl	m^3	dm^3	cm^3
Acceleration of gravity, g	32.17 ft/s^2	9.8 m/s^2	9.8 m/s^2	980 cm/s^2
Liquid density, ρ	lb_m/ft^3	kg/m^3	kg/m^3	g/cm^3
Wellbore fluid compressibility, c	psi^{-1}	Pa^{-1}	kPa^{-1}	atm^{-1}
α_w	3387	1	1/3600	1
α_l	144	1	10^4	9.869×10^5
g_c	32.17	1	1	1

for various flow regimes to develop that can be used in place of a complete test design simulation. It is usually not possible, even with continuous surface readout, to extend a test planned for less than a day to several days, because of a need to continue with other scheduled tasks. If the need to test for an extended period is justified in advance, such problems may be avoided.

Test initiation. Besides anticipating how to end a test, it is also important to plan how to begin. For formation and drillstem tests, the well has not yet been flowed, but for production tests, recent activity in the well to be tested and possibly in neighboring wells can cause superposition effects in the transient response. Further, including the well flow history in the computation of superposition time accounts for the superposition effects due to the well itself. Computations assuming infinite-acting radial flow for nearby wells that interfere with the transient response permit further correction for areal superposition effects but these computations are somewhat complex and error prone. In general, it is best to minimize these effects. Flow tests conducted with continuous downhole pressure and flow rate measurement will be less affected by interference from nearby wells than pressure buildup or falloff tests.

One procedure to consider concerns lowering the tool into the hole. Often the well cannot be flowing while the tool enters the hole. If the well was flowing just before preparing to lower the tool in a shutin condition, it may be helpful to bring the well back on production as soon as possible at about the same rate and maintain the well in stabilized flow for a long enough period of time to render negligible the effects of the brief shutin. If this is not practical, it is recommended to have the well shut in a day ahead of testing. In that case, the shutin condition is established before the beginning of the test.

Planning the rate sequence. A transient response can be initiated by either a step change in rate or a step change in pressure. Since continuous pressure measurements are usually more accurate than flow rate measurements, the step rate change is preferred. Ehlig-Economides and Ramey (1981) showed that analogous interpretation procedures can be derived for constant-pressure testing and for pressure buildup tests that follow constant-pressure production, but handling superposition is less straightforward. Whichever control mechanism is used, the main design concerns are the magnitude of each change and its direction.

The test sequence design indicates at what flow rates the test should be conducted. This aspect concerns both the vertical lift characteristics of the wellbore and the selection of sensors for transient acquisition. Using techniques in Chapter 7, predictions of downhole pressure for various surface flow rates are used to select a rate that should avoid multiphase flow in the formation. At the same time, the rate must be sufficiently high to produce a response that is well above the resolution of the pressure gauge selected. Since the test simulation indicates the expected variations in pressure with time, in some cases this exercise may suggest selection of a higher-resolution gauge. In other cases, large expected pressure variation may permit use of a lower-resolution gauge with little penalty in the final interpretation result. The same comments apply even for tests that may not flow to the surface; in that case, the cushion is designed to avoid multiphase flow but to permit sufficient pressure variation to be detectable by an available pressure gauge.

The direction of the change refers to whether the planned change will increase or decrease flow. Superposition effects are inherently more significant when the flow rate is decreased. However, superposition effects are less when the flow is stopped altogether than for a decrease from one nonzero rate to another. In general, whether the flow is increased or decreased, superposition effects are inversely related to the magnitude of the change in rate. A large rate change results in a transient response least affected by superposition effects. For reservoir limit characterization, drawdown testing with continuous downhole pressure and flow rate measurement is advantageous, because this avoids the inherent distortion due to superposition that occurs in late-time buildup data whenever there are boundary effects leading to a departure from the radial flow regime in late time . It is important to realize, however, that distortion due to superposition is absent in the buildup if the late-time flow regime is radial flow.

11-5.4 Hardware Selection

Frequently, testing hardware will be proposed by one or more service companies. The selection will be among the test string and gauge options described in this chapter and new equipment yet to be introduced. Having taken steps to carefully define the test objectives and to investigate their feasibility, informed decisions are ensured.

EXAMPLE 11-4
Test design for a horizontal well pilot hole

A horizontal well is planned in a fully developed field in which the vertical wells have reduced productivity due to water coning. Data from surrounding wells indicate good correlation of the pay zone with some intermittent shales and an oil zone thickness of 80 ft underlain by a 40-ft water zone. Average values for porosity and horizontal permeability are 0.23 and 20 md, respectively. The oil (which is highly undersaturated with a solution gas–oil ratio, R_s, equal to 40 SCF/STB) is 20°API, and reservoir temperature and pressure are 198°F and 4150 psi, respectively.

Optimum values for the horizontal well drilled length and standoff (above the oil–water contact) depend on the vertical permeability of the formation. Design a testing program to measure vertical and horizontal permeability in a 7 7/8-in.-diameter pilot hole to be drilled vertically through the pay thickness before drilling the horizontal segment.

Solution Further investigation about the formation to be tested and attempts to simulate the coning behavior in nearby wells have provided values for vertical permeability as low as 0.1 md, but most wells show values near 5 md. An explanation for the low vertical permeabilities in a well may be that it penetrates a shale lens that acts as a partial flow barrier. If so, the test for vertical permeability should avoid the shale if possible, because for a long horizontal well, the vertical permeability will probably be controlled by the sand properties.

Several of the test types described in this chapter can provide data that can be used to determine vertical permeability. The best way to determine the vertical permeability may be the multiprobe formation test, because after the pilot hole log has been interpreted on the well

site, the tool can be positioned to test the sand vertical permeability as in Fig. 11-27a. Further, if a shale is detected in the pilot hole, the tool can be positioned with the observation and sink probes above and below the shale as in Fig. 11-27b, and it may be possible to determine the vertical permeability of the shale and/or its extent. These measurements will also yield horizontal permeability near the pilot hole.

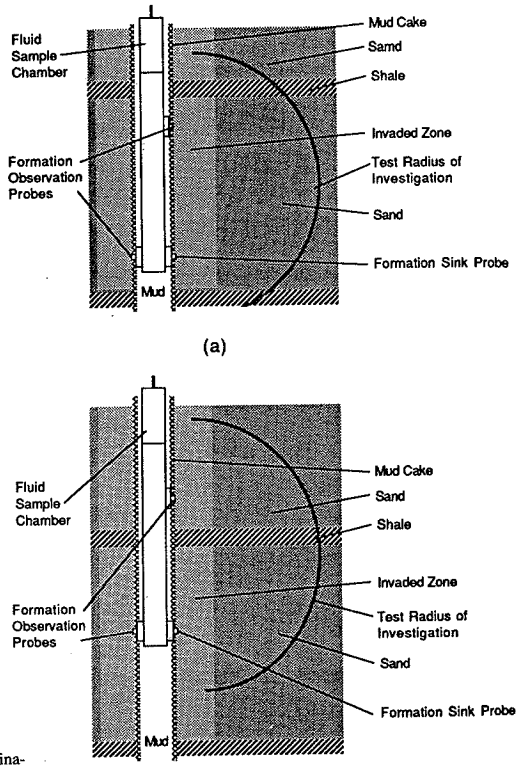

Figure 11-27
Multiprobe formation tests for determination of: (a) sand vertical permeability; (b) permeability and/or extent of shale lens.

Another possibility is to drill into the upper 10 ft of the interval. A drillstem test can be conducted in the partially drilled formation as shown in Fig. 11-28a. Then the pilot hole is drilled the rest of the way through the interval. If no shales are indicated on the log in the pilot hole for some distance below the tested interval, the vertical permeability determined from the DST should be representative of the sand. A second test should be conducted over the entire drilled hole as in Fig. 11-28b. This test will produce water and oil, and the interpretation must

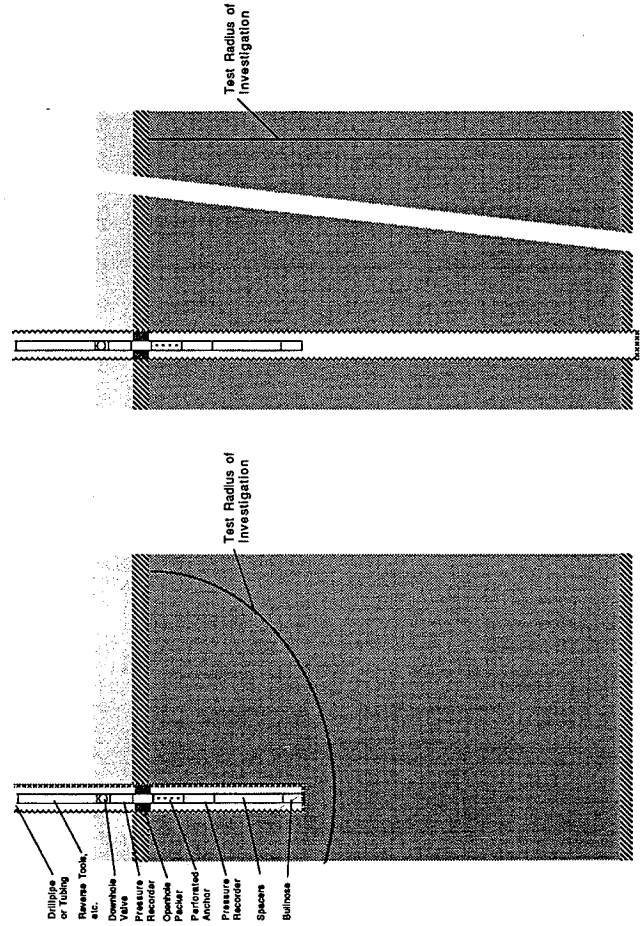

Figure 11-28
Testing in a pilot hole for a horizonal well: (a) in a partially drilled interval; (b) in a fully drilled interval.

account for the segregated flow of the two phases. The open-hole log will indicate the position of the oil–water contact required for this interpretation.

Oil viscosity, formation volume factor, and compressibility determined from correlations in Section 3–2 are 7 cp, 1.05 res bbl/STB, and 9.3×10^{-6} psi^{-1}, respectively. (The gas gravity is estimated as 0.65 from Fig. 3–2.) For a DST, assuming the shutin valve is 5 ft above the top of the formation, the wellbore storage duration is computed from the equation in Table 11-7 as

$$\begin{aligned}\text{time to end of wellbore storage} &= 50(3387)\frac{(7)(8.4\times10^{-6})}{(20)(15)}e^{0.14(0)} \\ &= 0.033 \text{ hr} = 2 \text{ min}\end{aligned} \tag{11-18}$$

where

$$V_w = \frac{\pi(0.328)^2(15)}{5.615} = 0.9 \text{ bbl} \quad \text{and} \quad C = (0.9)(9.3\times10^{-6}) = 8.4\times10^{-6} \text{ bbl/psi}$$

assuming negligible damage. The time to the end of wellbore storage for the test of the total interval is the same. A standard DST buildup of 2 hr should provide the required transient data for each of the two tests.

For the pressure sensor, from Eq. (11-16), the buildup pressure change from 1 to 2 hr is given by

$$\Delta p = \frac{(162.6)(q)(1)(1)}{20(120)}(\log 2) = 0.047q \text{ psi} \tag{11-19}$$

From Table 11-6, if the well is flowed at a rate of at least 100 STB/d, the pressure variation will be sufficient for even a low-cost gauge.

An even more conclusive way of testing in the pilot hole is shown in Fig. 11-29. Test 1 is conducted as in Fig. 11-28a, but the transient duration is extended long enough to detect radial flow. Then the pilot hole is drilled the rest of the way through the formation. Instead of testing the entire interval as in Fig. 11-28b, in test 2, packers are set 10 ft above the total well depth, again creating initial partial penetration conditions that will develop into radial flow in late time. If equal values for the vertical permeability are determined from each test, and if both tests provide the same estimate for kh from the late-time radial flow response, this suggests that the total interval flow behavior is homogenous. (The other conclusion consistent with this result is that there is a bed acting as a barrier that separates the upper and lower interval into two isolated layers each with the same kh, an unlikely possibility.)

For this case, it is important to estimate the time required to reach the radial flow response. From Chapter 5, the skin due to partial penetration exceeds 40. From Table 11-7, in the absence of an equation for estimating the end of spherical flow, the time to the end of the partial penetration and wellbore effects is estimated as

$$\text{time to end of wellbore storage} = 50(3387)\frac{(7)(8.4\times10^{-6})}{(20)(15)}e^{0.14(40)} \simeq 9 \text{ hr} \tag{11-20}$$

This implies that the buildup duration should exceed 1 day in order to establish radial flow in the transient response.

Figure 11-30 shows a test design simulation using the same parameters as the above computations. Although the wellbore storage ends at the expected time, the time to reach radial flow is more than 100 hr, which is much longer than that predicted by the computation

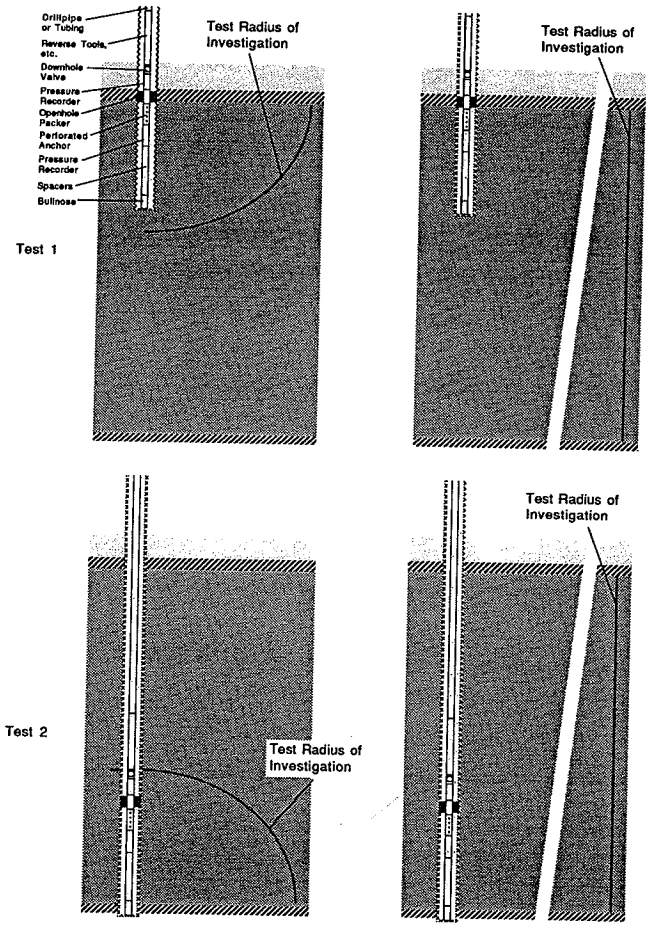

Figure 11-29
Testing in a pilot hole for a horizontal well: (a) in a partially drilled interval; (b) in fully drilled interval with packers isolating the deepest part of the hole.

in Eq. (11-19). The other curves for different penetration values show that greater penetration does not reduce the time to the start of radial flow. Hence, the simulation suggests that the test in Fig. 11-29 is not attractive for this reservoir.

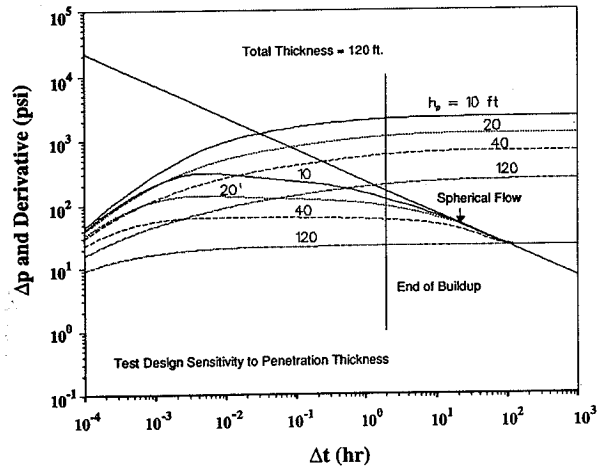

Figure 11-30
Test design simulation showing sensitivity of transient test response in a partially penetrated formation to penetration thickness (Example 11-4).

Figure 11-30 also shows that the test duration required to identify the spherical flow regime exceeds 24 hr. Hence, if a short-term buildup is run according to the design in Fig. 11-28, the data must be interpreted by type curve matching. Fortunately, as shown in Fig. 11-31, the transient response is highly sensitive to the vertical permeability, and thus, type curve matching should provide an accurate estimate for vertical permeability with data from a 2 hr buildup.

In this case, the test design simulation was highly instructive. In general, test design sensitivity studies like those in Figs. 11-30 and 11-31 are more reliable than computations based on the equations in Table 11-7, except for the simple case of a fully completed well in an unbounded homogeneous reservoir. ◇

EXAMPLE 11-5
Test design for a pumped well

Well F, in a 40-acre spacing, was hydraulically fractured 3 years ago. The treatment was designed to create a 500-ft fracture half-length. A sucker-rod pump was installed with a permanent downhole mechanical gauge attached to the tubing annulus and wireline strapped to the tubing after the stimulation treatment. The well produced at an average of 150 STB/d for 8 months, and then declined to an average rate of 90 STB/d up to the present. A recent reading from the permanent gauge gave a bottomhole flowing pressure of 1250 psi.

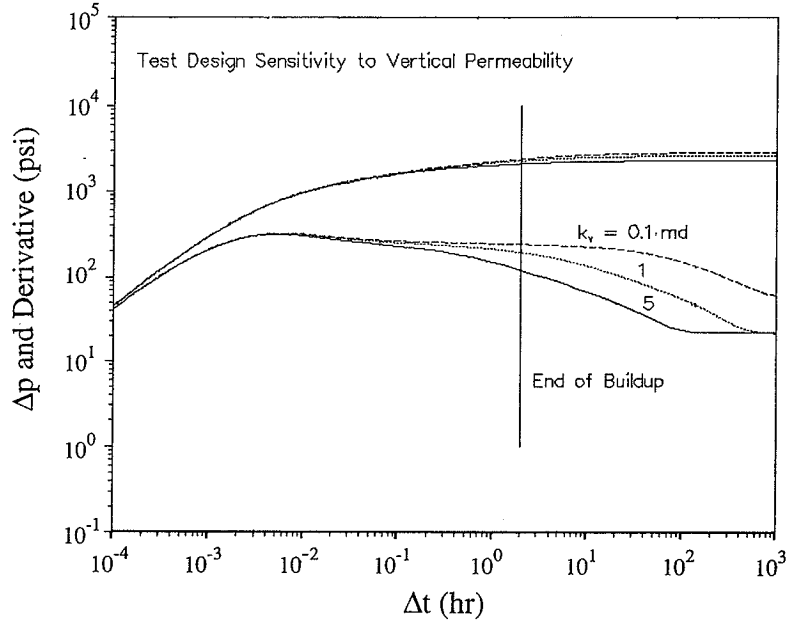

Figure 11-31
Test design simulation showing sensitivity of transient test response in a partially penetrated formation to vertical permeability (Example 11-4).

The core-derived formation porosity and permeability are 0.12 and 2.5 md, respectively.The net pay thickness is 47 ft in a laminated sand shale sequence of 63 ft. The fluids produced are oil and water, with a 60% water cut. Oil viscosity and compressibility are 1 cp and 10^{-5} psi^{-1}, respectively. The formation volume factor is assumed to be 1 res bbl/STB.

Design a test for this well.

Solution The first step is to evaluate known information about the reservoir and the well completion. The thickness of the sand and shale laminations is not indicated, but knowing the total interval thickness is 63 ft, and the net pay is about 75%, we may guess that sand beds average about 3 ft and shales 1 ft, and that the core permeability represented the permeability of the sand. More information about this interval and the core analysis would be helpful.

The productivity index is useful for evaluating known information about the well completion. The computed productivity index for the well is

$$J = \frac{(2.5)(47)}{(141.2)(1)(1)\{\ln[(0.472)(745)/0.3] - 6.7\}} = 2.27 \text{ psi/STB/d} \qquad (11\text{-}21)$$

assuming that the hydraulic fracture has infinite conductivity. In the above computation, the drainage radius is computed as

$$r_e = \sqrt{\frac{(40)(43{,}560)}{\pi}} = 745 \text{ ft} \tag{11-22}$$

and the skin was computed using Eq. (11-14). The assumption of an infinite-conductivity fracture provides an upper limit to the ideal productivity index. A finite-conductivity fracture providing a negative skin effect of -6 results in a productivity index of 0.78 psi/STB/d. [The small change in skin has an enormous impact on the productivity index because the effective wellbore radius resulting from the vertical fracture is nearly as large as the product (0.472)(745), making this term approach zero in the denominator.]

Without the hydraulic fracture and with negligible damage, the ideal productivity index for this well would be 0.12 psi/STB/d. The actual productivity index for the well is

$$J_{\text{actual}} = \frac{90}{650} = 0.14 \text{ psi/STB/d} \tag{11-23}$$

suggesting some stimulation, but far below the expected level.

There are other plausible explanations for the observed well performance. One possibility is that the hydraulic fracture is plugged. Even the initial flow rate after the treatment was not as large as would be expected. Further information may be available about the stimulation treatment, such as whether the flow back of the treatment fluids was adequate to clean up the fracture. If the fracture is choked, the conceptual model for flow to the well is radial.

A second possibility is that the formation permeability for the laminated sand shale sequence is lower than that derived from a core measurement in the sand. To explain a 10-fold reduction in the productivity index, the effective permeability may be only 0.25 md instead of 2.5 md. If this is the explanation for the observed behavior, the conceptual model for the test design is a hydraulically fractured well. Moreover, in this case no workover treatment or refracturing can substantially improve the productivity of the well.

A logical objective for the well test, then, is to distinguish between these possibilities. Before conducting the test, however, the questions concerning treatment fluid flow back and the nature of the sand shale sequence should be investigated, because either might resolve the stated objective without the need for a well test. Another possibility is to examine wellhead pressure and flow rate data in the manner of Chapter 18 to see whether these data can be used to characterize the fracture.

The test should be a buildup, and the conceptual models can be used to predict the necessary test duration. At 90 STB/d, if the well is shut in for 10 days, the cost of the test is (0.4)(90)(10) = 360 STB, since there is a permanent gauge in the hole. If the test determines that there is a problem with the stimulation treatment that can be corrected with a workover, the increased well performance should pay for the test in a few days.

Table 11-7 is used to estimate the required duration for the buildup. First, wellbore storage duration is computed as

$$\text{time to end of wellbore storage} = 50(3387)\frac{(1)(0.044)}{(2.5)(47)}e^{0.14(0)} > 60 \text{ hr} \tag{11-24}$$

$$= 2.5 \text{ d}$$

where

$$C = \frac{\pi(0.328^2 - 0.1875^2)/5.615}{62/144} = 0.044 \text{ bbl/psi} \tag{11-25}$$

In the above equation, the wellbore volume per unit length is computed for the annulus. As shown in Fig. 11-23, when the pump is shut off, formation fluids flow into the annulus between the tubing and the casing. This computation is for a wellbore radius of $7\frac{7}{8}$-in. and $2\frac{1}{4}$-in. tubing. If $k = 0.25$ md, the wellbore storage duration is estimated at 30 days.

If the well is fractured,

$$\text{time to end of linear flow} \geqq \frac{(0.016)(0.12)(1)(10^{-5})(500)^2}{0.0002637k} = \frac{18.2}{k} \text{ hr} \tag{11-26}$$

This is 7.3 hr if $k = 2.5$ md and more than 73 hr if $k = 0.25$ md. The above computation assumes that the fracture has effectively infinite conductivity. If not, the bilinear flow duration will be longer. These calculations imply that there is a likelihood that wellbore storage will obscure the linear or bilinear flow.

After wellbore storage and linear or bilinear flow have ended, to see at least $\frac{1}{2}$ log cycles of radial flow, the test must continue for approximately four times the time that radial flow begins. Hence a buildup of 10 to 12 days should suffice if the permeability is 2.5 md. If it is not, the hydraulic fracture behavior should appear in the transient response instead of radial flow, which will suggest that the permeability is lower than 2.5 md.

From Eq. (11-16), between 5 and 10 days,

$$\Delta p = \frac{(162.6)(90)(1)(1)}{k(47)}(\log 2) = \frac{94}{k} \text{ psi} \tag{11-27}$$

which will be from 37 to 370 psi. From Table 11-6, the drift of 10 psi per week may be sufficient to affect the analysis in late time. This possibility should be taken into account in the interpretation.

In summary, a 10- to 12-d pressure buildup has been designed to determine whether low well productivity is explained by unsuccessful stimulation or lower-than-expected formation permeability. The cost of the test is far outweighed by the opportunity cost of not improving the well productivity (if this can be done). In addition, the cost of the test is negligible compared to the cost of a workover, which may be avoided if the test shows that the performance problem cannot be corrected. ◇

REFERENCES

1. Ayoub, J. A., Bourdet, D. P., and Chauvel, Y. C., "Impulse Testing," *SPEFE*, 534–546, September 1988.
2. Beggs, H. D., and Brill, J. P., "A Study of Two-Phase Flow in Inclined Pipes," *JPT*, 607–617, May 1973.
3. Bourdet, D., Ayoub, J. A., and Pirard, Y.-M., "Use of Pressure Derivative in Well-Test Interpretation," *SPEFE*, 293–302, June 1989; *Trans. AIME* 293.
4. Burns, W. A., Jr., "New Single-Well Test for Determining Vertical Permeability," *JPT*, 743–752, June 1969.
5. Chatas, A. T., "Unsteady Spherical Flow in Petroleum Reservoirs," *SPEJ*, 102–114, June 1966.
6. Chauvel, Y. L., and Oosthoek, P., "Production Logging in Horizontal Wells: Applications and Experience to Date," SPE Paper 21094, 1990.
7. Earlougher, Robert C., Jr., *Advances in Well Test Analysis*, Society of Petroleum Engineers, Dallas, TX, 1977.
8. Economides, M. J., and Nolte, K. G., *Reservoir Stimulation*, 2nd ed., Prentice Hall, Englewood Cliffs, NJ, 1989.
9. Ehlig-Economides, C. A., "Computation of Test Area of Investigation in Nonradial Geometries", SPE Paper 25020, presented at the 1992 SPE European Petroleum Conference, Cannes, France, 1992.
10. Ehlig-Economides, C. A., Ambrose, R. W., and Joseph, J. A., "Pressure Desuperposition Technique for Improved Late-Time Diagnosis," SPE Paper 20550, 1990a.

11. Ehlig-Economides, C. A., and Economides, M. J., "Pressure Transient Analysis in an Elongated Linear Flow System," *SPEJ*, 839–847, December 1985.
12. Ehlig-Economides, C. A., Joseph, J. A., Ambrose, R. W., and Norwood, C., "A Modern Approach to Reservoir Test Interpretation," SPE Paper 19814, and *JPT*, 1554–1563, December 1990b.
13. Ehlig-Economides, C. A., and Ramey, H. J., Jr., "Pressure Buildup for Wells Produced at a Constant Pressure," *SPEJ*, 105–114, February 1981.
14. Govier, G. W., *Theory and Practice of the Testing of Gas Wells*, Energy Resources Conservation Board, Calgary, Alberta, Canada, 1975.
15. Horne, Roland N., *Modern Well Test Analysis: A Computer-Aided Approach*, Petroway, Inc., Palo Alto, CA, 1990.
16. Horner, D. R., "Pressure Build-up in Wells," *Proc. Third World Petroleum Congress*, The Hague, Sec. II, pp. 503–523, 1951.
17. Jacob, C. E., and Lohman, S. W., "Nonsteady Flow to a Well of Constant Drawdown in an Extensive Aquifer," *Trans. AGU*, 559–569, August 1952.
18. Joseph, J. A., Ehlig-Economides, C. A., and Kuchuk, F. J., "The Role of Downhole Flow and Pressure Measurements in Reservoir Testing," SPE Paper 18379, 1988.
19. Kamal, M. M., "Interference and Pulse Testing—A Review, *JPT*, 2257–2270, December 1983.
20. Kuchuk, F. J., "Applications of Convolution and Deconvolution to Transient Well Tests," *SPEFE*, 375–384, December 1990.
21. Moran, J. H., and Finklea, E. E., "Theoretical Analysis of Pressure Phenomena Associated with the Wireline Formation Tester," *JPT*, 899–908, August 1962.
22. Schlumberger Educational Services, *Formation MicroScanner* Service*, SMP-9100, Houston, TX, 1986a.
23. Schlumberger Educational Services, *Repeat Formation Tester*, SMP-9070, Houston, TX, 1986b.
24. Singh, P. K., Agarwal, R. G., and Krase, L. D., "Systematic Design and Analysis of Step-Rate Tests to Determine Formation Parting Pressure," SPE Paper 16798, 1987.
25. Stanislav, J. F., and Kabir, C. S., *Pressure Transient Analysis*, Prentice Hall, Englewood Cliffs, NJ, 1990.
26. Stewart, G., Wittmann, M. J., and Lefevre, D., "Well Performance Analysis: A Synergetic Approach to Dynamic Reservoir Description," SPE Paper 10209, 1981.
27. Vella, M., Veneruso, T., LeFoll, P., McEvoy, T., and Reiss, A., "The Nuts and Bolts of Well Testing," *Oilfield Review*, 14–27, April 1992.

PROBLEMS

11-1. Given $q = 1000$ bbl/d, $p_{wf} = 5000$ psi; $r_w = 0.3$ ft, and $\mu = 2$ cp, plot q versus p_{wf} for each of the following cases.

r_e (ft)	p (psi)	k (md)	s
1000	4500	100	0
1000	4500	100	10
1500	4500	100	0
1000	4200	100	0
1000	4200	1000	0

11-2. Data from an oil well flow-after-flow test are given in the following table:

q (bbl/d)	p_{wf} (psi)
2,170	4,598
4,340	4,196
6,510	3,794
7,590	3,592
10,850	2,989

For $\mu = 1.2$ cp, $B = 1.2$, $\frac{r}{w} = 0.32\%$ and $h = 112$ ft, determine the productivity index. Determine the missing values in the following table:

r_e (ft)	k (md)	s
1000	100	
1200		−2
	200	16

11-3. Derive the values for α_w and α_l in Table 11-3b for SI, preferred API standard, and cgs units.

11-4. For a 10,000-ft well with the following reservoir and fluid properties, compare wellbore storage duration for $k = 0.01$ md, $k = 0.1$ md, and $k = 100$ md for surface shutin: $\phi = 0.18$, $h = 96$ ft, $c_o = 3 \times 10^{-5}$ psi^{-1}, $c_t = 7 \times 10^{-6}$ psi^{-1}, $\mu_o = 2$ cp, $B_o = 1.02$ res bbl/STB, $r_w = 0.328$ ft. Repeat for downhole shutin with the valve located 8 ft above the formation top and with 35 ft of rathole below the formation bottom.

11-5. For the same well as in Problem 11-4, compare wellbore storage duration for $k = 10$ md and $s = 0$, $s = 1$, and $s = 10$ for surface and downhole shutin.

11-6. For the same well as in Problem 11-4, compute the time of the end of linear flow for $k = 0.01$ md, $k = 0.1$ md, and $k = 1$ md, for a 1200-ft fracture half-length.

11-7. An underbalance of 200 psi is planned for perforating well A. Given the following reservoir and fluid properties and an estimated value for permeability of 400 md, estimate at what rate the well will flow after the perforations are shot: $\phi = 0.26$, $h = 75$ ft, $c_o = 6 \times 10^{-5}$ psi^{-1}, $c_t = 10^{-5}$ psi^{-1}, $\mu_o = 1.2$ cp, $B_o = 1.1$ res bbl/STB, $r_w = 0.3$ ft, and $r_e = 1000$ ft.

11-8. For the same well as in Problem 11-7, estimate the wellbore storage duration and how long data can be acquired before the pressure variation decreases below the resolution of a strain gauge if the well is flowed for 5 min (assuming negligible skin). Assume the shutin valve is 10 ft above the formation top, and the rathole is 20 ft below formation bottom.

11-9. Reservoir and fluid properties for a posttreatment gas well buildup test are $r_w = 0.328$ ft, $\phi = 0.1$, $h = 84$ ft, $T_R = 175°F$, $\gamma_g = 0.709$, $\bar{\mu}_g = 0.013$ cp, $\bar{B}_g = 0.167$, $\bar{c}_t = \bar{c}_g = 0.000947\ \text{psi}^{-1}$, and $p_{wf} = 112$ psi, and the test sequence was the following:

Time (hr)	Flow Rate (MSCF/d)
12.1	0.9
14.95	0.61
17.83	1.34
18.8	0
20.6	End of test

Buildup data for this test are plotted in Fig. 11-7 and listed below.

Δt	Δp	$\Delta p'\ \Delta t$	Δt	Δp	$\Delta p'\ \Delta t$
0.003076	0.5151	0.6324	0.2110	4.793	1.859
0.01083	1.308	0.7635	0.2499	5.082	1.902
0.01375	1.495	0.7961	0.2866	5.308	1.977
0.01680	1.654	0.8293	0.5548	6.608	2.542
0.02968	2.162	1.007	0.6730	6.990	2.716
0.03426	2.308	1.063	0.7758	7.286	2.851
0.06229	3.001	1.313	0.8808	7.549	2.889
0.08732	3.334	1.431	1.044	7.889	2.887
0.09566	3.580	1.506	1.164	8.097	2.976
0.1077	3.751	1.543	1.340	8.378	3.165
0.1328	4.059	1.635	1.541	8.656	3.359
0.1555	4.306	1.702	1.758	8.928	3.473
0.1876	4.601	1.781			

If the formation permeability determined from a prefracture test is 6 md, determine $k_f w$ and estimate the fracture length. Estimate the test radius of investigation.

CHAPTER 12

Well Diagnosis with Production Logging

12-1 INTRODUCTION

Production engineers most commonly apply production logging as an aid in diagnosing the cause of poor well performance. As such, production logs can often indicate remedial action to be taken to improve well productivity. For example, if a well has begun to produce an excessive water cut compared with neighboring wells, the increased water rate may be due to channeling from another zone behind pipe, water coning, or premature breakthrough in a high-permeability zone. By running a suite of production logs that can locate channeling and measure the profile of water entry into the well, the engineer may be able to distinguish among these causes and, more important, properly plan a corrective workover, such as a cement squeeze treatment.

However, production logging is not a well diagnosis panacea and should not be applied in a vacuum; rather, it should be used as a supplement to the information gained from the well flow rate and pressure history and other well tests. In this chapter we will illustrate how production logging results can build upon other knowledge of well behavior to diagnose problem performance and assist in planning remediation.

The interpretation of production logs is not discussed here; rather, the results obtained from production logs (a well's flow profile, for example) serve as the starting point for illustrations of the application of production logging to well diagnosis. The engineer using production logging should always be mindful of the uncertainty that sometimes exists in these interpreted log results. For a thorough review of production logging practices and interpretation, the reader is referred to Hill (1990).

The chapter is organized according to the initial indicator of poor well performance or the objective of applying production logging. First, the use of production logs to diagnose low productivity is presented, followed by the evaluation of excessive gas and excessive water production. The application of production logging to well treatment planning and

evaluation is then discussed. The chapter concludes with a discussion of injection well problem diagnosis.

12-2 Abnormally Low Productivity

The cause of low productivity in a well can range from a fundamental reservoir problem to restrictions to flow in the near-wellbore vicinity or in the wellbore itself. Potential causes include lower-than-expected reservoir kh, low relative permeability to the hydrocarbon phase, formation damage, poorly penetrating or plugged perforations (or other restrictions in the completion, such as a partially plugged gravel pack), and wellbore restrictions. Here, we define a low-productivity well as one having an abnormally low productivity index (J); this is distinct from a well with a low *production rate*, as a low rate of production may be due to insufficient drawdown caused by a faulty lift mechanism or excessive pressure drop in the tubulars.

The first step, then, in evaluating a low-productivity well is to measure the productivity index. If it is found to be abnormally low (as compared with earlier in the well's life or with similar wells nearby, for example), it is then necessary to distinguish between low formation flow capacity and near-wellbore or completion restrictions to flow. This is best accomplished with a pressure transient test to measure the reservoir kh and skin factor as described in Chapter 11.

If the reservoir itself has been ruled out as the cause of low productivity, production logging can now be used to define more clearly the location and vertical extent of productivity impairment. If wellbore scale, fill in the wellbore, or casing collapse are considered possibilities, a caliper log should be run to locate wellbore restrictions. Barring any obstructions in the wellbore, production logs can then be run to measure the flow profile to determine if parts of the formation are contributing little or no flow or if the productivity is uniformly low. In this instance, the production logging results can be used to optimize remedial action.

EXAMPLE 12-1

Use of the flow profile to evaluate a damaged well

The production rate from Well A-1 in Reservoir Alpha had rapidly declined to less than half of its initial rate in a 6-month period. Estimates of the reservoir pressure and a measurement of the flowing bottomhole pressure showed that the well's PI was 50% below those of surrounding wells. A pressure buildup test was run and the skin factor found to be 20, while the kh product was near the expected value.

Production Logging Strategy and Analysis From the rapid decline and the high skin factor, near-wellbore formation damage is the likely culprit causing the well's low productivity. To help design a matrix acidizing treatment to remove the damage, temperature and spinner flowmeter logs were run to measure the flow profile. The interpreted results are shown in Fig. 12-1.

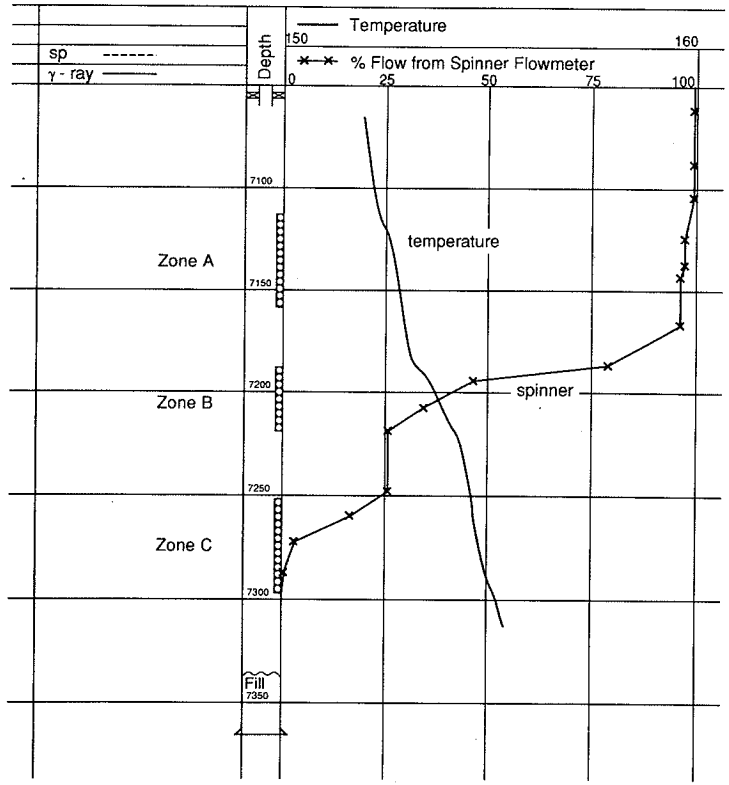

Figure 12-1

Temperature and spinner flowmeter-derived flow profile for Example 12-1.

The flow profile of the well from the spinner flowmeter log shows that zone A is producing less that 10% of the total flow, zone B is producing almost 70% of the total rate, and zone C is contributing about 25% of the production. The temperature log qualitatively confirms the interpretation of the spinner flowmeter log.

Apparently, zone A has been significantly damaged during the course of production, perhaps by fines migration near the wellbore. The production log shows that the needed treatment for this well is the selective stimulation of zone A, with perhaps a lesser amount of stimulation of zone C. Zone B does not need treatment; in fact, the flow profile shows that good diversion is needed during the stimulation treatment to minimize injection into zone B.

A matrix acidizing treatment to stimulate this well should begin with a diverter stage (ball sealers or particulate diverting agents) to prevent injection of acid into zone B. Subsequent treatment volumes and rates should be selected based on treating only zones A and C. In this example, the information from the production logs showed that the highly productive zone B should not be contacted with stimulation fluids (in oilfield parlance, "If it isn't broken, don't fix it") and allowed for the design of a smaller treatment than would otherwise be planned. ◇

12-3 Excessive Gas or Water Production

Excessive gas or water production is a common problem encountered in oil wells and can be caused by casing leaks, channeling behind the casing, preferential flow through high-permeability zones in the reservoir, or coning. Production logging can be used to locate the source of the gas or water production and to help determine the underlying cause of the unwanted production.

12-3.1 Channeling

Channeling between the casing and the formation caused by poor cement conditions [Figs. 12-2 and 12-3 (Clark and Schultz, 1956)] is sometimes the cause of high water or gas production rates. Cement bond or ultrasonic pulse-echo logs can indicate the possibility of channeling by measuring the mechanical properties of the cement behind the casing. To positively identify channeling, a production log that can respond to flow behind the casing is needed. Among the logs that can serve this purpose are temperature, radioactive tracer, and noise logs. The remedial treatment usually applied to eliminate channeling is a cement squeeze; to design a cement squeeze treatment, the location of the channel, preferably all the way to the source of the unwanted production, should be known.

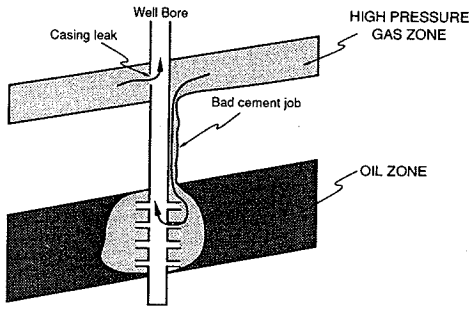

Figure 12-2
Gas channeling. (*From Clark and Schultz, 1956.*)

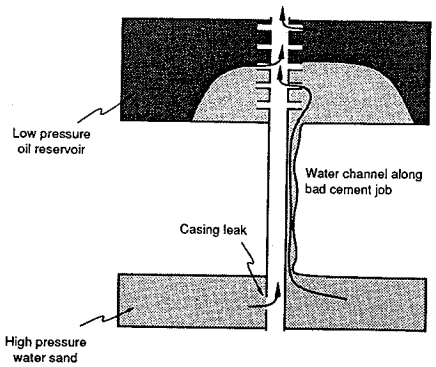

Figure 12-3
Water channeling. (*From Clark and Schultz, 1956.*)

EXAMPLE 12-2
Locating a gas channel with temperature and noise logs

The temperature and noise logs shown in Fig. 12-4 were obtained in an oil well producing at an excessively high GOR. Both logs clearly indicate that gas is being produced from an upper gas sand and channeling down to the upper perforations in the oil zone. Both logs respond to gas expanding through restrictions; the temperature log exhibits cool anomalies caused by Joule-Thomson cooling at gas expansion locations, while the noise log measures increased noise amplitude at the same locations. Thus both logs respond to gas flow at the gas source, at a restriction in the channel behind the casing, and at the location of gas entry into the wellbore.

To eliminate the excessive gas production, a cement squeeze can be performed to block the flow in the channel. This can best be accomplished by perforating near the gas source and circulating cement through the channel (Nelson, 1990).

Note that measuring the flow profile in this well would not be particularly helpful in locating the cause of high gas production or in planning corrective measures. A flow profile would show gas production into the wellbore from the upper part of the oil zone. This could be due to channeling (as was actually the case) or high gas saturation in the upper part of the oil zone, as can occur with secondary gas cap development. Only by applying logs that clearly identify channeling can the appropriate workover be planned. ◇

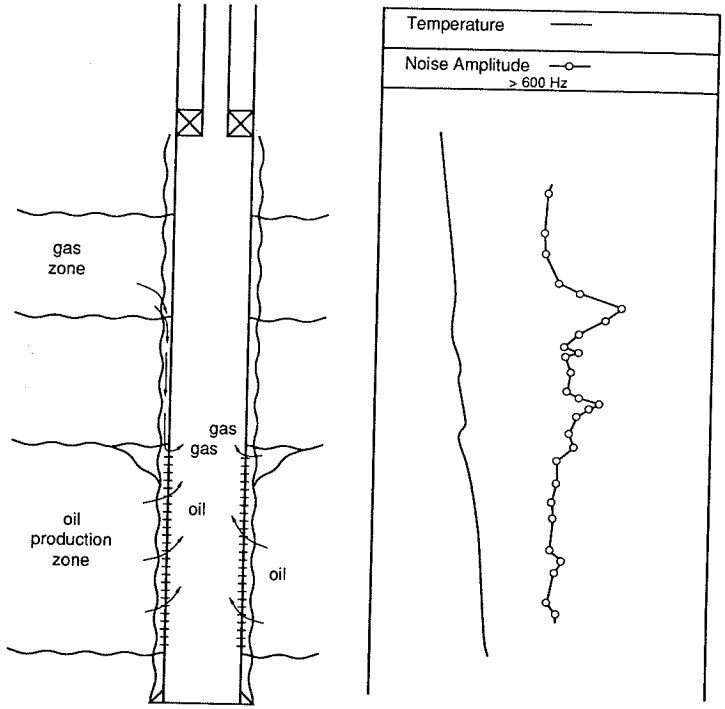

Figure 12-4
Temperature and noise logs identifying gas channeling for Example 12-2.

12-3.2 Preferential Gas or Water Flow through High-Permeability Layers

Preferential flow of water or gas through high-permeability layers (often referred to as thief zones), as illustrated in Figs. 12-5 and 12-6 (Clark and Schultz, 1956), is a common cause of high gas or water production in oil wells. Unwanted gas or water entries of this nature can sometimes be located with production logs.

Excessive water production may result from injected water in a waterflood or from water encroaching from an aquifer. An accurate flow profile of the production well can identify the location of the high-permeability zone or zones contributing the high production rate. However, the location of the water entry is not generally sufficient information to identify the cause of water production as being flow through a thief zone. Particularly if the water entry location is at the bottom of the completed interval, the water source may be

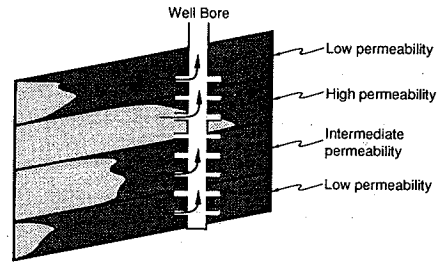

Figure 12-5
Early water breakthrough in high-permeability layers. (*From Clark and Schultz, 1956.*)

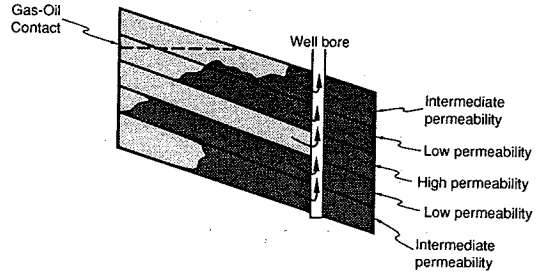

Figure 12-6
Early gas breakthrough in high-permeability layers. (*From Clark and Schultz, 1956.*)

channeling or coning from lower zones. Additional logs or tests are needed to distinguish among these possibilities (see Section 12-3.3). Because the measurement and interpretation of logs in the multiphase flow in production wells are generally less accurate (and more expensive) than those in a single-phase flow, in waterflood operations, water distribution in a reservoir is often monitored by measuring injection well profiles and assuming continuity of the reservoir layers between injectors and producers.

Excessive gas production can similarly result from flow of injected gas or from a gas cap. Again, a flow profile measured in a production well will identify the offending entry locations, or the high-permeability zones causing high gas production can be inferred from profiles measured in gas injection wells when gas is being injected into the reservoir. However, as with bottomwater production, if the gas production is from the upper part of the oil zone, it may be due to coning or channeling and further information beyond the flow profile is needed for complete diagnosis.

EXAMPLE 12-3

Excessive gas production from a thief zone

A well in Reservoir Beta is producing an unusually high gas rate, along with a lower oil rate, compared with similar wells in the field. What production logs or other tests should be run to determine whether the gas is migrating from the gas cap through a thief zone?

A prudent approach would be first to run temperature and fluid density logs. Both of these logs should locate the gas entry or entries qualitatively; in addition, the temperature log will help differentiate between production from a thief zone and gas production resulting from channeling.

Figure 12-7 shows temperature and Gradiomanometer (fluid density) logs that clearly indicate gas production from a thief zone in such a well. From the cool anomaly on the

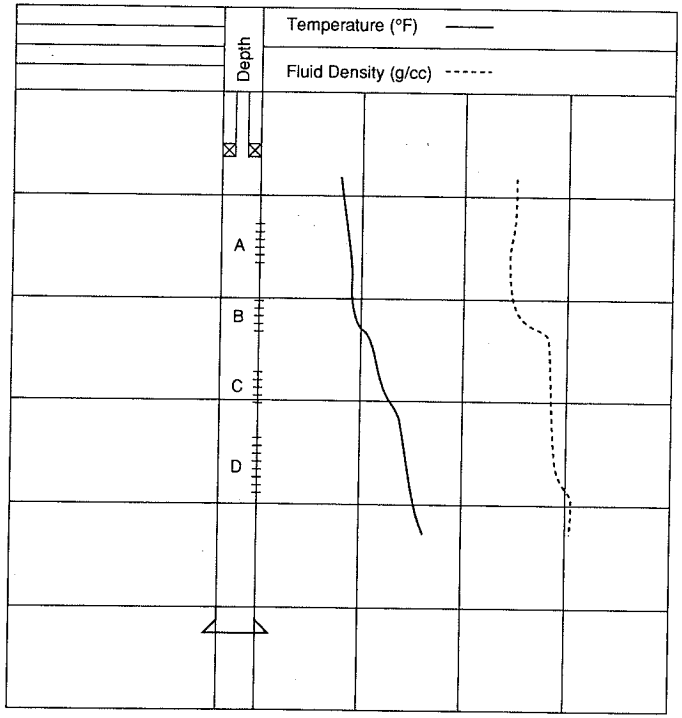

Figure 12-7

Temperature and fluid density logs locating gas entry for Example 12-3.

temperature log and the decrease in fluid density, zone B is identified as the thief zone. Since oil is being produced from zone A above this zone, as shown by the slight increase in fluid density across zone A, the gas production from zone B is not channeling or coning down to this level. The temperature log also gives no indication that channeling is occurring. ◇

12-3.3 Gas or Water Coning

Gas or water coning, illustrated in Figs. 12-8 and 12-9 (Clark and Schultz, 1956), is another possible source of excessive gas or water production. Gas coning results when a well is completed near a gas/oil contact and sufficient vertical permeability exists for gas to migrate downward to the wellbore as the pressure is drawn down around the well. Similarly, water can cone up from an underlying aquifer if vertical permeability is high enough. Discussions of the reservoir engineering aspects of coning are given by Frick and Taylor (1962) and Timmerman (1982).

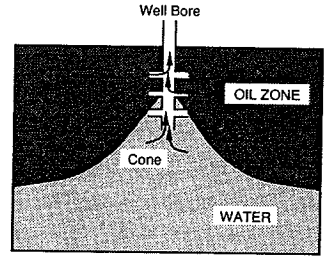

Figure 12-8

Water coning. (*From Clark and Schultz, 1956.*)

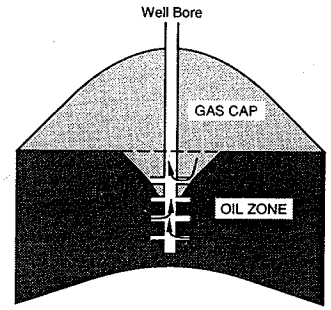

Figure 12-9

Gas coning. (*From Clark and Schultz, 1956.*)

Coning is a difficult phenomenon to identify conclusively with production logging. Consider a well that is experiencing water coning. A flow profile will indicate water production from the lowest part of the producing interval.

fluid movement in the fracture after shut-in or derivation of the fracture from intersection with the wellbore. The warm-anomaly region would then be included as part of the interpreted fractured zone.

The temperature logs run in Well D-2 after circulation of cool fluid before fracturing and after a short shut-in period after fracturing are shown in Fig. 12-10. The vertical extent of the fracture is indicated by the region where the two logs diverge, showing the fracture being located in this case from about 10,100 to about 10,300 ft. Temperature anomalies farther up the well on the postfracturing log are apparently due to variations in the thermal diffusivity of the formation.

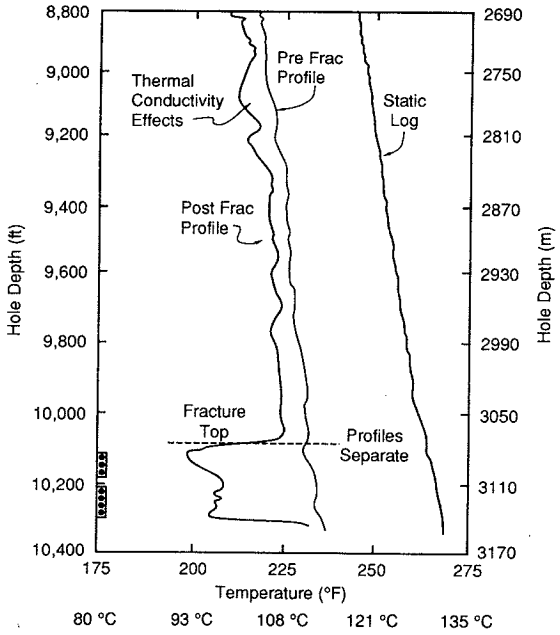

Figure 12-10
Pre- and postfracture temperature profiles for Example 12-5. (*From Dobkins, 1981.*)

Measuring Fracture Height with Radioactively Tagged Proppant A measure of propped fracture height can be obtained by radioactively tagging the final portion of the proppant, then running a postfracture γ-ray log to locate the tagged proppant. The fracture height interpreted in this manner can be misleading if the tagged proppant is not completely displaced from the wellbore or if the tagged proppant is displaced too far from the wellbore (the radiation from the tagged proppant can only be detected within about a foot from the wellbore). As with the temperature log, this method fails if the fracture plane is not coincident with the wellbore for the entire height of the fracture.

Figure 12-11 is the postfracture γ-ray survey from Well D-2 after injection of 10,000 lb of tagged proppant. The log shows tagged proppant detected from about 10,130 ft to about 10,340 ft. Comparing with the temperature log results, the top of the propped fracture is about 30 ft below the top of the created fracture. Proppant was also detected extending about 40 ft below the bottom of the fracture located by the temperature log. However, there is a good chance that the proppant detected below 10,300 ft is residual proppant in the wellbore. ◇

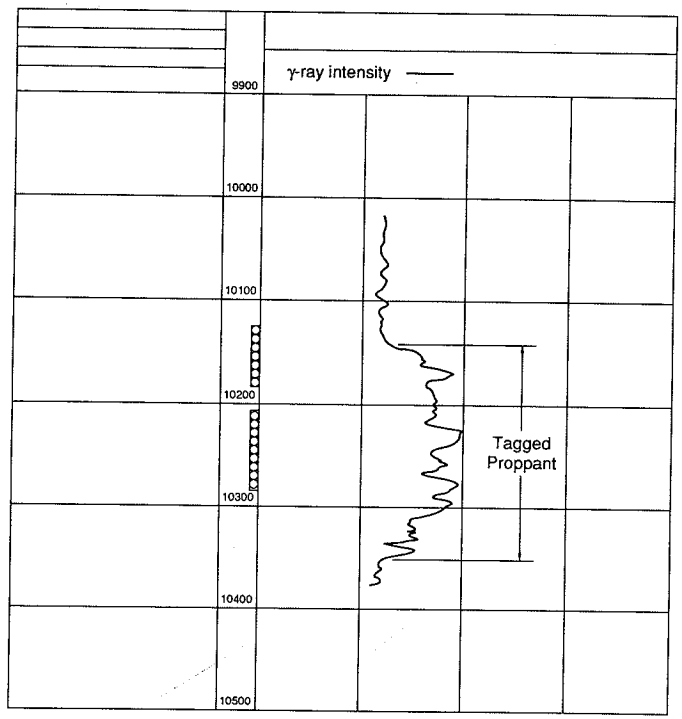

Figure 12-11
γ-Ray log after fracturing for Example 12-5.

12-5 INJECTION WELL DIAGNOSIS

Production logs are used in injection wells to monitor reservoir behavior and to evaluate problems observed with the individual injection well or the reservoir. Among

the problems that may arise are abnormally low or high injectivity, abnormal pressure or fluid level in the annulus, and low productivity or high water production in offset producers. Production logs are used to evaluate such problems in injection wells in a manner similar to that already described for production wells, that is, by measuring the amount of flow to each reservoir interval, by checking for interval isolation, by locating high-permeability zones, and by finding leaks in the well equipment.

The fundamental information sought with a production log in an injection well is the flow profile, the amount of fluid being injected into each interval. Flow profiles are measured in injection wells with temperature, radioactive tracer, and spinner flowmeter logs. A temperature log will yield a qualitative indication of the formation injection intervals, while the spinner flowmeter or radioactive tracer logs more precisely define the distribution of flow exiting the wellbore.

The flow profile shows where fluids leave the wellbore, but there is no guarantee that fluids are entering the formation at these same locations, because they may move through channels behind the casing and enter zones other than those intended. The capability of the well completion to isolate the injection zones from other formations is crucial to proper reservoir management and is thus an important property to be evaluated with production logs. To identify channeling positively, a production log that can respond to flow behind the casing is needed. Among the logs that will serve this purpose are temperature, radioactive tracer, and noise logs.

A change in rate and/or wellhead pressure often indicates a serious well or reservoir problem. Abnormally low injectivity or a marked drop in injection rate can result from formation damage around the wellbore, plugged perforations, restrictions in the casing or tubing, or scaling. An unusually high injection rate may be caused by leaks in the tubing, casing, or packer, by channeling to other zones, or by fracturing of the reservoir. Techniques that combine production logging with transient testing, such as the production log test, selective inflow performance, and the multilayer transient test provide the most complete information about abnormally high or low injectivity.

The cause of a rate change in a well is often easier to diagnose if production logs have been run periodically throughout the life of the well. For example, the flow profile in a water injection well may change gradually throughout the life of the well as the saturation distribution changes in the reservoir. Logs obtained occasionally through the life of the well would show this as being a natural progression in a waterflood. Without knowledge of this gradual change, a profile obtained several years after the start of injection might appear sufficiently different from the initial profile to lead to an erroneous conclusion that channeling had developed or that some other drastic change had taken place.

EXAMPLE 12-6
Abnormally high injection rate

In a waterflood operation in Reservoir A, water is being distributed to several injection wells from a common injection system; that is, water is supplied to all the wells at approximately the same wellhead pressure. Routine measurement of the individual well injection rates showed that one well was receiving approximately 40% more water than its neighbors. The sum of the kh products for all of the injection wells were approximately the same, and they were all completed at approximately the same depth. What are the possible causes of the abnormally high injection rate in this well, and what production logs or other tests might be run to diagnose the problem and plan remedial action?

The most likely causes of the high injection rate are leaks in the tubing, casing, or packer, or channeling to another zone. Fracturing is not a likely cause, because the similarly completed surrounding injectors have the same wellhead pressure, yet do not exhibit abnormally high rate. Another unlikely, but possible, cause is that all the surrounding injection wells are damaged to similar extents, while the high-rate well is relatively undamaged.

For this scenario, production logs that can detect leaks or channeling should be run on the high-rate injection well. A combination of a temperature and a noise log would be a good choice to attempt to locate the suspected leak or channel. ◇

EXAMPLE 12-7
Abnormally high injection rate

The temperature and noise logs shown in Fig. 12-12 were obtained in the injection well described in Example 12-6. What is the cause of the abnormally high injection rate in this well, and what corrective actions might be taken?

In a water injection well, the lowest point of water injection should be indicated clearly on the temperature log as the depth where the temperature (on both the flowing and shut-in logs) increases sharply toward the geothermal temperature. If such a sharp break does not occur, water is moving downward past the lowest depth logged.

The temperature logs in Fig. 12-12 show no sudden increase in the lower part of the well, indicating that injection water is moving downward at least to 9150 ft. Thus the excessive water injection is exiting the wellbore through a casing leak below the lowest perforations or is channeling down from the lowest perforations. A log measuring the flow profile (a spinner flowmeter or radioactive tracer log) would distinguish between these two possibilities. The noise log is not very diagnostic in this well. The small increase in noise amplitude at about 9140 ft could be due to flow through a restriction in a channel or flow through a casing leak.

To eliminate the unwanted injection, the well could be plugged back to about 9120 ft. This would plug any casing leak below this depth and would probably eliminate flow into a channel from the lowest perforations. ◇

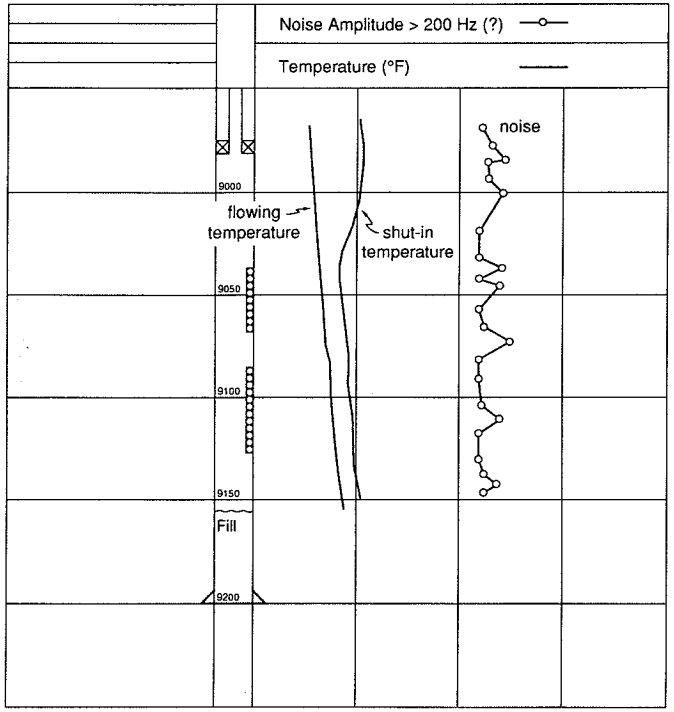

Figure 12-12
Noise and temperature logs for Example 12-6.

REFERENCES

1. Clark, N. J., and Schultz, W. P., "The Analysis of Problem Wells," *The Petroleum Engineer* (Sept. 1956) **28**: B30–B38, September 1956.
2. Dobkins, T. A., "Improved Methods to Determine Hydraulic Fracture Height," *JPT*, pp. 719–726, April 1981.
3. Frick, T. C., and Taylor, R. W., eds., *Petroleum Production Handbook, Volume II—Reservoir Engineering*, Society of Petroleum Engineers, Richardson, TX, pp. 43–46, 1962.
4. Hill, A. D., *Production Logging: Theoretical and Interpretive Elements*, Society of Petroleum Engineers Richardson, TX, 1990.
5. Muskat, Morris, *Physical Principles of Oil Production*, McGraw-Hill, New York, 1949.
6. Nelson, E. B., ed., *Well Cementing*, Elsevier, Amsterdam, 1990.
7. Timmerman, E. H., *Practical Reservoir Engineering, Volume II*, PennWell Books, Tulsa, OK, pp. 49–60, 1982.

PROBLEMS

12-1. A new zone (zone A) was perforated in a water injection well in Reservoir B. Prior to perforating the new zone, the injection rate into the well was 4500 bbl/d at 250 psi surface tubing presure; after perforating, the rate was 4700 bbl/d at 250 psi. It had been expected that the new zone would take at least 2000 bbl/d of injection water at this pressure. The old zone (zone B) in the well is located 20 ft below the new zone and has been on injection for 8 years.

It is important to know why perforating the new zone did not increase the total injection rate by the desired amount. First, list the possible causes of the apparent low injectivity into zone A. Then, describe the production logs or other tests that you would recommend to diagnose this problem, giving a priority ranking to the logs or tests recommended.

12-2. A production well in Reservoir A is producing an excessive amount of water (50% water cut). To locate the source of the excessive water production, the temperature, basket flowmeter, and fluid density logs shown (Fig. 12-13) were obtained. For this well, $B_o = 1.3$, $B_w = 1.0$, and at bottomhole conditions, $\rho_o = 0.85$ g/cm^3 and $\rho_w = 1.05$ g/cm^3. Which zone appears to be producing most of the water? From these logs, can the cause of the high water production be determined? Explain your answers.

12-3. An oil well is producing an excessive gas rate because of gas coning down from a gas cap. The well produces no water. Assuming that there are two perforated zones, sketch the temperature, noise, and fluid density logs you would expect to obtain in this well.

12-4. An injection well in a waterflood has abnormally high injectivity. Describe the production logs or other tests you would propose to diagnose the cause of the high injectivity.

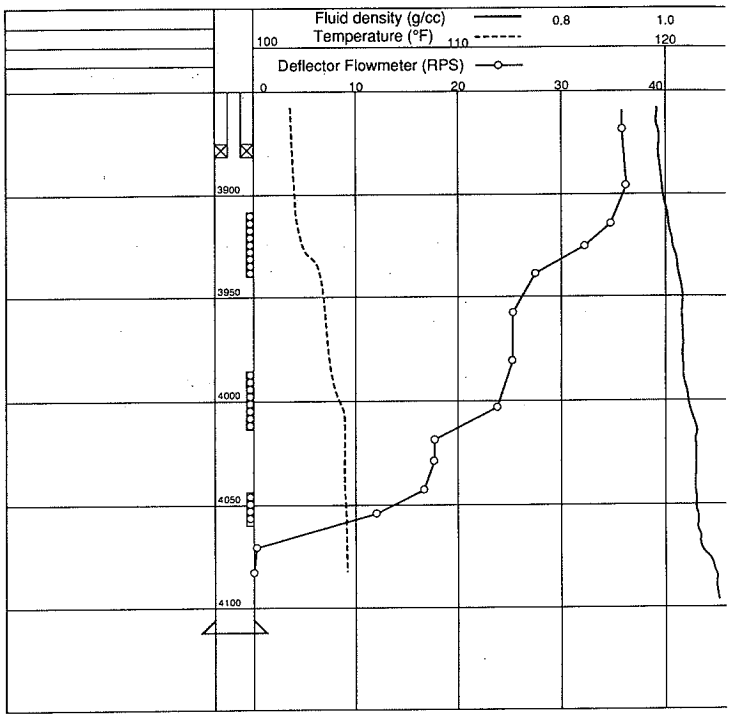

Figure 12-13
Fluid density, flowmeter, and temperature logs for Problem 12-2.

CHAPTER 13

Matrix Acidizing: Acid/Rock Interactions

13-1 INTRODUCTION

Matrix acidizing is a well stimulation technique in which an acid solution is injected into the formation in order to dissolve some of the minerals present, and hence, recover or increase the permeability in the near-wellbore vicinity. The most common acids used are hydrochloric acid (HCl), used primarily to dissolve carbonate minerals, and mixtures of hydrochloric and hydrofluoric acids (HF/HCl), for attacking silicate minerals such as clays and feldspars. Other acids, particularly some of the weak organic acids, are used in special applications. Matrix acidizing is a near-wellbore treatment, with all of the acid reacting within about a foot of the wellbore in sandstone formations, and within a few to perhaps as much as 10 ft of the wellbore in carbonates.

An acidizing treatment is called a "matrix" treatment because the acid is injected at pressures below the parting pressure of the formation, so that fractures are not created. The objective is to greatly enhance or recover the permeability very near the wellbore, rather than affect a large portion of the reservoir.

Matrix acidizing should not be confused with acid fracturing. While both types of stimulation treatments can be applied to carbonate formations and both use acids, their purpose of application and, consequently, the candidate reservoirs are often very different. Acid fracturing, resulting from the injection of fluids at pressures above the fracturing pressure of the formation, is intended to create a path of high conductivity by dissolving the walls of the fracture in a nonuniform way. Therefore, for the petroleum production engineer, acid fracturing has more in common with proppant fracturing than with matrix acidizing. Acid fracturing is sometimes used to overcome formation damage in relatively high-permeability formations. However, carbonate reservoirs of relatively low permeability may also be candidates for acid fracturing. For such reservoirs, a comparison with propped

fracturing must be done, taking into account the expected posttreatment production rate versus costs. Acid fracturing is discussed in Chapter 15.

Matrix acidizing can significantly enhance the productivity of a well when near-wellbore formation damage is present, and, conversely, is of little benefit in an undamaged well. Thus, matrix acidizing should generally be applied only when a well has a high skin effect that cannot be attributed to partial penetration, perforation efficiency, or other mechanical aspects of the completion.

EXAMPLE 13-1

The potential benefits of acidizing in damaged and undamaged wells

Assume that the well described in Appendix A has a damaged region extending 1 ft beyond the wellbore ($r_w = 0.328$ ft.) The well is on a 40-acre spacing ($r_e = 745$ ft). Calculate the ratio of the productivity index after removing this damage with acidizing to the productivity index of the damaged well for a permeability in the damaged region ranging from 5% to 100% of the undamaged reservoir permeability.

Next, assume that the well is originally undamaged and acid is used to increase the permeability in a 1-ft region around the wellbore up to 20 times the original reservoir permeability. Calculate the ratio of the stimulated productivity index to the productivity index of the undamaged well. In both cases, assume steady-state flow and no mechanical skin effects.

Solution The productivity index of a well in an undersaturated reservoir is given by Eq. (2-19). Taking the ratio of the stimulated productivity index to the damaged productivity index, noting that $s = 0$ when the damage has been removed, yields

$$\frac{J_i}{J_d} = \frac{\ln(r_e/r_w) + s}{\ln(r_e/r_w)} \tag{13-1}$$

The skin effect is related to the permeability and radius of the damaged region by Hawkins' formula [Eq. (5-4)]. Substituting for s in Eq. (13-1) gives

$$\frac{J_i}{J_d} = 1 + \left(\frac{1}{X_d} - 1\right)\frac{\ln(r_s/r_w)}{\ln(r_e/r_w)} \tag{13-2}$$

where X_d is the ratio of the damaged permeability to that of the undamaged reservoir [k_s/k in Eq. (5-4)]. Applying Eq. (13-2) for X_d ranging from 0.05 to 1, the results shown in Fig. 13-1 are obtained. For the case of severe damage, where the permeability of the damaged region is 5% of the original permeability, the skin effect of the damaged well is 26 and removal of the damage with acidizing increases the productivity index of the well by a factor of 4.5. With a damaged permeability of 20% of the original (a typical amount of damage from drilling), the original skin effect is 5.6 and complete removal of the damage increases the productivity index by about 70%.

For the case of stimulating an undamaged well, the ratio of the stimulated well productivity index to the original is

$$\frac{J_i}{J} = \frac{1}{1 + [(1/X_i) - 1][\ln(r_s/r_w)/\ln(r_e/r_w)]} \tag{13-3}$$

where X_i is the ratio of the stimulated permeability to the original permeability. Figure 13-2 is obtained by applying Eq. (13-3) for X_i ranging from 1 to 20. For this undamaged well,

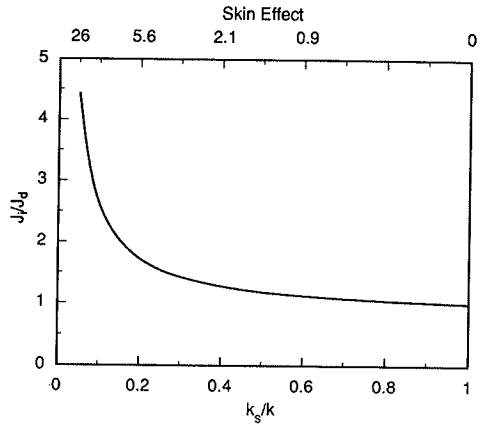

Figure 13-1
Potential productivity improvement from removing damage with acidizing.

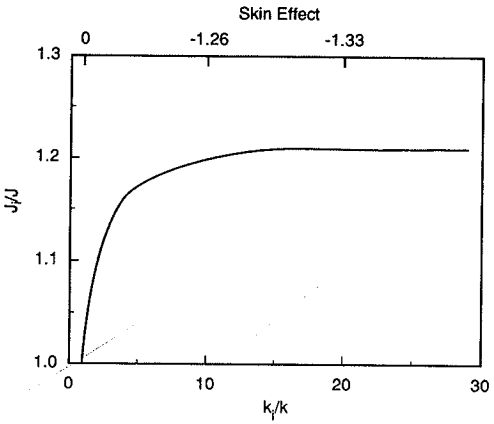

Figure 13-2
Potential productivity improvement from acidizing an undamaged well.

increasing the permeability by a factor of 20 in a 1-ft radius around the well increases the productivity index by only 21%. In fact, if the permeability in this 1-ft region were infinite (no resistance to flow), the productivity increase would be only 22%.

This example illustrates that matrix acidizing is primarily beneficial in removing damage. For lower-permeability reservoirs, significant stimulation of undamaged wells is generally possible only with hydraulic fracturing. ◇

The goal of a matrix acidizing treatment is to reduce the nonmechanical skin effect to near zero. Acidizing beyond the amount required to remove the damage is of little benefit. Among the design considerations important to matrix acidizing success are the type and concentration of acid to be used, the amount of acid needed to dissolve sufficient mineral around the wellbore, the optimal injection rate, and the placement of the acid solution.

In this chapter, the basic mechanisms by which acids and formation minerals interact are described. This includes the *stoichoimetry* of the acid-rock reactions, the amount of rock dissolved for a given amount of acid expended; the *reaction kinetics*, the rates at which acids react with various minerals; and *diffusion rates*, which control how rapidly acid is transported to the rock surfaces. With knowledge of these basic properties, design methods for sandstone and carbonate acidizing are developed in Chapters 14 and 15, respectively.

13-2 Acid-Mineral Reaction Stoichiometry

The amount of acid needed to dissolve a given amount of mineral is determined by the stoichiometry of the chemical reaction, which describes the number of moles of each species involved in the reaction. For example, the simple reaction between hydrochloric acid (HCl) and calcite ($CaCO_3$) can be written as

$$2HCl + CaCO_3 \longrightarrow CaCl_2 + CO_2 + H_2O \tag{13-4}$$

which shows that 2 moles of HCl are required to dissolve 1 mole of $CaCO_3$. The numbers 2 and 1 multiplying the species HCl and $CaCO_3$ are the stoichiometric coefficients, ν_{HCl} and ν_{CaCO_3}, for HCl and $CaCO_3$, respectively.

When hydrofluoric acid reacts with silicate minerals, numerous secondary reactions may occur that influence the overall stoichiometry of the reaction. For example, when HF reacts with quartz (SiO_2), the primary reaction is

$$4HF + SiO_2 \longleftrightarrow SiF_4 + 2H_2O \tag{13-5}$$

producing silicon tetrafluoride (SiF_4) and water. The stoichiometry of this reaction shows that 4 moles of HF are needed to consume one mole of SiO_2. However, the SiF_4 produced may also react with HF to form fluosilicic acid (H_2SiF_6) according to

$$SiF_4 + 2HF \longleftrightarrow H_2SiF_6 \tag{13-6}$$

If this secondary reaction goes to completion, 6 moles of HF, rather than 4, will be consumed to dissolve 1 mole of quartz. A complication is that the fluosilicates may exist in various forms (Bryant, 1991), so that the total amount of HF required to dissolve a given amount of quartz depends on the solution concentration.

The most common reactions involved in acidizing are summarized in Table 13-1. For the reactions between HF and silicate minerals, only the primary reactions are listed; secondary reactions will consume more HF per mole of mineral, thus changing the stoichiometry. For the reactions between HF and feldspars, for example, the primary reactions predict that 14 moles of HF are needed to consume 1 mole of feldspar. However, Schechter (1992) suggests that about 20 moles of HF are consumed for every mole of feldspar under typical acidizing conditions.

Table 13-1

Primary Chemical Reactions in Acidizing

HCl

Calcite:
$2HCl + CaCO_3 \longrightarrow CaCl_2 + CO_2 + H_2O$

Dolomite:
$4HCl + CaMg(CO_3)_2 \longrightarrow CaCl_2 + MgCl_2 + 2CO_2 + 2H_2O$

Siderite:
$2HCl + FeCO_3 \longrightarrow FeCl_2 + CO_2 + H_2O$

HF/HCl

Quartz:
$4HF + SiO_2 \longleftrightarrow SiF_4$(silicon tetrafluoride) $+ 2H_2O$
$SiF_4 + 2HF \longleftrightarrow H_2SiF_6$(fluosilicic acid)

Albite (sodium feldspar):
$NaAlSi_3O_8 + 14HF + 2H^+ \longleftrightarrow Na^+ + AlF_2^+ + 3SiF_4 + 8H_2O$

Orthoclase (potassium feldspar):
$KAlSi_3O_8 + 14HF + 2H^+ \longleftrightarrow K^+ + AlF_2^+ + 3SiF_4 + 8H_2O$

Kaolinite:
$Al_4Si_4O_{10}(OH)_8 + 24HF + 4H^+ \longleftrightarrow 4AlF_2^+ + 4SiF_4 + 18H_2O$

Montmorillonite:
$Al_4Si_8O_{20}(OH)_4 + 40HF + 4H^+ \longleftrightarrow 4AlF_2^+ + 8SiF_4 + 24H_2O$

A more convenient way to express reaction stoichiometry is with the dissolving power, introduced by Williams et al. (1979). The dissolving power expresses the amount of mineral that can be consumed by a given amount of acid on a mass or volume basis. First, the gravimetric dissolving power, β, the mass of mineral consumed by a given mass of acid, is defined as

$$\beta = \frac{\nu_{mineral} MW_{mineral}}{\nu_{acid} MW_{acid}} \tag{13-7}$$

Thus, for the reaction between 100% HCl and $CaCO_3$,

$$\beta_{100} = \frac{(1)(100.1)}{(2)(36.5)} = 1.37 \frac{lb_m\ CaCO_3}{lb_m\ HCl} \tag{13-8}$$

where the subscript 100 denotes 100% HCl. The dissolving power of any other concentration of acid is the β_{100} times the weight fraction of acid in the acid solution. For the commonly used 15 wt% HCl, $\beta_{15} = 0.15(\beta_{100}) = 0.21$ lb_m $CaCO_3/lb_m$ HCl. The stoichiometric coefficients for common acidizing reactions are found from the reaction equations in Table 13-1, while the molecular weights of the most common species are listed in Table 13-2.

Table 13-2

Molecular Weights of Species in Acidizing

Species	Molecular Weight (mass/mole)
Elements	
Hydrogen, H	1
Carbon, C	12
Oxygen, O	16
Fluorine, F	19
Sodium, Na	23
Magnesium, Mg	24.3
Aluminum, Al	27
Silicon, Si	28.1
Chlorine, Cl	35.5
Potassium, K	39.1
Calcium, Ca	40.1
Iron, Fe	55.8
Molecules	
Hydrochloric acid, HCl	36.5
Hydrofluoric acid, HF	20
Calcite, $CaCO_3$	100.1
Dolomite, $CaMg(CO_3)_2$	184.4
Siderite, $FeCO_3$	115.8
Quartz, SiO_2	60.1
Albite (sodium feldspar), $NaAlSi_3O_8$	262.3
Orthoclase (potassium feldspar), $KAlSi_3O_8$	278.4
Kaolinite, $Al_4Si_4O_{10}(OH)_8$	516.4
Montmorillonite, $Al_4Si_8O_{20}(OH)_4$	720.8

The volumetric dissolving power, X, similarly defined as the volume of mineral dissolved by a given volume of acid, is related to the gravimetric dissolving power by

$$X = \beta \frac{\rho_{\text{acid solution}}}{\rho_{\text{mineral}}} \tag{13-9}$$

A 15 wt% HCl solution has a specific gravity of about 1.07, and $CaCO_3$ has a density of 169 lb_m/ft^3. For the reaction of these species, the volumetric dissolving power is

$$X_{15} = 0.21 \left(\frac{lb_m\ CaCO_3}{lb_m\ 15\%\ HCl} \right) \left(\frac{(1.07)(62.4)(lb_m\ 15\%\ HCl)/(ft^3\ 15\%\ HCl)}{169(lb_m CaCO_3)/(ft^3 CaCO_3)} \right) \tag{13-10}$$

$$= 0.082 \frac{ft^3 CaCO_3}{ft^3\ 15\%\ HCl}$$

The dissolving powers of various acids with limestone and dolomite and for HF with quartz and albite are given in Tables 13-3 and 13-4 (Schechter, 1992).

Table 13-3

Dissolving Power of Various Acids[a]

Formulation	Acid	β_{100}	X 5%	10%	15%	30%
Limestone:	Hydrochloric (HCl)	1.37	0.026	0.053	0.082	0.175
$CaCO_3$	Formic (HCOOH)	1.09	0.020	0.041	0.062	0.129
$\rho CaCO_3 = 2.71$ g/cm^3	Acetic (CH_3COOH)	0.83	0.016	0.031	0.047	0.096
Dolomite:	Hydrochloric	1.27	0.023	0.046	0.071	0.152
$CaMg(CO_3)-2$	Formic	1.00	0.018	0.036	0.054	0.112
$\rho CaMg(CO_3)_2 = 2.87$g/cm^3	Acetic	0.77	0.014	0.027	0.041	0.083

[a]From Schechter, 1992.

Table 13-4

Dissolving Power for Hydrofluoric Acid [a, b]

Acid concentration (wt%)	Quartz(Sio_2) β	X	Albite ($NaAlSi_3O_8$) β	X
2	0.015	0.006	0.019	0.008
3	0.023	0.010	0.028	0.011
4	0.030	0.018	0.037	0.015
6	0.045	0.019	0.056	0.023
8	0.060	0.025	0.075	0.030

[a]From Schechter, 1992.

[b]β = Mass of rock dissolved/mass of acid reacted. X = Volume of rock dissolved/volume of acid reacted.

EXAMPLE 13-2
Calculating the HCl preflush volume

In sandstone acidizing treatments, a preflush of HCl is usually injected ahead of the HF/HCl mixture to dissolve the carbonate minerals and establish a low-pH environment. A sandstone with a porosity of 0.2 containing 10% (volume) calcite ($CaCO_3$) is to be acidized. If the HCl preflush is to remove all carbonates to a distance of 1 ft from the wellbore before the HF/HCl stage enters the formation, what minimum preflush volume is required (gallons of acid solution per foot of formation thickness)? The wellbore radius is 0.328 ft.

Solution The minimum volume is determined by assuming that the HCl-carbonate reaction is very fast so that the HCl reaction front is sharp (this is discussed in Chapter 14). The required preflush volume is then the volume of acid solution needed to dissolve all of the calcite to a radius of 1.328 ft plus the volume of acid solution that will be left in the pore space in this region. The volume of acid needed to consume the calcite is the volume of calcite present divided by the volumetric dissolving power:

$$\begin{aligned} V_{CaCO_3} &= \pi(r_{HCl}^2 - r_w^2)(1-\phi)x_{CaCO_3} \\ &= \pi(1.328^2 - 0.328^2)(1-0.2)(0.1) = 0.42 \text{ ft}^3/\text{ft } CaCO_3 \end{aligned} \tag{13-11}$$

$$V_{HCl,1} = \frac{V_{CaCO_3}}{X_{15}} = \frac{0.42}{0.082} = 5.01 \text{ ft}^3 \text{ HCl/ft} \tag{13-12}$$

The volume of pore space within 1 ft of the wellbore after removal of the carbonate is

$$\begin{aligned} V_p &= \pi(r_{HCl}^2 - r_w^2)[\phi + (x_{CaCO_3})(1-\phi)] \\ &= \pi(1.328^2 - 0.328^2)(0.2 + (0.1)(1-0.2)) = 1.46 \text{ ft}^3/\text{ft} \end{aligned} \tag{13-13}$$

so the total volume of HCl preflush is

$$V_{HCl} = V_{HCl,1} + V_p = [(5.01 + 1.46)\text{ft}^3/\text{ft}](7.48 \text{ gal/ft}^3) = 48 \text{ gal/ft} \tag{13-14}$$

This is a typical volume of HCl preflush used in sandstone acidizing. ◇

13-3 Acid-Mineral Reaction Kinetics

Acid-mineral reactions are termed "heterogeneous" reactions because they are reactions between species occurring at the interface between different phases, the aqueous phase acid and the solid mineral. The *kinetics* of a reaction is a description of the rate at which the chemical reaction takes place, once the reacting species have been brought into contact. The reaction between an acid and a mineral occurs when acid reaches the surface of the mineral by diffusion or convection from the bulk solution. The overall rate of acid consumption or mineral dissolution will depend on two distinct phenomena: the rate of transport of acid to the mineral surface by diffusion or convection, and the actual reaction rate on the mineral surface. Often, one of these processes will be much slower than the other. In this case, the fast process can be ignored, since it can be thought to occur in an insignificant amount of time compared with the slow process. For example, the reaction rate for the HCl-$CaCO_3$ reaction is extremely high, so the overall rate of this reaction is usually controlled by the rate of acid transport to the surface, the slower of the two processes. On the other hand, the surface reaction rates for many HF-mineral reactions are very slow compared with the acid transport rate, and the overall rate of acid consumption or mineral dissolution is reaction rate controlled. Surface reaction rates (reaction kinetics) are discussed in this section, while acid transport is detailed in Section 13-4.

A reaction rate is generally defined as the rate of appearance in the solution of the species of interest in units of moles per second. A surface reaction rate depends on the amount of surface exposed to reaction, so these reactions are expressed on a per-unit surface area manner. In general, the surface reaction rate of an aqueous species A reacting with mineral B is

$$R_A = r_A S_B \tag{13-15}$$

where R_A is the rate of appearance of A (moles/sec), r_A is the surface area-specific reaction rate of A (moles/sec-m^2), and S_B is the surface area of mineral B. When A is being consumed, the reaction rates, r_A and R_A, are negative.

The reaction rate, r_A, will generally depend on the concentrations of the reacting species. However, in the reaction between an aqueous species and a solid, the concentration of the solid can be ignored, since it will remain constant. For example, a grain of quartz has a fixed number of moles of quartz per unit volume of quartz, regardless of reactions that may be occurring on the surface of the grain. Incorporating the concentration dependence into the rate expression yields

$$-R_A = E_f C_A^{\alpha} S_B \tag{13-16}$$

where E_f is a reaction rate constant with units of moles A/[m^2-sec-(moles A/m^3)$^{\alpha}$], C_A is the concentration of species A at the reactive surface, and α is the order of the reaction, a measure of how strongly the reaction rate depends on the concentration of A. The reaction rate constant depends on temperature and sometimes on the concentration of chemical species other than A. Finally, Eq. (13-16) is written in the conventional manner for a species that is being consumed from solution, by placing a minus sign ahead of R_A, so that E_f is a positive number.

13-3.1 Laboratory Measurement of Reaction Kinetics

In order to measure the surface reaction rate of acid-mineral reactions, it is necessary to maintain a constant mineral surface area or measure its change during reaction, and to ensure that the rate of acid transport to the mineral surface is fast relative to the reaction rate. The two most common methods of obtaining these conditions are with a well-stirred slurry of mineral particles suspended in an acid solution (a stirred reactor) and with a rotating-disk apparatus (Fogler et al., 1976.) In the rotating-disk apparatus, a disk of the mineral is placed in a large container holding the acid solution. The disk is rotated rapidly, so that the acid mass transfer rate is high relative to the surface reaction rate. A third, more indirect method is by matching the core flood response to acidizing with a model of the process of flow with reaction. This approach has been common with sandstones and is discussed in Chapter 14.

13-3.2 Reactions of HCl and Weak Acids with Carbonates

Hydrochloric acid is a strong acid, meaning that when HCl is dissolved in water, the acid molecules almost completely dissociate to form hydrogen ions, H^+, and chloride ions, Cl^-. The reaction between HCl and carbonate minerals is actually a reaction of the H^+ with the mineral. With weak acids, such as acetic or formic acid, the reaction is also between H^+ and the mineral, with the added complication that the acid is not completely dissociated, thus limiting the supply of H^+ available for reaction. Because H^+ is the reactive species, the kinetics for the HCl reaction can also be used for weak acids by considering the acid dissociation equilibrium.

Lund et al. (1973, 1975) measured the kinetics of the HCl-calcite and HCl-dolomite reactions, respectively. Their results were summarized by Schechter (1992) as follows:

$$-r_{\mathrm{HCl}} = E_f C_{\mathrm{HCl}}^{\alpha} \tag{13-17}$$

$$E_f = E_f^0 \exp\left(-\frac{\Delta \mathrm{E}}{\mathrm{RT}}\right) \tag{13-18}$$

The constants α, E_f^0, and ΔE/R are given in Table 13-5. SI units are used in these expressions, so C_{HCl} has units of kg-mole/m^3 and T is in K.

Table 13-5

Constants in HCl-Mineral Reaction Kinetics Models

Mineral	α	$E_f^0 \left[\frac{\text{kg moles HCl}}{\text{m}^2\text{-s-(kg-moles HCl/m}^3\text{ acid solution)}^{\alpha}}\right]$	$\frac{\Delta E}{R}$(K)
Calcite ($CaCO_3$)	0.63	7.314×10^7	7.55×10^3
Dolomite ($CaMg(CO_3)_2$)	$\frac{6.32 \times 10^{-4} T}{1 - 1.92 \times 10^{-3} T}$	4.48×10^5	7.9×10^3

The kinetics of a weak acid-carbonate mineral reaction can be obtained from the HCl reaction kinetics by (Schechter, 1992)

$$-r_{\text{weak acid}} = E_f K_d^{\alpha/2} C_{\text{weak acid}}^{\alpha/2} \tag{13-19}$$

where K_d is the dissociation constant of the weak acid and E_f is the reaction rate constant for the HCl-mineral reaction.

13-3.3 Reactions of HF with Sandstone Minerals

Hydrofluoric acid reacts with virtually all of the many mineral constituents of sandstone. Reaction kinetics have been reported for the reactions of HF with quartz (Bergman, 1963; Hill et al., 1981), feldspars (Fogler et al., 1975) , and clays (Kline and Fogler, 1981.) These kinetic expressions can all be represented by

$$-r_{\text{mineral}} = E_f \left[1 + K(\mathrm{C_{HCl}})^{\beta}\right] C_{\mathrm{HF}}^{\alpha} \tag{13-20}$$

$$E_f = E_f^0 \exp\left(-\frac{\Delta E}{RT}\right) \tag{13-21}$$

and the constants α, β, E_f^0, and $\Delta E/R$ are given in Table 13-6.

These expressions show that the dependence on HF concentration is approximately first order ($\alpha = 1$). For the feldspar reactions, the reaction rate increases with increasing HCl concentration, even though HCl is not consumed in the reaction. Thus, HCl catalyzes the HF-feldspar reactions. Also, the reaction rates between clay minerals and HF are very similar in magnitude, except for the illite reaction, which is about two orders of magnitude slower than the others.

Example 13-3
Dissolution rate of a rotating disk of feldspar

A 2-cm.-diameter disk of albite (Na-feldspar) is immersed in a 3 wt% HF, 12 wt% HCl solution at 50°C and rotated rapidly for 1 hr. The density of the acid solution is 1.075 g/cm^3 and the density of the feldspar is 2.63 g/cm^3. If the acid concentration remains approximately constant during the exposure period, what thickness of the disk will be dissolved and what mass of HF will be consumed?

Solution The change in the number of moles of feldspar, M_f, is equal to the reaction rate, R_f, or

$$\frac{dM_f}{dt} = R_f = r_f S_f \tag{13-22}$$

The specific reaction rate, r_f, is constant, since the acid concentration is approximately constant, and, neglecting the reaction at the edge of the disk and any effects of surface roughness, the surface area of the disk is constant. Thus, Eq. (13-22) is readily integrated to yield

$$\Delta M_f = r_f s_f \Delta t \tag{13-23}$$

The surface area of the disk is π cm^2 or $\pi \times 10^{-4}$ m^2. The specific reaction rate is obtained from Eqs. (13-20) and (13-21), using the data in Table 13-6. First, the acid concentrations must be expressed in kg-moles/m^3 of solution:

$$C_{\mathrm{HF}} = \left(\frac{0.03\text{kg HF}}{\text{kg solution}}\right)\left(\frac{1075\text{ kg solution}}{\text{m}^3\text{ solution}}\right)\left(\frac{1\text{ kg-mole HF}}{20\text{ kg HF}}\right) \tag{13-24}$$

$$= 1.61\text{ kg-mole HF/m}^3\text{ solution}$$

$$C_{\mathrm{HCl}} = \left(\frac{0.12\text{ kg HCl}}{\text{kg solution}}\right)\left(\frac{1075\text{ kg solution}}{\text{m}^3\text{ solution}}\right)\left(\frac{1\text{ kg-mole HCl}}{36.5\text{ kg HCl}}\right) \tag{13-25}$$

$$= 3.53\text{kg-mole HCl/m}^3\text{ solution}$$

Then

$$K = 6.24 \times 10^{-2} \exp\left(\frac{554}{273 + 50}\right) = 0.347 \left(\frac{\text{kg moles HCl}}{\text{m}^3\text{ solution}}\right)^{-1} \tag{13-26}$$

Table 13-6

Constants in HF-Mineral Reaction Kinetic Models

Mineral	α	β	K [(kg-mole HCl/m^3)$^{-\beta}$]	E_f^0 $\left[\frac{\text{kg-mole mineral}}{\text{m}^2\text{-sec-(kg-mole HF)/m}^3\text{ acid})^\alpha}\right]$	$\Delta E/R(k)$
Quartz, SiO_2[a]	1.0	—	0	2.32×10^{-8}	1150
Orthoclase, K-Feldspar, $KAlSi_3O_8$	1.2	0.4	$5.66 \times 10^{-2} \exp(956/T)$	1.27×10^{-1}	4680
Albite, Na-Feldspar, $NaAlSi_3O_8$	1.0	1.0	$6.24 \times 10^{-2} \exp(554/T)$	9.50×10^{-3}	3930
Kaolinite, $Al_4Si_4O_{10}(OH)_8$	1.0	—	0	0.33	6540[b]
Sodium montmorillonite, $Al_4Si_8O_{20}(OH)_4$-nH_2O	1.0	—	0	0.88	6540[b]
Illite, $K_{0-2}Al_4(Al,Si)_8O_{20}(OH)_4$	1.0	—	0	2.75×10^{-2}	6540[b]
Muscovite, $KAl_2Si_3O_{10}(OH)_2$	1.0	—	0	0.49	6540[b]

[a]Based on 6 moles of HF per mole of SiO_2.

[b]Approximate values reported by Schechter (1992).

$$E_f = 9.5 \times 10^{-3} \exp\left(-\frac{3930}{273+50}\right) = 4.94 \times 10^{-8} \frac{\text{kg-mole feldspar}}{\text{m}^2\text{-sec-(kg-mole HFl / m}^3\text{ solution)}} \tag{13-27}$$

$$r_f = -4.94 \times 10^{-8}[1 + 0.347(3.53)](1.61) = -1.77 \times 10^{-7} \text{ kg-mole feldspar/m}^2 \text{ sec} \tag{13-28}$$

and the number of moles of feldspar dissolved in 1 hr is

$$\Delta M_f = (-1.77 \times 10^{-7})(\pi \times 10^{-4})(3600) = 2 \times 10^{-7} \text{ kg-moles feldspar} \tag{13-29}$$

The change in thickness of the disk is the volume dissolved divided by the surface area:

$$\Delta h = \frac{(-2 \times 10^{-7} \text{ kg-mole feldspar})(262 \text{ kg feldspar/kg-mole feldspar})(\text{m}^3 \text{ feldspar/2630 kg feldspar})}{\pi \times 10^{-4}\ m^2} = -6.3 \times 10^{-5}\ m = -0.063 \text{ mm} \tag{13-30}$$

The minus sign indicates that the surface is receding.

The mass of acid consumed is related to the mass of feldspar dissolved through the stoichiometry. Assuming that 20 moles of HF is consumed per mole of feldspar, the amount of acid consumed is

$$\Delta W_{HF} = (2 \times 10^{-7} \text{ kg moles feldspar})\left(\frac{20 \text{ kg-moles HF}}{\text{kg-mole feldspar}}\right)\left(\frac{20 \text{ kg HF}}{\text{kg-mole HF}}\right) = 8 \times 10^{-5} \text{ kg HF} = 0.08 \text{ g HF} \tag{13-31}$$

Only 0.063 mm of the feldspar surface is dissolved in 1 hr. Since feldspar is one of the faster-reacting constituents of sandstone, this indicates that the reaction rates in sandstone acidizing are quite small. However, in this example, it was assumed that the feldspar surface was smooth, making the available surface for reaction small. In sandstones composed of small grains of minerals, the specific surface areas of the grains (the surface area per unit volume) are much larger, making the overall reaction rate much larger. ◇

EXAMPLE 13-4

The relative reaction rates of sandstone minerals

A sandstone contains 85% quartz, 10% Na-feldspar, and 5% kaolinite by mass. The specific surface areas of the minerals are approximately 20 m^2/kg for the quartz and feldspar and 8000 m^2/kg for the clay [the reactive surface area of clays is less than the total surface area (Schechter, 1992)]. If this rock is contacted with a 3 wt% HF, 12 wt% HCl solution at 50°C, what proportion of the HF will initially be consumed by each of the three minerals?

Solution Per unit mass of rock, the specific surface area of each mineral is its specific surface area times the mass fraction of the mineral present in the sandstone. For example, the specific

surface area of quartz per mass of sandstone, S_q^*, is $(20\ m^2/kg)(0.85) = 17\ m^2/kg$ rock. Similarly, the specific surface areas of feldspar and kaolinite are 2 and 400 m^2/kg rock, respectively. The overall rate of reaction of HF with each mineral is

$$-R_{HF,q} = \gamma_q r_q S_q^* \tag{13-32}$$

$$-R_{HF,f} = \gamma_f r_f S_f^* \tag{13-33}$$

$$-R_{HF,k} = \gamma_k r_k S_k^* \tag{13-34}$$

where γ_i is the ratio of the stoichiometric coefficient of HF to that of mineral i ($\nu_{HF}/\nu_{\text{mineral } i}$). Obtaining the specific reaction rates with Eqs. (13-20), (13-21), and the data in Table 13-6, and using for γ, 6 moles HF/mole quartz, 20 moles HF/mole feldspar, and 24 moles HF/mole kaolinite,

$$-R_{HF,q} = 9.4 \times 10^{-8} C_{HF} \tag{13-35}$$

$$-R_{HF,f} = 4.4 \times 10^{-6} C_{HF} \tag{13-36}$$

$$-R_{HF,k} = 5.1 \times 10^{-6} C_{HF} \tag{13-37}$$

The fraction of HF expended in a particular reaction is the overall reaction rate for that mineral divided by the sum of the reaction rates, showing that 1% of the HF is reacting with quartz, 46% is reacting with feldspar, and 53% is reacting with kaolinite. This is a typical result, illustrating that the reaction rates of HF with clays and feldspars are approximately two orders of magnitude higher than that between HF and quartz. Because the clay and feldspar reaction rates are relatively high and they generally comprise a small portion of the total rock mass, they will be consumed first in sandstone acidizing. The quartz reaction becomes important in regions where most of the clay and feldspar have already been dissolved. ◇

13-3.4 Reactions of Fluosilicic Acid with Sandstone Minerals

As discussed in Section 13-2, fluosilicic acid, H_2SiF_6, is produced when HF dissolves silicate minerals, and the fluosilicic acid itself may then react with aluminosilicates. From models of core flood experiments, Bryant (1991) and da Motta et al. (1992) conclude that the reaction between fluosilicic acid and clays and feldspars is slow at room temperature, but that it is of the same order of magnitude as the HF reactions with these minerals at temperatures above 50°C. These conclusions have not been confirmed by more direct experimentation.

13-4 Acid Transport to the Mineral Surface

When the surface reaction rate is high, the overall rate of consumption of acid and dissolution of mineral will be controlled by the rate of acid transport to the mineral surfaces. This occurs most commonly with the reaction of HCl with carbonate minerals, but is possible with other reactions in acidizing, particularly at elevated temperatures. Acid is transported to the mineral surface by diffusion and by convection. The diffusional flux of acid is given by Fick's law,

$$J_y^A = D_A \frac{\partial C_A}{\partial y} \tag{13-38}$$

where J_y^A is the acid flux [moles or mass/(cm^2-sec)], D_A is the acid diffusion coefficient (cm^2/sec), and y denotes the direction of diffusion. Equation (13-38) shows that acid diffusion to the reactive surface is driven by the concentration gradient between the bulk solution and the surface. The effective diffusion coefficient for HCl has been determined by Roberts and Guin (1975) and is shown in Fig. 13-3.

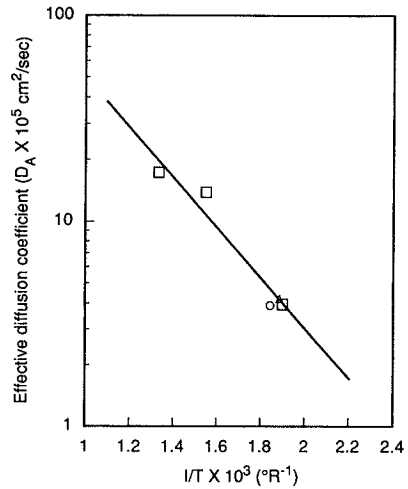

Figure 13-3
The effective diffusion coefficient of HCl. (*From Roberts and Guin, 1975.*)

In a porous medium composed of grains of rock and irregularly shaped, interconnected pore spaces, as reservoir rocks typically are, transport of acid to the mineral surfaces is likely due to both diffusion and convection. Modeling this process requires a hydrodynamic model of the flow through the pore structure, a model that is currently intractable except for a few idealized cases. Convective transport of acid to the reactive surface is more simply treated using the concept of fluid loss from a fracture or channel, as applied in hydraulic fracturing models. This application is presented in Chapter 15.

13-5 Precipitation of Acid Reaction Products

A major concern in acidizing, particularly acidizing of sandstones, is damage caused by the precipitation of acid-mineral reaction products. In acidizing of sandstone with HF, the formation of some precipitates is probably unavoidable. However, the amount of damage they cause to the well productivity depends on the amount and location of the precipitates. These factors can be controlled somewhat with proper job design.

The most common damaging precipitates that may occur in sandstone acidizing are calcium fluoride, CaF_2, colloidal silica, $Si(OH)_4$, ferric hydroxide, $Fe(OH)_3$, and asphaltene sludges.

Calcium fluoride is usually the result of the reaction of calcite with HF, according to

$$CaCO_3 + 2HF \longleftrightarrow CaF_2 + H_2O + CO_2 \tag{13-39}$$

Calcium fluoride is very insoluble, so precipitation of CaF_2 is likely if any calcite is available to react with the HF. Inclusion of an adequate HCl preflush ahead of the HF/HCl stage prevents the formation of CaF_2.

Production of some colloidal silica precipitate is probably unavoidable in sandstone acidizing. The equilibrium calculations of Walsh et al. (1982) show that there will virtually always be regions where the spent acid solution has the tendency to precipitate colloidal silica. However, laboratory core floods suggest that the precipitation is not instantaneous and in fact may occur at a fairly slow rate (Shaughnessy and Kunze, 1981.) To minimize the damage caused by colloidal silica, it is probably advantageous to inject at relatively high rates, so that the potential precipitation zone is rapidly displaced away from the wellbore. Also, spent acid should be produced back immediately after the completion of injection, since shutting in the well for even a relatively short time may allow significant silica precipitation to occur in the near-well vicinity.

When ferric ions (Fe^{3+}) are present, they can precipitate from spent acid solutions as $Fe(OH)_3$ when the pH is greater than about 2. Ferric ions may result from the dissolution of iron-bearing minerals in an oxidative environment or may derive from the dissolution of rust in the tubing by the acid solution. When a high level of ferric irons is likely in the spent acid solution, sequestering agents can be added to the acid solution to prevent the precipitation of $Fe(OH)_3$. However, Smith et al. (1969) suggest that these sequestrants be used with caution, as they may cause more damage through their own precipitation than would have been caused by the iron.

Finally, in some reservoirs, contact of the crude oil by acid can cause the formation of asphaltenic sludges. Simple bottle tests in which a sample of crude oil is mixed with the acid can indicate whether the crude has a tendency for sludge formation when contacted by acid. When sludge formation is a problem, emulsions of acid in aromatic solvents or surface-active additives have been used to prevent asphaltene precipitation (Moore et al., 1965.)

EXAMPLE 13-5

The effect of a precipitate zone on well productivity

A well with a radius of 0.328 ft in a 745-ft drainage radius has been treated with acid and all damage removed. However, 1 ft^3/ft of reservoir thickness of spent acid will form a precipitate that reduces the permeability to 10% of the original permeability. By the design of the overflush, this spent acid may be left next to the wellbore or displaced farther into the formation. Determine how the productivity of the well is influenced by the location of this zone of precipitate. The rock porosity is 0.15.

Solution When the precipitate zone is displaced away from the wellbore, there will be three zones around the well: the region between the well and the precipitate zone, where it can be assumed that the permeability is equal to the original reservoir permeability (the acid removed all damage); the precipitate zone, where the permeability is 10% of the original permeability; and the region beyond the precipitate zone, where the permeability is the original permeability of the reservoir. For steady-state radial flow with three regions in series, the productivity index is

$$J_p = \frac{h}{141.2B\mu\{[\ln(r_1/r_w)/k] + [\ln(r_2/r_1)/k_p] + [\ln(r_e/r_2)/k]\}} \tag{13-40}$$

where r_1 is the inner radius of the precipitate zone, r_2 is the outer radius of the precipitate zone, k_p is the permeability in the precipitate zone, and k is the original reservoir permeability. Dividing this equation by the equation describing the productivity index of the undamaged well and defining X_p as k_p/k yields

$$\frac{J_p}{J} = \frac{\ln(r_e/r_w)}{\ln(r_1/r_w) + (1/X_p)\ln(r_2/r_1) + \ln(r_e/r_2)} \tag{13-41}$$

Finally, since the volume of spent acid creating the precipitate zone is fixed,

$$r_2 = \sqrt{r_1^2 + \frac{V_{\text{spent acid}}}{\pi\phi}} \tag{13-42}$$

Using values of r_1 ranging from r_w to 2.5 ft., the results in Fig. 13-4 are obtained. When the precipitate is surrounding the wellbore, the productivity index of the well is less than 40% of its potential; displacing the precipitate to beyond 2 ft from the wellbore restores the PI to more than 80% of the undamaged case. ◇

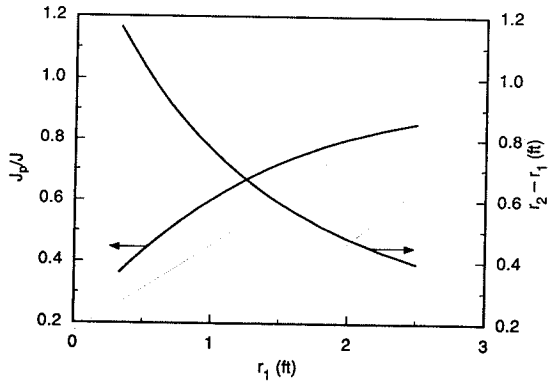

Figure 13-4
Effect of a zone of spent acid precipitate on well productivity.

REFERENCES

1. Bergman, I., "Silica Powders of Respirable Sizes IV. The Long-Term Dissolution of Silica Powders in Dilute Hydrofluoric Acid: An Anisotropic Mechanism of Dissolution for the Courser Quartz Powders," *J. Appl. Chem.*, **3**: 356–361, August 1963.
2. Bryant, S. L., "An Improved Model of Mud Acid/Sandstone Chemistry," SPE Paper 22855, 1991.
3. da Motta, E. P., Plavnik, B., Schechter, R. S., and Hill, A. D., "The Relationship between Reservoir Mineralogy and Optimum Sandstone Acid Treatment," SPE Paper 23802, 1992.
4. Fogler, H. S., Lund, K., and McCune, C. C., "Predicting the Flow and Reaction of HCl/HF Mixtures in Porous Sandstone Cores," *SPEJ*, pp. 248–260, October 1976, *Trans. AIME*, **234**.
5. Fogler, H. S., Lund, K., and McCune, C. C., "Acidization. Part 3. The Kinetics of the Dissolution of Sodium and Potassium Feldspar in HF/HCl Acid Mixtures," *Chem. Eng. Sci.*, **30** (11): 1325–1332, 1975.
6. Hill, A. D., Lindsay, D. M., Silberberg, I. H., and Schechter, R. S., "Theoretical and Experimental Studies of Sandstone Acidizing," *SPEJ*, **21**: 30–42, February 1981.
7. Kline, W. E., and Fogler, H. S., "Dissolution Kinetics: The Nature of the Particle Attack of Layered Silicates in HF," *Chem. Eng. Sci.*, **36**: 871–884, 1981.
8. Lund, K., Fogler, H. S., and McCune, C. C., "Acidization I: The Dissolution of Dolomite in Hydrochloric Acid," *Chem. Eng. Sci.*, **28**: 691, 1973.
9. Lund, K., Fogler, H. S., McCune, C. C., and Ault, J. W., "Acidization II—The Dissolution of Calcite in Hydrochloric Acid," *Chem. Eng. Sci.*, **30**: 825, 1975.
10. Moore, E. W., Crowe, C. W., and Hendrickson, A. R., "Formation, Effect, and Prevention of Asphaltene Sludges during Stimulation Treatments," *JPT*, pp. 1023–1028, September 1965.
11. Roberts, L. D., and Guin, J. A., "A New Method for Predicting Acid Penetration Distance," *SPEJ*, 277–286, August 1975.
12. Schechter, R. S., *Oil Well Stimulation*, Prentice Hall, Englewood Cliffs, NJ, 1992.
13. Shaughnessy, C. M., and Kunze, K. R., "Understanding Sandstone Acidizing Leads to Improved Field Practices," *JPT*, pp. 1196–1202, July 1981.
14. Smith, C. F., Crowe, C. W., and Nolan, T. J., III, "Secondary Deposition of Iron Compounds Following Acidizing Treatments," *JPT*, pp. 1121–29, September 1969.
15. Walsh, M. P., Lake, L. W., and Schechter, R. S., "A Description of Chemical Precipitation Mechanisms and Their Role in Formation Damage during Stimulation by Hydrofluoric Acid," *JPT*, pp. 2097–2112, September 1982.
16. Williams, B. B., Gidley, J. L., and Schechter, R. S., *Acidizing Fundamentals*, Society of Petroleum Engineers, Richardson, TX, 1979.

PROBLEMS

13-1. A well with a wellbore radius of 0.328 ft and a drainage radius of 745 ft has a perforation skin effect of 3. In addition, a damaged zone where the permeability is 10% of the original permeability extends 9 in. from the wellbore. Calculate the productivity improvement that can be obtained by removing the damage, and the skin effect before and after damage removal.

13-2. Based on the primary reactions in Table 13-1, calculate the gravimetric and volumetric dissolving powers of 3 wt% HF reacting with: (a) orthoclase feldspar; (b) kaolinite; (c) montmorillonite.

13-3. Calculate the specific reaction rate of 3 wt% HF with orthoclase feldspar at 120°F.

13-4. Determine which overall reaction rate is higher at 100°F: the reaction between 3 wt% HF and illite with a specific surface area of 4000 m^2/kg or the reaction between 3 wt% HF and albite with a specific surface area of 20 m^2/kg.

13-5. A 3 wt% HF/12 wt% HCl treatment is injected without an HCl preflush into a sandstone reservoir containing 10% $CaCO_3$. If half of the HF is consumed in reaction with $CaCO_3$ to form CaF_2, what will be the net porosity change, considering both $CaCO_3$ dissolution and CaF_2 precipitation? Assume that all $CaCO_3$ is dissolved in the region contacted by acid. The density of CaF_2 is 2.5 g/cm^3.

CHAPTER 14

Sandstone Acidizing Design

14-1 INTRODUCTION

As described in Chapter 13, matrix acidizing is a stimulation technique that is beneficial only when near-wellbore damage exists that can be removed with acid. Therefore, the first step in the planning of any matrix acidizing treatment should be a careful analysis of the cause(s) of impaired well performance. This analysis should begin with the measurement of the well skin effect. For highly deviated wells, there is a negative skin effect contribution from the extra exposure to the reservoir. A slightly positive or even zero skin effect that is obtained from a well test should be investigated. Potential recovery of a negative skin effect could greatly enhance well productivity. When a large positive skin effect is present, sources of mechanical skin (partial penetration, perforation skin, etc.) should be investigated as described in Chapter 5. If mechanical effects do not explain the flow impairment, formation damage is indicated. The well history should then be studied to determine if the damage present is amenable to removal with acid; in general, damage due to drilling mud invasion or fines migration can be successfully treated with acid.

Once acid-treatable formation damage has been identified as the cause of poor well productivity, acidizing treatment design can begin. A typical acid treatment in sandstones consists of the injection of an HCl preflush, with 50 gal/ft of formation being a common preflush volume, followed by the injection of 50 to 200 gal/ft of HF/HCl mixture. A postflush of diesel, brine, or HCl then displaces the HF/HCl from the tubing or wellbore. Once the treatment is completed, the spent acid should be immediately produced back to minimize damage by the precipitation of reaction products.

A sandstone acidizing treatment design begins with the selection of the type and concentration of acid to be used. The volume of preflush, HF/HCl mixture, and postflush required, and the desired injection rate(s), are considered next. In virtually all acid treat-

ments, the placement of the acid is an important issue—a strategy to ensure that sufficient volumes of acid contact all productive parts of the formation should be carefully planned. Proper execution of the treatment is critical to acidizing success, so the conduct of the treatment, including the mechanical arrangements for introducing the acid to the formation and the methods of treatment monitoring, should be planned in detail. Finally, numerous additives are incorporated with acid solutions for various purposes. The types and amounts of additives to be used in the treatment must be determined based on the completion, the formation, and the reservoir fluids. All of these design factors are considered in this chapter.

14-2 Acid Selection

The type and strength (concentration) of acid used in sandstones or carbonates is selected based primarily on field experience with particular formations. For years, the standard treatments consisted of 15 wt% HCl for carbonate formations and a 3 wt% HF, 12 wt% HCl mixture, preceded by a 15 wt% HCl preflush, for sandstones. In fact, the 3/12 HF/HCl mixture has been so common that it is referred to generically as "mud acid." In recent years, however, the trend has been toward the use of lower-strength HF solutions (Brannon et al., 1987.) The benefits of lower-concentration HF solutions are the reduction in damaging precipitates from the spent acid and lessened risk of unconsolidation of the formation around the wellbore.

McLeod (1984) presented guidelines for acid selection based on extensive field experience. His recommendations for sandstone reservoirs are shown in Table 14-1. These guidelines should not be taken as hard-and-fast rules, but rather as starting points in a treatment design.

For a more careful selection of optimal acid formulations, particularly when many wells may be treated in a particular formation, laboratory tests of the responses of cores to different acid strengths are worthwhile. Such tests usually consist of flowing the acid through a small core (typically 1 in. in diameter by 3 in. long) while monitoring the permeability response of the core by measuring the pressure drop across the core. A plot of the permeability of the core as a function of acid throughput in pore volumes is termed an "acid response curve" and is a common means of comparing different acidizing conditions. Figure 14-1 (Smith and Hendrickson, 1965) shows acid response curves for three different HF concentrations in Berea sandstone. These curves show that a lower-strength HF solution yields less damage in the early stages of injection; a conservative treatment design would select this low concentration as the best choice of those tested.

The results of a test in a short core cannot be expected to predict the response in a well accurately, but instead should be used as a guideline for field treatments or to provide input to a comprehensive acidizing model. Experiments in long cores, such as those reported by Cheung and Van Arsdale (1992), more accurately reflect field conditions; however, such experiments are expensive and difficult to perform.

Table 14-1

Sandstone Acidizing

HCl solubility > 20%	Use HCl only
High permeability (100 md plus)	
High quartz (80%), low clay (<5%)	10% HCl–3% HF[a]
High feldspar (>20%)	13.5% HCl–1.5 HF[a]
High clay (>10%)	6.5% HCl–1% HF[b]
High iron chlorite clay	3% HCl–0.5% HF[b]
Low permeability (10 md or less)	
Low clay (<5%)	6% HCl–1.5% HF[c]
High chlorite	3% HCl–0.5% HF[d]

[a]Preflush with 15% HCl.

[b]Preflush with sequestered 5% HCl.

[c]Preflush with 7.5% HCl or 10% acetic acid.

[d]Preflush with 5% acetic acid.

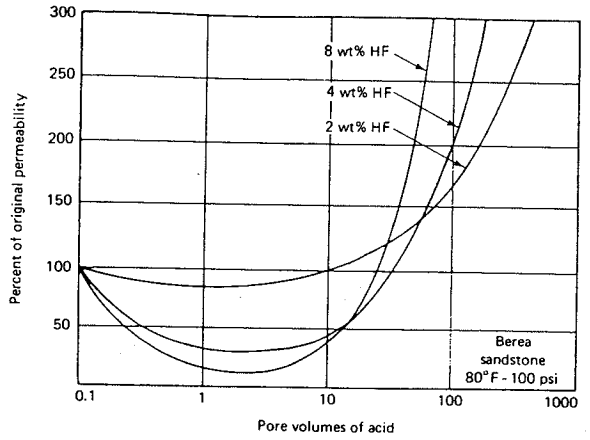

Figure 14-1
Acid response curves. (*From Smith and Hendrickson, 1965.*)

14-3 Acid Volume and Injection Rate

14-3.1 Competing Factors Influencing Treatment Design

The obvious goal of a sandstone acidizing treatment is to remove near-wellbore formation damage. A less obvious but equally important goal is to minimize the damage caused by the acidizing process itself. These two goals may at times be at odds. For example, if a shallow damaged zone exists around perforations (e.g., 2 in. or less of damaged region), the damage can be removed with the least amount of acid by injecting at a slow rate so that most of the acid is reacted within the 2-in. damaged region. However, such a slow rate may allow precipitates to form from the spent acid very near to the perforation, reducing the overall effectiveness of the acid. Thus, what may be an optimal rate based only on the dissolution of minerals in the damaged zone may be less than optimum when the overall acidizing process is considered.

The selection of an optimal acid volume is similarly complicated by competing effects. First, the volume of acid that is needed depends strongly on the depth of the damaged zone, and this depth is seldom known with any accuracy. With an assumption being made about the depth of the damaged zone, an optimal volume for a particular location in the well may be selected based on a laboratory acid response curve or an acidizing model. Such an analysis can yield a minimum recommended acid volume, such as 25 gal per perforation or 50 gal/ft of formation thickness. However, the acid will not in general be distributed equally to all parts of the formation. To ensure that an adequate amount of acid contacts most of the formation, a larger amount of acid may be necessary, depending mainly on the techniques used for proper acid placement.

Thus, design of a sandstone acidizing treatment will be imprecise. The approach recommended here will be to select a target acid volume based on a model of the acidizing process. The treatment should then be conducted in such as way that acidizing can be optimized "on the fly" for a particular well.

14-3.2 Sandstone Acidizing Models

The two-mineral model. Numerous efforts have been made over the years to develop a comprehensive model of the sandstone acidizing process that can then be used as a design aid. The most common model in use today is the two-mineral model (Hill et al., 1981; Hekim et al., 1982; Taha et al., 1989), which lumps all minerals into one of two categories: fast-reacting and slow-reacting species. Schechter (1992) categorizes feldspars, authogenic clays, and amorphous silica as fast-reacting, while detrital clay particles and quartz grains are the primary slow-reacting minerals.The model consists of material balances applied to the HF acid and the reactive minerals, which for linear flow, such as in a core flood, can bewritten as

$$\frac{\partial(\phi C_{\mathrm{HF}})}{\partial t} + u\frac{\partial C_{\mathrm{HF}}}{\partial x} = -\left(S_F^* V_F E_{f,F} + S_S^* V_S E_{f,S}\right)(1-\phi)C_{\mathrm{HF}} \tag{14-1}$$

$$\frac{\partial}{\partial t}\left[(1-\phi)V_F\right] = \frac{-\mathrm{MW}_{\mathrm{HF}} S_F^* V_F \beta_F E_{f,F} C_{\mathrm{HF}}}{\rho_F} \tag{14-2}$$

$$\frac{\partial}{\partial t}\left[(1-\phi)V_S\right] = \frac{-\mathrm{MW}_{\mathrm{HF}} S_S^* V_S \beta_S E_{f,S} C_{\mathrm{HF}}}{\rho_S} \tag{14-3}$$

In these equations, C_{HF} is the concentration of HF in solution, u is the acid flux, x is distance, S_F^* and S_S^* are the specific surface areas, V_F and V_S are the volume fractions, $E_{f,F}$ and $E_{f,S}$ are the reaction rate constants (based on the rate of consumption of HF), MW_F and MW_S are the molecular weights, β_F and β_S are the dissolving powers of 100% HF, and ρ_F and ρ_S are the densities of the fast- and slow-reacting minerals, respectively. When made dimensionless, assuming that porosity remains constant, these equations become:

$$\frac{\partial\psi}{\partial\theta} + \frac{\partial\psi}{\partial\epsilon} + \left(N_{\mathrm{Da},F}\Lambda_F + N_{\mathrm{Da},S}\Lambda_S\right)\psi = 0 \tag{14-4}$$

$$\frac{\partial\Lambda_F}{\partial\theta} = -N_{\mathrm{Da},F}N_{\mathrm{Ac},F}\psi\Lambda_F \tag{14-5}$$

$$\frac{\partial\Lambda_S}{\partial\theta} = -N_{\mathrm{Da},S}N_{\mathrm{Ac},S}\psi\Lambda_S \tag{14-6}$$

where the dimensionless variables are defined as

$$\psi = \frac{C_{\mathrm{HF}}}{C_{\mathrm{HF}}^0} \tag{14-7}$$

$$\Lambda_F = \frac{V_F}{V_F^0} \tag{14-8}$$

$$\Lambda_S = \frac{V_S}{V_S^0} \tag{14-9}$$

$$\epsilon = \frac{x}{L} \tag{14-10}$$

$$\theta = \frac{ut}{\phi L} \tag{14-11}$$

so that ψ is the dimensionless HF concentration, Λ is dimensionless mineral composition, ϵ is dimensionless distance, and θ is dimensionless time (pore volumes.) For a core flood, L is the core length. In Eqs. (14-4) through (14-6), two dimensionless groups appear for each mineral, N_{Da}, the Damkohler number, and N_{Ac}, the acid capacity number. These two groups describe the kinetics and the stoichiometry of the HF-mineral reactions. The Damkohler number is the ratio of the rate of acid consumption to the rate of acid convection, which for the fast-reacting mineral is

$$N_{\mathrm{Da},F} = \frac{(1-\phi_0)V_F^0 E_{f,F} S_F^* L}{u} \tag{14-12}$$

The acid capacity number is the ratio of the amount of mineral dissolved by the acid occupying a unit volume of rock pore space to the amount of mineral present in the unit

volume of rock, which for the fast-reacting mineral is

$$N_{\mathrm{Ac},F} = \frac{\phi \beta_F C^0_{\mathrm{HF}} \rho_{\mathrm{acid}}}{(1-\phi) V^0_F \rho_F} \tag{14-13}$$

The Damkohler and acid capacity numbers for the slow-reacting minerals are similarly defined. In this expression for the acid capacity number, the acid concentration is in weight fraction, not moles/volume.

As acid is injected into a sandstone, a reaction front is established by the reaction between the HF and the fast-reacting minerals. The shape of this front depends on $N_{\mathrm{Da},F}$. For low Damkohler numbers, the convection rate is high relative to the reaction rate and the front will be diffuse. With a high Damkohler number, the reaction front is relatively sharp because the reaction rate is high compared with the convection rate. Figure 14-2 (da Motta et al., 1992a), shows typical concentration profiles for high and low values of $N_{\mathrm{Da},F}$.

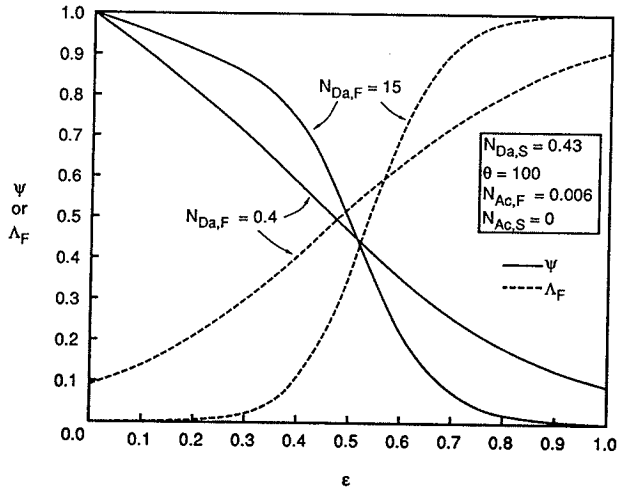

Figure 14-2
Acid and fast-reacting mineral concentration profiles. (*From da Motta et al., 1992a.*)

Equations (14-4) through (14-6) can only be solved numerically in their general form. However, analytical solutions are possible for certain simplified situations. Schechter (1992) presented an approximate solution that is valid for relatively high Damkohler number ($D_a^{(F)} > 10$) and is useful for design purposes. This solution approximates the HF-fast-reacting mineral front as a sharp front, so that behind the front all of the fast-reacting minerals have been removed. Conversely, ahead of the front, no dissolution has occurred. The reaction between slow-reacting minerals and HF behind the front serves to diminish

the HF concentration reaching the front. The location of the front is given by

$$\theta = \frac{\exp(N_{\mathrm{Da},S}\epsilon_f) - 1}{N_{\mathrm{Ac},F} N_{\mathrm{Da},S}} + \epsilon_f \tag{14-14}$$

which relates dimensionless time (or, equivalently, acid volume) to the dimensionless position of the front, ϵ_f, defined as the position of the front divided by the core length for linear flow. The dimensionless acid concentration behind the front is

$$\psi = \exp(-N_{\mathrm{Da},S}\epsilon) \tag{14-15}$$

A particularly convenient feature of this approximation is that it is applicable to linear, radial, and ellipsoidal flow fields with appropriate definition of dimensionless variables and groups. Radial flow represents the flow of acid from an open-hole completion and may also be a reasonable approximation to the flow from a perforated well with sufficient perforation density. The ellipsoidal flow geometry approximates the flow around a perforation and is illustrated in Fig. 14-3. The proper dimensionless variables and groups for these three flow fields are given in Table 14-2. For the perforation geometry, the position of the front, ϵ_f, depends on position along the perforation. In Table 14-2, expressions are given for the front position of the acid extending directly from the tip of the perforation and for the acid penetration along the wellbore wall. These two positions should be sufficient for design purposes; the reader is referred to Schechter (1992) for methods for calculating the complete acid penetration profile in this geometry.

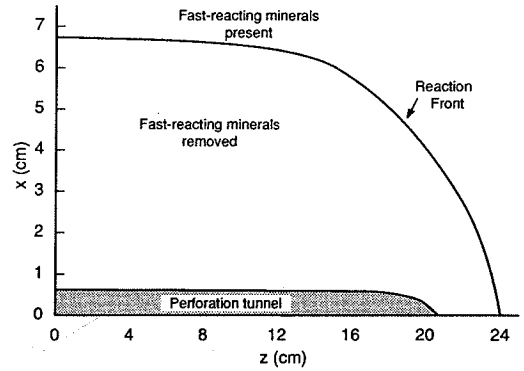

Figure 14-3
Ellipsoidal flow around a perforation. (*From Schechter, 1992.*)

It is interesting to note that the Damkohler number for the slow-reacting mineral and the acid capacity number for the fast-reacting mineral are the only dimensionless groups that appear in this solution. $N_{\mathrm{Da},S}$ regulates how much live HF reaches the front; if the slow

Table 14-2

Dimensionless Groups in Sandstone Acidizing Model

Flow Geometry	ϵ	θ	$N_{\mathrm{Da},S}$
Linear	$\frac{x}{L}$	$\frac{ut}{\phi L}$	$\frac{(1-\phi)V_S^0 E_{f,S} S_S^* L}{u}$
Radial	$\frac{r^2}{r_w^2} - 1$	$\frac{q_i t}{\pi r_w^2 h \phi}$	$\frac{(1-\phi)V_S^0 E_{f,S} S_S^* \pi r_w^2 h}{q_i}$
Ellipsoidal	Penetration from the tip of the perforation $\frac{1}{3}\bar{z}^3 - \bar{z} + \frac{2}{3};\ \bar{z} = \frac{z}{l_{\mathrm{perf}}}$	$\frac{q_{\mathrm{perf}} t}{2\pi l_{\mathrm{perf}}^3 \phi}$	$\frac{2\pi(1-\phi) l_{\mathrm{perf}}^3 S_S^* V_S^0 E_{f,S}}{q_{\mathrm{perf}}}$
	Penetration adjacent to the wellbore $\frac{1}{3}\left(\bar{x} + \frac{1}{\bar{x}+\sqrt{\bar{x}^2+1}}\right)^3 - \frac{1}{3}$ $\bar{x} = \frac{x}{l_{\mathrm{perf}}}$		

Note: Ψ, Λ, and $N_{\mathrm{Ac,f}}$ are the same for all geometries.

mineral reacts fast relative to the convection rate, little acid will be available to propagate the fast-mineral front. The acid capacity number for the slow-reacting mineral is not important, because the supply of slow-reacting mineral is almost constant behind the front. $N_{\mathrm{Ac},F}$ affects the frontal propagation rate directly: The more fast-reacting mineral is present, the slower the front will move. $N_{\mathrm{Da},F}$ does not appear because the front was assumed to be sharp, implying that $N_{\mathrm{Da},F}$ is infinite. This solution can be used to estimate the volume of acid needed to remove the fast-reacting minerals from a given region around a wellbore or perforation.

The dimensionless groups, $N_{\mathrm{Ac},F}$ and $N_{\mathrm{Da},S}$, can be calculated with Eq. (14-13) and Table 14-2 based on the rock mineralogy or can be obtained from experiments, as will be illustrated in the following example.

EXAMPLE 14-1

Determining $N_{\mathrm{Ac},F}$ and $N_{\mathrm{Da},S}$ from laboratory data

The effluent acid concentration measured in a core flood of a 0.87 in. diameter by 1.57-in.-long Devonian sandstone core with 1.5 wt% HF, 13.5 wt% HCl by da Motta et al. (1992a) is shown in Fig. 14-4. The acid flux was 0.346 cm/min (0.0114 ft/min). Determine $N_{\mathrm{Da},S}$ and $N_{\mathrm{Ac},F}$ from the data.

Solution In a typical acidizing core flood, the effluent acid concentration will start at a low value, then gradually increase as the fast-reacting minerals are removed from the core. The sharper the fast-reacting mineral front, the more rapid will be this rise in effluent concentration. When virtually all the fast-reacting minerals have been dissolved, the acid concentration will

level off to a plateau value that reflects the consumption of HF by the remaining quartz and other slow-reacting minerals in the core. The effluent concentration is the concentration at $\epsilon = 1$ as a function of time. Therefore, from Eq. (14-15), after all fast-reacting minerals have been dissolved,

$$N_{\mathrm{Da},S} = -\ln(\psi_e) \tag{14-16}$$

From Fig. 14-4, the dimensionless effluent acid concentration, ψ_e, gradually increases from 0.61 to 0.65 during the last 50 pore-volumes of the flood (the slight increase is due either to the removal of small amounts of fast-reacting mineral or decreasing surface area of the slow-reacting mineral). Using the average value of 0.63 in Eq. (14-16), $N_{\mathrm{Da},S} = 0.46$.

The acid capacity number for the fast-reacting minerals can be estimated from the breakthrough time of the reaction front, using Eq. (14-14). The location of the front can be approximated as that position where the acid concentration is half the value supplied to the front. Using the value of 0.63 as the dimensionless concentration supplied to the front, the front emerges from the core when the effluent concentration is 0.315. This occurs at about 180 pore volumes. Solving for $N_{\mathrm{Ac},F}$ from Eq. (14-14) when $\epsilon_f = 1$ gives

$$N_{\mathrm{Ac},F} = \frac{\exp N_{\mathrm{Da},S} - 1}{(\theta_{bt} - 1)N_{\mathrm{Da},S}} \tag{14-17}$$

so

$$N_{\mathrm{Ac},F} = \frac{\exp 0.46 - 1}{(180 - 1)(0.46)} = 0.0071 \tag{14-18}$$

These results compare well with the values of $N_{\mathrm{Da},S} = 0.43$ and $N_{\mathrm{Ac},F} = 0.006$ determined by da Motta et al. (1992a) with a more complex numerical model. ◇

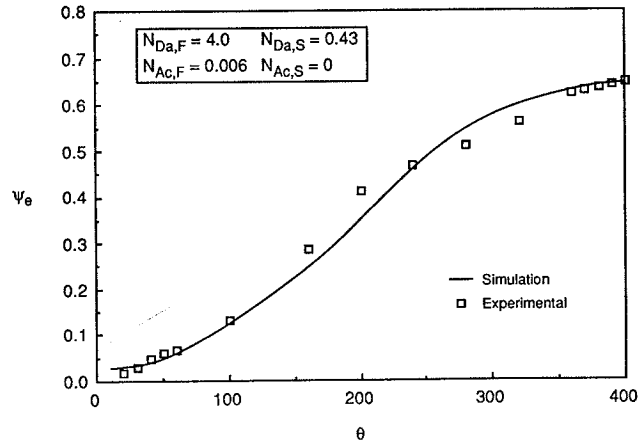

Figure 14-4
Effluent acid concentration from a core flood. (*From da Motta et al., 1992a.*)

EXAMPLE 14-2

Acid volume design for radial flow

Using the acid capacity and Damkohler numbers from Example 14-1, determine the acid volume (gal/ft) needed to remove all fast-reacting minerals to distances of 3 in. and 6 in. from a wellbore of radius 0.328 ft., assuming that the acid flows radially into the formation, such as would occur in an open-hole completion. The acid injection rate is 0.1 bbl/min-ft of thickness, and the porosity is 0.2.

Solution From Table 14-2, the radial flow Damkohler number is related to that for linear flow by

$$(N_{\mathrm{Da},S})_{\mathrm{radial}} = (N_{\mathrm{Da},S})_{\mathrm{linear}} \left(\frac{\pi r_w^2 h}{q_i}\right)_{\mathrm{well}} \left(\frac{u}{L}\right)_{\mathrm{core}} \tag{14-19}$$

so

$$(N_{\mathrm{Da},S})_{\mathrm{radial}} = (0.46)\left[\frac{(\pi)(0.328\mathrm{ft})^2}{(0.1\ \mathrm{bbl/min\text{-}ft})(5.615\ \mathrm{ft^3/bbl})}\right]\left(\frac{0.0114\ \mathrm{ft/min}}{(1.57/12)\ \mathrm{ft}}\right) = 0.024 \tag{14-20}$$

The dimensionless position of the front for radial flow is related to the radial penetration as shown in Table 14-2:

$$\epsilon_f = \left(\frac{0.328\ \mathrm{ft} + (3/12)\ \mathrm{ft}}{0.328\ \mathrm{ft}}\right)^2 - 1 = 2.1 \tag{14-21}$$

Using Eq. (14-14),

$$\theta = \frac{\exp[(0.024)(2.1)] - 1}{(0.007)(0.024)} + 2.1 = 310 \tag{14-22}$$

From the definition of θ for radial flow in Table 14-2 and recognizing that $q_i t/h$ is simply the volume injected per unit thickness,

$$\frac{q_i t}{h} = \theta \pi r_w^2 \phi_o \tag{14-23}$$

$$\frac{q_i t}{h} = (310)(\pi)(0.328\ \mathrm{ft})^2(0.2)\left(7.48\ \mathrm{gal/ft^3}\right) = 160\ \mathrm{gal/ft} \tag{14-24}$$

The dimensionless front position for a penetration of 6 in. from the wellbore is 5.37. Repeating the calculations yields an acid volume of 420 gal/ft, an unreasonably large volume. This particular formation has a high concentration of fast-reacting minerals (low $N_{\mathrm{Ac},F}$) and a relatively high slow-mineral reaction rate (high $N_{\mathrm{Da},S}$), making it difficult to propagate HF far into the formation. A higher acid concentration would be needed for deeper penetration with the same volume of acid. ◇

EXAMPLE 14-3

Acid volume design for ellipsoidal flow from a perforation

Calculate the acid volume needed (gal/ft) to remove all fast-reacting minerals a distance of 3 in. from the tip of the perforations for a well completed with 4 shots/ft, based on the laboratory data in Example 14-1. The perforation length is 6 in., the porosity is 0.2, and the injection rate is 0.1 bbl/min-ft of thickness. Also calculate the position of the acid front immediately adjacent to the wellbore for this volume of acid injection.

Solution From Table 14-2, the ellipsoidal flow Damkohler number is related to that for linear flow by

$$(N_{\mathrm{Da},S})_{\mathrm{ellipsoidal}} = (N_{\mathrm{Da},S})_{\mathrm{linear}} \left(\frac{2\pi l_{\mathrm{perf}}^3}{q_{\mathrm{perf}}}\right)\left(\frac{u}{L}\right) \tag{14-25}$$

Since there are 4 shots/ft., q_{perf} is $q_i/4$. Thus,

$$(N_{\mathrm{Da},S})_{\mathrm{ellipsoidal}} = (0.46)\left(\frac{(2\pi)(0.5\ \mathrm{ft})^3}{(0.025\ \mathrm{bbl/min})(5.615\ \mathrm{ft^3/bbl})}\right)\left(\frac{0.0114\ \mathrm{ft/min}}{(1.57/12)\ \mathrm{ft}}\right) = 0.224 \tag{14-26}$$

Using the expression from Table 14-2 relating the dimensionless frontal position to the acid penetration from the tip of the perforation, and noting that z is measured from the wellbore (the start of the perforation),

$$\bar{z} = \frac{z}{l_{\mathrm{perf}}} = \frac{6\ \mathrm{in.} + 3\ \mathrm{in.}}{6\ \mathrm{in.}} = 1.5 \tag{14-27}$$

$$\epsilon_f = \frac{1}{3}(1.5)^3 - 1.5 + \frac{2}{3} = 0.292 \tag{14-28}$$

Then

$$\theta = \frac{\exp[(0.224)(0.292)] - 1}{(0.007)(0.224)} + 0.292 = 43.4 \tag{14-29}$$

The volume injected per perforation is $q_{\mathrm{perf}}t$, so, from Table 14-2,

$$q_{\mathrm{perf}}t = 2\pi l_{\mathrm{perf}}^3 \phi\theta \tag{14-30}$$

$$q_{\mathrm{perf}}t = (2\pi)(0.5\ \mathrm{ft})^3(0.2)(43.4)(7.48\ \mathrm{gal/ft^3}) = 51\ \mathrm{gal/perf} \tag{14-31}$$

Since there are 4 shots/ft, the total acid volume per foot is 204 gal/ft.

The dimensionless acid penetration distance, ϵ_f, is the same at any location around the perforation. The acid penetration at the wellbore is found from the second expression in Table 14-2, using the value of 0.292 for ϵ_f and solving for x by trial and error. The result is a penetration distance of 4.3 in. around the base of the perforation adjacent to the wellbore. ◇

The two-acid, three-mineral model. Recently, Bryant (1991) and da Motta et al. (1992b) presented evidence that the sandstone acidizing process is not described adequately by the two-mineral model, particularly at elevated temperatures. In particular, these studies suggest that the reaction of fluosilicic acid (H_2SiF_6) with aluminosilicate (fast-reacting) minerals may be quite significant. This adds the following reaction to the two-mineral model:

$$H_2SiF_6 + \text{fast-reacting mineral} \longrightarrow \nu\ Si(OH)_4 + \text{Al fluorides} \tag{14-32}$$

The practical implications of this reaction being significant are that less HF will be needed to consume the fast-reacting minerals with a given volume of acid because the fluosilicic

acid will also be reacting with these minerals, and the reaction product, $Si(OH)_4$ (silica gel) will precipitate. This reaction allows live HF to penetrate further into the formation; the price is the risk of the formation of possible damaging precipitates.

The two-acid, three-mineral model has not been tested extensively. However, it suggests that using the two-mineral model for predicting required acid volumes will be a conservative approach, particularly for high-temperature applications.

Precipitation models. The two-acid, three-mineral model considers the precipitation of silica gel in its description of the acidizing process. However, there are numerous other reaction products that may precipitate. The tendency for reaction product precipitation has been studied with comprehensive geochemical models that consider a large number of possible reactions that may take place in sandstone acidizing.

The most common type of geochemical model used to study sandstone acidizing is the local equilibrium model, such as that described by Walsh et al. (1982). This type of model assumes that all reactions are in local equilibrium; i.e., all reaction rates are infinitely fast. A typical result from this model is shown in Fig. 14-5, a time–distance diagram for the injection of 4 wt%HF/11 wt%HCl into a formation containing calcite, kaolinite, and quartz. This plot shows regions where amorphous silica and aluminum fluoride will tend to precipitate. A vertical line on this plot represents the mineral species present as a function of distance if all reactions are in local equilibrium.

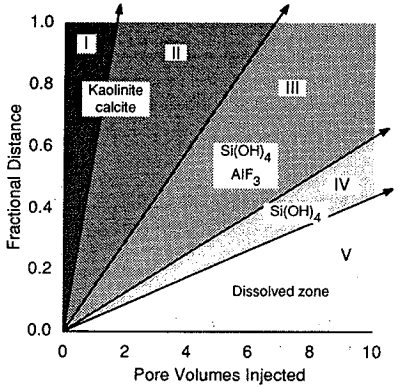

Figure 14-5
Time–distance diagram showing regions of possible precipitation. (*From Schechter, 1992.*)

Recently, Sevougian et al. (1992) presented a geochemical model that includes kinetics for both dissolution and precipitation reactions. This model shows that precipitation damage will be lessened if the either the dissolution or the precipitation reactions are not instantaneous. For example, Fig. 14-6 shows predicted regions and concentrations of precipitates for four different precipitation reaction rates (minerals AC and DB are precipitates). As the reaction rate decreased, the amount of damaging precipitate formed decreased.

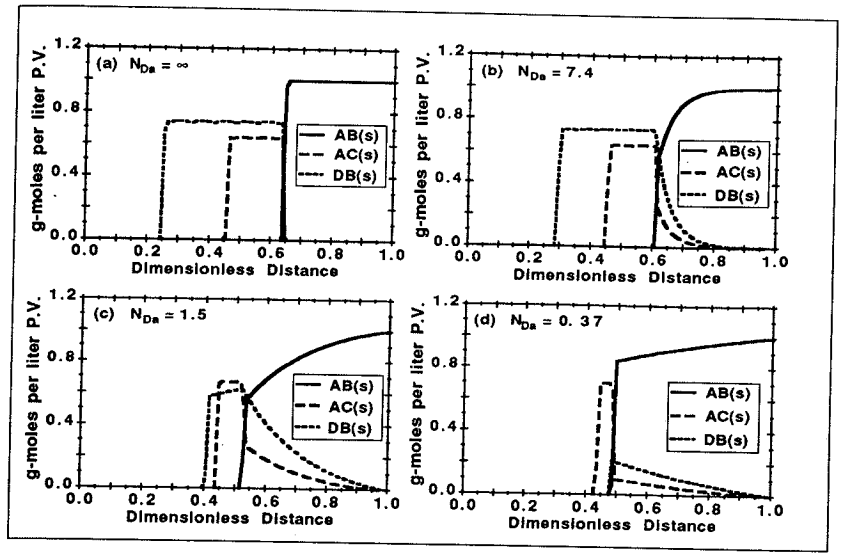

Figure 14-6
Effect of precipitation kinetics on regions of precipitate formation. (*From Sevougian et al., 1992.*)

Permeability models. To predict the response of a formation to acidizing, it is necessary to predict the change in permeability as acid dissolves some of the formation minerals and as other minerals precipitate. The permeability change as a result of acidizing is an extremely complicated process, since it is affected by several different, sometimes competing phenomena in the porous media. The permeability increases as pores and pore throats are enlarged by mineral dissolution. At the same time, small particles are released as cementing material is dissolved, and some of these particles will lodge (perhaps temporarily) in pore throats, reducing the permeability. Any precipitates formed will also tend to decrease the permeability. The formation of CO_2 as carbonate minerals are dissolved may also cause a temporary reduction in the relative permeability to liquids. The result of these competing effects is that the permeability in core floods usually decreases initially; with continued acid injection, the permeability eventually will increase to values considerably higher than the original permeability.

The complex nature of the permeability response has made its theoretical prediction for real sandstones impractical, though some success has been achieved for more ideal systems such as sintered disks (Guin et al., 1971). As a result, empirical correlations relating the permeability increase to the porosity change during acidizing are used. The most common correlations used are those of Labrid (1975), Lund and Fogler (1976), and

Lambert (1981). These correlations are:

$$\text{Labrid:} \qquad \frac{k_i}{k} = M\left(\frac{\phi_i}{\phi}\right)^n \tag{14-33}$$

where k and ϕ are the initial permeability and porosity and k_i and ϕ_i are the permeability and porosity after acidizing. M and n are empirical constants, reported to be 1 and 3 for Fontainbleau sandstone.

$$\text{Lund and Fogler:} \qquad \frac{k_i}{k} = \exp\left[M\left(\frac{\phi_i - \phi}{\Delta\phi_{\max}}\right)\right] \tag{14-34}$$

where $M = 7.5$ and $\Delta\phi_{\max} = 0.08$ best fit data for Phacoides sandstone.

$$\text{Lambert:} \qquad \frac{k_i}{k} = \exp[45.7(\phi_i - \phi)] \tag{14-35}$$

Lambert's expression is identical to Lund and Fogler's when $M/\Delta\phi_{\max} = 45.7$.

Using the values of the constants suggested, Labrid's correlation predicts the smallest permeability increase, followed by Lambert's, then Lund and Fogler's. The best approach in using these correlations is to select the empirical constants based on core flood responses, if such are available. Lacking data for a particular formation, Labrid's equation will yield the most conservative design.

EXAMPLE 14-4

Predicting the permeability response to acidizing

A sandstone with an initial porosity of 0.2 and initial permeability of 20 md contains a total of 10 vol% of carbonate and fast-reacting minerals in the damaged region. Calculate the permeability after removing all of these minerals using each of the permeability correlations.

Solution The change in porosity due to acidizing is the initial fraction of the bulk volume that is solid $(1 - \phi)$ multiplied by the fraction of solid dissolved,

$$\Delta\phi = (1 - 0.2)(0.1) = 0.08 \tag{14-36}$$

so the porosity after acidizing is 0.28. The predicted permeabilities after acidizing are as follows.

$$\text{Labrid:} \qquad k_i = (20\text{ md})\left(\frac{0.28}{0.2}\right)^3 = 55\text{ md} \tag{14-37}$$

$$\text{Lund and Fogler:} \qquad k_i = (20\text{ md})\exp\left[\frac{(7.5)(0.08)}{0.08}\right] = 3.6 \times 10^4\text{ md} \tag{14-38}$$

$$\text{Lambert:} \qquad k_i = (20\text{ md})\exp[(45.7)(0.08)] = 770\text{ md} \tag{14-39}$$

The predicted permeabilities with the three correlations differ by orders of magnitude, illustrating the great uncertainty involved in trying to predict the permeability response to acidizing in sandstones. Each of these correlations is based on experiments with particular sandstones and, clearly, the manner in which the pore structures of these formations responded to acid differed markedly. ◇

14-3.3 Monitoring the Acidizing Process; The Optimal Rate Schedule

Selecting an optimal injection rate for sandstone acidizing is a difficult process because of uncertainties about the damaged zone and the competing effects of mineral dissolution and reaction product precipitation. Based on mineral dissolution alone, and given the depth of the damaged zone, an optimal injection rate can be derived using the two-mineral model, with the optimal rate being the rate that maximizes the spending of the HF in the damaged zone. Such an approach has been presented by da Motta et al. (1992a.) However, the depth of the damage is seldom known with any certainty, and the detrimental effects of reaction product precipitates may be lessened by using rates higher than the optimum based on mineral dissolution alone. In fact, recent results with the two-acid, three-mineral model have shown that acidizing efficiency is relatively insensitive to injection rate, and that the highest rate possible yields the best results. Figure 14-7 (da Motta, 1993) shows that with shallow damage, injection rate has little effect on the skin effect after 100 gal/ft of acid injection; with deeper damage, the higher the injection rate, the lower the skin effect achieved by acidizing.

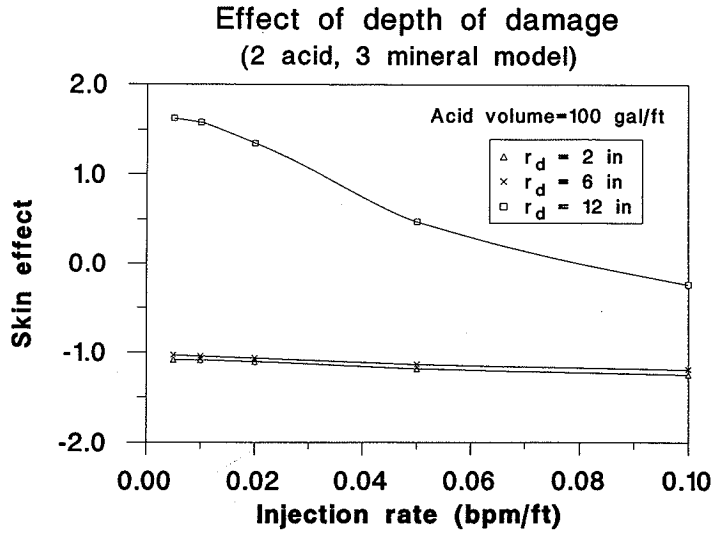

Figure 14-7

Effect on injection rate on skin evolution. (*From da Motta, 1993; courtesy of E. P. da Motta.*)

Field experience has also been contradictory regarding the optimal injection rate for sandstone acidizing. McLeod (1984) recommends relatively low injection rates, based on the observation that acid contact times with the formation of 2 to 4 hr appear to give good results. On the other hand, Paccaloni et al. (1988) and Paccaloni and Tambini (1990) reported

high success rates in numerous field treatments using the highest injection rates possible. It is likely that the success of Paccaloni's "maximum Δp, maximum rate" procedure is due to improved acid coverage (discussed in the next section) and the minimization of precipitation damage. Unless experience in a particular area suggests otherwise, Paccaloni's maximum Δp, maximum rate procedure is recommended and will be described here.

There is always an upper bound on injection rate since, to ensure a matrix treatment, the injection rate must be kept below the rate that will cause hydraulic fracture formation. The bottomhole pressure that will initiate a fracture (the breakdown pressure) is simply the fracture gradient, FG, times depth, or

$$p_{bd} = \text{FG}(H) \tag{14-40}$$

(See Chapter 16 for a thorough discussion of the breakdown pressure.) Assuming pseudo-steady-state flow, the breakdown pressure is related to the injection rate by Eq. (2-30), which for injection is

$$p_{\text{bd}} - \bar{p} = \frac{141.2 q_{i,\max} \mu}{kh}\left(\ln\frac{0.472 r_e}{r_w} + s\right) \tag{14-41}$$

Most commonly, only the surface rate and tubing pressure are monitored during an acid job, so it is necessary to relate the surface pressure to the bottomhole pressure by

$$p_{ti,\max} = p_{wf} - \Delta p_{\text{PE}} + \Delta p_F \tag{14-42}$$

where the potential energy and frictional pressure drops are both positive quantities. If the fluid is Newtonian, these can be computed using the methods described in Chapter 7. When foams or other non-Newtonian fluids are used, the bottomhole pressure should be monitored continuously (e.g., by monitoring annulus pressure), or pumping should occasionally be stopped for a brief period to determine the frictional pressure drop. Before a matrix acidizing treatment is begun, the relationship between the maximum rate and tubing pressure should be calculated so that the breakdown pressure is never exceeded. This should be done for a wide range of injection rates, since the injection rate that the formation can accommodate without fracturing will increase as the skin effect is reduced by the acid.

EXAMPLE 14-5

Maximum injection rate and pressure

A well in Reservoir A, at a depth of 9822 ft, is to be acidized with an acid solution having a specific gravity of 1.07 and a viscosity of 0.7 cp down 2-in.-I.D. coiled tubing with a relative roughness of 0.001. The formation fracture gradient is 0.7 psi/ft. Plot the maximum tubing injection pressure versus acid injection rate. If the skin effect in the well is initially 10, what is the maximum allowable rate at the start of the treatment? Assume that $r_e = 1000$ ft and $\bar{p} = 4500$ psi.

Solution The breakdown pressure from Eq. (14-40) is

$$p_{bd} = (0.7 \text{ psi/ft})(9822 \text{ ft}) = 6875 \text{ psi} \tag{14-43}$$

The maximum tubing injection pressure is given by Eq. (14-42). Using Eq. (7-22), the potential energy pressure drop, which is independent of flow rate, is

$$\Delta p_{\text{PE}} = (0.433 \text{ psi/ft})(1.07)(9822 \text{ ft}) = 4551 \text{ psi} \tag{14-44}$$

The frictional pressure drop is given by Eq. (7-31), which, for q_i in bpm and all other quantities in the usual oilfield units, is

$$\Delta p_F = \frac{1.525 \rho q_i^2 f L}{D^5} \tag{14-45}$$

The friction factor is obtained from the Reynolds number and the relative roughness using Eq. (7-35) or Fig. 7-7. The results for flow rates ranging from 0.5 to 10 bpm are given in Table 14-3 and plotted in Fig. 14-8. As injection rate is increased, the surface tubing pressure to maintain a constant bottomhole pressure increases because of the increased frictional pressure drop.

Table 14-3

Example 14-5 Results

q_i (bpm)	N_{Re}	f	Δp_F (psi)	$p_{ti,\max}$ (psi)
0.5	50,800	0.0061	48	2370
1.0	102,000	0.0056	175	2500
2.0	203,000	0.0053	660	2980
4.0	406,000	0.0051	2550	4870

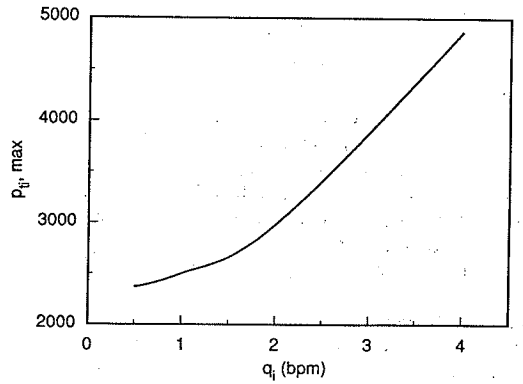

Figure 14-8
Maximum tubing injection pressure (Example 14-5).

The maximum injection rate at the start of the treatment can be obtained from Eq. (14-41). Solving for $q_{i,\max}$ yields

$$q_{i,\max} = \frac{(6875 - 4500)(8.2)(53)}{(141.2)(1.7)\{\ln[(0.472)(1000)/0.328] + 10\}} \qquad (14\text{-}46)$$
$$= 250 \text{ bbl/d} = 0.17 \text{ bpm}$$

Thus, the initial injection rate should be less than 0.2 bpm and the surface tubing pressure should be less than 2330 psi. The viscosity of the reservoir oil was used in this calculation since almost all of the pressure drop in the reservoir occurs where oil is flowing, even though an aqueous fluid is being injected.

As the skin effect decreases during acidizing, a higher injection rate is possible without fracturing the formation. To ensure that fracturing does not occur, it is usually recommended that the surface tubing pressure be maintained about 10% below the pressure that would initiate fracturing. For this well, a prudent design would begin with an injection rate of 0.1 bpm, which could be increased while keeping the surface pressure below 2000 psi. If the rate became higher than about 1 bpm, the tubing pressure could increase above 2000 psi, but should be held below 10% of the pressure shown in Fig. 14-8 for any particular rate. ◇

Paccaloni's Maximum Δp, Maximum Rate Procedure. Paccaloni's maximum Δp, maximum rate procedure has two major components: (1) The acid should be injected at the maximum rate and hence, maximum p_{wf} possible without fracturing the formation; and (2) the treatment should be monitored in real time to ensure that the maximum rate objective is being met and to determine when sufficient acid has been injected into the formation.

To monitor the progress of a stimulation treatment, Paccaloni calculates a steady-state skin effect, according to

$$s = \frac{0.00708kh\ \Delta p}{\mu q_i} - \ln\frac{r_b}{r_w} \qquad (14\text{-}47)$$

where all of the variables are in standard oilfield units. In Eq. (14-47), r_b is the radius affected by acid injection and Paccaloni suggests that a value of 4 ft be used. Equation (14-47) relates q_i, p_{wf} (through Δp), and s. To monitor a stimulation treatment, Paccaloni constructs a graph of p_{ti} versus q_i, with s as a parameter, where p_{ti} is related to p_{wf} by Eq. (14-42). As the treatment proceeds, the wellhead pressure is plotted against injection rate and the evolving skin effect can be read from the graph. The fracture pressure versus injection rate is also plotted on this graph, so that the rate can be held at the highest possible value without fracturing the formation. Figure 14-9 shows such a design chart for a matrix stimulation treatment.

A drawback to Paccaloni's method is that it will tend to overestimate the skin effect because it neglects transient flow effects, as pointed out by Prouvost and Economides (1988) and confirmed by Paccaloni and Tambini (1990.) This error can be severe when abrupt rate changes occur; however, in most treatments, it is not a serious problem because the error will be relatively constant and the evolution in skin effect is more important than its absolute value. Prouvost and Economides presented a procedure to calculate more accurately the changing skin effect during matrix acidizing, but this procedure may require the use of a

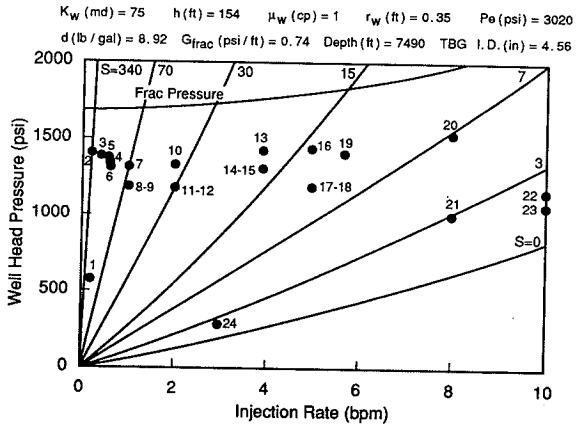

Figure 14-9
Paccaloni design chart for monitoring acidizing. (*From Paccaloni and Tambini, 1990.*)

simulator that will often not be available for real-time monitoring. This technique is more applicable to a careful posttreatment analysis, when the injection rate schedule from the treatment is known.

An alternative real-time monitoring procedure that draws on both Paccaloni's and Prouvost and Economides' approaches is as follows. Applying the approximation to the transient flow equation [Eq. (2-6)] for injection with a skin effect yields

$$\frac{p_{wf} - p}{q_i} = \frac{162.6\mu}{kh}\left(\log t + \log\frac{k}{\phi\mu c_t r_w^2} - 3.23 + s\right) \qquad (14\text{-}48)$$

Though this equation does not strictly apply during a matrix stimulation treatment (it assumes constant rate after the start of injection, for example), it suggests that the inverse of the injectivity will decrease as the skin effect is reduced by acidizing. Conversely, when no stimulation is occurring, the inverse injectivity will increase proportional to the log of time because of the transient nature of the flow.

To monitor a stimulation treatment, the inverse injectivity can be plotted against the log of time. As long as the inverse injectivity is decreasing, significant stimulation is occurring. When it levels off or begins to increase, little stimulation is occurring, indicating that injection of the treatment fluid should be discontinued, or a different fluid used.

A summary of the procedure is as follows.

1. Prior to the start of the treatment, develop the relationship between p_{wf} and p_{ti}, as in Example 14-5.
2. Begin injection at a rate such that $p_{wf} = 0.9p_{bd}$.
3. Plot $(p_{wf} - p)/q_i$ versus $\log(t)$ during the treatment. The reservoir pressure (p)

to use in the calculation is p_i in a new well, p_e in a well with pressure maintenance at the boundary, and $\bar{p}$ in a confined reservoir.

4. As stimulation proceeds, increase the rate to maintain $p_{wf} = 0.9p_{bd}$.
5. Stop injection when $\Delta p/q_i$ versus $\log(t)$ levels off or increases for a significant amount of injection (25–50 gal/ft). An oil or gas well should not be treated as an acid disposal well—when stimulation is no longer proceeding, injection of acid should be stopped.

EXAMPLE 14-6
Real-time treatment monitoring

Figure 14-10 shows the injection rate and surface tubing pressure for the matrix acidizing treatment of Well GW-1 presented by Paccaloni and Tambini (1990.) Other information about the treatment is given in Table 14-4. Analyze the response of this well to acidizing, using the method just presented.

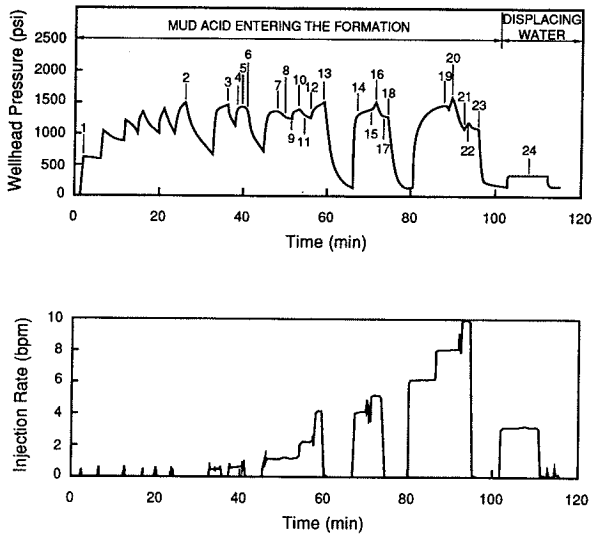

Figure 14-10
Injection rate and surface tubing pressure for acidizing treatment of Well GW-1 (Example 14-6). (*From Paccaloni and Tambini, 1990.*)

Solution From Eq. (14-40), the breakdown pressure is 5540 psi. Thus, to prevent fracturing, the bottomhole pressure should be restricted to less than about 5000 psi. For the acid injected

Table 14-4

Matrix Acidizing Design Data

Acid			
3%HF/12%HCl	Volume injected = 45 gal/ft		
$\rho = 66.72$ lb$_m$/ft^3	$\mu = 1$cp		
Formation			
$k = 75$ md	$h = 154$ ft	$p_e = 3020$ psi	FG = 0.74 psi/ft
Well			
$H = 7490$ ft	$r_w = 0.35$ ft	$D_{\text{tubing}} = 4.56$ in.	

and this depth, the potential energy pressure drop in the tubing is 3470 psi, and using Eq. (14-45), the frictional pressure drop is approximately

$$\Delta p_F = 1.92q^2 \tag{14-49}$$

so that p_{wf} is

$$p_{wf} = p_{ti} + 3470 - 1.92q^2 \tag{14-50}$$

The pressure drop, Δp, between the well and the reservoir, using the value of p_e given, is

$$\Delta p = p_{ti} + 450 - 1.92q^2 \tag{14-51}$$

Values of injection rate and tubing pressure versus time from Fig. 14-10 are tabulated in Table 14-5, along with p_{wf}, Δp, and $\Delta p/q_i$.

First, the bottomhole pressure versus time during the treatment is plotted in Fig. 14-11, which shows that p_{wf} was held just under the maximum safe level of about 5000 psi throughout most of the treatment. The diagnostic plot of inverse injectivity versus $\log(t)$ is shown in Fig. 14-12. Because the initial injectivity was so low (the initial skin effect was reported to be 340), the scale of this plot is so large that little detail is seen. Replotting the data starting after the first 56 min of injection yields Fig. 14-13, which gives a better picture of the progress of the second half of the treatment.

The inverse injectivity appears to level off three different times in this portion of the treatment. Paccaloni and Tambini attributed this behavior to successive portions of the formation receiving significant stimulation as the injection rate is boosted to maintain p_{wf} near the target value. The treatment was terminated after the third leveling off of inverse injectivity, and water was injected to displace the acid from the wellbore. The injectivity of this water was apparently lower than that of the acid. The acid treatment shown here was a very successful one—the skin effect measured with a pressure transient test after treatment was 1.2, indicating nearly complete removal of damage.

The analysis illustrated here should be applied during the course of a matrix stimulation treatment. However, such an analysis can also be applied after the treatment to diagnose the success or failure of the stimulation. ◇

Table 14-5

Example 14-6 Results

time (min)	q_i (bpm)	p_{ti} (psi)	p_{wf} (psi)	Δp (psi)	$\Delta p/q_i$ (psi/bpm)
2	0.2	600	4068	1048	5240
25	0.2	1500	4968	1948	9740
37	0.3	1450	4918	1898	6326
39	0.5	1450	4918	1898	3795
40	0.5	1400	4868	1848	3695
42	0.5	1400	4868	1848	3695
50	0.9	1350	4816	1796	1996
52	0.9	1300	4766	1746	1940
53	0.9	1200	4666	1646	1829
56	1.8	1330	4792	1772	984
57	1.8	1200	4662	1642	912
58	1.8	1350	4812	1792	995
60	3.9	1450	4889	1869	479
69	3.9	1300	4739	1719	441
72	3.9	1350	4789	1769	454
73	5	1500	4920	1900	380
74	5	1250	4670	1650	330
76	5	1200	4620	1600	320
87	6	1450	4849	1829	305
90	8	1520	4865	1845	231
93	8	1000	4345	1325	166
94	10	1180	4456	1436	144
97	10	1100	4376	1356	136
109	3	250	3701	681	227

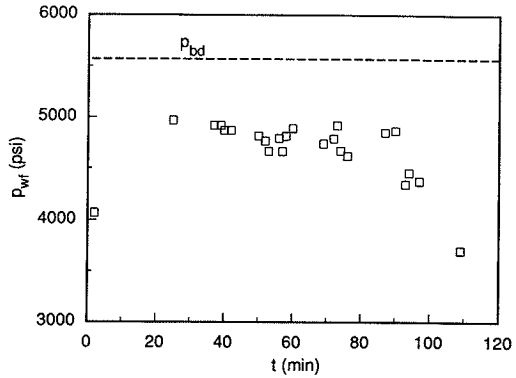

Figure 14-11
Bottomhole pressure record, Well GW-1 (Example 14-6).

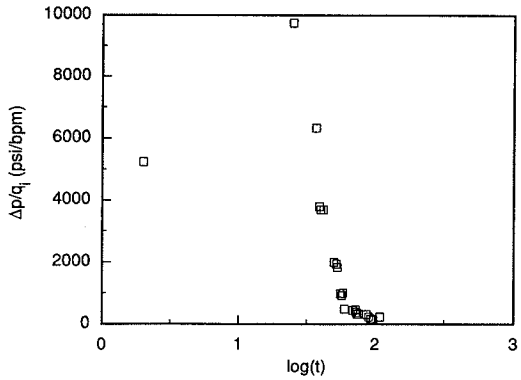

Figure 14-12
Inverse injectivity diagnostic plot (Example 14-6).

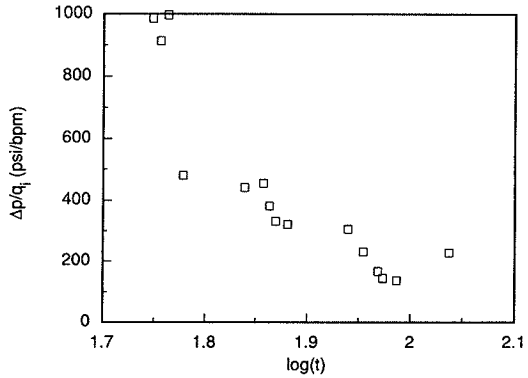

Figure 14-13
Inverse injectivity diagnostic plot after the first 56 min of injection (Example 14-6).

14-4 Fluid Placement and Diversion

A critical factor to the success of a matrix acidizing treatment is proper placement of the acid so that all of the productive intervals are contacted by sufficient volumes of acid. If there are significant variations in reservoir permeability, the acid will tend to flow primarily into the highest-permeability zones, leaving lower-permeability zones virtually untreated. Even in relatively homogeneous formations, the damage may not be distributed uniformly; without the use of techniques to improve the acid placement, much of the damage may be left untreated. Thus the distribution of the acid into the formation is a very important consideration in matrix acidizing, and a treatment design should include plans for acid placement. When it is determined that sufficient acid coverage cannot be obtained by allowing the acid to choose its own path, the acid should be diverted by mechanical means, with ball sealers, with particulate diverting agents, or with gels or foams.

14-4.1 Mechanical Acid Placement

The surest method for obtaining uniform acid placement is to isolate individual zones mechanically and treat all zones successively. Mechanical isolation can be accomplished with an opposed cup packer (perforation wash tool), the combination of a squeeze packer and a retrievable bridge plug, or inflatable straddle packers. These methods are described by McLeod (1984.) Mechanical placement techniques require the removal of tubulars from the well, adding significant cost to treatment. However, this cost may often be justified by the improved placement, particularly in horizontal wells.

14-4.2 Ball Sealers

Ball sealers are rubber-coated balls that are designed to seat in the perforations in the casing, thereby diverting injected fluid to other perforations. Ball sealers are added to the treating fluid in stages so that after a number of perforations have received acid, they are blocked, diverting acid to other stages. Most commonly, ball sealers are more dense than the treating fluid, so that after treatment, the ball sealers will fall into the rathole. However, Erbstoesser (1980) showed that ball sealers that are slightly buoyant in the carrying fluid seat more efficiently than dense ball sealers. Buoyant ball sealers will be produced back to the surface after completion of the treatment, so a ball trap must be added to the flow line. A general guideline for ball sealer use is to use twice as many dense ball sealers as perforations; with buoyant ball sealers, a 50% excess of ball sealers is recommended. The seating efficiency of ball sealers will increase as injection rate increases and are generally not recommended for low rate (< 1 bpm) treatments. Ball sealers are not effective in deviated or horizontal wells.

14-4.3 Particulate Diverting Agents

Perhaps the most common method of improving placement in matrix acidizing treatments is through the use of particulate diverting agents. Particulate diverting agents are fine particles that form a relatively low-permeability filter cake on the formation face. The pressure drop through this filter cake increases the flow resistance, diverting the acid to other parts of the formation where less diverting agent has been deposited. Diverting agents are either added to the treating fluid continuously, or in batches between stages of acid.

A particulate diverting agent must form a low-permeability filter cake and must be easily removed after treatment. To form a low-permeability filter cake, small particles and a wide range of particle sizes are needed. To ensure cleanup, materials that are soluble in oil, gas, and/or water are chosen. Commonly used particulate diverting agents and their recommended concentrations are given in Table 14-6 (McLeod, 1984).

Table 14-6

Summary of Particulate Diverters with Recommended Concentrations

Diverting Agent	Concentration
Oil-soluble resin or polymer	0.5 to 5 gal/1000 gal
Benzoic acid	1 lb_m/ft of perforations
Rock salt	0.5 to 2 lb_m/ft (do not use with HF acid)
Unibeads (wax beads)	1 to 2 lb_m/ft
Naphthalene flakes or moth balls	0.25 to 1 lb_m/ft (do not use in water-injection wells)

The presence of diverting agents complicates the diagnosis of acid treatments because the diverting agent is continuously adding a pressure drop at the wellbore. Simultaneously,

the acid is removing damage, decreasing the flow resistance near the wellbore. These two effects can be properly accounted for only with a comprehensive acidizing model, such as that presented by Taha et al. (1989). However, approximate models of the overall process can be helpful in designing diversion and interpreting the effect of diversion on the real-time rate/pressure behavior during an acid treatment.

Hill and Galloway (1984) presented a model of oil-soluble resin diverting agent performance that has been improved and extended by Doerler and Prouvost (1987), Taha et al. (1989), and Schechter (1992). These models all assume that the diverting agent forms an incompressible filter cake, and thus are applicable to any diverting agent that exhibits this behavior. Of the commonly used diverting agents, only Uni-Beads might be expected to deviate significantly from incompressible behavior.

The pressure drop across an incompressible filter cake can be expressed by Darcy's law as

$$\Delta p_{\text{cake}} = \frac{\mu u l}{g_c k_{\text{cake}}} \tag{14-52}$$

where u is the flux through the filter cake (q/A), l is the thickness of the filter cake, μ is the viscosity of the fluid carrying the diverting agent, and k_{cake} is the cake permeability. The thickness of the filter cake increases continuously as diverting agent is deposited and is related directly to the cumulative volume of diverting agent solution that has been injected. Incorporating this relationship into Eq. (14-52) yields

$$\Delta p_{\text{cake}} = \frac{\mu u C_{\text{da}} V}{g_c(1-\phi_{\text{cake}})k_{\text{cake}} A} \tag{14-53}$$

where C_{da} is the concentration of diverting agent particles in the carrying solution (volume of particles/volume of solution), V is the cumulative volume of solution injected, A is the cross-sectional area of the filter cake, and ϕ_{cake} is the porosity of the filter cake. This expression contains the intrinsic cake properties, ϕ_{cake} and k_{cake}, which are constant for an incompressible filter cake. However, these properties are difficult to measure independently. Instead, the pressure drop through the filter cake can be expressed in terms of the specific cake resistance, α, defined as

$$\alpha = \frac{1}{\rho_{\text{da}}(1-\phi_{\text{cake}})k_{\text{cake}}} \tag{14-54}$$

where ρ_{da} is the density of the diverting agent particles, so that

$$\Delta p_{\text{cake}} = \frac{\alpha \mu u C_{\text{da}} \rho_{\text{da}} V}{A g_c} \tag{14-55}$$

Taha et al. (1989) showed that α can be readily obtained from a variety of common laboratory tests. For example, if a diverting agent solution is injected into a core at constant rate and the pressure drop across the filter cake measured, Eq. (14-55) shows that α can be obtained from the slope of a Δp_{cake} versus cumulative volume curve. Taha et al. reported values of α for oil-soluble resin-diverting agents ranging from about 10^{13} to about 10^{15} ft/lb$_m$.

To calculate the effect of diverting agents during an acid treatment, the pressure drop through the filter cake can be expressed as a skin effect (Doerler and Prouvost, 1987):

$$s_{\text{cake}} = \frac{2\pi k h}{q\mu}\Delta p_{\text{cake}} \tag{14-56}$$

Substituting for Δp_{cake} with Eq. (14-55) and reconciling all units gives

$$s_{\text{cake}} = \frac{2.26 \times 10^{-16}\alpha C_{\text{da}}\rho_{\text{da}} k \bar{V}}{r_w^2} \tag{14-57}$$

where α is in ft/lb$_m$, C_{da} is ft^3 of diverting agent particles per cubic foot of solution, ρ_{da} is in lb$_m$/ft^3, k is the permeability of the formation in md, $\bar{V}$ is the specific cumulative volume injected (gal/ft), and r_w is the wellbore radius (ft). This expression for s_{cake} can now be incorporated into an equation describing the flow into a particular reservoir zone j. For example, assuming steady-state flow in the reservoir yields

$$\left(\frac{q_i}{h}\right)_j = \frac{(4.92 \times 10^{-6})(p_{wf} - p_e)k_j}{\mu\left[\ln(r_e/r_w) + s_j + s_{\text{cake},j}\right]} \tag{14-58}$$

where $(q_i/h)_j$ is in bpm/ft and all other quantities are in standard oilfield units. Recognizing that $(q_i/h)_j$ is the change in specific cumulative volume with time and incorporating the expression for $s_{\text{cake},j}$, Eq. (14-58) becomes

$$\frac{d\bar{V}_j}{dt} = \frac{(2.066 \times 10^{-4})(p_{wf} - p_e)k_j}{\mu[\ln(r_e/r_w) + s_j + c_{1,j}\bar{V}_j]} \tag{14-59}$$

where

$$c_{1,j} = \frac{2.26 \times 10^{-16}\alpha c_{\text{da}}\rho_{\text{da}} k_j}{r_w^2} \tag{14-60}$$

Equation (14-59) is an ordinary differential equation in $\bar{V}$ and t. If $p_{wf} - p_e$ remains constant, as in the maximum Δp, maximum rate method, Eqs. (14-58) and (14-59) can be solved directly to give the injection rate and cumulative volume injected into each layer as a function of time if the changing damage skin effect, s_j, is not considered. Alternatively, if the total injection rate is held constant, a system of J coupled ordinary differential equations result. Equations of this type and solutions for a few cases, neglecting the changing damage skin effect, were presented by Doerler and Prouvost (1987.)

To model the effects of diverting agents during acidizing more correctly, Eqs. (14-58) and (14-59) can be coupled with a comprehensive model of the acidizing process, as presented by Taha et al. (1989.) However, such an approach results in a complex numerical model. A simpler model can be obtained by assuming a relationship for the evolution of the damage skin effect and incorporating this relationship into Eqs. (14-58) and (14-59).

As acidizing proceeds, the skin effect will decrease until the damage has been almost entirely removed. After this point has been reached, the skin effect will change very slowly and can be approximated as being zero. The volume of acid needed to reduce the skin effect

to zero can be estimated based on an acidizing model, from laboratory results, or from field experience. The simplest approach is to assume that the skin effect will decrease linearly with cumulative acid injected until it reaches zero, and that it then remains constant. Thus,

$$s_j = s_{0,j} - c_{2,j}\bar{V}_j \qquad \bar{V}_j < \bar{V}_c \tag{14-61}$$

$$s_j = 0 \qquad \bar{V}_j > \bar{V}_c \tag{14-62}$$

where $s_{0,j}$ is the initial damage skin effect in layer j, $c_{2,j}$ is the rate of change of the skin effect as acid is injected, and $\bar{V}_{c,j}$ is the volume of acid needed to reduce the skin effect to zero. For example, if the initial skin effect is 10 and 50 gal/ft of acid are needed to reduce the skin effect to zero, $s_{0,j} = 10$, $c_{2,j} = 0.2$, and $\bar{V}_{c,j} = 50$. Bringing Eq. (14-61) to Eqs. (14-58) and (14-59) gives

$$\left(\frac{q_i}{h}\right)_j = \frac{(4.92 \times 10^{-6})(p_{wf} - p_e)k_j}{\mu\left[\ln(r_e/r_w) + s_{0,j} + (c_1 - c_2)_j\bar{V}_j\right]} \tag{14-63}$$

$$\frac{d\bar{V}_j}{dt} = \frac{(2.066 \times 10^{-4})(p_{wf} - p_e)k_j}{\mu\left[\ln(r_e/r_w) + s_{0,j} + (c_1 - c_2)_j\bar{V}_j\right]} \tag{14-64}$$

For convenience, these can be written as

$$\left(\frac{q_i}{h}\right)_j = \frac{a_{3,j}}{42(a_{1,j} + a_{2,j}\bar{V}_j)} \tag{14-65}$$

$$\frac{d\bar{V}_j}{dt} = \frac{a_{3,j}}{a_{1,j} + a_{2,j}\bar{V}_j} \tag{14-66}$$

where

$$a_{1,j} = \ln\left(\frac{r_e}{r_w}\right) + s_{0,j} \tag{14-67}$$

$$a_{2,j} = (c_1 - c_2)_j \tag{14-68}$$

$$a_{3,j} = \frac{2.066 \times 10^{-4}(p_{wf} - p_e)k_j}{\mu} \tag{14-69}$$

When it is integrated, Eq. (14-66) yields

$$t_j = \frac{a_{1,j}\bar{V}_j + (a_{2,j}/2)\bar{V}_j^2}{a_{3,j}} \tag{14-70}$$

$$\bar{V}_j = \frac{-a_{1,j} + \sqrt{a_{1,j}^2 + 2a_{2,j}a_{3,j}t}}{a_{2,j}} \tag{14-71}$$

Equations (14-63) through (14-71) apply to any layer for which $\bar{V}_j$ is less than $\bar{V}_{c,j}$. The injection time, $t_{c,j}$, at which $\bar{V}_j$ is equal to $\bar{V}_{c,j}$ is obtained from Eq. (14-70) by setting $\bar{V}_j$ equal to $\bar{V}_{c,j}$. For any layer in which $\bar{V}_j$ is greater than $\bar{V}_{c,j}$, $s_j = 0$ and the following equations hold:

$$a_{1,j} = \ln\left(\frac{r_e}{r_w}\right) \tag{14-72}$$

$$a_{2,j} = c_{1,j} \tag{14-73}$$

$$a_{4,j} = -\left[a_{3,j}(t - t_{c,j}) + a_{1,j}\bar{V}_{c,j} + \frac{a_{2,j}}{2}\bar{V}_{c,j}^2\right] \tag{14-74}$$

$$t_j = t_{c,j} + \frac{a_{1,j}\left(\bar{V}_j - \bar{V}_{c,j}\right) + (a_{2,j}/2)\left(\bar{V}_j^2 - \bar{V}_{c,j}^2\right)}{a_{3,j}} \tag{14-75}$$

$$\bar{V}_j = \frac{-a_{1,j} + \sqrt{(a_{1,j})^2 - 2a_{2,j}a_{4,j}}}{a_{2,j}} \tag{14-76}$$

The constant $a_{3,j}$ is independent of the injected volume, and Eq. (14-65) applies both before and after $\bar{V}_j$ is equal to $\bar{V}_{c,j}$ as long as the appropriate constants are used.

At any time during injection, the total injection rate and total injected volume are

$$\left(\frac{q_i}{h}\right)_t = \frac{\sum_{j=1}^{J}(q_i/h)_j h_j}{\sum_{j=1}^{J} h_j} \tag{14-77}$$

$$\bar{V}_t = \frac{\sum_{j=1}^{J}\bar{V}_j h_j}{\sum_{j=1}^{J} h_j} \tag{14-78}$$

The flow rate and cumulative volume injected for each layer as functions of injection time or total cumulative volume can be obtained from Eqs. (14-65) through (14-78) as follows. The highest-permeability layer, denoted as layer 1, serves as a convenient reference layer because the cumulative volume of acid will be highest for this layer at any given time. First, the injection rate and injection time as functions of the cumulative volume injected into the highest permeability layer are calculated with Eqs. (14-65) and (14-70) for $\bar{V}_1$ less than $\bar{V}_{c,1}$, and with Eqs. (14-65) and (14-75) for $\bar{V}_1$ greater than $\bar{V}_{c,1}$. Next, the cumulative volume injected into any other layer j *at the same time as when a known cumulative volume has been injected into the highest permeability layer* is calculated with Eq. (14-71) or Eq. (14-76), depending on whether $\bar{V}_j$ is less than or greater than $\bar{V}_{c,j}$. The injection rate for that layer is then calculated with Eq. (14-65). Finally, the total injection rate and cumulative volume injected for the time of interest are calculated by summing the contributions from all the layers, according to Eqs. (14-77) and (14-78).

EXAMPLE 14-7

Flow distribution during acidizing with diverting agents

Two reservoir zones of equal thickness and permeabilities of 100 and 10 md are to be acidized with an acid solution containing an oil-soluble resin diverting agent. The diverting agent is continuously added to the acid solution so that the concentration of diverting agent is 0.1 vol%.

The diverting agent has a specific gravity of 1.2 and a specific cake resistance of 10^{13} ft/lb$_m$, while the acid solution has a viscosity of 0.7 cp at downhole conditions.

The damage skin effect in both layers is initially 10, and 50 gal/ft of acid will remove all of the damage. The well radius is 0.328 ft, the drainage radius of the reservoir is 1980 ft, and the injection rate will be adjusted throughout the treatment to maintain $p_{wf} - p_e = 2000$ psi.

Calculate the injection rate and cumulative volume injected for each layer versus time up to a total injected volume of at least 100 gal/ft. Also, calculate and plot the total injection rate and the inverse injectivity as functions of time.

Solution First, the relevant constants for Eqs. (14-65) through (14-78) are calculated. From the given acidizing response, $\bar{V}_{c,j} = 50$ gal/ft and $c_{2,j} = 0.2$ for both layers. Labeling the high-permeability layer as layer 1, from Eq. (14-60),

$$c_{1,1} = \frac{(2.26 \times 10^{-16})(10^{13})(0.001)(1.2)(62.4)(100)}{(0.328)^2} = 0.157 \qquad (14\text{-}79)$$

and similarly, $c_{1,2} = 0.0157$. The constants $a_{i,j}$ are then calculated with Eqs. (14-67) through (14-69) for $\bar{V}_j$ less than $\bar{V}_{c,j}$, and with Eqs. (14-72) through (14-74) for $\bar{V}_j$ greater than $\bar{V}_{c,j}$. The results of these calculations are given in Table 14-7. The constants $a_{4,j}$ were not needed in this example, because the volume injected into the lower-permeability layer never exceeds 50 gal/ft.

Next the injection rate into layer 1 and the time that a given volume has been injected are calculated using Eqs. (14-65) and (14-70) for volumes up to 50 gal/ft. For example, at 50 gal/ft (which is $\bar{V}_{c,1}$),

$$\left(\frac{q_i}{h}\right)_1 = \frac{59.0}{42(18.7 - (0.043)(50))} = 0.085 \text{ bpm/ft} \qquad (14\text{-}80)$$

and

$$t_{c,1} = \frac{(18.7)(50) + (-0.043/2)(50^2)}{59.0} = 14.9 \text{ min} \qquad (14\text{-}81)$$

For larger injection volumes, the rate is again calculated with Eq. (14-65), but with the constants for $\bar{V}_j$ greater than $\bar{V}_{c,j}$, and the time corresponding to each volume is calculated with Eq. (14-75).

Table 14-7

Constants for Example 14-7

	$\bar{V}_j$ Less than $\bar{V}_{c,j}$			$\bar{V}_j$ Greater than $\bar{V}_{c,j}$		
Layer j	$a_{1,j}$	$a_{2,j}$	$a_{3,j}$	$a_{1,j}$	$a_{2,j}$	$a_{3,j}$
1	18.7	-0.043	59.0	8.7	0.157	59.0
2	18.7	-0.1843	5.90	8.7	0.0157	5.90

Now, for all injection times calculated previously, the flow rate and cumulative volume injected for layer 2 are calculated with Eqs. (14-65) and (14-71). Finally, the total injection rate and cumulative volume are calculated for each time with Eqs. (14-77) and (14-78). The results are given in Table 14-8.

Table 14-8

Example 14-7 Results

Time (min)	q_1 (bpm/ft)	q_2 (bpm/ft)	q_t (bpm/ft)	$\bar{V}_1$ (gal/ft)	$\bar{V}_2$ (gal/ft)	$\bar{V}_t$ (gal/ft)
0.00	0.075	0.0075	0.041	0.0	0.0	0.0
3.13	0.077	0.0076	0.042	10.0	1.0	5.5
6.20	0.079	0.0077	0.043	20.0	2.0	11.0
9.19	0.081	0.0077	0.044	30.0	2.9	16.5
12.10	0.083	0.0078	0.045	40.0	3.9	21.9
14.94	0.085	0.0079	0.046	50.0	4.8	27.4
18.15	0.077	0.0080	0.043	60.0	5.9	32.9
21.40	0.071	0.0081	0.040	70.0	7.0	38.5
24.71	0.066	0.0082	0.037	80.0	8.1	44.1
28.06	0.061	0.0083	0.035	90.0	9.3	49.6
31.47	0.058	0.0084	0.033	100.0	10.5	55.2
34.93	0.054	0.0085	0.031	110.0	11.7	60.8
38.45	0.051	0.0086	0.030	120.0	13.0	66.5
42.01	0.048	0.0087	0.028	130.0	14.3	72.1
45.63	0.046	0.0089	0.027	140.0	15.6	77.8
49.30	0.044	0.0090	0.026	150.0	17.0	83.5
53.03	0.042	0.0092	0.025	160.0	18.4	89.2
56.80	0.040	0.0093	0.025	170.0	19.9	94.9
60.63	0.038	0.0095	0.024	180.0	21.4	100.7
64.51	0.036	0.0097	0.023	190.0	22.9	106.5
68.44	0.035	0.0099	0.022	200.0	24.6	112.3

The injection rate and cumulative volume into each layer are shown in Figs. 14-14 and 14-15. The rate into layer 1 increases until 50 gal/ft have been injected, after which it declines. This behavior is due to the damage skin effect decreasing faster than the diverting agent skin increases until all damage is removed from the layer. After this time, the injection rate declines as diverting agent continues to build up on the sandface. The diverting agent was not very effective in this treatment, as the high-permeability layer received considerably more acid than necessary, while the low-permeability layer did not receive enough acid to remove all damage. Either a higher diverting agent concentration or a diverter with a higher specific cake resistance would result in better acid placement.

The total injection rate and inverse injectivity diagnostic plot are shown in Figs. 14-16 and 14-17. The total rate increases as the high-permeability layer responds to acid, then declines. This behavior results in a diagnostic plot much different from those for treatments without diverting agents. The positive slope on the diagnostic plot is the result of the increasing diverting agent pressure drop at the high-permeability layer. ◇

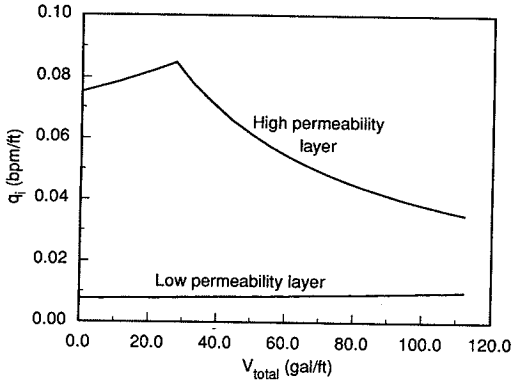

Figure 14-14
Injection rates into two layers (Example 14-7).

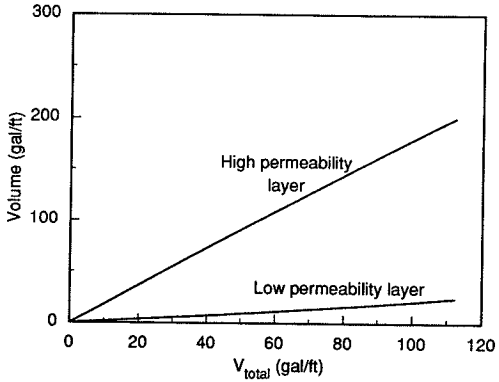

Figure 14-15
Cumulative volumes into two layers (Example 14-7).

EXAMPLE 14-8

The effect of the specific cake resistance on acid placement

Repeat the calculations of Example 14-7, but for the case of no diverting agent and for a diverting agent with a specific cake resistance of 10^{14} ft/lb$_m$. Compare the results for the three cases.

Solution The solutions for no diverting agent and a cake resistance of 10^{14} ft/lb$_m$ are obtained just as in Example 14-7. With no diverting agent, $s_{cake} = 0$, so all of the same equations can

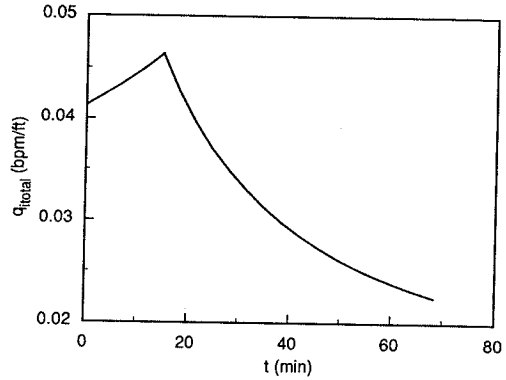

Figure 14-16
Total injection rate history (Example 14-7).

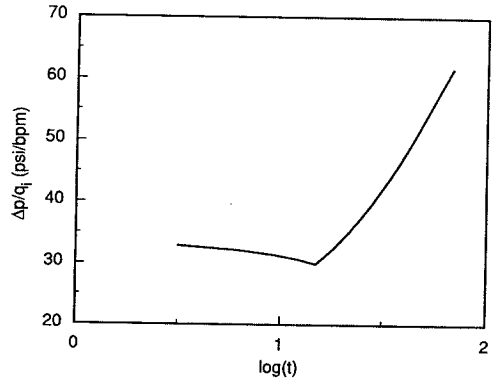

Figure 14-17
Inverse injectivity diagnostic plot (Example 14-7).

be used, with $c_{1,j} = 0$ in Eq. (14-60) for both layers. For the case of $\alpha = 10^{14}$, the volume injected into the low-permeability layer will exceed 50 gal/ft before a total of 100 gal/ft are injected. When $\bar{V}_2$ is greater than 50 gal/ft, $\bar{V}_2$ is calculated with Eq. (14-76), obtaining $a_{4,2}$ from Eq. (14-74).

The results are shown in Figs. 14-18 through 14-21. The effectiveness of diverting agent in decreasing injection to the highest-permeability layer is seen clearly in Fig. 14-18. Perhaps surprisingly, the injection rate into the lowest-permeability layer after 100 gal/ft of acid injection is highest when no diverting agent is used (Fig. 14-19), but paradoxically, the smallest cumulative amount of acid is injected into the low-permeability layer in this case. This is because the total injection rate is much higher with no diverting agent (recall that

the bottomhole pressure is being held constant), as shown in Fig. 14-20. With a high total injection rate, the time of injection is small, resulting in a small cumulative volume placed in the low-permeability layer. The diagnostic plots of inverse injectivity show much different characters for the three cases. When planning a treatment using diverting agents, it is helpful to prepare graphs such as these to assist in evaluating the diverting agent effectiveness during the treatment. ◇

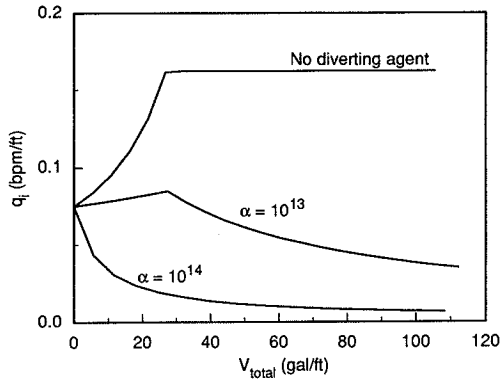

Figure 14-18
Injection rate into the high-permeability layer (Example 14-8).

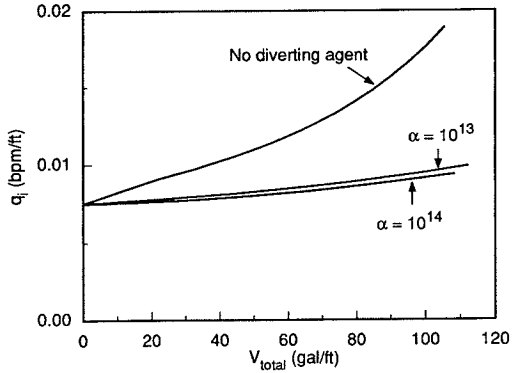

Figure 14-19
Injection rate into the low-permeability (Example 14-8).

The method presented here is based on particular assumptions about the effect of acid on damage removal; for example, it assumes that the damage skin effect decrease linearly with the cumulative acid injected. However, the same approach taken here can be applied with other relationships between damage skin effect and the amount of acid injected if better

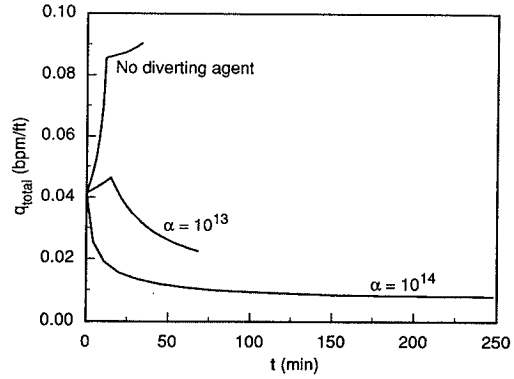

Figure 14-20
Total injection rate history (Example 14-8).

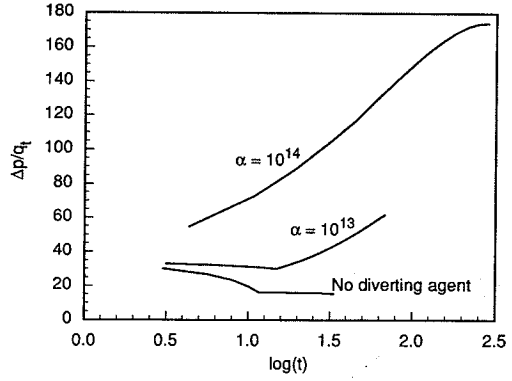

Figure 14-21
Inverse injectivity diagnostic plots (Example 14-8).

information is available for a particular formation.

The method presented is also based on the use of the wellbore cross-sectional area to represent the area on which diverting agent is deposited. For a cased, perforated completion, Doerler and Prouvost (1987) suggest approximating the perforations as cylinders, so that the cross-sectional area for diverting agent deposition is

$$A = 2\pi r_{perf} l_{perf} (SPF) h \tag{14-82}$$

Using this relationship for a perforated completion, r_w in Eqs. (14-57) and (14-60) is replaced by $(SPF) r_{perf} l_{perf}$ with SPF in shots/ft, and r_{perf} and l_{perf} in ft. Lea et al. (1991)

have shown that diversion within a perforation is not important to acidizing effectiveness, so this approach should give a reasonable model of diversion from one set of perforations to another.

14-4.4 Gels and Foams

Gelled and foamed acid solutions are being used increasingly as a means of improving acid placement. With gels, the mechanism of diversion is viscous diversion, the increase in flow resistance in higher-permeability regions due to the presence of a bank of viscous fluid. This can be modeled in a similar manner to that just shown for particulate diverting agents by defining a viscous skin effect as

$$s_{vis} = \left(\frac{\mu_{gel}}{\mu} - 1\right) \ln \frac{r_{gel}}{r_w} \tag{14-83}$$

where μ_{gel} is the viscosity of the gelled acid, μ is the viscosity of the formation fluid being displaced, and r_{gel} is the radius penetrated by the gel. Equation (14-83) is exactly analogous to Hawkins' formula, with viscosity instead of permeability being altered in the region near the well. The radius of gel penetration is related to the injected volume as done previously for acid solutions containing diverting agents.

Diversion by foams is a more complex phenomenon than viscous diversion, and is not well understood at present.

14-5 Preflush and Postflush Design

14-5.1 The HCl Preflush

Before the HF/HCl mixture is injected in a sandstone acidizing treatment, a preflush of hydrochloric acid, most commonly a 15 wt% solution, is usually injected. The primary purpose of the preflush is to prevent the precipitation of species such as calcium fluoride when the HF solution contacts the formation. The HCl preflush accomplishes this by dissolving the carbonate minerals, displacing ions such as calcium and sodium from the near-wellbore vicinity, and lowering the pH around the wellbore.

In situations where injectivity cannot be established with HCl, the HF/HCl mixture can be injected without a preflush. In this instance, the objective is not to obtain an optimal stimulation treatment, but to remove enough damage to establish communication with the formation for testing purposes. Paccaloni and Tambini (1990) reported several successful well responses without an HCl preflush in wells with very high skin effects that did not respond to conventional treatments using a preflush. It is likely that these wells had perforations clogged with drilling mud or other debris that was not HCl soluble.

When the HCl solution enters the formation, it dissolves carbonate minerals rapidly but does not react to a significant extent with other minerals. As seen in Chapter 13, the reaction rates between HCl and carbonate minerals are high, so that the movement of the HCl into the formation can be approximated as a shock front. Behind the front, all carbonate minerals have been dissolved and the HCl concentration is equal to the injected concentration. Ahead of the front, no reactions have occurred and a bank of spent HCl solution gradually builds up. Using the same dimensionless variables as defined for the

movement of the HF front in Table 14-2, the position of the HCl front is

$$\epsilon_{HCl} = \frac{\theta}{1 + [(1-\phi)/\phi]V^0_{CO_3} + (1/N_{Ac,HCl})} \tag{14-84}$$

where ϕ is the initial porosity in the region contacted by HCl, V^0_{CO3} is the initial volume fraction of the rock that is carbonate mineral, and the acid capacity number for HCl is defined similarly to that for HF, as

$$N_{Ac,HCl} = \frac{\phi \beta_{HCl} C^0_{HCl} \rho_{acid}}{(1-\phi) V^0_{CO_3} \rho_{CO_3}} \tag{14-85}$$

Equations (14-84) and (14-85) can be used to calculate the amount of HCl needed to remove all carbonates from a given region for radial flow around a wellbore or ellipsoidal flow around a perforation. The preflush volume is selected by assuming a distance to which all carbonates should be removed by the preflush and then calculating the acid volume required. A common procedure is to design the preflush to remove carbonates to a distance of 1 ft, as live HF is not likely to penetrate this far.

EXAMPLE 14-9
Preflush volume design for a perforated completion

Calculate the volume of 15 wt% HCl preflush needed to dissolve all carbonates to a distance of 1 ft beyond the tip of a 6-in.-long, 0.25-in.-diameter perforation if there are 4 shots/ft. The density of the acid solution is 1.07 g/cm^3. The formation contains 5 vol% $CaCO_3$ and no other HCl-soluble minerals and has an initial porosity of 0.2.

Solution The definition of the dimensionless penetration distance from the tip of a perforation is given in Table 14-2. For penetration of 1 ft from the tip of a 6-in. perforation, $\bar{z}$ = 1.5 ft/0.5 ft = 3. Then

$$\epsilon_{HCl} = \tfrac{1}{3}(3)^3 - 3 + \tfrac{2}{3} = 6\tfrac{2}{3} \tag{14-86}$$

From Table 13-3, $\beta_{100,HCl}$ = 1.37 and ρ_{CaCO3} = 2.71 g/cm^3. Using Eq. (14-85), the acid capacity number is

$$N_{Ac,HCl} = \frac{(0.2)(1.37)(0.15)(1.07)}{(1-0.2)(0.05)(2.71)} = 0.406 \tag{14-87}$$

Solving Eq. (14-84) for the dimensionless acid volume gives

$$\theta = \epsilon_{HCl}\left(1 + \frac{1-\phi}{\phi} V^0_{CO_3} + \frac{1}{N_{Ac,HCl}}\right) \tag{14-88}$$

and substituting the known values yields

$$\theta = 6.67\left[1 + \frac{(1-0.2)}{0.2}(0.05) + \frac{1}{0.406}\right] = 24.4 \tag{14-89}$$

From Table 14-2, the volume of acid per perforation is

$$V_{HCl} = q_{i,perf} t = (2\pi)(0.5)^3(24.4)(0.2) = 3.8 \text{ft}^3/\text{perf} = 29 \text{gal/perf} \tag{14-90}$$

With 4 shots/perf, 120 gal/ft of HCl preflush are needed. ◇

Designing the HCl preflush to remove all carbonates from 1 ft of formation before the injection of HF/HCl will be a conservative design because the HCl in the mud acid will continue to dissolve carbonates ahead of the live HF. Hill et al. (1991) showed that preflushes as small as 25 gal/ft ensured that live HF would not contact regions of high pH, even in heterogeneous formations. However, Gdanski and Peavy (1986) pointed out that some HCl will be consumed by ion exchange with clays, so an excess above that needed for carbonate dissolution may be appropriate.

14-5.2 The Postflush

After a sufficient volume of HF/HCl solution has been injected, it is displaced from the tubing and the wellbore with a postflush. A variety of fluids have been used for the postflush, including diesel, ammonium chloride (NH_4Cl) solutions, and HCl. The postflush displaces the spent acid farther from the wellbore so that any precipitates that may form will be less damaging. As a minimum, the postflush volume should be the volume of the tubing plus twice the volume of the wellbore below the tubing. Because of gravity segregation effects (Hong and Millhone, 1977), at least this much postflush is needed to displace all acid from the wellbore.

14-6 Acid Additives

Besides diverting agents, numerous other chemicals are frequently added to acid solutions, the most common of these being corrosion inhibitors, iron-sequestering compounds, surfactants, and mutual solvents. Acid additives should be tested carefully to ensure compatibility with other chemicals in the acid solution and with the formation fluids; only those that provide a clear benefit should be included in the treating fluids.

Corrosion inhibitors are needed in virtually all acid treatments to prevent damage to the tubulars and casing during acidizing. Corrosion of steel by HCl can be very severe without inhibition, particularly at high temperatures. The corrosion inhibitors used are organic compounds containing polar groups that are attracted to the metal surface. Corrosion inhibitors are usually proprietary formulations, so it is the responsibility of the service company supplying the acid to recommend the type and concentration of corrosion inhibitor to be used in a particular acid treatment.

An iron-sequestering compound, usually EDTA, is sometimes added to acid solutions when it is thought that ferric ions (Fe^{3+}) are present in the near-wellbore region in order to prevent the precipitation of $Fe(OH)_3$ in the spent acid solution. This situation should be rare, and the sequestering agents themselves are potentially damaging to the formation (see Chapter 13). In general, these materials should be used only when there is a clear indication of $Fe(OH)_3$ precipitation during acidizing.

Surfactants are added to acid solutions to prevent the formation of emulsions, to speed cleanup of spent acid, and to prevent sludge formation. Like sequestering agents, surfactants may have deleterious effects on the formation and should be used only after careful testing with the formation fluids and core samples.

An additive that has shown clear benefits in some sandstone acidizing applications is a mutual solvent, usually ethylene glycol monobutyl ether (EGMBE) (Gidley, 1971.) A mutual solvent is added to the postflush—it improves productivity apparently by removing corrosion inhibitor that has absorbed on formation surfaces (Crowe and Minor, 1985) and by restoring water-wet conditions.

14-7 Acidizing Treatment Operations

Three guiding principles should be followed when conducting an acidizing treatment: (1) All solutions to be injected should be tested to ensure that they conform to the design formulations; (2) all necessary steps should be taken to minimize the damage caused by the acidizing process itself; and (3) the acidizing process should be monitored by measuring the rate and pressure (surface and/or bottomhole). McLeod (1984), Brannon et al. (1987), Paccaloni and Tambini (1988), and numerous others have clearly shown the importance of these guidelines.

As mentioned previously, before an acidizing treatment is undertaken, there should be a clear indication that low well productivity is due, at least in part, to acid-soluble formation damage. This can be determined through a pretreatment pressure transient test to measure the skin effect, an analysis of other possible sources of skin, as shown in Chapter 5, and an assessment of the source of formation damage. A prestimulation production log is also helpful in some cases in planning the treatment and as a baseline for posttreatment analysis.

Before conducting the treatment, samples of the acid solutions should be taken, and as a minimum, the HCl concentrations should be checked on site with simple titrations. Some companies have developed acid quality control kits (Watkins and Roberts, 1983) that can be used to check acid concentrations rapidly.

A very important step in an acidizing treatment is cleaning of all surface tanks, surface flow lines, and the tubing used to inject the acid. Hydrochloric acid will partially dissolve and loosen rust, pipe dope, and other contaminants from pipe walls, so any source of such material should be cleaned before acid is introduced to the formation. Surface equipment can be cleaned prior to being brought to the location or on site with the acid solution itself. If the production tubing is to be used for acid injection, an HCl solution should be circulated down the tubing and back up the annulus before injection into the formation begins. Alternatively, clean coiled tubing can be employed for acid injection.

During the treatment, the injection rate and surface or bottomhole pressure should be monitored. The real-time monitoring discussed in this chapter can then be applied to optimize the treatment. Occasional samples of the injected solutions should also be taken; if any problems occur in the course of the treatment, samples of the injected solutions may be an important diagnostic aid.

When acid injection has been completed, the well should be flowed back immediately to minimize damage by reaction product precipitation. A posttreatment pressure transient test run shortly after a stabilized rate has been obtained is the most positive means of assessing the effect of the acid treatment. A production log will also be helpful in diagnosing the treatment outcome in some wells.

14-8 Acidizing of Horizontal Wells

Horizontal wells present a distinct challenge for matrix acidizing, if for no other reason than simply because of the extent of the region to be acidized. To attempt to obtain the same acid coverage in a horizontal well with a length of, for example, 2000 ft, would require an acid volume and treating time much greater than that typically needed for vertical wells. Besides the much greater cost, corrosion inhibition during long periods of acid injection may limit the extent of matrix acidizing that is feasible in a horizontal well.

However, the possible benefits of matrix acidizing in horizontal wells are clear. As seen in Chapter 5, a damaged zone around a horizontal well can greatly reduce the productivity. Economides et al. (1989) have shown that removal of such damage with acid is possible and very beneficial. The primary challenges for matrix acidizing in horizontal wells are to reduce the volume of acid needed and to find ways to properly place the acid.

It is likely that much of the productivity of a damaged horizontal well can be restored by acidizing only selected intervals, rather than the entire horizontal section. The result would be similar to the limited completion that Goode and Wilkinson (1989) demonstrated to be almost as productive as a fully completed horizontal well. This can best be accomplished with mechanical placement of the acid solution in selected locations along the horizontal section, using perforation wash tools or inflatable packers.

REFERENCES

1. Brannon, D. H., Netters, C. K., and Grimmer, P. J., "Matrix Acidizing Design and Quality-Control Techniques Prove Successful in Main Pass Area Sandstone," *JPT*, pp. 931–942, August 1987.
2. Bryant, S. L., "An Improved Model of Mud Acid/Sandstone Chemistry," SPE Paper 22855, 1991.
3. Cheung, S. K., and Van Arsdale, H., "Matrix Acid Stimulation Studies Yield New Results Using a Multi-Tap, Long-Core Permeameter," *JPT*, 98–102, January 1992.
4. Crowe, C. W., and Minor, S. S., "Effect of Corrosion Inhibitors on Matrix Stimulation Results," *JPT*, pp. 1853–1860, October 1985.
5. da Motta, E. P., "Matrix Acidizing of Horizontal Wells," Ph. D. dissertation, University of Texas at Austin, 1993.
6. da Motta, E. P., Plavnik, B., and Schechter, R. S., "Optimizing Sandstone Acidizing," *SPERE*, pp. 149–153, February 1992a.
7. da Motta, E. P., Plavnik, B., Schechter, R. S., and Hill, A. D., "The Relationship between Reservoir Mineralogy and Optimum Sandstone Acid Treatment," SPE Paper 23802, 1992b.
8. Doerler, N., and Prouvost, L. P., "Diverting Agents: Laboratory Study and Modeling of Resultant Zone Injectivities," SPE Paper 16250, 1987.
9. Economides, M. J., Ben-Naceur, K., and Klem, R. C., "Matrix Stimulation Method for Horizontal Wells," SPE Paper 19719, 1989.
10. Erbstoesser, S. R., "Improved Ball Sealer Diversion," *JPT*, pp. 1903–1910, November 1980.
11. Gdanski, R. D., and Peavy, M. A., "Well Return Analysis Causes Re-evaluation of HCl Theories," SPE Paper 14825, 1986.
12. Gidley, J. L., "Stimulation of Sandstone Formations with the Acid-Mutual Solvent Method," *JPT*, pp. 551–558, May 1971.
13. Goode, P. A., and Wilkinson, D. J., "Inflow Performance of Partially Open Horizontal Wells," SPE Paper 19341, 1989.
14. Guin, J. A., Schechter, R. S., and Silberberg, I. H., "Chemically Induced Changes in Porous Media," *Ind. Eng. Chem. Fund.*, **10** (1): 50–54, February 1971.
15. Hekim, Y., Fogler, H. S., and McCune, C. C., "The Radial Movement of Permeability Fronts and Multiple Reaction Zones in Porous Media," *SPEJ*, pp. 99–107, February 1982.

16. Hill, A. D., and Galloway, P. J., "Laboratory and Theortical Modeling of Diverting Agent Behavior," *JPT*, 1157–1163, July 1984.
17. Hill, A. D., Lindsay, D. M., Silberberg, I. H., and Schechter, R. S., "Theoretical and Experimental Studies of Sandstone Acidizing," *SPEJ*, pp. 30–42, February 1981.
18. Hill, A. D., Sepehrnoori, K., and Wu, P. Y., "Design of the HCl Preflush in Sandstone Acidizing," SPE Paper 21720, 1991.
19. Hong, K. C., and Millhone, R. S., "Injection Profile Effects Caused by Gravity Segregation in the Wellbore," *JPT*, pp. 1657–1663, December 1977.
20. Labrid, J. C., "Thermodynamic and Kinetic Aspects of Argillaceous Sandstone Acidizing," *SPEJ*, pp. 117–128, April 1975.
21. Lambert, M. E., "A Statistical Study of Reservoir Heterogeneity," MS thesis, The University of Texas at Austin, 1981.
22. Lea, C. M., Hill, A. D., and Sepehrnoori, K., "The Effect of Fluid Diversion on the Acid Stimulation of a Perforation," SPE Paper 22853, 1991.
23. Lund, K., and Fogler, H. S., "Acidization V. The Prediction of the Movement of Acid and Permeability Fronts in Sandstone," *Chem. Eng. Sci.*, **31** (5): 381–392, 1976.
24. McLeod, H. O., Jr., "Matrix Acidizing," *JPT*, **36**: 2055–2069, 1984.
25. Paccaloni, G., and Tambini, M., "Advances in Matrix Stimulation Technology," SPE Paper 20623, 1990.
26. Paccaloni, G., Tambini, M., and Galoppini, M., "Key Factors for Enhanced Results of Matrix Stimulation Treatments," SPE Paper 17154, 1988.
27. Prouvost, L. P., and Economides, M. J., "Applications of Real-Time Matrix Acidizing Evaluation Method," SPE Paper 17156, 1988.
28. Schechter, R. S., *Oil Well Stimulation*, Prentice Hall, Englewood Cliffs, NJ, 1992.
29. Sevougian, S. D., Lake, L. W., and, Schechter, R. S., "A New Geochemical Simulator to Design More Effective Sandstone Acidizing Treatments," SPE Paper 24780, 1992.
30. Smith, C. F., and Hendrickson, A. R., "Hydrofluoric Acid Stimulation of Sandstone Reservoirs," *JPT*, pp. 215–222, February 1965; *Trans. AIME*, **234**.
31. Taha, R., Hill, A. D., and Sepehrnoori, K., "Sandstone Acidizing Design with a Generalized Model," *SPEPE*, pp. 49–55, February 1989.
32. Walsh, M. P., Lake, L. W., and Schechter, R. S., "A Description of Chemical Precipitation Mechanisms and Their Role in Formation Damage during Stimulation by Hydrofluoric Acid," *JPT*, pp. 2097–2112, September 1982.
33. Watkins, D. R., and Roberts, G. E., "On-Site Acidizing Fluid Analysis Shows HCl and HF Contents Often Vary Substantially from Specified Amounts," *JPT*, pp. 865–871, May 1983.

PROBLEMS

14-1. Select the acid formulation or formulations to be used in the following formations:

(a) $k = 200$ md, $\phi = 0.2$, 5% carbonate, 5% feldspar, 10% kaolinite, 80% quartz
(b) $k = 5$ md, $\phi = 0.15$, 10% carbonate, 5% feldspar, 5% kaolinite, 80% quartz
(c) $k = 30$ md, $\phi = 0.25$, 20% carbonate, 5% chlorite, 75% quartz

14-2. In a core flood, $A_c^{(F)} = 0.024$ and $D_a^{(S)} = 0.6$. How many pore volumes of acid must be injected for the fast-reacting front to break through at the end of the core?

14-3. In a core flood in a 12-in.-long core, the dimensionless acid concentration at the fast-reacting mineral front is 0.7 when the front has moved 3 in. into the core. What is the dimensionless acid concentration at the front when the front has progressed 6 in.? 9 in.?

14-4. In a core flood in a 6-in.-long core, the fast-reacting mineral front breaks through at the end of the core after 50 pore volumes have been injected. The dimensionless acid concentration after breakthrough is 0.8. Calculate $A_c^{(F)}$ and $D_a^{(S)}$.

14-5. In a core flood of a 1-in.-diameter by 6-in.-long core, the acid flux is 0.04 ft/min. From this experiment, it was found that $D_a^{(S)} = 0.9$ and $A_c^{(F)} = 0.02$. For this formation and acid concentration and an injection rate of 0.1 bpm/ft, calculate and plot the acid volume as a function of the distance from the wellbore that the fast-reacting minerals have all been removed, out to a distance of 6 in. from the wellbore. Assume radial flow.

14-6. Repeat Problem 14-5, but for penetration of the front from the tip of a perforation.

14-7. For a particular sandstone, after all carbonates have been dissolved, the permeability is 10 md and the porosity is 0.15. The remaining minerals are 5 vol% clay, which reacts rapidly with HF. Calculate the permeability of this sandstone after all clays have been removed using the Labrid, Lund and Fogler, and Lambert correlations.

14-8. Calculate and plot the maximum tubing injection pressure and initial injection rate for matrix acidizing conditions if all parameters are the same as in Example 14-5, except instead of 2-in. tubing with a relative roughness of 0.001, injection is through:

(a) 1-in.-I.D. tubing, $\epsilon = 0.001$
(b) 3-in.-I.D. tubing, $\epsilon = 0.001$
(c) 2-in.-I.D. tubing, $\epsilon = 0.0001$

14-9. For the data given below for a matrix acidizing treatment, construct a diagnostic plot. What do you conclude about this treatment?

Fluid at Perfs.	Time (hr)	q_i (bpm)	p_{wf} (psi)
Water	0.15	2	4500
Water	0.30	2	4480
Water	0.45	2	4400
Aromatic solvent	0.60	2	4390
Aromatic solvent	0.75	2.5	4350
Aromatic solvent	0.90	2.4	4270
Aromatic solvent	1.05	2.7	4250
15% HCl	1.20	2.5	4200
15% HCl	1.35	3.2	3970
3%HF/12%HCl	1.50	3.7	3800
3%HF/12%HCl	1.65	4.1	3750
3%HF/12%HCl	1.80	4.4	3670
3%HF/12%HCl	1.95	1.0	2920
3%HF/12%HCl	2.10	3.9	3400
3%HF/12%HCl	2.25	5.6	3730
3%HF/12%HCl	2.40	5.6	3750
3%HF/12%HCl	2.55	5.6	3650
3%HF/12%HCl	2.70	5.7	3600
3%HF/12%HCl	2.85	5.8	3400

14-10. An acid solution containing an oil-soluble resin diverting agent is injected into a two-layer reservoir. The diverting agent concentration in the acid is 0.1 vol%, the diverting agent particles have a density of 1.2 g/cm^3, the specific cake resistance is 5×10^{13} ft/lb$_m$, and the viscosity of the acid solution at downhole conditions is 0.6 cp. For either layer, 50 gal/ft of acid will remove all damage. The wellbore radius is 0.328 ft, the drainage radius is 1490 ft, and the acid is injected at a pressure difference, $p_{wf} - p_e$, of 3000 psi. Layer 1 has a permeability of 75 md and an initial skin effect of 20, while layer 2 has a permeability of 25 md and an initial skin effect of 10. Plot $(q/h)_j$ and $\bar{V}_j$ for each layer as functions of the total cumulative volume per foot injected.

14-11. Repeat Problem 14-10, but for the case of no diverting agent in the acid.

14-12. Derive an equation for $(q/h)_j$ [analogous to Eq. (14-63)] for viscous diversion with a gel. Leave the expression in terms of μ_{gel}, μ, $\bar{V}_j$, and other constants.

14-13. Calculate the HCl preflush volume needed to remove all carbonates to a distance of 6 in. from the wellbore in radial flow. The acid is a 10 wt% solution with a specific gravity of 1.05. The formation contains 7 vol% $CaCO_3$ and has a porosity of 0.19.

CHAPTER 15

Carbonate Acidizing Design

15-1 INTRODUCTION

Carbonate acidizing is a more difficult process to predict than sandstone acidizing because, despite the chemistry of the process being much simpler than that of sandstone acidizing, the physics is decidedly more complex. In sandstones, the surface reaction rates are slow and a relatively uniform acid front moves through the porous medium. In carbonates, surface reaction rates are very high, so mass transfer often limits the overall reaction rate, leading to highly nonuniform dissolution patterns. Often, a few large channels, called wormholes, are created, such as shown in Fig. 15-1, caused by the nonuniform dissolution of limestone by HCl in a linear core flood (Hoefner and Fogler, 1988.) The structure of these wormhole patterns will depend on many factors, including (but not limited to) flow geometry, injection rate, reaction kinetics, and mass transfer rates. For example, Fig. 15-2 shows a casting of wormholes created by radial flow of water through plaster (Daccord and Lenormand, 1987); this wormhole pattern is much more branched than that shown in Fig. 15-1 and, clearly, the amounts of acid needed to propagate wormholes in these two systems would differ significantly.

Since wormholes are much larger than the pores in nonvugular carbonates, the pressure drop through the region penetrated by wormholes will be insignificant. Thus, in matrix acidizing, knowledge of the depth of penetration of wormholes allows a prediction of the effect of acidizing on the skin effect. Wormholing is also very significant in acid fracturing, as it will increase fluid loss rates, limiting the penetration of acid down the fracture. Thus, to predict acidizing results in carbonates, the physics of wormhole growth must be described. This inherently unstable process is not understood completely, but considerable progress has been made in recent years.

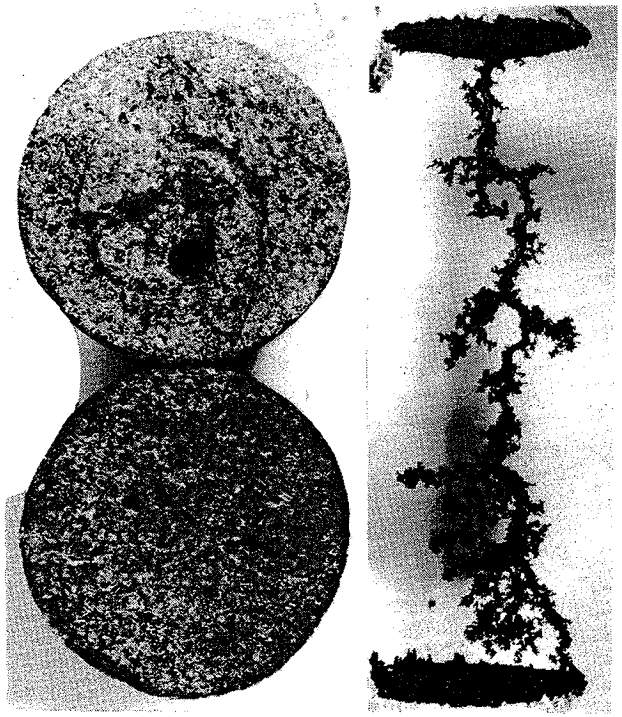

Figure 15-1
Wormholes created by acid dissolution of limestone. (*From Hoefner and Fogler, 1988; courtesy of AICHE.*)

15-2 Wormhole Formation and Growth

Wormholes form in a dissolution process when the large pores grow at a rate substantially higher than the rate at which smaller pores grow, so that a large pore receives an increasingly larger proportion of the dissolving fluid, eventually becoming a wormhole. This will occur when the reactions are mass transfer limited or mixed kinetics prevail, that is, the mass transfer and surface reaction rate are similar in size. For flow with reaction in a circular pore, the relative effects of mass transfer and surface reaction rates can be expressed by a kinetic parameter, P, the inverse of the Thiele modulus, defined as the ratio of the diffusive flux to the flux of molecules consumed by surface reaction (Daccord, 1989),

Figure 15-2
Molding of wormholes created by water dissolution of plaster. (*From Daccord and Lenormand, 1987; courtesy of Schlumberger.*)

$$P = \frac{u_d}{u_s} \tag{15-1}$$

or

$$P = \frac{D}{E_f r C^{n-1}} \tag{15-2}$$

where D is the molecular diffusion coefficient, E_f is the surface reaction rate constant, r is the pore radius, and C is the acid concentration. Since the overall reaction kinetics are controlled by the slowest step, $P \longrightarrow 0$ corresponds to mass transfer-limited reactions and $P \longrightarrow \infty$ indicates surface reaction rate-limited reactions. When P is near 1, the kinetics are mixed, and both surface reaction rate and mass transfer rate are important.

The natural tendency for wormholes to form when reaction is mass transfer limited has been demonstrated theoretically by Schechter and Gidley (1969), using a model of pore growth and collision. In this model, the change in the cross-sectional area of a pore can be expressed as

$$\frac{dA}{dt} = \Psi A^{1-n} \tag{15-3}$$

where A is the pore cross-sectional area, t is time, and Ψ is a pore growth function that does depend on time. Examination of Eq. (15-3) shows that if $n > 0$, smaller pores grow faster than larger pores and wormholes cannot form; when $n < 0$, larger pores grow faster than smaller pores, and wormholes will develop. From an analysis of flow with diffusion and surface reaction in single pores, Schechter and Gidley found that $n = 1/2$ when surface reaction rate controls the overall reaction rate, and $n = -1$ when diffusion controls the overall reaction rate.

Models of flow with reaction in collections of cylindrical pores can predict the tendency for wormhole formation, but do not give a complete picture of the wormholing process because they do not include the effects of fluid loss from the pores. As acid moves through a large pore or channel, acid moves to the reactive surface by molecular diffusion, but also by convective transport as acid flows to the smaller pores connected with the large pore. As the large pore grows, the fluid loss flux is a larger and larger portion of the flow of acid to the wormhole wall and is ultimately the limiting factor for wormhole growth. The fluid loss through the walls of the wormhole leads to the branches seen in Figs. 15-1 and 15-2.

Thus, whether or not wormholes will form, and the structure of the wormholes that do form, depend on the relative rates of surface reaction, diffusion, and fluid loss, all of which depend on the overall convection rate of the acid. A progression of dissolution patterns will occur as injection rate is increased. For a system with very high surface reaction rates, such as the HCl-limestone system, the modes of acid attack can be described as compact dissolution, diffusion-limited wormholing, fluid loss-limited wormholing, and uniform dissolution. These dissolution patterns are shown in Fig. 15-3, as predicted by the network model of Hoefner and Fogler (1988.) At a very low injection rate, the inlet face of the rock will be slowly consumed as acid diffuses to the surface, yielding compact dissolution of the rock face. This type of dissolution will not occur in a practical acidizing situation in limestone because the injection rate must be so low. However, it is of interest as the limiting case as flow rate approaches zero.

With increasing flow rate, a dominant wormhole (or a few dominant wormholes) forms and propagates into the porous medium. At relatively low injection rates there will be little branching, and only one or a few large wormholes will be formed. A characteristic of this mode of acid attack, called diffusion-limited wormholing, is that the volume of acid needed to propagate the wormhole a given distance decreases as injection rate increases.

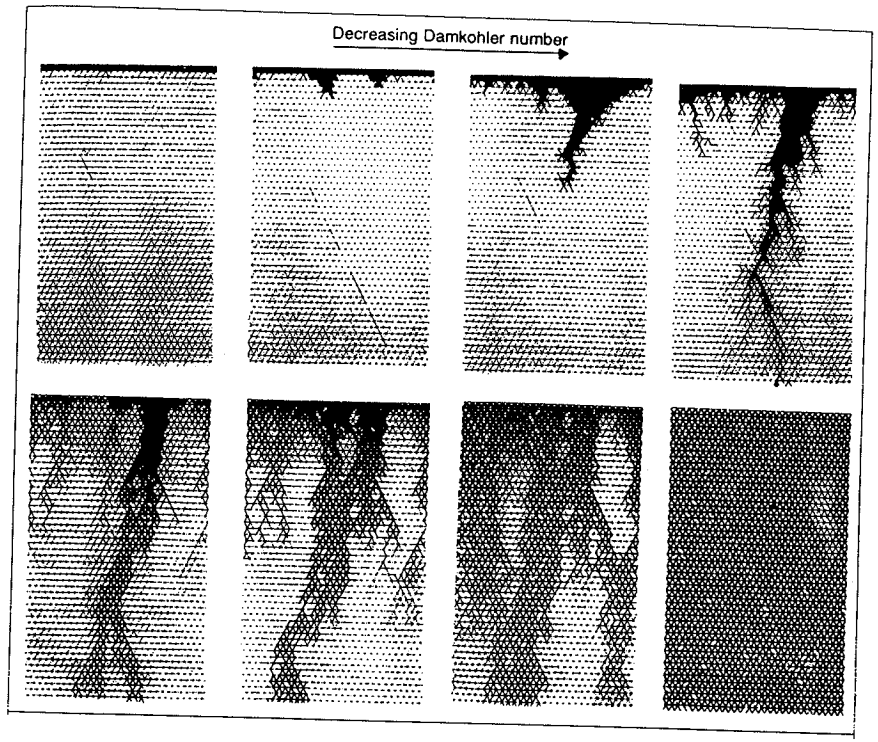

Figure 15-3
Network model simulations of wormhole patterns. (*From Hoefner and Fogler, 1988; courtesy of AICHE.*)

At even higher flow rates, more and more branches form, consuming significant amounts of acid and thus slowing the wormhole propagation rate. In this mode of attack, called fluid loss-limited wormholing, the branched wormhole structure may be fractal, as demonstrated by Daccord and Lenormand (1987.) Interestingly, the acidizing efficiency decreases as injection rate increases when fluid loss-limited wormholing occurs. This means that an optimal injection rate for efficient wormhole propagation will exist corresponding to the transition from diffusion limited to fluid loss-limited wormholing.

At sufficiently high injection rates, the mass transfer of acid is so rapid that the overall reaction rate becomes surface reaction rate limited, and uniform dissolution occurs,

analogous to that in sandstones. Since the injection rate is limited to avoid fracturing, uniform dissolution may never occur in a matrix treatment in highly reactive carbonates.

The progression presented here depends on the relative size of the diffusion and surface reaction rates and also on the flow geometry because of the role of fluid loss. Thus, wormholing behavior is much different in dolomites compared with limestones because of the different reaction rates. Also, predictions based on linear flow, such as standard core floods, may not be valid for other flow geometries, such as radial flow or flow from a perforation.

The transition from diffusion limited to fluid loss-limited wormholing has been demonstrated in linear core floods with HCl and limestone. Figure 15-4 shows the volumes of acid needed to propagate wormholes through Indiana limestone cores from the experiments of Wang (1993) and Hoefner and Fogler (1988.) A distinct minimum in the amount of acid required to propagate a wormhole through the core exists, showing the transition from diffusion-limited to fluid loss-limited wormholing. Notice that in the diffusion-limited regime, the volume of acid needed to propagate a wormhole a certain distance decreases rapidly as the injection rate increases, but when the wormhole propagation is fluid loss-limited, the volume of acid required increases only gradually with increasing injection rate. This means that it is better to inject at a rate above the optimum than at too low a rate.

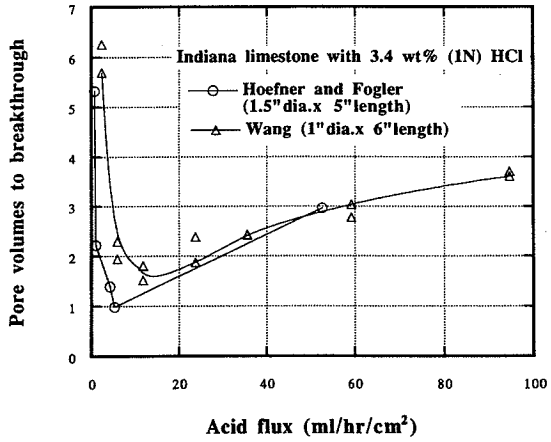

Figure 15-4
Acid volumes needed to propagate wormholes through linear limestone cores. (*From Wang, 1993.*)

The HCl-dolomite reaction rate is significantly lower than that for HCl and limestone. With a lower reaction rate, fluid loss-limited wormhole behavior occurs at lower rates and more acid is needed to propagate a wormhole a given distance, as shown in Fig. 15-5.

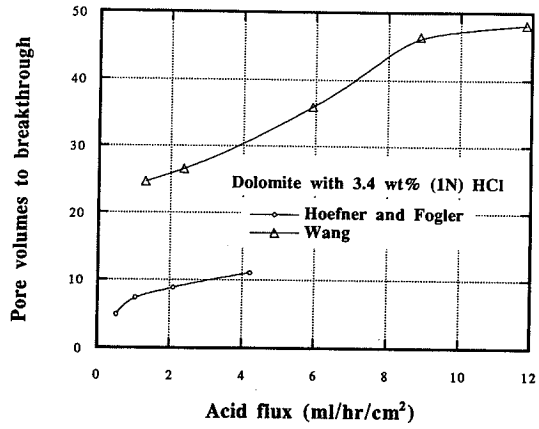

Figure 15-5
Acid volumes needed to propagate wormholes through linear dolomite cores. (*From Wang, 1993.*)

Three types of models of the wormholing process have been presented in the literature: mechanistic models of a single wormhole or a collection of wormholes (Hung et al., 1989; Schechter, 1992); network models (Hoefner and Fogler, 1988; Daccord et al., 1989); and fractal or stochastic models (Daccord et al., 1989; Pichler et al., 1992). Of these, the network models appear to give the best representation of wormhole behavior over a wide range of conditions. However, their application for treatment design is cumbersome. In addition to these models, a simple empirical model (the volumetric model) is also presented here.

A mechanistic model of wormhole propagation is illustrated in Fig. 15-6. If the reaction rate is high, all of the acid transported to the end of the wormhole will be spent dissolving rock at the wormhole tip, thus extending the wormhole. A mass balance gives the wormhole velocity (dL/dt) as

$$\frac{dL}{dt} = \frac{u_{end} C_{end} \rho_{acid} \beta_{100}}{(1-\phi)\rho_{rock}} \tag{15-4}$$

where u_{end} and C_{end} are the flux and acid concentration (mass fraction) at the end of the wormhole. This can also be written in terms of the acid capacity number as

$$\frac{dL}{dt} = \left(\frac{u_{end}}{\phi}\right)\left(\frac{C_{end}}{C_0}\right) N_{Ac} \tag{15-5}$$

Equation (15-5) shows the role of diffusion and fluid loss in wormhole propagation. The more acid diffuses to the wormhole wall, the lower is the concentration at the end of the

wormhole. Likewise, the greater the fluid loss along the wormhole, the lower is the flux to the end of the wormhole. Thus, diffusion and fluid loss tend to decrease the velocity of a wormhole. To complete the model of wormhole propagation, the diffusional and fluid loss fluxes to the wormhole wall must be calculated. Using a complex model of acid transport in a wormhole, Hung et al. (1989) found that the wormhole velocity increases linearly with the injection rate into the wormhole, implying that the volume of acid needed to propagate a wormhole a given distance is independent of injection rate. This model also predicts that the wormhole velocity will be constantly decreasing because the acid flux to the end of the wormhole is decreasing as the wormhole grows.

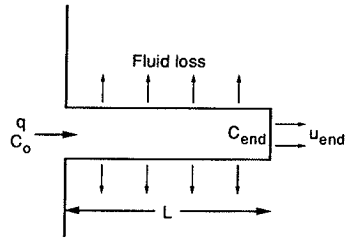

Figure 15-6
Idealization of a wormhole.

In a network model, the porous medium is approximated as a collection of interconnected capillaries. To model wormhole behavior, the acid concentration in each capillary is calculated and the radii of the capillaries are increased as dissolution occurs. With this type of model, results like those shown in Fig. 15-3 are obtained. Network models predict the types of wormhole patterns observed experimentally, but are difficult to generalize for treatment design.

Daccord et al. (1989) presented a model of wormhole propagation based on the nature of wormhole structures observed when fluid loss-limited behavior occurs. Based primarily on experiments with plaster and water, Daccord et al. found that, for linear flow,

$$L = \frac{aVN_{Ac}}{A\phi} D^{-2/3} q^{-1/3} \tag{15-6}$$

where a is an experimentally determined constant, V is the cumulative volume of acid injected, D is the molecular diffusion coefficient, and A is the cross-sectional area of flow. This equation shows that, for a fixed volume of acid injected, a longer wormhole will be obtained at a lower injection rate, as is observed in fluid loss-limited wormhole propagation. Since V is just qt, Eq. (15-6) can also be written as

$$\frac{dL}{dt} = \frac{aN_{Ac}}{A\phi} D^{-2/3} q^{2/3} \tag{15-7}$$

showing that the wormhole velocity increases with the injection rate to the 2/3 power.

For the fractal wormhole patterns observed in radial flow with water and plaster, Daccord et al. found

$$r_{wh} = \left[\frac{bN_{Ac}V}{\pi h\phi} D^{-2/3} \left(\frac{q}{h} \right)^{-1/3} \right]^{1/d_f} \tag{15-8}$$

where r_{wh} is the radius of wormhole penetration, b is a constant, and d_f is the fractal dimension, found to be equal to about 1.6. Again substituting qt for V and differentiating with respect to time yields

$$\frac{dr_{wh}}{dt} = \frac{1}{d_f} \left(\frac{bN_{Ac}D^{-2/3}}{\pi\phi} \right)^{(1/d_f)} \left(\frac{q}{h} \right)^{(2/3d_f)} t^{(1/d_f - 1)} \tag{15-9}$$

This predicts that the wormhole velocity in radial flow increases with injection rate to the 0.4 power and decreases with time. Daccord et al. report the constant b to be 1.5×10^{-5} in SI units for their experiments in small radial core floods with water and plaster. It is likely that b is smaller for field systems.

Daccord's model is based on diffusion being the limiting mechanism for acid transport to the rock surface and does not consider the role of fluid loss, which is the main limitation to wormhole growth in many cases. It is also based on the wormhole network geometry observed in water-plaster experiments, and these may not properly represent the patterns that occur in acid dissolution of carbonates. Thus, Daccord's model will likely overestimate the distance of wormhole penetration in carbonate acidizing and should be used with caution. Nevertheless, the application of this model is illustrated here so that it can be compared with other models.

EXAMPLE 15-1
Radius of wormhole penetration with Daccord's model

Calculate the radius of penetration of wormholes after the injection of 50 gal/ft of 15 wt% HCl at a rate of 0.1 bpm/ft into a limestone formation with a porosity of 0.2 using Daccord's fractal model. The molecular diffusion coefficient is 10^{-9} m^2/sec.

Solution The radius of wormhole penetration for Daccord's model is calculated with Eq. (15-8). Since the constant b is given in SI units and its units are complex, it is simplest to convert the units of injection rate and volume to SI units. Using conversion factors from Table 1-1, these are

$$\frac{q}{h} = \left(0.1 \frac{\text{bbl}}{\text{min-ft}} \right) \left(0.159 \frac{\text{m}^3}{\text{bbl}} \right) \left(\frac{\text{min}}{60\ \text{s}} \right) \left(\frac{\text{ft}}{0.3048\ \text{m}} \right) = 8.69 \times 10^{-4}\ \text{m}^3/\text{s-m}$$

$$\frac{V}{h} = \left(50 \frac{\text{gal}}{\text{ft}} \right) \left(3.785 \times 10^{-3} \frac{\text{m}^3}{\text{gal}} \right) \left(\frac{\text{ft}}{0.3048\ \text{m}} \right) = 0.621\ \text{m}^3/\text{m} \tag{15-10}$$

The acid capacity number for the injection of 15 wt% HCl into a 0.2-porosity limestone is

$$N_{Ac} = \frac{(0.2)(1.37)(0.15)(1.07)}{(1 - 0.2)(2.71)} = 2.03 \times 10^{-2} \tag{15-11}$$

Applying Eq. (15-8),

$$r_{wh} = \left[\frac{(1.5 \times 10^{-5})(0.0203)(0.621)}{\pi(0.2)}(10^{-9})^{-2/3}(8.69 \times 10^{-4})^{-1/3}\right]^{1/1.6} \quad (15\text{-}12)$$
$$= 2.05 \text{ m} = 6.74 \text{ ft}$$

This is very deep penetration of acid, particularly compared with sandstone acidizing. By comparison, a nonreacting tracer would penetrate only 1.3 m (4.3 ft) after 50 gal/ft of injection into a 20% porosity formation. The deep penetration is a result of the wormholing—acid is spent on (and flows through) only a fraction of the porous medium. The radius of penetration predicted here is probably significantly deeper than would occur in practice, because it is based on small-scale experiments where the wormhole velocities are high. ◇

Recently, Pichler et al. (1992) presented a stochastic model of wormhole growth, based on diffusion-limited kinetics and incorporating the randomness of diffusion-limited aggregation (DLA) models. This model predicts the branched wormhole structures found in carbonate acidizing, as shown in Fig. 15-7. With a large diffusion rate (Fig. 15-7a) the wormhole branches are thick, while lower diffusion rates lead to predictions of thinner wormhole branches (Fig. 15-7b.) This difference illustrates the transition in wormhole patterns from a pattern near to compact dissolution (Fig. 15-7a) to a more dominant wormhole structure (Fig. 15-7b.) Pichler et al. also included permeability anisotropy, permeability heterogeneity, and natural fractures in their model and illustrated how these factors bias the wormhole patterns created. With further development, stochastic models such as this one show great promise for predicting wormhole propagation quantitatively.

Another approach to predicting the volume of acid required to propagate wormholes a given distance is to assume that the acid will dissolve a constant fraction of the rock penetrated. When only a few wormholes are formed, a small fraction of the rock is dissolved; more branched wormhole structures dissolve larger fractions of the matrix. Defining η as the fraction of the rock dissolved in the region penetrated by acid, for radial flow it can be shown that

$$r_{wh} = \sqrt{r_w^2 + \frac{N_{Ac}V}{\eta\pi\phi h}} \quad (15\text{-}13)$$

The wormholing efficiency, η, can be estimated from linear core flood data as being

$$\eta = N_{Ac}PV_{bt} \quad (15\text{-}14)$$

where PV_{bt} is the number of pore volumes of acid injected at the time of wormhole breakthrough at the end of the core. This approach is equivalent to assuming that a fixed number of pore volumes of acid is needed to propagate wormholes a given distance.

The model presented here (the volumetric model) is an empirical one. If the wormholing efficiency is obtained from radial core floods, it should accurately predict wormhole propagation in a well treatment where the flow is radial, at least for wormhole propagation to the same distance as that tested in the core flood. If linear core floods are used to measure η, the wormhole propagation in radial flow will probably be somewhat overestimated.

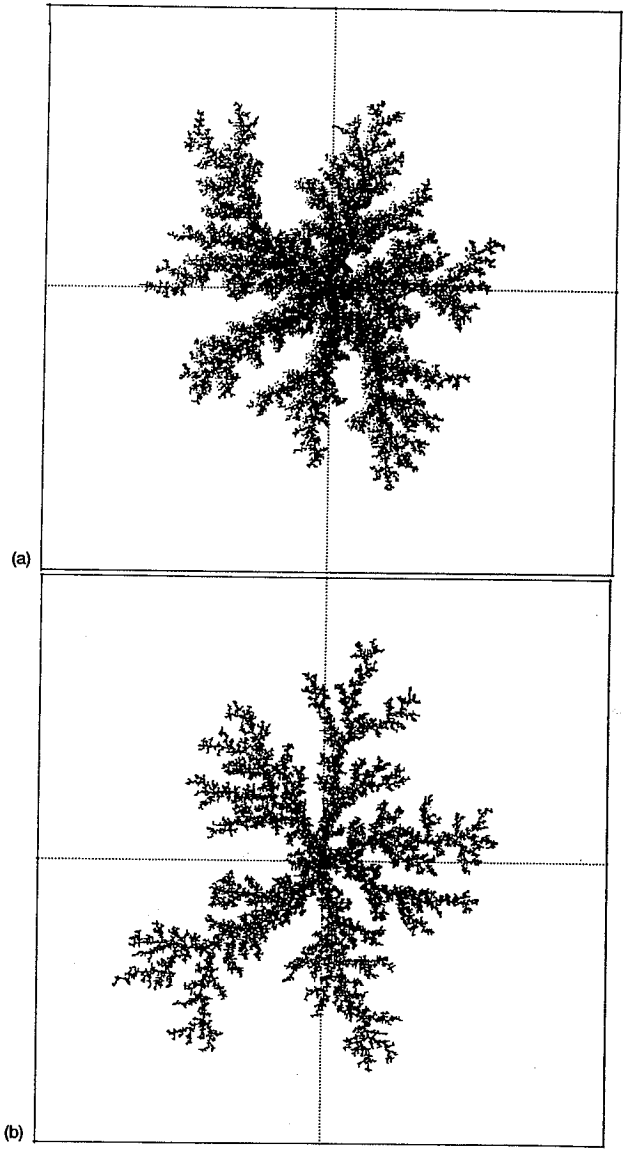

Figure 15-7
Wormhole patterns generated by a stochastic model. (*From Pichler et al., 1992.*)

EXAMPLE 15-2

Volumetric model of wormhole propagation

The data in Fig. 15-4 show that about 2 pore volumes of 1 N (3.4 wt%) HCl are required for wormholes to break through in a linear core flood in limestone, while Fig. 15-5 shows about 25 pore volumes of the same acid are needed for breakthrough in dolomite. Calculate the wormhole penetration after the injection of 50 gal/ft of 3.4 wt% HCl into limestone and dolomite, assuming that a constant fraction of the rock is dissolved. In both cases, the porosity is 0.2 and the wellbore radius is 0.328 ft.

Solution First, the acid capacity numbers are calculated. For limestone, the value obtained in Example 15-1 for 15 wt% HCl can be multiplied by the ratio of the concentrations:

$$N_{Ac} = (0.0203)\left(\frac{3.4}{15}\right) = 4.6 \times 10^{-3} \tag{15-15}$$

For dolomite, the acid capacity number is

$$N_{Ac} = \frac{(0.2)(1.27)(0.034)(1.01)}{(1-0.2)(2.87)} = 3.8 \times 10^{-3} \tag{15-16}$$

The wormholing efficiencies are calculated from Eq. (15-11):

$$\text{Limestone:} \quad \eta = (4.6 \times 10^{-3})(2) = 9.2 \times 10^{-3} \tag{15-17}$$

$$\text{Dolomite:} \quad \eta = (3.8 \times 10^{-3})(25) = 9.5 \times 10^{-2} \tag{15-18}$$

These efficiencies show that in limestone, less than 1% of the rock is dissolved in the region penetrated by wormholes, while in dolomite, almost 10% of the rock is dissolved. Applying Eq. (15-13), the radial penetration distance of wormholes is

$$\text{Limestone:} \quad r_{wh} = \sqrt{(0.328\text{ ft})^2 + \frac{(50\text{ gal/ft})(1\text{ ft}^3/7.48\text{ gal})(4.6 \times 10^{-3})}{(9.2 \times 10^{-3})(\pi)(0.2)}}$$

$$= 2.33\text{ ft} \tag{15-19}$$

$$\text{Dolomite:} \quad r_{wh} = \sqrt{(0.328\text{ ft})^2 + \frac{(50\text{ gal/ft})(1\text{ ft}^3/7.48\text{ gal})(3.8 \times 10^{-3})}{(9.5 \times 10^{-2})(\pi)(0.2)}} \tag{15-20}$$

$$= 0.73\text{ ft}$$

The wormhole penetration for limestone is 2.33 ft, while for dolomite it is only 0.73 ft, a penetration of 0.4 ft into the formation. This model, like Daccord's, will overpredict the wormhole penetration for large acid volumes, as neither considers the slowing of the wormhole because of increasing fluid loss. ◇

15-3 Matrix Acidizing Design for Carbonates

15-3.1 Acid Type and Concentration

Hydrochloric acid is by far the most common acid used in carbonate matrix acidizing. Table 15-1 shows the acids suggested by McLeod (1984) for various acid treatments of carbonate formations. Weak acids are suggested for perforation cleanup and perforating fluid, but otherwise, strong solutions of HCl are recommended. For a matrix treatment, HCl should be used unless corrosion considerations require a weaker acid (this would occur only in deep, hot wells.) All models of wormhole propagation predict deeper penetration for higher acid concentrations, so a high concentration of HCl is preferable. Also, in carbonates, there are no precipitation reactions to limit the acid concentrations used, as is the case in sandstones.

Table 15-1

Acid Use Guidelines: Carbonate Acidizing[a]

Perforating fluid:
5% acetic acid
Damaged perforations:
9% formic acid
10% acetic acid
15% HCl
Deep wellbore damage:
15% HCl
28% HCl
Emulsified HCl

[a]From McLeod, 1984.

15-3.2 Acid Volume and Injection Rate

An approach similar to that used in sandstone acidizing can be applied to determine the acid volume and injection rate schedule for carbonate acidizing, that being to determine the maximum volume needed based on a model of the acidizing process and then adjusting the injection rate and volume actually pumped based on real-time monitoring of the treatment. The acid volume is calculated with a model of wormhole propagation (Daccord's model or the volumetric model) for a desired penetration of wormholes.

Current models of wormhole propagation predict that wormhole velocity increases with injection rate to the power of 1/2 to 1. Thus, to propagate wormholes a given distance most rapidly, the maximum injection rate is preferable. However, this approach may not use the minimum amount of acid: If the acid volume is constrained, a slower injection rate may be preferable. In general, sufficient acid volumes are available (and not at great expense, if HCl is being used) so that injection at the maximum rate is recommended for limestone formations.

In dolomites, a lower injection rate may be preferable. As injection rate decreases, the temperature of the acid entering the formation increases, thereby increasing the reaction

rate. At a sufficiently high temperature, the dolomite-HCl reaction may become diffusion limited, leading to much faster wormhole propagation; that is, at an elevated temperature, dolomite will behave more and more like limestone. Thus, paradoxically, by increasing the reaction rate, acid will penetrate farther into the formation. This behavior is opposite that which occurs in uniform dissolution, such as in sandstones, and results from the fact that the reaction and diffusion rates are of similar size in dolomite.

EXAMPLE 15-3
Required acid volume

Calculate the volume (gal/ft) of 28% HCl needed to propagate wormholes 3 ft from a 0.328-ft-radius wellbore in a limestone formation with a porosity of 0.15, using both Daccord's model and the volumetric model. The injection rate is 0.1 bpm/ft, the diffusion coefficient is 10^{-9} m^2/sec, and the density of 28% HCl is 1.14 g/cm^3. In linear core floods, 1.5 pore volumes are needed for wormhole breakthrough at the end of the core.

Solution Daccord's model: Solving Eq. (15-8) for the volume of acid per unit thickness of formation yields

$$\frac{V}{h} = \frac{r_{wh}^{d_f} \pi \phi D^{2/3} (q/h)^{1/3}}{b N_{Ac}} \tag{15-21}$$

The acid capacity number for 28% HCl reacting with a 0.15 porosity limestone is

$$N_{Ac} = \frac{(0.15)(1.37)(0.28)(1.14)}{(1-0.15)(2.71)} = 2.85 \times 10^{-2} \tag{15-22}$$

It is more convenient to use SI units in Eq. (15-21); from Example 15-1, 0.1 bpm/ft is 8.69×10^{-4} m^3/sec-m. The desired wormhole radius is 3 ft + 0.328 ft = 3.328 ft, or 1.01 m. Then

$$\frac{V}{h} = \frac{(1.01)^{1.6}(\pi)(0.15)(10^{-9})^{2/3}(8.69 \times 10^{-4})^{1/3}}{(1.5 \times 10^{-5})(2.85 \times 10^{-2})} = 0.107 \text{ m}^3/\text{m} = 8.6 \text{ gal/ft} \tag{15-23}$$

The model predicts that only 8.6 gal/ft are needed to propagate wormholes 3 ft from the wellbore.

Volumetric model: First, substituting for η from Eq. (15-14) into Eq. (15-13) gives

$$r_{wh} = \sqrt{r_w^2 + \frac{V}{\pi \phi h P V_{bt}}} \tag{15-24}$$

and solving for V/h yields

$$\frac{V}{h} = \pi \phi (r_{wh}^2 - r_w^2) P V_{bt} \tag{15-25}$$

which shows that the acid volume needed is just the volume of the pore space in the region penetrated by wormholes multiplied by the number of pore volumes required to propagate wormholes through a given volume of rock. For the case given,

$$\frac{V}{h} = (\pi)(0.15)(3.328^2 - 0.328^2)(1.5) = 7.75 \text{ ft}^3/\text{ft} = 58 \text{ gal/ft} \tag{15-26}$$

A significantly larger volume is predicted by the volumetric model than by Daccord's model. Field experience suggests that the larger volume predicted by the volumetric model is more realistic than the small volume predicted by Daccord's model. ◇

15-3.3 Monitoring the Acidizing Process

A matrix acidizing treatment in a carbonate reservoir should be monitored by measuring the injection rate and pressure during injection, just as a sandstone acidizing treatment is monitored (see Section 14-3.) Because the wormholes created in carbonates are such large channels, it is generally assumed that the pressure drop through the wormholed region is negligible, so that the effect of the wormholes on the well skin effect is the same as enlarging the wellbore. With this assumption, the skin evolution in a carbonate matrix acidizing treatment can be predicted with the models of wormhole propagation.

In a well with a damaged region having a permeability k_s extending to a radius r_s, the skin effect during acidizing as a function of the radius of wormhole penetration is

$$s = \frac{k}{k_s} \ln \frac{r_s}{r_{wh}} - \ln \frac{r_s}{r_w} \tag{15-27}$$

Equation (15-27) applies until the radius of wormhole penetration exceeds the radius of damage. If the well is originally undamaged or the wormhole radius is greater than the original damage radius, the skin effect during acidizing is obtained from Hawkins' formula assuming that k_s is infinite [or from Eq. (15-27), setting $k_s = \infty$ and $r_s = r_{wh}$], which gives

$$s = -\ln \frac{r_{wh}}{r_w} \tag{15-28}$$

Using Eqs. (15-27) and (15-28), if the injection rate is held constant throughout the treatment, the skin effect predicted by Daccord's model is

with a damaged zone,

$$s = -\frac{k}{k_s} \ln \left\{ \frac{r_w}{r_s} + \left[\frac{b N_{Ac} V}{\pi r_s^{d_f} \phi h} D^{-2/3} \left(\frac{q}{h} \right)^{-1/3} \right]^{1/d_f} \right\} - \ln \frac{r_s}{r_w} \tag{15-29}$$

and, with no damage or the wormholes penetrating beyond the damaged region,

$$s = -\ln \left\{ 1 + \left[\frac{b N_{Ac} V}{\pi r_w^{d_f} \phi h} D^{-2/3} \left(\frac{q}{h} \right)^{-1/3} \right]^{1/d_f} \right\} \tag{15-30}$$

These equations do not apply if the injection rate is varying during the treatment because of the dependence of the wormhole velocity on injection rate in Daccord's model.

Using the volumetric model, the skin effect during injection is

with a damaged zone,

$$s = -\frac{k}{2k_s} \ln \left[\left(\frac{r_w}{r_s} \right)^2 + \frac{N_{Ac} V}{\eta \pi r_s^2 \phi h} \right] - \ln \frac{r_s}{r_w} \tag{15-31}$$

and, with no damage or the wormholes penetrating beyond the damaged region,

$$s = -\frac{1}{2}\ln\left(1 + \frac{N_{Ac}V}{\eta\pi r_w^2\phi h}\right) \tag{15-32}$$

Since the radius of wormhole penetration depends only on the volume of acid injected and not injection rate, Eqs. (15-31) and (15-32) apply for any injection rate schedule.

EXAMPLE 15-4

Skin evolution during carbonate matrix acidizing

Using the volumetric model, plot the skin effect as a function of volume of acid injected (up to 100 gal/ft) for the conditions described in Example 15-3, assuming an initial reservoir permeability of 100 md and a damaged region extending 3 ft from the wellbore, having a permeability of 10 md.

Solution In Example 15-3, it was found that 58 gal/ft of acid were needed for wormholes to penetrate a distance of 3 ft into the formation. Thus, up to this cumulative volume of injection, Eq. (15-31) applies; for volumes above 58 gal/ft, Eq. (15-32) should be used. Using Eq. (15-3), recognizing that η is $N_{Ac}PV_{bt}$,

$$s = -\frac{100}{(2)(10)}\ln\left[\left(\frac{0.328}{3.328}\right)^2 + \frac{(V/h)(\text{gal/ft})(1\ \text{ft}^3/7.48\ \text{gal})}{(\pi)(3.328)^2(0.15)(1.5)}\right] - \ln\left(\frac{3.328}{0.328}\right) \tag{15-33}$$

or

$$s = -5\ln\left[9.714\times10^{-3} + 1.708\times10^{-2}\left(\frac{V}{h}\right)\right] - 2.317 \tag{15-34}$$

When V/h is greater than 58 gal/ft, from Eq. (15-32),

$$s = -\frac{1}{2}\ln\left[1 + \frac{(V/h)(1/7.48)}{(\pi)(0.328)^2(0.15)(1.5)}\right] \tag{15-35}$$

or

$$s = -\frac{1}{2}\ln\left[1 + 1.758\left(\frac{V}{h}\right)\right] \tag{15-36}$$

Applying these equations for values of cumulative acid volume up to 100 gal/ft yields the results shown in Fig. 15-8. After the wormholes penetrate through the damaged region, very little further change in skin effect is obtained—the skin effect after penetration through the damaged region is −2.3, and it decreases to −2.6 after another 42 gal/ft of acid injection. Compared with sandstone acidizing, however, significantly lower skin effects are possible with matrix acidizing in carbonates, because of the relatively deep penetration of wormholes. ◇

15-3.4 Fluid Diversion

Adequate placement of acid into all zones to be stimulated is as important in acidizing carbonates as it is in sandstones, and the same fluid placement techniques are applicable.

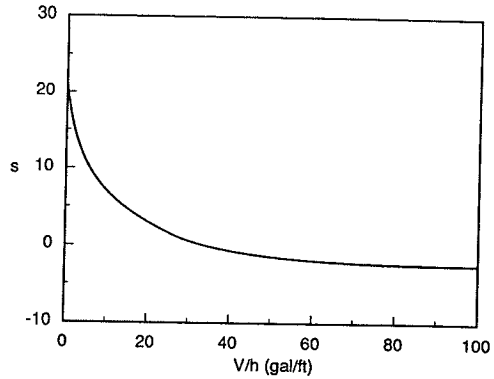

Figure 15-8
Skin evolution (Example 15-4).

These are covered in Section 14-4. One exception is in carbonate formations that are vugular or contain large natural fractures. In these types of formations, larger particle diverting agents are needed than would be necessary in sandstones. For a vuggy or fractured carbonate, diverting agents such as Unibeads or benzoic acid flakes are recommended.

The volume of acid that will be placed in different reservoir zones can also be predicted in a manner similar to that presented in Chapter 14 for sandstone acidizing. The flow rate into a layer j when particulate diverting agents are being used is given by Eq. (14-59),

$$\frac{d\bar{V}_j}{dt} = \frac{(2.066\times10^{-4})(p_{wf} - p_e)k_j}{\mu[\ln(r_e/r_w) + s_j + c_{1,j}\bar{V}_j]} \tag{14-59}$$

For sandstone acidizing, it was assumed that s_j decreased linearly with the volume of acid injected, leading to simple solutions for the flow rate and cumulative volume of acid injected into each layer. However, for carbonates, the models of wormhole propagation predict that the skin effect will depend logarithmically on the volume of acid injected [as shown in Eqs. (15-29) through (15-32)]. Since the flow rate will be changing into each zone when diverting agents are used, Daccord's model is not easily applied in Eq. (14-59). However, a solution can be obtained for the volumetric model. For a layer in which the wormholes have not penetrated beyond the damaged region, substituting for s_j from Eq. (15-31) into Eq. (14-59) yields

$$\frac{d\bar{V}_j}{dt} = \frac{a_{3,j}}{b_{1,j}\ln(b_{2,j} + b_{3,j}\bar{V}_j) + b_{4,j} + c_{1,j}\bar{V}_j} \tag{15-37}$$

where $a_{3,j}$ and $c_{1,j}$ are the same as defined in Chapter 14 [Eqs. (14-60) and (14-69)] and the other constants are

$$b_{1,j} = -\frac{k_j}{2k_{s,j}} \tag{15-38}$$

$$b_{2,j} = \left(\frac{r_w}{r_{s,j}}\right)^2 \tag{15-39}$$

$$b_{3,j} = \left(\frac{N_{Ac}}{\eta\pi r_{s,j}^2 \phi_j}\right) \tag{15-40}$$

$$b_{4,j} = \ln\frac{r_e}{r_{s,j}} \tag{15-41}$$

When it is integrated, this equation yields

$$b_{1,j}\left[\bar{V}_j \ln(b_{2,j} + b_{3,j}\bar{V}_j) + \frac{b_{2,j}}{b_{3,j}} \ln\left(\frac{b_{2,j} + b_{3,j}\bar{V}_j}{b_{2,j}}\right)\right] + \frac{c_{1,j}}{2}\bar{V}_j^2 + (b_{4,j} - b_{1,j})\bar{V}_j = a_{3,j}t_j \tag{15-42}$$

This equation cannot be solved explicitly for $\bar{V}_j$, so an iterative method must be used to solve for $\bar{V}_j$ as a function of injection time. Other than this difference, the same procedures presented in Chapter 14 can be used to predict acid placement using particulate diverting agents in carbonate acidizing.

15-4 Acid Fracturing

Acid fracturing is a stimulation technique in which acid is injected at pressures above the parting pressure of the formation, so that a hydraulic fracture is created. Usually, a viscous pad fluid is injected ahead of the acid to initiate the fracture, then plain acid, gelled acid, foamed acid, or an emulsion containing acid is injected. Fracture conductivity is created by the acid differentially etching the walls of the fracture; that is, the acid reacts nonuniformly with the fracture walls so that, after closure, the fracture props itself open, with the relatively undissolved regions acting as pillars that leave more dissolved regions as open channels. Thus, acid fracturing is an alternative to the use of proppants to create fracture conductivity after closure. The fracturing process itself is identical to that employed with proppant fracturing. The reader is referred to Chapter 16 for information about hydraulic fracturing in general.

The primary issues to be addressed in designing an acid fracturing treatment are the penetration distance of live acid down the fracture, the conductivity created by the acid (and its distribution along the fracture), and the resulting productivity of an acid-fractured well. Since acid fracturing should be viewed as an alternative means of creating fracture conductivity in a carbonate formation, a comparison with propped fracturing should generally be made when planning a possible acid fracturing treatment.

15-4.1 Acid Penetration in Fractures

To predict the distance to which fracture conductivity is created by acid and the final distribution of conductivity, the distribution of rock dissolution along the fracture is needed. This, in turn, requires a prediction of acid concentration along the fracture. The acid distribution along the fracture is obtained from an acid balance equation and appropriate boundary conditions. For linear flow down a fracture, with fluid leakoff and acid diffusion to the fracture walls (Fig. 15-9), these are

$$\frac{\partial C}{\partial t} + \frac{\partial(u_x C)}{\partial x} + \frac{\partial(u_y C)}{\partial y} - \frac{\partial}{\partial y}\left(D_{\text{eff}}\frac{\partial C}{\partial y}\right) = 0 \tag{15-43}$$

$$C(x, y, t = 0) = 0 \tag{15-44}$$

$$C(x = 0, y, t) = C_i(t) \tag{15-45}$$

$$Cu_y - C_L q_L - D_{\text{eff}}\frac{\partial C}{\partial y} = E_f C^n(1 - \phi) \tag{15-46}$$

where C is the acid concentration, u_x is the flux along the fracture, u_y is the transverse flux due to fluid loss, D_{eff} is an effective diffusion coefficient, C_i is the injected acid concentration, E_f is the reaction rate constant, n is the order of the reaction, and ϕ is porosity. To solve Eq. (15-43), continuity and transport equations are needed as well as a model of the fluid loss behavior. Complex numerical solutions of these equations that consider further complications such as the temperature distribution along the fracture, viscous fingering of low-viscosity acid through a viscous pad, the effect of the acid on leakoff behavior, and various fracture geometries have been presented by Ben-Naceur and Economides (1988), Lo and Dean (1989), and Settari (1991.)

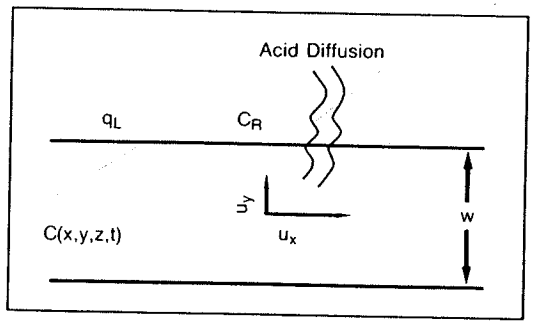

Figure 15-9
Acid transport in a fracture with diffusion and fluid loss. (*From Ben-Naceur and Economides, 1988.*)

By assuming steady-state, laminar flow of a Newtonian fluid between parallel plates with constant fluid loss flux along the fracture, Nierode and Williams (1972) presented a solution for the acid balance equation for flow in a fracture, adapted from the solution presented by Terrill (1965) for heat transfer between parallel plates. The solution for the concentration profile is presented in Fig. 15-10 as a function of the leakoff Peclet number, defined as

$$N_{\text{Pe}} = \frac{\bar{u}_y w}{2D_{\text{eff}}} \tag{15-47}$$

where $\bar{u}_y$ is average leakoff flux and w is the fracture width. The effective diffusion coefficient, D_{eff}, is generally higher than the molecular diffusion coefficient because of additional mixing caused by density gradients. Effective diffusion coefficients reported by Roberts and Guin (1974) are shown in Fig. 15-11, based on the Reynolds number in the fracture ($wu_x\rho/\mu$).

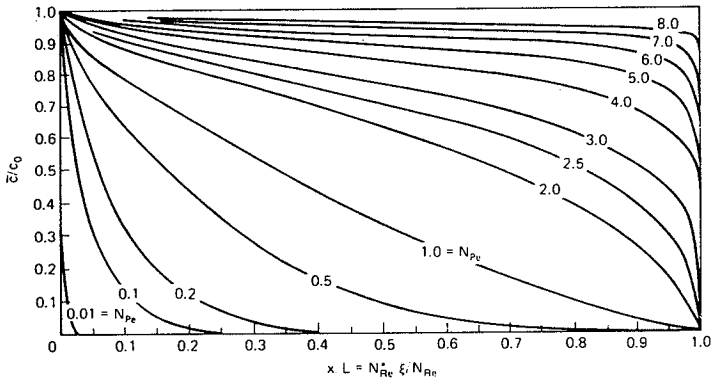

Figure 15-10
Mean acid concentration profiles along a fracture. (*From Schechter, 1992.*)

From Fig. 15-10, it is apparent that at low Peclet numbers, the acid concentration becomes very low before reaching the end of the fracture; at high Peclet numbers, high acid concentrations reach the end of the fracture. At low Peclet numbers, diffusion controls acid propagation, while at high Peclet numbers, fluid loss is the controlling factor. To complete the prediction of acid penetration, a model of fracture propagation is necessary, as the actual distance of acid propagation depends on the fracture length.

EXAMPLE 15-5
Acid penetration distance

For the fracturing conditions described in Examples 16-5 and 16-7 with $\eta \longrightarrow 0$, assuming that the fracturing fluid is a gelled acid, at what distance from the wellbore will the acid

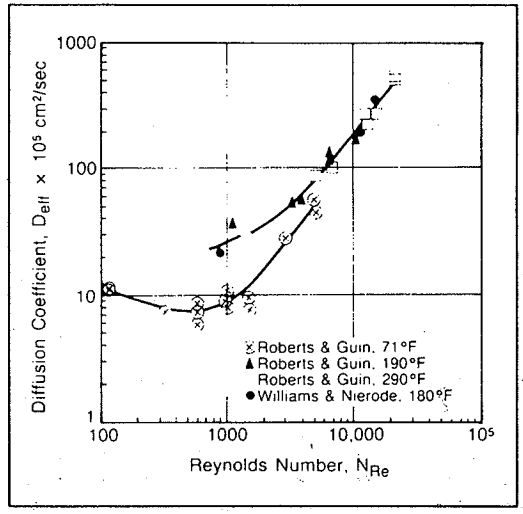

Figure 15-11
Effective acid diffusion coefficients. (*From Roberts and Guin, 1974; courtesy of SPE.*)

concentration be 50% of the injected concentration after 15 min of injection? 10% of the injected concentration? Assume an effective diffusion coefficient of 10^{-4} cm^2/sec.

Solution To answer this question, the fluid loss Peclet number is needed. When $\eta \longrightarrow 0$, the fluid loss rate is equal to the injection rate and the average fluid loss flux is the injection rate divided by the fracture surface area:

$$\bar{u}_y = \frac{q_i}{4hx_f} \tag{15-48}$$

From Example 16-7, after 15 min of injection, $x_f = 277$ ft. Thus,

$$\bar{u}_y = \frac{(40 \text{ bpm})(5.615 \text{ ft}^3/\text{bbl})}{(4)(100 \text{ ft})(277 \text{ ft})} = 2.03 \times 10^{-3} \text{ ft/min} \tag{15-49}$$

Following Example 16-5, for a fracture length of 277 ft, the average fracture width is 0.15 in. (0.01269 ft). When the units are converted to ft^2/min, the effective diffusion coefficient is 6.46×10^{-6}. From Eq. (15-47), the fluid loss Peclet number is

$$N_{\text{Pe}} = \frac{(0.01269 \text{ ft})(2.03 \times 10^{-3} \text{ ft/min})}{(2)(6.46 \times 10^{-6} \text{ ft}^2/\text{min})} = 2 \tag{15-50}$$

Reading from Fig. 15-10 for a Peclet number of 2, the acid concentration will be 50% of the injected value at a dimensionless distance of 0.69, or at (0.69)(277) = 191 ft. Similarly, a

concentration of 10% of the injected concentration penetrates to a dimensionless distance of 0.98, or an actual distance of 271 ft. ◇

15-4.2 Acid Fracture Conductivity

The conductivity ($k_f w$) of an acid fracture is difficult to predict because it depends inherently on a stochastic process: If the walls of the fracture are not etched heterogeneously, very little fracture conductivity will result after closure. Thus the approach taken to predict acid fracture conductivity is an empirical one. First, based on the acid distribution in the fracture, the amount of rock dissolved as a function of position along the fracture is calculated. Then an empirical correlation is used to calculate fracture conductivity based on the amount of rock dissolved. Finally, since the conductivity usually varies significantly along the fracture, some averaging procedure is used to obtain an average conductivity for the entire fracture. The methods for predicting fracture conductivity of an acid fracture should not be expected to be very accurate. By measuring the effective conductivity of acid fractures in the field using pressure transient testing, these techniques can be "field calibrated."

The amount of rock dissolved in an acid fracture is represented by a parameter called the ideal width, w_i, defined as the fracture width created by acid dissolution before fracture closure. If all the acid injected into a fracture dissolves rock on the fracture face (i.e., no live acid penetrates into the matrix or forms wormholes in the fracture walls), the average ideal width is simply the total volume of rock dissolved divided by the fracture area, or

$$\bar{w}_i = \frac{XV}{2(1-\phi)h_f x_f} \tag{15-51}$$

where X is the volumetric dissolving power of the acid, V is the total volume of acid injected, h_f is the fracture height, and x_f is the fracture half-length. For Peclet numbers greater than about 5, the acid concentration is almost equal to the injected concentration along most of the fracture length, and the actual ideal width is approximately equal to the mean ideal width. For lower Peclet numbers, more acid is spent near the wellbore than farther along the fracture, and the concentration distribution must be considered to calculate the ideal width distribution. Schechter (1992) presented one such solution (Fig. 15-12) based on the concentration profiles of Fig. 15-10.

From the ideal fracture width, the conductivity of an acid fracture is obtained from the correlation of Nierode and Kruk (1973.) This correlation is based on extensive laboratory measurements of acid fracture conductivity and correlates conductivity with the ideal width, the closure stress, σ_c, and the rock embedment strength, S_{rock}. Nierode and Kruk's correlation is

$$k_f w = C_1 e^{-C_2 \sigma_c} \tag{15-52}$$

where

$$C_1 = 1.47 \times 10^7 w_i^{2.47} \tag{15-53}$$

and

$$C_2 = (13.9 - 1.3 \ln S_{\text{rock}}) \times 10^{-3} \tag{15-54}$$

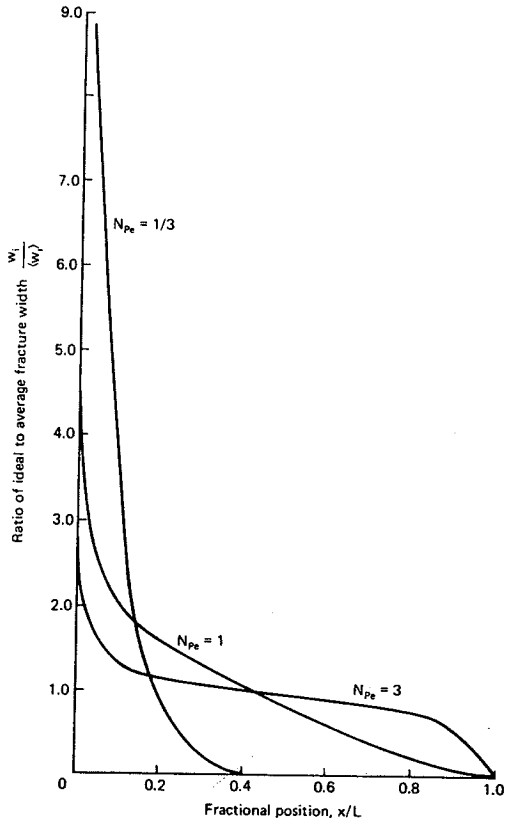

Figure 15-12
Ideal fracture width profile along a fracture. (*From Schechter, 1992.*)

for $S_{\text{rock}} < 20,000$ psi, and

$$C_2 = (3.8 - 0.28 \ln S_{\text{rock}}) \times 10^{-3} \tag{15-55}$$

for $S_{\text{rock}} > 20,000$ psi. [Note: In the original publication, there was a typographical error in the equation presented here as Eq. (15-54). The original publication has the constant 19.9 in this equation; the value of 13.9 given here is the correct one.]

For the constants given in these equations, $k_f w$ is in md-ft, w_i is in in., and σ_c and S_{rock} are in psi. The rock embedment strength is the force required to push a metal sphere a certain distance into the surface of a rock sample. Laboratory-measured values of embedment

strength and acid fracture conductivity for several common carbonate formations from Nierode and Kruk (1973) are given in Table 15-2.

Table 15-2

Effective Fracture Conductivity for Well-known Reservoirs as a Function of Rock Embedment Strength and Closure Stress[a]

			Conductivity (md-in.) versus Closure Stress (psi)				
Reservoir	Maximum Conductivity	S_{rock}	0	1000	3000	5000	7000
San Andres dolomite	2.7×10^6	76,600	1.1×10^4	5.3×10^3	1.2×10^3	2.7×10^2	6.0×10^0
San Andres dolomite	5.1×10^8	63,800	1.2×10^6	7.5×10^5	3.0×10^5	1.2×10^5	4.7×10^4
San Andres dolomite	1.9×10^7	62,700	2.1×10^5	9.4×10^4	1.9×10^4	3.7×10^3	7.2×10^2
Canyon limestone	1.3×10^8	88,100	1.3×10^6	7.6×10^5	3.1×10^5	4.8×10^4	6.8×10^3
Canyon limestone	4.6×10^7	30,700	8.0×10^5	3.9×10^5	9.4×10^4	2.3×10^4	5.4×10^3
Canyon limestone	2.7×10^8	46,400	1.6×10^6	6.8×10^5	1.3×20^5	2.3×10^4	4.4×10^3
Cisco limestone	1.2×10^5	67,100	2.5×10^3	1.3×10^3	3.4×10^2	8.8×10^1	2.3×10^1
Cisco limestone	3.0×10^5	14,800	7.0×10^3	3.4×10^3	8.0×10^2	1.9×10^2	4.4×10^1
Cisco limestone	2.0×10^6	25,300	1.4×10^5	6.2×10^4	1.3×10^4	2.7×10^3	5.7×10^2
Capps limestone	3.2×10^5	13,000	9.7×10^3	4.2×10^3	7.6×10^2	1.4×10^2	2.5×10^1
Capps limestone	2.9×10^5	30,100	1.8×10^4	6.8×10^3	9.4×10^2	1.3×10^2	1.8×10^1
Indiana limestone	4.5×10^6	22,700	4.6×10^5	1.5×10^5	1.5×10^4	1.5×10^3	1.5×10^2
Indiana limestone	2.8×10^7	21,500	7.9×10^5	3.0×10^5	4.3×10^4	6.3×10^3	9.0×10^2
Indiana limestone	3.1×10^8	14,300	7.4×10^6	2.0×10^6	1.4×10^5	1.0×10^4	7.0×10^2
Austin chalk	3.9×10^6	11,100	5.6×10^4	1.6×10^3	1.3×10^0	—	—
Austin chalk	2.4×10^6	5,600	3.9×10^4	1.2×10^3	1.2×10^0	—	—
Austin chalk	4.8×10^5	13,200	1.0×10^4	1.7×10^3	4.9×10^1	1.4×10^0	—
Clearfork dolomite	3.6×10^4	35,000	3.4×10^3	1.7×10^3	4.1×10^2	1.0×10^2	2.4×10^1
Clearfork dolomite	3.3×10^4	11,800	9.3×10^3	1.6×10^3	4.5×10^1	1.3×10^0	—
Greyburg dolomite	8.3×10^6	14,400	2.5×10^5	4.0×10^4	1.0×10^3	2.5×10^1	—
Greyburg dolomite	3.9×10^6	12,200	2.1×10^5	7.9×10^4	1.0×10^4	1.5×10^3	2.0×10^2
Greyburg dolomite	3.2×10^6	16,600	8.0×10^4	1.5×10^4	4.8×10^2	1.6×10^1	—
San Andres dolomite	1.0×10^6	46,500	8.3×10^4	4.0×10^4	9.5×10^3	2.2×10^3	5.2×10^2
San Andres dolomite	2.4×10^6	76,500	1.9×10^4	6.8×10^3	8.5×10^2	1.0×10^2	1.3×10^1
San Andres dolomite	3.4×10^6	17,300	9.4×10^3	2.8×10^3	2.5×10^2	2.3×10^1	—

[a]From Nierode and Kruk, 1973.

Once the conductivity variation along the fracture is obtained, an average conductivity for the entire fracture can be calculated in order to estimate the productivity of the acid-fractured well. If the variation in conductivity is not too great, Bennett (1982) has shown that a simple average of the conductivity predicts the well productivity after early production.

This average is

$$\overline{k_f w} = \frac{1}{x_f} \int_0^{x_f} k_f w \, dx \tag{15-56}$$

This average should be adequate when the fluid loss Peclet number is greater than 3. For lower values of Peclet number, this average will overestimate the well productivity because it is too strongly influenced by the high conductivity near the well. It is possible in some acid fractures that the conductivity is a maximum at some distance from the wellbore (caused, for example, by increasing diffusion or reaction rates as the acid warms up) (Elbel, 1989). For this type of distribution, a harmonic mean better approximates the behavior of the fractured well (Ben-Naceur and Economides, 1989):

$$\overline{k_f w} = \frac{x_f}{\int_0^{x_f} dx / k_f w} \tag{15-57}$$

EXAMPLE 15-6

Average acid fracture conductivity

The fracturing treatment described in Example 15-5 is conducted using 15 wt% HCl in a 15% porosity limestone formation. The formation has an embedment strength of 60,000 psi, and the closure stress is 4000 psi. Acid is injected for a total of 15 min. Calculate the average fracture conductivity after fracturing.

Solution First, the average ideal width is calculated with Eq. (15-51). For a total of 600 bbl of injection [(40 bpm)(15 min)] into a 100-ft-high, 277-ft-long fracture, average ideal width is

$$\bar{w}_i = \frac{(0.082)(600 \text{ bbl})(5.615 \text{ ft}^3/\text{bbl})}{(2)(1 - 0.15)(100 \text{ ft})(277 \text{ ft})} \left(\frac{12 \text{ in.}}{1 \text{ ft}} \right) = 0.0704 \text{ in.} \tag{15-58}$$

The fluid loss Peclet number was found to be 2 in Example 15-5. Interpolating between the curves for $N_{Pe} = 1$ and $N_{Pe} = 3$ in Fig. 15–12, values for $\bar{w}_f/w_i$ are read. These are shown in Table 15-3.

Using the Nierode-Kruk correlation, C_2 is given by Eq. (15-55),

$$C_2 = [3.8 - 0.28 \ln(60,000)] \times 10^{-3} = 7.194 \times 10^{-4} \tag{15-59}$$

and combining Eqs. (15-52) and (15-53),

$$k_f w = (1.47 \times 10^7) w_i^{2.47} e^{-(7.194 \times 10^{-4})(4000)} = (8.27 \times 10^5) w_i^{2.47} \tag{15-60}$$

The fracture conductivity for 10 equal increments along the fracture are shown in Table 15-3. Using the simple average, the average conductivity is 2300 md-ft. This value is probably high because of the high conductivity near the well. In contrast, using the harmonic average gives a value of 95 md-ft for the average conductivity. ◇

15-4.3 Productivity of an Acid-Fractured Well

The productivity of an acid-fractured well can be predicted in the same manner as for a well with a propped fracture (see Chapter 18 for details on propped fracture performance)

Table 15-3

Example 15-6 Results

x/x_f	$w_i/\bar{w}_i$	w_i (in.)	$k_f w$ (md-ft)
0.05	2.6	0.183	12,500
0.15	1.55	0.109	3500
0.25	1.3	0.092	2300
0.35	1.15	0.081	1700
0.45	1.0	0.070	1200
0.55	0.85	0.060	800
0.65	0.75	0.053	600
0.75	0.65	0.046	400
0.85	0.45	0.032	200
0.95	0.15	0.011	10

$k_f\bar{w} = 2300$ md-ft

if an average fracture conductivity adequately describes the well flow behavior. One complicating factor is that the conductivity of an acid fracture depends strongly on the closure stress, and the closure stress will be increasing as the bottomhole flowing pressure decreases during the life of the well. Since p_{wf} for a given flow rate depends on fracture conductivity and the fracture conductivity depends on closure stress, and hence, p_{wf}, an iterative procedure is required to determine the productivity of an acid fractured well. Ben-Naceur and Economides (1989) presented a series of performance type curves for acid-fractured wells producing at a constant p_{wf} of 500 psi. Four of these curves are reproduced in Figs. 15-13 through 15-16. The first three are for average ideal widths of 0.12 in., while the last curve is for an embedment strength of 60,000 psi. These curves are best used for Peclet numbers above 5, as they are based on uniform conductivity along the fracture.

In these curves, the dimensionless cumulative production, Q_D, and the dimensionless time, t_{Dxf}, are defined as

$$Q_D = \frac{3.73 \times 10^{-2} N_p B_o}{\phi h c_t x_f^2 (p_i - p_{wf})} \quad \text{for oil} \tag{15-61}$$

$$Q_D = \frac{0.376 G_p Z T}{\phi h c_t x_f^2 (p_i^2 - p_{wf}^2)} \quad \text{for gas} \tag{15-62}$$

$$t_{Dxf} = \frac{0.000264kt}{\phi \mu c_t x_f^2} \tag{15-63}$$

where N_p and G_p are the cumulative productions of oil (STB) and gas (MSCF), respectively, and all other variables and units are as defined in Chapter 18.

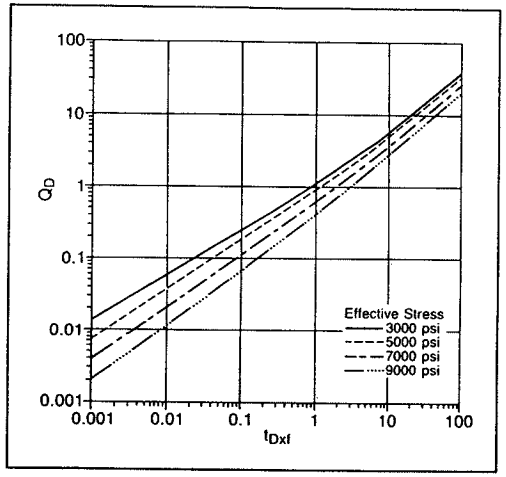

Figure 15-13
Performance curves for a 30,000-psi embedment strength formation as a function of closure stress. (*From Ben-Naceur and Economides, 1988.*)

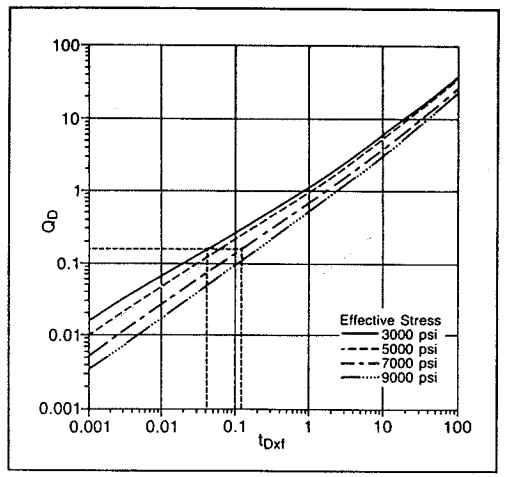

Figure 15-14
Performance curves for a 60,000-psi embedment strength formation as a function of closure stress. (*From Ben-Naceur and Economides, 1988.*)

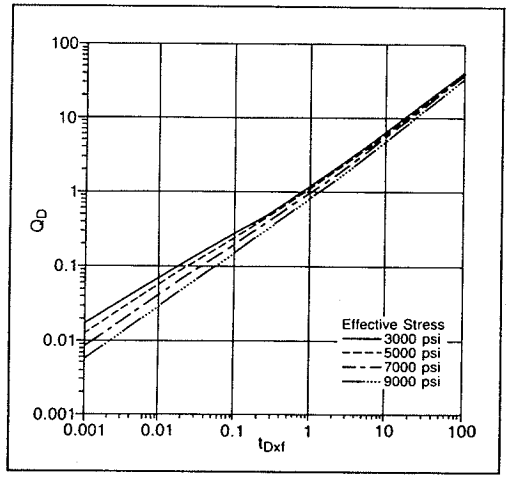

Figure 15-15

Performance curves for a 100,000-psi embedment strength formation as a function of closure stress. (*From Ben-Naceur and Economides, 1988.*)

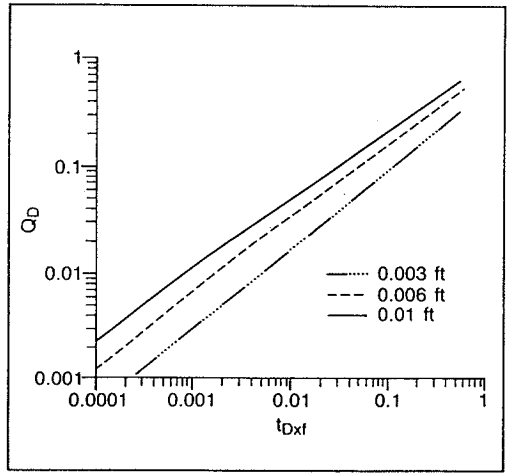

Figure 15-16

Performance curves for a 60,000-psi embedment strength formation and 7000-psi closure stress for different ideal widths. (*From Ben-Naceur and Economides, 1988.*)

15-4.4 Comparison of Propped and Acid Fracture Performance

The decision to place a propped instead of an acid fracture in a carbonate formation should be taken based on the expected posttreatment performance and the costs of the treatments. The fact that acid fracturing is intended specifically for carbonate formations should not preclude the use of a propped fracture if it can be placed and has economic advantages.

Acid fractures will be relatively short and and are by no means of infinite conductivity, particularly at high closure stress. On the other hand, propped fractures, which can be much longer, may be impossible to place in the (frequently) naturally fractured carbonate formations, because of screenouts. For both acid- and propped-fractured wells, an optimal fracture length (and hence an optimal treatment design) will exist. This optimum is determined based on the NPV of the fracturing treatment, as described in Chapter 18. To select between an acid and a propped fracture, the NPVs of the optimal treatments should be compared. In general, since acid fractures result in relatively short fractures, they will be favored in higher-permeability formations; propped fractures become more and more favorable as fracture length becomes more important, as is true for low-permeability formations.

REFERENCES

1. Ben-Naceur, K., and Economides, M. J., "The Effectiveness of Acid Fractures and Their Production Behavior," SPE Paper 18536, 1988.
2. Ben-Naceur, K., and Economides, M. J., "Acid Fracture Propagation and Production" in *Reservoir Stimulation*, M. J. Economides and K. G. Nolte, eds., Prentice Hall, Englewood Cliffs, NJ, Chap. 18, 1989.
3. Bennett, C. O., "Analysis of Fractured Wells," Ph. D. thesis, University of Tulsa, Tulsa, OK, 1982.
4. Daccord, G., "Acidizing Physics," in *Reservoir Stimulation*, M. J. Economides and K. G. Nolte, eds., Prentice Hall, Englewood Cliffs, NJ, Chap. 13, 1989.
5. Daccord, G., and Lenormand, R., "Fractal Patterns from Chemical Dissolution," *Nature*, **325**: 41–43, 1987.
6. Daccord, G, Touboul, E., and Lenormand, R., "Carbonate Acidizing: Toward a Quantitative Model of the Wormholing Phenomenon," *SPEPE*, pp. 63–68, February 1989.
7. Elbel, J., "Field Evaluation of Acid Fracturing Treatments Using Geometry Simulation, Buildup, and Production Data," SPE Paper 19773, 1989.
8. Hoefner, M. L., and Fogler, H. S., "Pore Evolution and Channel Formation during Flow and Reaction in Porous Media," *AICHE J.*, **34**: 45–54, January 1988.
9. Hung, K. M., Hill, A. D., and Sepehrnoori, K., "A Mechanistic Model of Wormhole Growth in Carbonate Matrix Acidizing and Acid Fracturing," *JPT*, **41** (1): 59-66, January 1989.
10. Lo, K. K., and Dean, R. H., "Modeling of Acid Fracturing," *SPEPE*, pp. 194–200, May 1989.
11. McLeod, H. O., Jr., "Matrix Acidizing," *JPT*, **36**: 2055–2069, 1984.
12. Nierode, D. E., and Kruk, K. F., "An Evaluation of Acid Fluid Loss Additives, Retarded Acids, and Acidized Fracture Conductivity," SPE Paper 4549, 1973.
13. Nierode, D. E., and Williams, B. B., "Characteristics of Acid Reactions in Limestone Formations," *SPEJ*, pp. 306–314, 1972.
14. Pichler, T., Frick, T. P., Economides, M. J., and Nittmann, J., "Stochastic Modeling of Wormhole Growth with Biased Randomness," SPE Paper 25004, 1992.
15. Roberts, L. D., and Guin, J. A., "The Effect of Surface Kinetics in Fracture Acidizing," *SPEJ*, pp. 385–396, August 1974; *Trans. AIME*, **257**.
16. Schechter, R. S., *Oil Well Stimulation*, Prentice Hall, Englewood Cliffs, NJ, 1992.
17. Schechter, R. S., and Gidley, J. L., "The Change in Pore Size Distribution from Surface Reactions in Porous Media," *AICHE J.*, **15**: 339–350, 1969.

18. Settari, A., "Modelling of Acid Fracturing Treatment," SPE Paper 21870, 1991.
19. Terrill, R. M., "Heat Transfer in Laminar Flow between Parallel Porous Plates," *Int. J. Heat Mass Transfer*, **8**: 1491–1497, 1965.
20. Wang, Y., "The Optimum Injection Rate for Wormhole Propagation in Carbonate Acidizing," Ph. D. dissertation, University of Texas at Austin, 1993.

PROBLEMS

15-1. Calculate the radius of wormhole penetration using Daccord's and the volumetric model for the injection of 100 gal/ft of 28% HCl at 0.05 bpm/ft into a 10% porosity limestone formation. The molecular diffusion coefficient is 10^{-9} m^2/sec, and 1.5 pore volumes of acid are required for wormhole breakthrough in a core flood.

15-2. Repeat Problem 15-1, but for dolomite in which 10 pore volumes of acid are needed for breakthrough.

15-3. Calculate the volume of 15 wt% HCl needed to propagate wormholes 2 ft beyond a 0.328-ft-radius wellbore into a 12% porosity limestone formation if the injection rate is 0.05 bpm/ft. Two pore volumes of acid are required for breakthrough in a core flood. Use both Daccord's and the volumetric model.

15-4. Derive Eqs. (15-31) and (15-32).

15-5. A well has a skin effect of 10 due to damage extending 2 ft beyond a 0.328-ft-radius wellbore. The undamaged reservoir permeability is 200 md. For the acidizing conditions described in Example 15-3, calculate and plot the skin evolution up to 100 gal/ft using Daccord's model.

15-6. Repeat Problem 15-5, but using the volumetric model.

15-7. A two-layer limestone reservoir ($k_1 = 100$ md, $k_2 = 20$ md) is to be acidized with a 15% HCl solution containing an organic resin diverting agent. Both layers have damaged regions where the permeability is 20% of the undamaged permeability extending 3 ft from the 0.328-ft-radius wellbore. Other data are given below. For a treatment conducted at a constant pressure difference ($p_{wf} - p_e$) of 2000 psi, at what time after the start of injection will 50 gal/ft of acid have been injected into the high-permeability layer?

Data: $C_{da} = 0.1$ vol%; $\alpha = 10^{13}$ ft/lb$_m$; $\rho_{acid} = 1.2$ g/cm^3; $\mu_{acid} = 0.7$ cp; $PV_{bt} = 2$; $\phi_1 = 0.15$; $\phi_2 = 0.10$.

15-8. An acid fracture in a 10% porosity dolomite formation is 100 ft high and 400 ft long after the injection of 400 bbl of 15% HCl solution. If the fracturing efficiency $\eta \longrightarrow 0$, at what distance from the wellbore will the acid concentration be half of the injected concentration? $D_{eff} = 10^{-4}$ cm^2/sec.

15-9. For the fracturing treatment described in Problem 15-8, assume that the rock is dissolved uniformly along the entire fracture. What is the resulting fracture conductivity if $S_{rock} = 40{,}000$ psi?

CHAPTER 16

Hydraulic Fracturing for Well Stimulation

16-1 INTRODUCTION

Wells in low to moderate-permeability reservoirs are candidates for hydraulic fracturing as a means of stimulating their performance.

A hydraulic fracture, like any other method of well stimulation, adjusts the skin effect (or the related effective wellbore radius). Suppose that a well in a 20-md reservoir had a prestimulation skin effect due to damage equal to 20. For typical reservoir and well variables ($h = 75$ ft, $\Delta p = 1000$ psi, $B = 1$ res bbl/STB, $\mu = 1$ cp, $r_e = 1500$ ft, and $r_w = 0.328$ ft), the steady-state flow rate would be 375 STB/d and 1260 STB/d for the pre- and poststimulation (s=0) conditions, respectively. This would mean an increase of 885 STB/d, a three-fold increase over the pretreatment rate. However, for a 1-md-permeability reservoir and with the same skin effects, the corresponding flow rates would be 19 and 63 STB/d, respectively. A hydraulic fracture that could result in an equivalent, negative skin effect of -6 would lead to a poststimulation rate equal to 220 STB/d, a 10-fold increase over the pretreatment rate.

Two conclusions should be drawn from the above. First, hydraulic fracturing is beneficial in low- to moderate-permeability formations, where damage removal would not be sufficient for an attractive well flow rate. Second, a hydraulic fracture cannot circumvent the reservoir's natural capacity to produce. A fracture resulting in an equivalent skin effect of -6 is a massive undertaking as will be shown later in this and the next chapters. In such a case the well flow rate from a 1-md reservoir cannot compare with simple damage removal from a 20-md reservoir, but the rationale for the treatment is not based solely on the magnitude of the rate increase.

It should be noted here that a hydraulic fracture bypasses the near-wellbore damage zone. Thus, any postfracture equivalent skin effect has no relation to the pretreatment value.

18. Settari, A., "Modelling of Acid Fracturing Treatment," SPE Paper 21870, 1991.
19. Terrill, R. M., "Heat Transfer in Laminar Flow between Parallel Porous Plates," *Int. J. Heat Mass Transfer*, **8**: 1491–1497, 1965.
20. Wang, Y., "The Optimum Injection Rate for Wormhole Propagation in Carbonate Acidizing," Ph. D. dissertation, University of Texas at Austin, 1993.

PROBLEMS

15-1. Calculate the radius of wormhole penetration using Daccord's and the volumetric model for the injection of 100 gal/ft of 28% HCl at 0.05 bpm/ft into a 10% porosity limestone formation. The molecular diffusion coefficient is 10^{-9} m^2/sec, and 1.5 pore volumes of acid are required for wormhole breakthrough in a core flood.

15-2. Repeat Problem 15-1, but for dolomite in which 10 pore volumes of acid are needed for breakthrough.

15-3. Calculate the volume of 15 wt% HCl needed to propagate wormholes 2 ft beyond a 0.328-ft-radius wellbore into a 12% porosity limestone formation if the injection rate is 0.05 bpm/ft. Two pore volumes of acid are required for breakthrough in a core flood. Use both Daccord's and the volumetric model.

15-4. Derive Eqs. (15-31) and (15-32).

15-5. A well has a skin effect of 10 due to damage extending 2 ft beyond a 0.328-ft-radius wellbore. The undamaged reservoir permeability is 200 md. For the acidizing conditions described in Example 15-3, calculate and plot the skin evolution up to 100 gal/ft using Daccord's model.

15-6. Repeat Problem 15-5, but using the volumetric model.

15-7. A two-layer limestone reservoir ($k_1 = 100$ md, $k_2 = 20$ md) is to be acidized with a 15% HCl solution containing an organic resin diverting agent. Both layers have damaged regions where the permeability is 20% of the undamaged permeability extending 3 ft from the 0.328-ft-radius wellbore. Other data are given below. For a treatment conducted at a constant pressure difference ($p_{wf} - p_e$) of 2000 psi, at what time after the start of injection will 50 gal/ft of acid have been injected into the high-permeability layer?

Data: $C_{da} = 0.1$ vol%; $\alpha = 10^{13}$ ft/lb$_m$; $\rho_{acid} = 1.2$ g/cm^3; $\mu_{acid} = 0.7$ cp; $PV_{bt} = 2$; $\phi_1 = 0.15$; $\phi_2 = 0.10$.

15-8. An acid fracture in a 10% porosity dolomite formation is 100 ft high and 400 ft long after the injection of 400 bbl of 15% HCl solution. If the fracturing efficiency $\eta \longrightarrow 0$, at what distance from the wellbore will the acid concentration be half of the injected concentration? $D_{eff} = 10^{-4}$ cm^2/sec.

15-9. For the fracturing treatment described in Problem 15-8, assume that the rock is dissolved uniformly along the entire fracture. What is the resulting fracture conductivity if $S_{rock} =$ 40,000 psi?

CHAPTER 16

Hydraulic Fracturing for Well Stimulation

16-1 INTRODUCTION

Wells in low to moderate-permeability reservoirs are candidates for hydraulic fracturing as a means of stimulating their performance.

A hydraulic fracture, like any other method of well stimulation, adjusts the skin effect (or the related effective wellbore radius). Suppose that a well in a 20-md reservoir had a prestimulation skin effect due to damage equal to 20. For typical reservoir and well variables (h = 75 ft, $\Delta p = 1000$ psi, $B = 1$ res bbl/STB, $\mu = 1$ cp, $r_e = 1500$ ft, and $r_w = 0.328$ ft), the steady-state flow rate would be 375 STB/d and 1260 STB/d for the pre- and poststimulation (s=0) conditions, respectively. This would mean an increase of 885 STB/d, a three-fold increase over the pretreatment rate. However, for a 1-md-permeability reservoir and with the same skin effects, the corresponding flow rates would be 19 and 63 STB/d, respectively. A hydraulic fracture that could result in an equivalent, negative skin effect of -6 would lead to a poststimulation rate equal to 220 STB/d, a 10-fold increase over the pretreatment rate.

Two conclusions should be drawn from the above. First, hydraulic fracturing is beneficial in low- to moderate-permeability formations, where damage removal would not be sufficient for an attractive well flow rate. Second, a hydraulic fracture cannot circumvent the reservoir's natural capacity to produce. A fracture resulting in an equivalent skin effect of -6 is a massive undertaking as will be shown later in this and the next chapters. In such a case the well flow rate from a 1-md reservoir cannot compare with simple damage removal from a 20-md reservoir, but the rationale for the treatment is not based solely on the magnitude of the rate increase.

It should be noted here that a hydraulic fracture bypasses the near-wellbore damage zone. Thus, any postfracture equivalent skin effect has no relation to the pretreatment value.

Execution of a hydraulic fracture involves the injection of fluids at a pressure sufficiently high to cause "tensile failure" of the rock. At the fracture initiation pressure, often known as the "breakdown pressure," the rock opens. As additional fluids are injected, the opening is extended and the fracture propagates.

A properly executed hydraulic fracture results in a "path," connected to the well, that has a much higher permeability than the surrounding formation. This path of large permeability (frequently five to six orders of magnitude larger than the reservoir permeability) is narrow but can be extremely long. Typical average widths of a hydraulic fracture are of the order of 0.25 in. (or less), while the effective length may be 3000 ft tip to tip. In a 100-ft-thick formation, this narrow structure would expose the wellbore to a 600,000-ft^2 fracture-to-formation surface area.

A reservoir at depth is under a state of stress. This situation can be characterized by the stress vectors. In a geologically stable environment, three principal stresses can be identified. Their directions coincide with the directions where all shear stresses vanish. Usually these directions are the vertical and two horizontal, that of the minimum and that of the maximum horizontal stresses.

A hydraulic fracture will be normal to the smallest of the three stresses because it will open and displace the rock against the least resistance. In the majority of reservoirs to be hydraulically fractured, the minimum horizontal stress is the smallest, leading to vertical hydraulic fractures (Hubbert and Willis, 1957). The direction of the hydraulic fracture will be analyzed in a subsequent section of this chapter.

What length or fracture permeability is desirable in a hydraulic fracture? While this issue will be dealt with extensively in later sections of this chapter, a conceptual analogy is instructive.

Suppose that a reservoir is depicted as a countryside, and the fracture is a road connecting two far-off points. In a countryside with an excellent and dense system of wide roads (high-permeability-reservoir analog), relative improvement of the traffic flow would require even wider and faster freeways. This translates to high-permeability fractures. The ratio of the fracture permeability to the reservoir permeability is proportional to the fracture *conductivity*. Therefore, in moderate- to high-permeability reservoirs (that are *candidates* for hydraulic fracturing), high conductivity is necessary, while the fracture length is of secondary importance.

Conversely, in a countryside with a sparse and poor road system (low-permeability analog), a long road connecting as much of the countryside as possible is indicated. Such a long road could bring about a major improvement in traffic flow. In fact, the worse the existing road system, the lower the relative requirements would be from the new road. By analogy, the length of the fracture in a lower-permeability reservoir is the priority; fracture permeability is secondary. Thus, in designing a hydraulic fracturing, these requirements must be addressed.

However, as in the case of posttreatment incremental production and the influence of reservoir permeability, the geometry of the fracture is affected by the state of stress and the rock properties. Fracture design for petroleum engineers must then take into account the natural state of the reservoir and rock and influence the fracture execution in an attempt to

create the optimum stimulation treatment. This chapter describes the important processes during hydraulic fractures, culminating in the fracture design, described in the next chapter.

16-2 In-Situ Stresses

Formations at depth are subjected to a stress field that can be decomposed in its constituent vectors. The most readily understood stress is the vertical stress, which corresponds to the weight of the overburden. For a formation at depth H, the vertical stress, σ_v, is simply

$$\sigma_v = g \int_0^H \rho_f \, dH \tag{16-1}$$

where ρ_f is the density of the formations overlaying the target reservoir. This stress can be calculated from an integration of the density log. If an average formation density is used in lb/ft^3 and the depth is in ft, Eq. (16-1) becomes

$$\sigma_v = \frac{\rho H}{144} \tag{16-2}$$

with σ_v in psi. For $\rho = 165$ lb/ft^3, the vertical stress gradient is approximately 165/144 ≈ 1.1 psi/ft.

This stress is the *absolute stress*, and in the case of a porous medium, since the weight of the overburden will be carried by both the grains and the fluid within the pore space, an *effective stress*, σ_v', is defined

$$\sigma_v' = \sigma_v - \alpha p \tag{16-3}$$

where α is Biot's (1956) poroelastic constant, which for most hydrocarbon reservoirs is approximately equal to 0.7.

The vertical stress is *translated* horizontally through the Poisson relationship, which in its simplest expression has the form

$$\sigma_H' = \frac{\nu}{1-\nu} \sigma_v' \tag{16-4}$$

where σ_H' is the effective horizontal stress and ν is the Poisson ratio. This variable is a rock property. For sandstones it is approximately equal to 0.25, implying that the effective horizontal stress is approximately one-third the effective vertical stress.

The absolute horizontal stress, σ_H, would then be equal to the effective stress plus αp in the same manner as the relationship in Eq. (16-3). The absolute horizontal stress decreases with fluid production.

The stress given by Eq. (16-4) is not the same in all directions in the horizontal plane. Because of tectonic components, this stress is the *minimum horizontal stress*, whereas the *maximum horizontal stress* is simply

$$\sigma_{H,\max} = \sigma_{H,\min} + \sigma_{\text{tect}} \tag{16-5}$$

where σ_{tect} is a tectonic stress contribution.

From the above, it is then obvious that three principal stresses can be identified in a formation, σ_v, $\sigma_{H,\min}$, and $\sigma_{H,\max}$. The fracture direction will be normal to the smallest of the three.

The magnitude of the breakdown pressure is characteristic of the values and the respective differences of the principal stresses, the tensile stress, and the reservoir pressure. An expression for the breakdown pressure has been given by Terzaghi (1923) and for a vertical well (i.e., coinciding with the direction of the vertical principal stress) this pressure, p_{bd}, is

$$p_{bd} = 3\sigma_{H,\min} - \sigma_{H,\max} + T_0 - p \tag{16-6}$$

where $\sigma_{H,\min}$ and $\sigma_{H,\max}$ are the minimum and maximum horizontal stresses, respectively, T_0 is the tensile stress of the rock, and p is the reservoir pressure.

For any other than the perfectly vertical direction, as in the case of deviated or horizontal wells, the breakdown pressure will be different than the one given by Eq. (16-6), since there will be a nonvanishing shear stress component. This new breakdown pressure may be less, but usually it will be more than the breakdown pressure for a vertical well (McLennan et al., 1989).

EXAMPLE 16-1

Calculation of stresses versus depth

Assume that a 75-ft sandstone formation is 10,000 ft deep. The density is 165 lb/ft^3, the poroelastic constant is 0.72, and the Poisson ratio is 0.25. Calculate and plot the absolute and effective vertical and minimum horizontal stresses.

The maximum horizontal stress is 2000 psi larger than the minimum horizontal stress. Plot the maximum stress also. Use hydrostatic reservoir pressure ($\rho_0 = 55$ lb/ft^3).

Repeat the calculation, but plot the stress profile of the target interval and overlaying and underlaying shale layers, each 50 ft thick. Use first a Poisson ratio for the shales equal to 0.25 (as in the sandstone layer), and then repeat for $\nu = 0.27$ and 0.3.

Finally, plot the absolute vertical and minimum horizontal stresses at 10,000 ft as functions of the reservoir pressure from hydrostatic to an overpressure of 4000 psi. What observations can be made?

Solution From Eq. (16-2) and $\rho = 165$ lb/ft^3, $\sigma_v = 1.15H$. From Eq. (16-3),

$$\sigma_v' = 1.15H - \frac{(0.72)(55)(H)}{144} = 0.88H \tag{16-7}$$

From Eq. (16-4),

$$\sigma_H' = \frac{0.25}{1-0.25}(0.88H) = 0.29H \tag{16-8}$$

and therefore

$$\sigma_{H,\min} = 0.29H + \frac{(0.72)(55)H}{144} = 0.57\,H \tag{16-9}$$

Figure 16-1 is a plot of all stresses: σ_v, σ_v', $\sigma_{H,\min}$, $\sigma_{H,\min}'$ and $\sigma_{H,\max}$ ($= \sigma_{H,\min} + 2000$). At 10,000 ft these stresses are 11,500, 8,800, 5,700, 2,900, and 7,700 psi, respectively. Of the three principal absolute stresses, $\sigma_{H,\min}$ is the smallest, suggesting that at any depth (under the assumptions of this problem), a hydraulic fracture would be vertical and normal to the minimum horizontal stress direction.

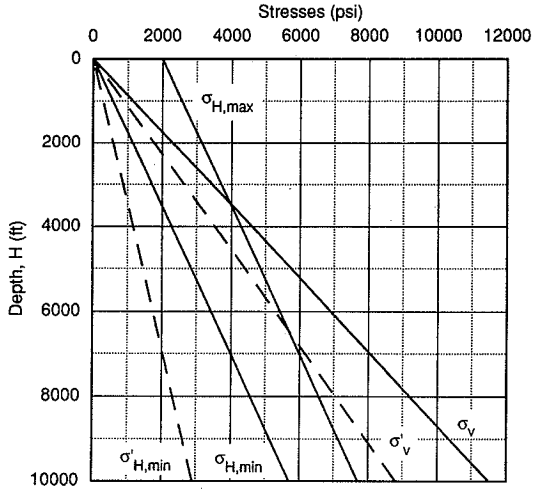

Figure 16-1

Absolute (σ_v, $\sigma_{H,\max}$, $\sigma_{H,\min}$) and effective (σ_v', $\sigma_{H,\min}'$) stresses for the formation of Example 16-1. Reservoir pressure is hydrostatic.

If a depth of 10,000 ft is the midpoint of the 75-ft formation, the difference between the horizontal stresses at the top and bottom of the formation would be only (0.57 ΔH) 43 psi.

When the two 50-ft shale layers are considered, the absolute vertical stresses at the top and bottom of the shale/sandstone and sandstone/shale sequence would be within 58 and 86 psi, respectively, and the absolute horizontal stresses would be within 29 and 43 psi, respectively (if $\nu = 0.25$ is used for all three layers). However, if $\nu = 0.27$ for the shales, while the horizontal stress in the sandstone remains the same, from Eq. (16-4), and similarly to Eq. (16-9), $\sigma_{H,\min} = 0.61\,H$, which at 10,000 ft results in an additional contrast of approximately 400 psi. For $\nu = 0.3$ this stress contrast is approximately 900 psi. A plot of the stress profiles in an expanded scale is shown in Fig. 16-2.

The single most important reason for fracture height containment is this natural stress contrast resulting from the differences in the Poisson ratios. Without this difference, fractures would have largely uncontrolled height.

Fracture height migration and calculations will be presented later in this chapter.

Finally, while σ_v is not affected by the reservoir pressure (σ_v' is), $\sigma_{H,\min}$ is a strong function of this overpressure, Δp. (Overpressure is the pressure difference above hydrostatic.) For this problem,

$$\sigma_v' = 0.88H - 0.72\,\Delta p \tag{16-10}$$

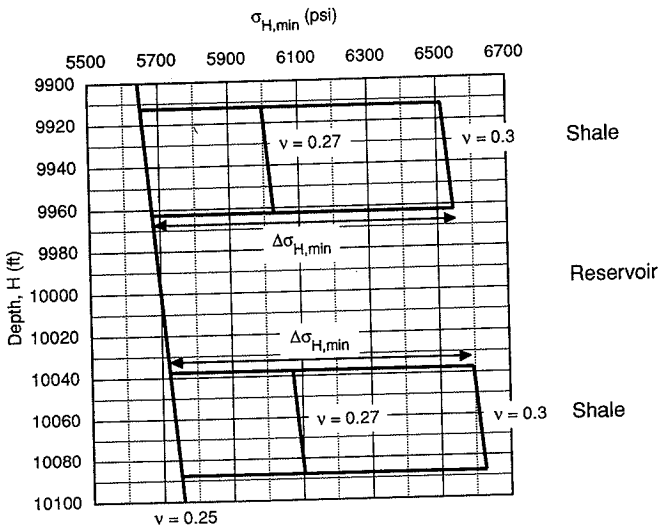

Figure 16-2

Idealized horizontal stress profiles and stress contrast between target, overlaying and underlaying shales (Example 16-1).

$$\sigma'_{H,\min} = 0.29H - 0.24\,\Delta p \tag{16-11}$$

and

$$\sigma_{H,\min} = 0.57H + 0.48\,\Delta p \tag{16-12}$$

Figure 16-3 is a plot of the vertical versus horizontal stresses at 10,000 ft. While the difference at $\Delta p = 0$ psi is (11,500 − 5,700) 5800 psi, it is 3800 psi when $\Delta p = 4000$ psi. It is then obvious that the fracture direction in shallower overpressured formations may not necessarily be vertical. As more and more wells are produced, decline in reservoir pressure will cause hydraulic fractures to be increasingly vertical. Furthermore, if, during fracturing, a contained fracture leads to an additional net pressure, then the fracture may *start* vertical and then turn horizontal. In the next section the issue of fracture direction will be dealt with in detail. ◇

EXAMPLE 16-2

Calculation of fracture initiation pressure

Estimate the fracture initiation pressure for a well in the reservoir described in the first paragraph of Example 16-1. The tensile stress is 1000 psi.

Solution From Eq. (16-6),

$$p_{bd} \approx 3(5700) - 7700 + 1000 - 3800 \approx 6600 \text{ psi} \tag{16-13}$$

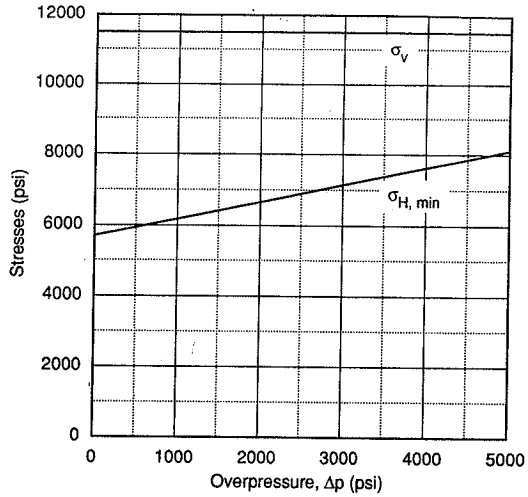

Figure 16-3

Vertical and minimum horizontal stresses for an overpressured formation (Example 16-1).

This breakdown pressure is bottomhole. The wellhead "treating" pressure, p_{tr}, would be

$$p_{tr} = p_{bd} - \Delta p_{PE} + \Delta p_F \tag{16-14}$$

where Δp_{PE} and Δp_F are the hydrostatic and friction pressure drops, respectively. ◇

16-3 FRACTURE DIRECTION

Fracture direction is normal to the minimum resistance. This is represented by the absolute minimum stress.

In the previous section, Eqs. (16-1) and (16-4) and results of Example 16-1 (see Fig. 16-1) suggest that the minimum horizontal stress is by definition smaller than the maximum horizontal stress and smaller than the vertical stress. Therefore the conclusion would be that all hydraulic fractures should be vertical and normal to the minimum stress direction.

There are exceptions. In Example 16-1, the role of the overpressure was addressed. More important, though, is the magnitude of the vertical stress itself.

The Poisson relationship [Eq. (16-4)] is valid during deposition, and the resulting horizontal stresses, contained within stiff boundaries, are "locked in place." The vertical stress, being directly proportional to the weight of the overburden, follows the geologic history (erosion, glaciation) of the top layers. Therefore, if ΔH is removed, the vertical stress at depth is $\rho g\ (H - \Delta H)$, where H is measured from the original ground surface.

The slope of the vertical stress versus depth curve remains constant, but the curve is shifted to the left (of the curve in Fig. 16-1).

Therefore, while the intersection of the original vertical and minimum horizontal stresses was at the original ground surface, the removal of a portion of the overburden, coupled with largely constant values of the minimum horizontal stress, result in a new curve intersection, which marks a critical depth. Above this depth the original minimum horizontal stress is no longer the smallest of the three stresses. Instead, the vertical stress is the smallest and a hydraulic fracture would be horizontal, lifting the overburden.

EXAMPLE 16-3

Calculation of critical depth for a horizontal fracture

Suppose that the formation described in the first paragraph of Example 16-1 lost 2000 ft of overburden. Assuming that the horizontal stresses are the original and the reservoir pressure is hydrostatic, based on the original ground surface, calculate the critical depth for a horizontal fracture.

Solution A graphical solution to the problem is shown in Fig. 16-4. The new ground surface, 2000 ft below the original, is marked. A line parallel to the original vertical stress is drawn from the new zero depth, and it intersects the original minimum horizontal stess at H=4000 ft from the original surface or 2000 ft from the current ground surface.

An algebraic solution is to set equal the stress values of the (new) vertical and minimum horizontal in their respective expressions and solve for H. If the original $\sigma_v = 1.15H$, after 2000 ft of overburden are removed, $\sigma_v = 1.15H - 2300$.

The horizontal stress is given by Eq. (16-9) ($\sigma_{H,\min} = 0.57\ H$).

Setting the two stresses equal results in

$$0.57H = 1.15H - 2300 \tag{16-15}$$

Therefore, at depths less than $H \approx 4000$ ft from the original ground surface or 2000 ft from the current surface, fractures will initiate horizontally.

Complex fracture geometries are likely to be encountered at depths below this level. Fractures may be *initiated* vertically but may turn horizontal (T-shape fractures) when (and if) the minimum stress plus the fracture net pressure exceed the overburden stress. A T-shape geometry is invariably undesirable, since the width of the horizontal branch is very small, resulting in substantial fluid loss during propped fracture propagation, slurry dehydration, and "screenouts." (These terms will be expounded upon in Section 16-7.)

Similar phenomena may occur during vertical fracture propagation if the values of the two horizontal stresses are nearly equal. The pressure in the fracture during execution may exceed the *seating* pressure of normal-to-the-trajectory natural fissures. Small widths will accept fluid but not proppant and increase the likelihood of a screenout. ◇

16-4 Length, Conductivity, and Equivalent Skin Effect

Every hydraulic fracture can be characterized by its length, conductivity and related equivalent skin effect. In almost all calculations, the fracture length, which must be the

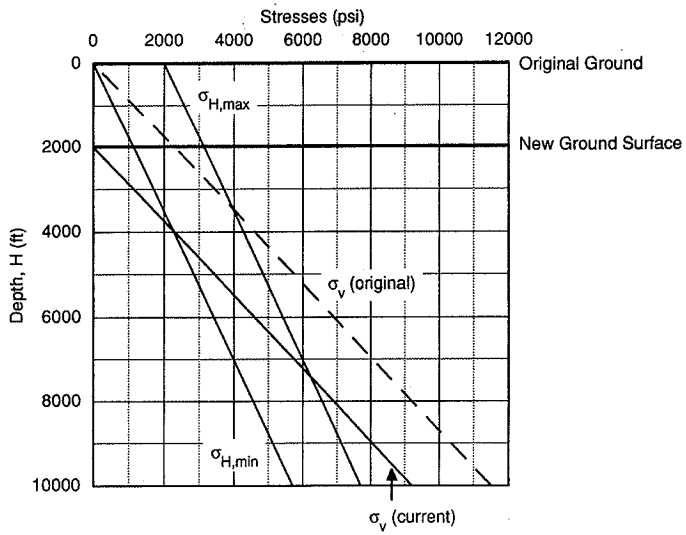

Figure 16-4

Critical depth for a horizontal fracture because of overburden removal (Example 16-2).

conductive length and not the created *hydraulic* length, is assumed to consist of two equal half-lengths, x_f, in each side of the well. (In the following definitions and in the remainder of this chapter and the following two chapters, the term "fracture length," denoted by x_f, will always refer to the conductive fracture half-length.)

In 1961, Prats provided pressure profiles in a fractured reservoir as functions of the fracture half-length and the relative capacity, a, which he defined as

$$a = \frac{\pi k x_f}{2 k_f w} \tag{16-16}$$

where k is the reservoir permeability, k_f is the fracture permeability, and w is the propped fracture width.

Small values of a imply large fracture permeability-width product or small reservoir permeability-fracture length product, thus a large *conductivity* fracture. In subsequent work, Argawal et al. (1979) and Cinco-Ley and Samaniego (1981) introduced the fracture conductivity, F_{CD}, which is exactly

$$F_{CD} = \frac{k_f w}{k x_f} \tag{16-17}$$

and is related to Prats's a by

$$F_{CD} = \frac{\pi}{2a} \tag{16-18}$$

Prats (1961) also introduced the concept of dimensionless effective wellbore radius in a hydraulically fractured well,

$$r'_{wD} = \frac{r'_w}{x_f} \tag{16-19}$$

where r'_w is

$$r'_w = r_w e^{-s_f} \tag{16-20}$$

The equivalent skin effect, s_f, is the result of a hydraulic fracture of a certain length and conductivity and can be added to the well inflow equations in the usual manner. For example, the steady-state equation for an oil well would be

$$q = \frac{kh(p_e - p_{wf})}{141.2B\mu[\ln(r_e/r_w) + s_f]} \tag{16-21}$$

Similarly, this skin effect can be added to all other "pseudo-radial" equations such as for the pseudo-steady-state and transient conditions after they have been established in the reservoir.

Transient, fracture-related, behavior was addressed in Chapter 11 and will be used extensively in Chapter 18, where the performance of hydraulically fractured wells is analyzed.

Prats (1961) correlated the relative capacity parameter, a, and the dimensionless effective wellbore radius. This is Fig. 16-5. From Fig. 16-5 for small values of a, or high conductivity fractures, the r'_{wD} is equal to 0.5, leading to

$$r'_w = \frac{x_f}{2} \tag{16-22}$$

which suggests that for these large-conductivity fractures the reservoir drains to a well with an effective wellbore equal to half of the fracture half-length. Furthermore, for these large-conductivity fractures, increasing the fracture length would result in additional benefits; increasing the fracture permeability would not.

A second conclusion can be drawn from Fig. 16-5. Since the effective wellbore must be as large as possible, values of a larger than unity must be avoided because the effective wellbore radius decreases rapidly. Therefore, hydraulic fractures should be designed for $a < 1$ or [from Eq. (16-18)] $F_{CD} > 1.6$.

A third important observation from Fig. (16-5) is that for large values of a, the slope of the curve is equal to 1, implying a linear relationship between r'_{wD} and a that is approximately

$$r'_{wD} = \frac{k_f w}{4kx_f} \tag{16-23}$$

or

$$r'_w = \frac{k_f w}{4k} \tag{16-24}$$

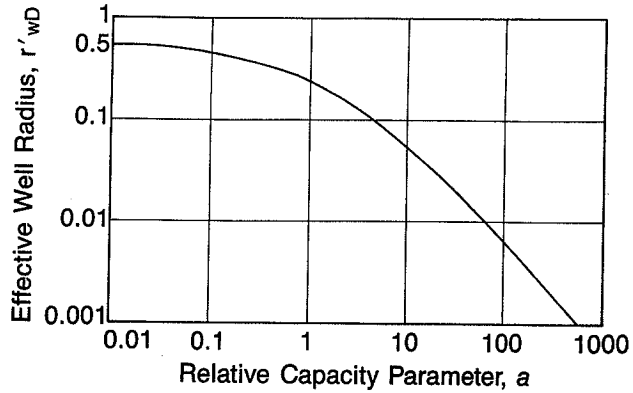

Figure 16-5
The concept of effective wellbore radius. (*From Prats, 1961.*)

Equation (16-24) suggests that for low-conductivity fractures, the increase in r'_w does not depend on fracture length but instead on the fracture permeability-width product, which must be maximized.

The results from Eq. (16-22) for high-conductivity fractures and Eq. (16-24) for low-conductivity fractures reinforce the analogy made in the introduction of this chapter. Low-permeability reservoirs, leading to high-conductivity fractures, would benefit greatly from length. Moderate- to high-permeability reservoirs, naturally leading to low-conductivity fractures, require good-fracture permeability (good-quality proppant and nondamaging fracturing fluids) and width. These guidelines must influence the fracture treatment design. A useful alternative graph of Fig. 16-5 is Fig. 16-6 (Cinco-Ley and Samaniego, 1981), relating F_{CD} and s_f directly.

EXAMPLE 16-4

Calculation of the equivalent skin effect from hydraulic fractures

Assuming that $k_f w = 2000$ md-ft, $k = 1$ md, $x_f = 1000$ ft, and $r_w = 0.328$ ft, calculate the equivalent skin effect and the folds of well productivity increase (at steady-state flow) for a reservoir with drainage radius, $r_e = 1490$ ft (160 acres) and no wellbore damage.

What would be the folds of increase for the same fracture lengths and $k_f w$ if $k = 0.1$ md and $k = 10$ md?

If the fracture length remains 1000 ft and k=10 md, what should be the $k_f w$ to deliver the same folds of increase as for $k = 1$ md and $k_f w = 1000$ md-ft?

Solution From Eq. (16-17),

$$F_{CD} = \frac{2000}{(1)(1000)} = 2 \tag{16-25}$$

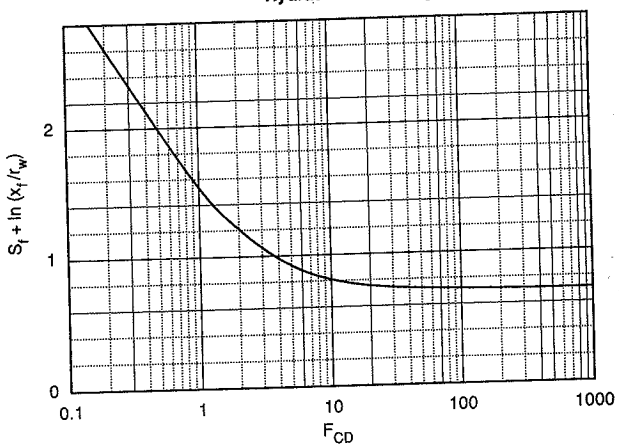

Figure 16-6

Fracture skin effect varying with fracture conductivity. *(From Cinco-Ley and Samaniego, 1981.)*

and therefore, from Fig. (16-6), $s_f + \ln(x_f/r_w) = 1.2$. Since $x_f = 1000$ ft and $r_w = 0.328$, then $s_f = -6.8$.

The folds of increase under steady state, denoted as J/J_0, where J and J_0 are the productivity indexes before and after stimulation, respectively, can be calculated:

$$\frac{J}{J_0} = \frac{\ln(r_e/r_w)}{\ln(r_e/r_w) + s_f} = \frac{\ln(1490/0.328)}{\ln(1490/0.328) - 6.8} = 5.2 \qquad (16\text{-}26)$$

That is, a 6.7-fold increase in productivity results from the treatment.

For $k = 0.1$ md, then $F_{CD} = 20$ and $s_f + \ln(x_f/r_w) = 0.7$. Therefore, s_f = -7.3 and $J/J_0 = 17.5$.

For $k = 10$ md, $F_{CD} = 0.2$ and $s_f + \ln(x_f/r_w) = 2.8$. Therefore, s_f = -5.2 and $J/J_0 = 2.6$. These results denote the impact of long fracture lengths in low-permeability reservoirs.

Finally, for $s_f + \ln(x_f/r_w) = 1.2$ to be constant, F_{CD} is equal to 2; if $k = 10$ md, then $k_f w = 20,000$ md-ft. This result (although such a $k_f w$ product with $w = 0.25$ in. would require a highly unrealistic value for the fracture permeability, $k_f = 10^6$ md—see Chapter 17) indicates the need to maximize the $k_f w$ product for a higher-permeability formation. ◇

16-5 Modeling of Fracture Geometry

Following the fracture initiation, additional fluid injection would result in fracture propagation. The geometry of the created fracture can be approximated by models that take into account the mechanical properties of the rock, the properties of the fracturing fluid, the conditions with which the fluid is injected (rate, pressure), and the stresses and stress distribution in the porous medium.

In describing fracture propagation, which is a particularly complex phenomenon, two sets of laws are required:

- Fundamental principles such as the laws of conservation of momentum, mass, and energy, and
- Criteria for propagation, i.e., what causes the tip of the fracture to advance. These include interactions of rock, fluid, and energy distribution. [See Ben-Naceur (1989) for an extensive treatment of the subject.]

Three general families of models are available: two-dimensional (2-D), pseudo-three-dimensional (p-3-D) and, fully three-dimensional (3-D) models. The latter allow full three-dimensional fracture propagation with full two-dimensional fluid flow. The fracture is discretized, and within each block calculations are done based on the fundamental laws and criteria for propagation. The fracture is allowed to propagate laterally and vertically, and change plane of original direction, depending on the local stress distribution and rock properties. Such fully 3-D models require significant amounts of data to justify their use, are extremely calculation intensive, and are outside the scope of this textbook. [They are also outside the scope of applications of the vast majority of hydraulic fracture treatments. However, fractures in horizontal and highly deviated wells may require full 3-D modeling because the fracture initiation, usually aligned with the well trajectory, is likely to be different from the direction of fracture propagation, which must be normal to the minimum, "far-field" stress (Economides et al., 1989).]

Two-dimensional models are closed-form analytical approximations assuming constant and known fracture height. For petroleum engineering applications, two mutually exclusive models have been used. For a fracture length much larger than the fracture height ($x_f >> h_f$), the Perkins and Kern (1961) and Nordgren (1972) or PKN model is an appropriate approximation. For $x_f << h_f$ the appropriate model has been presented by Khristianovic(h) and Zheltov (1955) and Geertsma and de Klerk (1969). This is frequently known as the KGD model. A limiting case, where $h_f = 2x_f$, is the radial or "penny-shape" model. The fracture height, h_f, used here is the dynamic value, that is, the fracture height at the time that the fracture length is equal to x_f.

The p-3-D models allow vertical fracture migration *along* the fracture path, and this migration depends on the stress contrast between the target and adjoining intervals. In Section 16-6, a fracture height migration model will be described.

For the purposes of this textbook the elegant 2-D models will be used for approximate calculations of the fracture width and the fracture propagation pressure. Both Newtonian and non-Newtonian fracturing fluids will be considered.

Recently, Valkó and Economides (1993) have introduced the concept of "continuum damage mechanics" (CDM) as a means to describe the additional phenomena of retarded fracture propagation and frequently observed, abnormally high treating pressures.

16-5.1 Hydraulic Fracture Width with the PKN Model

The PKN Model is depicted in Fig. 16-7. It has an elliptical shape at the wellbore. The maximum width is at the centerline of this ellipse, with zero width at the top and bottom. For a Newtonian fluid the maximum width, when the fracture-half length is equal to x_f, is given (in coherent units) by

$$w_{max} = 2.31\left[\frac{q_i\mu(1-\nu)x_f}{G}\right]^{1/4} \tag{16-27}$$

where G is the elastic shear modulus and is related to Young's modulus, E, by

$$G = \frac{E}{2(1+\nu)} \tag{16-28}$$

In Eqs. (16-27) and (16-28), q_i is the injection rate, μ is the apparent viscosity, and ν is the Poisson ratio. Equation (16-27) is particularly useful to understand the relationship among fracture width, treatment variables, and rock properties. The quarter-root relationship implies that to double the width, the viscosity of the fracturing fluid (or the injection rate) must be increased by a factor of 16. This is neither feasible nor desirable. Doubling the viscosity with all the potentially associated permanent damage to the proppant pack would result in a 19% increase of the fracture width. Thus, treatment variables have only moderate impact on the fracture width. Increasing the rate and/or viscosity will also result in an increase in the net pressure with potentially undesirable fracture height growth.

Rock properties have a much larger impact on the fracture width. The Young's modulus of common reservoir rocks may vary by almost two orders of magnitude, from 10^7 psi in tight and deep sandstones to 2×10^5 psi in diatomites, coals, and soft chalks. The difference in the fracture widths among these extremes will be more than 2.5 times. The implication is that in stiff rocks, where the Young's modulus is large for a given volume of fluid injected, the resulting fracture will be narrow but long. Conversely, in low-Young's-modulus formations, the same volume of fluid injected would result in wide but short fractures. This is one of those phenomena where the natural state helps the success of fracture stimulation, since low-permeability reservoirs that require long fractures usually have large Young's modulus values.

The corollary is not always true. Low Young's moduli are not necessarily associated with higher-permeability formations, although there are several cases where this is true.

The elliptical geometry of the PKN model leads to an expression for the average width by the introduction of a geometric factor. Thus,

$$\bar{w} = 2.31\left[\frac{q_i\mu(1-\nu)x_f}{G}\right]^{1/4}\left(\frac{\pi}{4}\gamma\right) \tag{16-29}$$

The factor γ is approximately equal to 0.75, and therefore the term in the second set of parentheses is equal to 0.59. In typical oilfield units, where $\bar{w}$ is calculated in in., q_i is in

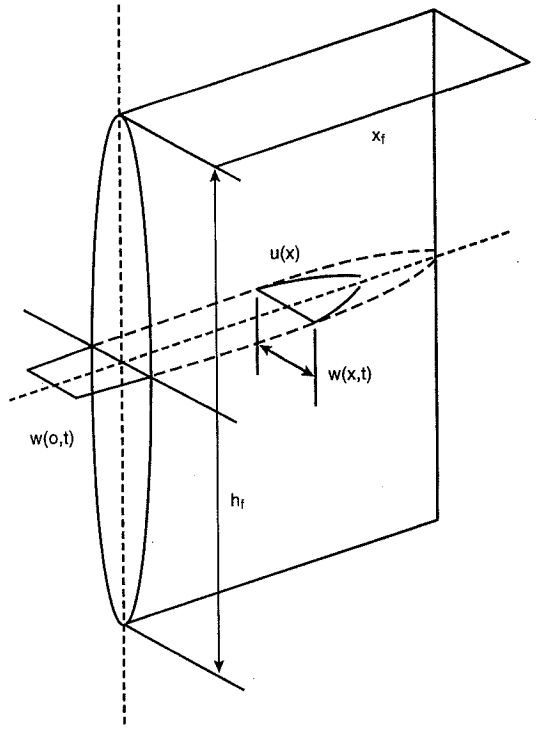

Figure 16-7
The PKN model geometry.

bpm, μ is in cp, x_f is in ft, and G is in psi, Eq. (16-29) becomes

$$\bar{w} = 0.3\left[\frac{q_i\mu(1-\nu)x_f}{G}\right]^{1/4}\left(\frac{\pi}{4}\gamma\right) \tag{16-30}$$

EXAMPLE 16-5
Calculation of the PKN fracture width with a Newtonian fluid

What would be the maximum and average fracture widths when the fracture half-length is 1000 ft, the apparent viscosity of the fluid is 100 cp, and the injection rate is 40 bpm? Assume that $\nu = 0.25$ and $E = 4 \times 10^6$ psi. What would be the average width when x_f=2000 ft?

Calculate the volume of the created fracture if h_f=100 ft when x_f=1000 ft for the formation described above. What fracture length would result in a chalk formation with $E = 4 \times 10^5$ psi for the same volume? Assume that h_f and ν are the same.

Solution From Eq. (16-28),

$$G = \frac{4 \times 10^6}{2(1 + 0.25)} = 1.6 \times 10^6 \text{ psi} \tag{16-31}$$

and from Eq. (16-30), when $x_f = 1000$ ft,

$$\bar{w} = 0.3\left[\frac{(40)(100)(1 - 0.25)(1000)}{1.6 \times 10^6}\right]^{1/4}\left(\frac{\pi}{4}\,0.75\right) \tag{16-32}$$
$$= (0.35)(0.59) = 0.21 \text{ in.}$$

In Eq. (16-32), the term 0.35 is the maximum fracture width (at the wellbore), and 0.21 is the average width.

When $x_f = 2000$ ft, the w_{max} and $\bar{w}$ are 0.42 and 0.25 in., respectively (simply the previous results multiplied by $2^{1/4}$).

The volume of the 1000-ft (half-length) fracture is

$$V = 2\,x_f h_f \bar{w} = (2)(1000)(100)\left(\frac{0.21}{12}\right) = 3500 \text{ ft}^3 \tag{16-33}$$

In the chalk formation, the product $x_f \bar{w}$ must also be 17.5 ft^2, since h_f is constant. From Eq. (16-28), $G = 1.6 \times 10^5$ psi and rearrangement of Eq. (16-30) results in

$$x_f = \left\{\left[\frac{12(x_f \bar{w})}{(0.3)(\pi\gamma/4)}\right]^4 \frac{G}{q_i \mu(1 - \nu)}\right\}^{1/5} \tag{16-34}$$

and therefore $x_f = 640$ ft. The corresponding average width is 0.33 in. ◇

16-5.2 Fracture Width with a Non-Newtonian Fluid

The expression for the maximum fracture width with a non-Newtonian fluid is (in oilfield units)

$$w_{max} = 12\left[\left(\frac{128}{3\pi}\right)(n' + 1)\left(\frac{2n' + 1}{n'}\right)^{n'}\left(\frac{0.9775}{144}\right)\left(\frac{5.61}{60}\right)^{n'}\right]^{1/(2n'+2)} \cdot \left(\frac{q_i^{n'} K' x_f h_f^{1-n'}}{E}\right)^{1/(2n'+2)} \tag{16-35}$$

where w_{max} is in in. The average width can be calculated by multiplying the w_{max} by $\pi\gamma/4$. The quantities n' and K' are the power-law rheological properties of the fracturing fluid. All other variables are as in Eq. (16-30) for the Newtonian fluid.

EXAMPLE 16-6
Fracture width with a non-Newtonian fluid

Use the treatment and rock variables in Example 16-5 to calculate the fracture width at $x_f = 1000$ ft for a fracturing fluid with $K' = 8 \times 10^{-3}$ lb$_f$ – sec$^{n'}$/ft^2 and $n' = 0.56$.

Solution From Eq. (16-35),

$$w_{max} = 12\left[(13.59)(1.56)(3.79)^{0.56}(0.0068)(0.0935)^{0.56}\right]^{0.32} \cdot \left[\frac{40^{0.56}(8 \times 10^{-3})(1000)(100)^{0.44}}{4 \times 10^6}\right]^{0.32} = 0.3 \text{ in.} \tag{16-36}$$

and therefore $\bar{w} = 0.18$ in. ◇

16-5.3 Fracture Width with the KGD Model

The KGD model, depicted in Fig. 16-8, is a 90° turn of the PKN model and is particularly applicable to approximate the geometry of fractures where $h_f >> x_f$. Thus, it should not be used in cases where long fracture lengths are generated.

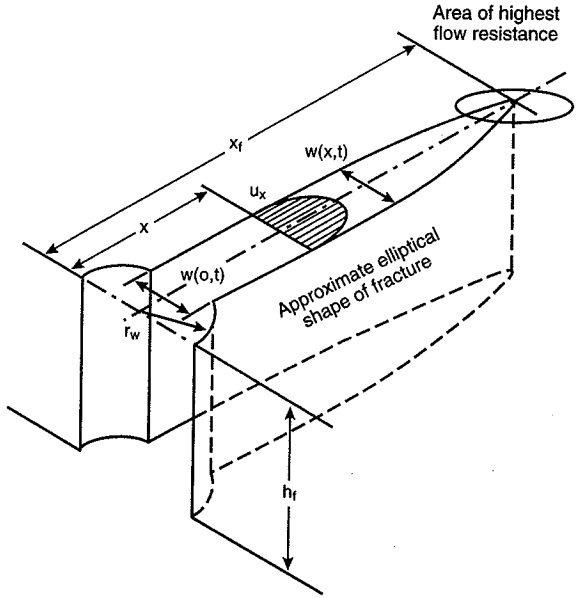

Figure 16-8
The KGD model geometry.

As can be seen from Fig. 16-8, the shape of the KGD fracture implies equal width along the wellbore, in contrast to the elliptical shape (at the wellbore) of the PKN model. This width profile results in larger fracture volumes when using the KGD model instead of the PKN model for a given fracture length.

The average hydraulic fracture width for the KGD model in coherent units and a Newtonian fluid is

$$\bar{w} = 2.27\left[\frac{q_i\mu(1-\nu)x_f^2}{Gh_f}\right]^{1/4}\left(\frac{\pi}{4}\right) \tag{16-37}$$

and in oilfield units, with $\bar{w}$ in in.,

$$\bar{w} = 0.29\left[\frac{q_i\mu(1-\nu)x_f^2}{Gh_f}\right]^{1/4}\left(\frac{\pi}{4}\right) \tag{16-38}$$

16-5.4 Net Fracturing Pressure

The creation of a two-dimensional crack, with one dimension of largely infinite extent and the other of finite extent, d, has been described by Sneddon and Elliot (1946). The maximum width of the crack, which is proportional to this characteristic dimension, is also proportional to the net pressure ($p_f - \sigma_{\min}$) and inversely proportional to the plane strain modulus, E'.

The maximum width is given by

$$w_{\max} = \frac{2(p_f - \sigma_{\min})d}{E'} \tag{16-39}$$

where

$$E' = \frac{E}{1-\nu^2} \tag{16-40}$$

The average width, $\bar{w}$, is

$$\bar{w} = \frac{\pi}{4}\gamma w_{\max} \tag{16-41}$$

For the PKN model the characteristic dimension d is the fracture height, h_f, while for the KGD model it is equal to the fracture length, tip to tip, $2x_f$. In Eq. (16-41), the value of γ is 0.75 for the PKN model and 1 for the KGD model.

Nolte and Economides (1989) have shown that for a fracturing operation with efficiency η ($= V_f/V_i$) $\longrightarrow$ 1, the volume of the fracture, V_f, must be equal to the volume of fluid injected, V_i, and therefore

$$\bar{w}A_f = q_i t \tag{16-42}$$

where A_f is the fracture area and equal to $2x_f h_f$.

For $\eta \longrightarrow 0$,

$$A_f = \frac{q_i\sqrt{t}}{\pi C_L r_p} \tag{16-43}$$

where C_L is the leakoff coefficient and r_p is the ratio of the permeable height to the fracture height. In a single-layer formation the permeable height is the net reservoir thickness, h.

For $\eta \longrightarrow 1$, Eq. (16-42) leads to

$$x_f\bar{w} = \frac{q_i t}{2h_f} \tag{16-44}$$

From Eq. (16-35) (maximum width of the PKN model) and Eq. (16-41) for the average width, and using all multipliers of $x_f^{1/(2n'+2)}$ as a constant C_1 (without the factor 12 to convert width in in.), Eq. (16-44) becomes

$$x_f(C_1 x_f^{1/(2n'+2)}) = \frac{5.615q_i t}{2h_f} \tag{16-45}$$

where q_i is in bpm and t is in minutes. Therefore,

$$x_f = \frac{1}{C_1}\left(\frac{5.615q_i t}{2h_f}\right)^{(2n'+2)/(2n'+3)} \tag{16-46}$$

For $\eta \longrightarrow 0$, x_f versus t can be obtained directly from Eq. (16-43), and thus

$$x_f = \frac{5.615q_i\sqrt{t}}{2\pi hC_L} \tag{16-47}$$

[The $h_f r_p$ product that would be in the denominator of Eq. (16-47) becomes simply h.]

From the Sneddon crack relationship [Eq. (16-39) with $d = h_f$ for the PKN model], the net fracturing pressure is given by

$$\Delta p_f = p_f - \sigma_{\min} = \frac{C_1}{(\pi\gamma/4)}x_f^{1/(2n'+2)}\frac{E}{2(1-\nu^2)h_f} \tag{16-48}$$

With Eq. (16-46) for $\eta \longrightarrow 1$ and using all multipliers of $t^{1/(2n'+3)}$ as C_2,

$$\Delta p_f = C_2 t^{1/(2n'+3)} \tag{16-49}$$

Similarly, from Eqs. (16-47) and (16-48), for $\eta \longrightarrow 0$,

$$\Delta p_f = C_3 t^{1/4(n'+1)} \tag{16-50}$$

where C_3 is the constant resulting from the combination of the equations.

Equations (16-46) and (16-47) for penetration and Eqs. (16-49) and (16-50) for net pressure represent the two extreme limits for $\eta \longrightarrow 1$ and $\eta \longrightarrow 0$, respectively.

The pressure expressions, in particular, are useful in monitoring the progress of a fracturing operation. Since n' is usually approximately equal to 0.5, the powers of time from Eqs. (16-49) and (16-50) should fall between 1/4 and 1/6. This observation was first made by Nolte and Smith (1981), who also presented analogous expressions for the KGD and Radial models. These are as follows:

KGD:

$$\Delta p_f \propto t^{-n'/(n'+2)} \qquad \text{for } \eta \longrightarrow 1 \tag{16-51}$$

$$\Delta p_f \propto t^{-n'/2(n'+1)} \qquad \text{for } \eta \longrightarrow 0 \tag{16-52}$$

Radial:

$$\Delta p_f \propto t^{-n'/(n'+2)} \qquad \text{for } \eta \longrightarrow 1 \tag{16-53}$$

$$\Delta p_f \propto t^{-3n'/8(n'+1)} \qquad \text{for } \eta \longrightarrow 0 \tag{16-54}$$

These results suggest that log-log plots during fracture execution can identify readily the morphology of the propagating fracture. In a plot of Δp_f versus time, positive slopes would suggest a normally extending, contained fracture, approximated by the PKN model. Negative slopes would imply either much larger fracture height than length growth, approximated by the KGD model, or radial fracture extension, approximated by the Radial model. This technique is currently in wide use.

Finally, there are also approximate and easy-to-use expressions for the net fracturing pressure for the PKN and KGD models using a Newtonian fracturing fluid.

For the PKN model, in coherent units, this expression is

$$\Delta p_f = 2.31 \left[\frac{G^3 q_i \mu x_f}{(1-\nu)^3 h_f^4} \right]^{1/4} \tag{16-55}$$

which in oilfield units becomes

$$\Delta p_f \text{ (psi)} = 0.0254 \left[\frac{G^3 q_i \mu x_f}{(1-\nu)^3 h_f^4} \right]^{1/4} \tag{16-56}$$

For the KGD model the analogous expression is

$$\Delta p_f \text{ (psi)} = 0.050 \left[\frac{G^3 q_i \mu}{(1-\nu)^3 h_f x_f^2} \right]^{1/4} \tag{16-57}$$

Again, it can be concluded readily that for the PKN model [Eq. (16-56)], as x_f grows, so does Δp_f. For the KGD model, as x_f grows, Δp_f declines [Eq. (16-57)].

EXAMPLE 16-7

Fracture penetration and net pressure versus time with the PKN model

Calculate the fracture penetration and the corresponding net pressure for the two extreme cases (i.e., $\eta \longrightarrow 1$ and $\eta \longrightarrow 0$). Use $n' = 0.5$, $K' = 8 \times 10^{-3}$ lb$_f$-sec$^{n'}$/ft^2, $q_i = 40$ bpm, $h = 100$ ft, $h_f = 150$ ft, $E = 2 \times 10^6$ psi, $\nu = 0.25$, and $C_L = 5 \times 10^{-3}$ ft/$\sqrt{\text{min}}$.

Plot the results of this calculation for the first 15 minutes.

Solution From Eqs. (16-35) and (16-41) and the given variables, the constant C_1 in Eq. (16-46) can be calculated:

$$C_1 = (0.59)(0.439)(6.8 \times 10^{-3}) = 1.76 \times 10^{-3} \tag{16-58}$$

From Eq. (16-46) for $\eta \longrightarrow 1$,

$$x_f = 457 t^{3/4} \tag{16-59}$$

For $\eta \longrightarrow 0$, from Eq. (16-47),

$$x_f = 71.5 t^{1/2} \tag{16-60}$$

In both Eqs. (16-59) and (16-60), the time is in minutes.

Finally, Eq. (16-49) for $\eta \longrightarrow 1$ becomes

$$\Delta p_f = 163 t^{1/4} \tag{16-61}$$

and for $\eta \longrightarrow 0$, Eq. (16-50) becomes

$$\Delta p_f = 87.9 t^{1/6} \tag{16-62}$$

Figure 16-9 is the plot of the results of this exercise. These net pressures increase with time, as should be expected from the PKN model. Of particular interest are the calculated fracture penetrations showing the enormous impact of the efficiency on fracture propagation. Thus, control of fluid leakoff should be of paramount importance for an effective hydraulic fracture treatment. ◇

16-5.5 Continuum Damage Mechanics in Hydraulic Fracturing

In certain cases, net treating pressures observed during hydraulic fracturing are several times greater than those predicted by simple propagation models. Palmer and Veatch (1989) give several examples of such abnormally high treating pressures. In such formations, using traditional design procedures would lead to unreliable results. An approach to understand and describe the phenomena is based on a fracture propagation criterion derived from continuum damage mechanics (CDM). According to CDM, under stress the material structure may begin to disintegrate. Small cracks may form, and such deterioration weakens the material and lowers its load-carrying capacity. The deterioration is characterized by the quantifiable damage variable. The damage growth rate can be described by a power-law-type constitutive relation, first introduced by Kachanov (1966). Starting from

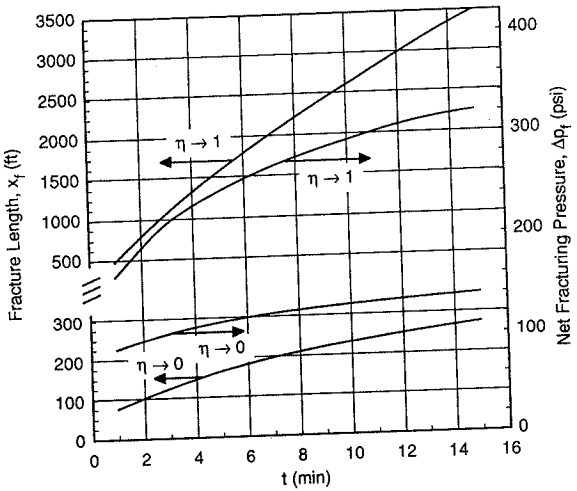

Figure 16-9

Penetration and net fracturing pressure using the PKN model for efficiency approaching 0 and 1 (Example 16-7).

the rupture criterion of continuum damage mechanics and assuming a stress distribution ahead of a moving crack, Valkó and Economides (1993) derived the following equation for the propagation rate of the fracture, u,

$$u = \frac{C\bar{l}^2}{\pi\sigma_{H,\min}}\left(\frac{K_I}{\bar{l}+L}\right)^2 \tag{16-63}$$

where u is in m/sec, C (1/Pa-sec) is the Kachanov parameter, $\bar{l}$ (m) is the average distance of microcracks, K_I (Pa-m$^{1/2}$) is the stress intensity factor, L is the fracture length, and $\sigma_{H,\min}$ (Pa) is the minimum principal stress. A small value of the Kachanov parameter and/or the average distance of the microcracks lead to retarded fracture propagation with treating pressures several times larger than usual. Applying the above equation as a boundary condition, a modified version of the Nordgren (1972) model can be introduced. The so-called CDM-PKN model is written in a dimensionless form using the following dimensionless variables:

$$x = c_1 x_D \qquad t = c_2 t_D \qquad w = c_3 w_D \qquad p_n = c_4 w_D \qquad L = c_1 L_D \tag{16-64}$$

where the constants c_1 through c_4 are given by

$$c_1 = \pi\left[\frac{(1-\nu)\mu(q_i/2)^5}{256C_L^8 G h^4}\right]^{1/3} \qquad c_2 = \pi^2\left[\frac{(1-\nu)\mu(q_i/2)^2}{32C_L^5 hG}\right]^{2/3}$$
$$c_3 = \left[\frac{16(1-\nu)\mu(q_i/2)^2}{C_L^2 Gh}\right]^{1/3} \qquad c_4 = \left[\frac{16G^2\mu(q_i/2)^2}{C_L^2(1-\nu)^2 h^4}\right]^{1/3} \tag{16-65}$$

The solution of the model is presented in Tables 16-1 through 16-3. The tables give the dimensionless length, wellbore width or net pressure, and fluid efficiency for a given dimensionless pumping time if the combined parameter, $C_D\bar{l}_D^2$, is known. The combined parameter can be obtained from calibration treatments, preferably from step rate tests. Though the dimensionless value of the combined parameter is not independent of the injection rate, the value determined for a given formation applying a given injection rate, can be easily recalculated to another injection rate using the formula

$$C_D l_D^2 = \left(\frac{q_i'}{q_i}\right)^{2/3}(C_D l_D^2)' \tag{16-66}$$

Therefore, the model can be used to predict the size of the fracture and the treating pressure for any specified injection rate and pumping time.

Table 16-1

Logarithm Base 10 of Dimensionless Length (L_D)

$\log_{10}(C_D\bar{l}_D^2) \longrightarrow$ $\log_{10}(t_D)$ $\downarrow$	−4	−3	−2	−1	0 (PKN)
−3	−3.2240	−2.9788	−2.7372	−2.5111	−2.4270
−2	−2.4779	−2.2363	−2.0004	−1.7815	−1.6787
−1	−1.7363	−1.5000	−1.2747	−1.0731	−0.9745
0	−0.9999	−0.7744	−0.5686	−0.4006	−0.3339
1	−0.2744	−0.06847	0.1028	0.2163	0.2435
2	0.4315	0.6029	0.7193	0.7729	0.7793
3	1.1029	1.2194	1.2757	1.2937	1.2947
4	1.7193	1.7757	1.7958	1.8010	1.8011
5	2.2760	2.2960	2.3025	2.3038	2.3038
6	2.7950	2.8022	2.8045	2.8048	2.8048

EXAMPLE 16-8

Prediction of fracture dimensions and net treating pressure using the CDM-PKN model

The following formation parameters are known: $h = 9.14$ m, $G = 1.3$ GPa, $\nu = 0.33$, $C_L = 7.87\times10^{-5}$ m/sec$^{1/2}$. A calibration test with a water injection rate $(q_i)' = 0.00262$ m^3/sec resulted in the combined parameter $(C_D\bar{l}_D^2)' = 0.000154$. Calculate the fracture length, the net treating pressure, and the fluid efficiency for a treatment with water ($\mu = 1$ mPa-sec) if the injection rate is $q_i = 0.005$ m^3/sec and the pumping time is t=60 min.

Solution First the parameter $C_D\bar{l}_D^2$, corresponding to the new injection rate, is calculated using Eq. (16-66):

$$C_D\bar{l}_D^2 = 0.65 \times 0.000154 = 0.0001 \tag{16-67}$$

Table 16-2

Logarithm Base 10 of Dimensionless Wellbore Width or Pressure (w_D)

$\log_{10}(C_D\bar{l}_D^2) \longrightarrow$ $\log_{10}(t_D)$ $\downarrow$	−4	−3	−2	−1	0 (PKN)
−3	0.2131	−0.04238	−0.2994	−0.5315	−0.6361
−2	0.4576	0.1987	−0.06606	−0.3202	−0.4505
−1	0.6986	0.4326	0.1547	−0.1267	−0.2802
0	0.9326	0.6538	0.3524	0.03177	−0.1258
1	1.1538	0.8517	0.5093	0.1399	0.01481
2	1.3517	1.0085	0.6041	0.2172	0.1469
3	1.5085	1.1027	0.6427	0.3045	0.2750
4	1.6027	1.1394	0.6606	0.4117	0.4013
5	1.6394	1.1504	0.6821	0.5302	0.5268
6	1.6496	1.1546	0.7315	0.6532	0.6520

Table 16-3

Logarithm Base 10 of Fluid Efficiency (η)

$\log_{10}(C_D\bar{l}_D^2) \longrightarrow$ $\log_{10}(t_D)$ $\downarrow$	−4	−3	−2	−1	0 (PKN)
−3	−0.01083	−0.02123	−0.03807	−0.06526	−0.1828
−2	−0.02115	−0.03765	−0.06731	−0.1182	−0.2540
−1	−0.03774	−0.06738	−0.1206	−0.2135	−0.3850
0	−0.06739	−0.1207	−0.2167	−0.3833	−0.5957
1	−0.1207	−0.2168	−0.3884	−0.6663	−0.8817
2	−0.2168	−0.3886	−0.6776	−1.0532	−1.2157
3	−0.3886	−0.6779	−1.0838	−1.4770	−1.5732
4	−0.6780	−1.0850	−1.5498	−1.8922	−1.9409
5	−1.0846	−1.5537	−2.0324	−2.2906	−2.3128
6	−1.5554	−2.0439	−2.5056	−2.6762	−2.6867

From Eq. (16-65), the coefficients, establishing the relations between the dimensionless and dimensioned variables, are

$$c_1 = 8.41 \text{ m} \qquad c_2 = 23.4 \text{ sec} \qquad c_3 = 9.70 \times 10^{-4} \text{ m} \qquad c_4 = 2.05 \times 10^5 \text{ Pa} \tag{16-68}$$

Now the base 10 logarithm of the combined parameter and the base 10 logarithm of the dimensionless time can be calculated:

$$\log_{10}(C_D\bar{l}_D^2) = -4 \qquad t_D = \frac{60 \times 60}{c_2} = 153 \qquad \log_{10}(t_D) = 2.19 \tag{16-69}$$

Knowing the logarithms from Tables 16-1, 16-2, and 16-3, the dimensionless length, width, or pressure, and fluid efficiency, respectively, can be obtained:

$$\log_{10}(L_D) = 0.560 \qquad \log_{10}(w_D) = 1.39 \qquad \log_{10}(\eta) = -0.242 \tag{16-70}$$

From the dimensionless length, the fracture length can be computed using Eq. (16-64):

$$L = c_1 L_D = 31 \text{ m} \tag{16-71}$$

Similarly, from the dimensionless wellbore width or pressure, the net treating pressure can be computed:

$$p_n = c_4 w_D = 5.0 \text{ MPa} \tag{16-72}$$

This pressure is considerably higher than what the traditional PKN model would calculate. Finally, the efficiency is calculated from its logarithm:

$$\eta = 0.57 \tag{16-73}$$

◇

16-6 HEIGHT MIGRATION

An appropriate p-3-D model would allow simultaneous lateral and vertical fracture height migration. An approximation for the fracture height at the wellbore (where it would have the maximum value) is presented below. The height prediction is based on log-derived mechanical properties and the wellbore net fracturing pressure. If this height were used with either the PKN or KGD model, it would lead to an overestimation of the required slurry volume to execute the treatment. Note that in the 2-D models the fracture height is considered to be constant along the fracture.

In Section 16-2, the distribution of horizontal stresses along the vertical column was discussed. It was suggested that because different lithologies have different Poisson ratios, the vertical stress (weight of the overburden) is translated horizontally unevenly, resulting in stress contrasts between layers. Example 16-1 showed several hundred psi differences between the horizontal stress of a target sandstone and overlaying or underlaying shales.

A simple model by Simonson (1978) relates this stress contrast, net fracturing pressure, and fracture height migration at the wellbore. Additionally, the effects of the interlayer critical stress intensity factor, K_{IC} (fracture toughness) and gravity have been incorporated. The latter was done by Newberry et al. (1985). Figure 16-10 is a schematic of the model. The horizontal stress value in the target layer of thickness, h, is σ. The overlaying layer has a stress σ_u, and the underlaying layer has a stress σ_d. Upward fracture migration h_u is

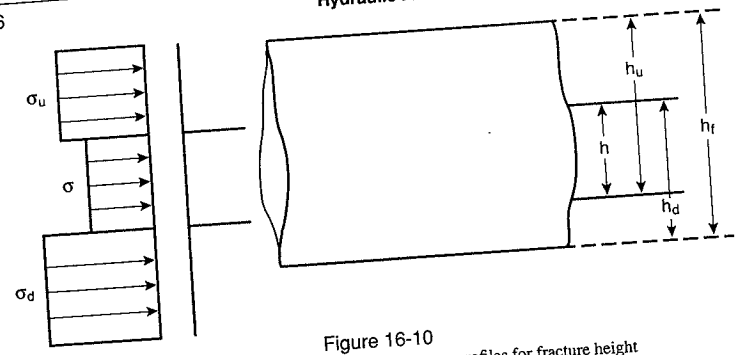

Figure 16-10
Geometry of target, adjoining intervals, and stress profiles for fracture height migration. (*After Newberry et al., 1985*)

measured from the bottom of the reservoir, and downward migration h_d is measured from the top of the reservoir.

The net fracturing pressure required to cause an upward fracture height migration h_u, is

$$\Delta p_f = \frac{C_1}{\sqrt{h_u}}\left[K_{IC}\left(1-\sqrt{\frac{h_u}{h}}\right) + C_2(\sigma_u-\sigma)\sqrt{h_u}\cos^{-1}\left(\frac{h}{h_u}\right)\right] + C_3\rho(h_u-0.5h) \tag{16-74}$$

Similarly, the net fracturing pressure required for a downward height migration h_d is

$$\Delta p_f = \frac{C_1}{\sqrt{h_d}}\left[K_{IC}\left(1-\sqrt{\frac{h_d}{h}}\right) + C_2(\sigma_d-\sigma)\sqrt{h_d}\cos^{-1}\left(\frac{h}{h_d}\right)\right] - C_3\rho(h_d-0.5h) \tag{16-75}$$

In the expressions above, the contribution from the interlayer stress contrast (second term on the right-hand side) for almost all reservoirs is the largest. The first term, that of the critical stress intensity factor, contributes only a small amount. Finally, in upward migration, gravity effects are retarding, while in downward migration they are accelerating.

The constants C_1, C_2, and C_3 for oilfield units (σ, σ_u, σ_d in psi, h, h_u, h_d in ft, ρ in lb/ft^3, and K_{IC} in psi/$\sqrt{\text{in.}}$) are 0.0217, 0.515, and 0.0069, respectively. The calculated net fracturing pressures would be in psi.

Finally, the inverse cosines must be evaluated in degrees.

EXAMPLE 16-9
Estimation of fracture height migration

A sandstone, 75 ft thick, has a minimum horizontal stress equal to 7100 psi. Overlaying and underlaying shales have stresses equal to 7700 and 8100 psi, respectively. $K_{IC} = 1000$ psi/$\sqrt{\text{in.}}$ and ρ=55 lb/ft^3. Calculate the fracture height migration for net fracturing pressures equal to 200 and 500 psi.

If the overlaying layer is 100 ft thick, what would be the critical net fracturing pressure above which an undesirable breakthrough into another permeable formation may occur?

Solution Figure 16-11 is a plot of $\Delta h_{u,d}(= h_{u,d} - h)$ versus Δp_f. An example calculation is presented below for the 100-ft migration above the target.

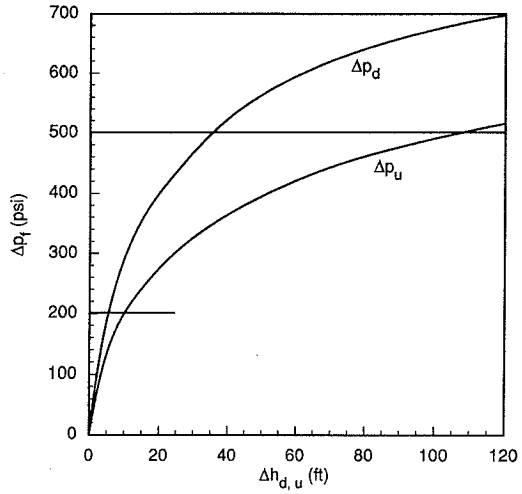

Figure 16-11
Pressures for upward and downward fracture height migration (Example 16-9).

Since $\Delta h_u = 100$, then h_u=175 ft and, from Eq. (16-74),

$$\Delta p_f = \frac{(0.0217)}{\sqrt{175}}\left[(1000)\left(1-\sqrt{\frac{175}{75}}\right) + (0.515)(7700-7100)\sqrt{175}\cos^{-1}\left(\frac{75}{175}\right)\right] + (0.0069)(55)[175-(0.5)(75)] \tag{16-76}$$

$$= -0.9 + 433 + 52 = 484 \text{ psi}$$

This is the critical net fracturing pressure that must not be exceeded during the treatment.

The three terms calculated above denote the relative contributions from the critical stress intensity factor, interlayer stress contrast, and gravity. For the type of stress contrast in this problem, the first term can be neglected and the gravity effects can be ignored for about a 10% error.

From Fig. 16-11, the fracture height migrations above the reservoir for 200 and 500 psi net pressure are 9 and 110 ft, respectively. In view of the calculation for 100-ft migration, the second net pressure would result in fracture growth into another permeable formation, usually an undesirable occurence.

Fracture migrations downward for 200 and 500 psi would be 6 and 35 ft, respectively.◇

16-7 Fluid Volume Requirements

A fracture execution consists of certain distinct fluid stages, each intended to perform a significant and specific task.

Pad is fracturing fluid that does not carry proppant. It is intended to initiate and propagate the fracture. During the fracture propagation, fluid *leakoff*, into the reservoir and normal to the created fracture area, is controlled primarily through the buildup of a wall filtercake. The volume of fluid leaking off is proportional to the square root of the residence time within the fracture. Therefore, pad, being the first fluid injected, acts as sacrificial to the following proppant-carrying slurry.

After the pad injection, *proppant slurry* is added to the fracturing fluid in increasing slurry concentrations until at the end of the treatment the slurry concentration reaches a predetermined value. This value depends on the proppant-transporting abilities of the fluid and/or the capacity the reservoir and the created fracture can accommodate.

In general, excessive fluid leakoff may be caused by reservoir heterogeneities, such as natural fissures. Another problem may be encountered as a result of fracture height migration. Breaking through a thin layer that separates two permeable formations is likely to create a narrow opening (remember Sneddon's relationship; for a shale with larger horizontal stress, the *net* pressure will be smaller and hence the fracture width will be smaller). This narrow opening can allow fluid to escape leaving proppant behind. These phenomena may result in excessive slurry dehydration and a "screenout." The latter refers to an inability of the slurry to transport the proppant, and it leads to an excessive pressure increase that prevents further lateral fracture growth.

The created hydraulic fracture length differs from the propped length because proppant cannot be transported beyond the point where the fracture width is smaller than three proppant diameters.

An approximation of the relationship between total fluid volume requirements, V_i, and the volume that is pad, V_{pad}, based on the fluid efficiency, η, was given by Nolte (1986) and Meng and Brown (1987):

$$V_{\text{pad}} \approx V_i \left(\frac{1-\eta}{1+\eta}\right) \tag{16-77}$$

Flush is intended to displace the slurry from the well into the fracture. It should be less than well volume, because overdisplacement would push the proppant away from the well and a "choked" fracture would result after the fracturing pressure dissipates and the fracture closes. This should be a major concern of the stimulation treatment and should be avoided at all cost.

A material balance between total fluid injected, created fracture volume V_f, and fluid leakoff V_L can be written:

$$V_i = V_f + V_L \tag{16-78}$$

Equation (16-78) can be expanded further by introducing constituent variables:

$$q_i t_i = A_f \bar{w} + K_L C_L (2A_f) r_p \sqrt{t_i} \tag{16-79}$$

where q_i is the injection rate, t_i is the injection time, A_f is the fracture area, C_L is the leakoff coefficient, and r_p is the ratio of the net to fracture height (h/h_f). The variable K_L is related to the fluid efficiency, and Nolte (1986) has shown that

$$K_L = \frac{1}{2}\left[\frac{8}{3}\eta + \pi(1-\eta)\right] \tag{16-80}$$

The fracture area in the leakoff term is multiplied by 2 to accommodate both sides of the fracture. The fracture area, A_f, is simply equal to $2x_f h_f$.

For a given fracture length, the average hydraulic width, $\bar{w}$, can be calculated under the assumption of a fracture model [e.g., Eq. (16-35) for the PKN model and a non-Newtonian fluid]. Knowledge of the fracture height, the leakoff coefficient, and the fluid efficiency would readily allow an inverse calculation using Eq. (16-79). This is a quadratic equation, and it can provide the required time to propagate a fracture of certain length (and implied width) while undergoing the penalty of fluid leakoff. Of the two solutions for the square root of time, one will be positive and the other negative. Squaring the positive solution would result in the calculation of the total injection time, t_i, and the product $q_i t_i$ is equal to the required total fluid (pad and proppant slurry) volume.

Since the portion of the total fluid volume that is pad can be calculated from Eq. (16-77), the onset of proppant addition can be obtained readily:

$$t_{\text{pad}} = \frac{V_{\text{pad}}}{q_i} \tag{16-81}$$

The leakoff coefficient, C_L in the material balance of Eq. (16-79), can be obtained from a fracture calibration treatment as described by Nolte and Economides (1989).

EXAMPLE 16-10

Total fluid and pad volume calculations

In Example 16-6, the average fracture width of a 1000-ft fracture was calculated to be equal to 0.18 in. Assuming that $r_p = 0.7$ (i.e., $h = 70$ ft), calculate the total volume and pad portion requirements. Use $C_L = 2 \times 10^{-3}$ ft/$\sqrt{\text{min}}$. Repeat the calculation for a large leakoff coefficient (2×10^{-2} ft/$\sqrt{\text{min}}$) and a small leakoff coefficient (2×10^{-4} ft/$\sqrt{\text{min}}$). The injection rate, q_i, is 40 bpm.

Solution

1. $C_L = 2 \times 10^{-3}$ ft/$\sqrt{\text{min}}$ The fracture area is $(2)(100)(1000) = 2 \times 10^5$ ft^2. Then, from Eq. (16-79), proper unit conversions, and assuming that $K_L = 1.5$,

$$(40)(5.615)t_i = 2 \times 10^5 \left(\frac{0.18}{12}\right) + (1.5)(2 \times 10^{-3})(4 \times 10^5)(0.7)\sqrt{t_i} \tag{16-82}$$

or

$$t_i - 3.74\sqrt{t_i} - 13.4 = 0 \tag{16-83}$$

which leads to t_i=36 min.

The total volume required is then

$$V_i = (40)(42)(36) = 6 \times 10^4 \text{ gal} \tag{16-84}$$

leading to an efficiency, η, of

$$\eta = \frac{V_f}{V_i} = \frac{(2 \times 10^5)\,(0.18/12)\,(7.48)}{6 \times 10^4} = 0.37 \tag{16-85}$$

where 7.48 is a conversion factor. From Eq. (16-80), $K_L = 1.48$, justifying the assumption of K_L=1.5. This calculation could be done by trial and error, although simple observation of Eq. (16-80) suggests that K_L is bounded between 1.33 and 1.57 and the use of $K_L \simeq 1.5$ is generally appropriate. From Eq. (16-77), the pad volume, V_{pad}, is

$$V_{\text{pad}} = (6 \times 10^4)\left(\frac{1 - 0.37}{1 + 0.37}\right) = 2.76 \times 10^4 \text{ gal} \tag{16-86}$$

representing 46% of the total volume. At an injection rate of 40 bpm, it would require 17 min of pumping.

2. $C_L = 2 \times 10^{-2}$ ft/$\sqrt{\text{min}}$ The corresponding quadratic equation would be

$$t_i - 37.4\sqrt{t_i} - 13.4 = 0 \tag{16-87}$$

The solution is then $t_i = 1425$ min. The required total volume is

$$V_i = (40)(42)(1425) = 2.39 \times 10^6 \text{ gal} \tag{16-88}$$

The efficiency η is very different from the previous calculation,

$$\eta = \frac{V_f}{V_i} = \frac{(2 \times 10^5)(0.18/12)(7.48)}{2.39 \times 10^6} = 9.4 \times 10^{-3} \tag{16-89}$$

and the pad volume would be also very different,

$$V_{\text{pad}} = (2.39 \times 10^5)\left(\frac{1 - 9.4 \times 10^{-3}}{1 + 9.4 \times 10^{-3}}\right) = 2.34 \times 10^6 \text{ gal} \tag{16-90}$$

representing 98% of the total volume and requiring 1397 min of pumping.

3. $C_L = 2 \times 10^{-4}$ ft/$\sqrt{\text{min}}$ The quadratic equation is

$$t_i - 0.374\sqrt{t_i} - 13.4 = 0 \tag{16-91}$$

and therefore $t_i = 15$ min.

The total volume requirements are

$$V_i = (40)(42)(15) = 2.5 \times 10^4 \text{ gal} \tag{16-92}$$

The efficiency is

$$\eta = \frac{V_f}{V_i} = \frac{(2 \times 10^4)(0.18/12)(7.48)}{2.5 \times 10^4} = 0.9 \tag{16-93}$$

and the pad volume is

$$V_{\text{pad}} = (2.5 \times 10^4)\left(\frac{1 - 0.9}{1 + 0.9}\right) = 1.3 \times 10^3 \text{ gal} \tag{16-94}$$

representing 5% of the total injected volume and requiring less than 1 minute of pumping.

From these calculations it is evident how important the leakoff coefficient is on the portion of the total fluid that must be injected before proppant is added to the slurry. Unavoidably, this has a major impact on the total amount of proppant that can be injected and the resulting propped fracture width for a given fracture length. ◇

16-8 PROPPANT SCHEDULE

Proppant addition, its starting point, and at what concentrations it is added versus time depend on the fluid efficiency. In the previous section the onset of proppant addition was determined after the pad volume was estimated [Eq. (16-77)].

Nolte (1986) has shown that, based on a material balance, the continuous proppant addition, "ramped proppant schedule" versus time, should follow a relationship expressed by

$$c_p(t) = c_f \left(\frac{t - t_{\text{pad}}}{t_i - t_{\text{pad}}}\right)^{\epsilon} \tag{16-95}$$

where $c_p(t)$ is the slurry concentration in pounds per gallon (ppg), c_f is the end-of-job (EOJ) slurry concentration, and t_{pad} and t_i are the pad and total times, respectively. The variable ϵ depends on the efficiency and is given by

$$\epsilon = \frac{1 - \eta}{1 + \eta} \tag{16-96}$$

Equations (16-95) and (16-96) simply denote the appropriate proppant addition mode so that the entire hydraulic length coincides with the propped length. This is not entirely realistic, since the fracture length, beyond the point where the hydraulic width is smaller than three

proppant diameters, cannot accept proppant; it will bridge (Note: Bridging can also occur at widths larger than three proppant diameters, which is the absolute minimum.) Hence, in designing a hydraulic fracture treatment, this type of criterion may be used as a check for the total mass of proppant that *can* be placed. Another consideration for the end-of-job slurry concentration, c_f, is the proppant-transporting ability of the fracturing fluid. Certainly, in all cases the calculated average propped width cannot exceed the average hydraulic width.

EXAMPLE 16-11
Determination of proppant schedule

Assume that the total injection time, t_i, is 245 min, and for efficiency $\eta = 0.4$, the pad injection time, t_{pad}, is 105 min. If the end-of-job slurry concentration, c_f, is 3 ppg, plot the continuous proppant addition schedule.

Solution From Eq. (16-96) and $\eta = 0.4$,

$$\epsilon = \frac{1-0.4}{1+0.4} = 0.43 \tag{16-97}$$

and from Eq. (16-95) and $c_f = 3$ ppg,

$$c_p(t) = 3\left(\frac{t-105}{245-105}\right)^{0.43} \tag{16-98}$$

For example, at $t = 150$ min $c_p(t) = 1.84$ ppg. Of course, at $t = 105$ min, $c_p(t) = 0$, and at $t = 245$ min, $c_p(t) = 3$ ppg.

Figure 16-12 is a plot of the injection with the onset of proppant addition and proppant schedule. ◇

16-9 Propped Fracture Width

In addition to the length, the propped width of the fracture describes the fracture geometry that controls posttreatment production. The fracture conductivity is simply the product of the propped width and the proppant pack permeability. The dimensionless conductivity was already given by Eq. (16-17). The width in that expression is the propped width of the fracture.

As should be obvious from the last two sections, the relationship between hydraulic width and propped width is indirect; it depends greatly on the fluid efficiency and especially on the possible end-of-job proppant concentration.

Assuming that a mass of proppant, M_p, has been injected into a fracture of half-length x_f and height h_f and the proppant is uniformly distributed, then

$$M_p = 2x_f h_f w_p (1-\phi_p)\rho_p \tag{16-99}$$

where the product $2x_f h_f w_p(1-\phi_p)$ represents the volume of the proppant pack and is characteristic of the proppant type and size. The density ρ_p is also a characteristic property of the proppant.

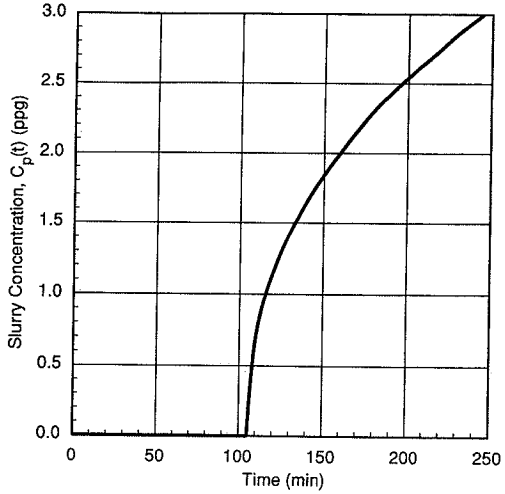

Figure 16-12
Onset of proppant slurry and continuous proppant addition (Example 16-11).

A frequently used quantity is the proppant concentration in the fracture, C_p, defined as

$$C_p = \frac{M_p}{2x_f h_f} \tag{16-100}$$

and the units are lb/ft^2. Traditionally, a good proppant pack concentration in a fracture would be 2 lb/ft^2. Therefore, Eq. (16-100), rearranged for the propped width, w_p, leads to

$$w_p = \frac{C_p}{(1-\phi_p)\rho_p} \tag{16-101}$$

To calculate the mass of proppant it is necessary first to integrate the ramped proppant schedule expression from t_{pad} to t_i and to obtain an average slurry concentration. From Eq. (16-95),

$$\bar{c}_p = \frac{1}{t_i - t_{pad}} \int_{t_{pad}}^{t_i} c_f \left(\frac{t-t_{pad}}{t_i - t_{pad}}\right)^{\epsilon} dt \tag{16-102}$$

leading to

$$\bar{c}_p = \frac{c_f}{\epsilon+1}(1-0) = \frac{c_f}{\epsilon+1} \tag{16-103}$$

The mass of proppant would then be

$$M_p = \bar{c}_p(V_i - V_{\text{pad}}) \tag{16-104}$$

Equations (16-99) through (16-104) are sufficient to calculate the average propped width of a fracture.

EXAMPLE 16-12
Calculation of the propped width

Suppose that 20/40 mesh sintered bauxite is injected ($\phi_p = 0.42$ and $\rho_p = 230$ lb/ft^3) into a fracture designed to have $x_f = 1000$ ft and $h_f = 150$ ft. If $c_f = 3$ ppg and $\epsilon = 0.43$ (see Example 16-11), calculate the total mass of proppant, the propped width, and the proppant concentration in the fracture. The volume of pad is $(4.12 \times 10^5) - (1.76 \times 10^5) = 2.36 \times 10^5$ gal.

Solution The average slurry concentration can be calculated from Eq. (16-103):

$$\bar{c}_p(t) = \frac{c_f}{1+\epsilon} = \frac{3}{1.43} = 2.1 \text{ ppg} \tag{16-105}$$

From Eq. (16-104), the mass of proppant can be determined:

$$M_p = (2.1)(2.36 \times 10^5) = 4.9 \times 10^5 \text{ lb} \tag{16-106}$$

The proppant concentration in the fracture, C_p, is [from Eq. (16-100)]

$$C_p = \frac{4.9 \times 10^5}{(2)(1000)(150)} = 1.63 \text{ lb/ft}^2 \tag{16-107}$$

Finally, from Eq. (16-101),

$$w_p = \frac{1.63}{(1-0.42)(230)} = 0.012 \text{ ft} = 0.15 \text{ in.} \tag{16-108}$$

◇

REFERENCES

1. Agarwal, R. G., Carter, R. D., and Pollock, C. B., "Evaluation and Prediction of Performance of Low-Permeability Gas Wells Stimulated by Massive Hydraulic Fracturing," *JPT*, pp. 362–372, March 1979; *Trans. AIME*, **267**.
2. Ben-Naceur, K., "Modeling of Hydraulic Fractures," in *Reservoir Stimulation*, 2nd ed., M. J. Economides and K. G. Nolte, eds., Prentice Hall, Englewood Cliffs, NJ, 1989.
3. Biot, M.A., "General Solutions of the Equations of Elasticity and Consolidation for a Porous Material," *J. Appl. Mech.*, **23**; 91–96, 1956.

4. Cinco-Ley, H., and Samaniego, F. "Transient Pressure Analysis for Fractured Wells," *JPT*, 1749–1766, September 1981.
5. Economides, M. J., McLennan, J. D., Brown, J. E., and Roegiers, J.-C., "Performance and Stimulation of Horizontal Wells," Part 1, *World Oil*, June 1989, Part 2, *World Oil*, July 1989.
6. Geertsma, J., and de Klerk, F., "A Rapid Method of Predicting Width and Extent of Hydraulically Induced Fractures," *JPT*, pp. 1571–1581, December 1969.
7. Hubbert, M. K., and Willis, D. G., "Mechanics of Hydraulic Fracturing," *Trans. AIME*, **210**: 153–168, 1957.
8. Kachanov, L. M., *Theory of Creep* (in Russian), Nauka, Moscow, 1966; also in *Advances in Creep Design*, Applied Science Publishers, London, 1971.
9. Khristianovic(h), S. A., and Zheltov, Y. P., "Formation of Vertical Fractures by Means of Highly Viscous Liquid," *Proc., Fourth World Petroleum Congress*, Sec. II, pp. 579–586, 1955.
10. McLennan, J. D., Roegiers, J.-C., and Economides, M. J., "Extended Reach and Horizontal Wells," in *Reservoir Stimulation*, 2nd ed., M. J. Economides and K. G. Nolte, eds., Prentice Hall, Englewood Cliffs, NJ, 1989.
11. Meng, H.-Z., and Brown, K. E., "Coupling of Production Forecasting, Fracture Geometry Requirements and Treatment Scheduling in the Optimum Hydraulic Fracture Design," SPE Paper 16435, 1987.
12. Newberry, B. M., Nelson, R. F., and Ahmed, U., "Prediction of Vertical Hydraulic Fracture Migration Using Compressional and Shear Wave Slowness," SPE/DOE Paper 13895, 1985.
13. Nolte, K. G., "Determination of Proppant and Fluid Schedules from Fracturing Pressure Decline," *SPEPE*, pp. 255–265, July 1986.
14. Nolte, K. G., and Economides, M. J., "Fracturing, Diagnosis Using Pressure Analysis," in *Reservoir Stimulation*, 2nd ed., M. J. Economides and K. G. Nolte, eds., Prentice Hall, Englewood Cliffs, NJ, 1989.
15. Nolte, K. G., and Smith, M. B., "Interpretation of Fracturing Pressures," *JPT*, pp. 1767–1775, September 1981.
16. Nordgren, R. P. "Propagation of Vertical Hydraulic Fracture," *SPEJ*, pp. 306–314, August 1972.
17. Palmer, I. D., and Veatch, R. W., Jr., "Abnormally High Fracturing Pressures in Step-Rate Tests," *SPEFE*, pp. 315–323, August 1990.
18. Perkins, T. K., and Kern, L. R., "Widths of Hydraulic Fracture," *JPT*, pp. 937–949, September 1961.
19. Prats, M., "Effect of Vertical Fractures on Reservoir Behavior—Incompressible Fluid Case," *SPEJ*, pp. 105–118, June 1961.
20. Simonson, E. R., "Containment of Massive Hydraulic Fractures," *SPEJ*, pp. 27–32, February 1978.
21. Sneddon, I. N., and Elliott, A. A., "The Opening of a Griffith Crack under Internal Pressure," *Quart. Appl. Math.*, **IV**:262, 1946.
22. Terzaghi, K, "Die Berechnung der Durchlässigkeitsziffer des Tones aus dem Verlauf der Hydrodynamischen Spannungserscheinungen," *Sber. Akad. Wiss., Wien*, **132**:105, 1923.
23. Valkó, P., and Economides, M. J., "A Continuum Damage Mechanics Model of Hydraulic Fracturing," *JPT*, 198–205, February 1993.

PROBLEMS

16-1. Assume that a formation is 6500 ft deep. What overpressure (above hydrostatic) is necessary to result in a horizontal fracture? The formation density, fluid density, and Poisson ratio are 165 lb/ft^3, 50 lb/ft^3, and 0.23, respectively.

16-2. If 2500 ft of overburden from the formation described in Problem 16-1 were removed, and if the formation fluid is at hydrostatic pressure, what fracturing net press would cause turning of the fracture from vertical to horizontal? Is it possible? Explain.

16-3. In Terzaghi's relationship [Eq. (16-6)], the breakdown pressure is in terms of absolute stresses and reservoir pressure. Assume that the reservoir described in Problem 16-1 is at hydrostatic pressure. Calculate its initial breakdown pressure and its value when the reservoir pressure declines by 500 and 1000 psi. The tensile stress is 500 psi.

16-4. Calculate the fracture equivalent skin effect, s_f, for a fracture length 500 ft and dimensioned conductivity, $k_f w$, equal to 1000 md-ft, for two wells, one in a 1-md reservoir and the other in a 0.01-md reservoir. If $r_e = 1500$ ft and $r_w = 0.328$ ft, calculate the corresponding productivity index increases.

16-5. If the permeabilities in two reservoirs are 1 md and 0.01 md, what should be the minimum (target) $k_f w$ products if $x_f = 500$ ft?

16-6. Derive Eq. (16-23) and plot the productivity index ratios for a reservoir with $r_e = 1500$ ft, $r_w = 0.328$ ft for a range of $k_f w$ and reservoir permeability k. What would be the limiting value for k if $k_f w$ cannot be smaller than 100 md-ft?

16-7. Calculate and plot the hydraulic fracture width versus fracture length for a sandstone reservoir with $E = 5 \times 10^6$ psi and a chalk formation with $E = 5 \times 10^5$ psi. Show the effect of doubling the injection rate, q_i, from 20 to 40 bpm. Use an apparent fracturing fluid viscosity equal to 100 cp and a Poisson ratio equal to 0.25.

16-8. If $q_i = 40$ bpm, $h_f = 100$ ft, $E = 4 \times 10^6$ psi, and $K' = 0.2$ lb$_f$ sec$^{n'}$/ft^2, plot the average fracture width, using the non-Newtonian fluid expression for $n' = 0.3, 0.4, 0.5$, and 0.6. Assuming that $n' = 0.5$, what is the ratio of the average widths for $q_i = 40$ bpm and 20 bpm?

16-9. Graph and compare the average fracture widths obtained with the PKN and KGD models for $q_i = 40$ bpm, $\mu = 100$ cp, $\nu = 0.25$, $E = 4 \times 10^6$ psi, and $h_f = 100$ ft. Perform the calculation for x_f up to 1000 ft (although the KGD model should not be used for such a length).

16-10. In Eq. (16-48), the constant C_1 is a function of the injection rate q_i and the consistency of the power law rheological model, K'. Assuming that all other variables are constant, develop an expression of the form $\Delta p_f = f(q_i, K', n')$.

If $n' = 0.5$, show the corresponding changes in q_i (with K' constant) or K' (with q_i constant) to allow a 10% reduction in Δp_f.

16-11. Develop a simple p-3-D fracture propagation model using Eqs. (16-74) and (16-75) for upward and downward fracture migration and Eqs. (16-35) (for width) and (16-39) relating this width with Δp_f. Note that $h_f = h_u + h_d - h$.

16-12. What would be the effect from the injection rate on the total fluid volume requirements? Using the non-Newtonian PKN width relationship and $n' = 0.56$, $K' = 8 \times 10^{-3}$ lb$_f$ sec$^{n'}$/ft^2, $E = 4 \times 10^6$ psi, $h_f = 100$ ft, $\eta = 0.3$, $C_L = 8 \times 10^{-3}$ ft/$\sqrt{\text{min}}$, and $r_p = 0.7$, graph V_i and the total time of injection, t_i versus q_i.

16-13. Repeat Problem (16-12) for $q_i = 40$ bpm but allow h_f to increase from 100 to 300 ft (still $h = 70$ ft). If the propped width w_p cannot exceed $0.8\bar{w}$, calculate and plot the allowable end-of-job proppant concentration c_f for increments of 50 ft in the h_f. Plot the proppant addition schedule for the same fracture heights.

16-14. If $c_f = 8$ ppg, $V_i = 10^6$ gal, and $\eta = 0.4$, calculate the total mass of proppant injected. What would be the propped width if $x_f = 1500$ ft, $h_f = 100$ ft, $\rho_p = 165$ lb/ft^3, and $\phi_p = 0.4$?

CHAPTER 17

Design of Hydraulic Fracture Treatments

17-1 INTRODUCTION

The design of a hydraulic fracture as a well stimulation treatment involves the selection and use of appropriate fracturing fluids and proppants. The amount of these materials and the mode of injection (rate and pressure) are related to the resulting fracture size. There is a large range of possible fracture sizes, and hence an attempt for optimization is warranted. An appropriate criterion for design optimization is production economics, that is, the maximizing of incremental benefits, above those that the unstimulated well could deliver, tempered by the costs of executing the fracture treatment.

Fluid selection should depend on two main criteria: to transport the proppant (adequate apparent fluid viscosity) and to cause relatively small residual damage to the proppant pack. Proppant selection should focus on the maximization of the proppant pack permeability/propped width of the fracture at the expected state of stress. (Note: Throughout this chapter, the term "viscosity" refers to the apparent viscosity of the largely non-Newtonian fracturing fluids.)

Injection rate and pressure should be kept below a level that would cause undesirable fracture height migration. High injection rate would result in a high net pressure [see Eqs. (16-56) and (16-57)] and hence the possibility of breaking into another formation or, at least, inefficient fracture growth. On the other hand, if height growth is tolerable, then a higher injection rate would result in a lower injection time and hence a more efficient fracture propagation, since fluid leakoff is proportional to the square root of the execution time [see Eq. (16-79)].

It is obvious from these considerations, which are affected by a few dozen variables, that a coherent design approach must first interconnect them and then employ a criterion to identify the optimum design. This is the purpose of this chapter.

17-2 Design Considerations for Fracturing Fluids

Almost all desirable and undesirable properties of fracturing fluids are related to their viscosity, which in turn is a function of the polymer load. Polymers such as guar, which is a naturally occuring material, or hydroxypropyl guar (HPG) have been used in aqueous solutions to provide substantial viscosity to the fracturing fluid. Polymer concentrations are often given in pounds of polymer per 1000 gallons of fluid (lb/1000 gal), and typical values range between 20 and 60 with, perhaps, 40 lb/1000 gal being the most common concentration in batch-mixed fracturing fluids that are currently in use.

Viscosity degrades with increasing temperature and shear. The largest degradation will be experienced by the first portion of the injected fracturing fluid, since it will experience the highest temperature and narrowest fracture width (i.e., highest shear). Subsequent portions will experience somewhat lower temperatures and, especially, lower shear, by virtue of the widening of the fracture. Hence viscosity requirements are likely to decrease during fracture execution, and the polymer load could be decreased. Today, continuous addition of polymer and on-time mixing is implemented as a preferred method over the traditional batch mixing of polymers in "frac tanks." Simply, mixed water and slurried polymers are blended together at the appropriate concentrations for the desired viscosity at any stage of the treatment.

Typical reservoir temperatures (175–200°F) would lead to relatively low viscosities of the straight polymer solutions. For example, while a 40-lb/1000-gal HPG solution would exhibit a viscosity of approximately 50 cp at room temperature at a shear rate of 170 sec^{-1}, the same solution at 175°F has a viscosity of less than 20 cp.

Experience has shown that the viscosity of fracturing fluids must be almost always above 100 cp at 170 sec^{-1} to transport the proppant. Thus crosslinking agents, usually organometallic or transition metal compounds, are used to boost the viscosity significantly. The most common crosslinking ions are borate, titanate, and zirconate. They form bonds with guar and HPG chains at various sites of the polymer, resulting in very high-molecular-weight compounds. The viscosity at 170 sec^{-1} of a 40-lb/1000-gal borate-crosslinked fluid is over 2000 cp at 100°F and about 250 cp at 200°F.

Borate-crosslinked fluids have an upper temperature of application about 225°F, while zirconate- and titanate-crosslinked fluids may be used up to 350°F. However, while borate-crosslinked fluids are not shear sensitive (bonds that may be sheared are readily regenerated), zirconate and titanate bonds, once broken, cannot be regenerated readily. This is an issue that can be remedied through "delayed crosslinking," which is activated after the fracturing fluid has traversed the pumps, tubing, and, ideally, the perforations where the maximum shear values are encountered.

An ideal fracturing fluid has very low viscosity while it is pumped down a well, leading to a low friction pressure drop, has the maximum required viscosity in the fracture to transport the proppant, and then reverts to very low viscosity upon the completion of the treatment. The latter is particularly important because although the polymer solutions serve a purpose in transporting the proppant, if they are left intact, they will effectively plug the proppant pack, leading to a highly reduced fracture permeability.

To accomplish these seemingly contradictory requirements, active research has identified a number of additives to modify the fracturing fluid properties at the appropriate time during the fracture execution. Some of the most common fracturing fluid additives are listed below:

Bactericides. Bacteria attack the organic polymers, destroying the bonds and, unavoidably, reducing the viscosity. Batch-mixed fracturing fluids, stored in "frac tanks" and in the absence of bactericides, are likely to lose an appreciable amount of viscosity.

Buffers. In batch-mixed systems, powdered polymers must be first dispersed and then hydrated. A higher pH (~9) is necessary for proper dispersion. This can be accomplished with a base. For hydration, though, the pH must be lowered. Materials such as weak organic acids are the preferred buffers. Continuous mixed systems disperse with the high agitation energy provided by the mixer and exhibit much faster hydration.

Guar and HPG can be crosslinked at pH between 3 and 10, depending on the crosslinking agent. The range of crosslinking is usually very narrow, requiring carefully metered acids or bases to accomplish the task.

Stabilizers. In addition to the inherent viscosity thinning caused by the elevated reservoir temperature, free oxygen attacks the polymers and, as should be expected, this degradation reaction increases with increasing temperature. Additives such as sodium thiosulfate or methanol are used as free oxygen "scavengers," trapping the oxygen and removing it from the reaction path.

Fluid loss additives. As shown in Section 16-7, fluid loss and its control are critical to a successful fracture execution. Usually, in largely homogeneous formations, a filter cake deposited on the walls of the fracture is an adequate means of leakoff control. Mayerhofer et al. (1991) have shown that 97–98% of the pressure drop from the fracture into the formation is controlled by a successfully placed filter cake. Crosslinked polymers can perform this task up to 5 md reservoir permeability.

Leakoff control can be augmented by the creation of oil-in-water emulsions with the addition of small quantities of diesel.

In fissured or naturally fractured formations, particulates such as silica flour or oil-soluble but water-insoluble resins can be used for additional leakoff control.

Surfactants. Wettability changes may result at the fracture face or in the associated invaded zone. Surfactants are added to facilitate the posttreatment cleanup.

Breakers. Perhaps the most important additives in a fracturing fluid are the polymer breakers. As mentioned earlier, unsuccessful degradation of the polymer chains, following the treatment execution, is highly detrimental to the well performance.

Breakers must strive toward certain ideal characteristics. In addition to their effectiveness, they must be activated *after* the treatment is over and yet as quickly as possible. Furthermore, their concentration in the fracturing fluid must be such as to accommodate the increasing polymer concentration in the fracture because of continuous water leakoff instead of the injected polymer concentration.

Thermally activated breakers are used at times in wells with temperatures over 225°F. Chemical breakers are added in cooler wells. Current research seeks "encapsulated" breakers, that is, additives that are inert during the execution but can be activated by physical or chemical means immediately after the treatment. Such products are currently becoming available in the industry.

More thorough outlines of fracturing fluid additives can be found in Gulbis (1989) and Economides (1991).

17-2.1 Fracturing Fluid Selection Guide

Figure 17-1 (Economides, 1991) is a fracturing fluid selection guide representing current and evolving industry practices. In addition to the aforementioned aqueous fracturing fluids, oil-base fluids and mixed formulations involving gas and liquid (foams) or oil and water (emulsions) have been developed and used.

Oil-base fluids and oil-and-water emulsions are obvious candidates for water-sensitive formations, whereas foams target, in addition to water-sensitive formations, reservoirs that are underpressured or with relative permeability problems. The expanding gas in the foams can aid in the lifting of the fracturing fluid back toward the surface, facilitating a rapid and more efficient cleanup following the stimulation treatment.

While cleanup and fracture face damage are important considerations (wettability or clay swelling problems), fracturing fluids should never be used exclusively on the basis of these criteria. As will be shown in Chapter 18, the performance impairment due to fracture face damage is always minor compared to the damage to the proppant pack or inadequate proppant pack. Thus the proppant-transporting ability of the fracturing fluid and its ability to deliver a substantial propped width with good fracture permeability should be the paramount consideration in fluid selection.

As was shown in Section 16-4, low-permeability reservoirs are candidates for long fractures where the fracture permeability is of lesser concern; moderate- to high-permeability reservoirs require higher-permeability fractures and the fracture length is secondary. This reservoir requirement should also influence the selection of the type of fracturing fluid, polymer load, and associated additives.

In Fig. 17-1 the first and obvious division is whether the reservoir is oil or gas. The temperature of 225°F is used as a dividing point, reflecting the applicable upper limit of borate-crosslinked fluids. These fluids, which are excellent proppant transporters, have been consistently proven in both posttreatment performance and laboratory experiments to be less damaging, retaining much of the ideal proppant pack permeability, and they should be used whenever possible.

In higher-pressure gas wells, if the temperature is very low, e.g., below 150°F, then linear fluids can be used if small fracture permeability or length is acceptable. Otherwise, borate-crosslinked fluids are recommended.

If the pressure is low or the formation is water sensitive, then 70- to 75-quality foams can be used.

If the gas reservoir temperature is more than 225°F, organometallic crosslinked fluids can be used. If the pressure is low, then these fluids can be energized with CO_2 or N_2.

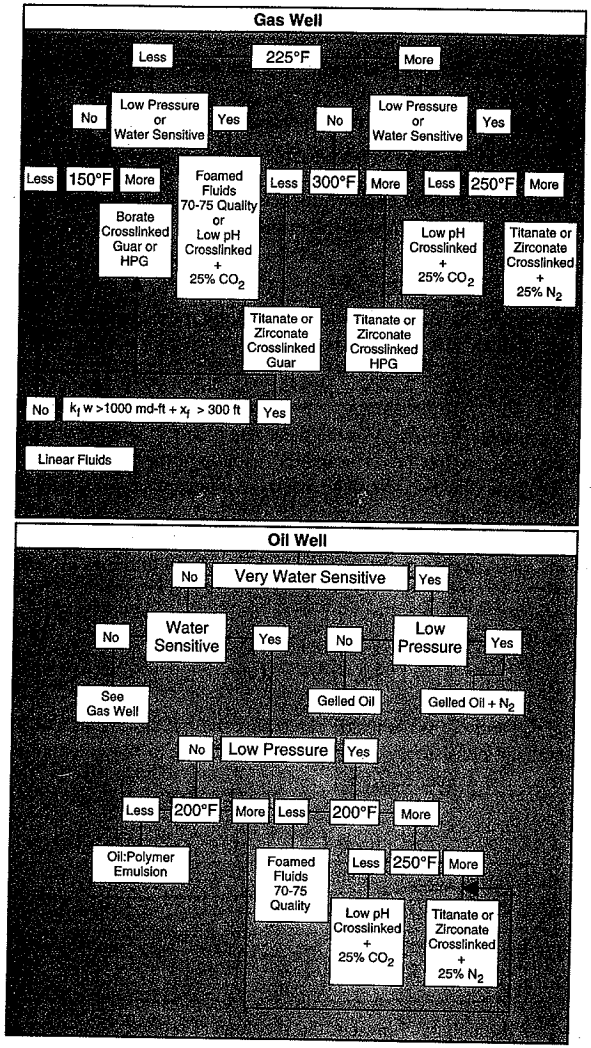

Figure 17-1
Fracturing fluid selection guide. (*From Economides, 1991.*) *Courtesy Schlumberger.*

In oil wells, *significant* water sensitivity is a concern. If the reservoir is only moderately water sensitive, then the same selection guidelines as applied to gas wells can be used. This encompasses a large majority of all oil wells.

If a reservoir is very water sensitive and with low pressure, then gelled oil with N_2 is recommended. If the pressure is high, then straight gelled oil can be used. If the reservoir is only moderately water sensitive, with higher pressure and less than 200°F, then a polymer emulsion can be used. Otherwise, foamed or energized organometallic crosslinked fluids can be injected.

While this selection guide allows a wide spectrum of fluids, borate-crosslinked fluids can be used effectively in the majority of fracturing treatments.

17-2.2 Rheological Properties

Most fracturing fluids are not Newtonian, and the most commonly used model to describe their rheological behavior is the power law

$$\tau = K\dot{\gamma}^n \tag{17-1}$$

where τ is the shear stress in lb_f/ft^2, $\dot{\gamma}$ is the shear rate in sec^{-1}, K is the consistency index in $lb_f\ sec^n/ft^2$, and n is the flow behavior index. A log-log plot of τ versus $\dot{\gamma}$ would yield a straight line, the slope of which would be n and the intercept at $\dot{\gamma}$=1 would be K.

Fracturing fluid rheological properties are obtained usually in concentric cylinders that lead to the geometry-specific parameters n' and K'. While the flow behavior index n is equal to n', the generalized consistency index K is related to the K' from a concentric cylinder by

$$K = K'\left[\frac{B^{2/n'}(B^2-1)}{n'(B^{2/n'}-1)B}\right]^{-n'} \tag{17-2}$$

where $B = r_{cup}/r_{bob}$ and r_{cup} is the inside cup radius and r_{bob} is the bob radius.

The generalized consistency index is in turn related to the consistency index for various geometries. For a pipe, K'_{pipe}, is

$$K'_{pipe} = K\left(\frac{3n'+1}{4n'}\right)^{n'} \tag{17-3}$$

and for a slot, K'_{slot}, is

$$K'_{slot} = K\left(\frac{2n'+1}{3n'}\right)^{n'} \tag{17-4}$$

Figures 17-2 through 17-5 present the rheological properties of the most common fracturing fluids. The first two contain n' and K' for the 40-lb/1000-gal borate-crosslinked fluid plotted with both temperature and exposure time. The last two figures represent n' and K' of the 40-lb/1000-gal zirconate-crosslinked fluid.

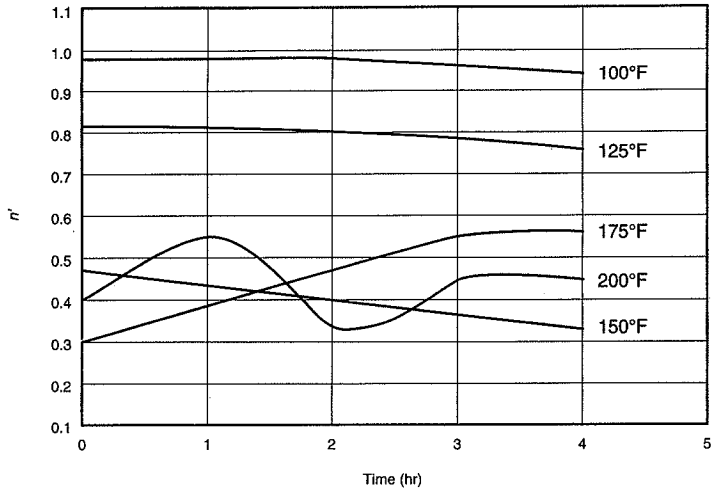

Figure 17-2
n' for 40-lb/1000-gal borate-crosslinked fluid. (*From Economides, 1991.*) *Courtesy Schlumberger.*

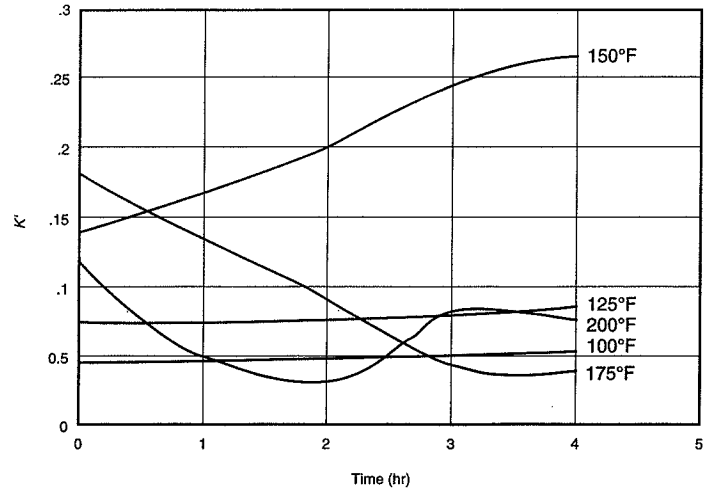

Figure 17-3
K' for 40-lb/1000-gal borate-crosslinked fluid. (*From Economides, 1991.*) *Courtesy Schlumberger.*

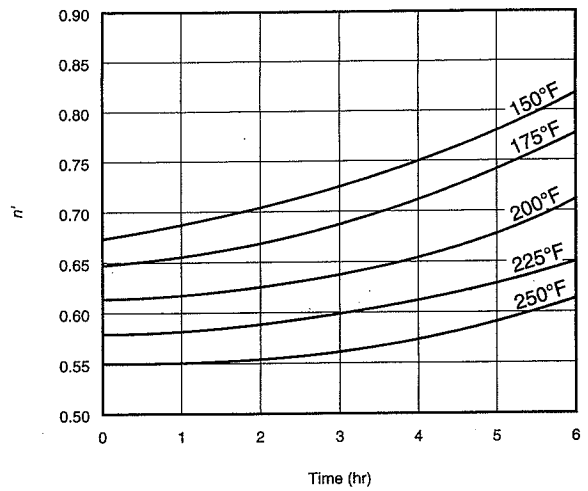

Figure 17-4
n' for 40-lb/1000-gal zirconate-crosslinked fluid. (*From Economides, 1991.*) *Courtesy Schlumberger.*

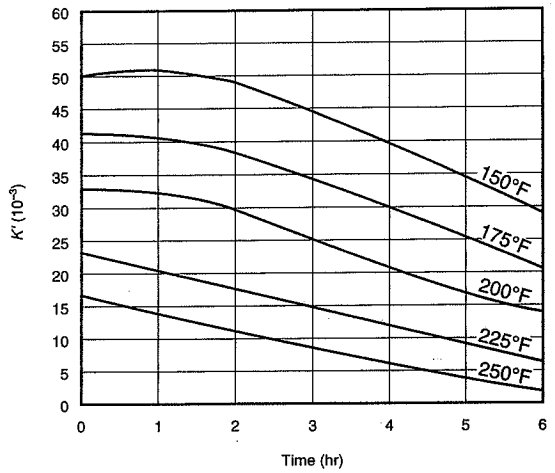

Figure 17-5
K' for 40-lb/1000-gal zirconate-crosslinked fluid. (*From Economides, 1991.*) *Courtesy Schlumberger.*

An interesting property is the apparent viscosity, μ_a, which is related to the geometry-dependent K', the n', and a given shear rate $\dot{\gamma}$:

$$\mu_a = \frac{47,880K'}{\dot{\gamma}^{1-n'}} \tag{17-5}$$

In Eq. (17-5), the viscosity is in cp.

Finally, the wall shear rate in a tube (well) for a power law fluid is

$$\dot{\gamma} = \left(\frac{3n'+1}{4n'}\right)\frac{8u}{d} \tag{17-6}$$

where d is the diameter and u is the superficial velocity and is equal to q/A.

For a slot, which could approximate the geometry of a fracture, the wall shear rate is

$$\dot{\gamma} = \left(\frac{2n'+1}{3n'}\right)\frac{6u}{w} \tag{17-7}$$

where w is the width of the slot.

For foam fluids, Valkó et al. (1992) showed that the consistency index in Eq. (17-1) can be expressed as

$$K = K_{\text{foam}}\epsilon^{1-n} \tag{17-8}$$

where ϵ is the specific volume expansion ratio:

$$\epsilon = \frac{\hat{v}_{\text{foam}}}{\hat{v}_{\text{liquid}}} = \frac{\rho_{\text{liquid}}}{\rho_{\text{foam}}} \tag{17-9}$$

and K_{foam} and n are characteristic for a given liquid–gas pair at a given temperature. In a well the superficial velocity of the foam changes with depth, since the pressure change causes a density variation. The important property of Eq. (17-8) is that the change in K will compensate for density variations and hence will result in a constant friction factor along the tube in both the laminar and turbulent flow regimes. Equation (17-8) is called the "volume equalized power law."

EXAMPLE 17-1
Determination of rheological properties of power law fluids

Calculate the K'_{pipe} and K'_{slot} for a 40-lb/1000-gal borate-crosslinked fluid at 175°F. Assume that the rheological properties were obtained in a concentric cylinder where B=1.3. If in a fracturing treatment the injection rate is 40 bpm, the fracture height is 250 ft, and the width is 0.35 in., calculate the apparent viscosity in the fracture.

Solution From Figs. 17-2 and 17-3 (at T=175°F and t = 0 hr), n' = 0.3 and K' = 0.18 $\text{lb}_f\ \text{sec}^{n'}/\text{ft}^2$. The generalized K is given by Eq. (17-2):

$$K = (0.18)\left[\frac{1.3^{2/0.3}(1.3^2-1)}{0.3(1.3^{2/0.3}-1)1.3}\right]^{-0.3} = 0.143\ \text{lb}_f\ \text{sec}^{n'}/\text{ft}^2 \tag{17-10}$$

Then, from Eq. (17-3),

$$K'_{\text{pipe}} = (0.143)\left[\frac{(3)(0.3)+1}{(4)(0.3)}\right]^{0.3} = 0.164 \text{ lb}_f\text{-sec}^n/\text{ft}^2 \tag{17-11}$$

and from Eq. (17-4),

$$K'_{\text{slot}} = (0.143)\left[\frac{(2)(0.3)+1}{(3)(0.3)}\right]^{0.3} = 0.17 \text{ lb}_f\text{-sec}^n/\text{ft}^2 \tag{17-12}$$

The shear rate in a fracture can be approximated by Eq. (17-7). At first the superficial velocity (with proper unit conversions) is

$$u = \frac{(40/2)(5.615)}{(60)(250)(0.35/12)} = 0.26 \text{ ft/sec} \tag{17-13}$$

The division of the flow rate by 2 implies that half of the flow is directed toward one wing of the fracture. Therefore,

$$\dot{\gamma} = \left[\frac{(2)(0.3)+1}{(3)(0.3)}\right]\left[\frac{(6)(0.26)}{(0.35/12)}\right] = 95 \text{ sec}^{-1} \tag{17-14}$$

The apparent viscosity is then [from Eq. (17-5)]

$$\mu_a = \frac{(47,880)(0.17)}{95^{0.7}} = 336 \text{ cp} \tag{17-15}$$

◇

17-2.3 Friction Pressure Drop during Pumping

The rheological properties of fracturing fluids are particularly useful for the estimation of the friction pressure drop. This is true not only for the calculation of the treating pressure [see Eq. (16-14)], it is especially necessary for the *prediction* of the downhole fracture propagation (net) pressure, since measurements are usually impractical. Downhole pressure gauges cannot be used unless they are permanently installed and insulated from the proppant-carrying slurry or they measure the pressure indirectly, as in the annulus.

The real-time measurement or extrapolation of the net fracturing pressure is a potent tool for the detection of the morphology of the created fracture. Interpretation of the net pressure and the meaning of the most commonly encountered patterns were outlined in Section 16-5.4.

To calculate the friction pressure drop for a power law fluid, at first the Reynolds number must be estimated.

$$N_{\text{Re}} = \frac{\rho u^{2-n'} D^{n'}}{K' 8^{n'-1}[(3n'+1)/4n']^{n'}} \tag{17-16}$$

Equation (17-16) is in consistent units. In oilfield units it becomes

$$N_{\text{Re}} = \frac{0.249\rho u^{2-n'} D^{n'}}{96^{n'} K'[(3n'+1)/4n']^{n'}} \tag{17-17}$$

where ρ is the density in lb/ft^3, u is the velocity in ft/sec, D is the diameter in in. and K' is in lb$_f$-sec$^{n'}$/ft^2.

The velocity in oilfield units is

$$u = 17.17\frac{q_i}{D^2} \tag{17-18}$$

where q_i is the injection rate in bpm.

For laminar flow ($N_{\text{Re}} < 2100$), the Fanning friction factor for smooth pipes can be calculated from the well-known expression

$$f_f = \frac{16}{N_{\text{Re}}} \tag{17-19}$$

If the flow is turbulent ($N_{\text{Re}} > 2100$), then the Fanning friction factor is

$$f_f = \frac{c}{N_{\text{Re}}^b} \tag{17-20}$$

where

$$b = \frac{1.4 - \log n'}{7} \tag{17-21}$$

and

$$c = \frac{\log n' + 2.5}{50} \tag{17-22}$$

The friction pressure drop is given by the well-known

$$\Delta p_F = \frac{2 f_f \rho L u^2}{D} \tag{17-23}$$

which in oilfield units, with Δp_F in psi, becomes

$$\Delta p_F = \frac{5.2 \times 10^{-3} f_f \rho L u^2}{D} \tag{17-24}$$

The calculation implied by the equations above would result in an upper limit of the friction pressure drop. Polymeric solutions are inherently friction pressure reducing agents, and the actual Δp_F is likely to be smaller than the one calculated.

EXAMPLE 17-2
Friction pressure drop calculation

Calculate the pressure drop of a 40-lb/1000-gal zirconate-crosslinked fluid per 1000 ft of vertical fracturing string with a 3-in. inside diameter. Assume that the average temperature is 150°F. The fluid density is 60 lb/ft^3. Use a range of injection rates from 1 to 60 bpm and plot the results on log-log paper.

What would be the pressure drop for the 40 bpm if the inside tubing diameter were 6 in.?

Solution Figure 17-6 is a graph of the friction pressure drops versus the injection rate for the 3-in. tubing. Up to a rate of 15 bpm, the flow is laminar. For higher injection rates, the flow is turbulent. Below is a calculation of the pressure drop for q_i=40 bpm.

First, from Figs. 17-4 and 17-5 at 150°F, $n' = 0.68$ and $K' = 0.05$ lb$_f$-sec$^{n'}$/ft^2?

Assuming that n' and K' (from a concentric viscometer) are also valid for the tubing and after the velocity is calculated from Eq. (17-18),

$$u = 17.17\left(\frac{40}{3^2}\right) = 76.3 \text{ ft/sec} \tag{17-25}$$

the Reynolds number can be obtained from Eq. (17-17):

$$N_{\text{Re}} = \frac{(0.249)(60)(76.3)^{1.32}3^{0.68}}{96^{0.68}(0.05)(1.18)^{0.68}} = 7700 \tag{17-26}$$

This value implies turbulent flow. The constants b and c are equal to 0.22 and 0.047, respectively [from Eqs. (17-21) and (17-22)]. Therefore the friction factor is

$$f_f = \frac{0.047}{7700^{0.22}} = 6.6 \times 10^{-3} \tag{17-27}$$

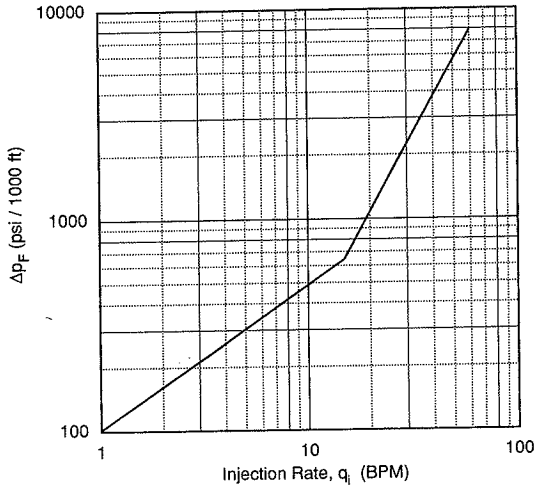

Figure 17-6
Friction pressure drop for a 1000-ft pipe with a 40-lb/1000-gal zirconate-crosslinked fluid (Example 17-2).

and, finally, from Eq. (17-24),

$$\Delta p_F = \frac{(5.2 \times 10^{-3})(6.6 \times 10^{-3})(60)(1000)(76.3)^2}{3} = 4000 \text{ psi} \tag{17-28}$$

This is a very large pressure drop, suggesting that the 3-in. tubing is not an appropriate size.

Repeating the calculation for $d = 6$ in. the velocity is 19.7 ft/sec, the Reynolds number is 2100 (assume turbulent flow), and the friction factor is 8.7×10^{-3}. The pressure drop is then

$$\Delta p_F = \frac{(5.2 \times 10^{-3})(8.7 \times 10^{-3})(60)(1000)(19.7)^2}{6} = 176 \text{ psi} \tag{17-29}$$

which is much more attractive. ◇

17-2.4 Power Demand for a Fracture Treatment

Equation (16-14) readily relates the wellhead treating pressure, p_{tr}, the fracture propagation pressure (p_{bd} for breakdown, p_f during fracturing), and the hydrostatic, Δp_{PE}, and friction, Δp_F, pressure drops. The treating pressure and the injection rate are related directly to the power demand. In HHP the relationship is

$$\text{HHP} = \frac{q_i p_{\text{tr}}}{40.8} \tag{17-30}$$

in oilfield units.

EXAMPLE 17-3
Power requirements for a fracturing treatment

Suppose that a reservoir is 10,000 ft deep, the injection rate is 15 bpm of 40-lb/1000-gal zirconate-crosslinked fluid, and the density is 60 lb/ft^3. Calculate the power demand if the expected maximum net fracturing pressure, Δp_f, is 1000 psi, the minimum stress is 7200 psi, and the Δp_F is 2000 psi.

Solution The maximum fracturing pressure is 8200 psi (1000 + 7200). The hydrostatic pressure is

$$\Delta p_{\text{PE}} = \frac{(60)(10,000)}{144} = 4170 \text{ psi} \tag{17-31}$$

Therefore,

$$p_{\text{tr}} = 8200 + 2000 - 4170 = 6030 \text{ psi} \tag{17-32}$$

From Eq. (17-30),

$$\text{HHP} = \frac{(15)(6030)}{40.8} = 2217 \text{ hhp} \tag{17-33}$$

The number of pumps available for the job should be able to provide at least this power plus whatever additional capacity is warranted in the event of breakdowns or other mechanical problems. ◇

17-2.5 Polymer-Induced Damage

Polymer solutions, with viscosities of several hundred centipoise at reservoir temperatures, would create a highly unfavorable mobility for the posttreatment production of reservoir fluids. Furthermore, while the injected concentrations may be 20 to 60 lb/1000 gal, slurry dehydration, because of filtrate leakoff into the reservoir, would rapidly increase the polymer concentration within the fracture to several hundred lb/1000 gal. Reduction of these detrimental effects is accomplished through the selection of less damaging fracturing fluid formulations and, especially, by the introduction of better breakers at the appropriate concentrations. In the late 1980s, STIM-LAB pioneered the testing of fracturing fluids under realistic pressure and temperature conditions and likely proppant concentrations in a fracture (1 to 2 lb/ft^2). Their results have shown that, in addition to the obvious—higher polymer loadings damage the fracture conductivity more than lower polymer loadings—the type of crosslinker has a major effect.

From the first finding, as should be expected, foams, coupled with their inherent ease of cleanup, are the least damaging fluids. The retained proppant pack permeability is frequently over 95%.

For aqueous polymer solutions and their retained proppant-pack permeability, the type of crosslinker is far more critical. Table 17-1 (Thomas and Brown, 1989) shows clearly that borate-crosslinked fluids are far less damaging than titanate- or antimonate-crosslinked fluids. Although the type of breaker has an impact (e.g., a persulfate/amine breaker performs better than an enzyme breaker), the difference from the type of crosslinker is dominant. Thus borate-crosslinked fluids should be used within their range of application ($T < 225$°F) instead of fracturing fluids with other crosslinkers.

Table 17-1

Long-Term Retained Permeability of 20/40 Jordan Sand at 2000 psi Closure Pressure, 100°F, and 1 lb/ft^2 Proppant Concentration with Various Fracturing Fluids[a]

Type of Fluid	Retained Permeability (%)
Borate-crosslinked 30-lb HPG with persulfate/amine breaker	95
Borate-crosslinked 40-lb HPG with persulfate/amine breaker	88
Borate-crosslinked 30-lb HPG with enzyme breaker	68
Titanate-crosslinked 40-lb HPG (low pH) with enzyme breaker	50
Antimonate-crosslinked 40-lb HPG (low pH) with enzyme breaker	40
Titanate-crosslinked 40-lb HPG (neutral pH) with enzyme breaker	19

[a]From Thomas and Brown, 1989.

Finally, the breaker concentration must be such as to accommodate the increased polymer concentration within the fracture. Figure 17-7 (Brannon and Pulsinelli, 1990) suggests that while the breaker concentration should be substantial (4 to 5 lb/1000 gal), larger concentrations (> 6 lb/1000 gal) would not result in appreciable improvement in the proppant pack permeability.

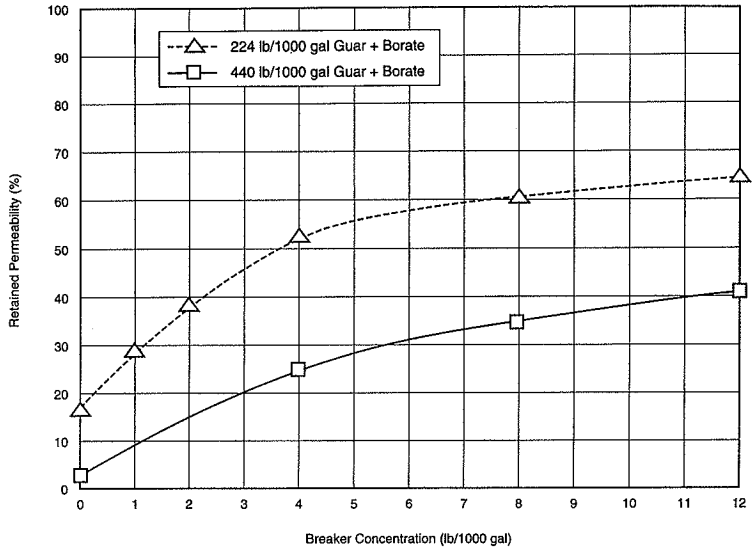

Figure 17-7
Effect of breaker concentration on retained permeability of 20/40 Northern White sand, 2 lb/ft^2, 160°F. (*From Brannon and Pulsinelli, 1990.*)

Ongoing research is continuously seeking better and more effective breakers, and several new products are emerging at the time of this writing.

17-3 Proppant Selection for Fracture Design

In the absence of a propping material, a created hydraulic fracture will heal shortly after the fracturing pressure dissipates into the reservoir. Natural sand is the most common proppant, especially in low-stress formations.

Much of the stress-induced permeability reduction of a proppant pack is caused by the crushing of the particles and the migration of fragments into the pore space of the pack. A thin coating of resin, applied to the sand grains, not only improves their strength but also retains fragments if already crushed. There are several varieties of resin-coated sand with the resin precured or hardened during manufacturing or in situ. Resins are also used with the proppant "tail-in" to prevent flowback after a treatment. Higher-stress formations

require higher-strength proppants. Manufactured ceramic intermediate-strength proppants (ISPs) and even higher-strength proppants such as sintered bauxite or zirconium oxide are used frequently.

The properties of proppants that affect the success of hydraulic fracturing include: grain size, grain size distribution, quality (amount of impurities), roundness and sphericity, proppant density, and the porosity of the proppant pack. All of these properties affect the initial and, especially, the long-term proppant pack permeability, which in turn affects the conductivity of the fracture. The product of the permeability/propped width, $k_f w$, is the dimensioned conductivity of the fracture in md-ft (see Section 16-4).

The grain size distribution, quality, and roundness and sphericity are all affected by the stress value (less roundness means greater possibility for fragments to be broken off.) The subsequent lodging of these broken fragments, along with preexisting impurities or smaller spheres (in a wider range of particles) into the pore space of the proppant pack results in an unavoidable reduction in the proppant pack permeability.

The other main properties, such as mesh size, porosity, and density of the most common proppants, are listed in Table 17-2.

Table 17-2

Typical Proppants and Their Characteristics

Type	Mesh Size	Particle Size (in.)	Density (lb/ft^3)	Porosity
Northern White sand	12/20	0.0496	165	0.38
	16/30	0.0350	165	0.39
	20/40	0.0248	165	0.40
Texas Brown sand	12/20	0.0496	165	0.39
	16/30	0.0350	165	0.40
	20/40	0.0248	165	0.42
Curable resin-coated sand	12/20	0.0496	160	0.43
	16/30	0.0350	160	0.43
	20/40	0.0248	160	0.41
Precured resin-coated sand	12/20	0.0496	160	0.38
	16/30	0.0350	160	0.37
	20/40	0.0248	160	0.37
ISP	12/20	0.0496	198	0.42
	20/40	0.0248	202	0.42
ISP-lightweight sintered bauxite	20/40	0.0248	170	0.40
	16/20	0.0400	231	0.43
	20/40	0.0248	231	0.42
	40/70	0.0124	231	0.42
Zirconium oxide	20/40	0.0248	197	0.42

If the proppant concentration within the fracture, C_p, is known, then the maximum propped width (i.e., without proppant embedment into the walls of the fracture) and the number of particle diameters can be calculated. For example, if 20/40-mesh Northern Sand is used and if $C_p = 2$ lb/ft^2 and $\phi_p = 0.4$ (from Table 17-2), the propped width [from Eq. 16-101)] is 0.02 ft. Since the particle diameter is 0.0248 in., the calculated propped width is equal to more than nine particle diameters.

As proppants are subjected to higher stress they crush, and the proppant pack permeability is reduced. Figure 17-8 is an example of the permeability and associated conductivity reduction versus stress for a sand. On the left side is the reduction with increasing stress. For a stress increase from 1000 to 5000 psi, the reduction is from 310 darcies to 95 darcies.

Prolonged exposure at higher stress leads to an additional reduction because of fatigue and final redistribution of the fragments. The right side of Fig. 17-8 shows this reduction where the permeability drops down to 40 darcies, representing almost an order-of-magnitude reduction from the original value at 1000 psi stress.

Long-term proppant permeability/conductivity testing is now the norm, and data exist for a variety of proppants, sizes, and concentrations within the fracture. Figure 17-9 (data from Penny, 1988) shows the reduction in the fracture conductivity for several 20/40-mesh proppants. Sands undergo a very severe conductivity reduction (more than 20-fold) for a stress increase from 2000 to 8000 psi. Resin-coated sand undergoes only a three-fold reduction within the same stress range. ISP also undergoes conductivity reduction, but both the relative reduction is lower (2- to 2.5-fold) and, especially, the magnitude remains high. The conductivity of ISP is more than an order of magnitude larger than that of sand at 8000 psi.

Larger proppant sizes have larger permeabilities. However, at higher stresses, larger-size particles are more susceptible to crushing because as grain size increases, strength decreases. Therefore, the relative reduction of the permeability/conductivity of larger-size proppants with increasing stress is larger. Coupled with the fact that large particles form larger pore sizes where fragments can migrate, their advantages may disappear at higher stresses. It is conceivable that the permeability/conductivity of a larger-size proppant at higher stress may be less than that of a smaller-size proppant. Complete sets of data for most common proppants can be found in Penny (1986) and Penny (1988).

Embedment is an additional factor for proppant-pack permeability reduction at higher stresses. It affects particularly higher-strength proppants. Lower-strength proppants may crush instead of embed. The relative reduction in lower proppant concentrations within a fracture will be more severe. Table 17-3 contains the fracture conductivity reduction for a sand and ISP but with C_p=1 lb/ft^2. Comparison with the data in Fig. 17-9 (for $C_p = 2$ lb/ft^2), the conductivity ratios for sand between the values at 2000, 4000, and 6000 psi are 2.2, 2.0, and 1.9, respectively. For ISP the ratios for 2000, 4000, 6000, 8000, and 10,000 psi are 2.2, 2.8, 3.8, 4.4, and 4.4, respectively, reflecting the larger relative impact of embedment at the lower proppant concentration. Thus, crushing and embedment are the two main stress-induced effects on the fracture permeability/conductivity reduction. In designing a hydraulic fracture treatment, the resulting conductivity must be balanced against the

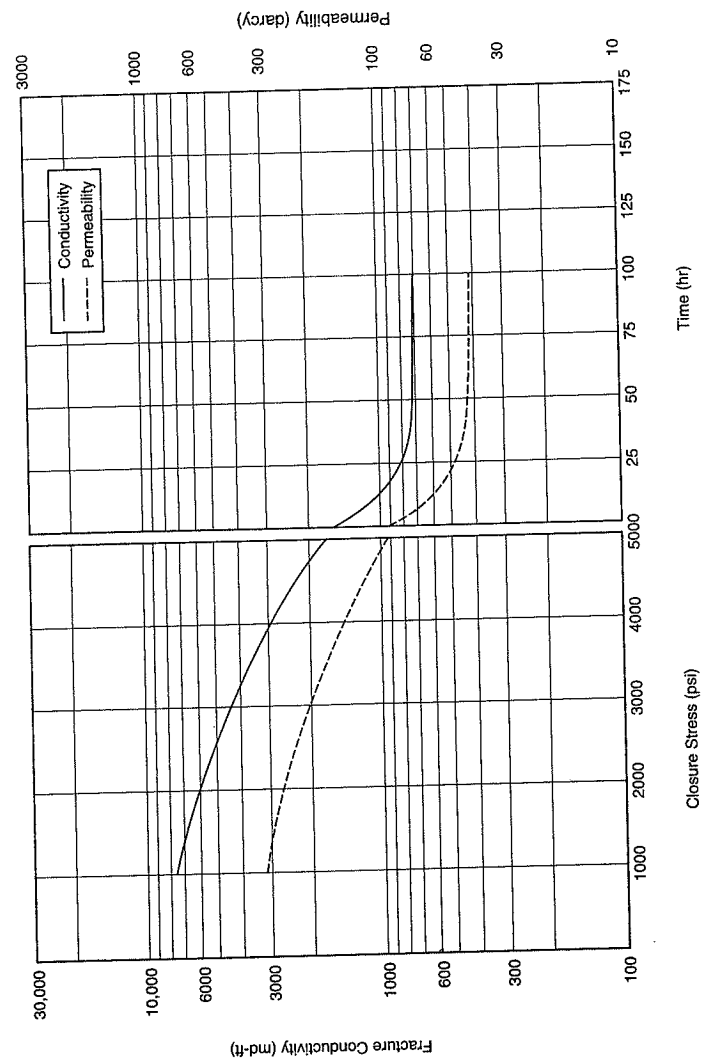

Figure 17-8
Fracture conductivity and proppant-pack permeability of 20/40 Brown sand at 2 lb/ft^2, 225°F. Time effects at 5000 psi closure stress. (*From Penny, 1986.*) *Courtesy STIM-LAB.*

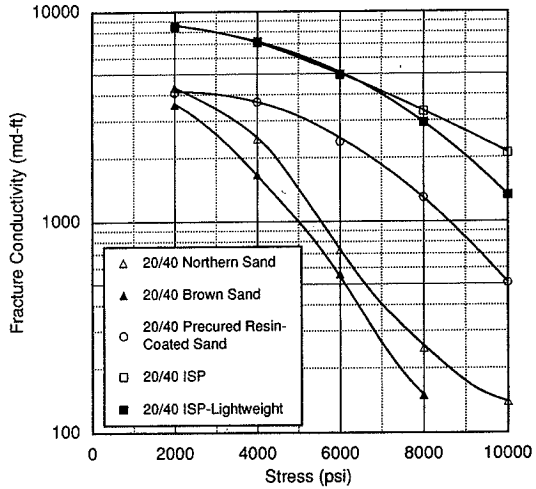

Figure 17-9
Long-term fracture conductivity for various proppants at 2 lb/ft^2. (*After Penny, 1988.*)

costs. While the costs of ISP or higher-strength proppants are greater, at higher stresses these materials retain their conductivity. Hence, in a design approach based on production economics, the optimum proppant selection must be based not only on costs but also on the posttreatment performance of the created proppant pack.

Table 17-3

Long-Term Conductivity for Various Proppants at 1 lb/ft^2 and 200°F[a]

	Fracture Conductivity (md-ft)				
Type	2000 psi	4000 psi	6000 psi	8000 psi	10,000 psi
20/40 Northern sand	1970	1210	380	—	—
20/40 ISP-lightweight	3770	2580	1330	660	310

[a]From Penny, 1988.

EXAMPLE 17-4
Calculation of stress on proppant and resulting permeability reduction

Assume that a reservoir is 10,000 ft deep with a formation density equal to 165 lb/ft^3, Poisson ratio equal to 0.25, Biot constant equal to 0.7, and initial reservoir pressure equal to 6500 psi.

Calculate the fracture conductivity of 20/40 sand and 20/40 ISP at 2000- and 4000-psi drawdowns. Will the stress on the proppant increase or decrease with time?

Solution Since a proppant pack can be considered as a porous medium, the effective horizontal stress on it could simply be calculated from Eqs. (16-2) through (16-4). Thus at the initial conditions of pressure:

$$\sigma'_{H,\min} = \frac{0.25}{0.75}\left[\frac{(165)(10{,}000)}{144} - (0.7)(6500)\right] = 2300 \text{ psi} \tag{17-34}$$

This is the stress that the proppants might have experienced without drawdown. However, 2000- and 4000-psi drawdowns ($p_{wf} = 4500$ and 2500 psi, respectively) would result in an increase in the effective stress by 1400 psi (0.7 × 2000) and 2800 psi (0.7 × 4000), respectively. Thus the effective stresses would be 3700 and 5100 psi. From Fig. 17-9, at 3700 psi the conductivity of (Northern) sand would be 2600 md-ft, while at 5100 psi it would be 1350 md-ft. For 20/40 ISP the corresponding values would be 7200 and 6000 md-ft, respectively.

The initial stress on the proppant would be the maximum value. After a time of production, the reservoir pressure would decline. If, for example, $\overline{p} = 5000$ psi, then the *absolute* horizontal stress would be

$$\sigma_{H,\min} = \frac{0.25}{0.75}\left[\frac{(165)(1000)}{144} - (0.7)(5000)\right] + (0.7)(5000) = 6150 \text{ psi} \tag{17-35}$$

and with $p_{wf} = 4500$ psi,

$$\sigma'_{H,\min} = 6150 - (0.7)(4500) = 3000 \text{ psi} \tag{17-36}$$

representing a 700-psi decrease.

For $p_{wf} = 2500$, the $\sigma'_{H,\min}$ would be 4400 psi instead of 5100 psi. ◇

17-3.1 Slurry Concentration

In Section 16-8 the slurry concentration $c_{p(t)}$ in pounds per gallon (ppg) of slurry was introduced as a function of the end-of-job slurry concentration, c_f. Furthermore, in Section 16-9 the average slurry concentration, $\overline{c}_p$, was related with c_f and the total mass of proppant placed in a fracture.

Equation (16-77) is a relation between the pad volume, V_{pad}, the total injected volume, V_i, and the efficiency, η. If V_{slurry} is the proppant-carrying fluid, then [with Eq. (16-77)]

$$V_{\text{slurry}} = V_i - \frac{1-\eta}{1+\eta}V_i = \frac{2\eta}{1+\eta}V_i \tag{17-37}$$

With Eq. (16-103), Eq. (17-37) leads to

$$M_p = \left(\frac{2\eta}{1+\eta}V_i\right)\left[\frac{c_f}{1+(1-\eta)/(1+\eta)}\right] = \eta c_f V_i \tag{17-38}$$

The mass of proppant was related to the fracture volume, proppant pack porosity, and proppant density by Eq. (16-99). Since, by definition,

$$\eta = \frac{V_f}{V_i} = \frac{2x_f h_f \overline{w}(7.48)}{V_i} \tag{17-39}$$

(the factor 7.48 is to convert from cubic feet into gallons), combination of Eqs. (17-38), (17-39), and (16-99) results in

$$w_p \rho_p (1-\phi_p) = 7.48\overline{w}c_f \tag{17-40}$$

It is essential that $w_p < \overline{w}$, and therefore

$$c_f < \frac{\rho_p(1-\phi_p)}{7.48} \tag{17-41}$$

This is the maximum allowable slurry concentration in pounds of proppant per gallon of slurry. If 20/40 sand is pumped (ρ_p =165 lb/ft^3 and $\phi_p = 0.4$, from Table 17-2) then,

$$c_f < \frac{(165)(0.6)}{7.48} < 13.2 \text{ ppg} \tag{17-42}$$

17-3.2 Proppant Mixing

In a continuous mixing, Eq. (16-95) provides the slurry concentration in ppg. Frequently the proppant concentration in pounds per gallon added, ppga, is used. This refers to pounds of proppant per gallon of fluid. The relationship is simple. Since c_p is ppg of slurry, then in 1 gal of slurry there are c_p/ρ_p gal of proppant (ρ_p must be density in lb/gal) and therefore $1 - c_p/\rho_p$ gal of fluid. The proppant concentration in ppga, c'_p, is then

$$c'_p = \frac{c_p}{1 - c_p/\rho_p} \tag{17-43}$$

For example, the c_f in Eq. (17-42) corresponds to

$$c'_p = \frac{13.2}{1 - 13.2/(165/7.48)} \simeq 33 \text{ ppga} \tag{17-44}$$

17-4 Fracture Design and Fracture Propagation Issues

In designing a hydraulic fracture, several variables are involved. Table 17-4 is a list of these variables. Typical values are listed for the calculations included in this and the two subsequent sections. There are three types of variables: those the designer can do little about, those where moderate control can be exercised, and those that are under complete control.

The first category includes the depth, reservoir permeability, reservoir thickness, minimum horizontal stress, initial reservoir pressure, and rock and fluid properties. In addition, the flowing bottomhole pressure (or the related wellhead pressure) are frequently dictated by surface production requirements or bottomhole constraints such as fines migration or coning. Therefore, fracture design must focus on the optimization of the treatment while taking into account these reservoir constraints.

Table 17-4

Well, Reservoir, Fracturing Fluid, and Treatment Variables for Example Fracture Design for an Oil Well

Depth, $H = 10,000$ ft	EOJ slurry concentration, $c_f = 8$ ppg
Reservoir permeability, $k = 0.1$ md	Proppant density, $\rho_p = 165$ lb/ft^3
Reservoir height, $h = 75$ ft	Proppant porosity, $\phi_p = 0.4$
Minimum horizontal stress, $\sigma_{H,\min} = 7000$ psi	Proppant diameter, $d_p = 0.0248$ in.
Initial reservoir pressure, $p_i = 5500$ psi	Fracture permeability, $k_f = 38,000$ md
Young's modulus, $E = 3 \times 10^6$ psi	Damage factor, 0.75
Poisson ratio, $\nu = 0.25$	$n' = 0.55$
Reservoir porosity, $\phi = 0.1$	$K' = 0.04$ lb$_f$-sec$^{n'}$/ft^2
Formation volume factor, $B_o = 1.1$ res bbl/STB	Proppant cost = \$0.4/lb
Total compressibility, $c_t = 10^{-5}$ psi^{-1}	Pumping cost = \$3.25/hr/hhp
Reservoir fluid viscosity, $\mu = 1$ cp	Fluid cost = \$1/gal
Flowing bottomhole pressure, $p_{wf} = 3500$ psi	Fixed cost = \$15,000
Fracture height, $h_f = 150$ ft	No. of years for NPV = 2
Leakoff coefficient, $C_L = 3 \times 10^{-3}$ ft/$\sqrt{\text{min}}$	Discount rate = 30%
Injection rate, $q_i = 40$ bpm	Oil price = \$15/bbl

Three other variables fall under the second category, where partial control may be in the hands of the designing engineer. These include the fracture height, leakoff coefficient, and the end-of-job proppant slurry concentration. These variables are classified under partial control because they also depend on reservoir and formation characteristics such as the presence of fissures, poor interlayer stress contrast, and high temperature, for which only limited capability is afforded to the designer.

The fracture height depends on the stress contrast between the target and adjoining layers and is a function of the net fracturing pressure. If the stress contrast is large, then a larger net pressure is tolerable. The opposite is true for a small stress contrast. This relationship was outlined in Section 16-6. From Eq. (16-56), providing the approximation for net fracturing pressure with the PKN model, it can be concluded readily that fracture length can grow at constant Δp_f (and thus keeping the fracture height largely constant) if the injection rate or the viscosity, or both, are reduced.

At first the efficiency for the given leakoff coefficient ($C_L = 3 \times 10^{-3}$ ft/$\sqrt{\text{min}}$) can be calculated. This is simply a solution of the material balance equation [Eq. (16-79)] for each fracture height for a range of fracture lengths as shown in Example 16-10. The results for various h_f/h ratios are shown in Fig. 17-10, where, as should be expected, the efficiency increases with increasing h_f. This is not a particularly attractive thing, since fracture height penetrating a nonproducing interval is useless. If it penetrates another permeable formation, it may be worse. During execution, excessive leakoff may lead to a screenout; during production, problems of zonal isolation may arise.

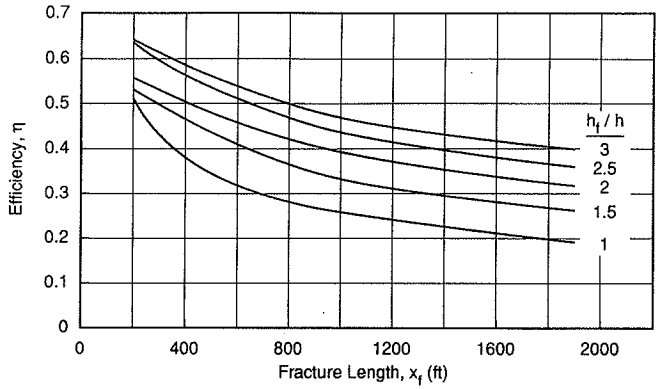

Figure 17-10
Efficiency calculation for several fracture height migrations.

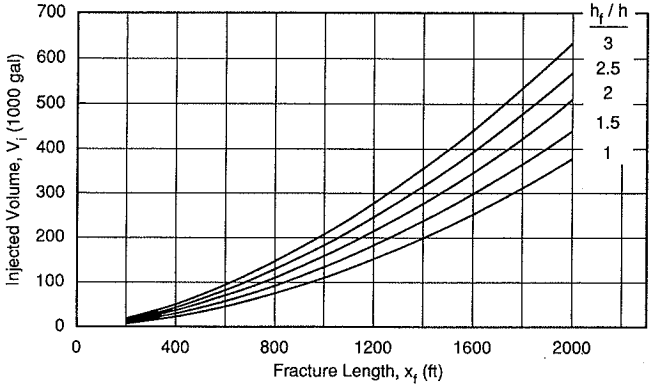

Figure 17-11
Total slurry volume requirements for several fracture height migrations.

Certainly, larger fracture height migration would lead to larger total fluid and proppant requirements. In Fig. 17-11 the total injected volume for various h_f/h ratios is plotted against x_f. At $x_f = 1600$ ft the volume requirements for $h_f/h = 1.5$ are 3×10^5 gal, whereas for $h_f/h = 3$ the volume requirements are 4.4×10^5 gal. At \$1/gal (considering only fluid), this would mean an additional cost of \$140,000.

Similarly, the mass of proppant would be substantially larger. This is shown in Fig. 17-12. Again, for $x_f = 1600$ ft the mass of proppant for $h_f/h = 1.5$ would be 8.4×10^5 lb, whereas for $h_f/h = 3$ it would be 1.85×10^6 lb, a difference of over 1 million pounds and at \$0.4/lb this would mean an additional cost of \$400,000.

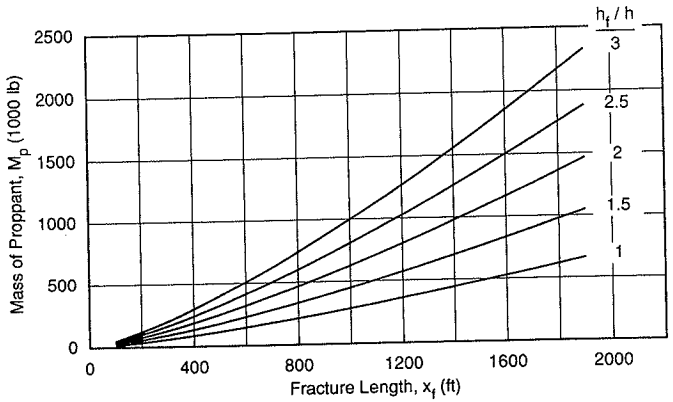

Figure 17-12
Mass of proppant requirements for several fracture height migrations.

The calculation of the mass of proppant requirements was presented in Section 16-9.

The leakoff coefficient is the second variable where the designer has partial control. In Section 16-7 the importance of reducing the leakoff coefficient was made evident by the presentation of the material balance during execution. In Section 17-2, methods of leakoff control were mentioned. Figure 17-13 shows the significant impact of the leakoff coefficient on the efficiency for a range of fracture lengths (and $h_f/h = 2$). At $x_f = 1600$ ft and $C_L = 3 \times 10^{-3}$ ft/$\sqrt{\text{min}}$, the efficiency η would be 0.34. However, for a leakoff coefficient five times larger ($C_L = 1.5 \times 10^{-2}$ ft/$\sqrt{\text{min}}$), the efficiency would be only 0.026. On the other hand, for a leakoff coefficient five times smaller ($C_L = 6 \times 10^{-4}$ ft/$\sqrt{\text{min}}$), the efficiency would be more than 0.8. Remembering that the efficiency controls the fraction of the fluid that is pad [Eq. (16-77)], control of leakoff has a major bearing on both costs and the proppant pack that can be generated.

Finally, the end-of-job proppant concentration, depending on the selection of the appropriate fracturing fluid and its proppant-transporting abilities, is the third variable under partial control of the designer. For the given leakoff coefficient ($C_L = 3 \times 10^{-3}$ ft/$\sqrt{\text{min}}$) and fracture height migration ($h_f/h = 2$), the masses of proppant that can be placed in the fracture are shown in Fig. 17-14.

At $x_f = 1600$ ft and with end-of-job proppant concentration c_f equal to 6, 8, and 10 ppg, the masses of proppant would be 7×10^5, 9.3×10^5, and 1.17×10^6 lb, respectively. The corresponding widths and fracture conductivities would follow the same trends. In a moderate- to high-permeability formation, an increase in the conductivity by 67% (1.17/0.7) would mean a major increase in posttreatment well performance.

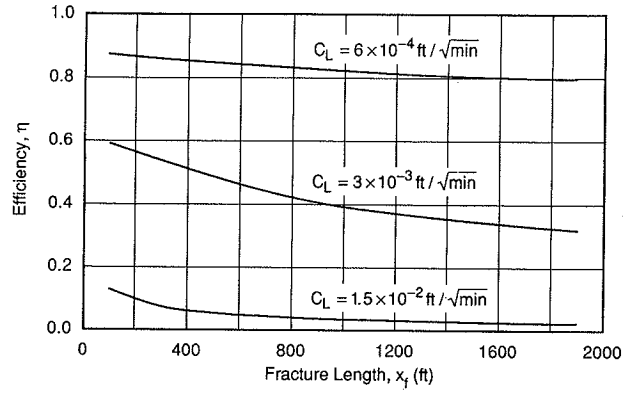

Figure 17-13
Effect of the leakoff coefficient on efficiency.

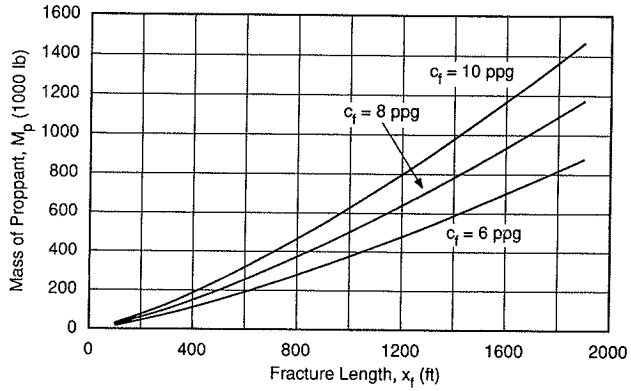

Figure 17-14
Total mass of proppant for a range of end-of-job proppant concentrations.

17-5 Net Present Value (NPV) for Hydraulic Fracture Design

The previous information in this chapter and in Chapter 16 dealt with the interactions among well, reservoir, fracturing fluid, and treatment variables in fracture propagation

and design. A number of design techniques combine the incremental, discounted revenue deriving from a fracturing treatment and the associated costs of execution. Veatch (1986) presented a comprehensive list of the various techniques, while Meng and Brown (1987) expounded upon the net present value (NPV) as an appropriate treatment optimization approach. Balen et al. (1988) presented a series of parametric studies and the components of the NPV calculation.

The NPV criterion is simple. The annual incremental revenue above the one that the unstimulated well would deliver is

$$\Delta R_n = \Delta N_{p,n}(\$/\text{bbl}) \tag{17-45}$$

where $\Delta N_{p,n}$ is the annual incremental cumulative production for year n for an oil well. (For a gas well it would be $\Delta G_{p,n}$.) The net present value of the revenue is then

$$\text{NPV}_R = \sum_{n=1}^{n} \frac{\Delta R_n}{(1+i)^n} \tag{17-46}$$

where i is the discount rate. Therefore

$$\text{NPV} = \text{NPV}_R - \text{cost} \tag{17-47}$$

Figure 17-15 is a schematic depiction of two cases, A and B, plotting the respective discounted revenues, costs, and NPV curves. The fracture half-length is graphed on the abscissa. For all cases the revenue curve will have a large slope for small values of x_f and will flatten out for larger x_f values. The posttreatment performance will be dealt with in Chapter 18, and the shape of this curve will be justified explicitly. The cost curve will be concave upward, reflecting the larger fracture volume with longer fractures and, especially, the much larger leakoff. Subtracting the cost curve from the revenue curves results in the NPV curve, which has a maximum. For case A this maximum is positive and corresponds to the optimum fracture size. For case B the NPV is negative, and the conclusion is that this well is not a candidate for hydraulic fracturing.

Figure 17-16 shows the steps and components for the optimization of fracture design as presented by Meng and Brown (1987) and Balen et al. (1988).

A fracture half-length, x_f, is selected. This is done incrementally, with each new fracture half-length longer than the previous, e.g., by 100 ft.

At first let us follow the lower branch on Fig. 17-16. For a reservoir, its lithology, its temperature, and the reservoir fluids would dictate the choice of the fracturing fluid, while the state of stress and the desired fractured well performance would point toward the proppant selection. A fracture propagation model such as the PKN, KGD, or p-3-D would then describe the fracture geometry, essentially the width (see Sections 16-5.1 through 16-5.3).

A treatment optimization is then done with imposed limits. These include critical fracture height, implied net pressure, maximum allowable injection rate, and leakoff coefficient. This calculation was outlined in Section 16-7 for the fluid volume requirements

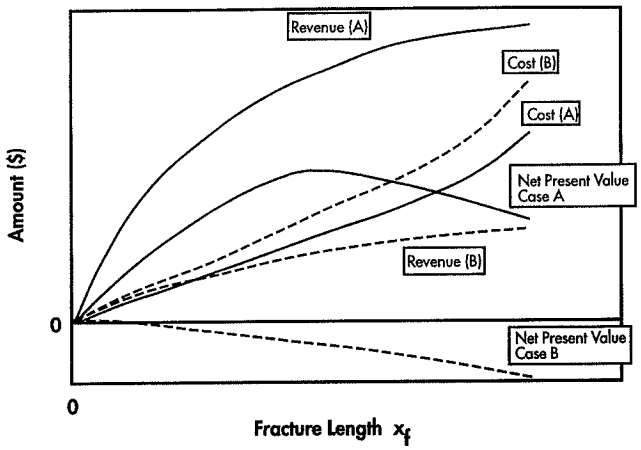

Figure 17-15
The net present value (NPV) concept. Fracture half-length versus revenue, cost, and NPV. Case A shows positive NPV with a maximum value corresponding to optimum fracture size. Case B has negative NPV.

and in Sections 16-8 and 16-9 for the proppant schedule (and its onset), propped width, and mass of proppant. Therefore, the end of the lower branch of Fig. 17-16 is the calculation of the fluid volume and mass of proppant and hence their costs. The net pressure, injection rate, and time of injection would lead to the service cost.

The calculated propped width and permeability of the created fracture, which are functions of the selected fracturing fluid and proppant (see Sections 17-2 and 17-3), the fracture half-length, and reservoir permeability, are sufficient to calculate the dimensionless fracture conductivity, F_{CD}, from Eq. (16-17). The conductivity and the fracture half-length are generally sufficient for a forecast of the posttreatment transient well performance.

The upper branch of Fig. 17-16 then describes the calculation for the incremental revenue. Coupling of the forecast of the fractured well performance with the tubing intake curve would readily allow the forecast of production decline and the associated cumulative production. Subtracting from the annual cumulative production what the unstimulated well would deliver (often zero) leads to the incremental cumulative production.

Then, as shown in Eqs. (17-45) and (17-46), the incremental net present value of the revenue can be calculated. Finally, the NPV can be obtained with Eq. (17-47). The calculation is repeated for additional x_f increments. Finally, it should be obvious that the NPV depends on the number of years for which the calculation is to be performed. Thus, there are 1-yr, 2-yr, 3-yr, etc., NPV optimizations. In general, the contribution to NPV from beyond the third year is negligible.

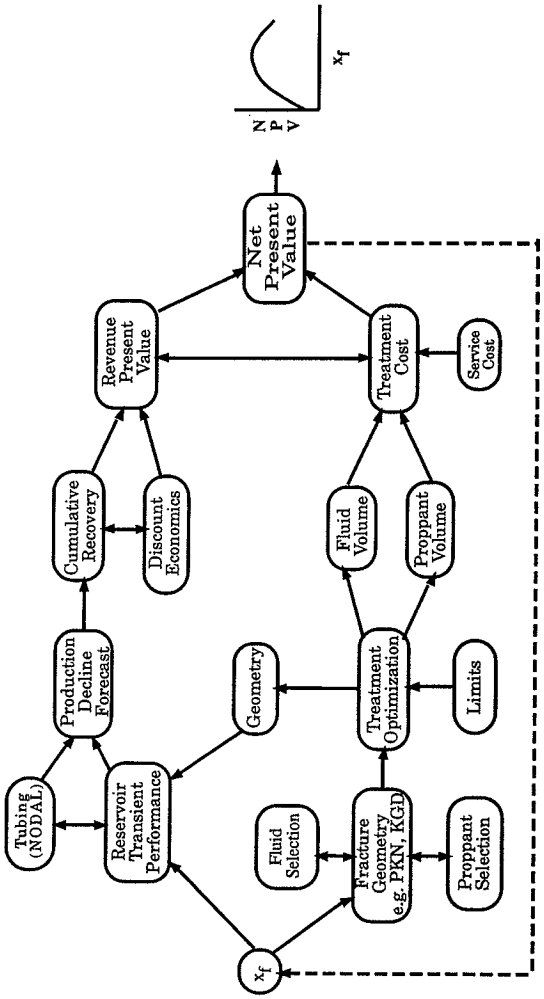

Figure 17-16
Components of the NPV fracture design optimization scheme.

17-6 PARAMETRIC STUDIES

One of the most useful products of a coherent design approach, such as the NPV, is the ability to perform parametric studies. As seen in the previous two sections, the design of a hydraulic fracture treatment as a well stimulation depends on a large number of variables.

Frequently, some of these are unknown. The main reason is economics. Tests to measure the permeability, logs to infer the fracture height, or fracture calibration treatments to estimate the leakoff coefficient are costly, often approaching the cost of the treatment itself in certain locations.

However, it should always be remembered that the cost of the treatment and the associated costs of testing are only one component of the NPV design approach. Benefits from an appropriate increase in the treatment size may dwarf the incremental costs. Similarly, in certain cases, knowledge of a particular variable may prevent a wasteful overtreatment.

In the parametric studies shown below, four of the most important variables affecting the fracture design are allowed to fluctuate within plausible ranges that have been observed in real cases. Interestingly, reservoir and formation properties such as the permeability and fracture height migration have a much larger impact on fracture design (both in the expected NPV and the optimum fracture half-length) than any of the treatment execution variables. One additional, extremely important, variable is the residual damage to the proppant pack. This will be observed in the case of inappropriate selection of fracturing fluids. In the parametric studies shown below, all other variables are taken from Table 17-4.

Figure 17-17 shows the effect of the reservoir permeability on NPV. In this study all optimum fracture half-lengths are 500 ft, corresponding to NPV values of $\$3.8 \times 10^5$, $\$1.1 \times 10^6$, and $\$1.8 \times 10^6$ for the 0.1-, 0.5-, 1-md permeabilities, respectively.

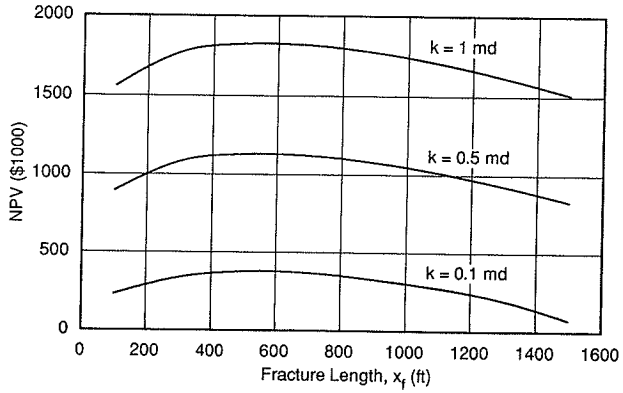

Figure 17-17
Effect of permeability on NPV.

Often, the posttreatment production rate (roughly proportional to the NPV) is used as a gauge for the success or failure of a treatment. This is true only if the reservoir permeability is the same. As can be seen in Fig. 17-17, no treatment in the 0.1-md reservoir can compete with a treatment in the 1-md reservoir. Conversely, a very small treatment (it is not even shown in the expanded scale of Fig. 17-17) in the 1-md reservoir could produce as much as the optimum treatment in the 0.1-md reservoir. Thus, posttreatment performance comparisons in the ignorance of the reservoir permeability are meaningless.

The effects of fracture height migration are shown in Fig. 17-18 for h_f/h ratios equal to 1.5, 2, 2.5, and 3, corresponding to fracture heights of 113, 150, 188, and 225 ft, respectively. Both the maximum NPV values and the associated optimum fracture lengths are reduced. For the four fracture heights, the corresponding optimum half-lengths are 700, 600, 500, and 400 ft, respectively. In general, any adversity in the fracture treatment will result in a decrease in the optimum half-length.

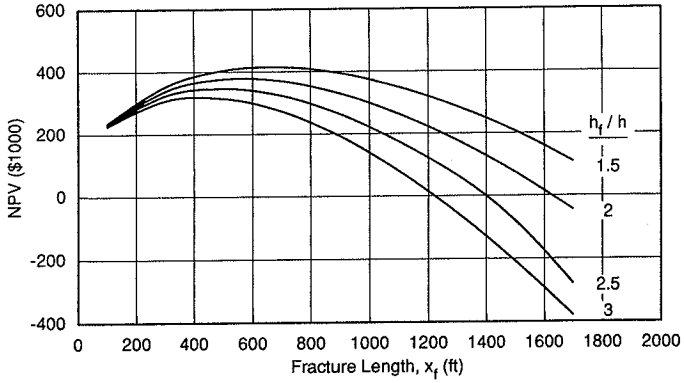

Figure 17-18
Effect of fracture height migration on NPV.

The same trends are evident in Fig. 17-19, where the effects of the leakoff coefficient are studied. Three values are used: a very large 1.5×10^{-2} ft/$\sqrt{\text{min}}$, a normal 3×10^{-3} ft /$\sqrt{\text{min}}$, and a small 6×10^{-4} ft/$\sqrt{\text{min}}$. Corresponding optimum fracture half-lengths are 400, 600, and 700 ft, respectively.

Finally, Fig. 17-20 shows the major impact of the polymer residual damage on the NPV and the optimum fracture length. If the damage is only 15% (i.e., a 15% reduction from the ideal proppant pack permeability at that stress), the maximum NPV would be $\$5.7 \times 10^5$, corresponding to an optimum fracture length of 900 ft. If the damage is 55%, the maximum NPV is $\$4.6 \times 10^5$ and the optimum length is 700 ft. For a severe 95% damage, the maximum NPV is only $\$ 2.3 \times 10^5$, corresponding to a 300-ft fracture half-length.

If this damage factor is not known, a 900-ft fracture treatment (the optimum for a 15% damage) would result in an NPV equal to zero for a 95% damage. The costs of such a stimulation treatment could not be offset by the performance of the damaged hydraulic fracture.

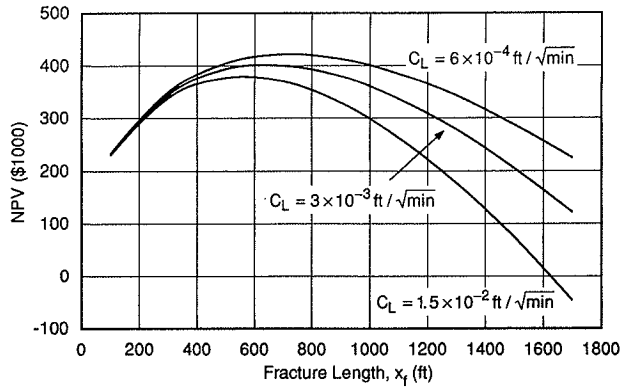

Figure 17-19
Effect of leakoff coefficient on NPV.

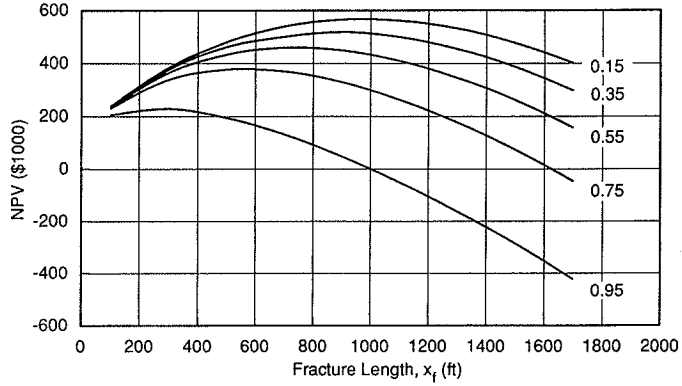

Figure 17-20
Effect of polymer residue damage on NPV.

The conclusion from these parametric studies is that lack of knowledge of a certain important variable carries a cost both in the expected performance and, very importantly, in the optimum sizing of a fracture stimulation treatment. The ability to perform parametric studies is perhaps the most important product of a coherent design approach such as the NPV, which allows the combination of treatment, well, and reservoir variables.

17-7 Fracture Design with Uncertainty: The Monte Carlo Technique

In the previous section the effects of variable fluctuations on the calculated NPV and the associated fracture length have been demonstrated through the use of parametric studies. Frequently, there are uncertainties in a large number of the variables that affect the fracture design. These uncertainties have several reasons. Many of the variables needed for the optimization of a fracture treatment must be measured and can have large variations within the same field (e.g., in-situ stresses, porosities, permeabilities). Others have different values at every well in the same field (e.g., reservoir thickness, reservoir pressure, rock properties); and, finally, certain variables may change during job execution in an unpredictable manner (e.g., fracturing fluid properties, proppant slurry concentrations). Others cannot be known at the moment of the job execution (e.g., oil price).

The Monte Carlo technique has been applied by Haid and Economides (1991) to fracture design to account for normal field and treatment uncertainties. Variables are given in ranges with probability distribution (probability to occur). Every variable is assigned a value completely randomly, within the range input, weighted by the given distribution.

Figure 17-21 shows the methodology of the Monte Carlo input and the assignment of a value to a variable within each design run. The probability and the magnitude of the variable are shown on the right. A random number generator picks a number between zero and one, and this number assigns a value to the variable from the cumulative probability graph shown on the right.

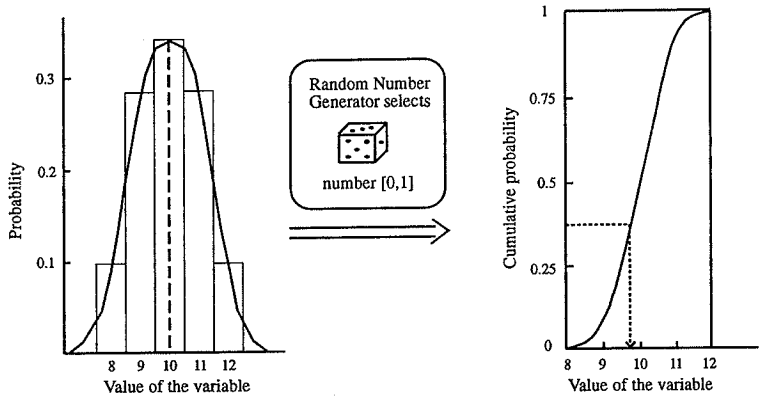

Figure 17-21

The Monte Carlo concept. Variables are given in terms of distribution and probability to occur. Values are selected randomly.

All calculations are done several times, and each time the variable is given another value by randomized assignment (from the range already defined). This leads to a result that generally looks the same as the input, a range of values, and a frequency curve.

Figure 17-22 is a modification of the NPV design procedure (shown in Fig. 17-16) to account for the Monte Carlo input and the uncertainty in reservoir variables. While for each run the calculations are similar to the standard NPV procedure, the result is a three-dimensional plot of NPV versus fracture half-length, with the probability to occur as the third variable. Thus for each fracture length there is a corresponding distribution of NPVs and an associated standard deviation.

This method of data input and design procedure is a significant improvement over all other existing methods, not only because natural facts and uncertainties are represented in a much more logical manner, but also because a more realistic impression of the results from a fracture treatment can be obtained, especially when the input parameters are not exactly known.

EXAMPLE 17-5

Case study for fracture design with Monte Carlo data input

The data in Table 17-4 are used for this design case study along with four variables that are offered as Monte Carlo inputs, shown in Fig. 17-23. These are the reservoir permeability, fracture height, leakoff coefficient and proppant pack damage. The permeability varies between 0.1 and 1 md, the fracture height between 75 and 225 ft, the leakoff coefficient between 3×10^{-4} and 3×10^{-3} ft/$\sqrt{\text{min}}$, and the damage factor between 0.35 and 0.75.

The results of the design appear in a three-dimensional plot on Fig. 17-24. Looking at just the fracture length versus NPV, the normal and characteristic shape is evident. However, for each fracture length there is a distribution of probabilities to occur for each NPV value. As should be expected, for smaller lengths the corresponding NPV values are smaller compared to the larger fracture lengths. However, the deviation between maximum and minimum NPV values is much smaller for smaller lengths. This is shown in Fig. 17-25. Therefore, smaller fractures are less risky but are likely to deliver smaller NPV values. Larger lengths result in riskier designs. Depictions such as the ones in Figs. 17-24 and 17-25 can be very useful in reservoir management. ◇

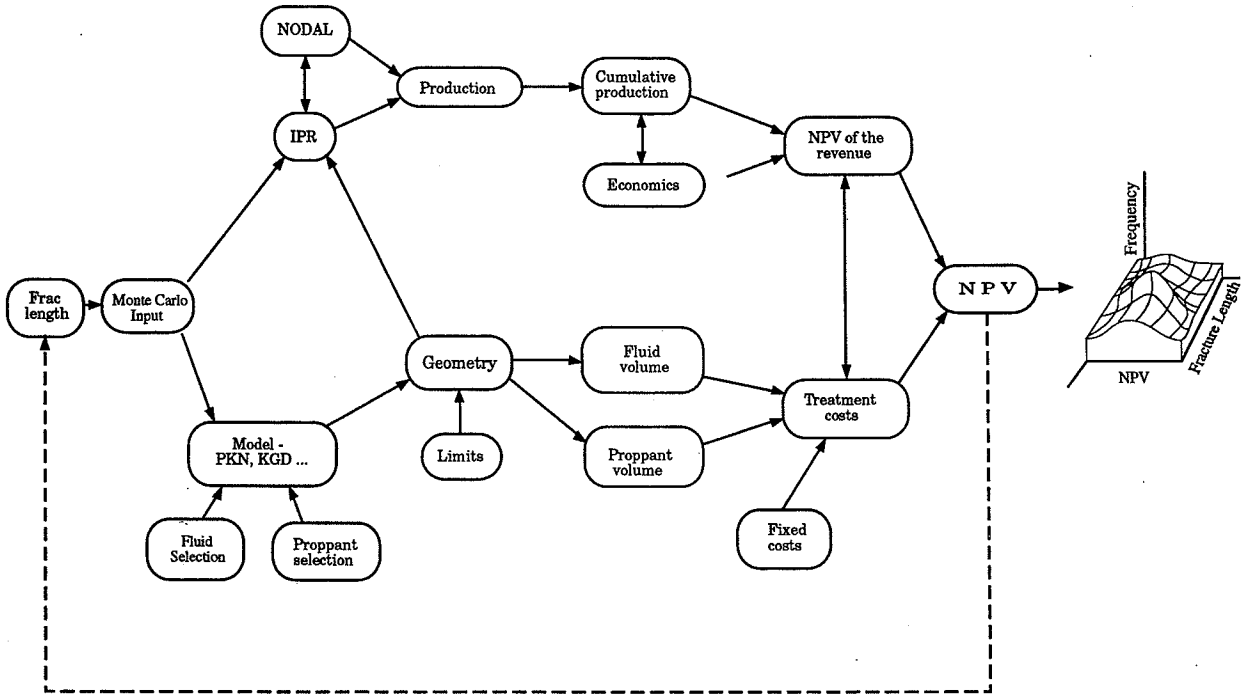

Figure 17-22
The components of the Monte Carlo fracture design optimization.

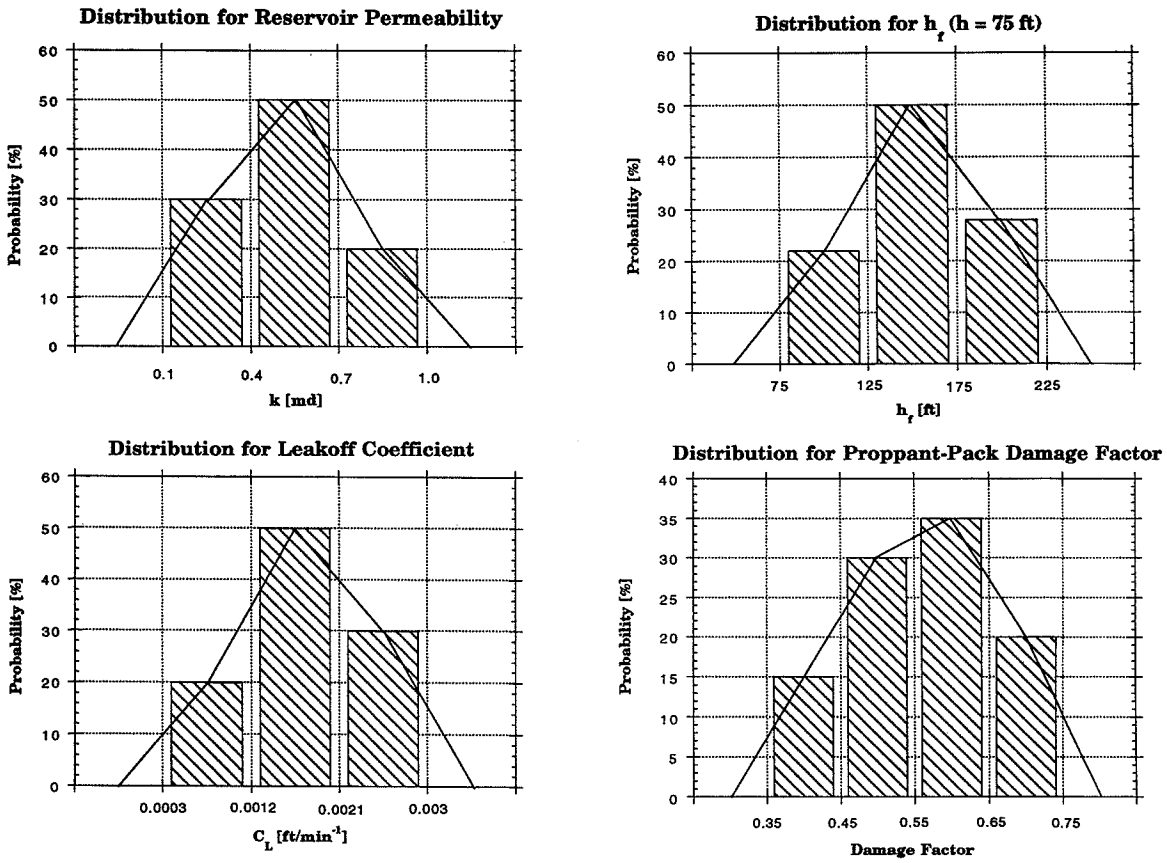

Figure 17-23
Four variables as Monte Carlo inputs for Example 17-5.

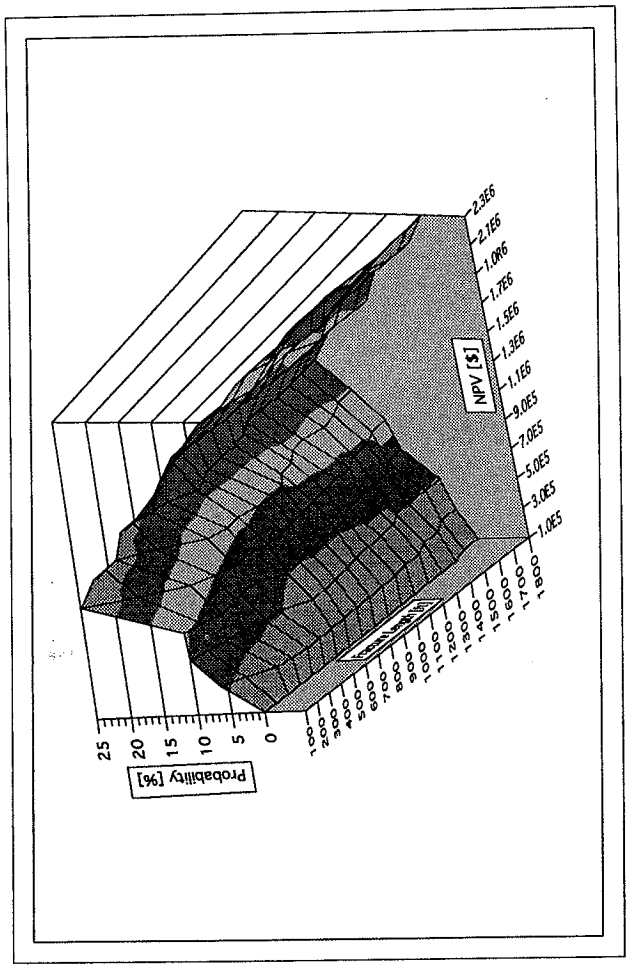

Figure 17-24
Three-dimensional NPV for Example 17-5.

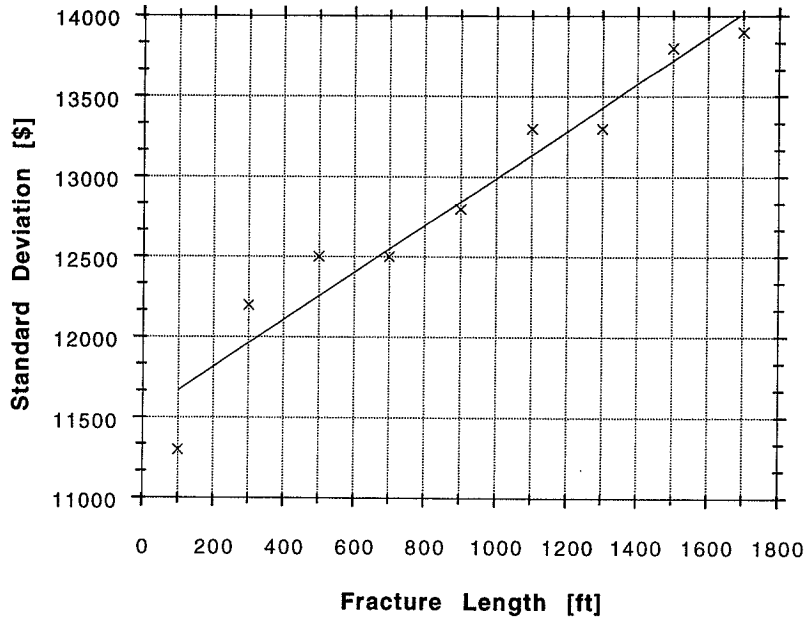

Figure 17-25
Standard deviation of NPV values for a range of fracture lengths for Example 17-5.

REFERENCES

1. Balen, M. R., Meng, H.-Z., and Economides, M. J., "Application of the NPV (Net Present Value) in the Optimization of Hydraulic Fractures," SPE Paper 18541, 1988.
2. Brannon, H. D., and Pulsinelli, R. J., "Breaker Concentrations Required to Improve the Permeability of Proppant Packs Damaged by Concentrated Linear and Borate-Crosslinked Fracturing Fluids," SPE Paper 20135, 1990.
3. Economides, M. J., *A Practical Companion to Reservoir Stimulation*, SES, Houston, 1991, and Elsevier, Amsterdam, 1991.
4. Gulbis, J. "Fracturing Fluid Chemistry", in *Reservoir Stimulation*, 2nd ed., M. J. Economides and K. G. Nolte, eds., Prentice Hall, Englewood Cliffs, NJ, 1989.
5. Haid, G., and Economides, M. J., "Optimierung Hydraulischer Frakbehandlungen bei der Erdölgewinnung mit Hilfe der Monte-Carlo-Technik und unter Anwendung des Barwertes," *BHM*, **12/91**: 467–474, 1991.
6. Mayerhofer, M. J., Economides, M. J., and Nolte, K. G., "An Experimental and Fundamental Interpretation of Filtercake Fracturing Fluid Loss," SPE Paper 22873, 1991.
7. Meng, H.-Z., and Brown, K. E., "Coupling of Production Forecasting, Fracture Geometry Requirements and Treatment Scheduling in the Optimum Fracture Design," SPE Paper 16435, 1987.
8. Penny, G. S., "An Investigation of the Effects of Fracturing Fluids upon the Conductivity of Proppants," Final Report STIM-LAB, Duncan, OK, 1986.

9. Penny, G. S., "An Investigation of the Effects of Fracturing Fluids upon the Conductivity of Proppants," Final Report STIM-LAB, Duncan, OK, 1988.
10. Thomas, R. L., and Brown, J. E., "Impact of Fracturing Fluids on Conductivity and Performance in Low-Temperature Wells," SPE Paper 18862, 1989.
11. Valkó, P., Economides, M. J., Baumgartner, S. A., and McElfresh, P. M., "The Rheological Properties of Carbon Dioxide and Nitrogen Foams," SPE Paper 23778, 1992.
12. Veatch, R. W., Jr., "Economics of Fracturing: Some Methods, Examples and Case Studies," SPE Paper 15509, 1986.

CHAPTER 18

Evaluating the Performance of Fractured and Long-Flowing Wells

18-1 INTRODUCTION

Production data, consisting of surface rates and pressures, are frequently the only information collected on a well. Calculations with these data are essential not only for the forecast of future performance but also for the evaluation of well design and past stimulation treatments.

In this chapter, first the performance of fractured vertical wells is treated. Because of the current wide use of hydraulic fracturing and its certain increase in the future, the performance of hydraulically fractured wells merits the special emphasis given here. Then, damage to the proppant pack, choked fractures, and fractures with face damage are examined. The possibility of substituting a fractured vertical well with an unfractured horizontal well and the potential benefits of fracturing horizontal wells are also discussed.

Many of these wells are economically marginal, and the cost of sophisticated well testing techniques described in Chapter 11 often cannot be justified. At the fracture pretreatment stage, testing is hindered not only by economics but also by the natural flow-retarding effects of the low permeability. A well test in a low-permeability reservoir is likely to require a long data acquisition time for satisfactory interpretation. Also, frequently these wells may not flow at all without hydraulic fracturing.

Similarly, the low permeability delays posttreatment evaluation. Coupled with economic constraints, this situation suggests the utilization of long-term surface production and pressure history for the evaluation of well performance and the calculation of fracture geometry and conductivity variables. The techniques described in this chapter, while they are particularly applicable to hydraulically fractured wells, can be used for any other long-flowing well where surface production and rate information are available. This methodology is a substitute in those cases where either a pretreatment well test is not available or posttreatment downhole testing is impractical.

Finally, decline curve analysis is presented in a section of this chapter. This traditional tool, available to production engineers, has been deemphasized in the recent past because of readily available reservoir simulation technologies and much more accessible formation evaluation data.

18-2 Pretreatment Testing of Hydraulic Fracture Candidate Wells

The well testing techniques described in Chapter 11 can be applied to wells that are candidates for hydraulic fracturing. However, low reservoir permeability prolongs wellbore storage, which masks the appearance of the recognizable and interpretable patterns from which reservoir permeability and other reservoir features may be determined. For example, from Table 11-8a, the expression for the end of wellbore storage (in oilfield units) is

$$t(\text{hr}) = 3387(60 + 3.5s)\frac{\mu C}{kh} \tag{18-1}$$

Using typical values for an oil well, μ=1 cp, C=10^{-3} bbl/psi, h=50 ft, and s=0 (best case), the time for the end of wellbore storage if k=100 md is 0.04 hr. However, for k=0.1 md this time becomes 40 hr. For a gas well with μ=0.025 cp but with C=10^{-1}bbl/psi, the corresponding time for k=0.1 md is 100 hr.

For the oil well case, an interpretable test typically requires a duration of 5 to 7 days. Consequently, low-permeability wells are not tested in a large number of reservoirs where hydraulic fracturing is indicated.

This shortcoming affects both the design procedure, outlined in Chapter 17, and also any posttreatment well test interpretation, using the techniques described in Chapter 11. The use of specialized plots or type curve matching for the determination of x_f or $k_f w$ requires knowledge of the reservoir permeability. These inherent difficulties are addressed in the posttreatment interpretation methodology outlined in Section 18-8.

18-3 Transient Response of a Hydraulically Fractured Well

The distinguishing responses of a high- (approaching infinite) conductivity fracture and that of a lower- or finite-conductivity fracture were introduced in Chapter 11. In Section 16-4 the dimensionless fracture conductivity, F_{CD}, and the fracture length were related with the effective wellbore radius. In the same section the inverse relationship between reservoir permeability and fracture conductivity was identified, and the impact of this relationship on the desirable treatment design was emphasized.

The pressure or rate transient response of a hydraulically fractured well depends on the well (the size of wellbore storage), the dimensionless fracture conductivity, the fracture length, the reservoir permeability and, at late time, boundary effects. Of interest is the difference in the response between high- and low-conductivity fractures.

As the solution by Gringarten and Ramey (1974) suggests, if an infinite-conductivity fracture controls the well response (F_{CD} > 300 and for practical purposes F_{CD} > 100), linear flow from the reservoir is developed, and a log-log plot of pressure and pressure derivative versus time yields a straight line with a slope equal to 1/2.

A plot of pressure versus the square root of time on Cartesian coordinates forms a straight line, from the slope of which the fracture half-length can be estimated if the reservoir permeability is known. This is shown in Chapter 11.

For finite-conductivity fractures (F_{CD} < 10), the solution by Cinco-Ley and Samaniego (1981a) suggests that while such fractures control the well response, bilinear flow (linear flow from the reservoir into the fracture and linear flow along the fracture into the well) will be dominant. During this time, a log-log plot of pressure versus time will form a straight line with a slope equal to 1/4. The slope of a Cartesian plot of pressure versus the quarter root of time yields the $k_f w$ product. This is also indicated in Chapter 11.

Figures 18-1 and 18-2 give comprehensive solutions for the pressure transient response under constant rate for a low- (F_{CD}=1) and a much higher-conductivity fracture (F_{CD}=100), respectively. These plots, presented by Economides (1987), are given in terms of the dimensionless pressure p_D and the fracture dimensionless time, t_{Dxf}, divided by the fracture dimensionless wellbore storage coefficient, C_{Df}, for a range of values of the latter. For the case of F_{CD}=1 (Fig. 18-1), after the 45° straight line characteristic of wellbore storage, and after a transition period, there is a long log-log straight line with slope equal to 1/4. Following an additional transition period, the well enters pseudo-radial, infinite-acting reservoir flow. For the much larger-conductivity fracture of Fig. 18-2, a long linear flow is evident (with a log-log slope equal to 1/2). Again, early-time 45° straight line and late-time pseudo-radial flow are also present.

The definition of the dimensionless variables for oil in oilfield units is

$$p_D = \frac{kh(p_i - p_{wf})}{141.2qB\mu} \tag{18-2}$$

$$t_{Dxf} = \frac{0.000264kt}{\phi\mu c_t x_f^2} \tag{18-3}$$

and

$$C_{Df} = \frac{5.615C}{2\pi\phi c_t h x_f^2} \tag{18-4}$$

The dimensionless fracture conductivity is given by Eq. (16-17).

EXAMPLE 18-1

Calculation of the beginning and end of bilinear, linear and pseudo-radial flow for a low- and a high-conductivity fractured well

Two oil wells, one with k=10 md and the other with k=0.1 md, are hydraulically fractured. The dimensionless fracture conductivity of the first well is 1 and of the second is 100. Assume that in both cases $k_f w$ (=10,000 md-ft) and x_f (=1000 ft) are the same.

If the following variables are common to both wells, estimate the beginning and end of bilinear and the beginning of pseudo-radial flow in the first well and the beginning and end of

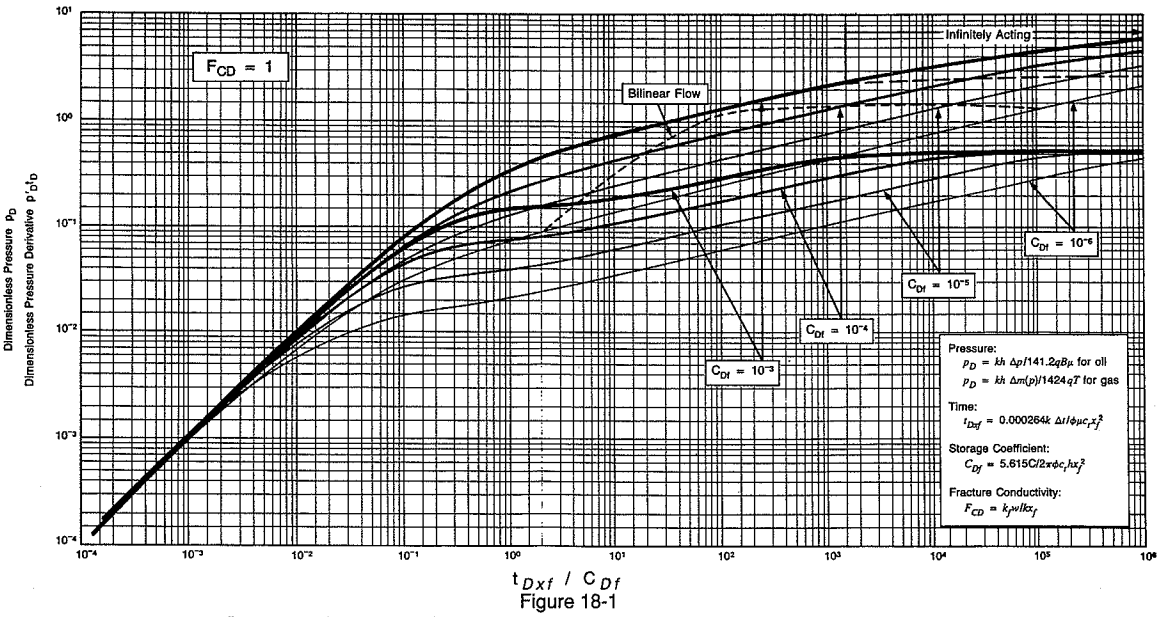

Figure 18-1

Pressure transient response of low-conductivity hydraulic fracture (F_{CD}=1) with wellbore storage.

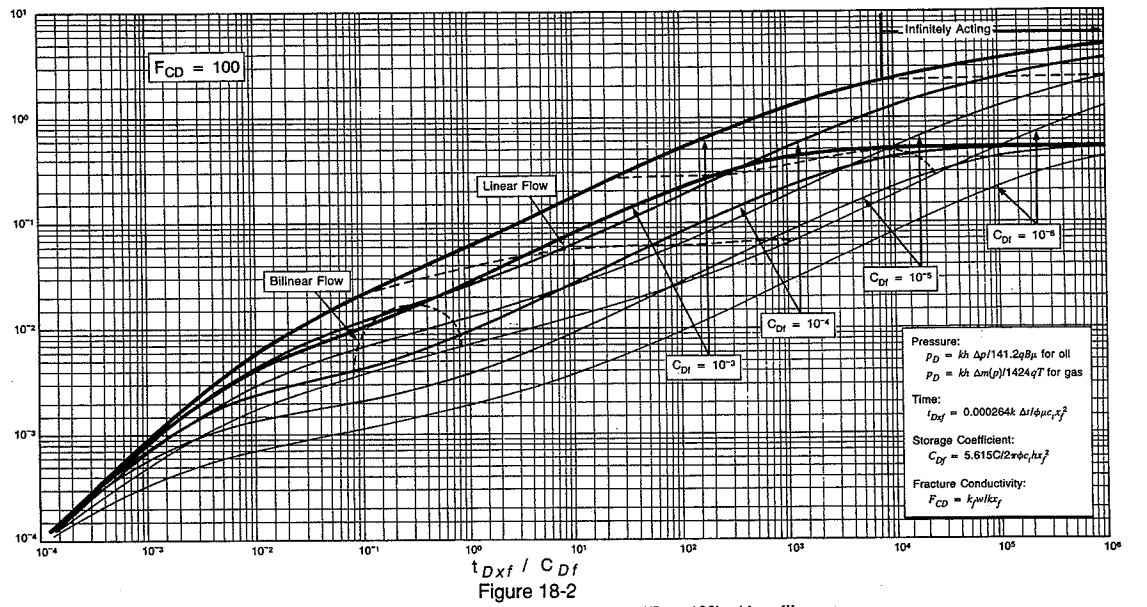

Figure 18-2

Pressure transient response of high-conductivity hydraulic fracture (F_{CD}=100) with wellbore storage.

linear and the beginning of pseudo-radial flow in the second: $C = 1 \times 10^{-3}$ bbl/psi, ϕ=0.1, h=60 ft, μ=1 cp, c_t=10^{-5} psi^{-1}.

Solution

k = 10 md The dimensionless fracture conductivity, F_{CD}=1 [=10,000/(10)(1000)]. From Eq. (18-4), the dimensionless wellbore storage coefficient is

$$C_{Df} = \frac{(5.615)(1 \times 10^{-3})}{(2)(3.14)(0.1)(10^{-5})(60)(1000^2)} = 1.5 \times 10^{-5} \tag{18-5}$$

The required real time for any milestone in the well performance can be obtained from a rearrangement of Eq. (18-3),

$$t = \frac{(t_{Dxf}/C_{Df})\phi\mu c_t x_f^2 C_{Df}}{0.000264k} \tag{18-6}$$

Since from Fig. 18-1 at $C_{Df} \simeq 1.5 \times 10^{-5}$ the beginning of bilinear flow is marked and is equal to t_{Dxf}/C_{Df}=6, then

$$t = \frac{(6)(0.1)(1)(10^{-5})(1000^2)(1.5 \times 10^{-5})}{(0.000264)(10)} = 0.034 \text{ hr} \tag{18-7}$$

Also marked is the end of bilinear flow, which is at t_{Dxf}/C_{Df}=10^4, leading to a real time of over 55 hr.

From the same figure, the beginning of the infinite-acting pseudo-radial flow is at $t_{Dxf}/C_{Df} = 1.5 \times 10^5$ and from Eq. (18-6) the real time would be almost 40 days.

The conclusion from this calculation is that while the $k_f w$ product could be estimated through a test within a reasonable time (e.g., a 24-hr buildup and if the reservoir permeability is known), the fracture half-length could not (no infinite-conductivity behavior is evident). In Section 18-8 it will be shown that, if it is present, the pseudo-radial behavior can be analyzed and therefore the fracture half-length can be estimated.

k = 0.1 md The F_{CD} for this case is equal to 100. From Fig. 18-2 and $C_{Df} = 1.5 \times 10^{-5}$, the beginning of linear flow is at t_{Dxf}/C_{Df}=70 and therefore, from Eq. (18-6) (and with k=0.1 md), the real time would be 40 hr. The end of the linear flow is at $t_{Dxf}/C_{Df} = 7 \times 10^3$, or at t=4000 hr (almost 6 months). Infinite-acting reservoir behavior would emerge after $t_{Dxf}/C_{Df} = 7 \times 10^5$ (t > 45 years) if no boundaries appear earlier.

In this example, the fracture half-length could be calculated after a few days' test duration. ◇

EXAMPLE 18-2

Flow rate versus pressure for a fractured well

Consider the k=10 md and F_{CD}=1 well of Example 18-1. All other variables are the same, and, in addition, B=1.1 res bbl/STB. If Δp (= $p_i - p_{wf}$) is held constant at 1000 psi, what would the flow rate be after 24 hr and after 15 days?

Solution From Eq. (18-3) and with t=24 hr,

$$\frac{t_{Dxf}}{C_{Df}} = \frac{(0.000264)(10)(24)}{(0.1)(1)(10^{-5})(1000^2)(1.5 \times 10^{-5})} = 4.2 \times 10^3 \tag{18-8}$$

and from Fig. 18-1, p_D=1.2. Therefore, from Eq. (18-2) and rearrangement,

$$q = \frac{(10)(60)(1000)}{(1.2)(141.2)(1.1)(1)} = 3220 \text{ STB/d} \tag{18-9}$$

After 15 days, $t_{Dxf}/C_{Df} \approx 6.3 \times 10^4$, p_D (from Fig. 18-1) = 2.1, and therefore q = 1840 STB/d.

In general, it should be noted that the decline in fractured well performance is considerably steeper than for unfractured wells. ◇

EXAMPLE 18-3

Production from a fractured gas well

The gas well in Appendix C is an obvious candidate for hydraulic fracturing. Develop a transient IPR relationship for a fractured well at t=10 days and compare it with the unfractured case of Example 4-9 [Eq. (4-64)]. The fracture half-length is 1500 ft, and the $k_f w$ is 2550 md-ft. Further, assume that H=8000 ft, and tubing I.D.=2.44 in. For the purposes of this calculation, assume that p_{wf}=1000 psi and p_{tf}=830 psi (calculated).

Solution The dimensionless fracture conductivity is [from Eq. (16-17)]

$$F_{CD} = \frac{2550}{(0.17)(1500)} = 10 \tag{18-10}$$

Now the wellbore storage coefficient must be calculated. Since the average flowing pressure in the well is 915 psi, the gas compressibility is approximately equal to 1/915 $\simeq$ 1.1×10^{-3} psi^{-1}. The wellbore storage coefficient is then (see Table 11-3)

$$C = \frac{(3.14)(2.44)^2(8000)(1.1 \times 10^{-3})}{(4)(144)(5.615)} = 5 \times 10^{-2} \text{ bbl/psi} \tag{18-11}$$

and from Eq. (18-4),

$$C_{Df} = \frac{(5.615)(5 \times 10^{-2})}{(2)(3.14)(0.14)(1.08 \times 10^{-4})(78)(1500)} = 1.7 \times 10^{-6} \tag{18-12}$$

(Note: The c_t was obtained in Example 4-9.)

At t=10 days and from Eq. (18-3),

$$t_{Dxf} = \frac{(0.000264)(0.17)(10)(24)}{(0.14)(0.0244)(1.08 \times 10^{-4})(1500^2)} = 1.3 \times 10^{-2} \tag{18-13}$$

and therefore t_{Dxf}/C_{Df}= 7.6×10^3.

From Fig. 18-3 (drawn for F_{CD}=10), at t_{Dxf}/C_{Df}= 7.6×10^3 and $C_{Df} \simeq 1.7 \times 10^{-6}$, p_D=0.27.

Similarly to Eq. (18-2), the dimensionless pressure for a gas well, cast in terms of real-gas pseudo-pressures, should be

$$p_D = \frac{kh[m(p_i) - m(p_{wf})]}{1424qT} \tag{18-14}$$

Substitution of the known variables and rearrangement yields

$$q = 5.39 \times 10^{-5}[1.265 \times 10^9 - m(p_{wf})] \tag{18-15}$$

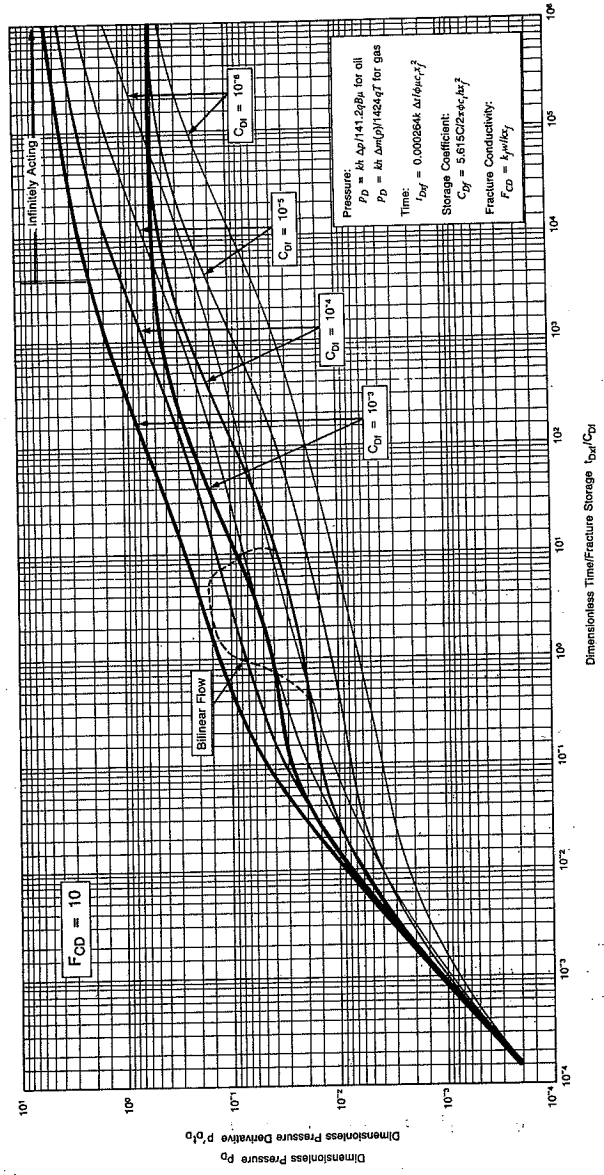

Figure 18-3
Transient response of a fracture with F_{CD}=10.

The coefficient of Eq. (18-15) is almost 25 times the one in Eq. (4-64).

Two comments are in order here:

1. The enhancement of the flow rate of the fractured over the unfractured well will decrease with time significantly, because the fractured well flow rate declines more steeply.
2. The larger flow rate implied by the fractured well could cause a marked increase in the influence of the non-Darcy coefficient. Thus the actual flow rate would be considerably less than the one obtained from Eq. (18-14).

Equation (18-14) with the non-Darcy contribution would become

$$m(p_i) - m(p_{wf}) = \frac{1424qTp_D}{kh} + \frac{1424TD}{kh}q^2 \tag{18-16}$$

Assuming that $D = 5 \times 10^{-5}$ (MSCF/d)$^{-1}$, then substitution of all known variables yields

$$m(p_i) - m(p_{wf}) = 1.86 \times 10^4 q + 3.44q^2 \tag{18-17}$$

Since p_i=4613 psi and p_{wf}=1000 psi, the $m(p)$ values from Table 4-5 are 1.265×10^9 and 8.396×10^7, respectively. While the flow rate from Eq. (18-15) is 64,000 MSCF/d (without considering turbulence effects), solution of Eq. (18-17) yields q=16,000 MSCF/d; the flow rate for the unfractured well [Eq. (4-64)] is 2570 MSCF/d. ◇

18-4 CHOKED FRACTURES

The fracture permeability is frequently far below the ideal proppant pack permeability, even after accounting for a stress-induced reduction. In Section 17-2.5 the polymer-induced damage was considered. Both of the above factors would result in a reduction in the dimensionless fracture conductivity. Well performance prediction can be handled appropriately with a transient solution using a lower F_{CD}.

Frequently, though, disproportionate damage occurs in the near-well zone of the hydraulic fracture. Flow in the fracture is likely to carry along reservoir fines and accumulate them. Higher drawdown, normal to the fracture path in the near-well portion, would result in a larger effective stress on the proppant and a larger stress-induced permeability reduction. Finally, overdisplacement of the proppant-laden slurry into the fracture during execution may reduce the fracture permeability (and perhaps the width) of the near-well zone.

A situation such as this results in a "choked" fracture, as named by Cinco-Ley and Samaniego (1981b). In their work they defined a choke skin effect, s_{ch}, given by

$$s_{ch} = \frac{\pi x_s k}{w_s k_{fs}} \tag{18-18}$$

where x_s, w_s, and k_{fs} are the damaged length, width, and permeability of the fracture, respectively. This skin effect can be added to the dimensionless pressure of Eq. (18-2):

$$p_D + s_{ch} = \frac{kh(p_i - p_{wf})}{141.2qB\mu} \tag{18-19}$$

Therefore, for a constant drawdown, the flow rate would be reduced accordingly.

EXAMPLE 18-4
Production rate reduction because of a choked fracture

Assume that in the k=10 md well of Examples 18-1 and 18-2, the permeability of the fracture in the nearest 100 ft has been reduced to one-fifth of the average fracture permeability. Calculate the well flow rate after 15 days. Assume that there is no reduction to the fracture width, that is, $w = w_s$.

Solution The choked fracture skin effect can be calculated from Eq. (18-18):

$$s_{ch} = \frac{(3.14)(100)(10)}{(10,000/5)} = 1.6 \tag{18-20}$$

The dimensionless pressure for this well after 15 days and without considering the damage was determined to be 2.1 (Example 18-2). Therefore, from Eq. (18-19),

$$q = \frac{(10)(60)(1000)}{(2.1 + 1.6)(141.2)(1.1)(1)} = 1040 \text{ STB/d} \tag{18-21}$$

which represents a 43% reduction from the rate calculated in Example 18-2.

(Note: This example is a further demonstration of the significance of fracture conductivity in the case of higher-permeability reservoirs.) ◇

18-5 Fracture Face Damage

A different and additional damage is the one that may develop on the fracture face because of filtrate or polymer invasion. Also described by Cinco-Ley and Samaniego (1981b), this damage can be quantified by a skin effect of the form

$$s_{fs} = \frac{\pi b_s}{2x_f}\left(\frac{k}{k_s} - 1\right) \tag{18-22}$$

where b_s is the penetration of damage into the reservoir normal to the fracture face and k_s is the damage zone permeability. The penetration of damage, b_s, is of the order of 0.2 ft or less.

This skin effect is *not* additive to the dimensionless pressure. Instead it affects the production rate indirectly through the reduction of the effective wellbore radius. Figure 18-4 (Cinco-Ley and Samaniego, 1981b) can be used for the determination of the effects of fracture face damage. Figure 18-4 is for a large-conductivity fracture.

In general, this damage is frequently inconsequential and insignificant compared to the previously described damage to the entire proppant pack (and F_{CD} reduction) or the choked fracture effects. The criteria for selection of a fracturing fluid should never be based solely on the formation/fracturing fluid compatibility (and thus avoiding fracture face damage), if that would be at the expense of fracture conductivity. Of course, if both can be avoided, it would be the ideal situation.

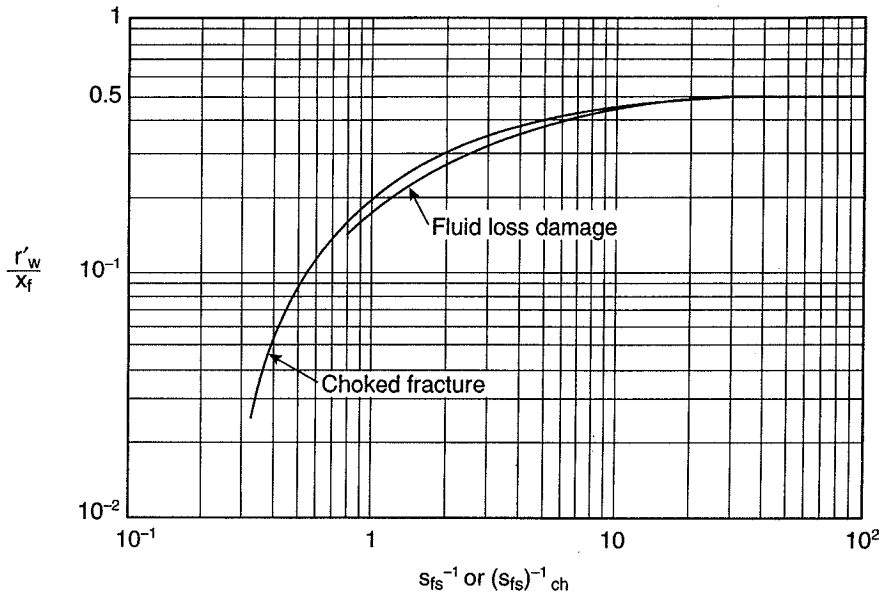

Figure 18-4
Dimensionless effective wellbore radius reduction for a damage fracture. (*From Cinco-Ley and Samaniego, 1981b.*)

EXAMPLE 18-5
Effect of fracture face damage

If b_s=0.2 ft and x_f=1000 ft, determine the effect of fracture face damage on well performance for k/k_s equal to 5 and 20 (80% and 95% permeability reductions).

Solution From Eq. (18-22) and k/k_s=5,

$$s_{fs} = \frac{(3.14)(0.2)}{(2)(1000)}(5 - 1) = 1.3 \times 10^{-3} \tag{18-23}$$

To use Fig. 18-4 the reciprocal of this skin effect is required. Thus $(s_{fs})^{-1} \simeq 800$, and from Fig. 18-4, r'_w/x_f=0.5, suggesting that there is no effect on the well performance. [Compare with Eq. (16-22), providing the effective wellbore radius of a large-conductivity fracture.]

Similarly, for k/k_s=20, $s_{fs} = 5.2 \times 10^{-3}$, $(s_{fs})^{-1} \simeq 200$, and again r'_w/x_f=0.5. ◇

EXAMPLE 18-6

Apparent fracture face damage

Inadvertently, a well may behave as if it has fracture face damage. This is the case when the pressure gradient, normal to the fracture face and into the reservoir, results in a phase change and an associated relative permeability reduction. For example, this would be the situation in a rich gas condensate reservoir with associated liquid knockout extending several feet into the reservoir.

Assume that b_s=50 ft, k/k_s=5, and x_f=1000. Calculate the impact on the effective wellbore radius. What fracture length would be required to offset the problem? Is it realistic?

Solution From Eq. (18-22),

$$s_{fs} = \frac{(3.14)(50)}{(2)(1000)}(5-1) = 0.31 \tag{18-24}$$

and $(s_{fs})^{-1} \simeq 3$. From Fig. 18-4, r'_w/x_f=0.35, which represents a considerable reduction. Assuming from Fig. 18-4 that at $(s_{fs})^{-1} > 20$ there is no impairment, then s_{fs}=0.05. If all other variables remain constant, then, from Eq. (18-22), an unrealistic fracture half-length equal to 6200 ft would be required. However, a 2000-ft fracture half-length would lead to s_{fs}=0.155, $(s_{fs})^{-1}$=6.4, and, from Fig. 18-4, an improved r'_w/x_f=0.42. ◇

18-6 FRACTURED VERTICAL VERSUS HORIZONTAL WELLS

Following the emergence of horizontal wells, it was natural to speculate whether they could substitute for a fractured vertical well. Mukherjee and Economides (1991) presented a relationship for equal productivity indices under pseudo-steady-state conditions between a fractured vertical well of half-length, x_f, and dimensionless effective wellbore radius r'_{wD} (see Fig. 16-5) with a horizontal well of length L draining an area with an equivalent radius r_{eV} in a reservoir of vertical-to-horizontal permeability anisotropy, I_{ani} (=$\sqrt{k_H/k_V}$). The relationship is

$$r'_{wD}x_f = \frac{r_{eV}L/2}{\left[a+\sqrt{a^2-(L/2)^2}\right]\left(\frac{I_{ani}h}{(I_{ani}+1)r_w}\right)^{I_{ani}h/L}} \tag{18-25}$$

In Eq. (18-25) the variable a is the large half-axis of the drainage ellipse formed by a horizontal well. It is given by Eq. (2-48) in Chapter 2. From the relationship of Eq. (18-25) it is possible to calculate the required horizontal well length that would deliver the same productivity index as would a fractured vertical well. The result would be optimistic for the horizontal well option, since no near-wellbore damage is considered. Ordinarily, longer lengths than the ones calculated from Eq. (18-25) would be required. Any possible combinations of r'_{wD} and x_f can be used. However, an appropriate choice would be the optimized x_f and F_{CD} (and therefore r'_{wD}) for a reservoir of a given permeability and other variables as shown in Chapter 17. Figure 18-5 (Brown and Economides, 1992) shows a series of example calculations for the required horizontal well lengths for equal productivity indexes as that of vertical wells with fracture half-lengths x_f. The plot is given for a range of

permeabilities. Marked are the optimum fracture half-lengths. As can be seen, the required horizontal well lengths are very large. A sample calculation to demonstrate this point and a discussion of the results are given in the next example.

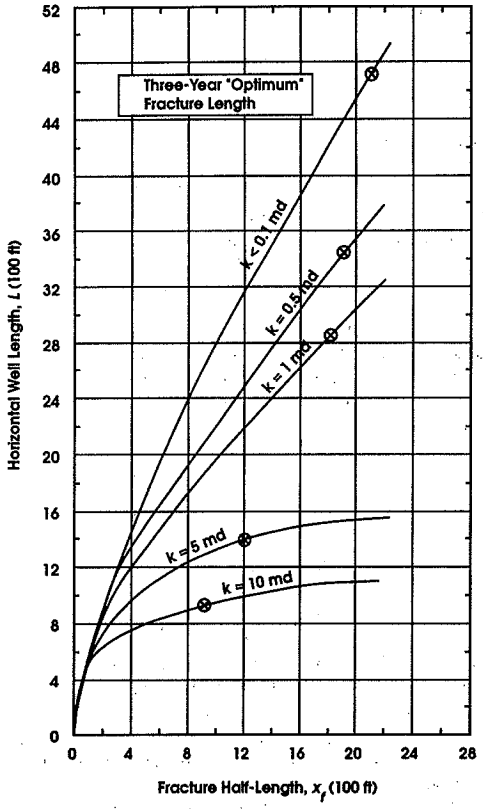

Figure 18-5

Fracture half-length in vertical well and required horizontal well length for equal productivity index ($I_{ani}h$=150 ft). (*From Brown and Economides, 1992.*)

If a is considered to be very near the value of r_{eH} [this is generally true, as any calculation using Eq. (2-48) can demonstrate], and since a^2 is usually considerably larger than $(L/2)^2$, and if $r_{eV} \approx r_{eH}$, then a simpler approximation of Eq. (18-25) is

$$r'_{wD}x_f = \frac{L/4}{[I_{ani}h/(I_{ani}+1)r_w]^{I_{ani}h/L}} \tag{18-26}$$

For most applications, the difference between the right-hand sides of Eqs. (18-25) and (18-26) would be less than 10%.

Finally, Eqs. (18-25) and (18-26) are for a reservoir with horizontal permeability isotropy. In highly horizontally anisotropic formations, the horizontal well direction is critical. Drilling such a well normal to the maximum permeability could result in a significant improvement to the productivity index. Brown and Economides (1992) have addressed these issues extensively and presented results for anisotropic formations.

EXAMPLE 18-7

Minimum required horizontal well length to deliver equal productivity index to that of a fractured well

In a reservoir of k=1 md, $I_{ani}h$=150 ft (e.g., I_{ani}=3 and h=50 ft), the optimum fracture half-length, using the NPV criterion, was found to be 1800 ft. The corresponding dimensionless fracture conductivity, F_{CD}, is 2.3. If r_w=0.328 ft and $r_{eH} = r_{eV}$=2980 ft, calculate the minimum required horizontal well length to deliver an equal productivity index.

Solution If F_{CD}=2.3, then the relative capacity parameter (to use in Fig. 16-5) is, from Eq. (16-18), equal to 0.7 [=3.14/(2)(2.3)]. From Fig. 16-5, the dimensionless effective wellbore radius, r'_{wD}, is equal to 0.3. Therefore, the left-hand sides of Eqs. (18-25) and (18-26) are both equal to 540 ft. Trial and error is required to solve for the horizontal well length L. If L=2000 ft, then, from Eq. (2-48),

$$a = \frac{2000}{2}\left[0.5 + \left[0.25 + \left(\frac{2980}{1000}\right)^4\right]^{0.5}\right]^{0.5} = 3065 \text{ ft} \qquad (18\text{-}27)$$

and thus the right-hand side of Eq. (18-25) yields

$$\frac{(2980)(2000)/2}{\left[3065 + \sqrt{3065^2 - 1000^2}\right](150/(4)(0.328))^{150/2000}} = 350 \text{ ft} \qquad (18\text{-}28)$$

If L=3000 ft, then a=3174 ft and the right-hand side of Eq. (18-25) is equal to 590 ft. Therefore, by interpolation, the required horizontal well length is 2800 ft.

Using the approximation of Eq. (18-26), with L=2000 ft, the right-hand side is identical to that calculated by Eq. (18-25) and equal to 350 ft. With L=3000 ft, the right-hand side is equal to 592 ft (compared with 590 ft). Thus the two expressions [Eq. (18-25) and Eq. (18-26)] give very nearly the same results.

The calculated large horizontal well length of 2800 ft is the required minimum, assuming total removal of damage. In general, a calculation such as the one in this example suggests that an unfractured horizontal well is not an economically attractive alternative to a fractured vertical well in most reservoirs that are candidates for hydraulic fracturing. Thus, in formations with large k_H/k_V and no horizontal permeability anisotropy, if a horizontal well is to be drilled, it must be fractured also (or not be drilled at all). However, as mentioned before this example, in formations with significant horizontal permeability anisotropy, a horizontal well drilled normal to the maximum permeability direction may be attractive, especially since a hydraulic fracture will propagate normal to the minimum permeability (aligned with minimum stress). See Brown and Economides (1992) for a comprehensive analysis. ◇

18-7 PERFORMANCE OF FRACTURED HORIZONTAL WELLS

As suggested in the previous section and example, an unfractured horizontal well is unlikely to be economically viable in most reservoirs where vertical wells are fractured. Therefore, for a horizontal well to be potentially attractive in a lower-permeability reservoir, it must be hydraulically fractured also.

The fracture direction has been discussed extensively in Chapter 16, where it was concluded that for most petroleum engineering applications a hydraulic fracture would be vertical and normal to the minimum horizontal stress. In the case of a perfectly vertical well, the fracture initiation direction and the fracture plane would coincide.

For a horizontal well the situation is far more complicated. First, the fracture direction and the well trajectory can coincide only if the well is drilled along the maximum horizontal stress direction. Second, for all other horizontal well directions, a hydraulic fracture will first initiate longitudinally and then will turn to become normal to the minimum horizontal stress (Yew and Li, 1987; McLennan et al., 1989). This fracture turning would be highly detrimental during execution because of potential screenouts, but it would also reduce the well production rate significantly.

There are therefore two limiting cases of horizontal well fracturing. First, the well can be drilled along the expected fracture trajectory. This is the longitudinal configuration. Second, the well may be drilled normal to the expected fracture trajectory (i.e., along the minimum horizontal stress), and in this case transverse hydraulic fractures can be generated, leading to the possibility that multiple fractures can be generated with proper zone isolation. In order to prevent the longitudinal-to-transverse turning of the fracture, it is necessary to minimize the perforated length. Economides et al. (1991) have shown that, if the perforated length is larger than one and one-half times the well diameter, an undesirable fracture width reduction will occur.

The ratio of the reduced fracture width, w', to that of a fracture that is not affected by near-wellbore turning, w, is

$$\frac{w'}{w} = \frac{1.5D}{L_p} \qquad (18\text{-}29)$$

where L_p is the perforated length.

18-7.1 Longitudinal Fracture Penetrating a Horizontal Well

Figure 18-6 shows the incremental productivity index of a longitudinally fractured horizontal well (with $2x_f = L$) versus the dimensionless vertical well fracture conductivity, F_{CD}. At early dimensionless time, t_{Dxf}, the productivity index increases are large. However, they decrease with time. For large values of F_{CD}, the PI ratio approaches unity. Large values of F_{CD} are likely to be obtained in lower-permeability reservoirs. In such cases there would be no justification to drill a horizontal well to accept a longitudinal fracture. A fractured vertical well would suffice (unless the transverse fractured configuration, described in the next subsection, is attractive).

From Fig. 18-6, it is then obvious that a longitudinally fractured horizontal well may be attractive in reservoirs where the fractured vertical well is likely to accept a low-conductivity fracture, that is, in relatively higher-permeability reservoirs.

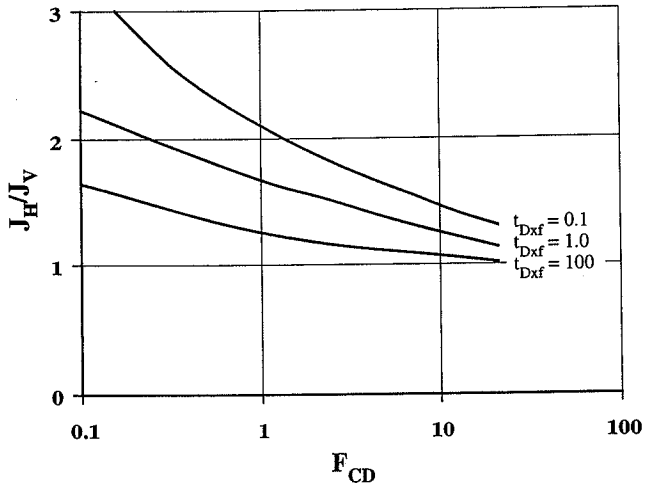

Figure 18-6
Productivity index ratio between longitudinally fractured horizontal well and fractured vertical well. (*From Economides et al., 1991.*)

18-7.2 Transverse Fractures Intersecting a Horizontal Well

The other limiting case is when the well is drilled in a direction normal to the expected fracture trajectory. Assuming that the entry point is minimized to prevent fracture turning, a configuration as shown in Fig. 18-7 can be expected. If the well is in the vertical center of a reservoir of thickness h, there exists a region of radius $h/2$ outside of which the flow in the fracture is linear. With the linear flow component from the reservoir into the fracture, this configuration could be described by the Cinco-Ley and Samaniego (1981a) solution.

The converging linear-to-radial flow within the fracture would result in an additional skin effect, s_c, which can be added to the dimensionless pressure of the transient fracture response. Mukherjee and Economides (1991) have developed an expression for this skin effect:

$$s_c = \frac{kh}{k_f w}\left[\ln\left(\frac{h}{2r_w}\right) - \frac{\pi}{2}\right] \tag{18-30}$$

The skin effect is small if kh is small, and can be reduced further if the near-wellbore $k_f w$ is large. "Tailing-in" with high-conductivity or resin-coated proppants may accomplish the task. Taking measures to avoid fracture width reduction because of turning may reduce this skin effect further. Whether the transverse fracture configuration is attractive, how many fractures are needed and of what size, is a matter of economic optimization and comparison with the base case of a fractured vertical well. The incremental benefits from multiple fractures (tempered by the production rate reduction from the skin effect and long-term

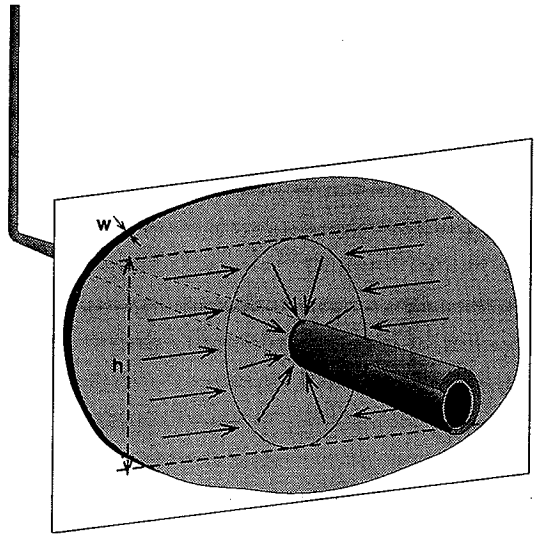

Figure 18-7
Transverse hydraulic fracture intersecting a horizontal well. Region of linear converging to radial flow.

interference effects) must be balanced against the treatment execution and zonal isolation costs and the additional costs of drilling the horizontal well.

EXAMPLE 18-8
Skin effect calculation for a transverse fracture

Assume that in a reservoir of k=1 md and h=100 ft, a horizontal well with r_w=0.328 ft is drilled and is hydraulically fractured. The fracture permeability-width product $k_f w$ is 1000 md-ft. Calculate the skin effect, s_c, because of converging linear-to-radial flow. The horizontal well is "notched" instead of perforated, and therefore there is no reduction to the fracture width.

If the well is perforated instead of "notched" and the perforated length is 200 ft, what would the skin effect be? Assume that the proppant permeability, k_f, is unchanged.

Solution From Eq. (18-30) with no fracture width reduction,

$$s_c = \frac{(1)(100)}{1000}\left\{\ln\left[\frac{100}{(2)(0.328)}\right] - \frac{3.14}{2}\right\} = 0.35 \tag{18-31}$$

If the perforated length, L_p, is 100 ft, then the corresponding width ratio would be, from Eq. (18-29),

$$\frac{w_{100}}{w} = \frac{1.5D}{L_p} = \frac{(1.5)(2)(0.328)}{100} = 9.8 \times 10^{-3} \tag{18-32}$$

Substituting this value in the denominator of Eq. (18-30) would lead to an extremely large s_c=36. This result demonstrates the need for the minimization of the perforated interval for such a stimulation treatment. ◇

EXAMPLE 18-9

Production rate from a horizontal well with a transverse fracture

Using the data and the results of Example 18-8 and Δp=1000 psi, ϕ=0.1, μ=1 cp, $c_t = 10^{-5}$ psi^{-1}, and B=1.1 res bbl/STB, calculate the well production rate for a 1000-ft fracture half-length after 30 days. Consider a fractured vertical well, a horizontal well with a transverse fracture, and a horizontal well with a transverse fracture but with L_p=100 ft. The dimensionless wellbore storage coefficient C_{Df} is equal to 10^{-5} for all cases.

Solution Since x_f=1000 ft, the F_{CD}=1 and Fig. 18-1 can be used. The dimensionless time, t_{Dxf}, is, from Eq. (18-3),

$$t_{Dxf} = \frac{(0.000264)(1)(30)(24)}{(0.1)(1)(10^{-5})(1000^2)} = 0.19 \tag{18-33}$$

Therefore $t_{Dxf}/C_{Df} = 1.9 \times 10^4$ and, from Fig. 18-1, p_D=1.5.

From Eq. (18-2) and rearrangement, the production rate from a fracture vertical well is

$$q = \frac{(1)(100)(1000)}{(141.2)(1.1)(1)(1.5)} = 430 \text{ STB/d} \tag{18-34}$$

From each transverse fracture in a horizontal well (infinite-acting reservoir with no intrafracture interference),

$$q = \frac{(1)(100)(1000)}{(141.2)(1.1)(1)(1.5+0.35)} = 349 \text{ STB/d} \tag{18-35}$$

representing a 19% reduction.

However, for L_p=100 ft and s_c=36, the flow from the fracture is

$$q = \frac{(1)(100)(1000)}{(141.2)(1.1)(1)(1.5+36)} = 17.2 \text{ STB/d} \tag{18-36}$$

which represents a 96% reduction from the unhindered fracture flow. This flow rate is also less than the flow rate that an unfractured horizontal well of length L_p would produce. [From Eq. (2-52), the latter would be 36 STB/d. Note that in fractured well performance the flow into a well from outside is usually and justifiably ignored.] ◇

18-8 Interpretation of Surface Rate and Pressure Data

This section demonstrates the use of surface production and pressure data as a practical alternative to downhole well testing. These data are routinely collected in almost all wells, and they have been commonly used in decline curve analysis (described in Section 18-9).

On the other side of the spectrum, these data are used for history matching with a numerical simulator.

The strategy is to process the data in such a way that they can be interpreted using conventional well testing techniques. Bottomhole pressures can be calculated using the methods presented in Chapter 7 and, once these pressures are calculated, bottomhole rates can be determined readily by simply multiplying the surface rate by the corresponding formation volume factor.

A number of authors (Jargon and van Poollen, 1965; Economides et al., 1979; Fetkovich and Vienot, 1984) have used rate-normalized pressure data for the determination of reservoir parameters. In its simplest form this function is $(p_i - p_{wf})/q$ for oil or $(p_i^2 - p_{wf}^2)/q$ and $[m(p_i) - m(p_{wf})]/q$ for gas.

Gladfelter et al. (1955) have shown that rate-normalized pressures versus time approximate the pressure behavior that would be observed under constant rate. Production data, however, are frequently too noisy to differentiate successfully, and thus trends are sought that are visible even without the derivative.

In the case of hydraulically fractured wells (and if the permeability is known), a very low-permeability formation ($k < 0.1$ md) is likely to exhibit an infinite-conductivity fracture behavior, and thus a log-log half-slope straight line may allow the determination of the fracture half-length. (See Example 18-1 for the expected onset of this behavior.) The equation in Table 11-3a could be used for this calculation, but without the factor q.

For a hydraulically fractured well in a relatively higher-permeability reservoir ($k > 1$ md), a finite-conductivity fracture behavior is likely and therefore the $k_f w$ product can be obtained from the portion of the data exhibiting bilinear flow, identified by 1/4-slope straight line on the log-log plot. Again the equation in Table 11-3a can be used but without the factor q.

If the reservoir permeability is not known, then it is necessary that pseudo-radial flow be observed in the transient response. From a semilogarithmic straight line, the permeability and the skin effect, s_f, resulting from the presence of the hydraulic fracture can be obtained. These equations can be found in Table 11-3a (again omitting the factor q).

If half-slope behavior is evident earlier, then the fracture half-length can be determined and the analysis is complete.

However, if quarter-slope behavior is observed, the $k_f w$ product can be obtained. The fracture half-length, x_f, can also be estimated with a trial-and-error approach. The procedure is as follows:

1. Assume x_f and calculate F_{CD}.
2. From Fig. 16-6, obtain $s_f + \ln(x_f/r_w)$.
3. Since s_f is already obtained from the pseudo-radial flow interpretation, calculate x_f and compare with the assumed.

EXAMPLE 18-10

Hydraulic fracture evaluation using production data

Interpret the transient response derived from wellhead pressure and flow-rate data acquired on a monthly basis for a hydraulically fractured gas well in a low-permeability reservoir. Data required for the analysis are the following: r_w=0.54 ft, ϕ=0.1, h=177 ft, p_i=6742 psi, T=356°F,

γ_g=0.852, mole% N_2=0.016, mole% CO_2=0.216. The formation permeability is estimated at 0.1 md, and wells are drilled on an approximate 40-acre spacing. Wellhead pressure and flow-rate data are shown as WHP and WHF in Fig. 18-8.

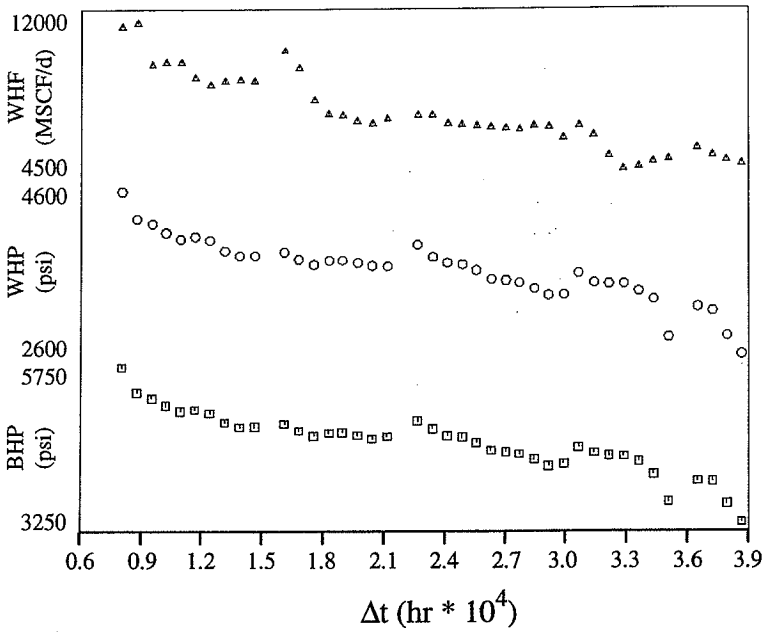

Figure 18-8
Wellhead production rate, wellhead pressure, and calculated bottomhole pressure for Example 18-10.

Solution To proceed with the analysis, the wellhead production data must first be converted to bottomhole pressure and flow-rate data. Bottomhole pressures computed using the standard Cullender and Smith technique explained in Chapter 7 are shown as BHP in Fig. 18-8. Bottomhole flow rates are computed using formation volume factors computed for the bottomhole pressure values. Using the gas gravity and impurities, reservoir temperature, and the average computed bottomhole pressure, Z=1.13, μ_g=0.04 cp, and $c_t = 5.5 \times 10^{-5}$ psi^{-1}. Each bottomhole pressure is transformed to normalized real-gas pseudo-pressure, $m_n(p)$ for the analysis. With this normalization, the plots used for analysis appear with a range of values approximately like the bottomhole pressures. Otherwise, the plotted values would be approximately like the bottomhole pressures squared.

Using the initial reservoir pressure, the change in the normalized real-gas potential, $\Delta m_n(p)$, is determined for each computed BHP value. Since the initial flow rate is 0, each $\Delta m_n(p)$ value is divided by the flow rate corresponding to the same month. This provides the rate-normalized pressure, RNP, for each point. The RNP can be treated as transient pressure in the analysis.

An appropriate model for the transient behavior is determined from a log-log diagnostic plot of RNP and its derivative, as shown in Fig. 18-9. On this plot, the RNP and RNP derivative data both show a half-slope trend initially, corresponding to pseudo-linear flow to the fracture, and a unit-slope trend in late time, corresponding to pseudo-steady state. Since the derivative response is never constant (flat), there is no pseudo-radial flow. Without the pseudo-radial flow regime, the reservoir permeability cannot be determined directly. Since the first data point corresponds to 1 month of production, it is apparent that a conventional pressure buildup test lasting up to 1 month would see the pseudo-linear flow regime in late time.

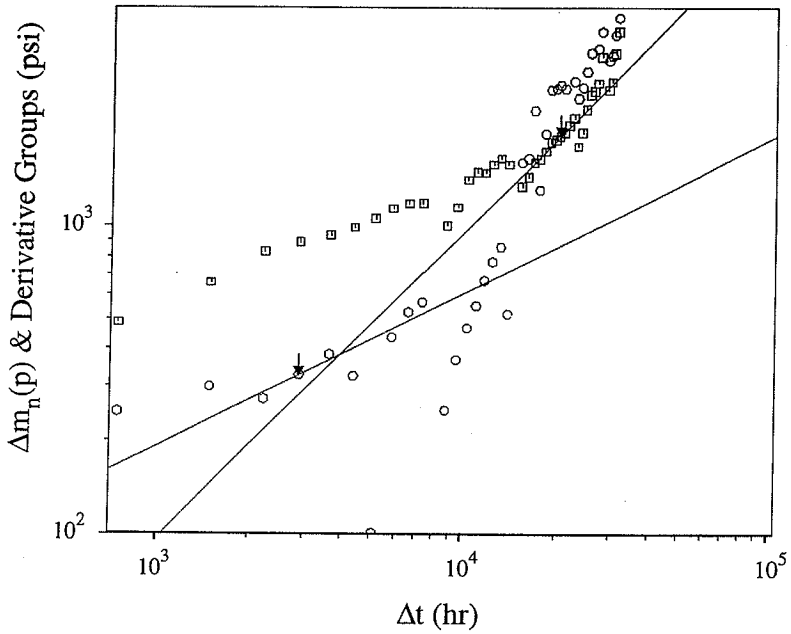

Figure 18-9
Diagnostic plot for Example 18-10 indicating the presence of a high-conductivity fracture and boundary effects.

The slope of the plot of RNP versus the square root of the elapsed production time as shown in Fig. 18-10 is used to determine kx_f^2. Using the estimated reservoir permeability of 0.1 md, this provides a fracture half-length of 600 ft.

Analysis of the pseudo-steady-state response in late time gives a drainage radius of approximately 600 ft, which compares well with the value expected for wells drilled with 40-acre spacing. ◇

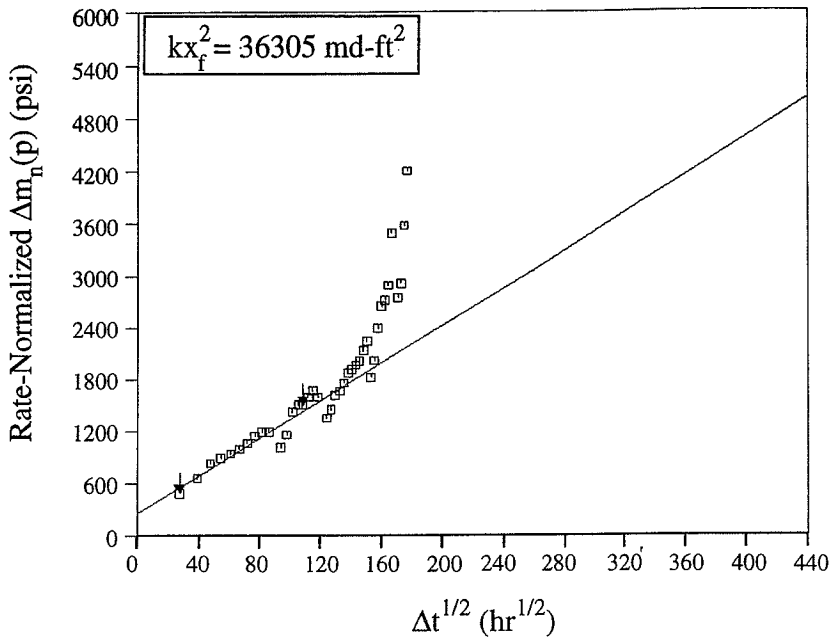

Figure 18-10
Specialized square-root-of-time plot for Example 18-10.

18-9 DECLINE CURVE ANALYSIS

A traditional, phenomenological means of well production study and forecast of performance is decline curve analysis. There is little fundamental justification to this method except empirical evidence that well performance data can be fitted with certain type functions. Under the sometimes tenuous assumption that the well flow performance will continue to obey the same mathematical function, a forecast of future performance can be performed.

It should be emphasized here that modern single-well transient analysis and numerical simulation, coupled with modern formation evaluation, render decline curve analysis obsolete. However, it is still in wide use and may be an alternative well performance evaluation methodology in those locations where more sophisticated techniques are uneconomical or unavailable.

Arps (1945) has presented several mathematical expressions that can be used in well flow rate decline analysis. Under constant flowing pressure, which is a reasonable assumption for normal production, the general expression for rate versus time is suggested to obey

$$\frac{dq/dt}{q} = -Kq^n \tag{18-37}$$

where K and n are constants. For constant fractional decline (exponential decline), n=0. For hyperbolic decline, $0 < n < 1$, and for the special case where n=1, the decline is called harmonic.

Of these cases, the exponential decline has been used extensively, because, as will be shown below, it forms a semilogarithmic straight line when log q is graphed versus time.

18-9.1 Constant Fractional Decline (Exponential Decline)

For n=0, Eq. (18-37) becomes

$$\frac{dq/dt}{q} = -K \tag{18-38}$$

amd after rearrangement it can be integrated between time 0 and t with corresponding flow rates q_i and q,

$$\int_{q_i}^{q} \frac{dq}{q} = -\int_0^t K\,dt \tag{18-39}$$

Equation (18-39) leads to

$$q = q_i e^{-Kt} \tag{18-40}$$

A semilogarithmic plot of log q versus t would form a straight line with a slope equal to $-K/2.3$. Since almost all production data can be fitted approximately with a semilog straight line, Eq. (18-40) has been used for a large number of wells.

18-9.2 Hyperbolic Decline

Equation (18-37), rearranged and integrated between q_i and q and 0 and t, leads to

$$\int_{q_i}^{q} q^{-1-n}\,dq = -\int_0^t K\,dt \tag{18-41}$$

and finally,

$$q^{-n} = nKt + q_i^{-n} \tag{18-42}$$

18-9.3 Harmonic Decline

For $n = 1$, Eq. (18-42) becomes simply

$$q^{-1} = Kt + q_i^{-1} \tag{18-43}$$

Equation (18-42) [Eq. (18-43) should be considered as a special case of Eq. (18-42)] can be used to fit data that do not form an apparent straight line on a semilog plot. After n and

K are obtained, Eq. (18-40) or Eq. (18-42) can be used to forecast the well performance at a future time t.

EXAMPLE 18-11

Decline analysis and forecast of future performance

Using the production performance for wells A and B in Table 18-1, calculate the projected rate at the end of 1995. Also calculate the incremental cumulative production from 1/1992 to 12/1995. The initial production rates were the ones recorded on 7/1986.

Table 18-1

Observed Production Rates for Wells A and B (Example 18-11)

Date	Well A q (STB/d)	Well B q (STB/d)
7/1986	2300	1568
1/1987	2155	970
7/1987	2015	664
1/1988	1885	478
7/1988	1760	363
1/1989	1650	285
7/1989	1545	230
1/1990	1440	191
7/1990	1347	161
1/1991	1260	137
7/1991	1179	118
1/1992	1102	103
7/1992	1031	90
1/1993	964	80

Solution Figure 18-11 is a semilog plot of the observed declines of wells A and B. Well A, exhibiting straight-line behavior, can be described by the exponential decline expression. The slope (with t in years) is -5.8×10^{-2} and therefore K=0.133 yr^{-1}. The expression providing the well production versus time is then

$$q = 2300e^{-0.133t} \tag{18-44}$$

At the end of 1995 (t=9.5 yr), the production rate would be

$$q = 2300e^{-(0.133)(9.5)} = 650 \text{ STB/d} \tag{18-45}$$

The incremental cumulative production from 1/1993 (6.5 yr) and 12/1995 (9.5 yr) would be simply (converting t in days)

$$\Delta N_p = \int_{(6.5)(365)}^{(9.5)(365)} q\,dt = 2300 \int_{(6.5)(365)}^{(9.5)(365)} e^{-3.65\times10^{-4}t}\,dt \tag{18-46}$$

Integration of Eq. (18-46) results in

$$\Delta N_p = \frac{(2300)}{(3.65 \times 10^{-4})}\left[e^{-(3.65\times10^{-4})(6.5)(365)} - e^{(-3.65\times10^{-4})(9.5)(365)}\right] \tag{18-47}$$
$$= 8.7 \times 10^5 \text{ STB}$$

For well B, fit of the data results in n=0.5 and $K = 2.7\times10^{-2}$ (with t in years) or $K = 7.4\times10^{-5}$ (with t in days). Thus, the decline expression is [after Eq. (18-42)]

$$q^{-0.5} = (1.35 \times 10^{-2})t + 1568^{-0.5} \tag{18-48}$$

After t=9.5 yr, solution of Eq. (18-48) results in q = 42 STB/d.

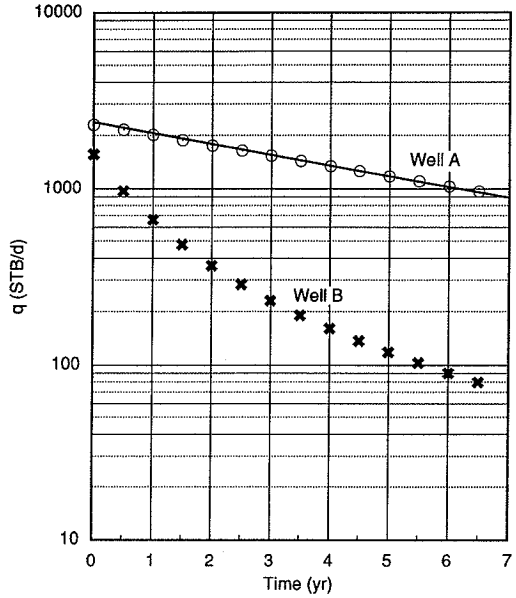

Figure 18-11
Decline curves for wells A and B (Example 18-11).

With t in days, Eq. (18-48) becomes

$$q = [(3.7 \times 10^{-5})t + 0.0253]^{-2} \tag{18-49}$$

and after integration,

$$\Delta N_p = \left\{ -\frac{1}{3.7 \times 10^{-5}} [(3.7 \times 10^{-5})t + 0.0253]^{-1} \right\}_{(6.5)(365)}^{(9.5)(365)} \quad (18\text{-}50)$$

$$= 6.3 \times 10^4 \text{ STB} \quad (18\text{-}51)$$

◇

REFERENCES

1. Arps, J. J., "Analysis of Decline Curves," *Trans. AIME*, **160**: 228–247, 1945.
2. Brown, J. E., and Economides, M. J., "An Analysis of Hydraulically Fractured Horizontal Wells," SPE Paper 24322, 1992.
3. Cinco-Ley, H., and Samaniego, F., "Transient Pressure Analysis for Fractured Wells," *JPT*, pp. 1749–1766, September 1981a.
4. Cinco-Ley, H., and Samaniego, F., "Transient Pressure Analysis: Finite Conductivity Fracture Case versus Damage Fracture Case," SPE Paper 10179, 1981b.
5. Economides, M. J., "Observations and Recommendations in the Evaluation of Tests of Hydraulically Fractured Wells," SPE Paper 16396, 1987.
6. Economides, M. J., Brigham, W. E., Cinco-Ley, H., Miller, F. G., Ramey, H. J., Jr., Barelli, A. and Mannetti, G., "Influence Functions and Their Application to Geothermal Well Testing," *GRC Trans.*, **3**: 177–180, 1979.
7. Economides, M. J., Deimbacher, F. X., Brand, C. W., and Heinemann, Z.E., "Comprehensive Simulation of Horizontal Well Performance," *SPEFE*, pp. 418–426, December 1991.
8. Fetkovich, M. J., and Vienot, M. E., "Rate Normalization of Buildup Pressure by Using Afterflow Data," *JPT*, pp. 2211–2224, December 1984.
9. Gladfelter, R. E., Tracy, G. W., and Wilsey, L.E., "Selecting Wells Which Will Respond to Production-Stimulation Treatment," *Drill. and Prod. Prac.*, API, Dallas, pp. 117–129, 1955.
10. Gringarten, A. C., and Ramey, A. J., Jr., "Unsteady State Pressure Distributions Created by a Well with a Single-Infinite Conductivity Vertical Fracture," *SPEJ*, pp. 347–360, August 1974.
11. Jargon, J. R., and van Poollen, H. K., "Unit Response Functions from Varying-Rate Data," *JPT*, pp. 965–972, August 1965.
12. McLennan, J. D., Roegiers, J.-C., and Economides, M. J., "Extended Reach and Horizontal Wells," in *Reservoir Stimulation*, 2nd ed., M. J. Economides and K. G. Nolte, eds., Prentice Hall, Englewood Cliffs, NJ, Chap. 19, 1989.
13. Mukherjee, H., and Economides, M. J., "A Parametric Comparison of Horizontal and Vertical Well Performance," *SPEFE*, pp. 209–216, June 1991.
14. Yew, C., and Li, Y., "Fracturing of a Deviated Well," *SPEFE*, pp. 429–437, November 1988.

PROBLEMS

18-1. Consider a fractured well with k=1 md, x_f=1000, and $k_f w$=1000 md-ft. Calculate the production rate after 30 days if C=10^{-3} bbl/psi, ϕ=0.1, h=90 ft, μ=1 cp, c_t=10^{-5} psi^{-1}, B=1.1 res bbl/STB, and $p_i - p_{wf}$=1000 psi. Repeat the calculation with $k_f w$=10,000 md-ft and x_f=1000 ft and also with $k_f w$=2000 md-ft but x_f=2000 ft. What observations can be made?

18-2. Use all variables as in Problem 18-1 but with k=10 md, x_f=500 ft, and $k_f w$=5000 md-ft. What would be the effect of reducing $k_f w$ to 2500 md-ft but increasing x_f to 1000 ft?

18-3. Develop a "folds" of increase versus time plot of an unfractured and fractured gas well as in Appendix C. Assume that $k_f w$=2550 md-ft and x_f=1500 ft. Use a non-Darcy coefficient, D=10^{-4} (MSCF/d)$^{-1}$.

18-4. Repeat Problems 18-1 and 18-2 but with a choked fracture with x_s=100 ft and $k_f w$ values one-third of the given. Comment on the relative impact of the choked fractures as a function of the reservoir permeability.

18-5. In Example 18-7, I_{ani} was equal to 3. Calculate the required horizontal well length to compete with the same fracture in the vertical well but in a reservoir where I_{ani}=1 and 0.25.

18-6. If in a reservoir with I_{ani}=1 and h=100 ft it is contemplated to drill a 2000-ft horizontal well (r_w=0.328 ft), develop a series of combinations of x_f and F_{CD} in a fractured vertical well to deliver the same productivity index. Make any reasonable assumptions.

18-7. Consider Example 18-9. A transversely fractured horizontal well produced 100 STB/d from each fracture. Calculate the linear-to-radial convergence skin effect, s_c. What is the likely perforated interval in each zone to deliver such a flow rate?

18-8. Use as a base case a fractured vertical well with k=1 md, $k_f w$=1000 md-ft, and x_f=1000 ft. A horizontal well is transversely hydraulically fractured with five equally spaced treatments. Assuming that no appreciable interference among the fractures will be observed in the first year, estimate the net present value of the incremental revenue from these treatments. Use x_f=500 ft and $k_f w$=2000 md-ft. In addition, use C=10^{-3} bbl/psi, ϕ=0.1, h=90 ft, μ=1 cp, c_t=10^{-5} psi^{-1}, B=1.1 res bbl/STB, and $p_i - p_{wf}$=1000 psi. The price of oil is $20/STB, and the time value of money is 25%.

18-9. What would be the forecast of well production rate at 9.5 years and the cumulative production between 6.5 and 9.5 years if the "best" straight line were to be drawn through the data of well B of Example 18-11, thus assuming exponential instead of hyperbolic decline? Compare these results with those in Example 18-11. What would be the difference if only the history of the first 4 years were to be considered?

18-10. The following well production history was observed.

Year	Production Rate (STB/d)
0	1100 (q_i)
1	980
2	867
3	769
4	684
5	609
6	543

Forecast the production rate at the end of years 7 through 10. Calculate the incremental cumulative production for each of these years.

CHAPTER 19

Gas Lift

19-1 INTRODUCTION

In Chapter 8 the relationship between tubing and inflow performance led to the well deliverability. If the bottomhole flowing pressure is smaller than the tubing pressure difference caused by a fluid with a given flowing gradient, then gas lift may be employed.

Gas lift is one method of artificial lift. The other is mechanical lift, and it will be discussed in Chapter 20. For gas lift, gas is injected continuously or intermittently at selected location(s), resulting in a reduction in the natural flowing gradient of the reservoir fluid, and thus reducing the hydrostatic component of the pressure difference from the bottom to the top of the well. The purpose is to bring the fluids to the top at a desirable wellhead pressure while keeping the bottomhole pressure at a value that is small enough to provide good driving force in the reservoir. This pressure drawdown must not violate restrictions for sand control and water or gas coning.

Two other considerations must enter the design. First, large amounts of gas injected into the well will affect the separation facilities at the top. Second, there exists a limit gas–liquid ratio (GLR) above which the pressure difference in the well will begin to increase because the reduction in the hydrostatic pressure will be offset by the increase in the friction pressure.

Figure 19-1 is a schematic of a typical gas-lift system showing the well, a blowup of a gas-lift valve, and the associated surface process equipment.

The positioning of the gas-lift valves and their number is a matter of wellbore hydraulics optimization. For continuous gas lift, an " operating valve" will be used to inject the appropriate amount of gas at the desirable tubing pressure at the injection point. Other valves may be placed below the injection point and may be put into service during the life of the well as the reservoir pressure declines or if the water–oil ratio increases.

For intermittent gas lift, both a single injection point and multiple injection points can be employed. First a liquid slug must be built in the tubing above the bottom valve. Then,

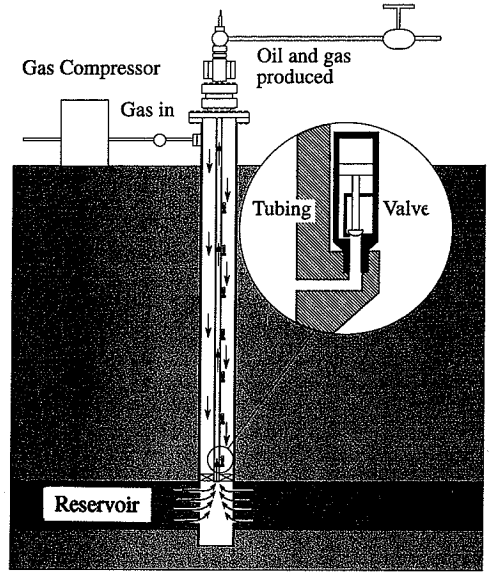

Figure 19-1
Gas-lift concept and gas-lift valves.

the valve opens, displacing the liquid slug upward. The valve remains open until the slug reaches the top, and then the valve closes. It reopens when a new liquid slug builds in the bottom of the well.

For multiple injection points, the bottom valve opens as described for the single-injection-point operation, but as the liquid slug moves upward, valves below the slug open. The valves close after the slug reaches the top. The actuation of the valves for intermittent gas lift can be done with a timing device or can depend on the pressure.

Valves can open and close based on the value of the casing or the tubing pressure. Other valves may be operated on the basis of the fluid level. A detailed discussion of the operating details of these valves can be found in Brown et al. (1980).

19-2 Natural versus Artificial Flowing Gradient

In Chapter 7 a number of correlations were introduced for pressure traverse calculations in two- and three-phase oil wells. For each production rate, these calculations result in gradient curves for a range of GLRs. Pressure differences are graphed against depth.

For a given flowing wellhead pressure, the required bottomhole pressure can be calculated. Thus, simply,

$$p_{tf} + \Delta p_{\text{trav}} = p_{wf} \tag{19-1}$$

where Δp_{trav} is the pressure traverse and is a function of the flow rate, the GLR, the depth, and the properties and composition of the fluid. The methodology was outlined in Chapter 7 and especially in Section 7-4.4. Example 7-10 (and associated Fig. 7-16) showed a typical calculation.

Equation (19-1) can be rewritten in terms of the flowing pressure gradient in the well. Thus,

$$p_{tf} + \frac{dp}{dz} H = p_{wf} \tag{19-2}$$

where dp/dz in Eq. (19-2) is considered constant. As can be seen from Fig. 7-16, this gradient is not constant throughout the depth of the well. For small values (< 100) or relatively large values (> 1500) of GLR, the gradient can usually be considered as largely constant for common well depths ($\approx$ 10,000 ft). For intermediate values, dp/dz is not constant but, instead, is a function of depth.

Suppose that the natural GLR (subscripted 1) would result in a pressure traverse requiring an unacceptably large p_{wf}. Then, for a more desirable p_{wf}, gas at a rate q_g would lead to a higher GLR (subscripted 2). If the rate is q_l, then

$$q_l(\text{GLR}_2 - \text{GLR}_1) = q_g \tag{19-3}$$

EXAMPLE 19-1
Calculation of required GLR and gas-lift rate

Suppose the well described in Example 7-10 (with q_o=400 STB/d and q_w=400 STB/d) is in a reservoir where H=8000 ft and GLR=300 SCF/STB. If the indicated bottomhole pressure is 1500 psi, what should be the working GLR, and how much gas should be injected at the bottom of the well? Would it be possible to inject (instead) at 4000 ft and still produce the same liquid rates? What would be the GLR above this alternative injection point?

Solution At 8000 ft and GLR=300 SCF/STB (see Fig. 7-16), the required flowing bottomhole pressure would be 1900 psi. Since the indicated pressure is 1500 psi, then (again from Fig. 7-16) the required GLR would be 450 SCF/STB. Therefore, from Eq. (19-3),

$$q_g = 800(450 - 300) = 1.2 \times 10^5 \text{ SCF/d} \tag{19-4}$$

Now for the alternative option. From Eq. (19-2) it can be written that

$$100 + \left(\frac{dp}{dz}\right)_a 4000 + 4000(0.3) = 1500 \tag{19-5}$$

where 0.3 is the pressure gradient for the GLR=300 SCF/STB curve (from Fig. 7-16) between depths of 4000 and 8000 ft. $(dp/dz)_a$ should be the pressure gradient above the injection point. Solution of Eq. (19-5) results in $(dp/dz)_a$=0.05 psi/ft, which is not possible as shown in Fig. 7-16. No fluid in this well can provide such a low flowing gradient. In addition to the

artificial GLR, two other variables must be reconciled—the possible gas injection pressure and the required compressor power demand, which is a function of both the gas injection rate and pressure. These will be outlined below. ◇

19-3 Pressure of Injected Gas

From the mechanical energy balance [Eq. (7-15)], ignoring changes in kinetic energy and the friction pressure drop in the casing (i.e., relatively small gas flow rates) and changing into oilfield units,

$$\int_{\text{surf}}^{\text{inj}} \frac{dp}{\rho} + \frac{1}{144}\int_0^H dH = 0 \tag{19-6}$$

From the real-gas law,

$$\rho = \frac{28.97\gamma p}{ZRT} \tag{19-7}$$

where γ is the gas gravity to air and 28.97 is the molecular weight of air. The gas constant R is equal to 10.73 psi ft^3/lb-mole-°R. The temperature is in °R.

Substitution of Eq. (19-7) into Eq. (19-6) and integration (using average values of $\bar{Z}$ and $\bar{T}$) results in

$$p_{\text{inj}} = p_{\text{surf}} e^{0.01875\gamma H_{\text{inj}}/\overline{ZT}} \tag{19-8}$$

EXAMPLE 19-2
Injection-point pressure

If gas of γ=0.7 (to air) is injected at 8000 ft and if p_{surf}=900 psi, T_{surf}=80°F and T_{inj}=160°F, calculate the pressure at the injection point, p_{inj}.

Solution Trial and error is required for this calculation. Assume that p_{inj}=1100 psi. From Chapter 4 (Fig. 4-2), p_{pc}=668 psi and T_{pc}=390°R and therefore

$$p_{pr} = \frac{(900+1100)/2}{668} = 1.5 \tag{19-9}$$

and

$$T_{pr} = \frac{(80+160)/2+460}{390} = 1.49 \tag{19-10}$$

From Fig. 4-1, $\bar{Z}$=0.86 and therefore

$$p_{\text{inj}} = 900e^{(0.01875)(0.7)(8000)/(0.86)(580)} = 1110 \text{ psi} \tag{19-11}$$

which agrees well with the assumed value. ◇

19-3.1 Point of Gas Injection

If Eq. (19-8) is expanded as a Taylor series and if common fluid properties for a natural gas and reservoir are considered such as γ=0.7, $\bar{Z}$=0.9, and $\bar{T}$=600R, then

$$p_{\text{inj}} \simeq p_{\text{surf}}\left(1 + \frac{H_{\text{inj}}}{40,000}\right) \tag{19-12}$$

where the pressures are in psi and H_{inj} is in feet. This relationship was offered first by Gilbert (1954). In current practice this type of approximation is usually not necessary, since the actual downhole injection pressure can be calculated readily with a simple computer program that considers the actual annulus geometry and accounts for both friction and hydrostatic pressure components. Equation (19-12), though, can be useful for first design approximations.

The p_{inj} in the production tubing must be reduced by an additional 100 to 150 psi for the pressure drop across the gas-lift valve. The value of this pressure drop will be supplied by the manufacturer.

The point of gas injection, H_{inj}, would create two zones in the well: one below, with a flowing pressure gradient $(dp/dz)_b$, and one above, with a flowing pressure gradient $(dp/dz)_a$. Thus,

$$p_{wf} = p_{tf} + H_{\text{inj}}\left(\frac{dp}{dz}\right)_a + (H - H_{\text{inj}})\left(\frac{dp}{dz}\right)_b \tag{19-13}$$

It should be obvious that the downhole gas injection pressure, p_{inj}, and the pressure within the tubing must be balanced for gas to enter the tubing at the injection point.

Figure 19-2 shows the concept of continuous gas lift in terms of the pressure values, pressure gradients, well depth, and depth of injection. With the available flowing bottomhole pressure and the natural flowing gradient $(dp/dz)_b$, the reservoir fluids would ascend only to the point indicated by the projection of the pressure profile in the well. This would leave a partially filled wellbore. Addition of gas at the injection point would lead to a marked alteration of the pressure gradient $(dp/dz)_a$, which would lift the fluids to the surface. The higher the required wellhead pressure, the lower the flowing gradient should be.

Also marked on Fig. 19-2 is the balance point, that is, the position in the tubing where the downhole pressure of the injected gas is equal to the pressure in the tubing. This pressure is related to the surface pressure as shown by Eq. (19-8) or its approximation, Eq. (19-12). The actual point of injection is placed a few hundred feet higher to account for the pressure drop across the gas lift value, Δp_{valve}.

EXAMPLE 19-3
Relating gas injection pressure, point of injection, and well flow rate

Suppose that the well at a depth of 8000 ft and a GLR=300 SCF/STB (as in Example 19-1) drains a reservoir with an IPR given by

$$q_l = 0.39(\bar{p} - p_{wf}) \tag{19-14}$$

What should be the surface gas injection pressure if the gas-lift valve is at the bottom of the well and $p_{\text{inj}} - \Delta p_{\text{valve}} = p_{wf}$=1000 psi? [The average reservoir pressure, $\bar{p}$, is 3050 psi for q_l=800 STB/d, as can be calculated readily from Eq. (19-14).]

What should be the point of gas injection for a production rate of 500 STB/d? Figure 19-3 is the tubing performance curve for q_l=500 STB/d with 50% water and 50% oil. Note from Fig. 19-3 that $(dp/dz)_b$=0.33 psi/ft for GLR=300 SCF/STB between H=5000 and 8000 ft. Use Δp_{valve}=100 psi.

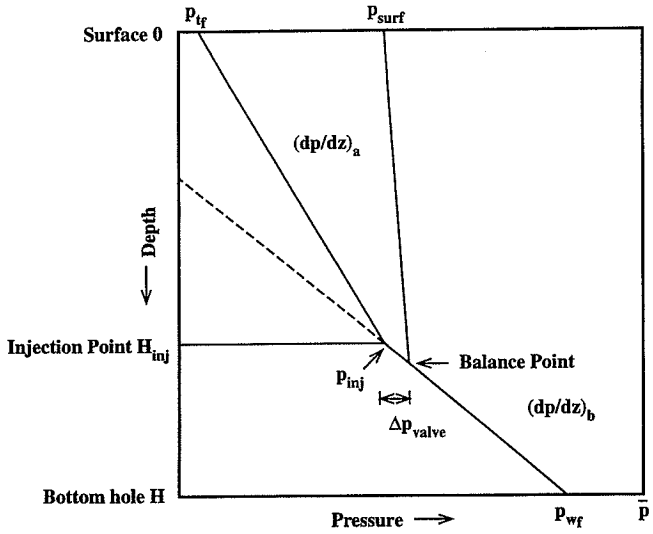

Figure 19-2
Continuous gas lift with pressures and pressure gradients versus depth.

Solution From Eq. (19-12) and rearrangement and noting that p_{inj}=1100 psi,

$$p_{surf} = 1100/\left(1 + \frac{8000}{40{,}000}\right) = 915 \text{ psi} \tag{19-15}$$

For q_l=500 STB/d, then from the IPR relationship [Eq. (19-14)],

$$p_{wf} = 3050 - \frac{500}{0.39} = 1770 \text{ psi} \tag{19-16}$$

The injection point must be where the pressure between the injected gas and the pressure in the production string must be balanced. Thus,

$$915\left(1 + \frac{H_{inj}}{40{,}000}\right) - 100 = 1770 - 0.33(8000 - H_{inj}) \tag{19-17}$$

and therefore H_{inj}=5490 ft.

Finally, the p_{inj} at H_{inj} is

$$p_{inj} = 915\left(1 + \frac{5490}{40{,}000}\right) \approx 1040 \text{ psi} \tag{19-18}$$

Inside the tubing the pressure is 940 psi, since Δp_{valve}=100 psi.

The intersect between p=940 psi and H_{inj}=5490 is at GLR=340 SCF/STB (see Fig. 19-4). Therefore the gas injection from Eq. (19-3) would be $q_g = 2 \times 10^4$ SCF/d. ◇

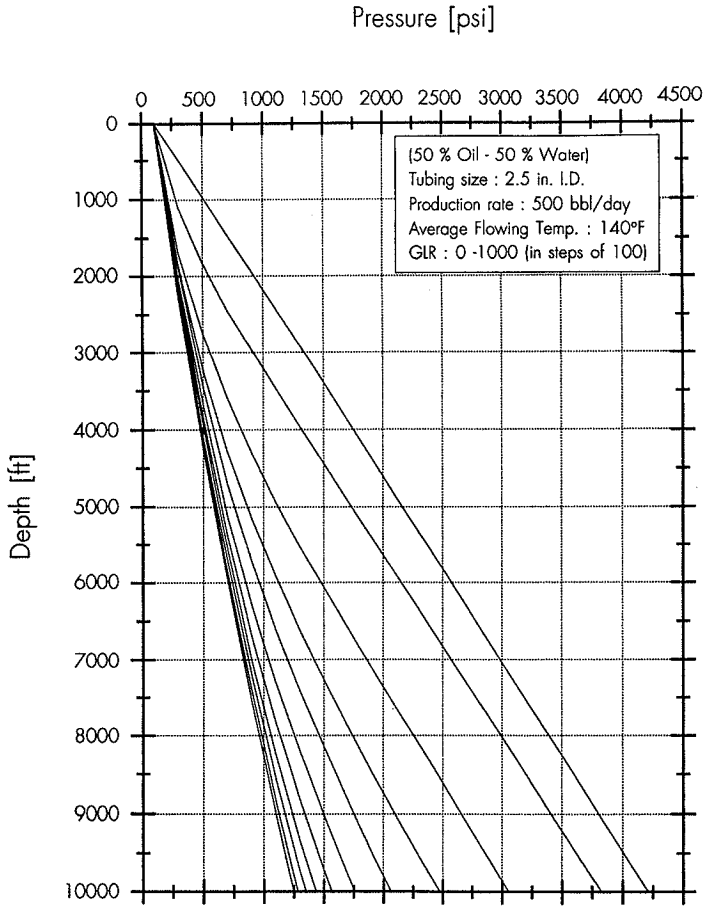

Figure 19-3
Gradient curves for q_l=500 STB/d (Example 19-3).

19-4 Power Requirements for Gas Compressors

The horsepower requirements can be estimated from the following equation:

$$\text{HHP} = 2.23 \times 10^{-4} q_g \left[\left(\frac{p_{surf}}{p_{in}}\right)^{0.2} - 1\right] \tag{19-19}$$

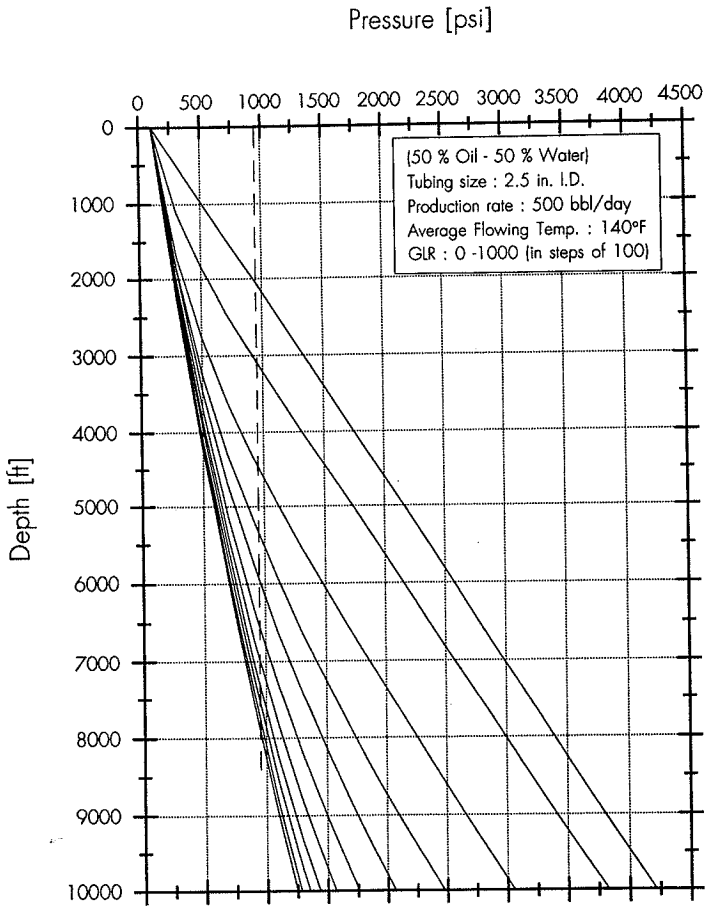

Figure 19-4
Point of gas injection. Intersection of gas injection pressure with gradient curves (Example 19-3).

where p_{in} is the inlet compressor pressure. Thus for a given gas injection rate in a well and the surface pressure, the calculated horsepower would be an important variable in gas-lift optimization design.

EXAMPLE 19-4
Calculation of gas-lift compressor horsepower

Suppose that the gas injection rate is 1.2×10^5 SCF/d, p_{surf} is 1330 psi, and the compressor inlet pressure, p_{in}, is 100 psi. Calculate the horsepower requirements.

Solution From Eq. (19-19),

$$\text{HHP} = 2.23 \times 10^{-4}(1.2 \times 10^5)\left[\left(\frac{1330}{100}\right)^{0.2} - 1\right] = 18.4 \text{ hhp} \qquad (19\text{-}20)$$

◇

19-5 Impact of Increase of Gas Injection Rate; Sustaining of Oil Rate with Reservoir Pressure Decline

Figure 19-4 can be used to investigate the effect of increasing the gas injection rate, and therefore increasing the GLR in the wellbore. First, increasing the gas injection rate allows the injection at a lower point in the tubing without increasing the injection pressure.

From Eq. (19-13), as H_{inj} increases [with the associated smaller $(dp/dz)_a$] and since $(dp/dz)_b$ remains constant within a smaller interval $H - H_{inj}$, then p_{wf} will necessarily decrease. Therefore larger oil production rates are likely to be achieved with higher GLR and a lower injection point.

Similarly, to *sustain* a production rate while the reservoir pressure depletes, the flowing bottomhole pressure must be lowered. This can be accomplished by lowering the injection point and by increasing the gas injection rate. This has a limit, and it will be addressed in the next section.

EXAMPLE 19-5
Effect of injection rate and injection point on the flowing bottomhole pressure

Assuming that Fig. 19-4 represents a gas-lift graph, calculate the flowing bottomhole pressure at 8000 ft for the injection points described by the intersection of the gas injection curve and the pressure traverse curves for GLR values equal to 500, 600, and 700 SCF/STB, respectively. The flowing gradient below the injection point is 0.33 psi/ft (GLR=300 SCF/STB).

Solution From Fig. 19-4, the wellhead pressure is 100 psi. Also, the following table can be constructed from the intersection of the gas and pressure traverse curves:

GLR	Injection Point	Pressure at Injection Point
500	6250	960 psi
600	6800	970 psi
700	7050	975 psi

The pressures at the injection points shown above are obtained from Eq. (19-12) using p_{surf}=915 psi and subtracting 100 psi across the gas-lift valve. Therefore the bottomhole pressure can be calculated readily by

$$p_{wf} = p_{inj} + (H - H_{inj})\left(\frac{dp}{dz}\right)_b \tag{19-21}$$

where p_{inj} is the pressure at the injection point.

Substituting the values for p_{inj} and the corresponding H_{inj} results in p_{wf} equal to 1538, 1366, and 1288 psi, for GLRs equal to 500, 600, and 700 SCF/STB, respectively. Assuming that Fig. 19-4 describes approximately the pressure traverse of flow rates larger than 500 STB/d, these lower bottomhole pressures would lead to larger oil production rates. If Eq. (19-14) in Example 19-3 describes the IPR for this well, then the lower bottomhole pressures (using $\bar{p}$=3050 psi as in Example 19-3) would result in q_l equal to 590, 657, and 687 STB/d, respectively. ◇

EXAMPLE 19-6

Sustaining a production rate while the reservoir pressure depletes

Repeat Example 19-3 with the IPR described by Eq. (19-14). Where should the injection point be after the reservoir pressure drops by 500 psi? What should be the gas injection rate to sustain a liquid production rate equal to 500 STB/d? Use Fig. 19-4 and the data of Example 19-5 for the analysis.

Solution From Eq. (19-14) and rearrangement if $\bar{p}$=2550 psi (500 psi less than the original 3050 psi).

$$p_{wf} = 2550 - \frac{500}{0.39} = 1268 \text{ psi} \tag{19-22}$$

The injection point must then be obtained from the solution of

$$915\left(1 + \frac{H_{inj}}{40{,}000}\right) - 100 = 1268 - 0.33(8000 - H_{inj}) \tag{19-23}$$

leading to H_{inj}=7120 ft.

From Fig. 19-4 at H_{inj}=7120 ft and (calculated) p_{inj}=980 psi, the GLR must be equal to 750 SCF/STB.

Finally, the gas injection rate is

$$q_g = (750 - 300)500 = 2.25 \times 10^5 \text{ SCF/d} \tag{19-24}$$

This injection rate is more than 10 times the gas injection rate calculated in Example 19-3, which would be required at the reservoir pressure of 3050 psi. The injection point is also deeper: from 5490 to 7120 ft. ◇

19-6 Maximum Production Rate with Gas Lift

As stated in the introduction to this chapter, there exists a limit value of GLR referred to here as "limit" (Golan and Whitson, 1991, have referred to it as "favorable") GLR, where the flowing pressure gradient is minimum. For GLR values that are larger than the minimum, the flowing gradient begins to increase. As discussed already, the well flowing pressure gradient is a combination of the hydrostatic pressure head and the friction pressure drop. While increase of the GLR from small values would result in fluid density reduction with modest friction pressures, continued GLR increase would lead to a disproportionate increase in the friction pressure. Thus the limit GLR is that value at which the increase in friction pressure will offset the decrease in the hydrostatic pressure.

Figure 19-5 represents pressure traverse calculations for a specific liquid production rate (q_l=800 STB/d) in a given tubing size. The values of the GLR have been selected to be large enough to observe the behavior reversal at the limit GLR value. For this example, the limit GLR is approximately equal to 4000 SCF/STB.

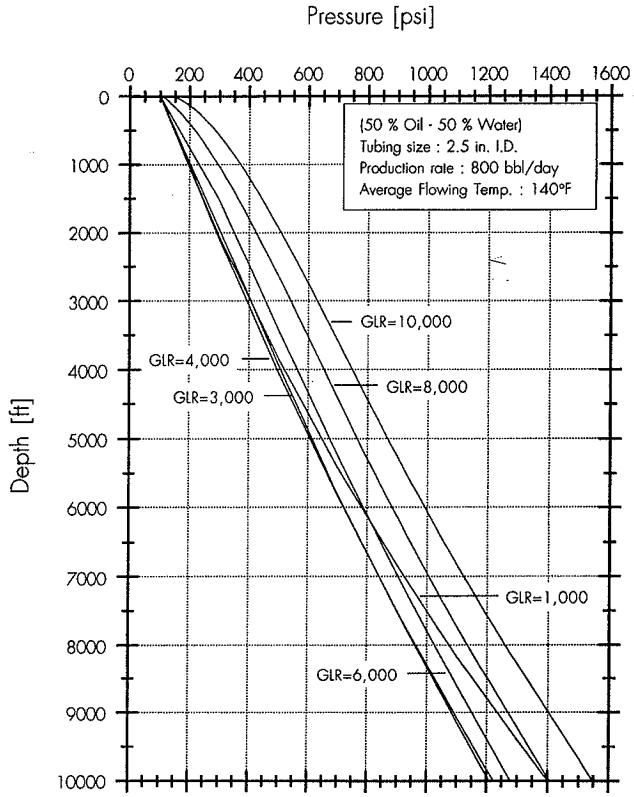

Figure 19-5
Large GLR values and limit GLR for q_l=800 STB/d.

The limit GLR increases as the production rate decreases. Figure 19-6 is for a smaller liquid production rate (q_l=500 STB/d) in the same size well. In this example the limit GLR is approximately 7000 SCF/STB. This limit GLR for which the minimum p_{wf} will be obtained is rarely the natural GLR of the reservoir fluids. Thus it can be reached only through artificial gas lift. While the above apply to an already completed well, appropriate production engineering must take into account these concepts before the well is completed. A larger well size would lead to a larger limit GLR, with, of course, a larger gas injection rate. These design issues, balancing benefits and costs, will be dealt with in Section 19-8.

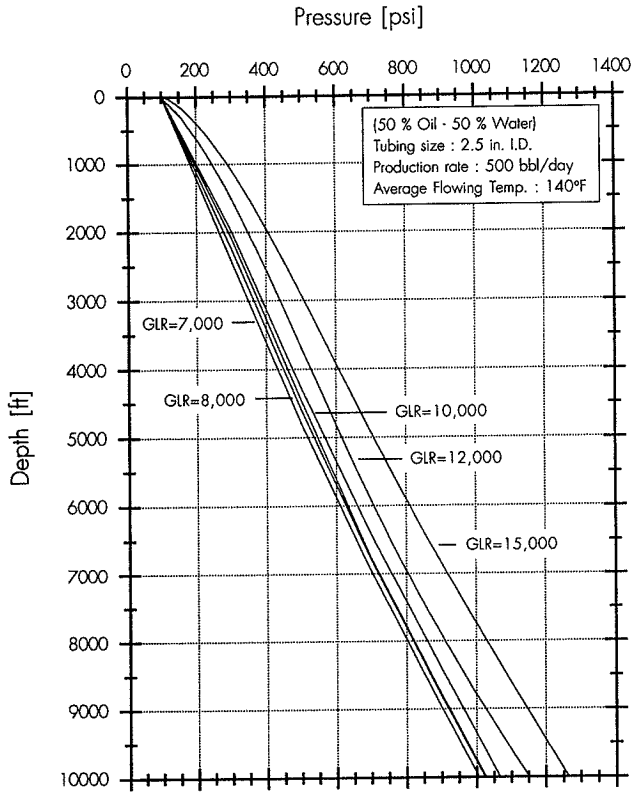

Figure 19-6
Large GLR values and limit GLR for $q_l = 500$ STB/d.

19-7 GAS-LIFT PERFORMANCE CURVE

Poettmann and Carpenter (1952) and Bertuzzi et al. (1953), in developing design procedures for gas-lift systems, introduced the "gas-lift performance curve," which has been used extensively in the petroleum industry ever since.

Optimized gas-lift performance would have an important difference from natural well performance. Based on the information presented in the previous section, for each liquid production rate there exists a limit GLR where the minimum p_{wf} will be observed. Thus, a plot similar to the one shown in Fig. 19-7 can be drawn. The IPR curve, as always, characterizes the ability of the reservoir to deliver certain combinations of production rates and flowing bottomhole pressures. Intersecting this IPR curve is the optimum gas-lift performance curve of minimum flowing bottomhole pressures (minimum pressure intake curve), and for each production rate they correspond to the limit GLR. Other values of GLR *above* or *below* the limit GLR will result in smaller production rates. This is shown conceptually in Fig. 19-8. Each gas-lift performance curve in the *vicinity* of the maximum production rate will result in a larger pressure intake and therefore lower production. In summary, the intersection of the IPR curve with the intake curves from various GLR values in a given tubing can be depicted as shown in Fig. 19-9.

The gas-lift GLR minus the natural GLR times the liquid production rate is the required gas injection rate as shown by Eq. (19-3). A plot of the gas injection rate versus the production rate is the gas-lift performance curve. This is shown in Fig. 19-10, where the maximum production rate corresponds to the gas injection rate for the limit GLR. This graph corresponds to an instant in time in the life of the reservoir. For later times a new gas-lift performance curve will be in effect.

EXAMPLE 19-7
Development of gas-lift performance curve

With the IPR curve described by Eq. (19-14) (Example 19-3) and a well at 8000 ft depth whose gradient curves for 800 and 500 STB/d were given in Figs. 19-5 and 19-6, develop a gas-lift performance curve assuming that the gas injection valves are at the bottom of the well. The average reservoir pressure, $\bar{p}$, is 3050 psi, and the natural GLR is 300 SCF/STB.

Solution Figure 19-11 is a graph of the intersection of the IPR and the optimum gas-lift performance curve, that is, the locus of the points corresponding to the limit GLR for each production rate. Maximum production rate is 825 STB/d, which corresponds to a limit GLR of 3800 SCF/STB (gradient curves are not shown for this rate).

From Eq. (19-3), the gas injection rate for the maximum production rate of 825 STB/d and limit GLR=3800 SCF/STB is

$$q_g = 825(3800 - 300) = 2.89 \times 10^6 \text{ SCF/d} \tag{19-25}$$

Figure 19-12 is the gas-lift performance curve for this well. For production rates other than the maximum, the gas injection rate could be larger or smaller. This performance curve will change with time, as will be shown in Example 19-12. ◇

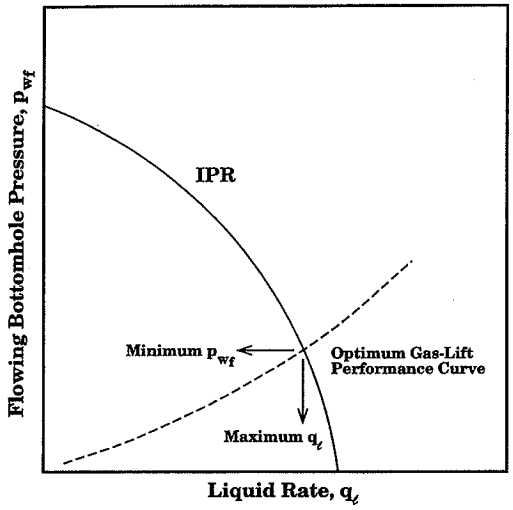

Figure 19-7
IPR and optimum gas-lift performance (at limit GLR).

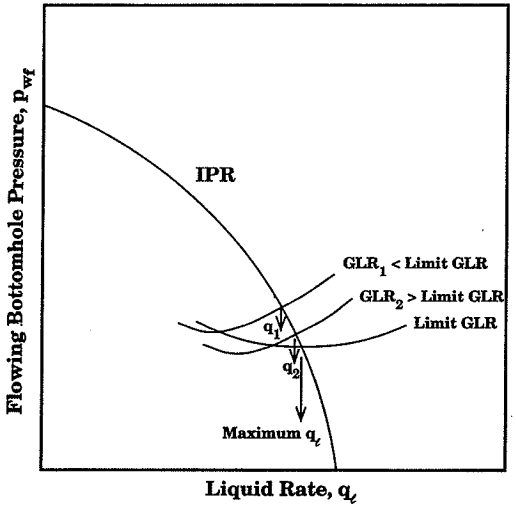

Figure 19-8
Maximum production rate is at the limit GLR. Larger or smaller values of GLR will result in smaller production rates.

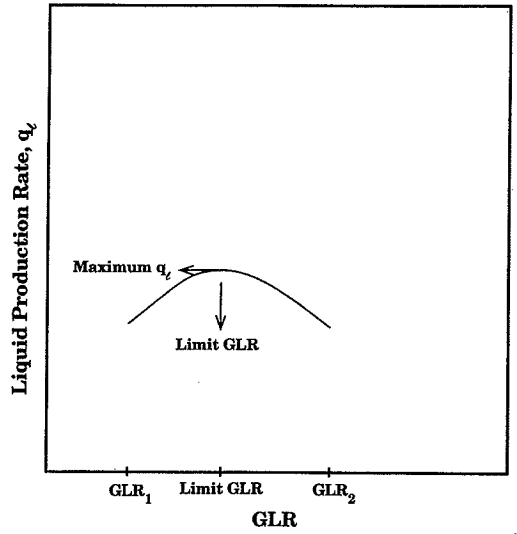

Figure 19-9
Liquid production rate versus GLR. Limit GLR corresponds to maximum q_l.

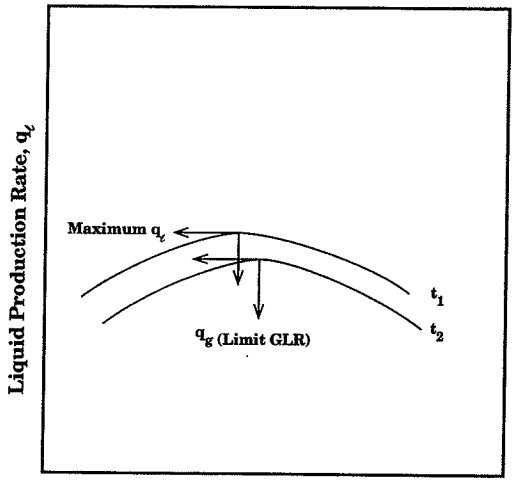

Figure 19-10
Gas-lift performance curve. Time dependency.

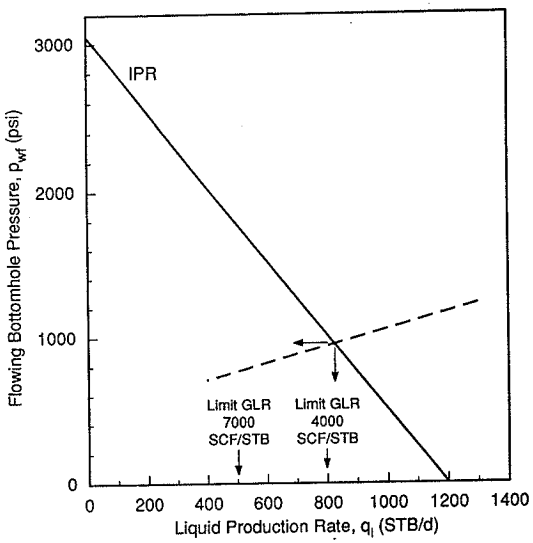

Figure 19-11
IPR and optimum gas lift (Example 19-7).

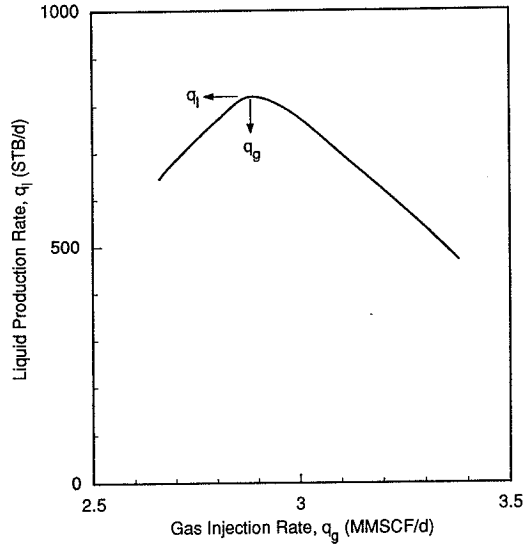

Figure 19-12
Gas-lift performance curve (Example 19-7).

EXAMPLE 19-8
Near-wellbore damage and gas lift

Suppose that wellbore damage ($s \approx +9$) would reduce the IPR curve used in Examples 19-3 and 19-7 to

$$q_l = 0.22(\bar{p} - p_{wf}) \tag{19-26}$$

what would be the maximum production rate and the associated gas-lift requirements?

Solution Figure 19-13 shows the new IPR curve and its intersection with the optimum gas-lift curve. The point of intersection is at q_l=500 STB/d. From Fig. 19-12 (done for Example 19-7) at 500 STB/d, the gas injection rate, q_g, is 3.35×10^6 SCF/d. If q_l=500 STB/d, then, from Eq. (19-26),

$$p_{wf} = 3050 - \frac{500}{0.22} = 780 \text{ psi} \tag{19-27}$$

If, though, the gas injection rate for the undamaged well were maintained ($q_g = 2.89 \times 10^6$ SCF/d for q_l = 825 STB/d—see Example 19-7), then the GLR would be

$$\text{GLR} = \frac{q_g}{q_l} + (\text{GLR})_{\text{natural}} \tag{19-28}$$

and therefore

$$\text{GLR} = \frac{2.89 \times 10^6}{500} + 300 = 6100 \text{ SCF/STB} \tag{19-29}$$

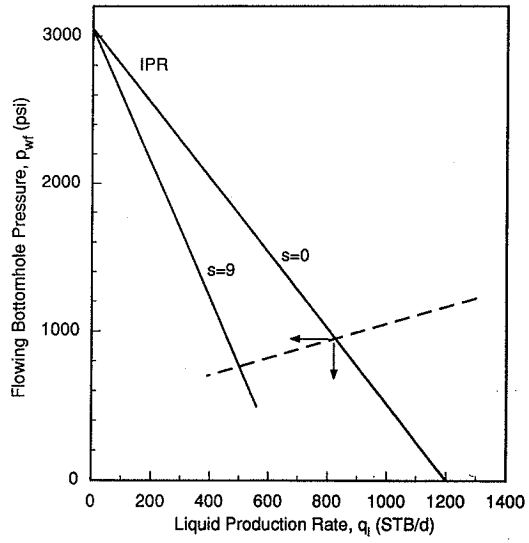

Figure 19-13
Wellbore damage and its effect on gas-lift performance (Example 19-8).

It can be calculated readily that at GLR=6100 SCF/STB and H=8000 ft the flowing bottomhole pressure would be 810 psi rather than 780 psi. This would tend to reduce the production rate further. It should be remembered always that for a given production rate there is always one specific limit GLR. This example also shows that optimized gas lift not only cannot offset wellbore damage but will require a larger gas injection rate (larger GLR) to lift the maximum possible liquid production rate. It is then evident that matrix stimulation must be a continuous concern of the production engineer, and any production-induced damage should be removed periodically to allow optimum well performance. ◇

EXAMPLE 19-9

Limited gas supply; economics of gas lift

In Example 19-8 the required gas injection rate for maximum production was the one corresponding to the limit GLR. This would assume unlimited gas supply. Since this is frequently not the case, repeat the well deliverability calculation for 0.5, 1, and 5×10^5 SCF/d gas injection rates, respectively. If the cost of gas injection is \$0.5/HHP-hr, the cost of separation is \$1/(MSCF/d), and the price of oil is \$30/STB, develop a simple economic analysis (benefits minus costs) versus available gas rate. Use the IPR curve for Example 19-3, $\bar{p}$=3050 psi, and natural GLR=300 SCF/STB.

Solution If only a gas injection rate of 5×10^4 SCF/d is available, then if, for example, q_l=500 STB/d, the GLR would be [from Eq. (19-8)]

$$\text{GLR} = \frac{5 \times 10^4}{500} + 300 = 400 \text{ SCF/STB} \tag{19-30}$$

From Fig. 19-3 at GLR=400 SCF/STB, the flowing bottomhole pressure (with p_{tf} =100 psi) is 1500 psi. Similar calculations can be done with the gradient curves for other flow rates. The resulting gas-lift performance curve is shown in Fig. 19-14. In addition to $q_g = 5 \times 10^4$ SCF/d, the two other curves, corresponding to 1 and 5×10^5 SCF/d, are also drawn. Intersections with the IPR curve would lead to the expected production rates and flowing bottomhole pressures. With the help of Eq. (19-12), the surface pressure can be calculated (assuming 100 psi pressure drop across the valve). Finally, from Eq. (19-19), the horsepower requirements are calculated (using p_{in}=100 psi). The results are shown in Table 19-1.

Table 19-1

Well Performance with Unlimited and Limited Gas Injection Rates

q_g (SCF/d)	q_l (STB/d)	p_{wf} (psi)	p_{surf} (psi)	HHP
5×10^4	615	1475	1310	7.5
1×10^5	660	1360	1220	14.5
5×10^5	750	1130	1025	66
2.89×10^6	825	935	865	348

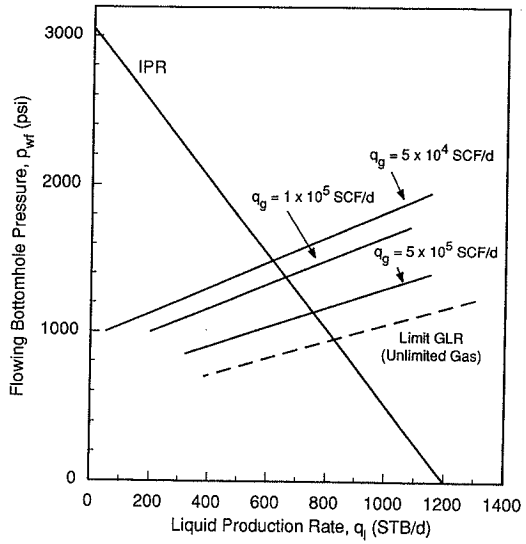

Figure 19-14
Production with gas lift with unlimited and limited gas injection rate (Example 19-9).

An economic comparison between the various options is made below considering the 5×10^4 SCF/d injection rate as a base case. Incremental benefits between this and the 1×10^5 SCF/d rate are $\Delta q_l \times$ (\$/STB) = $(660-615) \times 30$ = \$1350/d. Incremental costs are ΔHHP $\times$ 24$\times$ (\$/HHP - hr)= $(14.5 - 7.5)(24)(0.5)$ = \$84/d and $\Delta q_g \times$ \$1/MSCF = $[(1 \times 10^5) - (5 \times 10^4)](1/1000)$ = \$50/d. Therefore the incremental benefits are 1350 − 134 = \$1220/d.

Similarly, for $q_g = 5 \times 10^5$ SCF/d, incremental benefits are \$2900/d. Finally, for the limit GLR ($q_g = 2.89 \times 10^6$), the incremental benefits are −\$720/d; that is, the incremental production rate cannot compensate for the incremental compression and separation costs.

This type of calculation, of course, is indicated always. It depends heavily on local costs and, especially, like everything else in production engineering, on the price of oil. ◇

EXAMPLE 19-10

Tubing size versus gas-lift requirements

The IPR for a high-capacity reservoir with producing water–oil ratio equal to 1 is

$$q = 1.03(\bar{p} - p_{wf}) \tag{19-31}$$

If the average reservoir pressure, $\bar{p}$, is 3550 psi and the natural GLR is 300 SCF/STB, calculate the required rate of gas to be injected at the bottom of the well (H=8000 ft) for three different tubing sizes (2.5 in., 3.5 in., and 4.5 in., respectively) in order to produce 2000 STB/d of liquid. The wellhead pressure is 100 psi.

Solution If q=2000 STB/d, then, from Eq. (19-31), p_{wf} must be equal to 1610 psi. Figures 19-15, 19-16, and 19-17 are the gradient curves for q_l=2000 STB/d (50% water, 50% oil) for the three tubing sizes.

From Fig. 19-15, at H=8000 ft and p_{wf}=1610 psi, the GLR must be 800 SCF/STB. Since the natural GLR is 300 SCF/STB, the required gas injection rate, q_g, must be $2000(800-300) = 1 \times 10^6$ SCF/d.

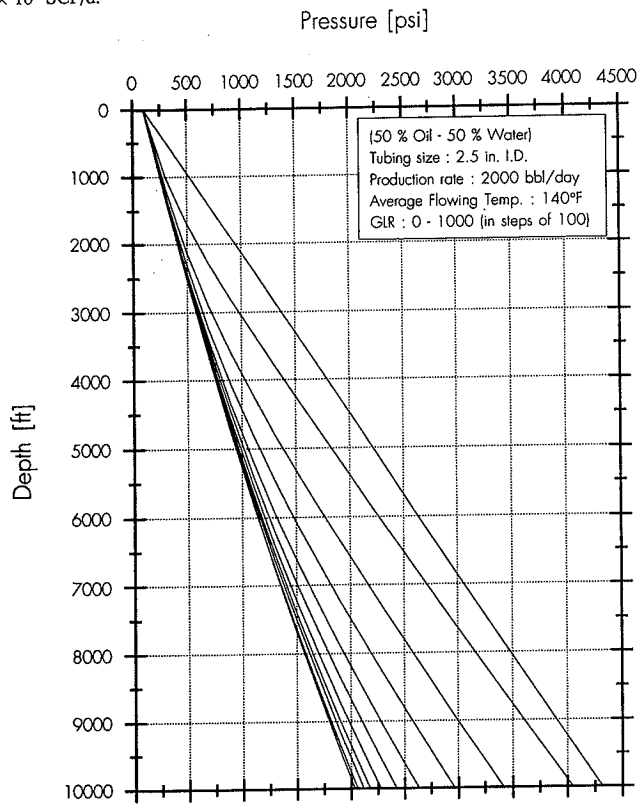

Figure 19-15
Gradient curves for q_l=2000 STB/d and tubing I.D.=2.5 in. (Example 19-10).

From Fig. 19-16 (for the 3.5-in. well), the required GLR for the same H and p_{wf} would be only 350 SCF/STB and therefore the gas injection rate would be only $2000(350-300) = 1 \times 10^5$ SCF/d, an order of magnitude smaller. Finally, as can be seen readily from Fig. 19-17, the natural GLR would be sufficient to lift the liquid production rate if the tubing diameter is 4.5 in.

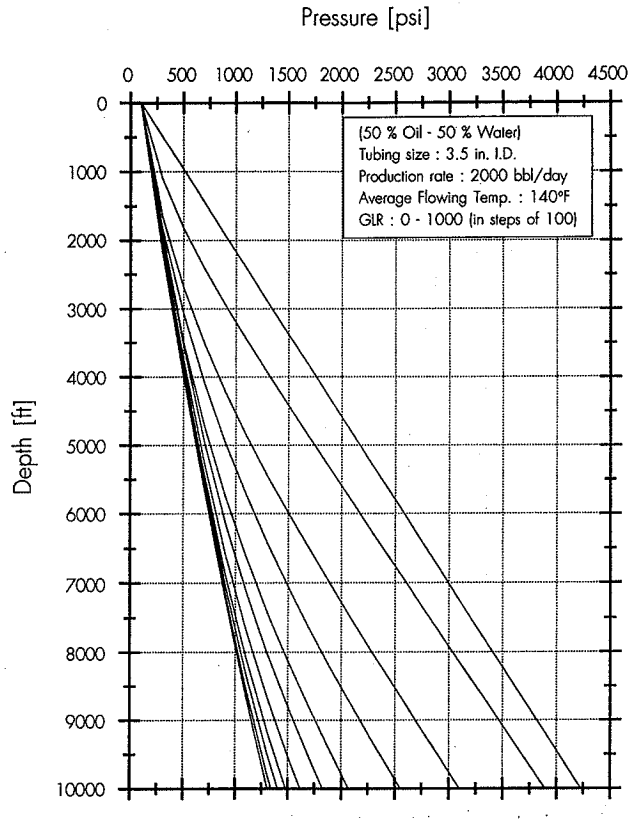

Figure 19-16
Gradient curves for q_l=2000 STB/d and tubing I.D.=3.5 in. (Example 19-10).

This calculation shows the importance of the tubing size selection (and the associated economics of well completion) versus gas-lift requirements (i.e., volume of gas, compression and separation costs). ◇

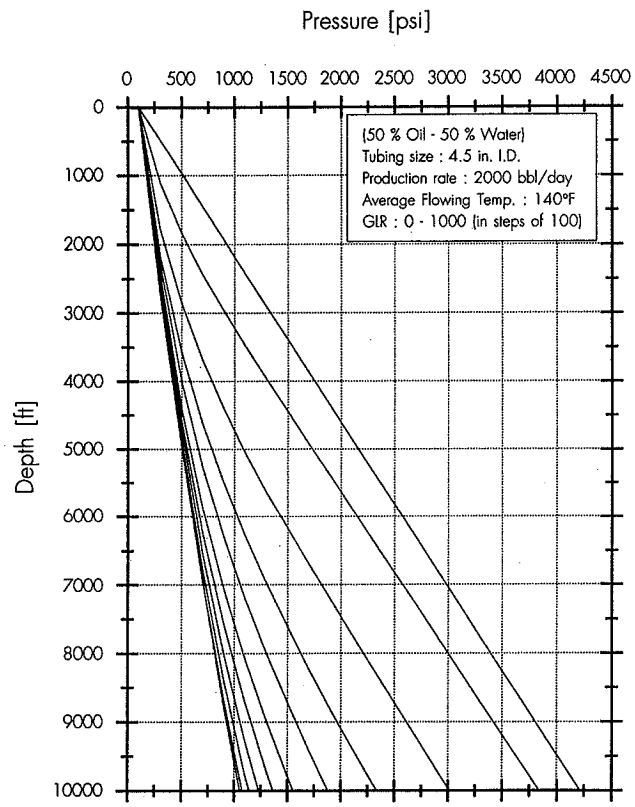

Figure 19-17
Gradient curves for q_l=2000 STB/d and tubing I.D.=4.5 in. (Example 19-10).

19-8 GAS-LIFT REQUIREMENTS VERSUS TIME

As the reservoir pressure declines, the driving force in the reservoir is reduced and therefore, in order to sustain a given production rate, the flowing bottomhole pressure must be reduced accordingly. This was discussed in Section 19-5 and was shown in Example 19-6. In that example it was concluded that sustaining a production rate would require an increase in the gas injection rate as the reservoir pressure declines. In the same example the production rate was not the maximum possible for the given reservoir pressure (500 STB/d

versus 825 STB/d, as shown in Example 19-7, where maximized gas-lift performance was calculated).

Maximizing the liquid production rate with gas lift requires an increase in the gas injection rate, since the limit GLR is larger for smaller production rates in a given tubing size. Again, design of gas lift versus time must be the subject of economic evaluation.

An appropriate method for forecasting gas-lift requirements versus time is as follows.

1. Establish an optimum gas-lift performance curve for the given tubing and reservoir fluid.
2. For each average reservoir pressure, develop a new IPR curve.
3. The intersection of the IPR curves with the optimum gas-lift performance curve is the maximum production rate.
4. This maximum production rate is at the limit GLR, which is also associated with the minimum p_{wf}.
5. Material balance calculations as shown in Chapter 9 can provide the reservoir cumulative production within each reservoir pressure decline interval, $\Delta\bar{p}$.
6. The production rate within this interval and the calculated cumulative production easily allow the calculation of the time required for this pressure decline.
7. Well performance and gas injection rate requirements versus time can then be forecasted.

EXAMPLE 19-11
Maximized production rate with gas lift in a depleting reservoir

What would be the average reservoir pressure for a maximized production rate of 500 STB/d. Use the IPR curve described by Eq. (19-14) (the same as for Examples 19-3 and 19-7). Calculate the flowing bottomhole pressure.

Solution The simplest solution to this problem can be obtained graphically from Fig. 19-11. The maximum production rate must be at the intersection of the new IPR curve (slope 0.39) and the optimum gas-lift curve. Thus, a parallel IPR (Fig. 19-18) is drawn, which intersects the vertical axis at an average reservoir pressure, $\bar{p}$, equal to 2050 psi. From the same figure or from the IPR equation, the corresponding flowing bottomhole pressure, p_{wf}, is 770 psi. ◇

EXAMPLE 19-12
Onset of gas lift in the life of a well; need for gas lift

Use the well described in Appendix B. Suppose that the depth is 8000 ft. If there is to be an attempt to sustain the production rate at 1000 STB/d, could gas lift play a role? If so, *when* should it begin, and what should be the location of the gas lift valves versus time? Assume that the well is completed with a 2 3/8-in. tubing (≈ 2-in. I.D.) and that the wellhead pressure requirement is 300 psi.

Solution From the data in Appendix B, the IPR curve for this well, using Eq. (3-11) and allowing for different average reservoir pressures $\bar{p}$ and formation volume factors B_o, is

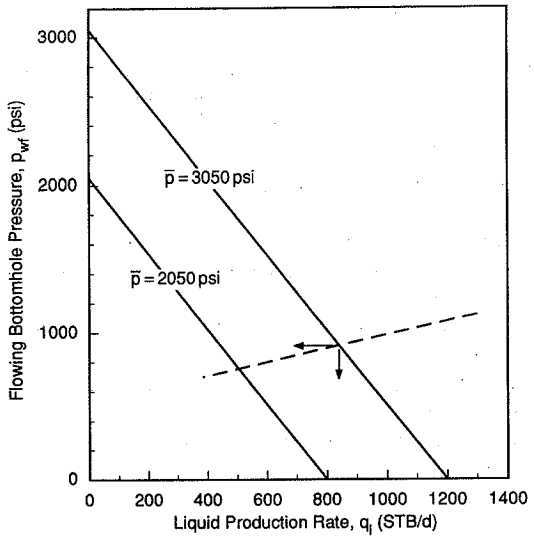

Figure 19-18
IPR curves with declining reservoir pressure for optimized gas lift (Example 19-11).

$$q_o = \frac{0.46\bar{p}}{B_o}\left[1 - 0.2\frac{p_{wf}}{\bar{p}} - 0.8\left(\frac{p_{wf}}{\bar{p}}\right)^2\right] \tag{19-32}$$

Figure 19-19 shows the series of IPR curves for this problem for average reservoir pressures ranging from the initial value (4350 psi) to 3350 psi in increments of 200 psi. The corresponding required flowing bottomhole pressures for q=1000 STB/d can be readily extracted from this figure.

Figure 19-20 is an expanded scale of the flowing gradients for this well for different GLR values. The maximum GLR is 2000 SCF/STB. The curves for GLR > 1600 are practically indistinguishable. The natural GLR for this well is 840 SCF/STB (= R_s). Of course, as the well matures, the producing GLR will increase, reflecting the emergence of a gas cap (although the solution R_s will decrease). To allow for decisions on gas lift, a material balance calculation as suggested by Havlena and Odeh (1963) and a deliverability relationship for solution gas drive as introduced by Tarner (1944) are indicated. This type of calculation was presented in detail in Chapter 9. Table 9-4 gives the physical properties (obtained from Fig. B-1 in Appendix B) and the calculated values of Φ_n and Φ_g for reservoir pressures from $\bar{p}$=4350 to 3350 psi.

The incremental cumulative productions and cumulative productions for oil and gas and the producing GLR (listed as R_{av}) are shown in Table 9-5. The incremental time and total time versus average reservoir pressure for this example are listed in Table 19-2.

The way to interpret these results is as follows. From Fig. 19-19, in the interval between $\bar{p}$=4350 psi and $\bar{p}$=4150 psi for q=1000 STB/d, the p_{wf} should be 2000 psi. From Table

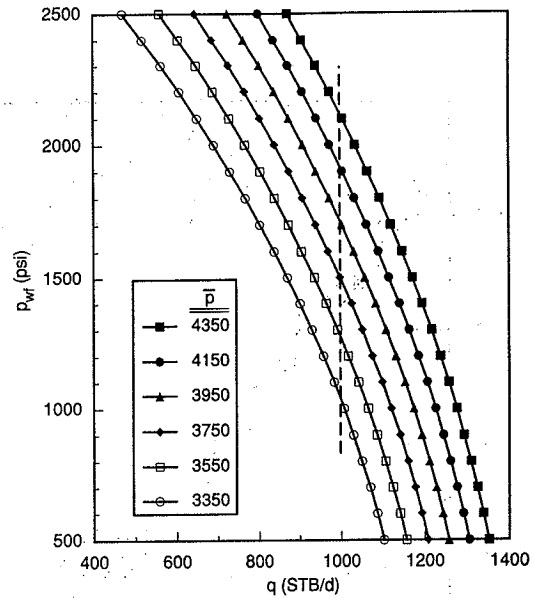

Figure 19-19
IPR curves at different reservoir pressures for Example 19-12.

9-5, the producing natural GLR is 845 SCF/STB. From the gradient curves in Fig. 19-10 at H=8000 ft and GLR=845 SCF/STB, the required p_{wf} would be only 1710 psi. Therefore the well would naturally move the fluid to the top.

At p_{wf}=1710 psi, the producing rate, q, (at average $\bar{p}$=4250 psi) would be [from Eq. (19-32)] equal to 1090 STB/d.

Similar calculations can be done until the reservoir pressure is 3750 psi. The increasing producing natural GLR would shift the required bottomhole pressure to the left, allowing the minimum production rate of 1000 STB/d without the need of artificial lift.

In the interval between 3550 and 3750 psi for q=1000 STB/d, the required p_{wf} is 1400 psi [from Fig. 19-19 or Eq. (19-32)]. From Table 9-5, the producing GLR is 1280 SCF/STB, which would require a bottomhole flowing pressure of 1600 psi (from Fig. 19-20). Gas lift could then be possible. However, as can be seen from Fig. 19-20, the maximum GLR curve at that depth would require a p_{wf} equal to 1560 psi. Therefore, increasing the GLR would require an even larger p_{wf}. The conclusion from this problem is that gas lift cannot be used as a means of artificial lift. Furthermore, the production rate cannot be sustained at 1000 STB/d after the reservoir pressure drops below 3750 psi. The example shown here is the type of calculation that is needed in every well in order to design an artificial lift system in anticipation of future production behavior. ◇

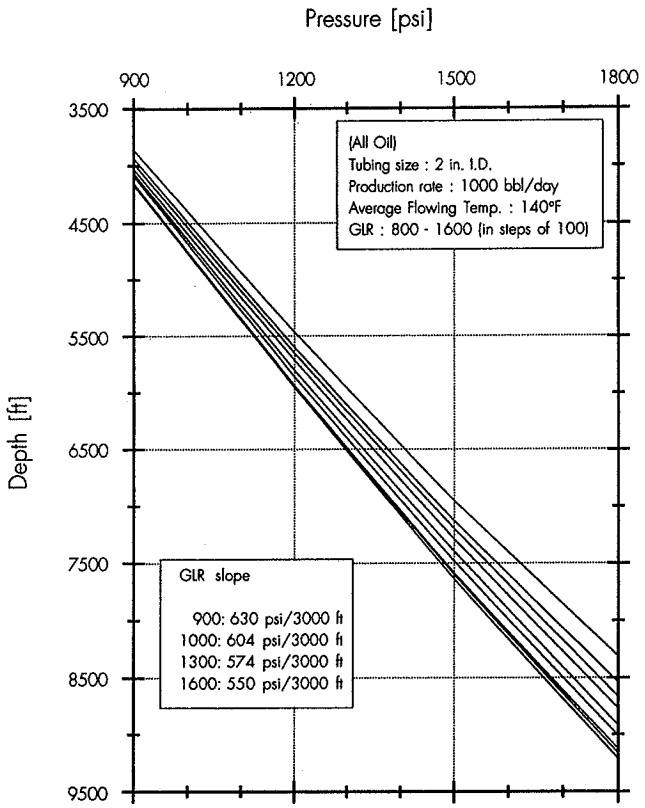

Figure 19-20
Expanded-scale gradient curves for well in Example 19-12.

Table 19-2

Production Prediction versus Time for Well in Example 19-12 (Initial Oil in Place 5.87×10^7 STB for A = 640 acres)

$\bar{p}$ (psi)	ΔN_p (STB)	Δt (days)	t (days)
4350			
	1.71×10^5	171	
4150			171
	4.94×10^5	494	
3950			665
	7.04×10^5	704	
3750			1370
	7.4×10^5	740	
3550			2110
	6.46×10^5	646	
3350			2756

REFERENCES

1. Bertuzzi, A. F., Welchon, J. K., and Poettman, F. H., "Description and Analyses of an Efficient Continuous Flow Gas-Lift Installation," *JPT*, pp. 271–278, November 1953.
2. Brown, K. E., Day, J. J., Byrd, J. P., and Mach., J., *The Technology of Artificial Lift Methods*, Petroleum Publishing, Tulsa, OK, 1980.
3. Gilbert, W. E., "Flowing and Gas-Lift Well Performance," *Drill. and Prod. Prac.*, API, p. 143, 1954.
4. Golan, M., and Whitson, C. H., *Well Performance*, 2nd ed., Prentice Hall, Englewood Cliffs, NJ, 1991.
5. Havlena, D., and Odeh, A. S., "The Material Balance as an Equation of a Straight Line," *JPT*, pp. 896–900, August 1963.
6. Poettman, F. H., and Carpenter, P. G., "Multiphase Flow of Gas, Oil and Water through Vertical Flow Strings with Application to the Design of Gas-Lift Installations," *Drill. and Prod. Prac.*, API, pp. 257–317, 1952.
7. Tarner, J., "How Different Size Gas Caps and Pressure Maintenance Programs Affect Amount of Recoverable Oil," *Oil Weekly*, pp. 32–34, June 12, 1944.

PROBLEMS

19-1. Use Fig. 19-3. Suppose that the natural GLR is 200 SCF/STB and the well depth is 10,000 ft. What would be the natural bottomhole pressure to lift this liquid rate? What should be the working GLR for the bottomhole pressure to be 1500 psi? If the average reservoir pressure is 3500 psi, what is the governing IPR for this well? What would be the gas injection rate for this case?

19-2. What would be the production rate if gas with p_{surf}=1000 psi were injected at 5000 ft and if the flowing gradient below the injection point were 0.37 psi/ft? The IPR from Problem 19-1 is

$$q = 0.25(\bar{p} - p_{wf})$$

and the average reservoir pressure, $\bar{p}$, is 3500 psi. The well depth is 8000 ft. What should be the injection point for q_l=400 STB/d?

19-3. Use Fig. 19-3. Gas surface injection pressure is 1000 psi. Calculate the bottomhole pressures at 10,000 ft if the points of injection are at the curves for GLR equal to 400, 600, and 800 SCF/STB, respectively, and if the flowing gradient below the injection points is 0.37 psi/ft. At what average reservoir pressures should these points be activated to sustain a production rate of 500 STB/d? Use the IPR from Problem 19-2.

19-4. Suppose that the following limit GLR values and bottomhole pressures (at H=10,000 ft) correspond to the three production rates listed below.

q_l (STB/d)	GLR (SCF/STB)	p_{wf} (psi)
500	7000	1020
1000	2500	1200
2000	1000	2000

What would be the maximum production rate if the IPR multiplier were 0.6 and if $\bar{p}$=3500 psi? What would be the maximum production rate after the reservoir pressure declines to 3000 and 2500 psi, respectively?

19-5. Calculate the gas injection rates, injection pressure, and horsepower requirements for Problem 19-4. Assume that the natural GLR is 300 SCF/STB.

19-6. Start with the IPR of Problem 19-4. Use Figs. 19-3 (for q_l=500 STB/d) and 19-15 (for q_l=2000 STB/d) for your calculations. Assume that the available gas is only 3×10^5 SCF/d. If the natural GLR is 200 SCF/STB, calculate the expected production rate from this well.

19-7. Suppose that the price of oil is \$30/bbl, the cost of injection is \$0.5/hhp-h, and the cost of separation is \$1/(MSCF/d). If for a production of 1000 STB/d there is a need for 5×10^5 SCF/d of additional gas, what should be the gas rate demand for a production rate of 1200 STB/d? Make any reasonable assumptions for gas injection pressures and depth of injection point.

CHAPTER 20

Pump-Assisted Lift

20-1 INTRODUCTION

Downhole pumps are a common means of boosting the productivity of a well by lowering the bottomhole flowing pressure. Rather than lowering the pressure gradient in the tubing to reduce the bottomhole pressure, as in gas lift, downhole pumps increase the pressure at the bottom of the tubing a sufficient amount to lift the liquid stream to the surface. In fact, the pressure gradient in the tubing is actually higher in a pumped well than it would be without the pump, because most of the gas produced with the liquids is vented through the casing-tubing annulus. A typical well configuration and pressure profiles in the well are shown in Fig. 20-1.

Two types of pumps are used: positive-displacement pumps, which include sucker rod pumps and hydraulic piston pumps; and dynamic displacement pumps, the most common of which are electrical submersible centrifugal pumps and jet pumps. Of these, sucker rod pumps and electrical submersible pumps are the most common, and will be treated in more detail here.

For any well with a downhole pump, the work supplied by the pump is related to the increase in pressure across the pump by the mechanical energy balance equation, which for an incompressible fluid is

$$W_s = \frac{p_2 - p_1}{\rho} + \frac{u_2^2 - u_1^2}{2g_c} + F \tag{20-1}$$

For liquids, the kinetic energy term is usually small compared to the other terms, so the equation simplifies to

$$W_s = \frac{p_2 - p_1}{\rho} + F \tag{20-2}$$

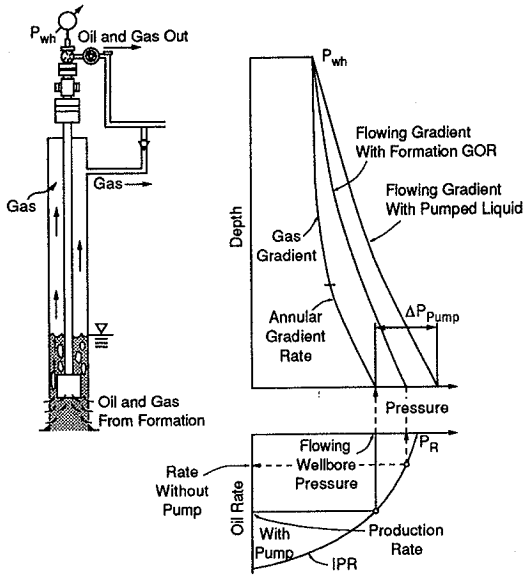

Figure 20-1
Well configuration and pressure profiles for an oil well. (*After Golan and Whitson, 1991.*)

where W_s is the work supplied by the pump, p_2 is the pressure in the tubing just above the pump, p_1 is the pressure just below the pump, and F is the frictional loss in the pump.

To determine the size and power requirements for a downhole pump, the pressures on either side of the pump are related to the the bottomhole flowing pressure by the pressure gradient in the gas-liquid stream below the pump and to the surface pressure by the single-phase liquid gradient in the tubing. Thus, a design procedure is as follows: From the IPR relationship, the p_{wf} needed for a desired production rate is determined; from a two-phase flow calculation, the pressure just below the pump, p_1, is calculated from p_{wf} (when the pump is near the production interval, $p_1 \approx p_{wf}$); from the surface tubing pressure, p_2 is determined based on single-phase liquid flow at the desired rate. Once the pressure increase required from the pump is known, the work required from the pump is found, usually based on empirical knowledge of the frictional losses in the pump (the pump efficiency.) The flow relationships presented in Chapter 7 can be used to calculate the needed pressure profiles in the wellbore below the pump and in the tubing.

EXAMPLE 20-1
The pressure increase needed from a downhole pump

For the well described in Appendix A, it is desired to obtain a production rate of 500 STB/d at a time when the average reservoir pressure has declined to 3500 psi. Calculate the pressure increase needed from a downhole pump, assuming the pump is set at 9800 ft, just above the production interval, and that the surface tubing pressure is 100 psig. The well has 2 7/8-in., 8.6-lb$_m$/ft tubing (I.D. = 2.259 in.) and a relative roughness of 0.001.

Solution IPR curves for this well for different reservoir pressures are presented in Fig. 2–7. From this figure, when the average reservoir pressure is 3500 psi, for a production rate of 500 STB/d, p_{wf} is 1000 psi. Since the pump is set near the production interval, $p_1 = 1000$ psi. p_2 is calculated from Eq. (7-15) for single-phase liquid flow. From Appendix A, the API gravity of the oil is 28°, equivalent to a specific gravity of 0.887, and the oil viscosity is 1.7 cp. From Eq. (7-22), we calculate the potential energy pressure drop to be 3760 psi. Since we can assume the oil to be incompressible, the kinetic energy pressure drop will be 0. To determine the frictional pressure drop, the Reynolds number is found with Eq. (7-7) to be 10,665 and the friction factor from the Moody diagram (Fig. 7-7) or the Chen equation [Eq. (7-35)] is 0.0073. The average velocity is 1.165 ft/s. Using Eq. (7-31),

$$\Delta p_F = \frac{(2)(0.0073)(0.887)(62.4)(1.165)^2(9,800)}{(32.17)(2.259/12)} = 1775 \text{ lb}_f/\text{ft}^2 = 12.3 \text{ psi} \qquad (20\text{-}3)$$

so

$$\Delta p = \Delta p_{PE} + \Delta p_F = 3760 + 12.3 = 3770 \text{ psi} \qquad (20\text{-}4)$$

and

$$p_2 = p_{surf} + \Delta p = 100 + 14.7 + 3770 = 3885 \text{ psi} \qquad (20\text{-}5)$$

so $p_2 - p_1$, the pressure increase needed from the pump, is $3885 - 1000 = 2885$ psi. ◇

20-2 POSITIVE-DISPLACEMENT PUMPS

20-2.1 Sucker Rod Pumping

Sucker rod pump equipment. The surface and downhole equipment for a rod-pumped well are shown in Fig. 20-2. The rotary motion of the crank is translated to a reciprocating motion of the polished rod by the Pitman and the walking beam; the sucker rods transmit the reciprocating motion from the polished rod to the downhole pump. The pump (Fig. 20-3) consists of a barrel with a ball-and-seat check valve at its bottom (the standing valve) and a plunger containing another ball-and-seat check valve (the traveling valve.) When the plunger moves up, the standing valve opens, the traveling valve closes, and the barrel fills with fluid. On a down stroke, the traveling valve opens, the standing valve closes, and the fluid in the barrel is displaced into the tubing. For a detailed review of rod pump equipment, see Brown (1980a).

Volumetric dispacement with sucker rod pumps. Positive-displacement pump performance is evaluated based on the volume of fluid displaced, not the pressure increase generated by the pump, since the compression of the wellbore fluid in the pump will create enough pressure to displace the fluid in the tubing. The volumetric flow rate displaced by a rod pump is

$$q = 0.1484 N E_v A_p S_p \qquad (20\text{-}6)$$

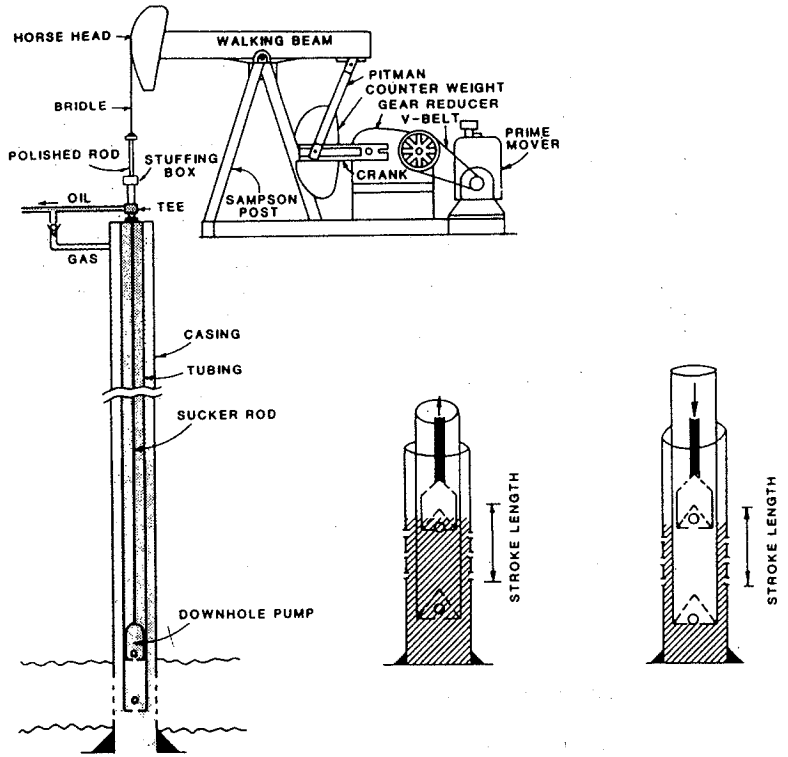

Figure 20-2
Rod-pumped well. (*From Golan and Whitson, 1991.*)

where q is the downhole volumetric flow rate (bbl/d), N is the pump speed (strokes per minute, spm), E_v is the volumetric efficiency, A_p is the plunger cross-sectional area (in.^{2}), and S_p is the effective plunger stroke length (in.). The surface production rate will be the downhole rate divided by the formation volume factor.

The volumetric efficiency is less than 1 because of leakage of the fluid around the plunger. The volumetric efficiency is usually 0.7 to 0.8 for a properly working rod pump.

EXAMPLE 20-2
Calculation of required pump speed

Determine the pump speed (spm) needed to produce 250 STB/d at the surface with a rod pump having a 2-in.-diameter plunger, a 50-in. effective plunger stroke length, and a volumetric efficiency of 0.8. The oil formation volume factor is 1.2.

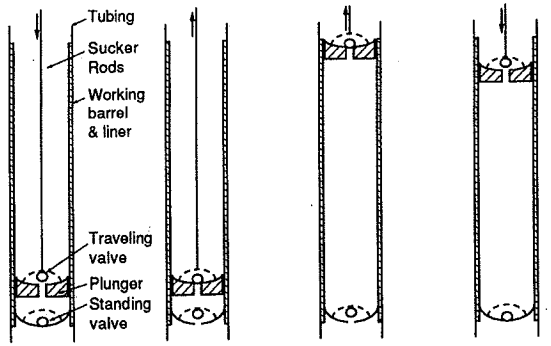

Figure 20-3
Sucker rod pump. (*From Brown, 1980a.*)

Solution The downhole volumetric flow rate is calculated by multiplying the surface rate by the formation volume factor. The cross-sectional area of the 2-in.-diameter plunger is π in.^{2}. Then, using Eq. (20-5),

$$N = \frac{qB_o}{0.1484E_vA_pS_p} = \frac{(250 \text{ STB/d})(1.2)}{(0.1484)(0.8)(\pi \text{ in.}^2)(50 \text{ in.})} = 16 \text{ spm} \qquad (20\text{-}7)$$

The required pump speed is found to be 16 spm. Sucker rod pumps are typically operated at speeds ranging from 6 to 20 spm. The highest speed is limited to avoid excessive vibration of the rods due to resonation. For steel rods, the lowest pump speed that can cause the rods to vibrate at their natural frequency is (Craft et al., 1962)

$$N = \frac{237{,}000}{L} \qquad (20\text{-}8)$$

where L is the length of the rod string (in ft). Pump speed should be kept below this limiting value. ◇

Effective plunger stroke length. The effective plunger stroke length will differ from and generally be less than the polished rod stroke length because of the stretching of the tubing and the rod string and because of overtravel caused by the acceleration of the rod string. Thus,

$$S_p = S + e_p - (e_t + e_r) \qquad (20\text{-}9)$$

where S is the polished rod stroke length, e_p is the plunger overtravel, e_t is the length the tubing is stretched, and e_r is the length the rod string is stretched. Note that if the tubing is anchored, the tubing stretch will be zero. Assuming harmonic motion of the polished rod and elastic behavior of the rod string and tubing, the effective plunger stroke length is

$$S_p = S + \frac{(5.79 \times 10^{-4})SL^2N^2}{E} - \frac{5.20\gamma_1 HA_pL}{E}\left(\frac{1}{A_t} + \frac{1}{A_r}\right) \qquad (20\text{-}10)$$

In this equation, E is Young's modulus (about 30×10^6 psi for steel), γ_l is the specific gravity of the fluid, H is the fluid level depth in the annulus ($H = L$ if the fluid level is at the pump), A_t is the cross-sectional area of the tubing, A_r is the cross-sectional area of the rods, and all other variables are defined as before. Cross-sectional areas of common sizes of rods and tubing are given in Table 20-1.

Table 20-1

Sucker Rod and Tubing Cross-Sectional Areas

Sucker Rods			
Rod Size (in.)	Weight (lb_m/ft)		Area (in.^{2})
5/8	1.16		0.307
3/4	1.63		0.442
7/8	2.16		0.601
1	2.88		0.785
1 1/8	3.64		0.994
Tubing			
Nominal Size (in.)	Weight (lb_m/ft)	O.D. (in.)	Area (in.^{2})
1 1/2	2.90	1.900	0.800
2	4.70	2.375	1.304
2 1/2	6.50	2.875	1.812
3	9.30	3.500	2.590
3 1/2	11.00	4.000	3.077
4	12.75	4.500	3.601

EXAMPLE 20-3
Effective plunger stroke length

Calculate the effective plunger stroke length for a well with a rod pump set at 3600 ft. The well has 3/4-in. sucker rods and 2 1/2-in. tubing, and the specific gravity of the produced liquid is 0.90. The pump speed is 20 spm, the plunger is 2 in. in diameter, and the polished rod stroke length is 64 in. The well is pumped off, so the fluid level is at the pump depth.

Solution From Table 20-1, the cross-sectional areas of the rods and the tubing are 0.442 and 1.812 in.^{2}, respectively. Since the fluid level is at the pump, $H = L = 3600$ ft. Applying Eq. (20-9),

$$S_p = 64 + \frac{(5.79 \times 10^{-4})(64)(3600)^2(29)^2}{30 \times 10^6} - \frac{(5.2)(0.9)(3600)(3.14)(3600)}{30 \times 10^6}\left(\frac{1}{1.812} + \frac{1}{0.442}\right) \tag{20-11}$$

$$= 64 + 6.4 - 17.9 = 52.5 \text{ in.}$$

◇

Prime mover power requirements. The next step in designing a sucker rod pump installation is the determination of the power requirements for the prime mover. The prime mover must supply sufficient power to provide the useful work needed to lift the fluid; to overcome frictional losses in the pump, the polished rod, and the rod string; and to allow for inefficiencies in the prime mover and the surface mechanical system. Thus the required prime mover power is

$$P_{pm} = F_s(P_h + P_f) \tag{20-12}$$

where P_{pm} is the prime mover horsepower, P_h is the hydraulic horsepower needed to lift the fluid, P_f is the power dissipated as friction in the pump, and F_s is a safety factor accounting for prime mover inefficiency. The safety factor can be estimated as 1.25 to 1.5 (Craft et al., 1962); for several empirical approaches to determining this factor, the reader is referred to Brown (1980a).

The hydraulic power is usually expressed in terms of net lift, L_N,

$$P_h = (7.36 \times 10^{-6})\, q \gamma_l L_N \tag{20-13}$$

where the flow rate is in bbl/d and the net lift is in ft of produced fluid. The net lift is the height to which the work provided by the pump alone can lift the produced fluid. If the tubing and casing pressure is zero at the surface and the fluid level in the annulus is at the pump, the net lift is simply the depth at which the pump is set. More generally, the fluid in the annulus above the pump exerts the force of its weight in helping to lift the fluid in the tubing and the tubing pressure is an additional force that the pump must work against. In this case, the net lift is

$$L_N = H + \frac{p_{tf}}{0.433\gamma_l} \tag{20-14}$$

where H is the depth to the liquid level in the annulus and p_{tf} is the surface tubing pressure in psig. To obtain Eq. (20-14), we have assumed that the pressure at the liquid surface in the annulus is atmospheric pressure (i.e., the casing surface pressure is atmospheric and the hydrostatic head of the column of gas in the annulus is negligible) and that the average density of the liquid in the annulus is the same as that in the tubing (we are neglecting the gas bubbling through the liquid in the annulus.)

The horsepower needed to overcome frictional losses is empirically estimated as

$$P_f = 6.31 \times 10^{-7} W_r S N \tag{20-15}$$

where W_r is the weight of the rod string (lb_m), S is the polished rod stroke length (in.), and N is the pump speed (spm).

EXAMPLE 20-4
Prime mover power requirements

For the well described in Example 20-3, calculate the power requirement for the prime mover if the surface tubing pressure is 100 psig and the fluid level in the annulus is 200 ft above the pump.

Solution Since the fluid level is 200 ft above the pump, the fluid level, H, is $3600 - 200 = 3400$ ft. Then, from Eq. (20-14), the net lift is

$$L_N = 3400 + \frac{100}{(0.433)(0.9)} = 3657 \text{ ft} \tag{20-16}$$

The flow rate, obtained from Eq. (20-6) using a volumetric efficiency of 0.8 and the results from Example 20-3, is

$$q = (0.1484)(20)(0.8)(3.14)(52.5) = 391 \text{ bbl/d} \tag{20-17}$$

The hydraulic horsepower is then calculated with Eq. (20-13):

$$P_h = (7.36 \times 10^{-6})(391)(0.9)(3657) = 9.5 \text{ hp} \tag{20-18}$$

Using the data in Table 20-1, the weight of 3600 ft of 3/4-in. sucker rods is 5868 lb_m. The frictional horsepower from Eq. (20-15) is

$$P_f = (6.31 \times 10^{-7})(5868)(64)(20) = 4.7 \text{ hp} \tag{20-19}$$

Finally, using a safety factor of 1.25 in Eq. (20-12), the prime mover horsepower requirement is

$$P_{pm} = (1.25)(9.5 + 4.7) = 18 \text{ hp} \tag{20-20}$$

◇

The effect of gas on pump efficiency. Any downhole pump is adversely affected by the presence of free gas in the fluid being pumped; with sucker rod pumps, the effect can be particularly severe. When gas is present in the pump barrel, much of the pump energy is expended in compressing the gas instead of lifting the liquid. Figure 20-4 illustrates this effect. When gas is present in the pump, on an upstroke, the gas must be compressed until the pressure in the barrel is equal to the pressure in the tubing above the pump before the traveling valve will open and allow fluid to pass into the tubing. On a down stroke, the gas must expand until the pressure is below p_1, the pressure in the casing just below the pump, before the standing valve will open and let wellbore fluids enter the barrel. In extreme cases, essentially nothing will occur in the pump except the expansion and compression of gas; in this instance, the pump is said to be "gas-locked."

Because of these deleterious effects, some means must be employed to exclude most, if not all, of the free gas from entering a sucker rod pump. This is accomplished by setting the pump below the perforations so that the gas will rise out of the liquid stream moving to the pump or by employing various mechanical means to separate the gas from the liquid stream. Downhole devices installed on rod pumps to separate the gas from the liquid are called "gas anchors."

Analysis of rod pump performance from dynamometer cards. The performance characteristics of sucker rod pumps are commonly monitored by measuring the

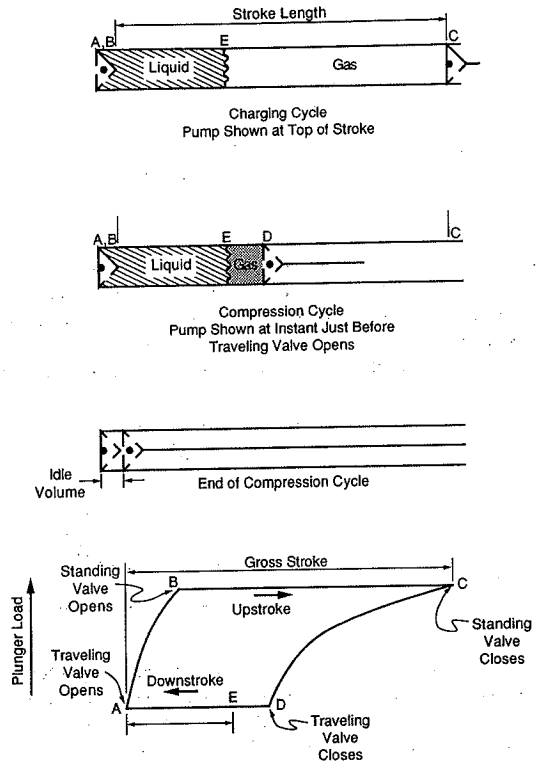

Figure 20-4
Effect of gas on rod pump performance. (*From Golan and Whitson, 1991.*)

load on the polished rod with a dynamometer. A recording of the polished rod load over one complete pump cycle is referred to as a "dynamometer card." The dynamometer card plots polished rod load as a function of rod position.

An ideal dynamometer card for elastic rods is shown in Fig. 20-5. At point a, an upstroke begins and the polished rod load gradually increases as the rods stretch until at point b the polished rod supports the weight of the rods in the fluid and the weight of the fluid. The load remains constant until the downstroke begins at point c. At this time, the standing valve closes and the standing valve supports the weight of the fluid; the polished rod load decreases as the rods recoil until, at point d, the polished rod supports only the weight of the rods in the fluid. The load then remains constant until another cycle begins at point a.

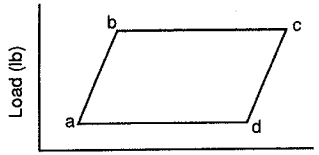

Figure 20-5
Ideal dynamometer card for elastic rods.

Numerous factors will cause an actual dynamometer card to differ from this idealization—a dynamometer card from a properly working rod pump is shown in Fig. 20-6. The acceleration and deceleration of the rod string accounts for most of the difference between the ideal load history and the actual history of the polished rod in a properly operating rod-pumped well. The character of the dynamometer card can sometimes be used to diagnose abnormal characteristics of the pump or well behavior.

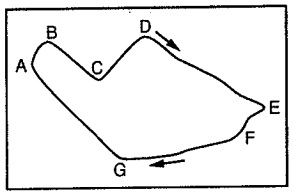

Figure 20-6
Actual dynamometer card. (*From Craft et al., 1962.*)

Figure 20-7 illustrates characteristic dynamometer card shapes for a number of adverse conditions that can be encountered in a rod-pumped well (Craft et al., 1962). A well being pumped at synchronous speed will exhibit the distinctive card shown in Fig. 20-7a. Notice the decreasing load on the upstroke and the loop in the curve at the end of the upstroke. A restriction in the well leads to an increasing load on the upstroke and little pump work, as indicated by the area of the region enclosed by the load curve (Fig. 20-7b).

Excessive friction in the pumping system results in erratic dynamometer responses, like those shown in Fig. 20-7c (sticking plunger) or Fig. 20-7d. Liquid pound occurs when the pump barrel does not fill completely on the upstroke and is characterized by a sudden decrease in load near the end of the downstroke (Fig. 20-7e). Gas pound (Fig. 20-7f) occurs when the pump partially fills with gas and exhibits a similar character to liquid pound, but the decrease in load is not as pronounced on the downstroke. When the pump is almost completely filled with gas, gas lock has occurred, resulting in a dynamometer card like that in Fig. 20-7g. This card shows a decreasing load on the upstroke and little pump work. Finally, plunger undertravel and overtravel are indicated by cards like those in Figs. 20-7h and 20-7i. With plunger undertravel, the load increases throughout the upstroke; while with overtravel, the load w decreases throughout the upstroke.

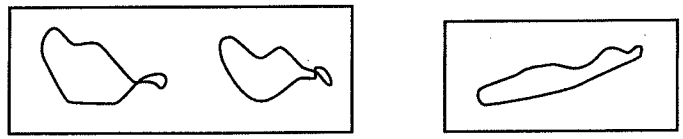

(a) Well being pumped at synchronous speed

(b) Restriction in well

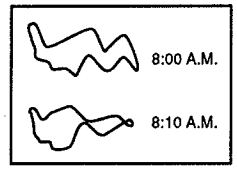

(c) Sticking plunger

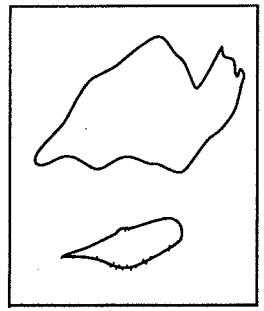

(d) Excessive friction in the pumping system

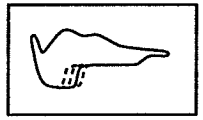

(e) Liquid pound

(f) Gas pound

(g) Gas lock

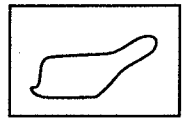

(h) Plunger undertravel

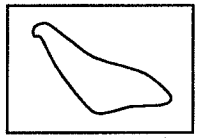

(i) Plunger overtravel

Figure 20-7
Characteristic dynamometer card shapes. (*From Craft et al., 1962.*)

20-2.2 Hydraulic Piston Pumping

The use of sucker rod pumps is not feasible in deep or highly deviated wells because of the weight or large amount of friction of the rods. A positive-displacement pump that can be used in these applications is the hydraulic piston pump. A hydraulic piston pump (Fig. 20-8) consists of an engine with a reciprocating piston driven by a power fluid connected by a short shaft to a piston in the pump end. The pump acts much like a rod pump, except that hydraulic pumps are usually double acting, meaning that fluid is being displaced from the pump on both the up and the down strokes. The high-pressure power fluid is injected down a tubing string from the surface and is either returned to the surface through another string of tubing or is commingled with the produced fluid in the production string. Either water or oil may be used as the power fluid.

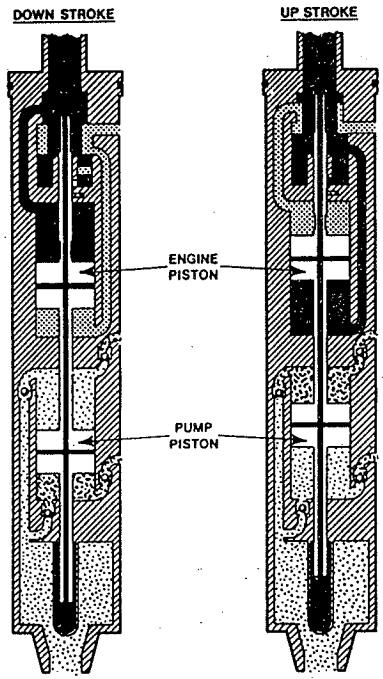

Figure 20-8
Hydraulic piston pump. (*From Brown, 1980b.*)

The production rate from a hydraulic piston pump is related simply to the power fluid flow rate by

$$q = q_{PF}\frac{A_{pump}}{A_{engine}} \tag{20-21}$$

where q_{PF} is the flow rate of the power fluid and A_{pump} and A_{engine} are the piston cross-sectional areas for the pump and the engine, respectively. Thus the production rate is easily changed by changing the power fluid injection rate.

20-3 Dynamic Displacement Pumps

20-3.1 Electrical Submersible Pumps

An electrical submersible pump (ESP) is a multistage centrifugal pump that offers a great deal of flexibility. ESPs are capable of producing very high volumes of fluid, can be used efficiently in deeper wells than sucker rod pumps, and are able to handle some free gas in the pumped fluid. A typical ESP completion is shown in Fig. 20-9. The pump is driven by an electric motor connected by cables to a three-phase power source at the surface. In the United States, ESPs typically operate at 3500 rpm driven by a 60-Hz AC electrical supply, while in Europe, operation at 2915 rpm with a 50-Hz AC power supply is common. The motor is situated so that the produced fluids flow around the motor, providing cooling, either by setting the pump above the producing interval, or by equipping the pump with a shroud that directs the fluids past the motor before entering the pump intake.

Centrifugal pumps do not displace a fixed amount of fluid, as do positive-displacement pumps, but rather create a relatively constant amount of pressure increase to the flow stream. The flow rate through the pump will thus vary, depending on the back pressure held on the system. The pressure increase provided by a centrifugal pump is usually expressed as pumping head, the height of produced fluid that the Δp created by the pump can support:

$$h = \frac{\Delta p}{\rho}\frac{g_c}{g} \tag{20-22}$$

which in field units can be expressed as

$$h = \frac{\Delta p}{0.433\gamma_1} \tag{20-23}$$

The pumping head is independent of the density of the fluid. For a multistage pump, the total head developed is equal to the sum of the pumping head from each stage, or

$$h = N_s h_s \tag{20-24}$$

The pumping head of a centrifugal pump will decrease as the volumetric throughput increases; however, the efficiency of the pump, defined as the ratio of the hydraulic power transferred to the fluid ($q\Delta p$) to the power supplied to the pump, has a maximum at some flow rate for a given pump. The developed head and efficiency of a centrifugal pump depend on the particular design of the pump and must be measured. These characteristics are provided by the pump manufacturer as a pump characteristic chart, such as

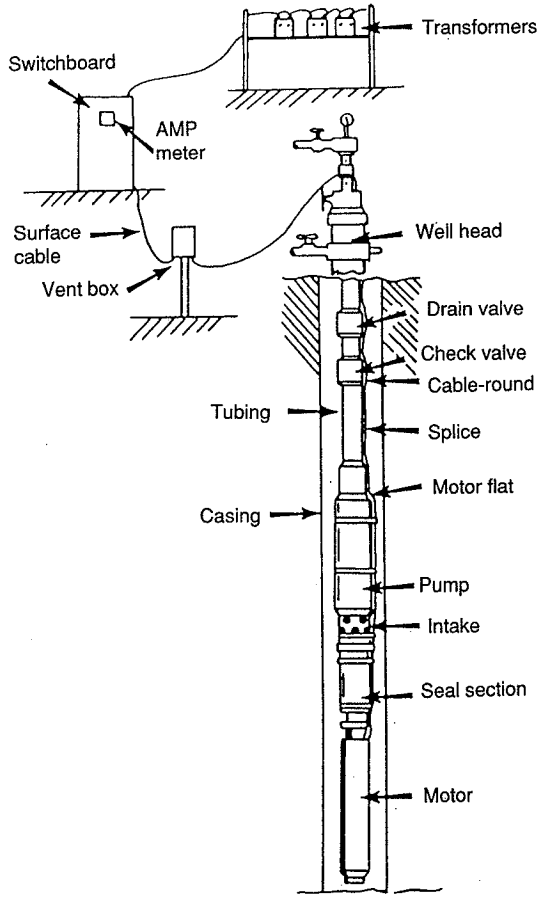

Figure 20-9
Electrical submersible pump completion. (*From Centrilift, 1987.*)

that shown in Fig. 20-10. These characteristics are measured with fresh water. With another fluid of about the same viscosity, the pumping head will be the same, but the power requirements will differ, since the Δp will vary with specific gravity according to Eq. (20-23). Thus, for a fluid of a different density,

$$P_h = P_{h,\text{water}}\gamma_l \tag{20-25}$$

The pump characteristic chart for an ESP is usually for a 100-stage pump, so the head developed per stage is the total head from the chart divided by 100.

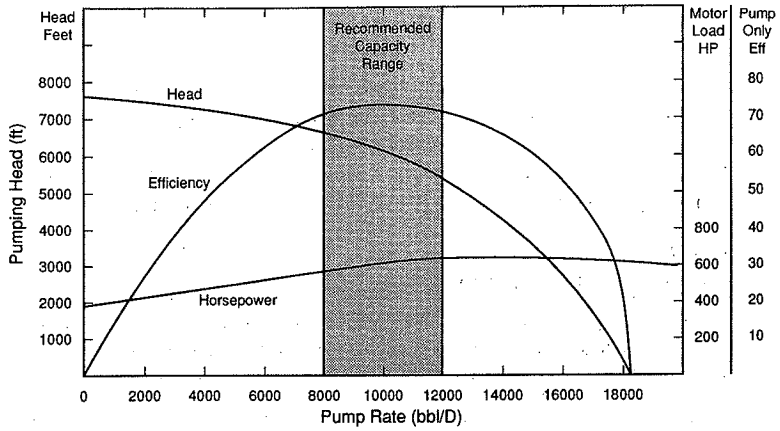

Figure 20-10
Pump characteristic chart.

To design an electrical submersible pump installation, the Δp (pumping head) needed to produce the desired volumetric flow rate must be determined from the well's IPR and the pressure drop that will occur from the pump to the surface. The steps needed to select an appropriate ESP to produce a desired volumetric flow rate are as follows:

1. Determine the appropriate size pump from manufacturer's specifications. An efficient throughput for an ESP depends on the size of the pump, not the Δp developed by the pump. Thus the pump size can be selected based only on the flow rate.
2. From the IPR relationship for the well, determine p_{wf} for the desired production rate.
3. Calculate the minimum pump depth based on p_{wf} and the necessary pump suction pressure. ESPs generally require a suction pressure of 150–300 psi. For zero casing pressure and neglecting the hydrostatic pressure of the gas column in the annulus, the pump depth is

$$H_{\text{pump}} = H - \left(\frac{p_{wf} - p_{\text{suction}}}{0.433\gamma_l}\right) \tag{20-26}$$

where H is the depth of the producing interval, H_{pump} is the pump depth, and p_{suction} is the required suction pressure of the pump. The pump can be set at any depth below this minimum depth, and will often be located nearer the production interval. The pump suction pressure can be calculated from Eq. (20-26) for any pump depth.

4. Determine the required pump discharge pressure from a pressure traverse calculation for the flow in the tubing, using the equations presented in Chapter 7.
5. The Δp needed from the pump is then

$$\Delta p = p_{\text{discharge}} - p_{\text{suction}} \tag{20-27}$$

and the total head from the pump can be calculated with Eq. (20-23).

6. From the pump characteristic curve, the head per stage is read. The number of stages needed is then calculated with Eq. (20-24).
7. The total power requirement for the pump is obtained by multiplying the power per stage from the pump characteristic chart by the number of stages.

EXAMPLE 20-5
Electrical submersible pump design

A 10,000-ft-deep well in the reservoir described in Appendix B is to be produced at a rate of 1000 STB/d with an ESP when the average reservoir pressure is 4350 psi. The well will be equipped with 2 7/8-in. tubing ($\epsilon = 0.001$), the surface tubing pressure is 100 psig, and the well casing is 7 in. Assume that the minimum suction pressure required by the pump is 200 psi. Determine the required specifications for an electrical submersible pump for this application.

Solution The first step is to choose a pump with a capacity range suitable for the desired flow rate. The flow rate through the pump is the downhole volumetric oil rate, assuming that all free gas is excluded from the pump. To determine the formation volume factor for this saturated oil , we must know the pressure.

From Vogel's equation [Eq. (3–54)] or Fig. 3–6, p_{wf} for a rate of 1000 STB/d is 2300 psi. Then, from Fig. B-1, B_o is 1.26, so the flow rate through the pump is (1000 STB/d)(1.26) = 1260 bbl/d. We now choose a pump that will fit in the 7-in. casing and that has a suitable capacity. Figure 20-11 is the pump characteristic chart for one such pump.

Next we check the minimum depth for setting the pump. The specific gravity of the 32°API stock tank oil is 0.865. We will use this value throughout to calculate the hydrostatic head of the oil, even though it will vary somewhat with temperature and pressure. Using Eq. (20-26),

$$H_{\text{pump}} = 10{,}000 - \frac{2300 - 200}{(0.433)(0.865)} = 4390 \text{ ft} \tag{20-28}$$

The pump can be set at any depth below this point. We will assume that the pump is set at 9800 ft; the pump suction pressure is then

$$p_{\text{suction}} = 2300 - (0.433)(0.865)(10{,}000 - 9{,}800) = 2225 \text{ psi} \tag{20-29}$$

The pressure drop in the tubing must now be calculated to determine the pump discharge pressure. Following Example 20-1,

$$\Delta p_{PE} = (0.433)(0.865)(9800) = 3670 \text{ psi} \tag{20-30}$$

The Reynolds number is 26,210, the friction factor is 0.0068, and the mean velocity is 2.94 ft/sec, so

$$\Delta p_F = \frac{(2)(0.0068)(0.865)(62.4)(2.94)^2(9800)}{(32.17)(2.259/12)(144)} = 71 \text{ psi} \tag{20-31}$$

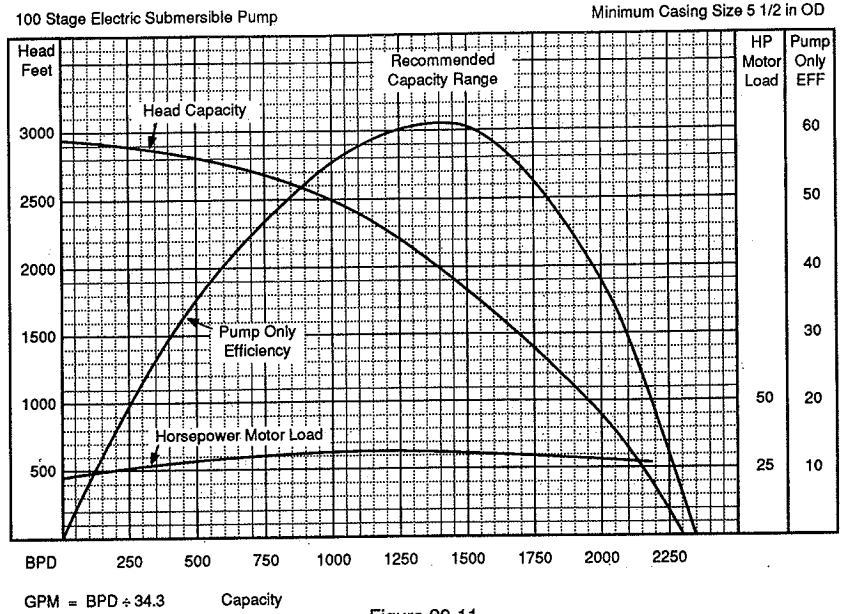

Figure 20-11
Pump characteristic chart for Example 20-5.

so the total Δp is $3670 + 71 = 3741$ psi. The discharge pressure is

$$p_{\text{discharge}} = p_{\text{surf}} + \Delta p = 100 \text{ psig} + 14.7 \text{ psia} + 3741 \text{ psia} = 3856 \text{ psi} \tag{20-32}$$

and the pressure increase from the pump, from Eq. (20-27), is

$$\Delta p = 3856 - 2225 = 1631 \text{ psi} \tag{20-33}$$

The pressure increase from the pump can be expressed as feet of head using Eq. (20-23):

$$h = \frac{1631}{(0.433)(0.865)} = 4350 \text{ ft} \tag{20-34}$$

Reading from Fig. 20-11, for a flow rate of 1260 bbl/d, the head for a 100-stage pump is 2180 ft, or 21.8 ft/stage. The required number of stages is then

$$N_s = \frac{4350}{21.80} = 200 \text{ stages} \tag{20-35}$$

Finally, the horsepower required for the 100-stage pump at 1260 bbl/d from Fig. 20-11 is 35 hp. For the 200-stage pump, the power requirement will be 70 hp.

This example illustrates the optimal pump to produce this well at a fixed rate and fixed average reservoir pressure. As the reservoir pressure declines, the IPR curve will change, and hence, the optimal pump design will gradually change. To design an ESP that will be optimal over a finite life span of the well involves a trade-off between pumping requirements early in the life of the well and later in the life of the reservoir and is ultimately an economic question. Particularly in water-flooded reservoirs, where the water production rate may rise dramatically over the life span of the well, the pumping requirements may change drastically. ◇

The pump characteristics given by ESP manufacturers are for pumping water and must be corrected if the fluid being pumped has a higher viscosity. High fluid viscosity decreases the efficiency of a centrifugal pump and can affect the head developed. Pump manufacturers provide correction charts to account for behavior with high-viscosity fluids.

20-3.2 Jet Pumps

A jet pump is a dynamic-displacement pump that differs dramatically from a centrifugal pump in the manner in which it increases the pressure of the pumped fluid. A schematic of a jet pump is shown in Fig. 20-12. A power fluid is accelerated through a nozzle and then mixed with the produced fluid in the throat of the pump. As the fluids mix, some of the momentum of the power fluid is transferred to the produced fluid; in the diffuser, some of the kinetic energy of the mixed stream is converted to static pressure. A schematic of a typical downhole jet pump is presented in Fig. 20-13.

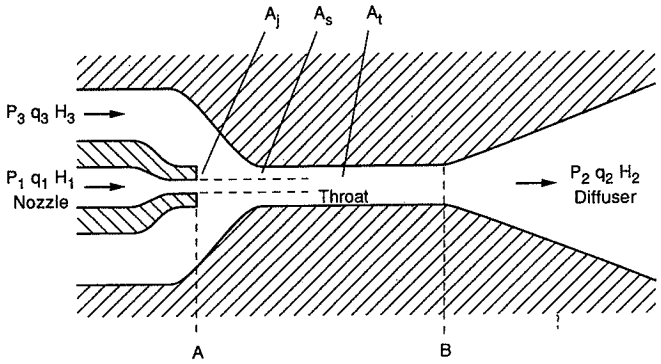

Figure 20-12
Schematic of a jet pump. (*From Brown, 1980b.*)

Jet pumps offer the advantage of having no moving parts, so dirty or gassy fluids can be produced without the wear that will result in positive-displacement pumps. They can also be used at any depth. Drawbacks to jet pumps are their low efficiency (generally in the 20–30% range) and the need for high suction pressure to prevent cavitation in the pump. Jet pump installations are designed using characteristic pump charts in a manner analogous to the design of centrifugal pumps. In addition, careful calculation of the pump depth needed

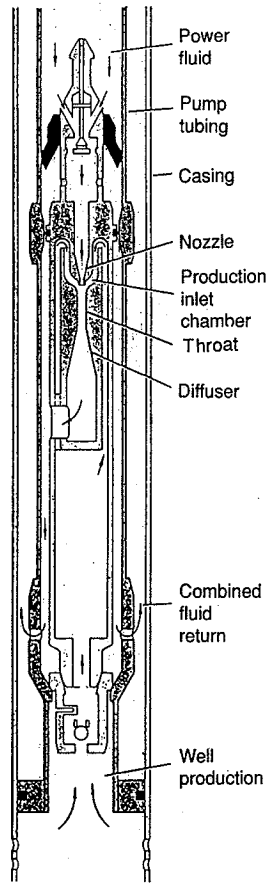

Figure 20-13
Schematic of a downhole jet pump. (*From Brown, 1980b*)

to provide sufficient suction pressure to prevent cavitation is required in designing a jet pump for a well. For further details about jet pumping, the reader is referred to Brown (1980b) or Petrie et al. (1983).

20-4 Selection of Artificial Lift Method; Gas Lift versus Pump-Assisted Lift

The production engineer designing an artificial lift scheme can choose among gas lift and the various types of pumping systems. The optimal system is ultimately based on

economic considerations, requiring a careful comparison among alternatives over the life of the well or the reservoir. However, there are constraints that may eliminate one or more possible lift methods, simplifying the design procedure.

A first consideration is available space, particularly in offshore development. The space limitations of an offshore platform generally preclude the use of rod pumps, with their large surface beam-pumping units. Likewise, in certain environmentally sensitive areas, where minimizing surface facilities is important, rod pumps may not be feasible.

For gas lift to be the lift method of choice, a gas supply must be available, either from the produced associated gas or from other nearby sources, and the reservoir performance must be amenable to gas lift. The amount of gas needed for gas lift is approximately the amount that is required to power the gas compressors, since most of the gas is recycled. As shown in Example 19-12, some wells cannot benefit from gas lift. In general, the higher the natural GLR, the less benefit will be obtained from gas lift. In these wells, pump-assisted lift is the lift mechanism of choice, as illustrated in the following example.

EXAMPLE 20-6

Feasibility of pump-assisted lift instead of gas lift

In Example 19-12, it was shown that for the well of Appendix B that a production rate of 1000 STB/d could not be maintained with gas lift after the average reservoir pressure had declined below 3750 psi. Check the feasibility of using an electrical submersible pump to maintain the target rate by designing an ESP for an average reservoir pressure of 3350 psi.

Solution From Fig. 19-19, for $\bar{p} = 3350$, $p_{wf} = 1050$ psi. From Appendix B, at 1050 psi, B_o is 1.18, so the downhole production rate is 1180 bbl/d. This difference in flow rate from that in Example 20-5 will result in a slight difference in the frictional pressure drop, but will not affect the potential energy pressure drop and thus can be ignored. Following Example 20-5, for the pump set at 9800 ft, $p_{\text{suction}} = 975$ psi and $p_{\text{discharge}} = 3856$ psi (the same as in Example 20-5). Then, $\Delta p_{\text{pump}} = 3856 - 975 = 2881$ psi, equivalent to 7690 ft of head. With the pump of Fig. 20-1 delivering 21.8 ft of head per stage, the number of stages needed is 7690/21.8 = 353 stages. The horsepower required is (350/100) × 35 = 122.5 hp. Thus, an ESP with about 350 stages can deliver the required rate after the average reservoir pressure has declined to 3350 psi. ◇

REFERENCES

1. Brown, K. E., *The Technology of Artificial Lift Methods*, Vol. 2a, Petroleum Publishing Co., Tulsa OK, 1980a.
2. Brown, K. E., *The Technology of Artificial Lift Methods*, Vol. 2b, Petroleum Publishing Co., Tulsa OK, 1980b.
3. Centrilift, *Submersible Pump Handbook*, 4th ed., 1987.
4. Craft, B. C., Holden, W. R., and Graves, E. D., Jr., *Well Design: Drilling and Production*, Prentice Hall, Englewood Cliffs, NJ, 1962.
5. Golan, M., and Whitson, C. H., *Well Performance*, 2nd ed., Prentice Hall, Englewood Cliffs, NJ, 1991.
6. Petrie, H. L., Wilson, P. M., and Smart, E. E., "Jet Pumping Oil Wells," *World Oil*, Part 1, pp. 51–56, November 1983; Part 2, pp. 109–114, December 1983; Part 3, pp. 101–108, January 1984.

PROBLEMS

20-1. For the well described in Example 20-1, calculate the required pressure increase needed from a downhole pump if, in addition to 500 STB/d of oil, the well is producing 500 bbl/d of water. The water has a specific gravity of 1.05 and a viscosity of 2 cp.

20-2. What diameter rod-pump plunger is needed to produce 600 STB/d of oil at a pump speed of 18 spm with a 60-in. effective plunger stroke length? The oil formation volume factor is 1.1, and the volumetric efficiency of the pump is 0.75.

20-3. A rod pump with 3/4-in. rods is set at 6000 ft, and the liquid level in the annulus is 5000 ft. The well is equipped with 2 1/2-in., 6.5-lb_m-ft tubing, and the pump plunger diameter is 2 1/4-in. The polished rod stroke length is 72 in., and the volumetric efficiency of the pump is 0.8. What would be the production rate (STB/d) of a 30°API oil with a formation volume factor of 1.2 if the pump speed is 16 spm?

20-4. Calculate the prime mover horsepower requirement for the pump in Problem 20-3.

20-5. The well described in Example 20-5 is to be produced at a rate of 1300 STB/d using the pump with the characteristics given in Fig. 20-11. The pump is to be set at 9800 ft. Determine the number of pump stages, the horsepower requirements of the pump, and the liquid level above the pump.

CHAPTER 21

Systems Analysis

21-1 INTRODUCTION

In this textbook the petroleum production system, shown schematically in Fig. 1-6, is decomposed into individual parts, each representing a pressure difference in series.

The system and the corresponding pressure drops describe the path of a petroleum fluid beginning in the reservoir, through the completion zone (which can be damaged, equipped with gravel packs and screens or perforations), up the tubing, through the wellhead, and finally along the horizontal lines into separators or other surface facilities. The individual components of the system are interdependent. At any point along the system the rate that the upstream pressure drop may deliver must coincide with the rate that the downstream pressure drop may allow. This concept is demonstrated amply in Chapter 8, where appropriate flow performance relationships (IPR—describing what the reservoir can deliver) are combined with the well vertical lift performance for a given wellhead pressure (as shown in Chapter 7). The combination of the two is the expected production rate *at exactly* the expected flowing bottomhole pressure. Thus, this rate, resulting from the pressure difference between the reservoir and bottomhole pressures, is equal to the flow rate that would result in a pressure difference in the tubing equal to the determined flowing bottomhole pressure minus the given wellhead pressure.

Well deliverability is one use of system analysis. All individual pressure differences depend on well-understood variables but whose values in certain cases may be unknown. By deducing the corresponding pressure difference, the value of an unknown or group of variables may be determined, and remedial action may be taken.

The idea of analyzing individual components of a production system becomes possible because pressure measurements—either direct, such as at the surface, across a choke, or downhole, or indirect (e.g., determining average reservoir pressure from a buildup test)—can be readily available.

Well performance analysis then becomes an exercise of determining the total pressure difference, identifying the components, and isolating the pressure difference that may cause a problem. This type of analysis leads to the determination of near-wellbore damage, turbulence effects, number of open perforations, etc., or even more basic issues such as the optimization of choke or tubing size. Thus, systems analysis is crucial to any petroleum production management strategy, and it may encompass one or more wells.

Brown et al. (1984) have presented an extensive procedure for decoupling the individual components of a petroleum production system and solving for the corresponding pressure and flow rate at any point along the fluid path. They labeled their analysis Nodal (trademark of Schlumberger) analysis.

Traditional systems analysis examines each component individually, allowing a plausible solution but not necessarily an optimum one. Multivariate optimization of production systems can be done with the aid of presently available computers. Thus, the most optimum (profitable) configuration of the entire system can be identified, considering all components simultaneously. Carroll and Horne (1992) have presented such a generalized approach to multivariate optimization. Haid and Economides (1991) offered a similar technique, focusing on the design of hydraulically fractured wells, using the Monte Carlo approach.

21-2 Pressure Drop Components of the System

Depending on the beginning and the end point of the petroleum production system, a total pressure drop Δp can be defined. Usually, for convenience, the pressure difference is between a reservoir pressure, p_i, p_e, or $\bar{p}$, and the inlet pressure to a separator, p_{sep}. The total pressure drop would then be

$$\Delta p = \bar{p} - p_{sep} \tag{21-1}$$

This total pressure drop may be decomposed into a number of individual parts,

$$\Delta p = \Delta p_{res} + \Delta p_s + \Delta p_{comp} + \Delta p_{tub} + \Delta p_{hor} \tag{21-2}$$

where the pressure drops on the right-hand side of Eq. (21-2) are for the reservoir, skin zone, completion, vertical tubing, and horizontal lines, respectively. In turn, these individual pressure drops may be subdivided further, accounting for restrictions, safety valves, chokes, etc.

In Chapter 8, the system was considered between the reservoir and the wellhead. The well bottomhole was the selected point for the reconciliation of two individual components of the total pressure drop, that is, $\bar{p} - p_{wf}$ and $p_{wf} - p_{tf}$.

For each flow rate and the given reservoir pressure, a corresponding p_{wf} can be calculated, taking into account the near-wellbore zone and the completion.

Similarly, for each flow rate and the given wellhead pressure, a corresponding p_{wf} can be determined, accounting for friction and hydrostatic effects while considering the fluid's physical and thermodynamic properties (Chapter 7). If these two, independently derived, relationships have a point of intersection, it will be the required solution to the problem,

that is, the well deliverability at the determined flowing bottomhole pressure. While the choice of the well bottomhole, as a location for such an analysis, has been in wide use in the past, it is certainly not mandatory. The wellhead, or any other point along the path, can serve the same purpose adequately.

In this textbook, methods for calculating the pressure drop in oil, two-phase, and gas reservoirs for all types of conditions (infinite-acting, pseudo-steady-state, and steady-state) are presented in Chapters 2, 3, and 4.

Pressure drops across the near-wellbore zone are treated in Chapter 5. A variety of skin effects are introduced to account for damage, completion configurations, perforations, and phase and rate phenomena. The pressure drop through a gravel pack is presented in Chapter 6.

Chapter 7 contains an extensive treatment of the pressure drop associated with the vertical lift of a petroleum fluid through a well. Most of the prominent correlations necessary for this task are included in the chapter.

Finally, Chapter 10 contains the necessary correlations and calculational procedures for the estimation of the pressure drop through the wellhead chokes and horizontal lines.

For wells under artificial (gas or pump-assisted) lift, Chapters 19 and 20, respectively, can be used for the calculation of the corresponding pressure drops in the tubing and the pressure increase provided by a pump.

21-3 System Design and Diagnosis

In addition to the obvious use of the analysis of an existing or contemplated, adequately defined system in determining well deliverability or forecast of well performance (Chapter 9), a most appropriate application is for the design of individual components or the diagnosis of suspected problems. These tasks can be accomplished through parametric studies.

For design, the procedure is straightforward. Suppose that the tubing size is at issue. Starting from the separator pressure, the corresponding wellhead pressures can be calculated for a series of flow rates (Chapter 10). For a pair of wellhead pressure and flow rate and for *each* tubing size, the corresponding bottomhole pressure can be obtained (Chapter 7).

Since the well bottomhole is the chosen point of analysis, graphs of flow rate versus p_{wf} can be constructed for each tubing size. Combination with the IPR (accounting for all relevant near-wellbore conditions) leads to the expected flow rates from each tubing size. Figure 21-1 is a schematic depiction for such a calculation.

This type of exercise, several examples of which are presented in Chapter 8, is invaluable during well design because the incremental benefits, if any, can be compared against the incremental costs of different completion schemes.

All components of the system can, and must, be subjected to such a scrutiny both at the planning stage *and* during the life of the well. This approach should include potential modifications to the IPR (such as fracturing—Chapter 17) and certainly a continuous attention to the crucial near-wellbore zone and the inherent need for matrix stimulation (Chapters 13, 14, and 15). Figure 21-2 is a schematic depiction for this exercise. Again, examples were presented in Chapter 8.

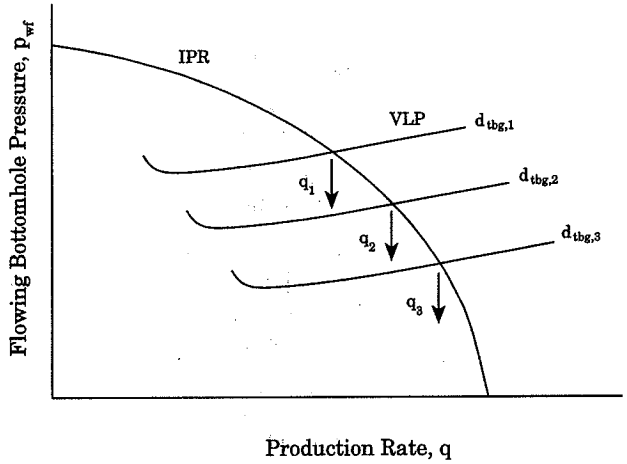

Figure 21-1
Method for a design parametric study for tubing size.

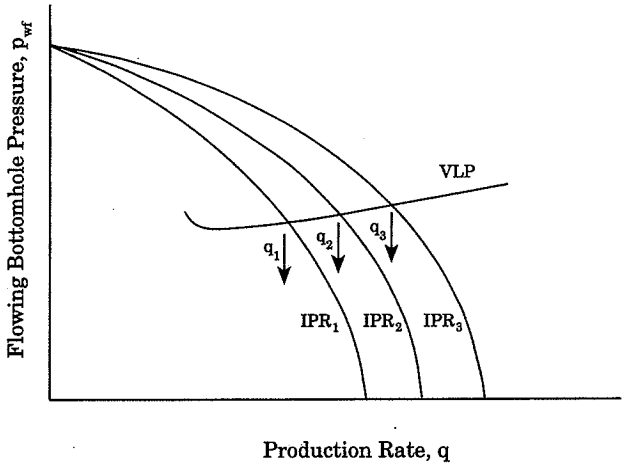

Figure 21-2
Parametric study with IPR modifications (e.g., corresponding to different hydraulic fracture designs).

Problem diagnosis uses a similar approach. If the well does not perform as designed, appropriate investigation should attempt to identify (1) the problematic pressure drop component and (2) the responsible culprit.

Often, the discrepancy between expectations and actual performance is caused by incorrect assumptions about important variables such as the permeability, reservoir discontinuities, or heterogeneities. Testing techniques, as described in Chapter 11, can resolve discrepancies.

If the knowledge of the reservoir is adequate, then any other part of the system may be causing the problem. The problem can be isolated by a process of elimination through parametric studies or, in cases of doubt, by actual measurements at any point along the system.

For example, nonflowing perforations constitute a frequent problem. Assuming a series of pressure drops across the total perforated interval, a series of IPR curves can be constructed. Intersections with the VLP curve provide the corresponding production rates. Comparison with the observed actual rate yields the corresponding pressure drop across the perforations. Since the pressure drop is directly proportional to the perforation skin effect (Chapter 5), the number of open perforations may be approximated. Figure 21-3 is a schematic depiction for this problem.

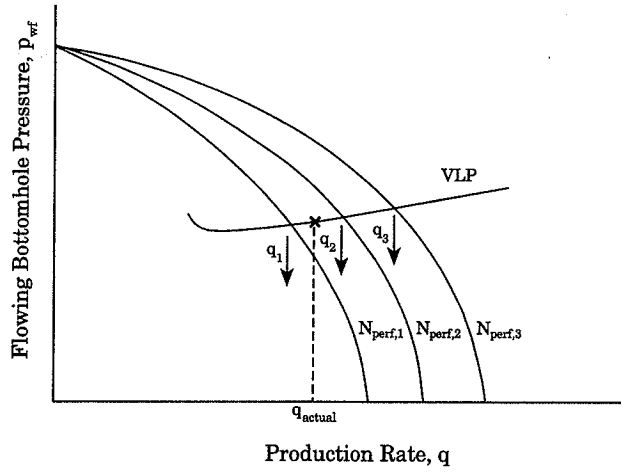

Figure 21-3
Use of system analysis for problem diagnosis (e.g., number of open perforations).

Two observations are in order here:

- Individual pressure drop components and the corresponding pressure values may affect neighboring parts of the system. For example, the previously mentioned

pressure drop through the perforations, affecting the sandface pressure, may result in different phase distribution in the near-wellbore zone and thus a different phase-dependent skin effect (and pressure drop)

- There is always an issue of uniqueness in problem diagnosis. System analysis through parametric studies can be augmented by measurements. Production logging (Chapter 12) can provide invaluable information for this purpose. In the previous perforation example, while parametric studies may provide an estimate of actual open perforations (versus number of shots), production logs can indicate whether closed perforations are distributed throughout or whether they are concentrated in specific, nonflowing but shot intervals.

In conclusion, analysis of the petroleum system and its individual parts, using the techniques presented in this textbook, must be an essential exercise for the production engineer during the design and subsequent operation of a well. Necessary aids include testing and production logging. Appropriate decisions for hardware selection, surface facilities, lift mechanisms, and stimulation can thus be made for optimum petroleum production.

REFERENCES

1. Brown, K. E., et al., *The Technology of Artificial Lift Methods*, Pennwell Publishing, Tulsa, OK, 1984.
2. Carroll, J. A., III, and Horne, R. N., "Multivariate Optimization of Production Systems," *JPT*, pp. 782–789, July 1992.
3. Haid, G., and Economides, M. J., "Optimierung Hydraulischer Frakbehandlungen bei der Erdölgewinnung mit Hilfe der Monte-Carlo-Technik und unter Anwendung des Barwertes," *BHM*, **12/91**: 467–474, 1991.

CHAPTER 22

Environmental Concerns in Petroleum Production Engineering

22-1 INTRODUCTION

A petroleum production engineer must exercise prudent care in all phases of oil and gas production. Two of the most important aspects of this care are protection of the environment and concern for safety. These concerns may constitute a large part of the costs of petroleum production. Godic and Biglarbigi (1990) have shown that costs for environmental compliance may result in a 42% reduction in future drilling- and enhanced oil recovery (EOR)-related additions to U.S. reserves. This reduction is from an estimate in which environmental costs are not considered.

Governmental regulations and rules vary significantly with each country and are modified with great regularity. The production engineer must be environmentally sensitive and aware of applicable laws, rules, and regulations in the area of operations. Further, many environmental issues are unique to various production operations, especially offshore, Arctic areas, wetlands, urban areas, etc. The production engineer must also be familiar with these issues.

This chapter reviews some of the environmental considerations common to oilfield operations. Environmental issues for onshore and offshore operations are discussed in Section 22-2. While most of these issues are concerned with specific pollutants, other environmental impacts are discussed. In Section 22-3 the techniques for handling oilfield production operations are discussed. Arctic issues are dealt with in Section 22-4.

22-2 WASTES GENERATED IN PRODUCTION OPERATIONS

Production operations include normal well operations, separation and treating at production facilities and gas plants, and workovers. Typical wastes generated within these areas are discussed below.

22-2.1 Well Operations

During the course of normal well production and injection operations, pollution is possible through spills or leaks on the surface and from unwanted migration of fluids underground. Regulations generally require that efforts be taken to ensure that no fluids can migrate into freshwater aquifers. Thus, wells must be cemented properly so that produced or injected fluids are isolated from aquifers that may lie above the productive zones. If flow behind pipe that could allow communication with potable water sources is suspected, production logs to detect channeling should be run (see Chapter 12.) Remedial cementing to eliminate fluid migration should be conducted if fluid migration to freshwater aquifers is detected.

22-2.2 Production Facilities

Production facilities gather produced vapors, fluids, and solids from wells, separate liquid hydrocarbons and natural gas, and prepare them for sale. Salable products generally have restrictions as to allowable contaminants. In the case of oil, a maximum limit is set on basic sediment and water (BS&W), typically 0.5 to 1.0%. In the case of gas, there are limits on water content, energy content (BTU content), and mole fractions of nonhydrocarbon gases such as N_2, CO_2, and H_2S (API, 1989).

Oil and gas wells generate a variety of wastes, including paraffin, oil, produced water, used lubricator oils, etc. Oil and produced water contaminants are occasionally produced as a result of stuffing box leaks or spillage during well site operations. Paraffin is generated in operations such as cutting paraffin in tubing with downhole tools and pigging flow lines. Sand and scale contamination with traces of hydrocarbons and other hydrocarbon sludge are generated from flow lines, separators, free water knockouts, heater-treaters, stock tanks, desanders, etc. Filters used to improve water quality generate potential contaminants when the filter medium is replaced or cleaned.

Steam generators for thermal oil recovery generate a variety of air emissions (CO_2, NO_x, etc.), with the amounts varying strongly with the technology and fuel used for steam generation. Even the cleanest and most efficient of these technologies (cogenerating electricity using natural gas as a fuel and making steam from waste heat) generates contaminated water in the water-softening and deionization systems. Air pollution controls to decrease SO_2 emissions for oil-fired generators generate sulfur compounds in a liquid solution called "sulfur liquor."

Other facilities, such as compressors, dehydrators and sweetening units, gas scrubbers, line heaters, and methanol injection pumps, generate a variety of low-level contaminants. These include air pollution, waste lubrication oils, filters, spent glycol, amine, caustic and iron sponge material, and empty containers.

22-2.3 Natural Gas Plants

Natural gas plants provide a centralized facility to efficiently dehydrate, compress, and extract nonhydrocarbon diluents from natural gas and to extract natural gas liquids (NGLs). The relative roles of gas plants and well production facilities vary. Some gas plants accept full well stream, some accept gas separated at the lease, and others essentially "straddle" a gas pipeline that is transporting marketable natural gas. While methane is the principal component of natural gas, many natural gases contain significant fractions of ethane, propane, butanes, and heavier NGLs. Nonhydrocarbon diluents such as CO_2, N_2, and H_2S are very common. Water, free hydrocarbon liquids, mercaptan, solids, scale, sludge, and other impurities may also be present.

The types of pollutants generated in natural gas processing operations are similar to those in production facilities. However, because of the greater number, longer life, and larger scale of operations, certain problems are exacerbated. The large number of engines, compressors, pumps, sumps, etc., involve larger volumes of lubrication and hydraulic oils, cooling waters, cleaners, oily debris, glycol, amines, solid desiccants, filters, etc.

22-2.4 Workover Operations

Workover operations range from very clean operations involving minimal environmental risks to operations that are identical in risk to drilling operations. Workover rigs themselves generate waste hydraulic fluids, used oils, and filters. Workover fluids include muds, residual hydrocarbons, solids, acids, gels, fracturing fluids and related chemicals, sand, solvents, surfactant, etc.

Reserve pits must be handled with care as will be discussed later.

22-2.5 Offshore Operations

While all offshore operations are generally similar to onshore production operations, certain differences are significant. Production operations from fixed platforms, ships, caissons, etc., are more compact and isolated than their onshore counterparts. Fewer wells are involved; generally, however, these are (on average) higher-flow-capacity wells. Numerous wellheads are close together, complicating well access. The compact location and necessity of transporting equipment by barge, ship, or helicopter affects logistics. More important, spilled pollutants reach navigable waterways almost immediately.

Accidents are responsible for the majority of serious offshore pollution incidents. Potential sources of significant oil spills due to accidents include:

- Well blowouts
- Platform collapses
- Ship collisions
- Pipeline ruptures
- Equipment failures
- Fires and explosions
- Human error

Several of these potential problems are unique to the offshore environment; all have potentially greater damage and are more difficult to contain and to remediate compared to onshore locations.

Sources of air pollution in offshore operations include ship engine exhaust, drilling/power supply equipment, and treatment processes. Pollutants include NO_x, hydrocarbons,

CO, and particulates. While air quality is typically degraded in the immediate platform vicinity, the dynamic offshore environment quickly disperses these pollutants. Nearshore operations near inhabited areas may be required to mitigate such pollutants.

Numerous offshore areas have live bottom characteristics that make offshore development particularly difficult. Most of these environments cannot be developed except by extended-reach drilling from areas with less sensitive locations. Live bottom characteristics include:

- Sea grass communities
- Sessile invertebrates (sea fans, corals, anemones, etc.)
- Lithotypes favoring accumulation of turtles, fishes, and other fauna

Another measure required in offshore facilities design is the installation of protective devices over subsea equipment in areas of shrimp harvesting (or other drag net fishing).

Produced water from onshore wells is typically reinjected after removal of entrained oil, down to an amount dictated by purely economic constraints—that is, can more oil be recovered at a cost less than its value? The remaining water with entrained oil typically is injected into subterranean formations. Offshore operations have extremely limited storage space and volumes; most produced water will ultimately be dumped into the ocean or sea. This requires a better level of cleaning than for onshore operations. The specific technologies of recovering low concentrations of oil and grease from produced waters depend on the volumes involved. Selection of the technology should include the following criteria:

- Cost versus reduction in pollutants
- Age of the equipment
- Process specifics and engineering details
- Process changes required
- Energy demand

Devices to detect low concentrations of oil and grease in water include infrared monitors, calorimetric devices, and extraction gravimetric devices. Produced water contains both free and dissolved oil as well as water-soluble organic compounds (WSOs). WSOs include organic acids and light hydrocarbons (Arscott, 1989). While produced water may be the most important source of oil and grease in water, deck drainage (water runoff) from cleanup activities or rain may also carry enough hydrocarbons to impart a surface "sheen" on the ocean. The relative amounts of oil spillage that must be reported vary according to location and specific regulations. However, most locations require that all spills that impart a visible sheen be reported. Acceptable oil and grease concentration can be quantified as generally less than 48 mg/liter.

Produced sands and other solids are also routinely dumped overboard after cleanup and removal of free hydrocarbons. Typical requirements are to remove enough hydrocarbons so that no visible sheen results on the surface of the ocean and that there is no discharge of free oil.

Most large offshore production facilities are manned—that is, personnel live on location on a continuous basis. This also creates the potential for new pollution sources

associated with sewage and trash. Trash is typically burned during daylight hours and is subject to volume constraints. Sanitary waste must be treated and is subject to restrictions on chlorine concentration, total and suspended solids, total flows, and biological oxygen demand (BOD).

Other pollutants that are unique to offshore operations include cathodic metal discharge. Sacrificial anodes are frequently designed into the platform legs, which are preferentially consumed to protect the structural integrity of the platform material. The total amount of such material and the types of metals permitted are often subject to regulation.

A final concern in offshore environments involves the ultimate removal of platform structures. Platform structures are typically removed by explosive charges approximately 5 m below the mudline. Because the presence of platforms frequently attracts fish, turtles, and marine mammals, explosive removal of platforms can potentially kill such marine creatures.

In fact, because of their beneficial effect as artificial reefs, in some cases offshore structures are severed at a depth below the water surface, deep enough not to interfere with ship traffic, and the structures are then left on the ocean floor.

22-3 Operating Issues—Handling Oilfield Wastes

The following areas of environmental concern deal with production operations and the minimization and disposition of potential pollutants. At the end of this section are some example applications and calculations of environmentally related problems. No attempt is made to cover all issues, as this is beyond the scope of this book.

22-3.1 Chemical Concerns

A "release" of substances can include spilling, leaking, dumping, pumping, pouring, emitting, emptying, discharging, injecting, escaping, and disposing into the environment. The number of substances to be reported to government regulatory bodies depends on specific regulations and may depend on the volume released. Most oilfield chemicals, including oil and condensate, and in some instances even produced water, may be reportable.

Certain chemicals must be treated as toxic substances. Specific labeling, storage, transport, disposal, and record-keeping requirements will generally apply to these substances. Example chemicals frequently considered toxic include polychlorinated biphenyls (PCBs), chlorofluoroalkanes (CFAs), and polybrominated biphenyls (PBBs).

22-3.2 Open Burning and Incincerators

The open burning of nonhazardous hydrocarbon-containing materials with properties that make recycling unsuitable is appropriate when it is allowed by regulations. Burning should be restricted to materials such as paraffins and oily sorbents. Burning should be conducted during daylight hours, and should not cause excessive black smoke or particulates.

22-3.3 Road Spreading

Certain hydrocarbon wastes such as tank bottoms, heavy hydrocarbons, solids contaminated with crude oil, and emulsions may be used for road oil or road building material

under certain conditions. Typically, these require that the materials are not ignitable (flash point > 140°F) and that they have a density and metals content consistent with approved road oils and mixes. The use of such materials should be at a rate that minimizes surface runoff. Produced waters that are brackish (salinities > 300 ppm) should not be used for road spreading or dust suppression. The use of such waters in lieu of road salting for snow/ice control may be acceptable if approved by appropriate regulations.

22-3.4 Land Spreading/Biodegration

Low-toxicity wastes may be treated and disposed of by land spreading. This process reduces organic and inorganic constituents by natural processes such as biodegration, dilution, and absorption. This process must be carefully managed to eliminate the chance for groundwater contamination or harm to animals, soil, or vegetation. Solid and liquid wastes may be treated this way after free oil and water have been removed. The material is spread evenly, and materials to accelerate biodegration (nitrogen, water, specific bacteria selected for the process) may be added. Numerous precautions are required, and the presence of toxic substances and significant metals eliminates this method of disposition. Land spreading may also generate other materials that will be unsuitable in areas immediately adjacent to populated areas.

22-3.5 Pits

Unlined pits for production, gas plants, or drilling operation are an invitation to disaster (Jones and Hulse, 1982). Existing unlined disposed pits should be evaluated, phased out, and closed. Pits that are not closed should be lined with synthetic or clay liners and should be inspected annually for integrity. Historically, operators may have disposed of field brines and other materials in unlined pits to "evaporate." In many such cases, rates of leaching into the subsurface (with potential contamination of shallow aquifers) exceed rates of evaporation.

Pits designed to provide pressure relief during emergency conditions only are acceptable if they are pumped and cleaned promptly after use. Frac tanks should be used where feasible in lieu of blowdown pits. Freshwater pits (e.g., less than about 10,000 ppm total dissolved solids) may be unlined if they comply with applicable standards where freshwater is produced. Reserve pits use should be limited only to drilling muds, cuttings, and completion fluids. Upon well completion or plugging, reserve pits should be promptly closed and reclaimed.

22-3.6 Produced Water

Produced water for onshore wells should be disposed of at an approved injection well, in an approved synthetic or clay-lined evaporation pond, or pursuant to a discharge permit in accordance with applicable requirements. Leaks, spills, or other releases of produced waters must be reported to the appropriate agencies.

22-3.7 Injection Wells for Produced Water

Underground disposal of produced water in injection wells must be carried out strictly within approved parameters to prevent any risk of contamination to underground water supplies or to the environment. The facility supervisor should ensure that all injection wells are operated and tested according to the approved and applicable permit conditions. The facility supervisor should obtain assurance that third-party disposal and produced water injection wells also meet these conditions. A written agreement should be required with all third-party disposal well operators.

Disposal of produced water in injection wells requires equipping with tubing, casing, and a packer. Pressure monitoring devices should be installed and routinely observed measurements recorded for the evaluation of the tubing and casing annulus pressure. Shut-in disposal water injection wells should be monitored and pressures recorded at least quarterly. Wells that do not meet operating requirements should be immediately shut in until they are adequately repaired and successfully retested.

All disposal of produced water in injection wells should undergo a formal mechanical integrity assessment at least every 2 years, or more frequently if required by regulations. This includes pressure testing or an assessment of tubing and casing annulus pressure-monitoring records. If significant pressure anomalies or trends are noted, a mechanical integrity test pursuant to the well's permit should be properly performed. A temperature/radioactive (RA) tracer log or its equivalent should be required once every 4 years or within 12 months after a well has been acidized or subjected to other activities that could affect the integrity of the well or the injection zone. Copies of disposal well water injection reports, tests, surveys, and other reporting relevant to permits, compliance, monitoring, and maintenance of underground disposal and injection wells should be maintained at the facility.

22-3.8 Radiation

Naturally occurring radioactive materials (NORMs) have been known to be present in varying concentrations in hydrocarbon reservoirs throughout the world for many years. These materials may produce radioactive scale, film, and sludge in equipment associated with oil and gas production and processing.

Surplus materials must be evaluated for NORMs. Only equipment that has been in service in the production fields and gas plants (i.e., pipes, valves, vessels, pumps, compressors, etc.) are affected. NORM contaminated surplus material may be returned to like service without any remedial action, but may not be used for any other service outside oil and gas production or sold for scrap unless NORMs are below acceptable levels.

22-3.9 Underground Petroleum Storage Tanks and Sumps

Installation of new underground petroleum storage tanks is discouraged due to the substantial risk of future leaks. Existing underground petroleum storage tanks should be phased out. Timing of the underground removals should be planned to allow for notifi-

cation of the appropriate regulating agencies. Sumps for petroleum collection should be constructed so that its walls are self-supporting (i.e., fiberglass tanks or concrete), and they must be approved for use prior to installation.

A soil/groundwater assessment program should be implemented upon removal of any tank or sump found to have been leaking. Adequate testing and record-keeping procedures for a monitoring program must be implemented.

22-3.10 Waste Management and Minimization

Wastes must be handled in a manner that protects the environment within the area of production operations and complies with all applicable laws and regulations and good housekeeping practices. Waste-minimization and recycling programs and practices should be implemented in all operations to the extent practicable.

All operating waste for disposal must be tested to characterize its composition and/or to identify the presence of any hazardous substances. If testing indicates the presence of a hazardous substance, the waste must be stored, manifested, and transported according to government regulations, and disposed of at a permitted disposal facility.

Appropriate tests should be conducted to identify the presence of a hazardous substance in wastes from tank bottoms, residues from heater treaters and separators, frac fluids, nondischargeable drilling muds, workover fluids, and additives. Hazardous waste procedures must be followed when hazardous substances or regulated levels of radiation are present in any waste.

Substances used in operations that are generally identified as hazardous waste include chromates, solvents, lead-based paints, acid or caustic solutions, methanol, inhibitors, distillate, pesticides, treating chemicals, residues of hazardous waste, and other wastes that are hazardous by "characteristic" (corrosive, reactive, ignitable, or toxic).

All used or waste oil sent offsite to an approved recycler/reclaimer needs to be manifested to protect from future liability in the event of improper handling by a third party. Used oil that is not recycled or reclaimed either at the generating facility or at an approved third-party reclaimer should be manifested as hazardous waste and disposed of properly at an approved hazardous waste facility.

Hazardous and nonhazardous waste substances should be stored in separate storage facilities. Hazardous and nonhazardous waste materials should not be mixed or consolidated. If hazardous and nonhazardous materials are mixed, the resultant mixture is considered hazardous and must be disposed of as hazardous waste, resulting in increased disposal costs.

Waste Management. Operating facilities should develop and implement a waste management plan to effectively manage, reduce, and recycle wastes generated within their area. Practices should include minimizing the number of chemical drums at locations, requiring vendors to take back the drums they deliver, utilizing products/chemicals that do not contain hazardous substances when possible, avoiding the mixing of hazardous wastes with nonhazardous wastes, eliminating waste-generating activities where alternatives exist, and preventing leaks and spills. Preventative measures include employing and maintaining leak- and spill-prevention mechanisms and substituting nonhazardous components for hazardous ones.

EXAMPLE 22-1
Water treatment plant sizing

A water treatment plant is to handle 600,000 bbl/d. Suppose that a coagulation/flocculation time of 30 min and a sedimentation time of 2 hr are required. Assuming that three sets of tanks, each 60 ft long are to be used, the coagulation/flocculation tanks are 10 ft deep, and the sedimentation tanks are 15 ft deep, calculate the required widths. If the throughput per filter box is 0.05 bpm/ft^2 and if 12 units will be used, calculate the required filtration area per unit.

Solution The volumetric capacity of each coagulation/flocculation tank (and remembering the need of 30 min residence time) is

$$V_{\text{tank}} = \frac{600{,}000}{3}\frac{(5.615)(30)}{(24)(60)} = 2.34 \times 10^4 \text{ ft}^3 \tag{22-1}$$

Therefore, the width of each tank should be

$$w_{\text{tank}} = \frac{2.34 \times 10^4}{(60)(10)} = 39 \text{ ft} \tag{22-2}$$

Similarly, the volumetric capacity of each sedimentation tank should be 9.36×10^4 ft^3, and the corresponding width should be 104 ft.

Each of the 12 filter boxes will handle 50,000 bbl/d or 34.7 bpm. Since the throughput is 0.05 bpm/ft^2, the required area is 694 ft^2(= 34.7/0.05). Each of the 12 filter boxes is 30 ft long (two for each tank), and therefore the corresponding width is 23.3 ft. ◇

EXAMPLE 22-2
Discharge in surface waters

A group of wells produce a great deal of water that is ultimately discharged into a nearby estuary. Total flow into the estuary is restricted to a rate of 320 gpm with no more than 10 ppm oil and grease. An oil spill results in 50 bbl of oil being released out of the lease. Cleanup efforts recover 30 bbl of oil, with 20 bbl contained in a wastewater pond. Further reclamation will be costly and difficult. One alternative is to regulate the release of the oil with the water stream into the estuary. Assuming that oil flow can be controlled with the water, how long will it take to discharge the trapped oil under permitted conditions? Is this a practical solution?

Solution Since the allowable oil concentration is 10 ppm, then the total volume of water required to dilute 20 bbl of oil is

$$V_w = \frac{(20)(1{,}000{,}000)}{10} = 2 \times 10^6 \text{ bbls} = 8.4 \times 10^7 \text{ gal} \tag{22-3}$$

The time required would be

$$t = \frac{(8.4 \times 10^7) + (8.4 \times 10^2)}{320} = 2.63 \times 10^5 \text{ min} = 182 \text{ d} \tag{22-4}$$

The calculated time assumes zero oil concentration in the produced water and thus it is the minimum required time. Such a time is inordinately long and not a likely solution.

EXAMPLE 22-3
Bioremediation of sludge

A small "bug farm" is operated for bioremediation of produced sludge. Permit restrictions limit oil and grease in the soil to 10%. The bug farm contains 9.4 acres, and the measured oil and grease content is 4.1%. From a cleanup operation of a spill, 9470 yd^3 of oily sludge is produced. The oil and grease content of the sludge is 16.2%. The density of the sludge is 78 lb/ft^3, while the soil density in the 1-ft-thick zone of incorporation is 91 lb/ft^3. Costs to move the sludge off-lease are large, so it is necessary to incorporate as much as possible within the facility. How much can be incorporated within permit limits?

Solution If all the sludge, with 16.2% oil and grease content, were to be dumped in the 9.4 acres and with the 10% limit, it would be the weighted equivalent of

$$V_{\text{sludge}} = \frac{(0.1)(91)(9.4)(43{,}560)(1)}{(0.162)(78)(27)} = 1.09 \times 10^4 \text{ yd}^3 \tag{22-5}$$

However, since the current oil and grease content is 4.1%, the weighted equivalent of the sludge-in-place is 4500 yd^3[= (0.041)(10,921)/0.1]. Thus a maximum of 6400 yd^3 can be added, which means that 3070 yd^3(= 9470 − 6400) must be disposed of elsewhere.

22-4 ARCTIC ENVIRONMENTS

Arctic regions are characterized by mean temperatures during their warmest months of less than 10°C and average annual temperatures below 0°C. The subarctic region extends to areas with no more than 4 months with a mean temperature above 10°C. Total arctic and subarctic areas include 26 million km^2 of water and 5 million km^2 of land area. This constitutes more than 20% of the earth's surface area.

Arctic and subarctic areas contain vast quantities of identified and prospective hydrocarbon-bearing formations. The environmental risks associated with onshore and offshore operations include all of the risks associated with warmer climates; however, the arctic environment includes numerous additional risks. These include:

- Unique flora and fauna with unusual susceptibilities to damage
- Permafrost zones and arctic tundra soils and subsoils
- Limited access by land, sea, and air, especially during winter
- Isolated from infrastructure associated with exploration and production activities
- Unusually large transportation risks

Permafrost consists of water saturated-soils that are frozen year-round. An "active layer" of soils that thaw and refreeze may exist to depths up to a few feet. The permafrost layer in arctic regions can be hundreds of feet thick. Permafrost conditions require special well completions, drilling operations, production facilities, etc.

Oil production in permafrost environments requires special insulation to prevent thawing of the permafrost (and subsequent instabilities). This can be accomplished by setting an additional casing string and leaving an insulating material (typically a gelled crude oil mixture) in this annulus. Insulated tubing and insulating fluids in the tubing/casing annulus may also be used.

Actual pollution of groundwater and waterways is not generally as great a problem as in warmer areas, since many spills will not travel readily to waterways in the lower temperatures and the liquid-phase groundwater below the permafrost is frequently brackish to saline, making it nonpotable. Damage to sensitive arctic flora and fauna is certainly possible from E&P operations.

Travel and operations in the most severe arctic environments is severely limited. Extreme cold, high winds, and limited loading facilities make helicopter and fixed-wing aircraft travel difficult. Ship and barge access is restricted to summer months. Land transportation over the arctic tundra requires specially designed vehicles with extraordinary large tires at low air pressure. These complications increase costs, slow operations, and limit the time period during which operations may be conducted. Cleanup of spills and other remediation efforts are also seriously hampered (Lidell et al., 1991).

Installation of permanent facilities and pipelines is also complicated by permafrost environments. Pipelines must be elevated and wrapped for insulation. Pipes, skids, and other facilities must be either placed on gravel skids or elevated. The costs of developing permanent infractures are very high.

One of the greatest environmental risks in the arctic is product transportation. A pipeline failure could cause significant local damage. However, oil spillage from tankers and barges remains the largest threat to the arctic environment. Tanker collisions, accidental or deliberate discharging of crude oil into the sea, and other tanker damage have the most significant potential for spill events.

A wide variety of cleanup technologies are available (booms, oil barriers, skimmers, dispersants, absorbants, burning, beodegrations, etc.), which work on land or on water and can be applied with varying success in the arctic and subarctic environments. Temperature-related technology issues, the presence of ice in the water, human discomfort, and limited visibility conditions affect the degree of success and the costs of cleanup (McLeod and McLeod, 1974).

REFERENCES

1. API, *API Environmental Guidance Document: Onshore Solid Waste Management in Exploration and Production Operations*, 1st ed., American Petroleum Institute, Washington, DC, 1989.
2. Arscott, R. L., "New Directions in Environmental Protection in Oil & Gas Operations," *JPT*, pp. 336–342, April 1989.
3. Godic, M. L. and Biglarbigi, K., "The Economic Impacts of Environmental Regulations on the Costs of Finding and Developing Crude Oil Resources in the United States," SPE Paper 20619, 1990.
4. Jones, M. and Hulse, M., "Drilling Fluid Bioassays and the OCS," *O&GJ*, June 21, 1982.
5. Liddell, V. B., Smallback, D. R., and Ramert, P. C., "Arctic Bioremediation: A Case Study," SPE Paper 22215, 1991.
6. McLeod, W. R. and McLeod, D. L., "Measures to Combat Arctic & Subarctic Oil Spills," *JPT*, pp. 269–278, March 1974.

APPENDIX A

Well in an Undersaturated Oil Formation

$k_H = 8.2$ md
$k_V = 0.9$ md
$h = 53$ ft
$p_i = 5651$ psi
$p_b = 1323$ psi
$c_o = 1.4 \times 10^{-5}$ psi^{-1}
$c_w = 3 \times 10^{-6}$ psi^{-1}
$c_f = 2.8 \times 10^{-6}$ psi^{-1}
$c_t = 1.29 \times 10^{-5}$ psi^{-1}
$\mu = 1.7$ cp
$B = 1.1$ res bbl/STB
$R_s = 150$ SCF/STB
$\phi = 0.19$
$S_w = 0.34$
API° = 28
$r_w = 0.328$ ft (7 7/8 well)

APPENDIX B

Well in a Two-Phase Reservoir

$k_H = 13$ md (from cores)
$h = 115$ ft
$p_i = 4350$ psi
$p_b = 4350$ psi
$c_o = 1.2 \times 10^{-5}$
$c_w = 3 \times 10^{-6}$ psi^{-1}
$c_f = 3.1 \times 10^{-6}$ psi^{-1}
$c_t = 1.25 \times 10^{-5}$ psi^{-1}
$\overline{\mu}_o = 1.7$ cp
$\gamma_o = 32°$ API
$\gamma_g = 0.71$
$T = 180°$F
$T_{pc} = 395°$R
$p_{pc} = 667$ psi
$S_w = 0.3$
$\phi = 0.21$
$r_w = 0.406$ ft

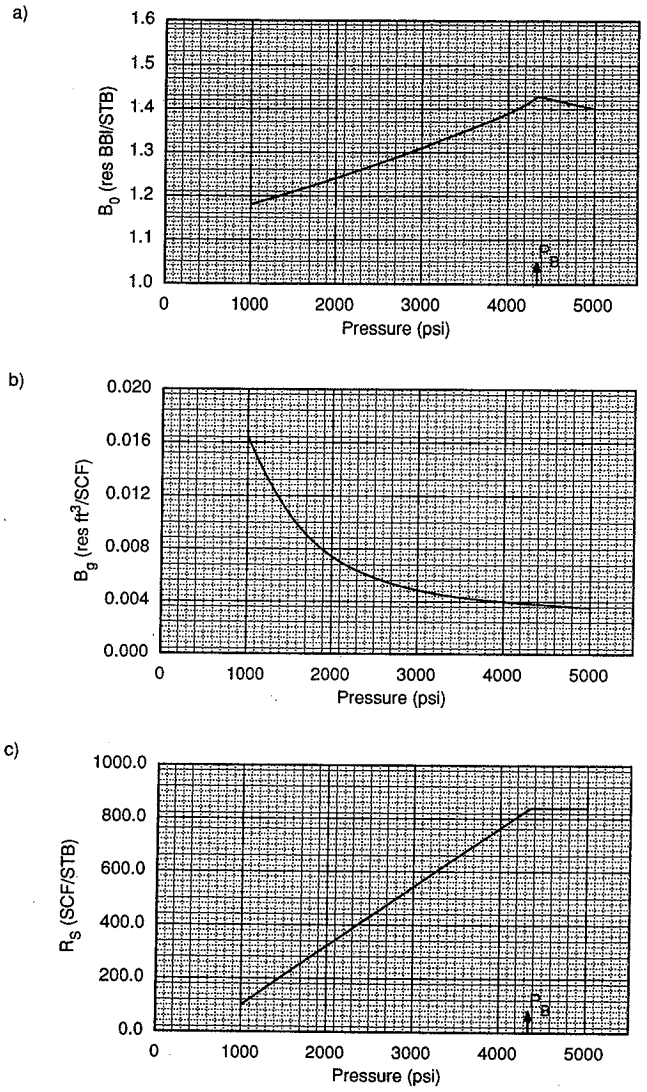

Figure B-1
Thermodynamic properties for fluid.

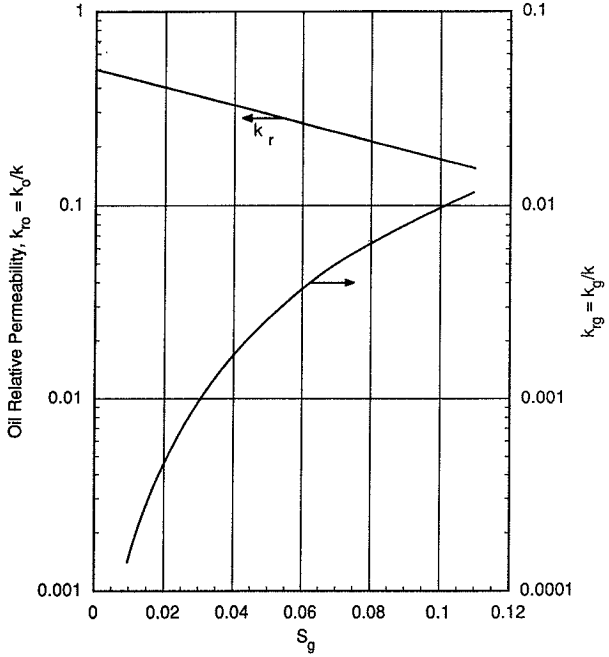

Figure B-2
Relative permeabilities for fluid.

APPENDIX C

Well in a Natural Gas Reservoir

Composition of gas and properties:

$C_1(0.875)$	$C_2(0.083)$	$C_3(0.021)$
$i\text{-}C_4(0.006)$	$n\text{-}C_4(0.002)$	$i\text{-}C_5(0.003)$
$n\text{-}C_5(0.008)$	$n\text{-}C_6(0.001)$	$C_7\text{+}(0.001)$
$T_{pc} = 378°\text{R}$	$p_{pc} = 671$ psi	$\gamma_g = 0.65$

Well and Reservoir Variables

$$
\begin{aligned}
T &= 180°\text{F} = 640°\text{R} \\
p_i &= 4613 \text{ psi} \\
Z_i &= 0.945 \\
\mu_i &= 0.0244 \text{ cp} \\
h &= 78 \text{ ft} \\
S_w &= 0.27 \\
S_g &= 0.73 \\
\phi &= 0.14 \\
r_w &= 0.328 \text{ ft (7 7/8-in. well)} \\
k &= 0.17 \text{ md}
\end{aligned}
$$

APPENDIX D

Nomenclature

a = half-axis of horizontal well damage ellipse, ft, m
A = drainage area, ft^2, acres, m^2
A_f = fracture area, ft^2, m^2
b = reservoir width, ft, m
B_g = gas formation volume factor, res ft^3/SCF, m^3/Sm^3
B_o = oil formation volume factor, res bbl/STB, m^3/Sm^3
B_t = total formation volume factor, res bbl/STB, m^3/Sm^3
B_w = water formation volume factor, res bbl/STB, m^3/Sm^3
c_f = end-of-job slurry concentration, ppg, kg/m^3
c_g = gas compressibility, psi^{-1}, Pa^{-1}
c_o = oil compressibility, psi^{-1}, Pa^{-1}
C_{pf} = heat capacity, BTU/lb, J/kg
C_p = proppant concentration, bl/ft^2, kg/m^2
$c_p(t)$ = slurry concentration, ppg, kg/m^3
c_t = total system compressibility, psi^{-1}, Pa^{-1}
c_w = water compressibility, psi^{-1}, Pa^{-1}
C = wellbore storage, bbl/psi, m^3/Pa
C = choke flow coefficient (Chap. 10)
C = species concentration, $moles/m^3$ (Chap. 13)
C = damage constant, cp^{-1}, $(Pa\text{-}s)^{-1}$ (Chap. 16)
C_A = drainage shape factor, dimensionless
C_A = concentration of mineral A, moles $/m^3$ (Chap. 13)
C_L = leakoff coefficient, $ft/\sqrt{min}$, $m/\sqrt{sec}$
D = diameter, ft, m

D = non-Darcy coefficient, $(\text{STB/d})^{-1}$, $(\text{m}^3/\text{sec})^{-1}$
E = Young's modulus, psi, Pa
E_f = reaction rate constant, m^2-sec $(\text{moles/m}^2)^{\alpha}$
f_f = Fanning friction factor, dimensionless
F_{CD} = dimensionless fracture conductivity
g = acceleration of gravity, ft/sec^2, m/sec^2
G = gas-in-place, SCF, m^3
G = elastic modulus, psi, Pa (Chap. 16)
GLR = gas–liquid ratio, SCF/STB, m^3/m^3
GOR = gas–oil ratio, SCF/STB, m^3/m^3
h = reservoir thickness, ft, m
h_f = fracture height, ft, m
h_w = completion interval, ft, m
H = depth, ft, m
I_{ani} = index of permeability anisotropy, dimensionless
J = productivity index, STB/d/psi, m^3/sec/Pa
k = permeability, md, m^2
k_f = fracture permeability, md, m^2
k_g = gas permeability, md, m^2
k_H = horizontal permeability, md, m^2
k_o = oil permeability, md, m^2
k_{rg} = gas relative permeability, dimensionless
k_{ro} = oil relative permeability, dimensionless
k_{rw} = water relative permeability, dimensionless
k_V = vertical permeability, md, m^2
k_w = water permeability, md, m^2
K' = power law consistency index, lb_f-$\text{sec}^{n'}/\text{ft}^2$, Pa-$\text{sec}^{n'}$
K_I = stress intensity factor, psi $\sqrt{\text{in.}}$ Pa $\sqrt{\text{m}}$
L = horizontal well length, ft, m
L = linear distance, ft, m
m = gas cap fraction
$\dot{m}$ = mass flow rate, lb/hr, kg/sec
$m(p)$ = real gas pseudo-pressure, psi^2/cp, Pa/sec
M_p = mass of proppant, lb, kg
MW = molecular weight
n = number of moles
n' = power law exponent, dimensionless
N = oil-in-place, STB, m^3
N = pump speed, strokes per minute (Chap. 20)
N_{Ac} = acid capacity number
N_{Da} = Damkohler number
N_{Fr} = Froude number
N_L = liquid viscosity number
N_p = oil cumulative production, STB, m^3

N_{Re} = Reynolds number
N_{vg} = gas velocity number
N_{vl} = liquid velocity number
p = pressure, psi, Pa
$\overline{p}$ = average reservoir pressure, psi, Pa
p_{bd} = breakdown pressure, psi, Pa
p_D = dimensionless pressure
p_f = fracturing pressure, psi, Pa
p_i = initial reservoir pressure, psi, Pa
p_s = pressure due to skin, psi, Pa
p_{tf} = flowing wellhead pressure, psi, Pa
p_{ti} = wellhead injection pressure, psi, Pa
p_{tr} = fracture treatment pressure, psi, Pa
p_{wf} = flowing bottomhole pressure, psi, Pa
q = production rate, STB/d, m^3/sec
q_g = gas production rate, MSCF/d, m^3/sec
q_i = injection rate, STB/d, m^3/sec (bpm in Chap. 16)
q_o = oil production rate, STB/d, m^3/sec
r = radial distance, ft, m
r_A = area specific reaction rate, moles/sec-m^2
r_e = drainage radius, ft, m
r_{eH} = horizontal drainage radius, ft, m
r_{eV} = vertical drainage radius, ft, m
r_s = radius of damage zone, ft, m
r_w = well radius, ft, m
r'_w = effective wellbore radius, ft, m
R = universal gas constant, 10.73 psi ft^3/lb-mole-°R
R_s = solution gas–oil ratio, SCF/STB, m^3/m^3
R_A = rate of appearance of species A, moles/sec
s = skin effect, dimensionless
$s_{c+\theta}$ = skin effect for partial completion and slant
s_{ch} = choke skin effect
s'_{eq} = horizontal well equivalent + skin effect
s_g = gravel pack skin factor
s_p = perforation skin effect
S_b = surface area of mineral B, ft^2, m^2 (Chap. 13)
S_g = gas saturation, fraction
S_o = oil saturation, fraction
S_w = water saturation, fraction
S_{wc} = connate water saturation, fraction
t = time, hr, sec
t_p = producing time, hr, sec
T = temperature, °F, °C
u = velocity, ft/sec, m/sec

u_s = slip velocity, ft/sec, m/sec
U = overall heat transfer coefficient, BTU/hr-ft^2-°F, J/sec-m^2-°C
V = volume, ft^3, m^3
V_b = bulk volume, ft^3, m^3
V_{HC} = hydrocarbon pore volume, ft^3, m^3
V_i = injected volume, gal, m^3 (Chap. 16)
V_p = pore volume, ft^3, m^3
w = fracture width, ft, m
w_p = propped fracture width, ft, m
W = weight, lb, kg
x_f = fracture half-length, m, ft
X = acid volumetric dissolving power, ft^3/ft^3, m^3/m^3
y = mole fraction
y_α = void holdup fraction
y_β = holdup, dimensionless
z = elevation, ft, m
z_w = elevation of perforation midpoint, ft, m
Z = gas compressibility (gas deviation factor), dimensionless

α = order of reaction (Chap. 13)
α = Biot's constant, dimensionless (Chap. 16)
β = acid dissolving power, lb/lb, kg/kg
γ_g = gas gravity, fraction (to that of air)
γ_l = liquid specific gravity, dimensionless
γ_o = oil gravity, °API
γ_w = water specific gravity, dimensionless
Δ = as a prefix for difference
ϵ = pipe roughness, dimensionless
η = efficiency, dimensionless
θ = angle of well deviation
λ = thermal conductivity, BTU/hr-ft-°F, J/sec-m-°C
$\lambda_{\alpha,\beta}$ = input volume fractions
μ = viscosity, cp, Pa-sec
ν = Poisson ratio, dimensionless
ρ = density, lb/ft^3, kg/m^3
σ = surface tension, psi, Pa
σ = stress, psi, Pa (Chap. 16)
σ' = effective stress, psi, Pa
ϕ = porosity, fraction

Subscripts

b = bubble point
D = dimensionless

g = gas
i = initial
l = liquid
o = oil
pc = pseudo-critical
pr = pseudo-reduced
sc = standard conditions
w = water

Index

N

O

P

R

S